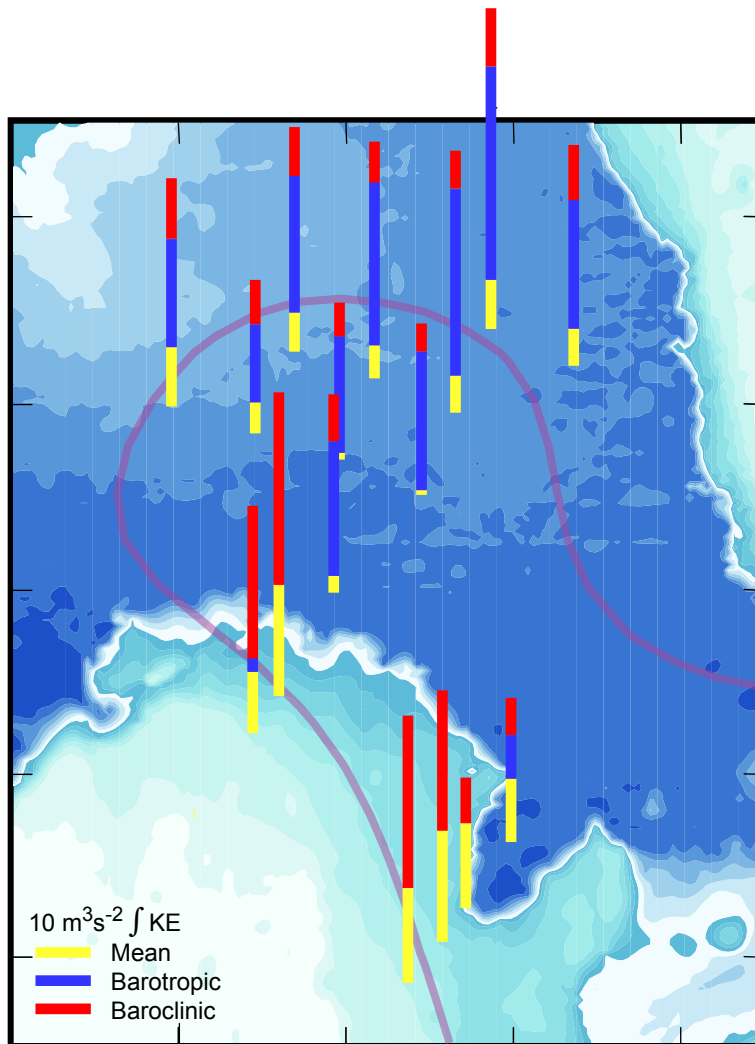




Observations and Dynamics of the Loop Current



Observations and Dynamics of the Loop Current

Authors

Peter Hamilton
Kathleen Donohue
Cody Hall
Robert Leben
Hui Quian
Julio Sheinbaum
Randolph Watts

Prepared under BOEM Contract
M08PC20043

by

Leidos, Inc.

615 Oberlin Road, Suite 100
Raleigh, North Carolina 27605

Published by

**U.S. Department of the Interior
Bureau of Ocean Energy Management
Gulf of Mexico OCS Region**

**New Orleans, LA
February 2015**

DISCLAIMER

Study concept, oversight, and funding were provided by the US Department of the Interior, Bureau of Ocean Energy Management, Environmental Studies Program, Washington, DC, under Contract Number M08PC20043. This report has been technically reviewed by BOEM and it has been approved for publication. The views and conclusions contained in this document are those of the authors and should not be interpreted as representing the opinions or policies of the US Government, nor does mention of trade names or commercial products constitute endorsement or recommendation for use.

REPORT AVAILABILITY

To download a PDF file of this Gulf of Mexico OCS Region report, go to the US Department of the Interior, Bureau of Ocean Energy Management, [Environmental Studies Program Information System](#) website and search on OCS Study BOEM 2015-006.

The report may also be obtained from the BOEM Gulf of Mexico Regional OCS Office.

US Department of the Interior, Bureau of Ocean Energy Management
Gulf of Mexico OCS Region, Public Information Office (MS GM 355A)
1201 Elmwood Park Boulevard
New Orleans, LA 70123-2394
Phone: (504) 736-2519, 1-800-200-GULF, Fax: (504) 736-2620

CITATION

Hamilton, P., K. Donohue, C. Hall, R. R. Leben, H. Quian, J. Sheinbaum, and D. R. Watts. 2014. Observations and dynamics of the Loop Current. US Dept. of the Interior, Bureau of Ocean Energy Management, Gulf of Mexico OCS Region, New Orleans, LA. OCS Study BOEM 2015-006. 417 pp.

ABOUT THE COVER

The cover figure shows the topography of the study region (contours every 250 m with the addition of 100 m; greenish shades down to 2000 m, blue shades from 2000 m to 3500 m). The vertical bars, which extend above the frame, represent depth integrated (whole water column) kinetic energy (KE) at each mooring in the US and Mexican arrays. The depth-integrated KE is proportioned between that due to mean flow (yellow), barotropic or depth-independent velocity fluctuations (blue), and baroclinic or surface intensified (mostly from the surface to about 900 m) velocity fluctuations (red). The period for the calculations is June 2009 to June 2011. The purple line denotes the mean edge of the Loop Current as defined by the 17-cm sea-surface-height contour for the study period. The figure shows the dominance of the depth-independent, whole water column velocity fluctuations that are generated after the Loop Current leaves the continental slope that borders the Campeche Bank.

ACKNOWLEDGEMENTS

The enthusiastic and timely support of Dr. Alexis Lugo-Fernández, the BOEM Contract Officer's Technical Representative, is gratefully acknowledged. The suggestions and support from the Science Review Group (Dr. John Bane, Dr. Eric Chassignet, Dr. Allan Clarke, Dr. William Johns and Dr. Susan Lozier) were positive, constructive and greatly appreciated. Dr. Lie-Yauw (Leo) Oey and his colleagues at Princeton University are thanked for their numerical modeling and data analysis contributions to the contract that resulted in a number of important publications on Loop Current dynamics. Leidos program personnel, Paul Blankinship (Data Management) and James Singer (Field Operations and Logistics Manager), were crucial to data processing and the excellent data return from field activities. These two also played key roles in the deployment, rotation and recovery cruises as cruise leaders, and were involved in instrument servicing and deck operations. Special thanks are also expressed to Craig Boyd, Scott Sharpe (Specialty Devices, Inc.), John Evans (Leidos) and John Morris for their "can do" attitude handling mooring recovery and deployment operations, as well as their involvement in servicing instruments. Mr. Erran Sousa (URI), with the able assistance of Gary Savoie and Stuart Bishop, was responsible for and successfully conducted all aspects of PIES instrument servicing and related field operations. Many others were important to the program success, including a number of students and technicians and the captains and crews of the R/V *Pelican* and the R/V *WeatherBird II*. Finally, special thanks are expressed to Chuck Guidry at LUMCON for his valuable logistical support over the 2.5-year field effort.

Contents

LIST OF FIGURES.....	V
LIST OF TABLES	XVII
ABBREVIATIONS AND ACRONYMS.....	XXI
CHAPTER 1: INTRODUCTION	1
1.1 BACKGROUND	1
1.2 GENERAL PROGRAM DESCRIPTION	4
1.3 STUDY PARTICIPANTS	6
1.4 LOOP CURRENT EDDY SHEDDING	7
1.5 MAJOR EVENTS.....	10
<i>Eddy Separations</i>	10
<i>Deepwater Horizon Oil Spill</i>	10
<i>Hurricanes</i>	12
1.6 REPORT ORGANIZATION	12
CHAPTER 2: EXPERIMENTAL DESIGN AND METHODOLOGY	13
2.1 MOORED ARRAYS.....	13
2.1.1 <i>Array Design</i>	13
2.2 EQUIPMENT AND INSTRUMENTS	13
2.2.1 <i>Introduction</i>	13
2.2.2 <i>Moored and PIES Instruments</i>	14
2.2.3 <i>Instrumentation</i>	14
2.2.4 <i>Instrument Calibration, Performance and Data Return</i>	19
2.3 CTD DATA	29
2.3.1 <i>CTD Data Acquisition Systems</i>	29
2.4 CICESE MOORING DATA	31
2.4.1 <i>Introduction</i>	31
2.4.2 <i>Instrumentation</i>	31
2.5 PIES	34
2.5.1 <i>Gravest Empirical Mode Method</i>	34
2.5.2 <i>Conversion of Measured τ to $\tau(150-1000) = \tau_{index}$</i>	43
2.5.3 <i>Upper-Ocean Maps</i>	49
2.5.4 <i>Bottom Pressure</i>	49
2.5.5 <i>Reference-Level Maps</i>	51
2.5.6 <i>Total Maps</i>	51
2.5.7 <i>Mooring Comparisons</i>	55
2.6 REMOTE SENSING.....	67
2.6.1 <i>Satellite Altimetry</i>	67
2.6.2 <i>Satellite Radiometry</i>	78
2.6.3 <i>Ancillary Satellite Altimeter Datasets</i>	79
2.7 PIES AND ALTIMETRY EVALUATION AND COMPARISON	79
2.7.1 <i>Altimetric Sampling and Aliasing</i>	80
2.7.2 <i>Signal-to-Noise</i>	88
2.7.3 <i>Sea-Surface-Height Time Scales</i>	89
2.7.4 <i>Comparison of CCAR Mesoscale, AVISO, and PIES Mapped Absolute SSH</i>	93

2.8 NUMERICAL MODEL	98
2.8.1 Model Skill Metrics for In-Situ Measurements	101
2.9 METHODS	101
2.9.1 Vertical Velocities	101
2.9.2 Relative Vorticity	104
2.9.3 Potential Vorticity.....	104
2.9.4 Streamlines and Velocity Potentials	107
2.9.5 Wavelet Analysis	109
2.9.6 Complex Demodulation	109
2.9.7 Notes on EOF Analysis	109
CHAPTER 3: BASIC DESCRIPTIONS AND STATISTICS	111
3.1 INTRODUCTION	111
3.2 EDDY FORMATION AND SEPARATION	117
3.2.1 Ekman.....	117
3.2.2 Franklin.....	119
3.2.3 Hadal.....	126
3.3 NUMERICAL MODELING OF HADAL’S SEPARATION	132
3.3.1 Introduction.....	132
3.3.2 Model Forecast Skill.....	133
3.4 STATISTICS	139
3.4.1 Mean Flows	139
3.4.2 Depth Variability of Velocities	142
3.4.3 Horizontal Variability in the Upper Layer	147
3.4.4 Horizontal Variability in the Lower Layer	166
CHAPTER 4: DYNAMICS.....	185
4.1 INTRODUCTION	185
4.2 RELATIVE VORTICITY, UPWELLING AND LC EDDY SEPARATIONS	185
4.3 LOOP CURRENT FRONTAL VARIABILITY	187
4.4 RELATIVE VORTICITY	193
4.5 BAROCLINIC INSTABILITY ANALYSIS	204
4.5.1 Eddy Potential Energy	222
4.6 TOPOGRAPHIC ROSSBY WAVES.....	232
4.7 NUMERICAL MODELING	235
CHAPTER 5: LONG TERM AND SEASONAL VARIABILITY	241
5.1 INTRODUCTION	241
5.2 RE-ANALYSIS OF THE “PRE-ALTIMETRIC” LOOP CURRENT RECORD	244
5.3 COMPARISONS OF PREVIOUSLY PUBLISHED SEPARATION DATES WITH THE RE-ANALYSIS	256
5.4 THE ALTIMETRIC LOOP CURRENT RECORD	260
5.5 STATISTICAL ANALYSIS OF LOOP CURRENT SEASONALITY	277
General Conclusions	294
5.6 INVESTIGATION OF DYNAMICS CONTRIBUTING TO LOOP CURRENT SEASONALITY	294
Deepwater EOF Analysis.....	295
Coastal EOF Analysis	316
Conclusions.....	325
CHAPTER 6: INERTIAL OSCILLATIONS	327
6.1 INTRODUCTION	327

6.2 DATA AND METHODS.....	328
6.3 DESCRIPTION OF INERTIAL RESPONSE TO HURRICANE IDA.....	332
6.4 DISCUSSION	338
6.4.1 <i>The Effect of Relative Vorticity on the Distribution of Inertial Oscillations</i>	338
6.4.2 <i>The Effect of the Loop Current on the Distribution of Inertial Oscillations</i>	338
6.5 LONG-TERM VARIABILITY OF INERTIAL OSCILLATIONS	340
6.6 SUMMARY AND CONCLUSIONS	344
CHAPTER 7: SUMMARY DISCUSSION AND RECOMMENDATIONS	351
7.1 INTRODUCTION	351
7.2 LC EDDY SHEDDING EVENTS.....	352
<i>Ekman</i>	353
<i>Franklin</i>	353
<i>Hadal</i>	353
7.3 STATISTICS AND DYNAMICS	354
7.4 LC EDDY SEPARATION DYNAMICS.....	356
7.5 LONG-TERM AND SEASONAL VARIABILITY	358
7.6 RECOMMENDATIONS	359
7.7 DEEPWATER HORIZON OIL SPILL	363
CHAPTER 8: REFERENCES	365
APPENDIX: BAROTROPIC TIDES.....	385

LIST OF FIGURES

Figure 1.1-1.	A high resolution SST image (left panel) and SSH altimeter map (right panel) showing an extended LC and a partially detached LC eddy (Hadal) on 21 April 2011.....	2
Figure 1.2-1.	Locations of moorings and PIES deployed in the U.S. and Mexican sectors in the eastern Gulf of Mexico during the study of Loop Current dynamics.....	5
Figure 1.2-2.	Schedule and relationships of data types collected and used during this study.	6
Figure 1.5-1.	Time series of LC area (green) and LC+eddy area (blue) as delineated by the 17-cm SSH contour from the altimeter maps.	11
Figure 2.2-1.	Schematic of tall mooring.	18
Figure 2.2-2a.	Timeline of data return for instruments on tall moorings A1 and A2.	23
Figure 2.2-2b.	Timeline of data return for instruments on tall moorings A3 and A4.	24
Figure 2.2-2c.	Timeline of data return for instruments on tall moorings B1 and B2.	25
Figure 2.2-2d.	Timeline of data return for instruments on tall moorings B3 and C1.	26
Figure 2.2-2e.	Time lines of data return for tall mooring C2 and short moorings D1, D2, D3, D4, D5, D7, and D8.	27
Figure 2.4-1a.	Time lines of data return from CICESE moorings N3, N4, E1, E2, E3, E4, and E5.	32
Figure 2.4-1b.	Time lines of data return from CICESE moorings N1, N2, Y1, Y2, Y3, Y4, YN, Y5, Y6, and Y7.	33
Figure 2.5-1.	Time series of tau anomaly in seconds in panels arranged according to approximate geographic location.	35
Figure 2.5-2.	Time series of bottom pressure anomaly in dbar arranged according to approximate geographic location.	36
Figure 2.5-3.	Several views of the current and temperature structure in the region for 5 May 2009 provided by the PIES and current meter measurements.	37
Figure 2.5-4.	Spatial and temporal distribution of hydrocasts used to construct the Gravest Empirical Mode.	39
Figure 2.5-5.	Temperature profiles interpolated every 10 dbar and sorted by $\tau(150-1000) = \tau_{\text{index}}$	40
Figure 2.5-6.	Scatter plots of temperature versus $\tau_{\text{index}} = \tau(150 - 1000)$ for six representative pressure levels.	41
Figure 2.5-7.	Contour plot of the cubic smoothing spline fits for the temperature GEM field.	42
Figure 2.5-8.	Scatter plots of temperature versus $\tau(150-1000)$ for surface (left) and 50 dbar (right) with the cubic spline fit shown as a solid dark line.	44

Figure 2.5-9.	Seasonal temperature correction/amplitude contoured as a function of yearday and pressure.	45
Figure 2.5-10.	Upper panel: Scatter plots of surface geopotential anomaly referenced to 150 dbar with the cubic spline fit shown as a solid dark line.	46
Figure 2.5-11.	Time series of $\tau(150-1000)$ in seconds, with panels arranged according to approximate geographic location.	47
Figure 2.5-12.	Scatter plots of $\tau(0-150)$ versus $\tau(150-1000)$	48
Figure 2.5-13.	Correlation coefficient between pairs of PIES $\tau(150-1000)$ records.	50
Figure 2.5-14.	All the individual pressure records (thin black) and their array-average (red), called the common mode.	52
Figure 2.5-15.	Time series of bottom pressure anomaly (dbar) with the common mode removed.	53
Figure 2.5-16.	Correlations between pairs of pressure records.	54
Figure 2.5-17.	Comparison between the A4 mooring (red) and PIES-derived (blue) temperature.	56
Figure 2.5-18.	Summary of the temperature comparisons.	57
Figure 2.5-19.	Observed rms and predicted differences between measured and PIES-estimated temperature.	58
Figure 2.5-20a.	Comparison between the A4 mooring (red) and PIES-derived (blue) zonal and meridional velocities at 200 and 400 dbar.	60
Figure 2.5-20b.	Comparison between the A4 mooring (red) and PIES-derived (blue) zonal and meridional velocities at 600 and 900 dbar.	61
Figure 2.5-20c.	Comparison between the A4 mooring (red) and PIES-derived (blue) zonal and meridional velocities at 1300 and 2000 dbar.	62
Figure 2.5-21.	Summary of the zonal velocity comparisons.	63
Figure 2.5-22.	Summary of the meridional velocity comparisons.	64
Figure 2.5-23.	Rms and predicted differences between measured and PIES-estimated zonal (left) and meridional (right) velocities.	65
Figure 2.5-24.	PIES-estimated total SSH anomaly (red) and Jason SSH anomaly (blue) for the seven PIES sites along groundtracks.	66
Figure 2.5-25.	Rms differences between altimeter SSH anomaly and PIES-estimated total SSH anomaly as a function of γ	68
Figure 2.5-26.	Multiplicative factor, γ , applied to the reference SSH (velocity).	69
Figure 2.6-1.	Satellite altimeter exact repeat groundtrack coverage in study region.	70
Figure 2.6-2.	Plot showing daily “actual”, “available”, “windowed”, and “used” data from operational altimeter satellites during the study program.	76

Figure 2.7-1.	Maps of PIES barotropic unaliased variance for 10-day, 17-day, and 35-day sampling.	82
Figure 2.7-2.	Maps of PIES baroclinic unaliased variance for 10-day, 17-day, and 35-day sampling.	83
Figure 2.7-3.	Maps of PIES SSH unaliased variance for 10-day, 17-day, and 35-day sampling.	84
Figure 2.7-4.	Maps of PIES SSH signal-to-noise ratio (SNR) for 10-day, 17-day, and 35-day sampling.	90
Figure 2.7-5.	Spatial maps of the half-power period, $T_{0.5}$, computed from the PIES barotropic, baroclinic, and combined SSH anomaly time series.	92
Figure 2.7-6.	Spatial map of the temporal correlation between the PIES mapped SSH time series and the CCAR Mesoscale SSH and AVISO SSH time series coincident with the LC study.	94
Figure 2.7-7.	Spatial map of the temporal correlation between the PIES mapped SSH time series and the AVISO SSH time series with and without the seasonal steric signal removed.	95
Figure 2.7-8.	Rms SSHA (standard deviation about the mean) during the program time period of the CCAR Mesoscale, AVISO, and PIES mapped datasets.	96
Figure 2.7-9.	Regression of the daily means of the PIES mapped SSH on to the means of the CCAR Mesoscale and AVISO mapped SSH in the study region.	97
Figure 2.7-10.	CCAR Mesoscale and AVISO mean SSH maps over the program time period with the PIES mean SSH as an inset.	99
Figure 2.7-11.	Comparison of the CCAR Mesoscale and AVISO mean SSH maps over the program time period.	100
Figure 2.9-1.	Average temperature, salinity and sigma-t profiles for CTD casts taken during the LC study.	103
Figure 2.9-2.	Mapping array and CICESE transects showing the locations of relative vorticity points and their surrounding triangles and rectangles.	105
Figure 2.9-3.	Comparison of relative vorticity at two depths for location 82 using the triangle E2-E3-EN and the E2-E3 pair to estimate velocity gradients.	106
Figure 2.9-4.	Geostrophic velocities from mapped geopotential, and observed 2-day averaged 40-HLP currents at 160 m.	108
Figure 3.1-1a.	40-HLP temperature and velocity records from the A2 mooring at the indicated depths.	112
Figure 3.1-1b.	40-HLP temperature and velocity records from the C2 mooring at the indicated depths.	113
Figure 3.1-2a.	Surface-layer (~ 100 m) currents on the N2 to C1 transect where up is normal to the transect.	115

Figure 3.1-2b.	Lower-layer currents at ~1300 and ~2000 m on the N2 to C1 transect where up is normal to the transect.....	116
Figure 3.2-1.	The growth and detachments of Ekman using the SSH 17-cm contour from altimeter maps at 15-day intervals.....	118
Figure 3.2-2.	Maps of the separation of Ekman for the indicated dates.	120
Figure 3.2-3.	Loop Current 17-cm frontal boundaries from SSH altimeter maps for Franklin for the indicated dates.	121
Figure 3.2-4.	Mean surface velocities and standard deviation ellipses from drifter tracks (gray lines) for May and June 2010.....	123
Figure 3.2-5.	The first detachment of Franklin showing the depth of the 6 °C isotherm and 80 to 100-m velocity vectors from the moorings.	124
Figure 3.2-6.	Franklin detachment 1: Upper and lower-layer circulation for indicated dates.	125
Figure 3.2-7.	Five-day average velocity components for transect E moorings.....	127
Figure 3.2-8.	Loop Current 17-cm frontal boundaries from SSH altimeter maps for Hadal for the indicated dates.....	128
Figure 3.2-9.	Maps of the separation of Hadal for the indicated dates in 2011 showing upper and lower-layer circulations.	130
Figure 3.2-10.	Surface Chlorophyll-A from Modis Aqua overlaid with SSH from altimeter maps for 12 August 2011.	131
Figure 3.3-1.	Daily averaged SSH and surface currents for every 10 days of the forecast simulation, starting from 1 July 2011.....	134
Figure 3.3-2.	Comparison between AVISO and forecast SSHA.	135
Figure 3.3-3.	Full-depth ADCP mooring (A1-A4, B1-B3 and C1-C2) locations from the US array superimposed on the July mean model forecast SSH.	137
Figure 3.3-4.	Vertical profiles of complex correlation R_s and Q_s , ratio of model-to-observed standard deviations, skill, ratio of model-to-observed mean speeds, and angle of modeled observed mean velocity.....	138
Figure 3.4-1.	Mean 40-HLP currents for all moorings overlaid with mean SSH and mean depths of the 6 °C isotherm.	140
Figure 3.4-2.	Mean near-bottom 40-HLP currents and standard deviation ellipses for the indicated interval.	141
Figure 3.4-3.	Depth range weighted CEOF modes for mooring A3.	143
Figure 3.4-4.	CEOF modes for the 2-year common interval.	145
Figure 3.4-5.	Normalized mode amplitudes for CEOFs by mooring for the 2-year interval.	146
Figure 3.4-6.	EKE spectra in variance preserving form of selected normalized mode amplitudes.....	148

Figure 3.4-7.	Cummulative depth-integrated KE for mean flow, and the QB and SI CEOF modes.....	149
Figure 3.4-8.	200-m depth mapped and measured mean current vectors (bold) and standard deviation ellipses superimposed on the time-mean 200-m depth eddy kinetic energy.....	151
Figure 3.4-9.	Standard deviation of baroclinic sea-surface height referenced to the bottom as a function of frequency band.....	152
Figure 3.4-10.	Loop Current area, and array mean baroclinic sea-surface height referenced to the bottom.....	154
Figure 3.4-11.	CCAR SSH determined Loop Current positions during CEOF time periods. .	155
Figure 3.4-12.	CEOFs determined from band-passed baroclinic sea-surface height referenced to the bottom, during the Ekman time period.....	156
Figure 3.4-13.	CEOFs determined from band-passed baroclinic sea-surface height referenced to the bottom during the Franklin time period.....	159
Figure 3.4-14.	CEOFs determined from band-passed baroclinic sea-surface height referenced to the bottom during the Hadal time period.....	161
Figure 3.4-15.	CEOFs determined from band-passed baroclinic sea-surface height referenced to the bottom during the Icarus time period.....	163
Figure 3.4-16.	Wavenumber versus phase speed.....	165
Figure 3.4-17.	Near-bottom mapped and directly-measured mean currents with standard-deviation ellipses superimposed on the time-mean near-bottom eddy kinetic energy.....	167
Figure 3.4-18.	Standard deviation of reference sea-surface height as a function of frequency band.....	169
Figure 3.4-19.	Loop Current area with array-mean baroclinic sea-surface height referenced to the bottom and CCAR sea-surface height.....	170
Figure 3.4-20.	CCAR SSH-determined Loop Current positions during Ekman_deep CEOF time period.....	171
Figure 3.4-21.	CCAR SSH-determined Loop Current positions during Franklin_deep CEOF time period.....	172
Figure 3.4-22.	CCAR SSH-determined Loop Current positions during Hadal_deep CEOF time period.....	173
Figure 3.4-23.	CEOFs determined from band-passed deep reference sea-surface height during the Ekman_deep time period.....	174
Figure 3.4-24.	CEOFs determined from band-passed deep reference sea-surface height during the Franklin_deep time period.....	175
Figure 3.4-25.	CEOFs determined from band-passed deep reference sea-surface height during the Hadal_deep time period.....	176

Figure 3.4-26.	Snapshots of 100 to 40 day band-passed deep reference sea-surface height for a portion of the Franklin_deep time interval.	178
Figure 3.4-27.	Snapshots of 40 to 25 day band-passed deep reference sea-surface height for a portion of the Franklin_deep time interval.	179
Figure 3.4-28.	Snapshots of 100 to 40 day band-passed deep reference sea-surface height for a portion of the Hadal_deep time interval.	181
Figure 3.4-29.	Snapshots of 40 to 25 day band-passed deep reference sea-surface height for a portion of the Hadal_deep time interval.	182
Figure 3.4-30.	Snapshots of 25 to 16 day band-passed deep reference sea-surface height for a portion of the Hadal_deep time interval.	183
Figure 4.2-1.	Array averaged relative vorticity anomaly, eddy kinetic energy at 200 m and 100 mab, with area averaged 7-DLP vertical velocities at 900 m.	186
Figure 4.2-2.	A schematic illustration of the three stages of the LC cycle.	188
Figure 4.3-1.	Depth of the 6 °C isotherm along the N3-C1 transect.	190
Figure 4.3-2.	Velocity components, directed 310°T, at 120 m for moorings along the N1-C1 transect.	191
Figure 4.3-3.	Along-front velocity vectors for the E and N1-C1 transects for the west and east sides, respectively.	192
Figure 4.3-4.	EKE spectra of the along-front interpolated velocities on the N2-C1 and E transects.	194
Figure 4.4-1.	Mean along-front velocities and relative vorticity for the indicated interval and sections across the Campeche slope during the LC formation of Hadal. ...	195
Figure 4.4-2.	Time series of relative vorticity for locations 78, and 82 as a function of depth.	197
Figure 4.4-3.	Time series of relative vorticity for location 56 as a function of depth.	198
Figure 4.4-4.	Frequency domain EOFs of vertical profiles of relative vorticity at locations 56 and 67.	199
Figure 4.4-5.	Time series of relative vorticity for location 67 as a function of depth.	200
Figure 4.4-6.	Normalized wavelet power for relative vorticity at 160 m at locations 82 and 78 using the Morlet wavelet.	202
Figure 4.4-7.	Cross-wavelet normalized power between 166 and 2000 m at locations 56 and 67.	203
Figure 4.5-1.	Near-bottom mapped and directly measured mean currents with standard deviation ellipses superimposed on the time-mean near-bottom eddy kinetic energy.	205
Figure 4.5-2.	Schematic representation of the characteristic phase offset between upper and lower-layer cyclonic or anticyclonic perturbations that favor baroclinic instability.	206

Figure 4.5-3.	Coherence and phase between upper, SSH_bcb, and lower, SSH_ref, streamfunction for three frequency bands.	208
Figure 4.5-4a.	Loop Current eddy-shedding event Ekman, 4 May through 18 July 2009, shown using maps of baroclinic SSH referenced to the bottom embedded within altimetric SSH.	209
Figure 4.5-4b.	Loop Current eddy-shedding event Ekman, 4 May through 18 July 2009, shown using maps of 100-40 day band-passed baroclinic SSH referenced to the bottom embedded within altimetric SSH.....	210
Figure 4.5-4c.	Loop Current eddy-shedding event Ekman, 23 July through 16 September 2009 (Full frequency band).	211
Figure 4.5-4d.	Loop Current eddy-shedding event Ekman, 23 July through 16 September 2009 (100-40 day frequency band).....	212
Figure 4.5-5a.	Loop Current eddy-shedding event Franklin, 11 April through 25 June 2010, shown using maps of baroclinic SSH referenced to the bottom (SSH_bcb) embedded within altimetric SSH.	213
Figure 4.5-5b.	Loop Current eddy-shedding event Franklin, 11 April through 25 June 2010, shown using maps of 100-40 day band-passed baroclinic SSH referenced to the bottom embedded within altimetric SSH.....	214
Figure 4.5-5c.	Loop Current eddy-shedding event Franklin, 30 June through 13 September 2010 (Full frequency band).	215
Figure 4.5-5d.	Loop Current eddy-shedding event Franklin, 30 June through 13 September 2010 (100-40 day frequency band).....	216
Figure 4.5-6a.	Loop Current eddy-shedding event Hadal, 9 March through 23 May 2011, shown using maps of baroclinic SSH referenced to the bottom embedded within altimetric SSH.	218
Figure 4.5-6b.	Loop Current eddy-shedding event Hadal, 9 March through 23 May 2011, shown using maps of 100-40 day band-passed baroclinic SSH referenced to the bottom embedded within altimetric SSH.....	219
Figure 4.5-6c.	Loop Current eddy-shedding event Hadal, 28 May through 11 August 2011 (Full frequency band).	220
Figure 4.5-6d.	Loop Current eddy-shedding event Hadal, 28 May through 11 August 2011 (100-40 day.....	221
Figure 4.5-7.	A linear relationship (black line) exists between mean ψ_{bcb} and mean T at 400 m (grey dots).....	224
Figure 4.5-8.	Eddy heat flux vectors at 400-m depth for the three LC eddy-shedding events superimposed on the 400-m depth temperature variance.....	225
Figure 4.5-9.	Four terms in the steady eddy potential-energy budget determined for the Ekman event, 3 May through 31 August 2009 at 400-m depth.....	228

Figure 4.5-10.	BC and PKC at 400-m depth determined for the Ekman event.	229
Figure 4.5-11.	Four terms in the steady eddy potential-energy budget determined for the Franklin event, 15 February through 14 September 2010 at 400-m depth.....	230
Figure 4.5-12.	BC and PKC at 400-m depth determined for the Franklin event.	231
Figure 4.5-13.	Four terms in the steady eddy potential-energy budget determined for the Hadal event, 1 March through 14 September 2011, at 400-m depth.....	233
Figure 4.5-14.	BC and PKC at 400-m depth determined for the Hadal event.	234
Figure 4.6-1.	Wavenumbers from 100 to 20-day EOFs for the 100-mab currents for Franklin where the propagation is compatible with TRWs.....	236
Figure 4.7-1.	Schematic illustrations of the dominant flow anomalies in the northwestern Caribbean Sea for the indicated months based on monthly composites derived from EOF analysis of model SSH.	239
Figure 5.2-1.	Examples of the “best” LC images from CZCS ocean color and AVHRR SST in the time period before EddyWatch analyses from Horizon Marine, Inc. became available in 1984.	246
Figure 5.2-2.	Sample HMI EddyWatch map from week of 10-17 January 1986 showing frontal analysis of “Fast Eddy”, “Hot Core Eddy”, and the Loop Current.	247
Figure 5.2-3.	LC eddy 1978 as observed by Seasat approximately two weeks after eddy separation.....	249
Figure 5.2-4.	LC eddy separation events with LC retreat latitude following separation shown by dashed black lines (February 1980 through August 1982).	251
Figure 5.2-5.	LC eddy separation events with LC retreat latitude following separation shown by dashed black lines (March 1983 through January 1986).	252
Figure 5.2-6.	LC eddy separation events with LC retreat latitude following separation shown by dashed black lines (Sept. 1986 through Nov. 1991).	253
Figure 5.2-7.	LC eddy 1992 “Unchained” as observed by ERS-1 on the date of separation, 10 August 1992.....	254
Figure 5.4-1.	Satellite usage in the CCAR gridded altimeter dataset during the time period from 1993 through 2012.	261
Figure 5.4-2.	Monthly histograms of separation and detachment dates determined from the CCAR, AVISO, and AVISO-CUPOM SSH datasets.	267
Figure 5.4-3.	Daily LC area, volume, anticyclonic circulation, westernmost longitude, and northernmost latitude time series and corresponding histograms.	268
Figure 5.4-4.	Monthly mean plots of LC area, area including detachments, northernmost latitude, volume, anticyclonic circulation, and westernmost longitude statistics.	269
Figure 5.5-1.	LC eddy separation dates binned monthly from reanalysis and Vukovich (2012) pre-altimetry (1978-1992).....	279

Figure 5.5-2.	Monthly-binned histograms of pre-altimetry, altimetry, and combined LC eddy separation date datasets.....	281
Figure 5.5-3.	LC eddy separation dates binned monthly from CCAR, AVISO, and AVISO-CUPOM altimetry (1993-2012).....	282
Figure 5.5-4.	LC eddy separation dates binned monthly from combined pre-altimetry reanalysis (1978-1992) and CCAR, AVISO, and AVISO-CUPOM altimetry (1993-2012).....	286
Figure 5.5-5.	LC eddy separation dates binned monthly (1978-2012) from combined Vukovich (2012) pre-altimetry (1978-1992) and CCAR, AVISO, and AVISO-CUPOM altimetry (1993-2012).....	287
Figure 5.5-6.	Pre-altimetry reanalysis LC eddy separation dates from 1978-1992 plotted as days-of-year on the unit circle in the complex plane, divided into two seasons.....	289
Figure 5.5-7.	LC eddy separation dates from CCAR, AVISO, and AVISO-CUPOM altimetry (1993-2012) plotted as days-of-year on the unit circle in the complex plane, and divided into two seasons.....	290
Figure 5.5-8.	LC eddy separation dates (1978-2012) combining the reanalysis pre-altimetry with CCAR, AVISO, and AVISO-CUPOM altimetry dates plotted as days-of-year on the unit circle in the complex plane, and divided into two seasons.....	291
Figure 5.6-1.	Deepwater EOF mode 1, and EOF mode 2 loading vectors, derived from monthly AVISO SSH with the steric signal removed.....	296
Figure 5.6-2.	Deepwater EOF mode 3, and EOF mode 4 loading vectors, derived from monthly AVISO SSH with the steric signal removed.....	298
Figure 5.6-3.	Deepwater principal component time series PCTS 1 and PCTS 2, and PCTS 3 and PCTS 4, derived from monthly AVISO SSH with the steric signal removed.....	299
Figure 5.6-4.	CACs generated from deepwater EOF mode PCTS 1 and PCTS 2, and PCTS 3 and PCTS 4.....	301
Figure 5.6-5.	Sum variance of monthly AVISO maps, and fraction of total variance captured by first four deepwater EOF modes including correlated signals at depths less than 200 m.....	302
Figure 5.6-6.	CAC of Loop Current northern boundary latitude.....	303
Figure 5.6-7.	CAC of Loop Current area.....	304
Figure 5.6-8.	CAC_raw deepwater EOF mode 1, and EOF mode 2.....	306
Figure 5.6-9.	CAC_raw deepwater EOF mode 3, and EOF mode 4.....	308
Figure 5.6-10.	CAC_raw deepwater PCTS for EOF mode 1 and EOF mode 2, and EOF mode 3 and EOF mode 4.....	309
Figure 5.6-11.	CAC1234 deepwater EOF mode 1, and EOF mode 2.....	310

Figure 5.6-12.	CAC1234 deepwater EOF mode 3, and EOF mode 4.....	311
Figure 5.6-13.	CAC of Loop Current northern boundary latitude.	312
Figure 5.6-14.	CAC of Loop Current area.	313
Figure 5.6-15.	Coastal EOF mode 1 loading vector derived with monthly AVISO data from 1993 through 2012 with CAC removed, low-pass-filtered, and detrended and unfiltered.....	318
Figure 5.6-16.	Interannual EOF mode 1 from monthly tide gauge SSH data for June 1993 through October 2001 compared to EOF mode 1 derived from coastal AVISO SSH data low-pass filtered with CAC/linear trend removed and unfiltered.....	319
Figure 5.6-17.	Gulf Western Boundary Current ship drift speed anomaly CAC as compared to the northward geostrophic speed anomaly derived from CAC_raw.	320
Figure 5.6-18.	CAC1234 EOF mode 1 loading vector, and CM1 loading vector with 5.07-cm offset applied.	321
Figure 5.6-19.	Sum variance of monthly AVISO maps, and fraction of total variance generated by monthly reconstruction of CM1.....	323
Figure 5.6-20.	CAC of Loop Current northern boundary latitude, and CAC of Loop Current area.	324
Figure 6.1-1.	Locations for the mooring array in the Gulf of Mexico, the NDBC buoy and the track of Hurricane Ida.....	329
Figure 6.2-1.	Six-kilometer Intra-Americas Sea circulation model domain.	330
Figure 6.2-2.	Time series comparison of east and north wind components between hourly 42003 buoy observations and the merged 6-hourly product used to drive the model in late 2009.	331
Figure 6.2-3.	Winds during the passage of Hurricane Ida over the eastern Gulf from merged Hurricane Center and NCEP 10-m data.	333
Figure 6.2-4.	Model simulated Sea-Surface Height in early November 2009. Purple line is the 17-cm SSH contour.	334
Figure 6.3-1.	Time series of high-pass filtered horizontal velocity at various depths from 450-m ADCP measurements at mooring A4 and from model simulations at the same location.	335
Figure 6.3-2.	Time series of high-pass filtered horizontal velocity at various depths from 500-m ADCP measurements at mooring E5.	336
Figure 6.3-3.	Clockwise rotary power spectra for high-pass filtered horizontal velocity at moorings for the upper 500 m.	337
Figure 6.4-1.	Mean normalized relative vorticity plot for 6 November to 6 December 2009 at 200 m for the LC study moorings, and vertical plot of mean normalized relative vorticity at the E-transect moorings for the same period.....	339

Figure 6.4-2.	Time series evolution of zonal momentum budget at moorings A4 and E5 during the Hurricane Ida period.	341
Figure 6.5-1.	Time series of inertial frequency velocity amplitudes from complex demodulation at moorings A4, B2 and C1 for depths of 100 and 300 m, respectively.	342
Figure 6.5-2.	Time series of high-pass filtered horizontal velocity components at various depths from the 450-m ADCP measurements at mooring A4 for two periods, November 2009 and January 2011.	343
Figure 6.5-3.	Time series of atmospheric pressure, atmospheric temperature, and wind vectors for two winter periods for NDBC buoy 42003.	345
Figure 6.5-4.	Time series of high-pass filtered horizontal velocity components at various depths from the 450-m ADCP measurements at mooring B2 for two periods, November 2009 and January 2011.	346
Figure 6.5-5.	Time series of high-pass filtered horizontal velocity components at various depths from the 450-m ADCP measurements at mooring B2 for the 2010-2011 winter.	347
Figure 6.5-6.	Time series of atmospheric pressure, atmospheric temperature, and wind vectors for the 2010-2011 winter periods for NDBC buoy 42003.	348
Figure 7.3-1.	Depth range weighted CEOF modes for LC mooring A3 and Exploratory mooring L4.	355
Figure 7.6-1.	PIES/mooring arrays deployed in the eastern Gulf for this and prior BOEM/MMS programs.	361
Figure 7.6-2.	A possible configuration of PIES and moorings for a LC radiation experiment.	362
Figure A-1.	Amplitude and phase of the O1, K1, Q1, and P1 constituents determined with the tidal response method from the 25 bottom pressure records.	386
Figure A-2.	Amplitude and phase of the M2, K2, N2, and S2 constituents determined with the tidal response method from the 25 bottom pressure records.	387

LIST OF TABLES

Table 2.2-1.	Triangulated Mooring Locations and Depths by Deployment for the Loop Current Study.....	15
Table 2.2-2.	Mooring Deployment Periods for the Loop Current Study.....	16
Table 2.2-3.	PIES Deployment Locations and Periods for the Loop Current Study.....	17
Table 2.2-4a.	Mooring Locations and Moored Instrument Levels for the Loop Current Study (American Sector) with Nominal Instrument Depths (Tall Moorings A1, A2, A3 and A4).....	20
Table 2.2-4b.	Mooring Locations and Moored Instrument Levels for the Loop Current Study (American Sector) with Nominal Instrument Depths (Tall Moorings B1, B2 and B3).....	21
Table 2.2-4c.	Mooring Locations and Moored Instrument Levels for the Loop Current Study (American Sector) with Nominal Instrument Depths (Tall Moorings C1, C2 and Short Moorings D1, D2, D3, D4, D5, D7 and D8).....	22
Table 2.2-5.	Moored Instrument Data Return (by Good Record Count) during the Loop Current Study.....	28
Table 2.3-1.	Listing of CTD Casts made at PIES Sites during the Loop Current Study.....	30
Table 2.4-1.	Mexican Mooring Locations and Deployment Periods during the Loop Current Study.....	31
Table 2.6-1.	Satellite Altimeter Missions Active During the LC Study Program.....	71
Table 2.7-1.	Satellite Altimeter Mission Exact-Repeat Periods and Periods Associated with the Nyquist Sampling Frequency.....	80
Table 2.7-2.	Unaliased Variance Statistics for 10-day, 17-day, and 35-day Exact-Repeat Sampling of the PIES Barotropic, Baroclinic, and Combined SSH Signals.....	85
Table 2.7-3.	PIES SSH, Baroclinic, and Barotropic Statistics and Percent of Unaliased Variance Measured by Satellites in 10-day, 17-day, and 35-day Exact-Repeat Orbits.....	86
Table 2.7-4.	Signal-to-Noise Ratio (SNR) Statistics for 10-day, 17-day, and 35-day Exact-Repeat Sampling of the PIES Barotropic, Baroclinic and Combined SSH Signals.....	89
Table 2.7-5.	Half-Power Period of PIES Barotropic, Baroclinic, and Total SSH Signals.....	91
Table 3.3-1.	A Summary of Various Skill Metrics Computed Using Currents from the Model and ADCP Measurements from Moorings A1 to C2.....	139
Table 3.4-1.	Percent Variance Accounted for by Depth-Range Weighted CEOF Modes (7 June 2009 to 1 May 2011).....	144
Table 3.4-2.	Average Propagation Speeds Determined from the CEOF Analysis.....	166

Table 5.2-1.	Eddy separation events with the corresponding retreat latitudes and separation periods from July 1978 through December 1992.....	245
Table 5.2-2.	Date ranges for LC eddy separation events shown in Figures 5.2-4, 5.2-5 and 5.2-6.....	255
Table 5.3-1.	Comparison of re-analysis LC eddy separation dates with those from Vukovich (2012).....	257
Table 5.4-1.	LC eddy separation event dates with the corresponding retreat latitudes and separation periods from January 1993 through December 2012, derived from CCAR SSH dataset.....	262
Table 5.4-2.	Comparison of LC eddy separation event dates derived from CCAR, AVISO, and AVISO-CUPOM SSH datasets from January 1993 through December 2012.....	263
Table 5.4-3.	Comparison of LC eddy detachment event dates derived from CCAR, AVISO, and AVISO-CUPOM SSH datasets from January 1993 through December 2012. The HMI industry name of the LC eddy separation event following each date is also listed.....	265
Table 5.4-4.	Comparison of altimetry record LC eddy separation dates from AVISO re-analysis (from Table 5.4-2), Chang and Oey (2013b), Vukovich (2012), and Lindo-Atichati et al. (2013).....	271
Table 5.4-5.	LC eddy separation timing of the 19 events where each source – the AVISO re-analysis (from Table 5.4-2), Chang and Oey (2013b), Vukovich (2012), and Lindo-Atichati et al. (2013) – reported a separation event, excluding events #25 and 34.....	272
Table 5.4-6.	Comparison of LC eddy separation events.....	274
Table 5.5-1.	Results of significance testing of various sources of LC eddy separation event dates.....	283
Table 5.5-2.	Centers (means) and standard deviations (std.) of Table 5.2-1 and 5.4-2 separation events analyzed separately and combined, separated into spring and fall seasons and presented circularly and linearly.....	293
Table 5.6-1.	Proportion of LC northern latitude and area variance explained by first four deepwater EOF modes reconstructed as monthly time series and as CACs (CAC1, CAC12, CAC123, and CAC1234) with reference to complete monthly time series and CAC of original AVISO data (CAC_raw).....	305
Table 5.6-2.	Proportion of CAC_Raw and CAC1234 LC northern latitude and area variance explained by CACs of reconstructions of first four deepwater EOF modes of CAC1234.....	314
Table 5.6-3.	Proportion of CAC_Raw and CAC1234 LC northern latitude and area variance explained by the monthly reconstruction of CM1.....	322
Table A-1.	Amplitude in CM and Phase in Degrees for Four Major Tidal Constituents (O1, K1, Q1, P1).....	388

Table A-2.	Amplitude in CM and Phase in Degrees for Four Major Tidal Constituents (M2, K2, N2, S2).....	389
------------	---	-----

ABBREVIATIONS AND ACRONYMS

ADCP:	Acoustic Doppler Current Profiler
APEX:	Autonomous Profiling Explorer
ARGOS:	Advanced Research Global Observation Satellite (nolonger an acronym)
AVHRR:	Advanced Very High Resolution Radiometer
AVISO:	Archiving, Validation and Interpretation of Satellite Oceanography
BC:	Baroclinic Conversion
BCB:	Baroclinic Referenced to the Bottom
BOEM:	Bureau of Ocean Energy Management
BT:	Barotropic Streamfunction
CAC:	Composite Annual Cycles
CASE/EJIP:	Climatology and Simulation of Eddies/Eddy Joint Industry Project
CCAR:	Colorado Center for Astrodynamics Research
CCMP:	Cross-Calibrated Multi-Platform
CEOF:	Complex EOF
CICESE:	Centro de Investigacion Cientifica y de Educacion Superior de Ensenada
CLS:	Carrere and Lyard (2003) Sea state bias
CM1:	Coastal EOF Mode 1
CNES:	Centre National d'Etudes Spatiales, France
CPD:	Cycles per Day
CPIES:	PIES with an attached Doppler current sensor suspended 50 m above the PIES
CT:	Conductivity/Temperature
CTD:	Conductivity/Temperature/Depth
CTW:	Coastal-Trapped Wave
CUPOM:	University of Colorado version of the Princeton Ocean Model
CWT:	Continuous Wavelet Transform
CZCS:	Coastal Zone Color Scanner
DBAR:	Decibars
DGPS:	Digital Global Positioning System
DLP:	Day Low Pass
DOF:	Degrees of Freedom
DOY:	Days of Year
DT:	Delayed Time
DWH:	<i>Deepwater Horizon</i>
EAP:	Eddy Potential Energy
EEZ:	Exclusive Economic Zone
EKE:	Eddy Kinetic Energy
EOF:	Empirical Orthogonal Function
ERM:	Exact Repeat Mission
ERS-2:	Earth Resources Satellite – 2
ESA:	European Space Agency
FIO:	Florida Institute of Oceanography
GEM:	Gravest Empirical Mode or Gulf Eddy Model
GEOSAT:	Geodetic Satellite

GERG:	Geochemical and Environmental Research Group (TAMU)
GFE:	Government Furnished Equipment
GFO:	Geosat Follow-On
GFS:	Global Forecast System
GHR SST:	Group for High Resolution Sea-Surface Temperature
GIM:	Global Ionosphere Map
GMT:	Greenwich Mean Time or UTC
GOES:	Geostationary Operational Environmental Satellite
GOM:	Gulf of Mexico
GOMRI:	Gulf of Mexico Research Initiative
GPS:	Global Positioning System
GS:	Gulf Stream
GSFC:	Goddard Space Flight Center
GVAR:	Global Vector Auto-Regression
HCMM:	Heat Capacity Mapping Mission
HHP:	Hour High Pass
HLP:	Hour Low Pass
HMI:	Horizon Marine, Inc.
HRD:	Hurricane Research Division
HYCOM:	Hybrid Coordinate Ocean Model
IAS:	Intra-American Sea
IES:	Inverted Echo Sounder
JPL:	Jet Propulsion Laboratory
KE:	Kinetic Energy
LC:	Loop Current
LCFE:	Loop Current Frontal Eddy
LCS:	Lagrangian Coherent Structures
LCT:	Loop Current Toolbox
LH:	Left Hand
LSU:	Louisiana State University
LUMCON:	Louisiana Universities Marine Consortium
MAB:	Meters above Bottom
MADT:	Maps of Absolute Dynamic Topography
MAP:	Mean Advection of Eddy Potential Energy
MCSST:	Microwave Instrument for SST
MICOM:	Miami Isopycnic Coordinate Ocean Model
MMS:	Minerals Management Service
MODIS:	Moderate Resolution Imaging Spectroradiometer
MPI:	Message Passing Interface
MUR:	Multi-Scale Ultra-High Resolution
NAD 83:	North American Datum of 1983
NASA:	National Aeronautics and Space Administration
NCEP:	National Center for Environmental Prediction
NDBC:	National Data Buoy Center
NEPA:	National Environmental Policy Act
NGDC:	National Geophysical Data Center

NOAA:	National Oceanic and Atmospheric Administration
NODC:	National Ocean Data Center
NOS:	National Ocean Survey
NRT:	Near Real Time
NSF:	National Science Foundation
OA:	Objective Analysis
OBPG:	Ocean Biology Processing Group
PCTS:	Principal Component Time Series
PDR:	Precision Depth Recorder
PE:	Potential Energy
PI:	Principal Investigator
PIES:	Inverted Echo Sounder with Pressure
PKC:	Eddy Potential to Kinetic Energy Conversion
PO:	Physical Oceanography
PO.DAAC:	Physical Oceanography Distributed Active Archive Center
POM:	Princeton Ocean Model
PROFS:	Princeton Regional Ocean Forecast System
PSU:	Practical Salinity Unit
PV:	Potential Vorticity
PVA:	Potential Vorticity Anomaly
QB:	Quasi-Barotropic
R:	Correlation Coefficient
RADS:	Radar Altimeter Database System
RAFOS:	Ranging and Fixing of Sound (SOFAR spelled backwards)
RDI:	RD Instruments
Re:	Regression Coefficient
RFP:	Request for Proposal
RG:	Reduced Gravity
RH:	Right Hand
RHS:	Right Hand Side
RMS:	Root Mean Square
ROMS:	Regional Ocean Modeling System
RV:	Relative Vorticity
SAIC:	Science Applications International Corporation
SAR:	Synthetic Aperture Radar
SI:	Surface Intensified
SLA:	Sea-Level Anomaly
SNR:	Signal-to-Noise Ratio
SOFAR:	Sound Fixing and Ranging
SSH:	Sea Surface Height
SSHA:	Sea Surface Height Anomaly
SST:	Sea Surface Temperature
SUW:	Subtropical Underwater
Sv:	Sverdrups
T:	Temperature
TAMU:	Texas A&M University

T/C/P:	Temperature/Conductivity/Pressure
TOPEX	Ocean Topography Experiment
TOP/POS:	TOPEX/Poseidon
TRW:	Topographic Rossby Wave
T/S/P:	Temperature/Salinity/Pressure (or T/P/S: Temperature/Pressure/Salinity)
UCK:	Universal Co-Kriging
URI:	University of Rhode Island
USCG:	United States Coast Guard
USGS:	United States Geological Survey
UTC:	Coordinated Universal Time or GMT
USF:	University of South Florida
VHRR:	Very High Resolution Radiometry
WFS:	West Florida Shelf
WGS 84:	World Geodetic System of 1984
XBT:	Expendable Bathythermograph
XCP:	Expendable Current Profiler
XCTD:	Expendable CTDs
YC:	Yucatan Channel

CHAPTER 1: INTRODUCTION

1.1 BACKGROUND

Over the last decade, the Bureau of Ocean Energy Management (BOEM), formerly the Minerals Management Service (MMS), of the U.S. Department of the Interior, has conducted major physical oceanographic measurement programs in the deep waters of the Gulf of Mexico. These studies provided information on circulation and physical processes for aiding the safe exploration for oil and gas in U.S. waters in water depths of 1000 m or more, as well as for assessing environmental impacts of such activities. These observational studies included the DeSoto Canyon Eddy Intrusion Study (Hamilton et al. 2000; Hamilton and Lee 2005), Deepwater Observations in the Northern Gulf of Mexico from In-Situ Current Meters and PIES (Hamilton et al. 2003), Exploratory Study of Deepwater Currents in the Gulf of Mexico (Donohue et al. 2006), Survey of Deepwater Currents in the Northwestern Gulf of Mexico (Donohue et al. 2008), and Study of Deepwater Currents in the Eastern Gulf of Mexico (Cox et al. 2010). These programs have advanced the state of knowledge of the deep Gulf, and have included the first use in the Gulf of pressure-equipped inverted echo sounders (PIES), and deep Lagrangian RAFOS floats.

The deep waters of the Gulf, including the lower continental slope and abyssal depths, can be characterized as being in two layers. Current variation in the upper layer, from the surface to 800 – 1200 m, is dominated by mesoscale eddies, both cyclonic and anticyclonic (anti-clockwise and clockwise rotations, respectively when viewed from above). Also, the Loop Current (LC), a segment of the Gulf Stream system, enters the Gulf through the Yucatan Channel (YC), extends northward as a quasi-stationary clockwise turning meander and exits through the Straits of Florida. The LC sheds large anticyclonic eddies or rings (200 – 400 km in diameter) at irregular intervals of between 4 and 18 months (Sturges and Leben 2000). After the eddy detachment is complete, a LC eddy will typically translate westward and southwestward across the basin. These large energetic LC eddies dominate the upper-layer circulation and appear to have a major role in generating smaller-scale cyclones and anticyclones (diameters 30 – 150 km) that are often found over the continental slope and in deep water. Figure 1.1-1 illustrates the LC and a partially detached LC eddy along with the mesoscale eddy field using satellite remote sensing of sea-surface temperature (SST), and sea-surface-height anomalies (SSHA) derived from altimeters. There are a number of examples in the above reports and in the literature of eddy-eddy and eddy-topography interactions that make the Gulf upper-layer circulation complex and highly dynamic.

Whereas the upper-layer eddy flows are surface intensified with the strongest currents occurring in the top 100 m, the lower-layer flows, from ~ 1000 m to the seabed, are either slightly bottom intensified or nearly depth independent. These lower-layer motions have been attributed to propagating planetary waves (e.g., topographic Rossby waves (TRWs) discussed in Hamilton (1990; 2009)), though lower-water-column eddies are not ruled out. Near-bottom currents with speeds ~ 90 cm/s have been measured near the base of the Sigsbee escarpment in the northern Gulf (Hamilton and Lugo-Fernandez 2001). TRWs have wave periods of between 10 and 100 days, and length scales ~ 70-200 km and, for the most part, are decoupled from the surface-layer eddies where they have been observed. However, because TRWs propagate generally westward

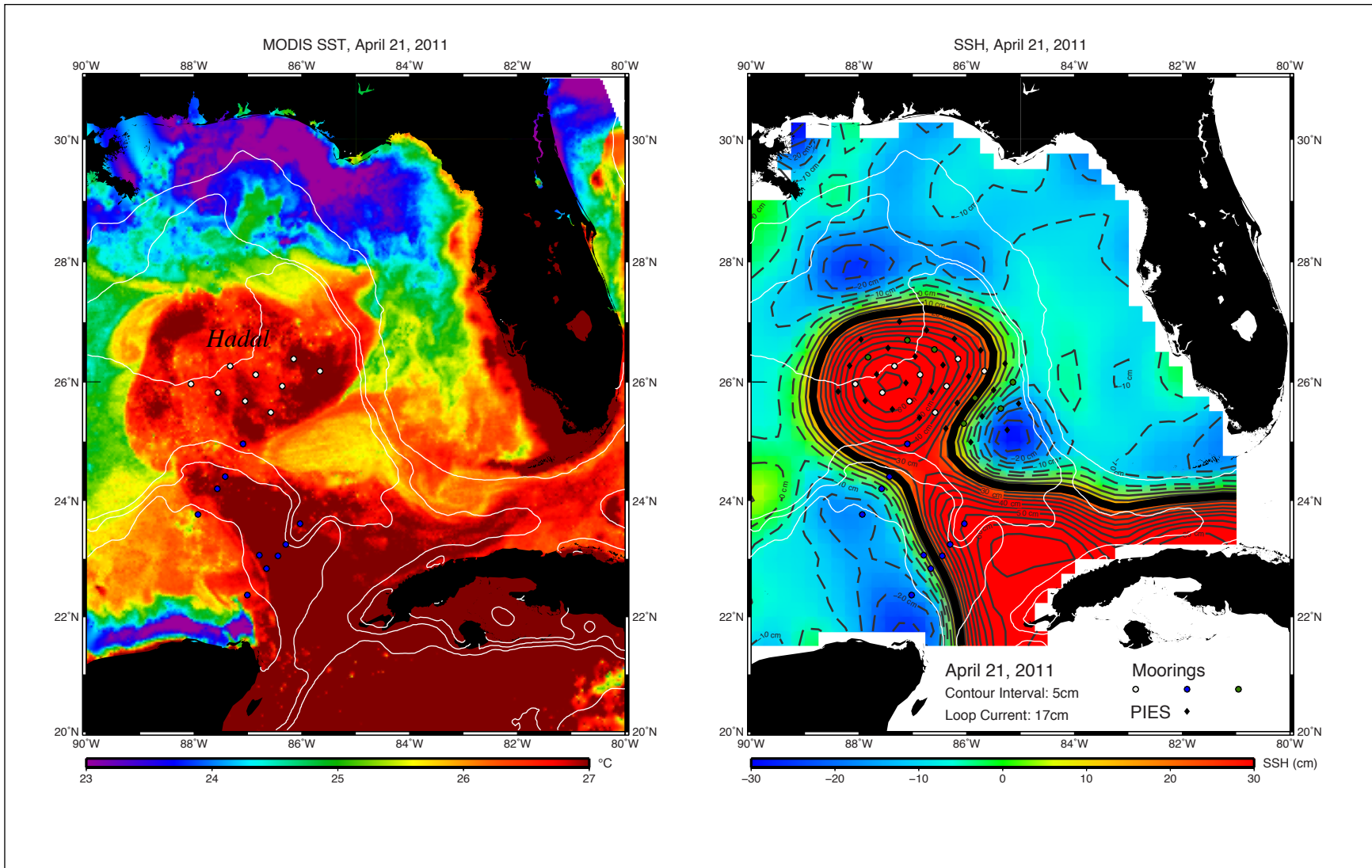


Figure 1.1-1. A high resolution SST image (left panel) and SSH altimeter map (right panel) showing an extended LC and a partially detached LC eddy (Hadal) on 21 April 2011. The fine white lines are isobath contours at 200, 1500 and 3000 m, and the dots are mooring and PIES locations (full depth only on left panel; complete array on right panel).

with shallower water on the right-hand-side (RHS) of the direction of propagation, major generation sources for these deep energetic flows are expected to be the LC, and secondarily the westward propagating LC eddies (Oey and Lee 2002).

The LC is, therefore, of major importance to the circulation in the Gulf of Mexico both as a direct and indirect generator of surface-layer eddies, and as a source of deep lower-layer flows. Until this study, the LC had surprisingly few in-situ observations commensurate with the time scales of the LC eddy-shedding cycle. Much of what is known has come from remote sensing studies of surface layer variability (Leben 2005; Leben and Born 1993; Vukovich 1986; Vukovich et al. 1979), and numerical modeling studies (Oey et al. 2005). Clockwise circulating, frontal propagating frontal cyclones, known as LC frontal eddies (LCFEs), were identified as a possible trigger for the pinch-off of a LC eddy by the larger scale meander variability of the LC front (Schmitz 2005). However, a number of mechanisms, which may act in combination, have been identified as playing roles in the separation of a major LC eddy. These include the large scale “momentum paradox” of Pichevin and Nof (1997), to baroclinic instabilities (Hurlburt and Thompson 1982), to potential vorticity fluxes through the YC (Candela et al. 2002). Longer-term moored current measurements were not attempted until the early 1980s (Science Applications International Corporation 1989) when the energetic and depth-independent nature of flows below 1000 m were established for the east side of the LC. Later, a single long-term mooring was deployed for several (not contiguous) years on the west side of the LC (Inoue et al. 2008). In order to advance understanding of the LC role in the Gulf, BOEM funded the present study and a complementary study in Mexican waters, to deploy a comprehensive array of instruments in the eastern Gulf, supplemented by remote sensing and numerical modeling. The resulting 2 to 2.5 year long observational database is being used to study LC variability, LC eddy shedding, and the controlling dynamics from the basin scale to the small LCFE scales. The database will also be invaluable for determining the realism, particularly in the lower layer, of numerical model simulations of the Gulf, and will be exploited for many years to come.

The overarching goal of this study is to increase knowledge of the dynamics of the LC in the eastern Gulf of Mexico through a combined analysis of observations and numerical modeling output. Specific objectives are to:

Increase understanding of the causes of the LC incursions into the Gulf,

1. Describe oceanographic conditions leading up to and during eddy shedding, and reattachment and to help understand the dynamics of these processes;
2. Understand how the LC interacts with and drives the lower-layer circulation;
3. Provide statistics from *in situ* observations supplemented by numerical modeling output that describes the general circulation patterns inferred from remote sensing and geostrophic calculations;
4. Analyze the available data and model output to develop an understanding of processes and interactions from the large basin to small eddy scales that control the variability of the LC, including the separation of rings; and
5. Provide information for BOEM to fulfill its regulatory mission and to comply with data and information needs for National Environmental Policy Act (NEPA) requirements.

1.2 GENERAL PROGRAM DESCRIPTION

The study design for the in-situ measurements consisted of an array of nine full-depth (or tall) moorings, six near-bottom moorings, and 25 PIES deployed in U.S. waters. Instrumentation used on the moorings is given in Chapter 2. The location of the array, referred to as the mapping array in this report, is given in Figure 1.2-1. The location of the array was determined partly by the location of the Exclusive Economic Zone (EEZ) boundary between the U.S. and Mexico, and an analysis of 19 eddy separations from the altimeter record. Based on these data, the mapping array is centered on the region that has the highest probability of capturing the separation zone between a recently detached LC eddy and the LC, as well as encompassing both the northwest and east sides of an extended LC. The spacing of moorings and PIES was set to resolve the coherence scales of both the upper and lower layers based on previous deepwater studies that showed that length scales in the lower layer tend to be shorter than at the surface. The mapping array was deployed for 2.5 years beginning in April 2009 with the final retrieval in November 2011. The moorings were rotated half way through at 15 months into the deployment. The PIES were deployed for the whole observational period without rotation, though the first 15 months of data were retrieved in July 2010 through uploads via a hydrophone. Two 1500-meter depth CTD casts were taken at most of the PIES sites. These were used for calibration of round-trip travel times during the deployment period (see Chapter 2 for details).

Because this study was restricted to deploying moorings inside the U.S. EEZ, BOEM funded complementary arrays in Mexican waters that were deployed by the CANEK group at the Centro de Investigación Científica y Educación Superior de Ensenada (CICESE), Mexico. The locations of the CICESE moorings are also given in Figure 1.2-1, where all Mexican moorings were full depth. Instrumentation and mooring design, which differs from the mapping array, are again given in Chapter 2. The CICESE moorings were deployed in June 2009 and rotated on an annual basis, providing a two-year overlap with the mapping array data (see Figure 1.2-2). BOEM funded the work associated with transects E and N across the Campeche Bank eastern slope. The Yucatan Channel (YC) moorings were part of an already established Mexican funded study, and BOEM provided some assistance with instrumentation for this transect. For these reasons, the data from transects E and N will be integrated into the analysis, but YC data will only be used for some derived products (such as volume transport) that have been supplied by our colleagues at CICESE. Many of the CICESE moorings were still deployed (as of June 2013) for a third year of measurements that naturally will not be included in the combined datasets.

Monitoring LC variability at the larger scales is important so as to place the in-situ measurements in context. Therefore, the study included a remote sensing task using satellite altimetry for SSHA, and ocean color and SST for examining features at higher resolution. The SSHA altimetric database that resolves mesoscale eddies in the Gulf of Mexico now extends over nearly three decades, and is used herein to place the in-situ LC observations in historical context, as well as for analysis of longer term and larger space-scale processes such as upstream and downstream influences on the eddy separation processes.

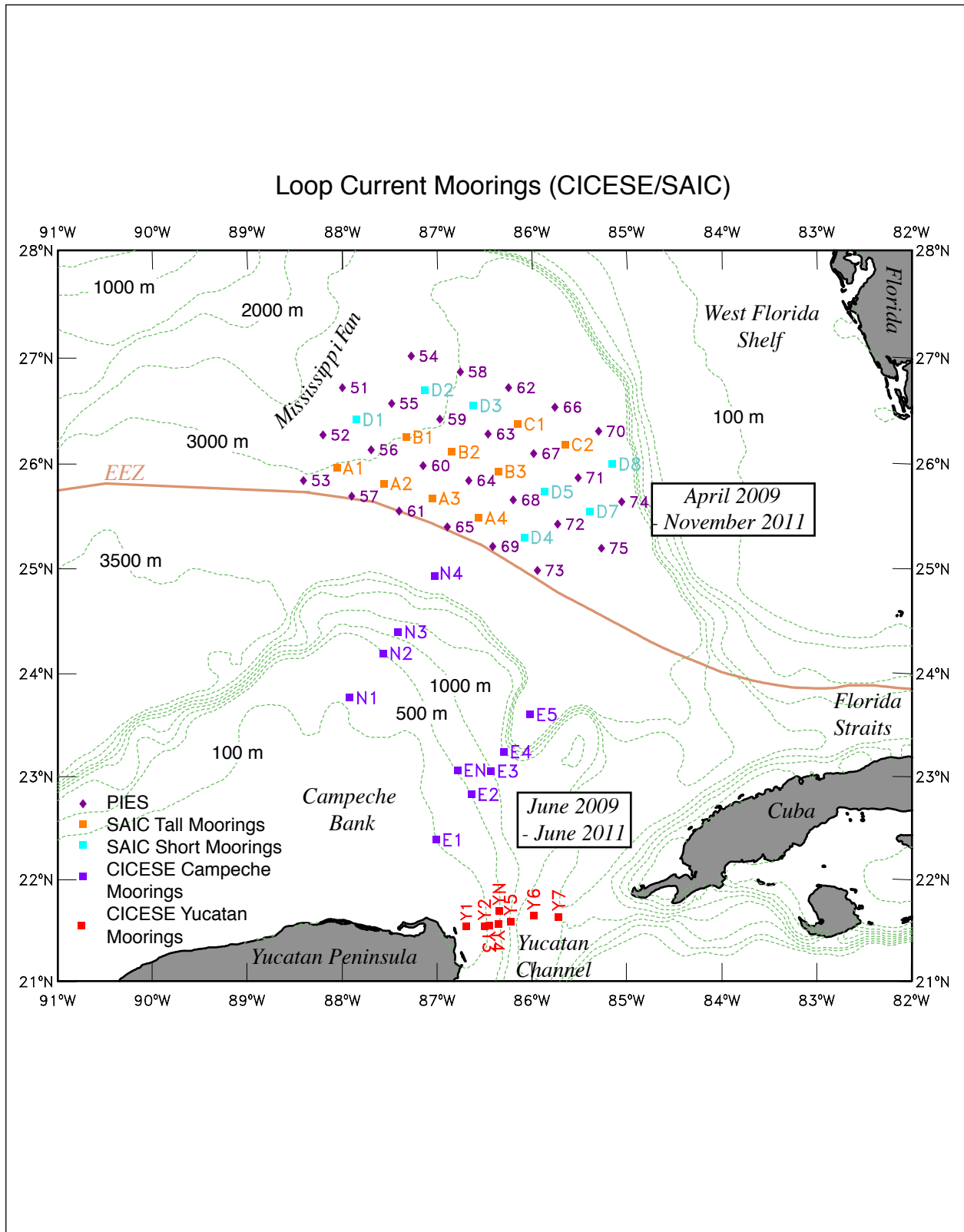


Figure 1.2-1. Locations of moorings and PIES deployed in the U.S. and Mexican sectors in the eastern Gulf of Mexico during the study of Loop Current dynamics.

Data Acquisition Intervals

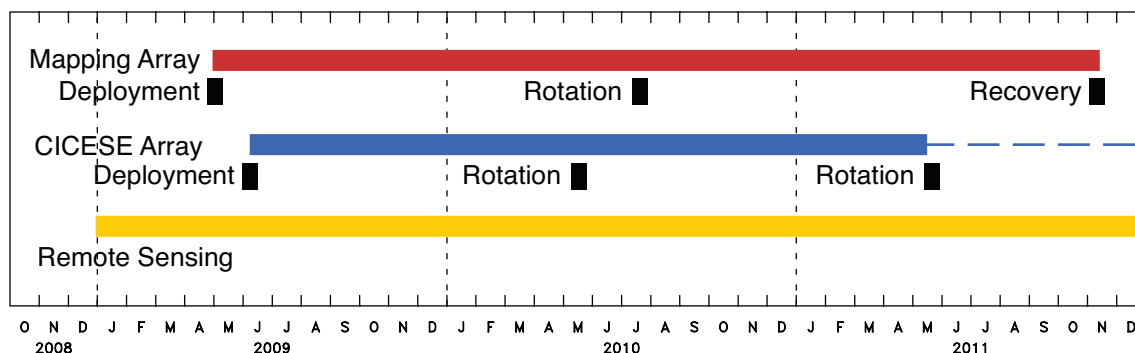


Figure 1.2-2. Schedule and relationships of data types collected and used during this study. Dashed line represents additional CICESE data collected but not discussed in this report.

A numerical modeling component is included in this study, and was designed to primarily assist in the analysis of LC processes by performing experiments on LC growth and eddy-shedding processes, and relating them to the observations. Model studies are also used in a similar manner to the long time series of altimetric SSHA maps to examine remote influences and basin-scale processes in three dimensions.

The general schedule for the measurement programs and data acquisition is shown above. The Science Applications International Corporation (SAIC¹) contract was awarded in September 2008 with mobilization taking place over the first six months. The deployment, rotation and recovery cruises for the mapping-array moorings and PIES were complex logistical operations requiring several legs because of the amount and weight of the hardware. Subsequently, the cruises lasted three to four weeks, with staging at Cododrie, Louisiana (LUMCON), and St. Petersburg, Florida (FIO), and use of the R/V *Pelican* (LUMCON) and the R/V *Weatherbird II* (FIO).

1.3 STUDY PARTICIPANTS

Participants in the study included the science team of principal investigators (PIs), support personnel, both at SAIC and the home institutions of the science team, and PIs of co-operating studies. The science team and their primary areas of responsibility were:

	Affiliation	Responsibility
Dr. Peter Hamilton	Science Applications International Corporation (SAIC)	Moorings, upper and lower; layer circulation; inertial currents
Dr. Kathleen Donohue	University of Rhode Island	PIES; upper- and lower-layer subtidal circulation
Dr. Randy Watts	University of Rhode Island	PIES; upper- and lower-layer subtidal circulation

¹ SAIC was split into two companies on September 27, 2013; the newly-named Leidos Corporation inherited the contract.

	Affiliation	Responsibility
Dr. Robert Leben	University of Colorado	Remote sensing and altimetry
Dr. Leo Oey	Princeton University	Modeling and data synthesis

It is important to note that the complete data set from the U.S. and Mexican sectors was available to both the science team and investigators at CICESE. Dr. Julio Sheinbaum was the program manager for the CICESE measurements, and he made many contributions through the program meetings of this study, and through informal collaborations with SAIC’s team members. Collegial interactions within the team and with cooperating studies were an important part of the approach to the analysis tasks so that combined expertise was brought to bear on complex physical processes.

Ms. Hui Quian worked as an intern under the supervision of Dr. Hamilton and her advisor Dr. Ruoying He of North Carolina State University. As part of her dissertation (Ph.D. awarded in December 2013), she performed a statistical and model-based analysis of inertial currents measured by the array, which contributed to Chapter 6 in this report. Mr. Cody Hall worked as a graduate research assistant under the supervision of Dr. Robert Leben at the University of Colorado. He was awarded a Ph.D. in Aerospace Engineering Sciences on May 8, 2014 based on his dissertation titled “Loop Current Seasonality”, which contributed substantially to Chapter 5 in this report.

The science team was supported by SAIC Management and Logistic personnel as follows:

Dr. Peter Hamilton, Program Manager

Mr. James Singer, Logistics Manager and Cruise Chief Scientist

Mr. Paul Blankinship, Data Manager

All moored current-meter arrays in the U.S. sector were the responsibility of SAIC. The University of Rhode Island was responsible for PIES instrumentation, including preparation, deployment, at-sea interrogation, and recovery. The University of Colorado handled satellite remote sensing, and Princeton University handled the facilities for numerical modeling. The CICESE physical oceanographic group was responsible for moorings in the Mexican sector.

Until he left the company, Dr. Scott McDowell was the program manager for the first year of the program. Dr. Nick Shay of the University of Miami was the PI for a cooperative study involving aircraft AXBT/AXCTD/AXCP surveys of the LC related to hurricane activity in the eastern Gulf of Mexico.

1.4 LOOP CURRENT EDDY SHEDDING

As outlined in Section 1.1, the Loop Current (LC) provides the dominant influence on upper-layer circulations in the Gulf. It can have a wide variety of configurations ranging from turning directly eastward from the Yucatan Current to the Straits of Florida along the coast of Cuba (port

to port mode) to extending in a loop far northwards or northwestwards so as to directly impact the continental slopes south of Mississippi and Alabama (Huh et al. 1981). The upper-layer current is characterized by strong velocity shears laterally and vertically with flow limited to a depth of ~ 800 to 1000 m; it carries warmer water and a saline core (>36.5 psu) of subtropical underwater (SUW) at about 200 m depth. In this study, the upper layer is defined from the surface to the depth of the 6 °C isotherm, and the lower layer from the 6 °C isotherm depth to the bottom. The 6 °C surface corresponds to the lowest part of the LC and also corresponds to the sill depth (~ 800 m) in the Straits of Florida (Bunge et al. 2002).

At irregular intervals, as the LC extends northwards or northwestwards towards the Mississippi delta, it sheds a warm anticyclonic ring called a Loop Current eddy of diameter ~ 200 to 400 km. The separated LC eddies subsequently move into the western Gulf, eventually interacting with the topography of the western Mexican slope and dissipating there. Often a recently detached LC eddy will reattach to the LC. Detachment and reattachment may happen several times, over intervals as long as a few months, before the final detachment, when the eddy separates and moves into the western Gulf. In this report, reference to a detachment implies that there may be a subsequent reattachment, and only the last detachment is referred to as a separation, i.e., the eddy is shed.

In this report, reference will often to be made to the LC or LC eddy front or boundary. In most cases this is defined to be the 17 cm SSH contour, which approximates the position the maximum horizontal shear on the cyclonic side of the jet, and is close to the maximum velocity of the surface jet. There is also a distinct surface temperature front (Figure 1.1-1) ~ 20 to 50 km to the left of the 17 cm SSH contour, looking downstream along the jet (Leben 2005), that is often blurred by the advective effects of cyclonic frontal eddies, and has a very small temperature contrast in the summer months. This front, and its associated subsurface downward sloping pycnocline, separates the warmer LC water mass with its high salinity SUW core, from external Gulf waters.

Immediately following LC eddy separation, the northern boundary of the LC itself has generally reformed south of 26°N (the retreat latitude), and the northward extension begins again. Leben (2005) showed that there is a strong correlation between the retreat latitude and the time to the next subsequent eddy shedding that may be explained as a consequence of mass conservation and vorticity changes between retreated and extended positions (Lugo-Fernandez and Leben 2010). A 54-year free-running HYCOM numerical model of Gulf circulation has been able to reproduce this retreat latitude correlation. The mean time interval between eddy sheddings, based on the altimeter record, is ~ 9 to 11 months. However, based on a new, longer and improved database of eddy sheddings, there is evidence of seasonality in the probability that some months have higher incidences of separation events (see Chapter 5). Causes of this seasonality in the mean annual cycle may be related to the biannual variation in the strength of Caribbean trade winds (Chang and Oey 2013b), or alternatively, sea-level variability along the southeastern U.S. Atlantic and Gulf of Mexico continental shelf and slope (Chapter 5).

Eddy-shedding dynamics, including the effects of external influences, have been primarily explored using numerical models, where there seem to be as many explanations as there are models (see Oey et al. (2005) for a review). At one end of the spectrum, LC eddy separation is

purely an upper-layer phenomenon that occurs once the LC extends northwards due to increases in upper-layer volume transport through the YC. Westward translation of the extended LC arises from momentum imbalance, analyzed by Pichevin and Nof (1997), that stretches the LC and effects a separation, whereupon the LC eddy translates westward at the long Rossby wave speed (referred to as β -advection). Separation is often preceded by a reduction in Yucatan Current volume transport. On the one hand, for example, Chang and Oey (2013a) suggest that the Pichevin-Nof mechanism is the only dynamics necessary for eddy separation. On the other hand, the model-based analyses of Chérubin et al. (2005) propose a more complex scenario in which instabilities that couple the upper and deepest layers in and under the LC, can develop suddenly, with a deepening of an extended LC, and pinch off a ring. Similarly, Le Hénaff et al. (2012) use potential vorticity arguments to account for the generation of lower-layer cyclones in their model when the upper-layer LC flows across the topography of the Mississippi Fan.

Frontal cyclones or LCFEs are observed, in remote sensing data, translating clockwise along the LC front, and have long been thought to play a role in LC eddy separations. The LCFEs are assumed to grow along the extended loop and effect a separation by extending from the west Florida slope across the neck. They are sometimes assisted by the appearance of a cyclone between the western LC front and the Campeche Bank slope that is assumed to propagate northwards through the Yucatan Channel (see Schmitz (2005) for further discussion). Model results of Chérubin et al. (2006) and Oey (2008) interpret deep lower-layer cyclones as being generated by LCFEs through instability processes that Chérubin et al. (2006) analyzed as barotropic and baroclinic vortex rim instabilities. In this report, LCFEs, originating along the Campeche Bank slope, are distinguished from large amplitude meanders of the north and east-side LC front (Chapter 4).

The pioneering model studies of Hurlburt and Thompson (1982) showed that the LC is inherently unstable and will shed eddies even if Yucatan Channel transports are unvarying. Moreover the ring formation process requires an active lower layer for the model to generate realistic eddy shedding intervals. The role of the lower layer, which spans two-thirds of the water column in the deep eastern basin, has had relatively few observations, most of which are summarized by Hamilton (2009). Lower-layer flows in the eastern basin are observed to be either depth-independent or slightly bottom intensified, and are quite energetic, and can be considered to arise from a mixture of TRWs plus cyclonic and anticyclonic eddies. Their role in eddy-shedding dynamics has not been established, as the above discussion of model studies indicates. The results of Chapter 4 will show that energetic lower-layer currents are generated by intervals of baroclinic instability, and these deep eddy currents directly influence LC eddy detachments.

On longer time scales of LC growth and eddy separation, Bunge et al. (2002) showed that observed lower-layer transport in the Yucatan Strait is directly related to change in LC area, approximately consistent with mass conservation. Chang and Oey (2011) have a more sophisticated view of this connection that involves exchange vertically between upper and lower layers and laterally between eastern and western basins (see Chapter 4).

The major thrusts in the present study combining observations and companion modeling activities are: (1) To study the variability of LC incursions into the Gulf, on time scales that span

eddy-shedding, interannual, and multi-decadal processes; (2) To describe circulation processes that lead to detachments, reattachments, and separations during eddy shedding; (3) To understand how the LC interacts with and forces the lower-layer circulation; and (4) To incorporate observations from the Mexican sector of the Eastern Gulf into the investigation of circulation and dynamics. Many of the scientific topics outlined above, such as baroclinic instability, the influence of LCFEs on detachments and deep cyclones, are addressed in subsequent chapters, and in some cases the results differ from preceding paradigms.

1.5 MAJOR EVENTS

Eddy Separations

One of the primary aims of the study was to document and analyze LC eddy-shedding processes. A brief outline of the formation and eddy-shedding events is given here so as to place in context the following analysis and statistics chapters. The measurement program documented the formation and separation of three LC eddies: Ekman, Franklin, and Hadal, where the names were defined by an oil industry group (Eddy Watch). The study also documented the formation and first detachment of Icarus over the last three months of the U.S. observational period. Eddy Icarus did not fully separate from the LC until January 2012. Figure 1.5-1 gives an overview of the eddy detachments, showing the deepening of the isotherms over the array as the LC extended to the north and northwest. Both Ekman and Franklin were large eddies with multi detachments and re-attachments over several months, before finally separating, where the detachment points were south of the mapping array in the vicinity of transect E. Hadal was almost a canonical LC eddy that was preceded by the LC extending far to the northwest in a sequence of growth spurts. The eddy separated on its first detachment with the separation point being in the center of the mapping array. Eddy Watch also identified eddy Galileo as separating at the end of June 2011 when the LC was fully extended to the northwest. However, it was not a true LC eddy, but rather a small region of anticyclonic circulation that was extruded from the northwest tip of the forming Hadal that rapidly dissipated.

Deepwater Horizon Oil Spill

During the first deployment of the mapping array, the *Deepwater Horizon* (DWH) disaster occurred. DWH, situated about 80 km southeast of the Mississippi delta in about 1200-m water depth, exploded on 20 April 2010, claiming 11 lives. The subsequent discharge of oil and gas continued from the seafloor until the wellhead was capped three months later (Liu et al. 2011a). The oil discharge took place during the latter stages of the formation and first detachments of Franklin, and concern was expressed that the extensive surface oil would find its way into the eddy and be transported south to the Florida Keys and beyond (Maltrud et al. 2010; Weisberg 2011). This did not occur, however, even though a large quantity of surface oil was present in mid-May 2010 in a large cyclone immediately north of the northern part of the LC/Franklin front (Walker et al. 2011). To support the national response to the disaster, BOEM funded the taking of water samples on the July 2010 rotation cruise for analysis for hydrocarbons by the Texas A&M University Geochemical and Environmental Research Group (GERG). No significant hydrocarbon concentrations, at any depth, were found south of the LC front implying that entrainment of oil-polluted water into Franklin was minimal. Wade et al. (2011) published an analysis of these hydrocarbon measurements, and therefore, they are not included in this report.

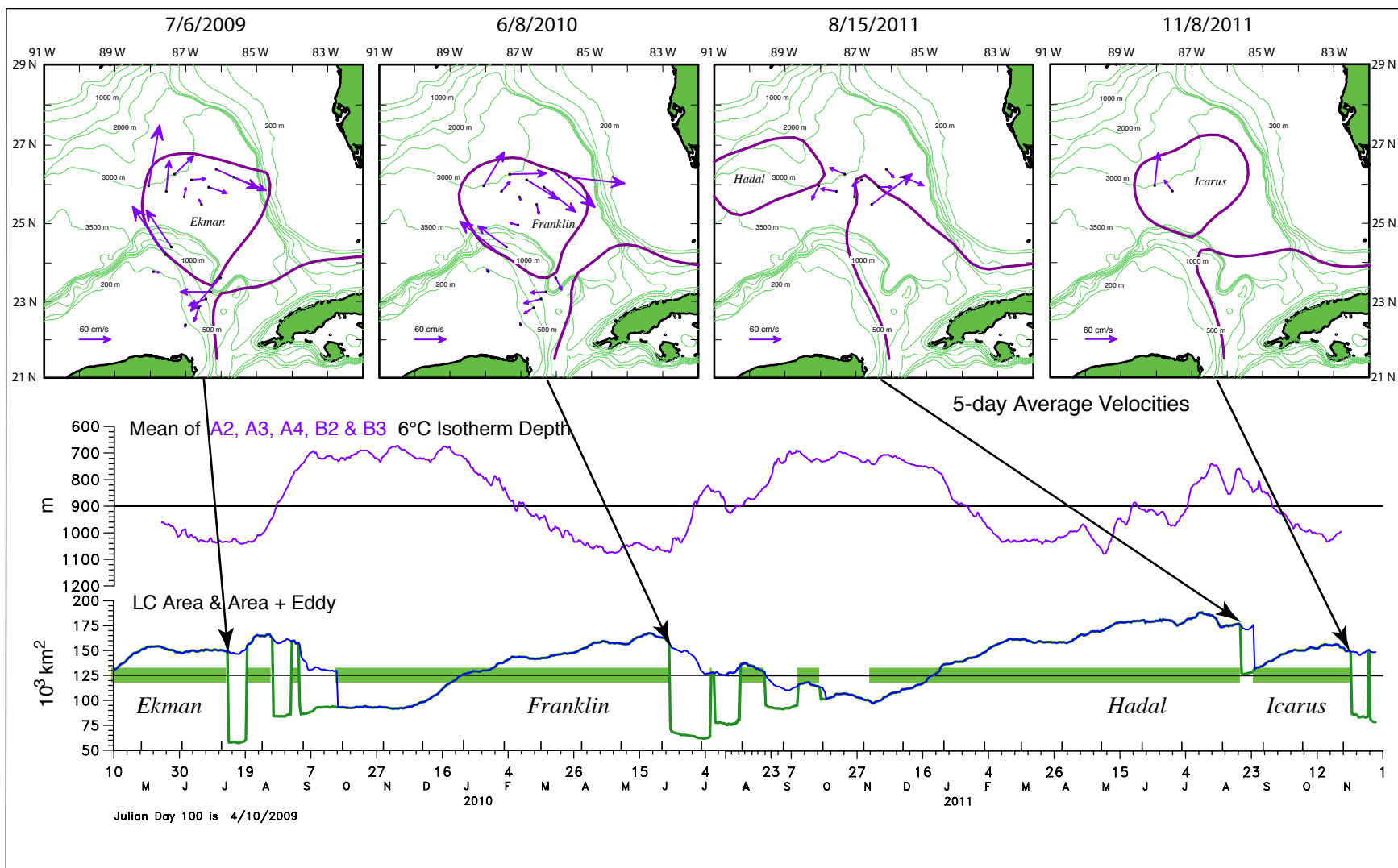


Figure 1.5-1. Time series of LC area (green) and LC+LCE area (blue) as delineated by the 17-cm SSH contour from the altimeter maps. The second panel shows the mean depth of the 6 °C isotherm from the center of the mapping array. The maps show the 17-cm contour on the day of the first detachment along with the 5-day average currents at 80 to 100 m depth, centered on the detachment date.

The circulation of Franklin during the oil spill was also analyzed using in-situ velocity and temperature measurements from the mapping array (Hamilton et al. 2011).

Hurricanes

Unlike the summers previous to, and after the deployment of the mapping array, no major hurricanes occurred in the eastern Gulf of Mexico during the three summer-hurricane periods encompassed by the deployments. The only hurricane/tropical storm that passed close to the array was the late season Hurricane Ida (8–10 November 2009) that tracked northwards through the Yucatan Channel making landfall close to the Mississippi delta.

1.6 REPORT ORGANIZATION

The following chapters of the report are organized as follows. Except where noted, all the principal PIs contributed to the chapters.

Chapter 2: A description of the experiment and experimental methodology, along with the major analysis methods used in the remainder of the report.

Chapter 3: A detailed description of eddy formation, detachments and separation events, including a numerical simulation of Hadal's separation, followed by a statistical analysis of the observed flow fields.

Chapter 4: A dynamical analysis of eddy growth and separation, including the role of LCFEs and a baroclinic instability analysis of meander growth. Principal authors are Dr. Donohue, Dr. Watts and Dr. Hamilton.

Chapter 5: Multi-decadal analysis of the historical record with a newly constructed record mainly from remote sensing and altimetry. Principal authors are Dr. Leben and Dr. Hall.

Chapter 6: An observational and numerical model analysis of the inertial response caused by hurricane Ida. Principal authors are Dr. Quian and Dr. Hamilton.

Chapter 7: Summary discussion of the major results from the study, followed by recommendations for further studies to fill knowledge gaps for the Gulf of Mexico.

CHAPTER 2: EXPERIMENTAL DESIGN AND METHODOLOGY

2.1 MOORED ARRAYS

2.1.1 Array Design

The U.S. component of the moored current-meter array consisted of nine full-depth, tall moorings and seven near-bottom, 100-meter-tall, short moorings deployed in the U.S. part of the LC region in the eastern Gulf of Mexico (GOM). These were embedded in an array of 25 inverted echo sounders with pressure (PIES). Further south, in the Mexican sector, ten current-meter moorings were deployed along two sections north and northeast of the Yucatan Peninsula off Campeche Bank, and eight additional moorings extended from the Yucatan Peninsula halfway across the Yucatan Channel opposite Cuba. The locations were shown earlier in Figure 1.2-1. Mooring deployments, rotations, and recoveries were undertaken by separate entities (SAIC and CICESE for the U.S. and Mexican sectors, respectively). The initial deployments of the Mexican sector moorings occurred 1-2 months after the U.S. sector deployment, and they were recovered after 24 months, approximately 5-6 months before the U.S. sector moorings and PIES were recovered.

The U.S. sector full-depth moorings were grouped to both span the major part of the LC and be in the most likely locations to capture a LC eddy separation, with the limitation that they had to be north of the EEZ. By embedding these moorings in an array of PIES and near-bottom or short moorings, this placed the tall mooring measurements in a wider context by mapping fields of temperature, salinity, geostrophic velocity, bottom pressure and sea-surface height (SSH). It was expected that a comparison of current profiles from the tall moorings with geostrophic velocity profiles would allow evaluation of the non-linear ageostrophic components of the dynamics expected to be important for peripheral eddies and eddy-separation events. The spacing of the PIES array was ~53 km, which was less than that used in both the Exploratory and NW GOM programs (~60 km) but a little more than that used for the small PIES array in the Eastern Gulf program. The PIES were also laid out along TOPEX/Jason interleaved ground tracks to facilitate incorporation of altimetry into the analyses. The inevitable compromise between area covered and spatial resolution of the array resulted in the roughly rectangular array in the U.S. sector (Figure 1.2-1) with approximately equal north and east spacing of about 53 km. The regular spacing of the array also makes the calculation of dynamical quantities involving horizontal gradients (e.g., relative vorticity) less error prone. The addition of PIES to the array was designed in part to increase the horizontal resolution, because for geostrophic dynamics, full-depth moorings and PIES can be considered as providing equivalent information.

2.2 EQUIPMENT AND INSTRUMENTS

2.2.1 Introduction

Moored data collection consisted primarily of in-situ moored current, temperature, conductivity and pressure measurements at nine full-depth, tall mooring sites and current and temperature measurements at seven near-bottom, short mooring sites. In addition, 48 conductivity/temperature/depth (CTD) casts (one, two or three at each PIES site) were made to support calibration of inverted echo sounder measurements made at 25 locations during the field effort.

2.2.2 Moored and PIES Instruments

Moored measurements in the U.S. sector were made from 16 current meter moorings (nine tall and seven short) deployed in the eastern Gulf of Mexico, north of 25°00'N to ~27°00'N, and west of 85°00'W to ~88°30'W, in waters ranging in depth from 2700 to 3350 meters. Tall mooring tops were at 60 to 70 meters depth. Measurements at these sites were made continuously for 30 + months beginning in late April 2009 and, except for one short mooring, were completed in early November 2011. One of the short moorings was not recovered until mid-January 2012. The moorings were rotated after ~15.0 months. The locations and deployment periods for all 16 moorings are listed in Tables 2.2-1 and 2.2-2, respectively, and the locations and deployment periods for the 25 PIES are listed in Table 2.2-3. A map showing the mooring and PIES locations was presented earlier in Figure 1.2-1.

The navigation datum used for mooring placement was the World Geodetic System of 1984 (WGS 84), which is nearly the same as the North American Datum of 1983 (NAD 83). After deployment, mooring locations were triangulated and depth determined based on DGPS fixes, precision depth recorder (PDR) readings corrected for the speed of sound, and minimum acoustic ranges to the mooring releases. Later, instrument pressure data were evaluated as another check on mooring depth. Fallback of each mooring from the anchor-drop site to the final resting place on the bottom was also determined. This ranged from a minimum of approximately 130 meters to 450 meters for the short moorings, and from approximately 400 meters to 900 meters for the tall moorings. Fallback was affected primarily by the magnitude and direction of upper layer currents during deployment.

Each tall mooring was equipped to measure near-surface currents with an upward looking 75-kHz ADCP using 8-meter bins and was deployed at 450 meters depth. Currents were also measured at 600, 900, 1300, and 2000 meters depth and 100 meters above bottom (MAB). Temperature data were collected at each current-meter level on the tall moorings as well as at 75, 150, 250, 350, 525, 750, 1100, and 1500 meters depth. Salinity data were collected only at the 150-meter and 750-meter levels and pressure data were generally collected at 150, 450, 750, 900, 1300 and 2000 meters depth on each tall mooring. Short moorings measured only current and temperature at 100 MAB. A schematic of a tall mooring is shown in Figure 2.2-1.

2.2.3 Instrumentation

The moorings were instrumented with a number of different type current meters. These included Aanderaa RCM-7/8s (rotor type) at 900 and 1300 meters depth on the tall moorings and 100 MAB on the short moorings; and RCM-11s (Doppler type) at 2000 meters and 100 MAB on each tall mooring. In addition, an InterOcean S4 (electromagnetic) current meter was deployed at 600 meters depth and an RDI 75-kHz LongRanger ADCP at 450 meters depth on each of the tall moorings. A small number of additional current meters were deployed during the second deployment period on the B1 and B2 tall moorings and included the following:

Table 2.2-1. Triangulated Mooring Locations and Depths by Deployment for the Loop Current Study

Mooring (DD)	Deployment 1 Triang. Location	Triang. Depth (M)	Deployment 2 Triang. Location	Triang. Depth (M)	Dist. Between
A1 (3036 M)	25°57.666'N 88°03.159'W	3035 [3024]	25°57.658'N 88°03.113'W	3023 [3025]	0.078 km
A2 (3208 M)	25°49.012'N 87°33.126'W	3200 [3190]	25°49.029'N 87°32.970'W	3195 [3190]	0.262 km
A3 (3302 M)	25°40.531'N 87°02.891'W	3293 [3283]	25°40.540'N 87°02.953'W	3295 [3282]	0.105 km
A4 (3270 M)	25°29.164'N 86°33.565'W	3262 [3255]	25°29.152'N 86°33.677'W	3270 [3255]	0.189 km
B1 (3049 M)	26°15.245'N 87°18.998'W	3049 [3031]	26°15.319'N 87°19.069'W	3053 [3032]	0.181 km
B2 (3138 M)	26°06.701'N 86°50.359'W	3132 [3123]	26°06.744'N 86°50.321'W	3146 [3121]	0.102 km
B3 (3160 M)	25°55.617'N 86°21.301'W	3156 [3147]	25°55.663'N 86°21.370'W	3167 [3146]	0.143 km
C1 (3190 M)	26°22.536'N 86°08.597'W	3182 [3161]	26°22.647'N 86°08.497'W	3182 [3166]	0.265 km
C2 (3257 M)	26°10.737'N 85°38.921'W	3250 [3236]	26°10.644'N 85°38.860'W	3254 [3237]	0.200 km
D1 (100 MAB)	26°24.986'N 87°51.007'W	2827	26°24.878'N 87°51.050'W	2832	0.213 km
D2 (100 MAB)	26°41.751'N 87°07.587'W	2885	26°41.614'N 87°07.638'W	2866	0.268 km
D3 (100 MAB)	26°32.949'N 86°37.301'W	3098	26°33.077'N 86°37.200'W	3101	0.291 km
D4 (100 MAB)	25°17.993'N 86°04.783'W	3259	25°18.144'N 86°04.939'W	3264	0.382 km
D5 (100 MAB)	25°44.336'N 85°51.744'W	3234	25°44.507'N 85°51.765'W	3236	0.319 km
D7 (100 MAB)	25°33.042'N 85°22.986'W	3311	25°32.967'N 85°22.412'W	3293	0.973 km
D8 (100 MAB)	25°59.946'N 85°09.216'W	3309	26°00.014'N 85°09.200'W	3299	0.129 km

Deployment 1: 04/20/2009–07/26/2010 (11/11/2010 end for B1 & B2)

Deployment 2: 07/01/2010–11/28/2011 (01/14/2012 end for D4)

(DD) = Design Depth following adjustments for bathymetric survey at target site.

[] = Mooring Depth calculated from 150 m MicroCat/SeaCat or 450 m ADCP pressure-sensor data, whichever produced smaller variation from planned instrument depth.

Table 2.2-2. Mooring Deployment Periods for the Loop Current Study

Mooring	Deployment Number	Deployment Periods (UTC)
A1	1	05/05/2009 – 07/19/2010
	2	07/20/2010 – 11/13/2011
A2	1	05/04/2009 – 07/17/2010
	2	07/18/2010 – 11/13/2011
A3	1	04/30/2009 – 07/10/2010
	2	07/11/2010 – 11/08/2011
A4	1	04/30/2009 – 07/08/2010
	2	07/09/2010 – 11/03/2011
B1	1	05/14/2009 – 11/09/2010
	2	11/10/2010 – 11/01/2011
B2	1	05/11/2009 – 11/11/2010
	2	11/12/2010 – 11/08/2011
B3	1	05/10/2009 – 07/02/2010
	2	07/03/2010 – 11/09/2011
C1	1	04/20/2009 – 07/12/2010
	2	07/15/2010 – 10/28/2011
C2	1	04/22/2009 – 07/04/2010
	2	07/07/2010 – 10/27/2011
D1	1	05/15/2009 – 07/19/2010
	2	07/20/2010 – NR
D2	1	05/06/2009 – 07/16/2010
	2	07/16/2010 – 11/14/2011
D3	1	05/09/2009 – 07/12/2010
	2	07/12/2010 – NR
D4	1	04/27/2009 – 07/01/2010
	2	07/02/2010 – 01/14/2012
D5	1	04/27/2009 – 06/30/2010
	2	07/01/2010 – 11/02/2011
D7	1	04/21/2009 – 07/26/2010
	2	07/26/2010 – 11/02/2011
D8	1	04/21/2009 – 07/26/2010
	2	07/26/2010 – 10/27/2011

NR = Not Recovered. Note: There was no D6 Mooring.

Table 2.2-3. PIES Deployment Locations and Periods for the Loop Current Study

PIES	Latitude	Longitude	Water Depth (M)	Deployment Period (UTC)
P51	26°42.845'N	87°59.480'W	2733	04/23/2009 – 11/01/2011
P52	26°16.459'N	88°11.953'W	2823	04/26/2009 – 11/05/2011
P53	25°50.150'N	88°24.455'W	3114	05/01/2009 – 11/05/2011
P54	27°00.635'N	87°16.318'W	2882	04/19/2009 – 10/26/2011
P55	26°34.062'N	87°28.821'W	2833	04/23/2009 – 11/01/2011
P56	26°07.733'N	87°41.468'W	3029	04/26/2009 – 11/01/2011
P57	25°41.472'N	87°53.975'W	3209	05/01/2009 – 11/05/2011
P58	26°51.826'N	86°45.471'W	3065	04/19/2009 – 10/26/2011
P59	26°25.386'N	86°58.320'W	3023	04/23/2009 – 10/29/2011
P60	25°59.034'N	87°11.058'W	3184	04/26/2009 – 11/02/2011
P61	25°32.876'N	87°23.817'W	3332	05/01/2009 – 11/04/2011
P62	26°43.025'N	86°14.809'W	3169	04/19/2009 – 10/27/2011
P63	26°16.683'N	86°27.902'W	3108	04/23/2009 – 10/29/2011
P64	25°50.267'N	86°40.210'W	3247	04/26/2009 – 11/02/2011
P65	25°24.073'N	86°53.477'W	3326	04/30/2009 – 11/04/2011
P66	26°31.902'N	85°45.658'W	3226	04/19/2009 – 10/27/2011
P67	26°05.497'N	85°58.772'W	3240	04/21/2009 – 10/28/2011
P68	25°39.161'N	86°11.594'W	3213	04/27/2009 – 11/02/2011
P69	25°12.893'N	86°24.497'W	3293	04/30/2009 – 11/04/2011
P70	26°18.275'N	85°17.950'W	3298	04/20/2009 – 10/27/2011
P71	25°51.902'N	85°31.001'W	3278	04/21/2009 – 10/28/2011
P72	25°25.562'N	85°43.943'W	3286	04/27/2009 – 11/03/2011
P73	24°59.229'N	85°56.835'W	3325	04/29/2009 – 11/04/2011
P74	25°38.033'N	85°03.289'W	3336	04/21/2009 – 10/28/2011
P75	25°11.899'N	85°16.260'W	3341	04/28/2009 – 11/03/2011

Note: Water depth was calculated from the record mean PIES pressure converted to depth in meters using seawater depth with the PIES site latitudes.

Full-Depth Mooring Schematic

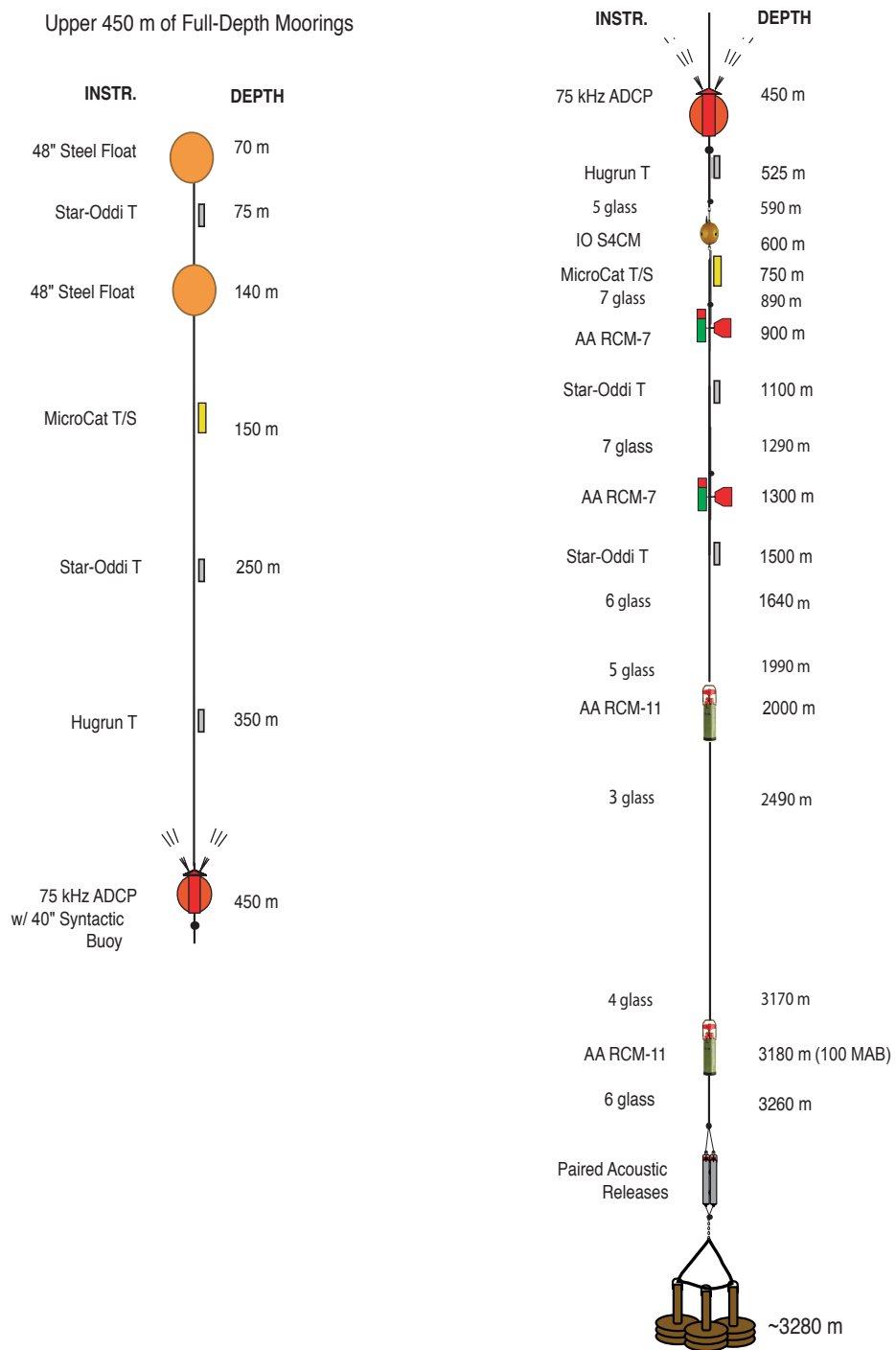


Figure 2.2-1. Schematic of tall mooring.

- 300-kHz RDI Sentinel ADCP (at 90 meters depth on the B1 mooring)
- RCM-8 current meter (at 599 meters depth on the B1 mooring)
- S4 current meter (at 90 meters depth on the B2 mooring)
- RCM-11 current meter (at 91 meters depth on the B2 mooring)

The tall moorings also included Hugnún Seamon mini temperature recorders, Sea-Bird MicroCat and SeaCat conductivity/temperature recorders, and Star-Oddi Starmon mini temperature recorders at the following levels:

- Hugnún recorders (primarily at 250 and 350 meters depth)
- Sea-Bird recorders (at 150 and 750 meters depth)
- Star-Oddi recorders (primarily at 75, 525, 1100 and 1500 meters depth)

Table 2.2-4a–c summarizes the measurement levels for each of the data logging instruments deployed on the moorings during the program. All of the tall moorings were equipped with paired-Teledyne Benthos 865-A acoustic releases, and the short moorings were equipped with various single acoustic releases including Teledyne Benthos 865-A, ORE/EdgeTech 8202 or ORE/EdgeTech 8242XS. The PIES instruments (manufactured by the University of Rhode Island) were deployed on low profile stands and were mounted about one meter above the bottom.

2.2.4 Instrument Calibration, Performance and Data Return

Except for the Hugnún temperature recorders, all of the moored data logging instruments used in the field effort were serviced and calibrated by their respective original manufacturer prior to deployment on the Loop Current study moorings. The Hugnún recorders were serviced and calibrated by Star-Oddi as the original manufacturer was no longer in business.

Figure 2.2-2a–e presents a timeline of the data return by each mooring instrument level for the American Sector moorings deployed by SAIC. Note that not all levels were instrumented on each mooring during each deployment period. This is due to the fact that a few extra instruments were added to the B1 and B2 moorings during the second deployment period to permit instrument comparison or backup. Also, periods where some data were lost are identified as having occurred for a variety of reasons including instrument malfunctions, battery failures and instrument leaks.

A total of 272 instrument deployments were made on the moorings over the course of the 30 + month field effort, and the total data return from these was approximately 93.8%. This return was calculated based on the maximum number of "good" data points expected for the various type instruments at their respective settings. However, since an ADCP generally works or does not work, the data return for these instruments reflects only that "good data" were obtained for at least one level, though anywhere from 20 depth cells on the Sentinel to 51 depth cells on the LongRanger may have provided useful data. Table 2.2-5 summarizes the moored instrument data return by instrument type.

Table 2.2-4a. Mooring Locations and Moored Instrument Levels for the Loop Current Study (American Sector) with Nominal Instrument Depths (Tall Moorings A1, A2, A3 and A4)

Mooring	Location	Water Depth (M)	Instrument Depth (M)	Instrument Type (Serial Number)
A1	25°57.666'N 88°03.159'W	3036	75 150 250 350 450 525 600 750 900 1100 1300 1500 2000 2930 (100 MAB)	TEMP (T1277) T/S/P (2698) TEMP (C959) TEMP (D634) 75 kHz ADCP (4913) TEMP (T1156) S4 (08161755) (08161753) T/S/P (3392) (2702) RCM-7 (10881) TEMP (T1160) RCM-8 (12789) TEMP (T1162) RCM-11 (360) RCM-11 (354)
A2	25°49.012'N 87°33.126'W	3208	75 150 250 350 450 525 600 750 900 1100 1300 1500 2000 3108 (100 MAB)	TEMP (T1276) T/S/P (2697) TEMP (C946) TEMP (C950) 75 kHz ADCP (4856) TEMP (T1155) S4 (08161753) (08111779) T/S/P (3391) RCM-7 (9949) TEMP (T2943) RCM-8 (12788) TEMP (T2944) RCM-11 (683) RCM-11 (353)
A3	25°40.531'N 87°02.891'W	3302	75 150 250 350 450 525 600 750 900 1100 1300 1500 2000 3202 (100 MAB)	TEMP (T1275) (T1278) T/S/P (2696) TEMP (C943) TEMP (C944) 75 kHz ADCP (4817) TEMP (T1154) S4 (08111779) (08161757) T/S/P (3390) RCM-7 (10350) TEMP (T2989) RCM-7 (9950) TEMP (T2995) RCM-11 (675) RCM-11 (351)
A4	25°29.164'N 86°33.565'W	3270	75 150 250 350 450 525 600 750 900 1100 1300 1500 2000 3170 (100 MAB)	TEMP (T1271) T/S/P (2695) TEMP (C933) TEMP (C939) 75 kHz ADCP (4866) TEMP (T1153) S4 (07961708) (07961709) T/S/P (3388) RCM-7 (11450) TEMP (T2966) RCM-7 (9948) TEMP (T3001) RCM-11 (362) RCM-11 (350)

Table 2.2-4b. Mooring Locations and Moored Instrument Levels for the Loop Current Study (American Sector) with Nominal Instrument Depths (Tall Moorings B1, B2 and B3)

Mooring	Location	Water Depth (M)	Instrument Depth (M)	Instrument Type (Serial Number)
B1	26°15.245'N 87°18.998'W	3049	75 90 [2] 150 250 350 450 525 599 [2] 600 750 900 1100 1300 1500 1990 2949 (100 MAB)	TEMP (T1280) 300 kHz ADCP (209) T/S/P (1341) (2699) TEMP (D617) (D595) TEMP (D620) 75 kHz ADCP (4855) TEMP (T1159) RCM-8 (7356) S4 (07801678) (08161755) T/S/P (3394) RCM-7/8 (11791) (12804) TEMP (T3030) RCM-7/8 (10533) (7582) TEMP (T3031) RCM-11 (677) RCM-11 (357) (349)
B2	26°06.701'N 86°50.359'W	3138	75 90 [2] 91 [2] 150 250 350 450 525 600 750 900 1100 1300 1500 2000 3038 (100 MAB)	TEMP (T1279) S4 (08111746) RCM-11 (356) T/S/P (2700) TEMP (D597) (T1157) TEMP (D614) (T3034) 75 kHz ADCP (4888) TEMP (T1158) S4 (08291851) (07801678) T/S/P (3393) RCM-7 (11389) (11791) TEMP (T3032) RCM-8 (7528) TEMP (T3033) RCM-11 (682) RCM-11 (356) (357)
B3	25°55.617'N 86°21.301'W	3160	75 150 250 350 450 525 600 750 900 1100 1300 1500 2000 3060 (100 MAB)	TEMP (T1278) (T1624) T/S/P (2699) (1342) TEMP (D591) (D581) TEMP (D595) (D621) 75 kHz ADCP (4865) TEMP (T1157) (T1625) S4 (08161757) (08582010) T/S/P (2702) (2701) RCM-7 (11432) (7077) TEMP (T3034) (T2260) RCM-8/7 (7582) (11432) TEMP (T3037) (T3485) RCM-11 (361) (364) RCM-11 (355)

MAB = Meters above bottom.

[] = Deployed during indicated deployment only.

Table 2.2-4c. Mooring Locations and Moored Instrument Levels for the Loop Current Study (American Sector) with Nominal Instrument Depths (Tall Moorings C1, C2 and Short Moorings D1, D2, D3, D4, D5, D7 and D8)

Mooring	Location	Water Depth (M)	Instrument Depth (M)	Instrument Type (Serial Number)
C1	26°22.536'N 86°08.597'W	3190	75 150 250 350 450 525 600 750 900 1100 1300 1500 1995 3090 (100 MAB)	TEMP (T1187) T/S/P (1719) TEMP (C919) TEMP (C926) 75 kHz ADCP (4918) TEMP (D583) S4 (08111746) (07961708) T/S/P (2693) RCM-7 (6892) TEMP (T3038) RCM-7 (6922) TEMP (T1981) RCM-11 (358) RCM-11 (348)
C2	26°10.737'N 85°38.921'W	3257	75 150 250 350 450 525 600 750 900 1100 1300 1500 1990 3157 (100 MAB)	TEMP (T1270) T/S/P (1720) TEMP (C932) TEMP (C929) 75 kHz ADCP (4914) TEMP (D585) S4 (07961709) (08161758) T/S/P (2694) RCM-7 (9524) TEMP (T1982) RCM-7/8 (9525) (9266) TEMP (T1983) RCM-11 (349) (361) RCM-11 (359)
D1	26°24.986'N 87°51.007'W	2827	2727 (100 MAB)	RCM-8 (12806) (12809)
D2	26°41.751'N 87°07.587'W	2885	2785 (100 MAB)	RCM-8 (12809) (12810)
D3	26°32.949'N 86°37.301'W	3098	2998 (100 MAB)	RCM-8 (12804) (12808)
D4	25°17.993'N 86°04.783'W	3259	3159 (100 MAB)	RCM-8 (9266) (12803)
D5	25°44.336'N 85°51.744'W	3234	3134 (100 MAB)	RCM-8 (12808) (12805)
D7	25°33.042'N 85°22.986'W	3311	3211 (100 MAB)	RCM-8 (7356) (12806)
D8	25°59.946'N 85°09.216'W	3309	3209 (100 MAB)	RCM-8 (7355) (12807)

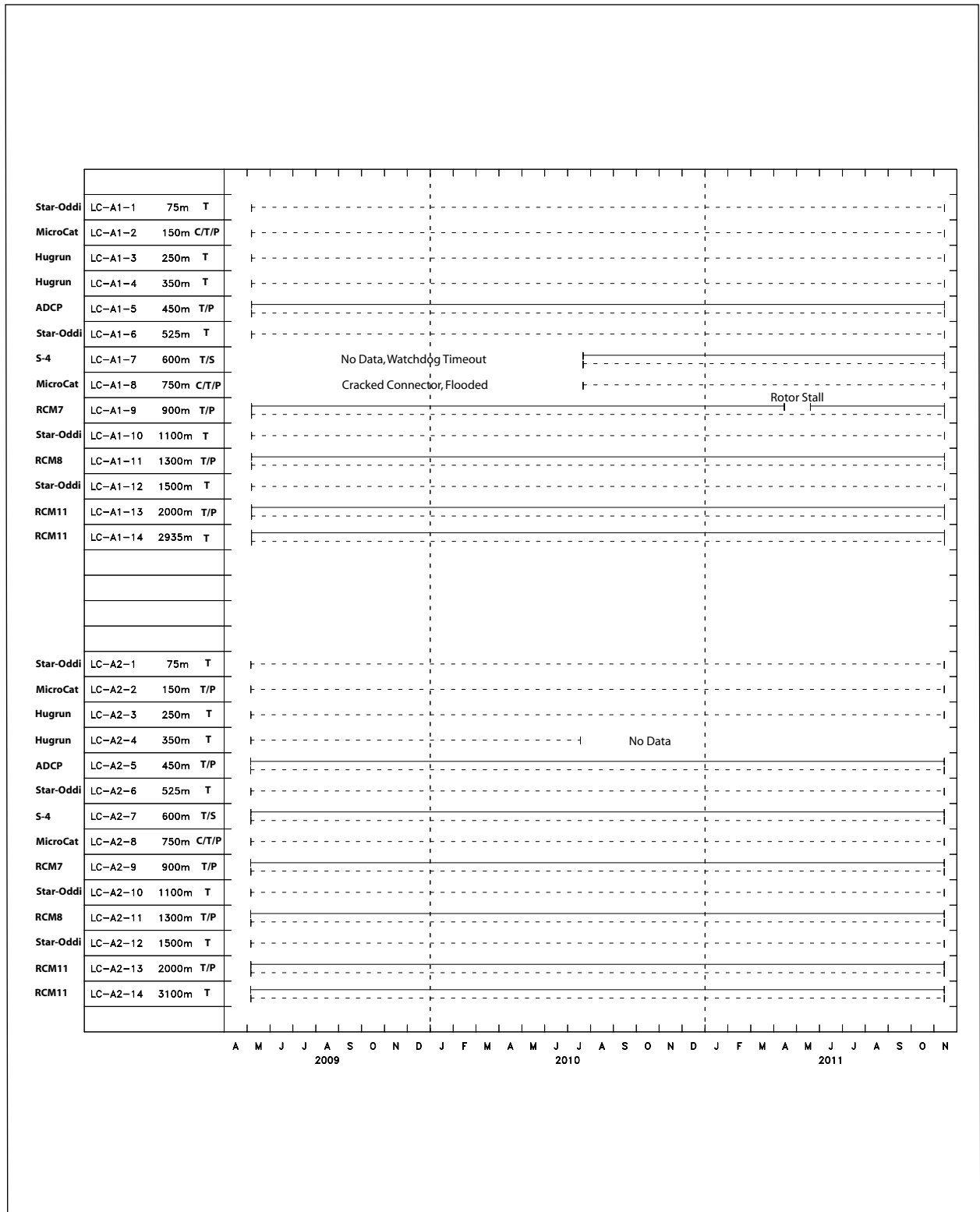


Figure 2.2-2a. Time lines of data return from moorings A1 and A2. Solid and dashed lines are velocity and scalar data, respectively.

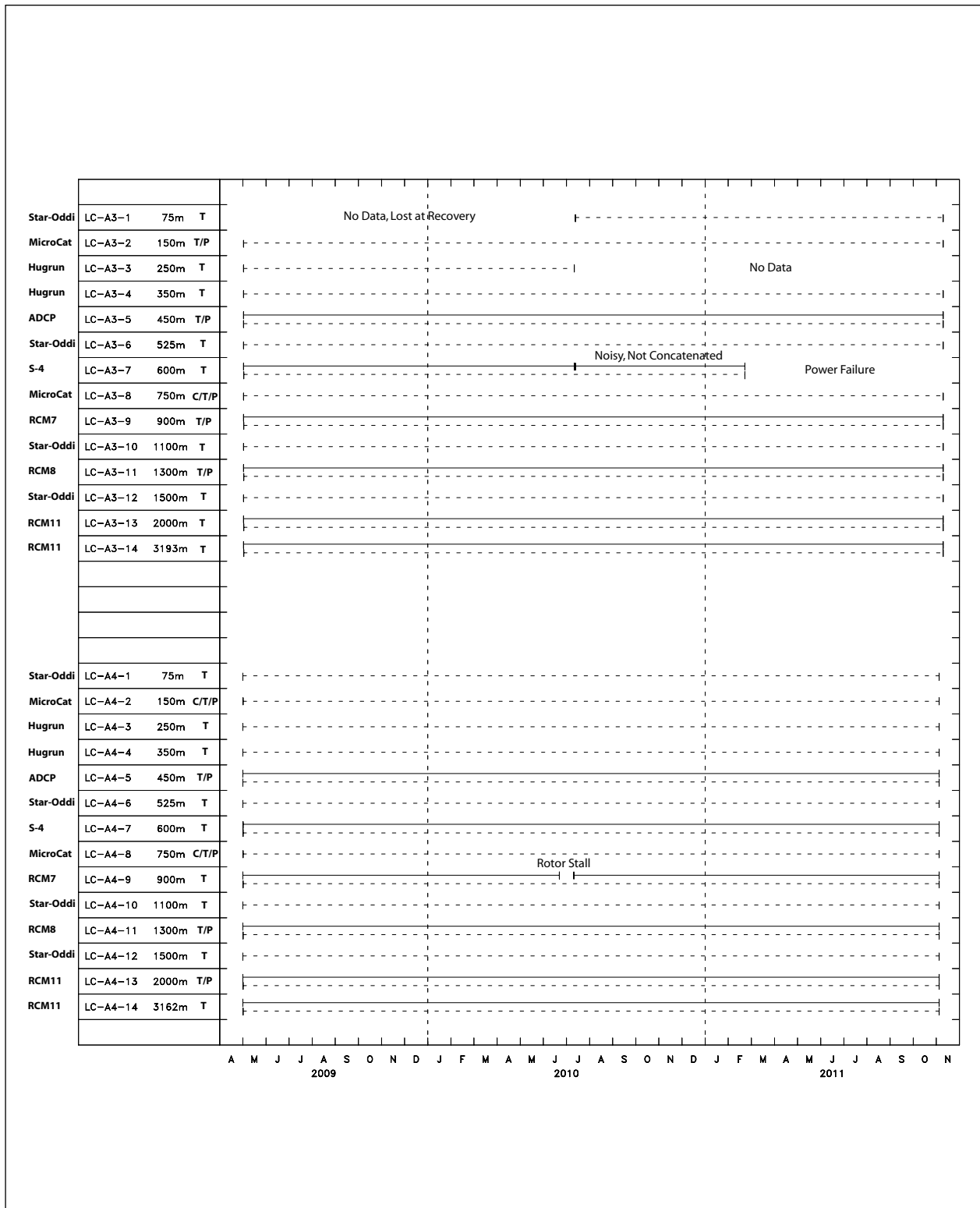


Figure 2.2-2b. Time lines of data return from moorings A3 and A4. Solid and dashed lines are velocity and scalar data, respectively.

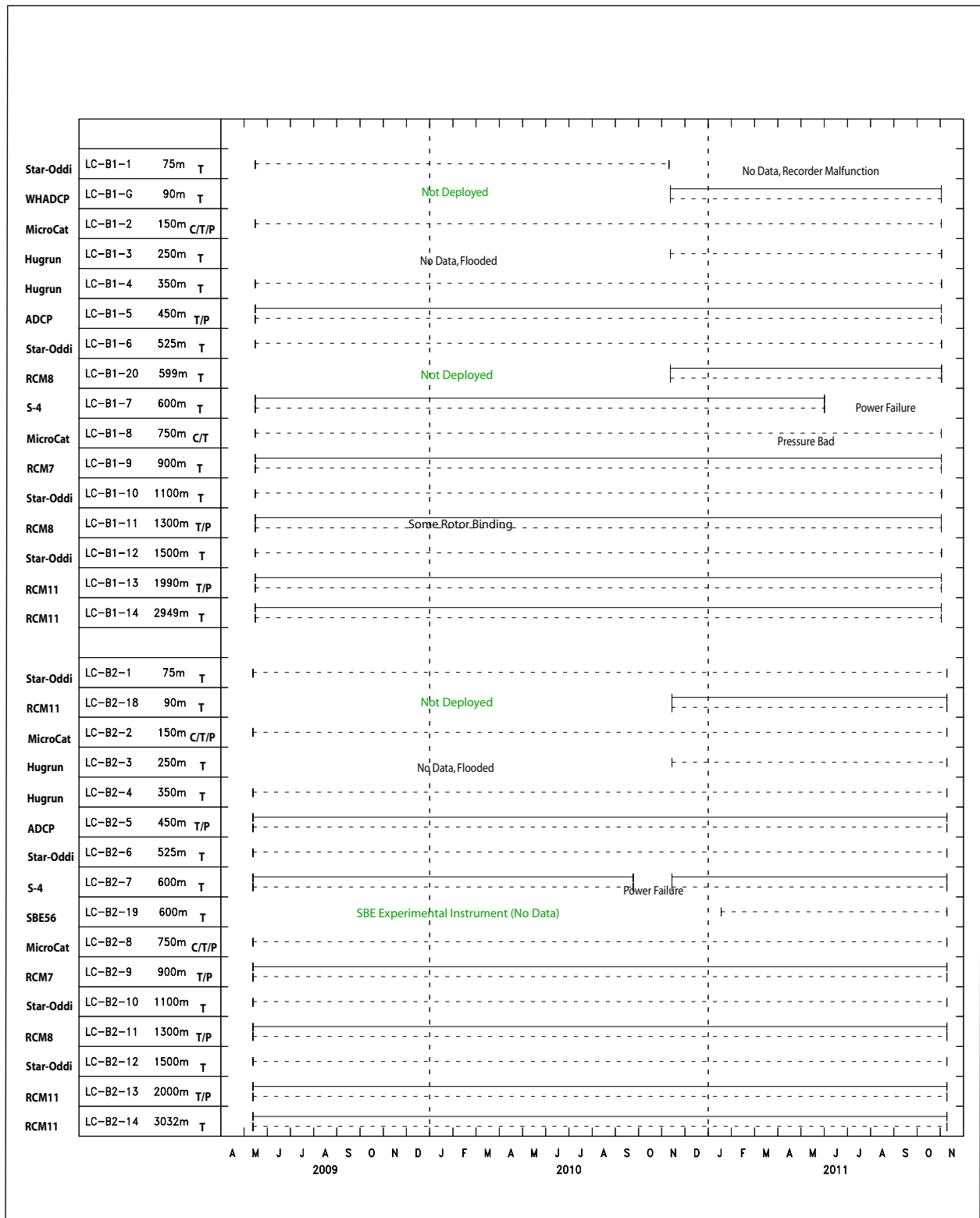


Figure 2.2-2c. Time lines of data return from moorings B1 and B2. Solid and dashed lines are velocity and scalar data, respectively.

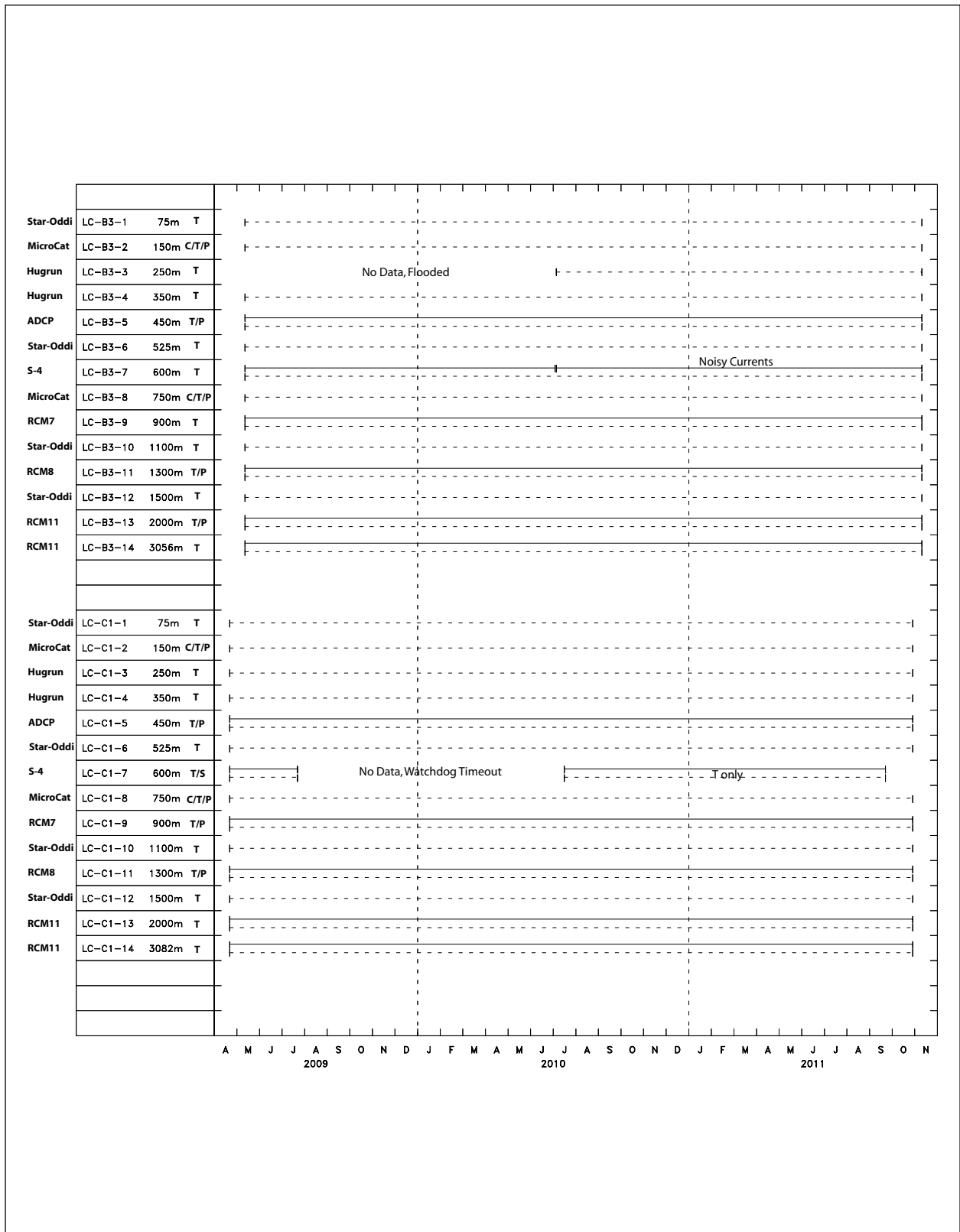


Figure 2.2-d. Time lines of data return from moorings B3 and C1. Solid and dashed lines are velocity and scalar data, respectively.

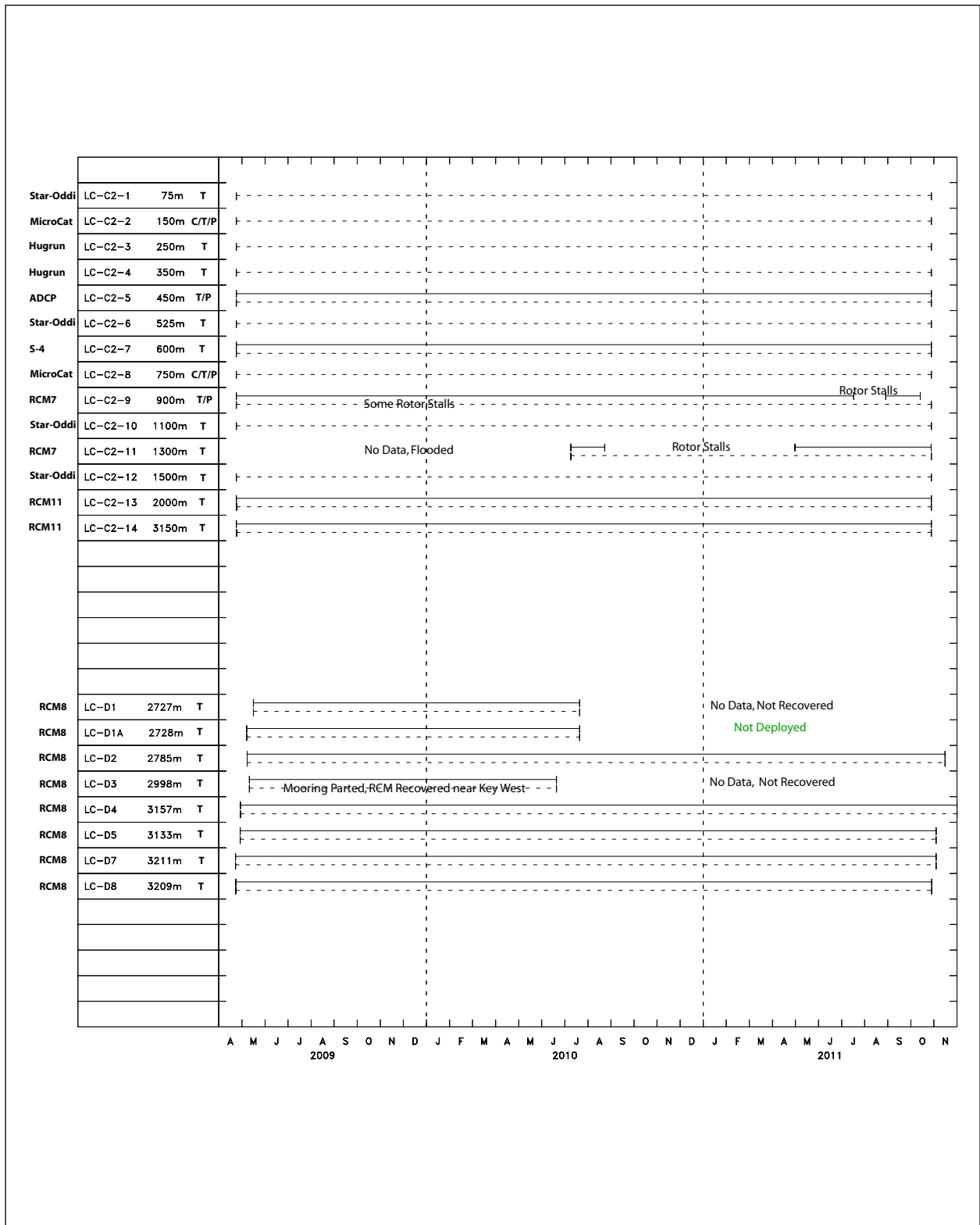


Figure 2.2-2e. Time lines of data return for tall mooring C2 and short moorings D1, D2, D3, D4, D5, D7, and D8. There was no D6 mooring. Solid lines are velocity and scalar data, respectively.

Table 2.2-5. Moored Instrument Data Return (by Good Record Count) during the Loop Current Study

Deployment	Aanderaa RCM-7/8 (CUR+T)	Aanderaa RCM-11 (CUR+T)	Hugrun Seamon Mini (T)
1	355,719/ 367,781 (25)	198,842/ 198,842 (18)	183,862/ 220,091 (20)
2	305,184/ 360,156 (28)	196,116/ 196,116 (19)	178,324/ 201,543 (18)
TOTALS	660,903/ 727,937 (53)	394,958/ 394,958 (37)	362,186/ 421,634 (38)
Percent Good	90.8%	100%	85.9%
Deployment	InterOcean S4 (CUR+T)	RD Instruments ADCP* (CUR+T)	Sea-Bird MicroCat (T+S)
1	158,300/ 198,844 (9)	198,844/ 198,844 (9)	334,106/ 355,202 (16)
2	163,661/ 196,113 (10)	196,118/ 196,118 (10)	346,820/ 346,820 (16)
TOTALS	321,961/ 394,957 (19)	394,962/ 394,962 (19)	680,926/ 702,022 (32)
Percent Good	81.5%	100%	97.0%
Deployment	Sea-Bird SeaCat (T+S)	Star-Oddi Starmon Mini (T)	GRAND TOTAL
1	42,488/ 42,488 (2)	366,006/ 376,458 (34)	1,838,167/ 1,958,550 (133)
2	45,434/ 45,434 (2)	378,314/ 386,844 (36)	1,809,971/ 1,929,144 (139)
TOTALS	87,922/ 87,922 (4)	744,320/ 763,302 (70)	3,648,138/ 3,887,694 (272)
Percent Good	100%	97.5%	93.8%

* All ADCP bin levels for each instrument counted as one (1) time series record.
 (#) = Number of instrument deployments.

A number of instrument types provided 100% data return. These included the Aanderaa RCM-11 Doppler current meter, the RD Instruments 75-kHz LongRanger and 300-kHz Sentinel ADCPs, and the SeaBird SeaCat conductivity/temperature/pressure recorders. One Sea-Bird MicroCat failure out of 32 deployments occurred where the instrument was found to have a sheared off I/O connector at recovery. The resultant data return for this instrument type was 97.0%. Also, one Star-Oddi temperature recorder failed to collect data and a second was lost during mooring recovery operations, yet the data return for this type instrument (from 70 deployments) was 97.5%.

Four data logging instruments were found to be flooded at recovery. One of these was an Aanderaa RCM-7 rotor-type current meter for which the source of the leak was not obvious. Three others were Hugrún temperature recorders with plastic housings. In addition to these, two other Hugrúns had non-responsive recorders at recovery, so no data were recovered from them, as well. The large number of Hugrún failures (only 85.9% data return) is thought to be due to age-related fatigue of the plastic housing and the instrument electronics. These GFE instruments have since been retired.

Two Aanderaa RCM-8 rotor-type current meters deployed on short moorings were not recovered. It is believed that these losses were due to release failures as acoustic release problems had been experienced at a number of the short mooring sites. In spite of the loss of two

instruments and the flooding of a third, the data return for the Aanderaa rotor-type current meters was 90.8% from 53 instrument deployments.

Finally, the InterOcean S4 electromechanical current meter had an 81.5% data return from 19 instrument deployments. Two instruments were affected by firmware mismatches that caused them to stop collecting data early or to collect no data at all. Three others experienced power failures during the deployment which caused them to also stop collecting data before the moorings were recovered.

2.3 CTD DATA

Forty-eight CTD casts were made with planned profiling depths of 1500 meters at each of the PIES deployment sites. Their purpose was to help in creating an appropriate Gravest Empirical Mode (GEM) to be used to calibrate the PIES data. These casts are documented in Table 2.3-1.

2.3.1 CTD Data Acquisition Systems

The CTD data acquisition system used on most of the cruises consisted of a Sea-Bird 911 Plus system provided and operated by the technical staff onboard the R/V PELICAN, a UNOLS vessel operated by Louisiana Universities Marine Consortium (LUMCON) at Cocodrie, Louisiana. This particular CTD system was equipped with redundant Sea-Bird CT sensors, a Datasonics altimeter and a Sea-Bird Carousel Water Sampler with Niskin water sample bottles. A second system used onboard the R/V WEATHERBIRD II in July 2010 consisted of a Sea-Bird SBE 25 and a Rosette Water Sampler with Niskin water sample bottles. This latter system was provided by Florida Institute of Oceanography (FIO) and operated by one of their technical staff.

The CTD system sensors were calibrated periodically at the manufacturer's facilities over the course of the study, and bottle salinities were taken at the bottom of each cast as a further check on instrument salinity calibration. These were run on a Guildline 8400B Autosal Laboratory Salinometer. No calibration problems were detected during the 30-month study period. Also, the lowering speed of the CTD was varied from 15 meters per minute for the first 90 meters of descent to 30 meters per minute from 90 to 200 meters depth, and then increased to 60 meters per minute once below the 200 meter level. This was to eliminate or reduce the possibility of CT sensor mismatch which can cause salinity spiking when passing through a sharp thermocline.

Table 2.3-1. Listing of CTD Casts made at PIES Sites during the Loop Current Study

Sta. /CTD Depth (M)	Date (UTC)	Time (UTC)	Cruise
P51 / 1500	05/06/2009	1137 - 1407	PE09-34
P51 / 1500	07/20/2010	0035 - 0138	PE11-01
P52 / 1501	05/06/2009	0150 - 0245	PE09-34
P52 / 1425	11/09/2010	2210 - 2321	PE11-16
P53 / 1500	07/19/2010	0621 - 0723	PE11-01
P54 / 1501	07/16/2010	0502 - 0555	PE11-01
P54 / 1500	07/16/2011	2026 - 2153	PE12-02
P55 / 1501	07/16/2010	2005 - 2124	PE11-01
P55 / 1439	11/13/2010	0735 - 0850	PE11-16
P56 / 1501	07/17/2010	0328 - 0457	PE11-01
P56 / 1500	11/10/2010	0437 - 0521	PE11-16
P57 / 1384	05/05/2009	0255 - 0419	PE09-34
P57 / 1502	07/17/2010	2205 - 2312	PE11-01
P57 / 1500	07/19/2011	2200 - 2301	PE12-02
P58 / 1501	07/15/2010	0537 - 0654	PE11-01
P58 / 1500	10/26/2011	1209 - 1320	PE12-16
P59 / 1500	06/28/2010	2320 - 0043	PE11-01
P59 / 1418	11/11/2010	2006 - 2050	PE11-16
P60 / 1501	07/03/2010	0015 - 0122	PE11-01
P60 / 1501	07/10/2010	2342 - 0040	PE11-01
P60 / 1237	11/11/2010	0420 - 0549	PE11-16
P61 / 1501	07/10/2010	1755 - 1904	PE11-01
P61 / 1499	11/04/2011	2149 - 2248	PE12-16
P62 / 1500	06/29/2010	1455 - 1626	PE11-01
P62 / 1499	10/26/2011	2252 - 0000	PE12-16
P63 / 1501	06/29/2010	0405 - 0510	PE11-01
P63 / 1369	11/12/2010	0200 - 0304	PE11-16
P64 / 1501	05/11/2009	0619 - 0805	PE09-34
P64 / 1500	07/02/2010	1840 - 1957	PE11-01
P64 / 1331	11/12/2010	0652 - 0800	PE11-16
P65 / 1501	07/10/2010	0227 - 0332	PE11-01
P65 / 1500	07/19/2011	1205 - 1314	PE12-02
P65 / 1499	11/03/2011	2238 - 2359	PE12-16
P66 / 1500	06/29/2010	2022 - 2137	PE11-01
P66 / 1500	07/17/2011	1824 - 1920	PE12-02
P67 / 1501	06/30/2010	0154 - 0301	PE11-01
P67 / 1200	10/28/2011	1353 - 1515	PE12-16
P68 / 1502	06/30/2010	1510 - 1630	PE11-01
P69 / 1498	07/28/2010	0635 - 0923	WB10-016
P70 / 1990	07/29/2010	0455 - 0725	WB10-016
P70 / 1500	07/18/2011	2222 - 2322	PE12-02
P71 / 1500	07/04/2010	0600 - 0656	PE11-01
P71 / 1496	10/28/2011	0710 - 0820	PE12-16
P72 / 1498	07/27/2010	1545 - 1902	WB10-016
P73 / 1371	07/27/2010	2218 - 0307	WB10-016
P74 / 1501	07/27/2010	0237 - 0615	WB10-016
P74 / 1500	07/18/2011	1621 - 1719	PE12-02
P75 / 1497	07/27/2010	0910 - 1242	WB10-016

2.4 CICESE MOORING DATA

2.4.1 Introduction

In addition to the American sector moorings, current meter data are available from 10 BOEM-funded moorings (N1-N4, E1-E5 and EN in Figure 1.2-1) deployed by CICESE within the Mexican EEZ in water depths ranging from 127 m to 3354 m. Also, CICESE deployed eight additional moorings extending halfway across the Yucatan Channel (Moorings Y1-Y7 and YN). The locations and deployment periods for these moorings are presented in Table 2.4-1 and timelines for each instrument level on each mooring are presented in Figure 2.4-1a-b.

2.4.2 Instrumentation

The CICESE moorings were instrumented with a number of different type current meters. These included Aanderaa RCM-11 and SeaGuard (Doppler type) current meters, Nortek Aquadopp current meters, and RD Instruments 75-kHz LongRanger and 300-kHz WorkHorse ADCPs. Teledyne Benthos 865-A acoustic releases were used with each of the current meter moorings. In addition to providing a timeline of the data return for each instrument level on each mooring during the deployment period, Figure 2.4-1a-b also indicates which type instruments were used at each depth on each mooring.

Table 2.4-1. Mexican Mooring Locations and Deployment Periods during the Loop Current Study

Mooring	Location	Water Depth (M)	Deployment Period
N1	23°45.70'N, 87°55.11'W	130	05/31/2009 - 05/07/2011
N2	24°11.80'N, 87°34.01'W	500	05/31/2009 - 05/07/2011
N3	24°23.90'N, 87°24.68'W	1205	05/31/2009 - 05/07/2011
N4	24°57.47'N, 87°04.95'W	3352	06/01/2009 - 05/06/2011
E1	22°23.01'N, 87°00.43'W	127	06/02/2009 - 05/09/2011
E2	22°49.81'N, 86°38.36'W	501	06/02/2009 - 05/09/2011
E3	23°03.37'N, 86°25.98'W	998	06/02/2009 - 05/08/2011
E4	23°14.48'N, 86°17.58'W	1994	06/02/2009 - 05/08/2011
E5	23°36.17'N, 86°01.37'W	3354	06/01/2009 - 05/08/2011
EN	23°04.09'N, 86°47.01'W	500	06/02/2009 - 04/26/2010
Y1	21°32.42'N, 86°42.00'W	23	04/24/2010 - 04/18/2011
Y2	21°32.44'N, 86°29.74'W	68	06/05/2009 - 05/11/2011
Y3	21°33.46'N, 86°27.00'W	124	06/04/2009 - 05/11/2011
Y4	21°33.96'N, 86°21.30'W	526	06/04/2009 - 04/18/2010
Y5	21°35.55'N, 86°13.64'W	1206	06/12/2009 - 05/11/2011
Y6	21°38.81'N, 85°59.16'W	1880	06/04/2009 - 05/11/2011
Y7	21°38.37'N, 85°42.97'W	2030	06/03/2009 - 05/10/2011
YN	21°41.65'N, 86°20.50'W	495	06/03/2009 - 08/29/2009

Note: The initial deployments of the Mexican sector moorings occurred 1–2 months after the U.S. sector deployments, and were recovered after 24 months, approximately 5–6 months before the U.S. sector moorings were recovered.

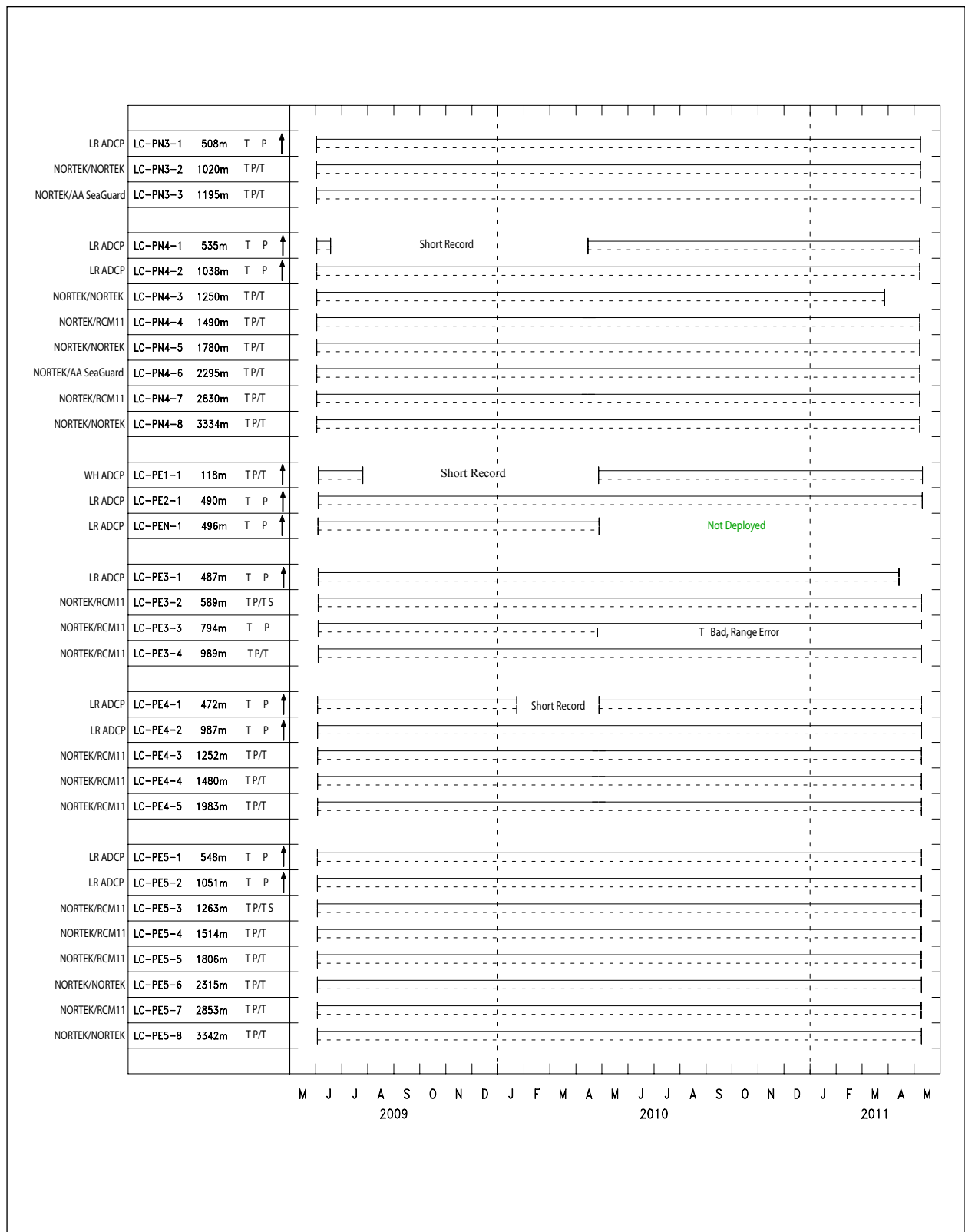


Figure 2.4-1a. Time lines of data return from CICESE moorings N3, N4, E1, E2, E3, E4, and E5. Solid and dashed lines are velocity and scalar data, respectively.

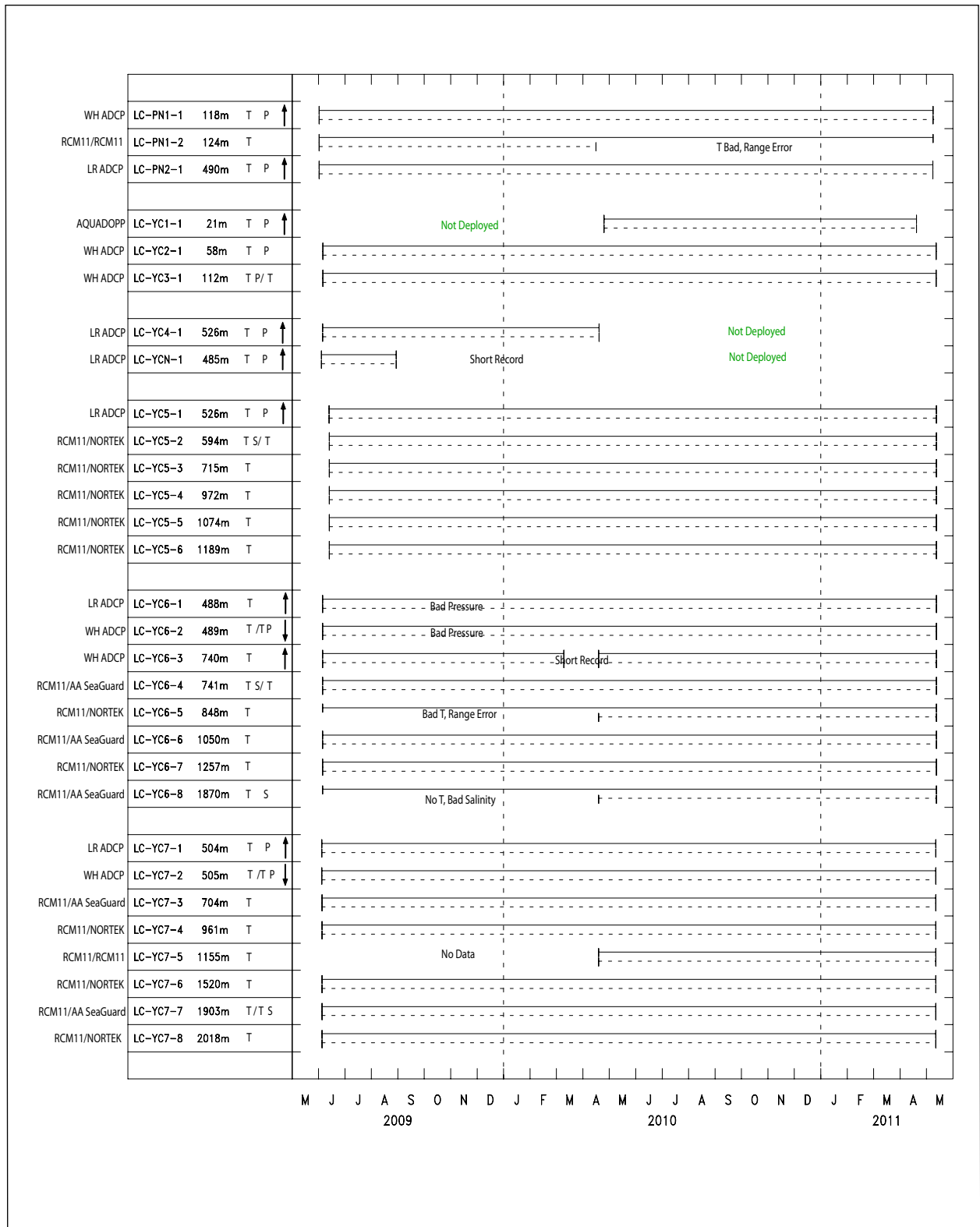


Figure 2.4-1b. Time lines of data return from CICESE moorings N1, N2, Y1, Y2, Y3, Y4, YN, Y5, Y6, and Y7. Solid and dashed lines are velocity and scalar data, respectively.

2.5 PIES

A mesoscale-resolving array of twenty-five inverted echo sounders with pressure gauges (PIES) was deployed in April 2009 and recovered in October-November 2011 as part of the Loop Current study (Figure 1.2-1). The PIES is a bottom-mounted instrument that emits 12 kHz sound pulses and measures the round trip travel times, τ (tau), of these pulses from the sea floor to the sea surface and back. It is also equipped with a pressure gauge, and measures bottom pressure. A detailed description of the instrument and the initial data processing may be found in Hamilton et al. (2003) and Donohue et al. (2006). Here, aspects of data processing specific to this data set are reported. The data return from the PIES was excellent (Figures 2.5-1 and 2.5-2), and full deployment records are available from each of the instruments.

The broad extent of the array of PIES, nominally 89°W to 85°W, and 25°N to 27°N, combined with measurements from the tall moorings enabled a quantitative mapping of the regional circulation. Knowledge of deep correlation scales from previous Gulf experiments and our science objective to map deep relative vorticity, set the nominal 50 km spacing of the PIES and current meter moorings. The array placement within the Gulf was guided by historical analysis that indicated where eddy separation was most likely to occur. The array size encompassed the Loop Current from east to west. The experiment duration of 30 months captured three Loop Current Eddy formation events: Ekman, Franklin, and Hadal. Round-trip acoustic travel time measured by the inverted echo sounders produced estimates of vertical profiles of temperature, salinity, and density, by utilizing empirical relationships established with historical hydrography. An exponential-linear drift curve was fitted to the difference between each bottom pressure record and the time series of current-meter-derived geostrophic pressure maps, as described in Donohue et al. (2010). This methodology de-drifted and leveled the pressure records simultaneously. Further details are given in Section 2.5.4. Deep pressure records combined with estimated horizontal density gradients yielded referenced geostrophic velocities. With this array, 4-D maps of temperature, salinity, density, velocity and sea-surface height (SSH) were produced (Figure 2.5-3).

2.5.1 Gravest Empirical Mode Method

For this experiment PIES τ measurements were converted into profiles of temperature, salinity, and specific volume anomaly through the use of a look-up table. A relationship has been established between a τ index and vertical profiles of temperature and salinity using historical hydrography. This has been designated the Gravest Empirical Mode (GEM) representation (e.g., Meinen and Watts 2000). The procedure consists of two steps. First, the empirical look-up table is calculated, and second, the PIES-measured τ is converted to the τ_{index} of the look-up table.

2.5.1.1 Determine τ_{index}

Round-trip travel time between the 150 and 1000 dbar surface, $\tau(150-1000)$ was used as the τ_{index} . The 150-dbar upper limit of the τ integration avoided the influence of the seasonal cycle most evident in this upper layer. Further refinements discussed below detail a seasonal correction. The 1000-dbar lower limit of the τ integration balanced two needs: extend the integration below the thermocline and retain as many of the acquired historical hydrocasts as possible.

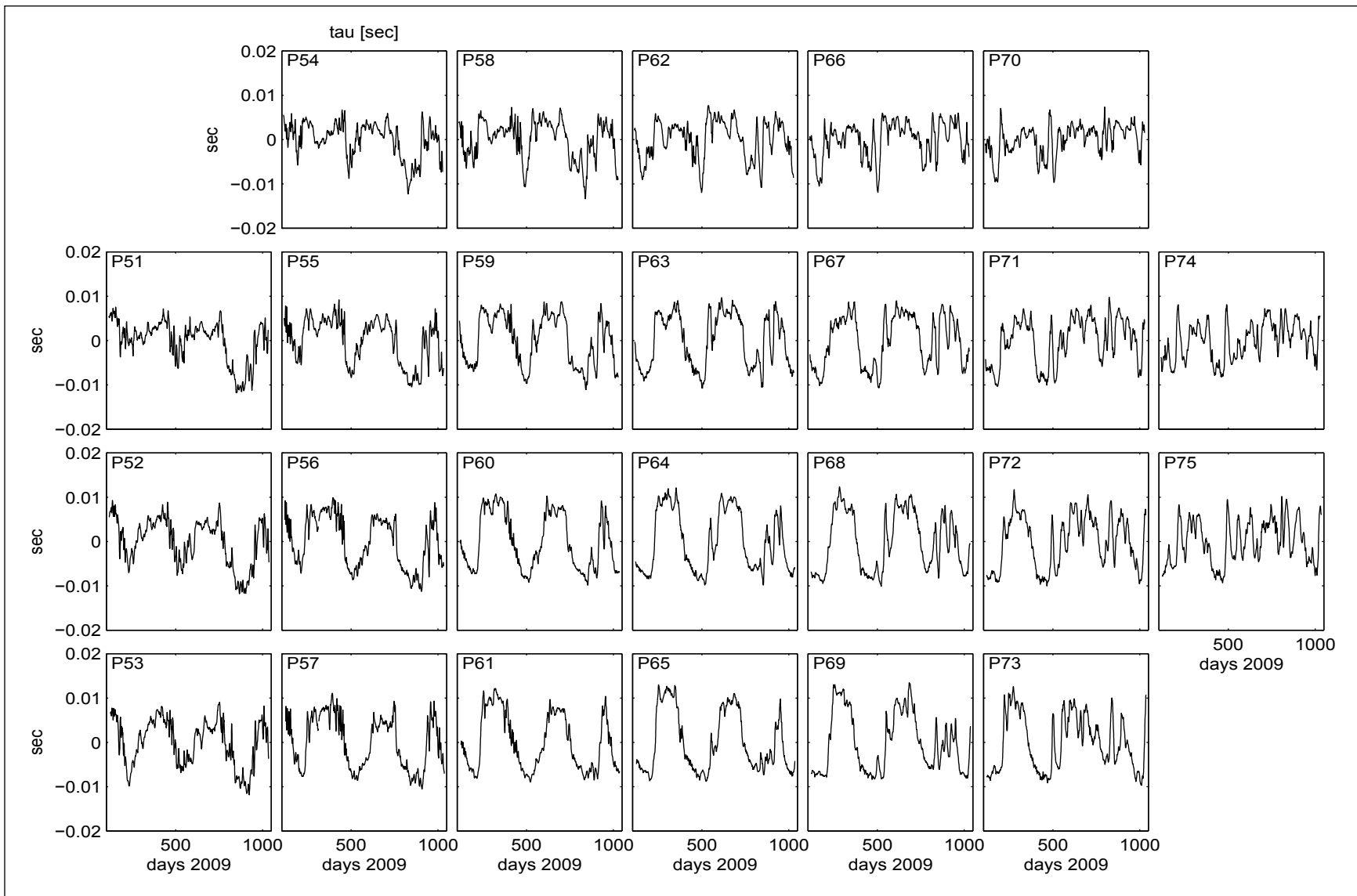


Figure 2.5-1. Time series of tau anomaly in seconds in panels arranged according to approximate geographic location. Instrument number is noted in the upper left corner of each subplot.

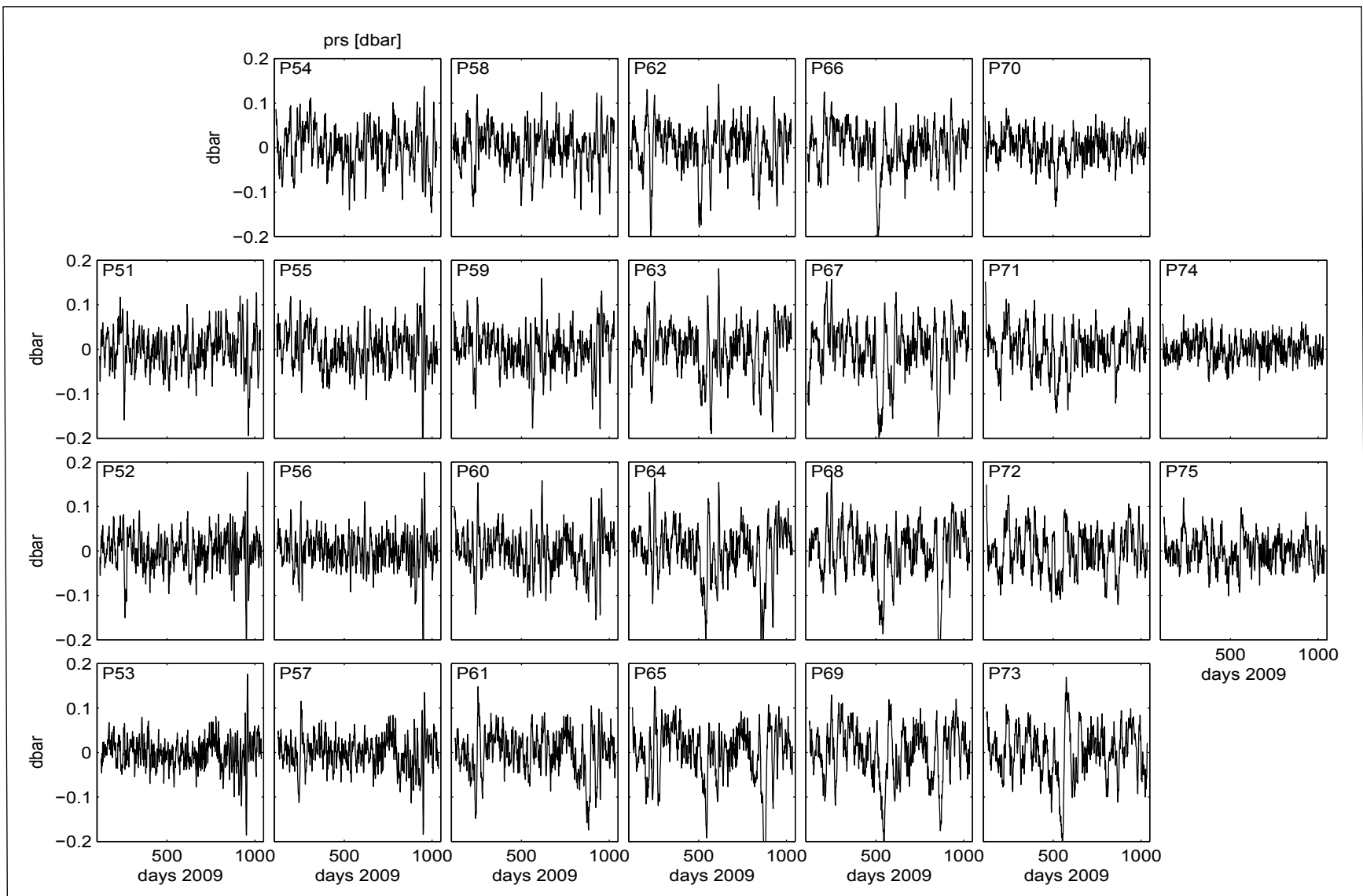


Figure 2.5-2. Time series of bottom pressure anomaly in dbar arranged according to approximate geographic location. Instrument number is noted in the upper left corner of each subplot.

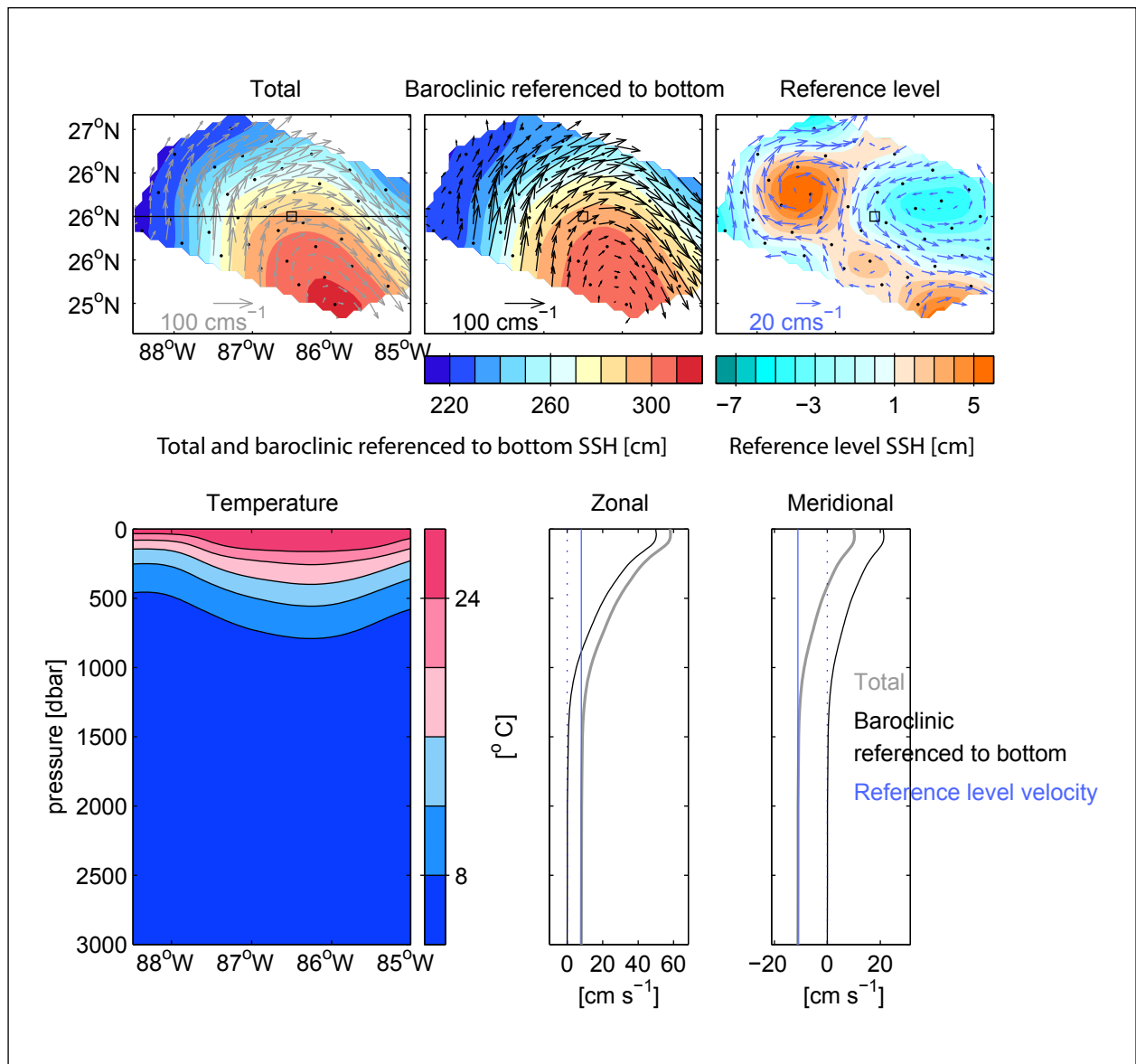


Figure 2.5-3. Several views of the current and temperature structure in the region for 5 May 2009 provided by the PIES and current meter measurements. Top panels: Total sea surface height in plan view (left), displaying its baroclinic contribution referenced to the bottom, $\varphi(z=0)_{3000}/g$ (middle), and reference level contribution, $p_b/(\rho g)$ (right), both scaled to sea surface height. $\varphi(z=0)_{3000}$ is geopotential height at the surface relative to 3000 dbar, p_b is bottom pressure, ρ is near-bottom density and g is gravity. Anticyclonic circulations are shown by reddish hues; cyclonic circulations by bluish hues. Mapped current vectors plotted at 20 km spacing. PIES and current meter mooring sites are denoted by black filled circles. Bottom left panel: Cross-section of temperature in $^{\circ}\text{C}$ along the horizontal black line in the top left panel. Bottom two right panels: Zonal and meridional velocity (total: grey, reference level velocity: blue, and baroclinic referenced to the bottom: black) at the black square shown in the upper panels.

2.5.1.2 Assemble Regional Hydrographic Data Set

The regional hydrographic data set accumulated for the Exploratory Study of Deepwater Currents in the Gulf of Mexico (Donohue et al. 2006), consisting of 777 casts, was initially used. An additional 359 profiles were added from four sources: hydrocasts taken during the Loop Current Study field program (49 casts), NOAA casts taken following the Deepwater Horizon oil spill (48 casts), Argo float profiles (27 casts) and historical data from CICESE (235 casts). The spatial and temporal distribution of the resulting data set (of 1136 casts) is shown in Figure 2.5-4. Hydrocasts represent about 30 years of sampling. The bulk of casts extend between 1000 to 2000 dbar with relatively few casts below 2000 dbar.

2.5.1.3 Sort Hydrographic Data by τ_{index}

Hydrocasts were linearly interpolated to a uniform 10-dbar grid and sorted by $\tau(150-1000)$. Samples are sparse for the lowest τ_{index} range (<1.122 sec) that would be found in the very center of the loop in the Loop Current. It was found that measured τ when converted to τ_{index} (see discussion below for the methodology to convert measured τ to τ_{index}) could occasionally extend to lower values than the minimum GEM τ_{index} . Therefore, the GEM had to be extended to lower τ_{index} values. Synthetic profiles were constructed from temperatures measured by the tall moorings to extend the low τ_{index} portion of the GEM. First, a τ_{index} time series was determined for each mooring by mapping PIES τ_{index} time series to each mooring site. Second, a time series of temperature as a function of pressure was calculated for each temperature record. Recall that pressure gauges on each mooring tracked mooring motion. Data were restricted to times when the mooring drawdown was relatively small (within ± 15 dbar of nominal level). Third, temperature was averaged in 0.5 ms τ_{index} bins from 1.1145 to 1.1222 sec and interpolated onto a 10 dbar grid from the surface to 1500 dbar. A total of 124 synthetic profiles were added to the database (Figure 2.5-5).

To make synthetic salinity profiles, the mean θ/S relationship for $\tau_{index} < 1.122$ sec (41 profiles) was created. A salinity profile was then obtained for every synthetic temperature profile by interpolating the mean θ/S relationship.

Every 10 dbar, a cubic smoothing spline was fitted to temperature as a function of $\tau_{index} = \tau(150-1000)$ (Figure 2.5-6). Root-mean-square residual, rms, for each curve provides an indication of the departure any individual profile might have from the GEM curve. The rms values for temperature are small, 0.30°C within the thermocline, decreasing further with increasing depth. The curves show that a functional relationship exists between the integrated variable, $\tau(150-1000)$ and vertical profiles of temperature. The two-dimensional GEM fields are shown in Figure 2.5-7. Note that there is little structure in the fields below 1000 dbar and this reflects the uniform deep-water properties in the Gulf of Mexico.

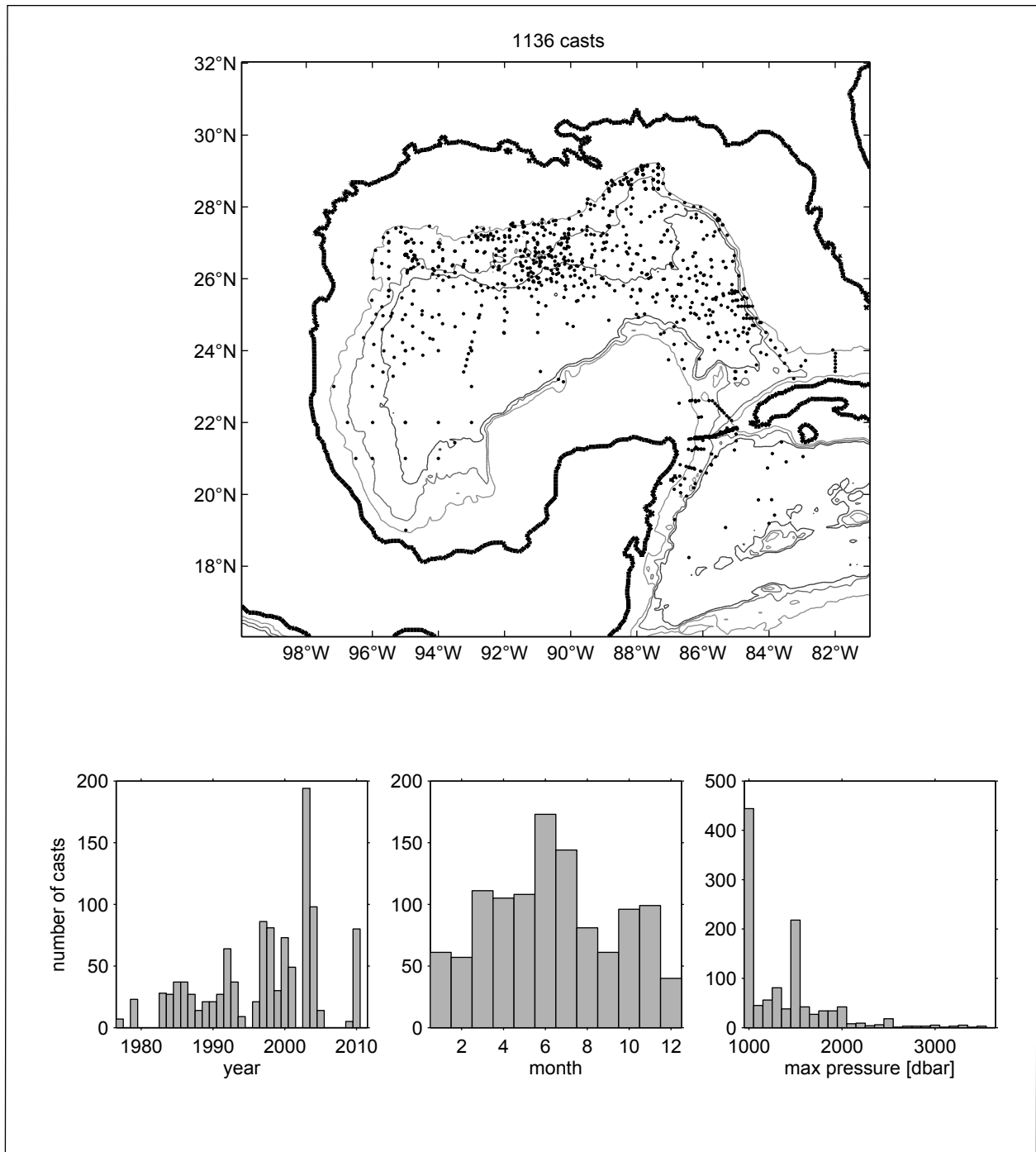


Figure 2.5-4. Spatial and temporal distribution of hydrocasts used to construct the Gravest Empirical Mode. Data provided by the Gulf of Mexico HYDRO Database compiled by TAMU as part of the MMS-funded Deepwater Reanalysis and additional stations provided by SAIC, NOAA casts taken following the Deepwater Horizon oil spill, historical data from CICESE and Argo profiling float hydrocasts. Top panel: Spatial distribution of the hydrocasts with bathymetry contoured every 1000 m. Bottom panels: Histograms of the year of hydrocast (left), month of hydrocast (middle) and maximum hydrocast pressure (right).

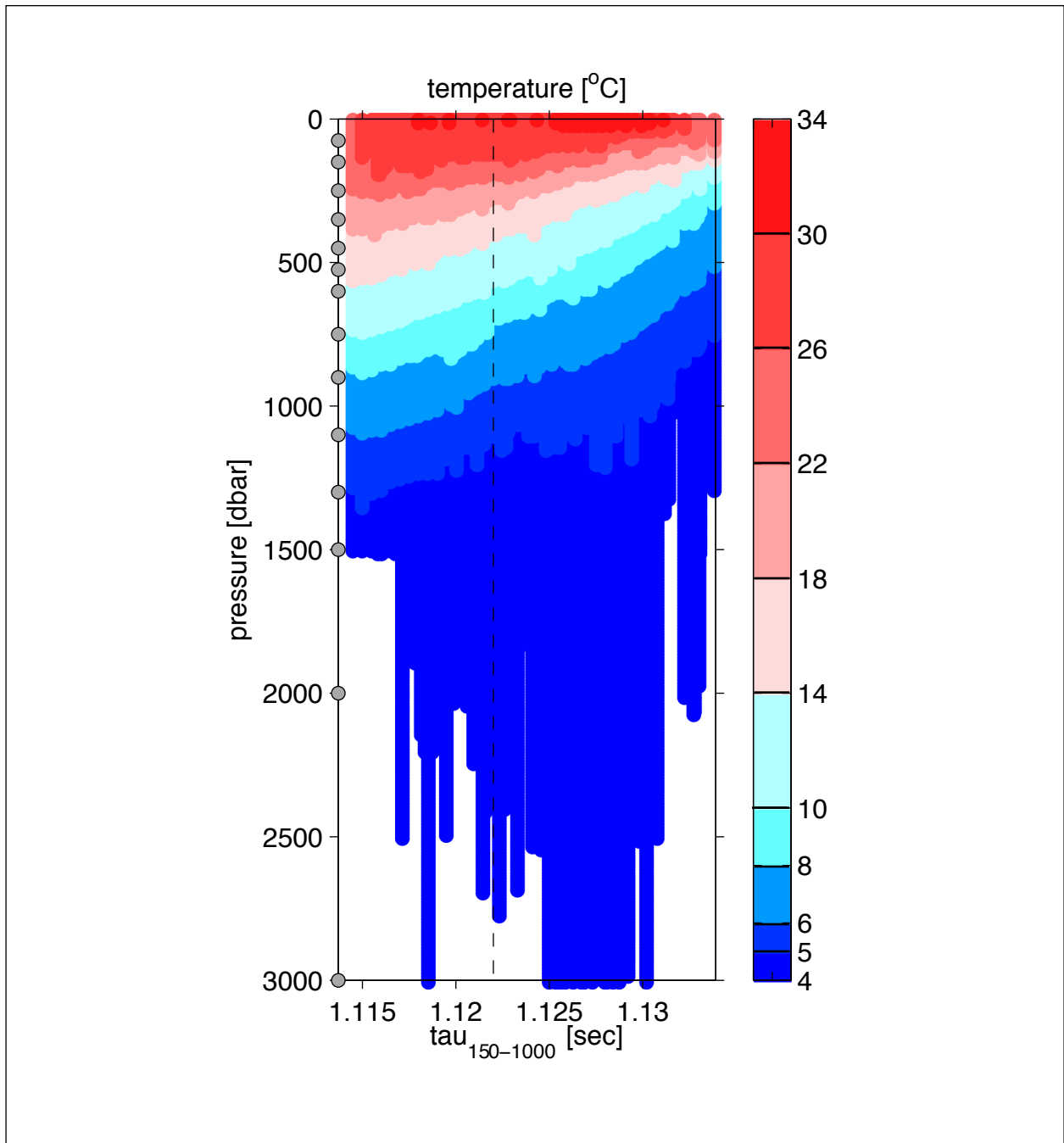


Figure 2.5-5. Temperature profiles interpolated every 10 dbar and sorted by $\tau_{150-1000} = \tau_{\text{index}}$. Synthetic profiles supplemented the CTDs to the left of the dashed line in the deepest-thermocline portion on the warm side of the Loop Current, where we otherwise had only a sparse non-representative distribution. The dots along the y-axis (up to 1500 m) show the nominal depths at which moored temperatures and pressures gave $T(p)$ profiles to join with PIES mapped tau measurements to contribute to the GEM lookup table. We did not use the two deepest sensors (2000 and bottom) because of the large vertical sensor spacing and small temperature gradient below 1500 m.

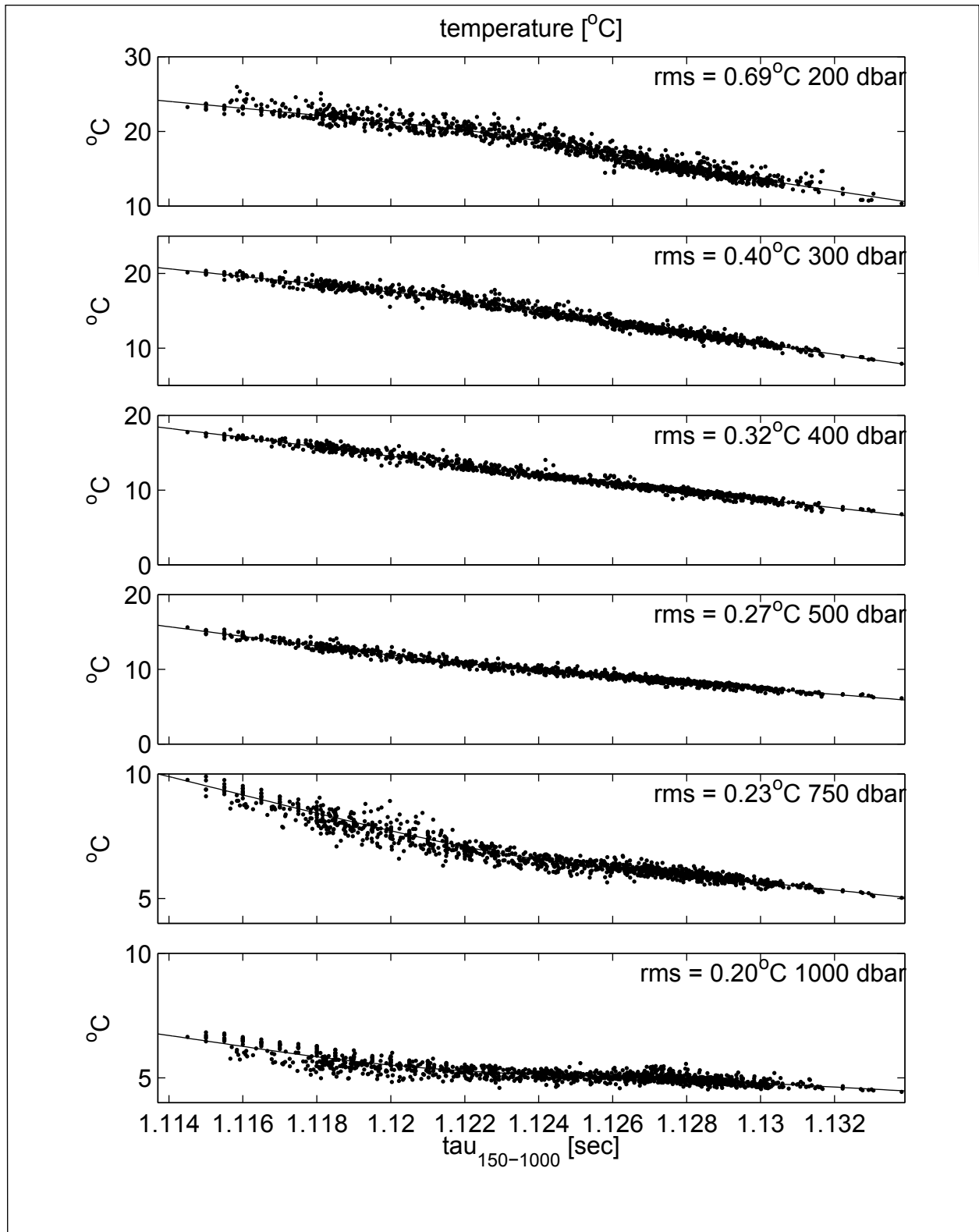


Figure 2.5-6. Scatter plots of temperature versus $\tau_{\text{index}} = \tau(150 - 1000)$ for six representative pressure levels. At each pressure, temperature versus $\tau(150 - 1000)$ data were fit by a cubic smoothing spline (solid curve).

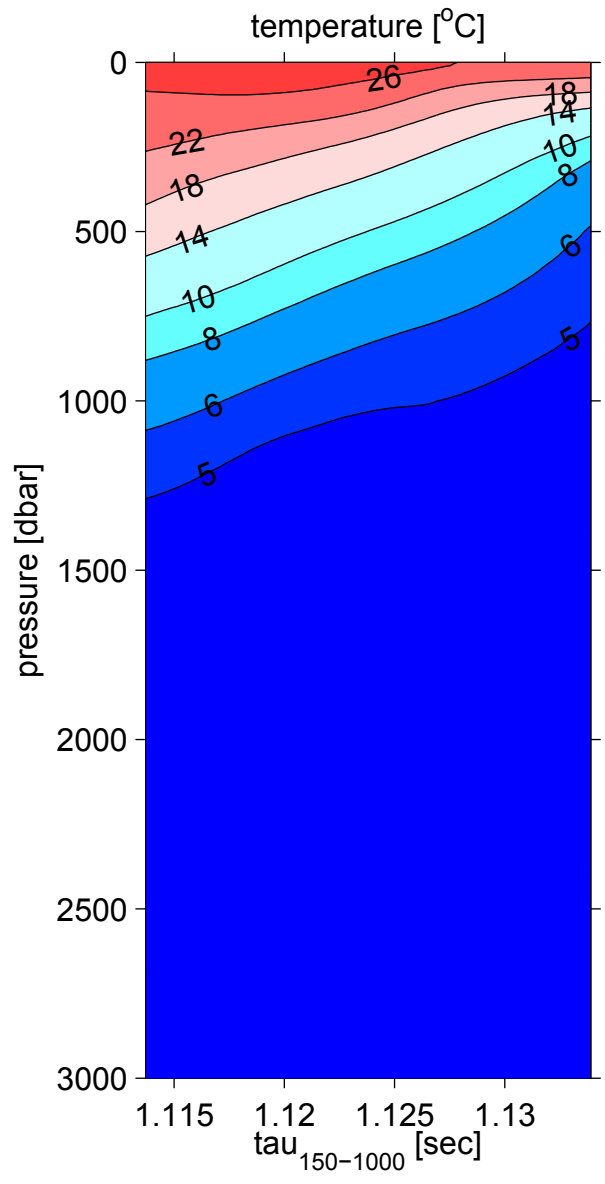


Figure 2.5-7. Contour plot of the cubic smoothing spline fits for the temperature GEM field.

2.5.1.4 Seasonal Correction

A seasonal depth-dependent temperature model can be added to the upper 150 m of the GEM lookup table, generated from the observed monthly-averaged departures of hydrographic profiles from the GEM temporal-mean structure. It incorporates seasonal variations in SSH due to thermal expansion/contraction. The seasonal model is shown in Figures 2.5-8 and 2.5-9. Because the model does not depend on location within the Gulf, it has no effect upon the velocities. A seasonal correction for τ_{index} is described later in this section.

A seasonal depth-dependent model, generated in a manner similar to that described above for temperature, was added to the geopotential anomaly calculated from the GEM temperature and salinity fields. The model is shown in Figure 2.5-10. Adding the seasonal cycle improved agreement between altimetric SSH and PIES-estimated SSH shown later. The peak-to-peak range of the seasonal cycle is $1.16 \text{ m}^2\text{s}^{-2}$.

2.5.2 Conversion of Measured τ to $\tau(150-1000) = \tau_{\text{index}}$

In order to use the GEM fields with the PIES τ measurements, measured τ was converted to $\tau(150-1000)$. Advantage was taken of the fact that τ at any deep pressure is linearly related to τ at any other deep pressure, $\tau(150-1000) = A \times \tau_{p_1} + B$. Historical hydrography established the slope of this relationship and hydrocasts taken during the PIES deployment, current meter turnaround and PIES recovery cruises determined B for each time series. The majority of sites had two calibration casts. Sites P53, P68, P69, P72, P73 and P75 had only a single calibration cast, while three sites, P57, P64 and P65 had three calibration casts. Calibrations at PIES sites with two or more hydrocasts generally agreed with each other within 1 millisecond, except where casts were taken during periods of rapidly changing τ (sites P57, P58, P64 and P67). The mean pressure of each instrument was determined from the record average pressure adjusted for the vertical offset between the pressure sensor and the transducer (0.6 dbar) and mean atmospheric pressure (10.16 dbar). Time series were filtered with a 72-hour 4th order Butterworth filter and subsampled at 12-hour intervals. The final $\tau(150-1000)$ records are shown in Figure 2.5-11.

Before measured τ records were converted to $\tau_{\text{index}} = \tau(150-1000)$, a seasonal τ signal was subtracted from the τ records. This seasonal signal was determined from the historical hydrography in a manner similar to the seasonal temperature adjustment model described above. Here, the influence of the seasonal cycle in τ between the surface and 150 dbar was considered since the hydrography showed that there is little seasonal signal below 150 dbar. The scatter plot of $\tau(0-150)$ versus $\tau(150-1000)$ was largely due to the seasonal cycle and it was determined that the amplitude of the residual was 0.3147 milliseconds (Figure 2.5-12). The correction was small, about 2% of the total range in $\tau(150-1000)$.

The error in the time series of $\tau_{\text{index}} = \tau(150-1000)$ was estimated to be near 1.07 ms. The methodology to determine the errors in τ follows Donohue et al. (2010). This error derives from the measured hourly τ error, 0.05 ms; the residual of the seasonal correction to τ , 0.3 ms; the conversion from τ to τ_{index} , 0.25 ms, and a τ_{index} calibration error (from the CTDs at a given site) of 1.0 ms.

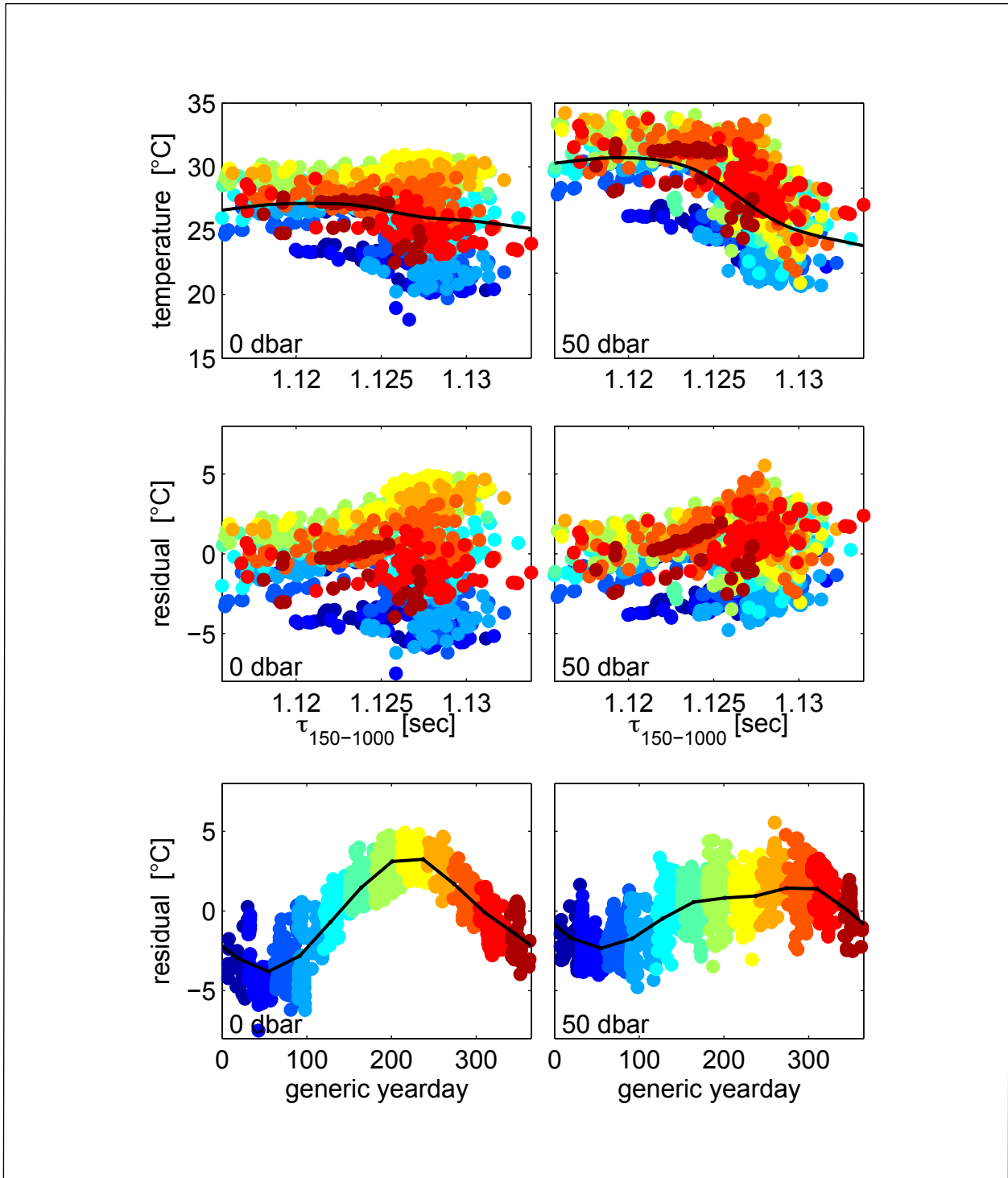


Figure 2.5-8. Upper panels: Scatter plots of temperature versus $\tau(150-1000)$ for surface (left) and 50 dbar (right) with the cubic spline fit shown as a solid dark line. All samples in all panels are color coded by generic yearday transitioning from blue in January to red in December. Middle panels: Residual from the cubic spline fit. Lower panels: A clear seasonal signal in temperature emerges when the residual is sorted by time of year.

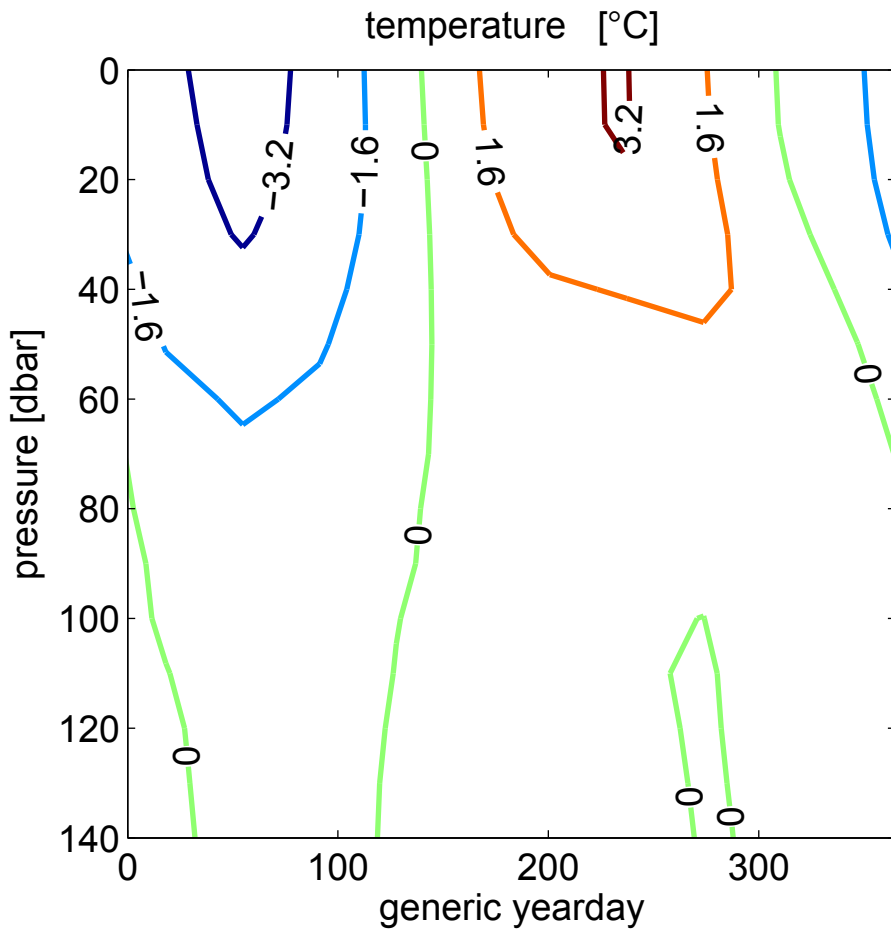


Figure 2.5-9. Seasonal temperature correction/amplitude contoured as a function of yearday and pressure. The amplitude of the temperature seasonal correction is about 3°C at the surface and decays to less than 0.5°C by 90 dbar.

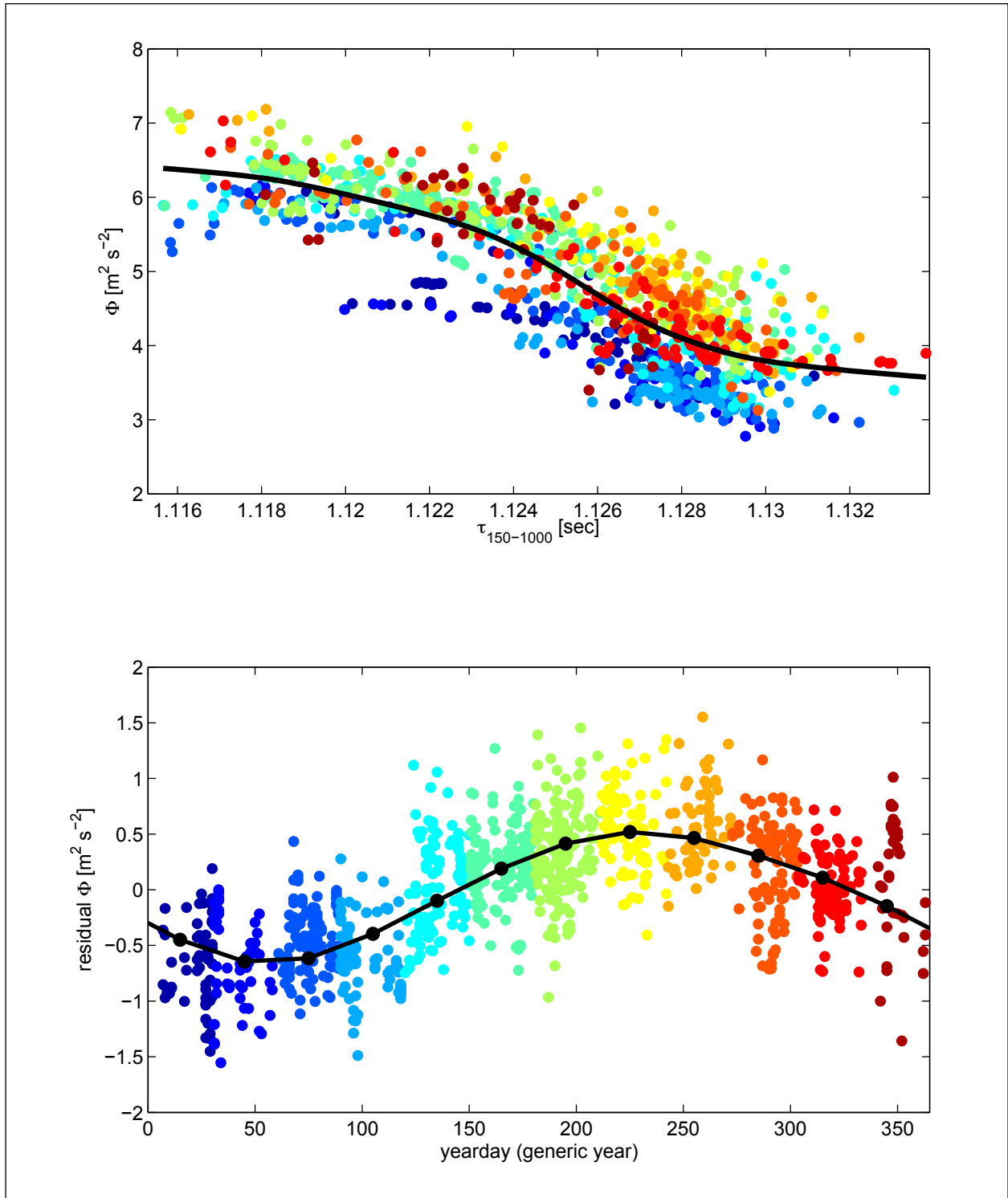


Figure 2.5-10. Upper panel: Scatter plots of surface geopotential anomaly referenced to 150 dbar with the cubic spline fit shown as a solid dark line. All samples in all panels are color coded by generic yearday transitioning from blue in January to red in December. Lower panel: A clear seasonal signal emerges when the residual is sorted by time of year.

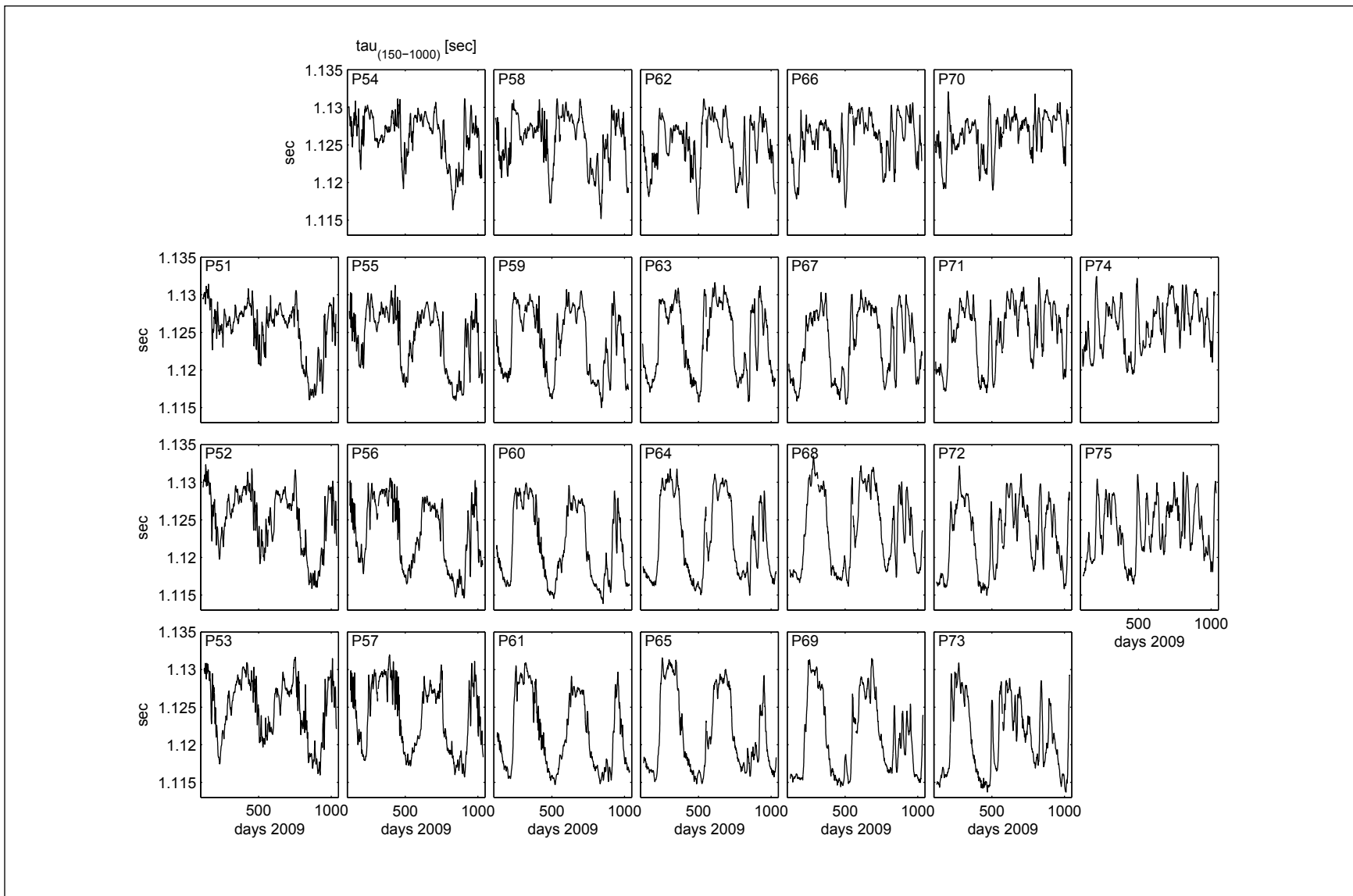


Figure 2.5-11. Time series of $\tau(150-1000)$ in seconds, with panels arranged according to approximate geographic location. Instrument number is noted in the upper left corner of each subplot.

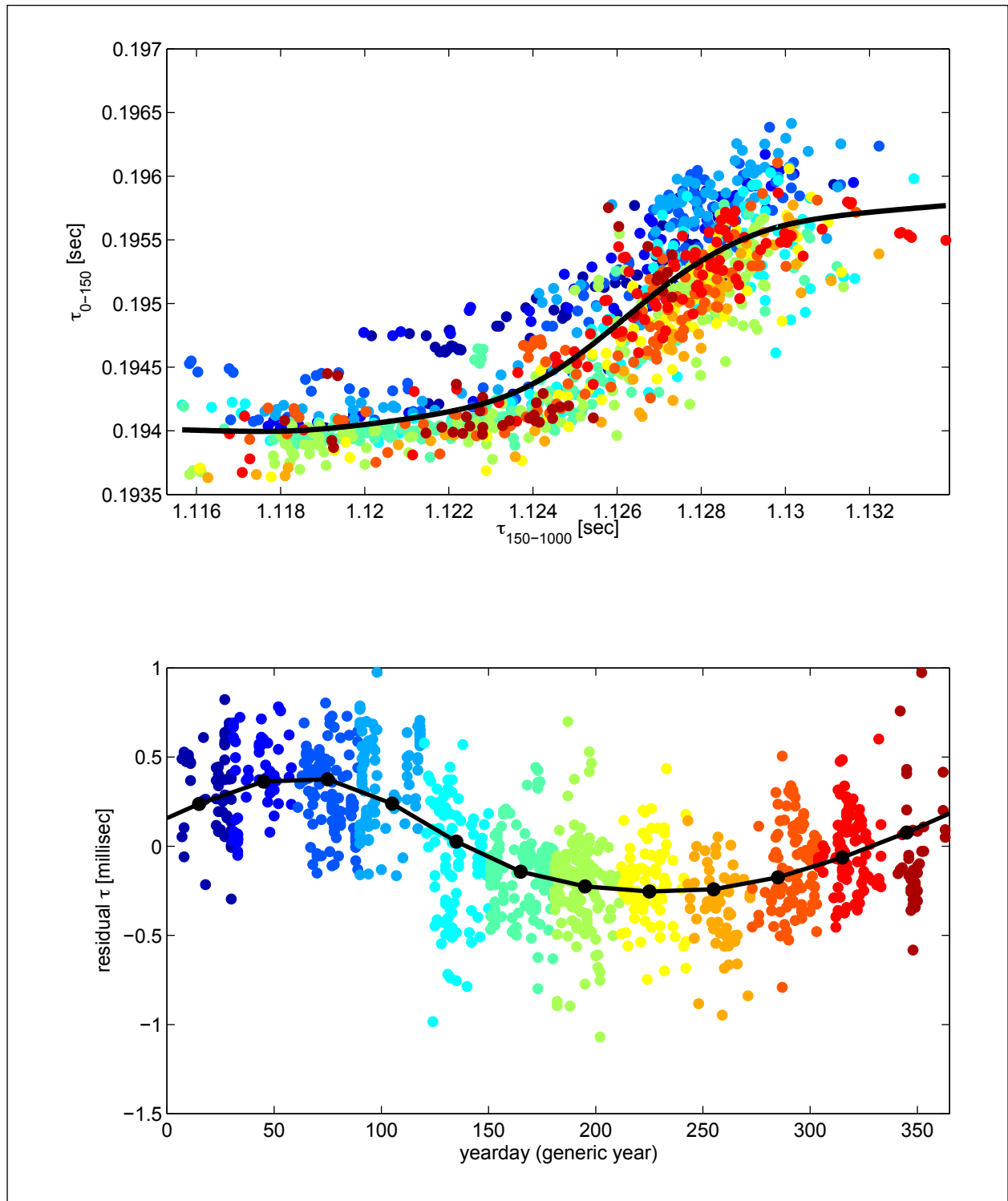


Figure 2.5-12. Upper panel: Scatter plots of $\tau(0 - 150)$ versus $\tau(150 - 1000)$. Each point is color coded by generic yearday transitioning from blue in January to red in December. The scatter about the spline fit (solid dark line) is largely due to the seasonal cycle. Lower panel: The residual from the cubic spline fit shown in the upper panel sorted by generic yearday shows a clear annual signal.

2.5.3 Upper-Ocean Maps

Maps were produced with optimal interpolation techniques adapted from Bretherton et al. (1976) and outlined in Watts et al. (1989; 2001). Optimal interpolation requires that the input fields have zero mean and uniform variance. In order to meet this requirement a mean field must be subtracted from the fields before mapping and then added back to produce maps of the total field. The mean has been removed in such a way that the mapped fields behaved well outside the measurement sites. Additionally, the cross-correlations among the measurements determined the correlation function and length scales utilized in the optimal interpolation to map anomalies. A Gaussian correlation function was employed to construct maps. Multivariate optimal interpolation mapped geopotential, pressure and velocity. Mapping was constrained to be geostrophic.

Maps of τ were calculated by subtracting a 60-day low-passed field mapped with a correlation length scale of 160 km. The residual anomaly field was then mapped with a shorter correlation length scale of 70 km. Correlation functions of the measurement anomalies determined the correlation length scales (Figure 2.5-13). The measurement correlation functions were nearly isotropic indicating that the use of an isotropic Gaussian correlation function for the objective analysis was appropriate. Maps of τ are used to map temperature at desired depths using the GEM look-up tables.

Maps of upper-ocean geopotential and baroclinic velocity relative to 3000 dbar were constructed at each desired depth as follows: Time series of geopotential $\Phi(t)$ for each PIES site were looked up from $\tau_{\text{index}}(t)$ using the GEM fields. The Φ time series were 60-day low-pass filtered and these time series are optimal interpolation mapped (OI-mapped) using a correlation length scale of 160 km. At each site the residual time series was determined by subtracting the low-passed mapped field from the total. The anomaly field was then mapped using a shorter correlation length scale of 70 km to create a high-passed field. The low-passed and high-passed fields of geopotential and baroclinic velocity were summed to produce the combined best estimate. The suite of depths was every 20 dbar from 0 to 1000 dbar; 100 dbar from 1100 to 1500 dbar, and the following deep levels: 1750, 2000, 2500, and 3000 dbar.

2.5.4 Bottom Pressure

Several bottom-pressure processing details are noteworthy. Pressure data were de-tided. Tidal response analysis (Munk and Cartwright 1966) determined the eight major tidal constituents for each instrument (See Appendix). Tidal amplitudes are generally small. The largest tidal amplitudes are near 13 cm for O1 and K1, near 5 cm for P1 and M2, and less than 5 cm for the remaining four constituents. Estimated tides and phases vary smoothly across the array. Pressure records were de-drifted and leveled simultaneously using the techniques described in Donohue et al. (2010). ‘Leveled bottom pressures’ refers to bottom pressures that have been adjusted to the same geopotential surface. Mean near-bottom currents and bottom pressures were jointly mapped by optimal interpolation to be in geostrophic balance. A linear drift curve was removed from 16 of the pressure records, while an exponential-plus-linear drift curve was removed from the other nine pressure records. Fifteen instruments have drifts less than 0.1 dbar (equivalent to 10 cm); seven instruments have drifts between 0.1 and 0.2 dbar; three instruments have drifts between 0.3 and 0.6 dbar. The final de-drift curves are constrained to yield a slope difference between PIES pressures and pressures determined from optimally interpolated current-meter

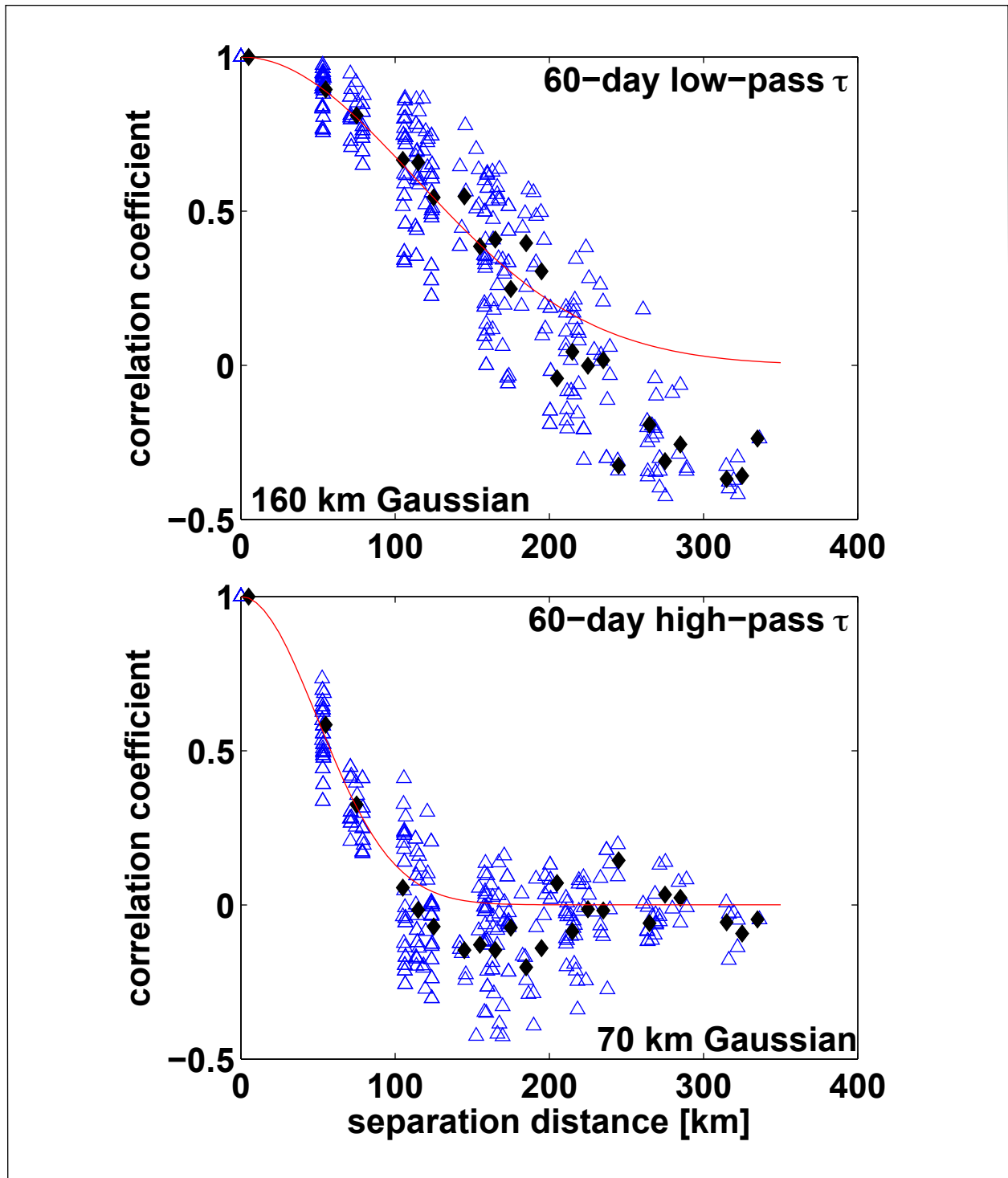


Figure 2.5-13. Correlation coefficient between pairs of PIES τ (150 -1000) records. Correlation coefficient plotted as a function of separation distance and binned every 10 km (black diamonds). Upper panel: Time series have been 60-day low-pass filtered. A 160 km Gaussian function is plotted with red line. Lower panel: Time series have been 60-day high-pass filtered. A 70 km Gaussian function is plotted with red line.

records of $\pm 1.0 \times 10^{-5}$ dbar day⁻¹. With this criterion, the residual error resulting from drift is less than 0.01 dbar.

2.5.5 Reference-Level Maps

Lower-ocean mapping paralleled the upper-ocean procedure. In preparation, a common mode or array-average pressure was subtracted from the bottom pressures (Figure 2.5-14). The common mode in the deep pressures simply adds a time-dependent array-wide constant which has no dynamical significance for the mesoscale circulation. The spectrum of the common mode reveals three broad spectral peaks near 50, 30 and 18 days as well as a narrow-band spectral peak near 9 days. A 16-day peak was found in the Exploratory bottom-pressure data set. We hypothesize that the low-frequency signals are driven by atmospheric forcing. The 9-day peak is the Mt tide (Richard Ray, personal communication). Note that the Mf tide, calculated by the TPXO 7.2 model, appears as a spectral peak near periods of 13.66 days. TPXO 7.2 is the current version of a global model of ocean tides which best fits, in a least-squares sense, the Laplace Tidal Equations and along track averaged data from TOPEX/Poseidon and Jason. The methods used to compute the model are described in Egbert and Erofeeva (2002). Figure 2.5-15 shows the bottom pressure records with the common mode removed.

Reference level maps were calculated, after removing the common mode pressure, in a similar way to those calculated for the upper ocean. First, a 40-day low-passed field mapped with a correlation length scale of 70 km was subtracted. Then, an anomaly field with a shorter correlation length scale of 65 km was mapped. Correlation functions of the measurement anomalies determined the correlation length scales (Figure 2.5-16). Similar to the τ time series, the near-bottom-pressure autocorrelations are nearly isotropic (not shown). Streamfunction maps were created with inputs from both pressure and current-meter data. The inclusion of the current-meter data sharpens gradients. The mapped low-passed fields were first calculated, then the residual at each site was used as input to map the high-passed fields, and the two maps were summed at each time step to produce the combined final fields of reference-level pressures and velocities.

2.5.6 Total Maps

The vector sums of mapped baroclinic velocity profiles plus deep reference velocities give the estimated absolute geostrophic velocities at each desired level. Upper-ocean baroclinic velocities were created by mapping geopotential referenced to 3000 dbar. This component is termed as baroclinic referenced to the bottom ('bcb'). The 3000 dbar-level ('ref') velocities mapped with the bottom pressure and current-meter records provided the reference for the upper-ocean baroclinic velocities to generate absolute velocities throughout the water column.

Absolute sea-surface heights were also determined. First, 3000-dbar pressures were converted to their height equivalent (pressure divided by gravity and density). This component is termed as the reference level sea-surface height (ref). Second, surface geopotentials referenced to 3000 dbar were converted to their height equivalent (geopotential divided by gravity). This component is termed as the baroclinic SSH referenced to the bottom (bcb). The bcb and the ref contributions to sea-surface height are combined to yield absolute sea-surface height.

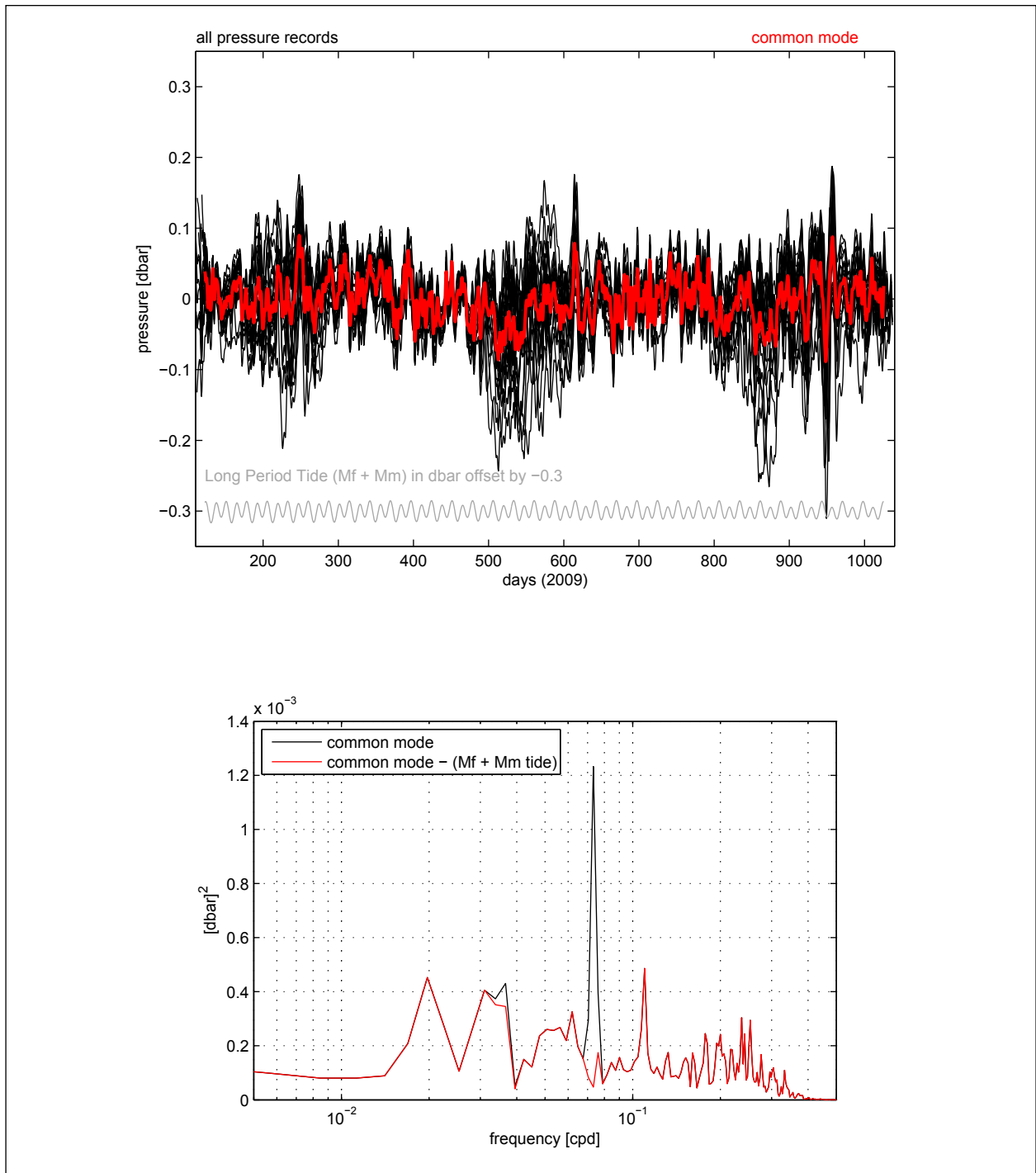


Figure 2.5-14. Top panel: All the individual pressure records (thin black) and their array-average (red), called the common mode, which was subtracted from each bottom pressure record before mapping deep water reference velocities and pressure anomaly fields. Offset from the common mode is the time series of the long period tide ($M_f + M_m$) from the TPXO 7.2 model. Bottom panel: Spectrum of common mode, (black) before and (red) after removing the dominant M_f peak near 14 days and the smaller M_m peak (Spectra calculated on window length 355 days).

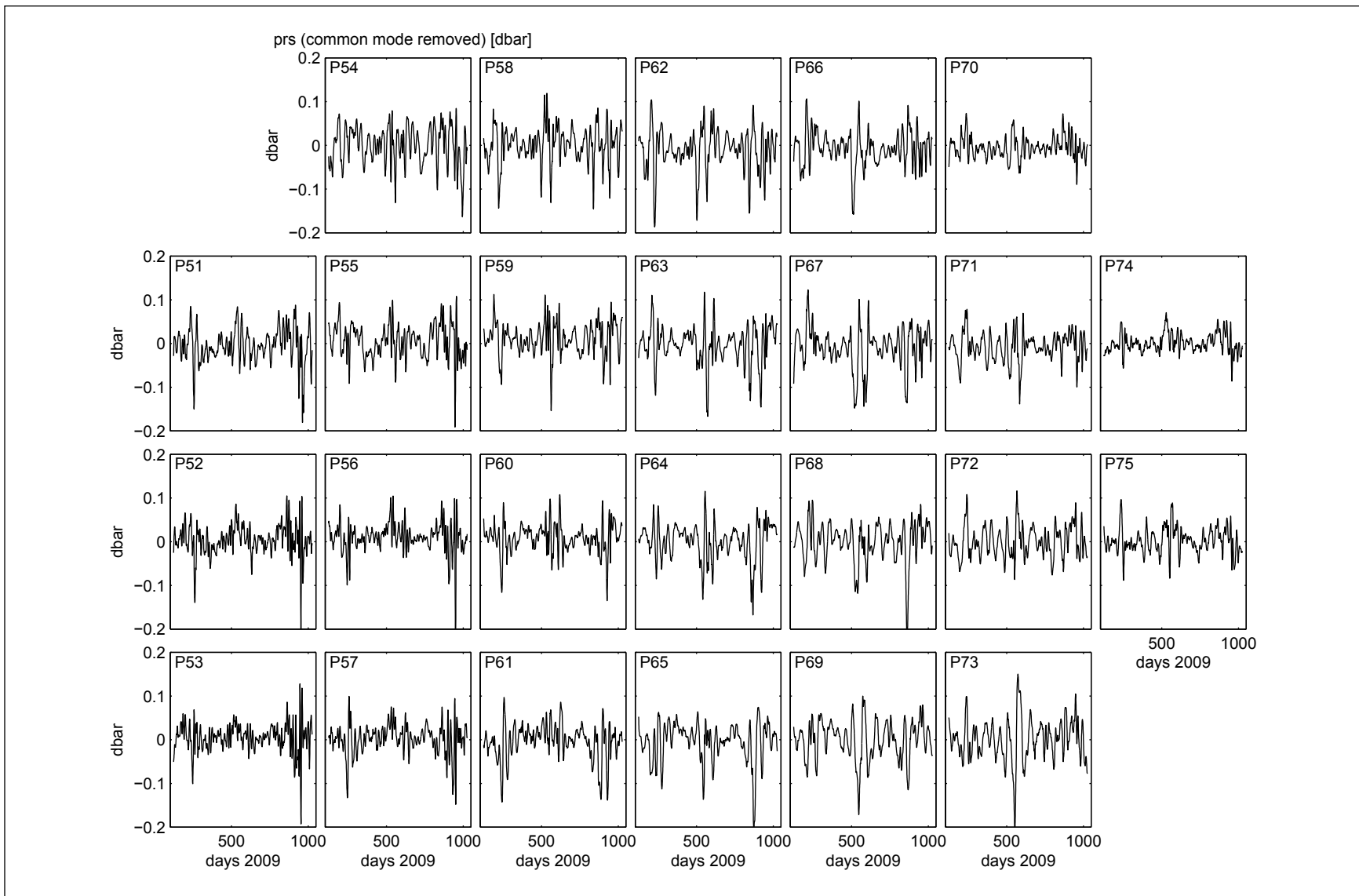


Figure 2.5-15. Time series of bottom pressure anomaly (dbar) with the common mode removed. Panels are arranged according to approximate geographic location. The instrument number is noted in the upper left corner of each subplot.

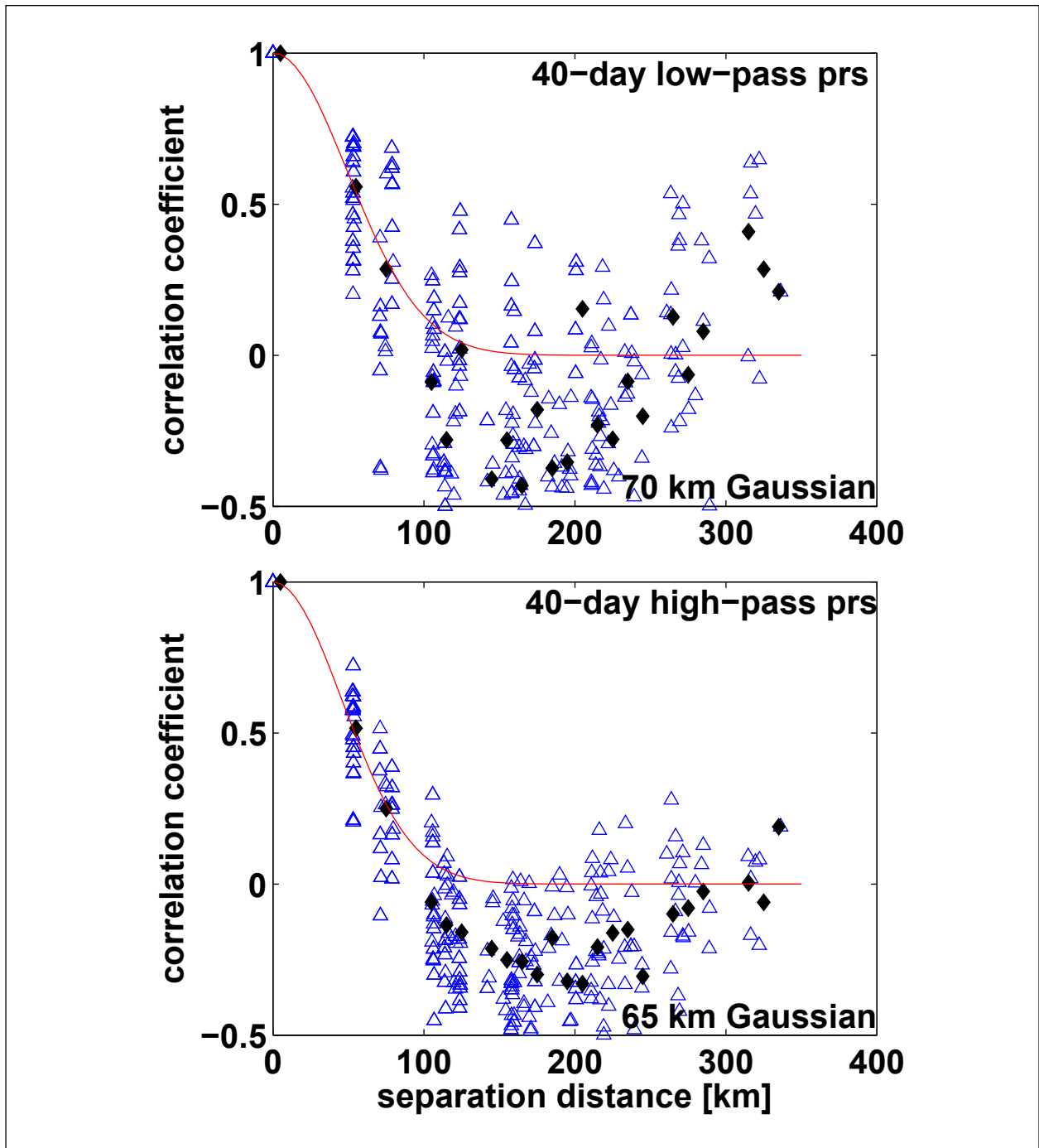


Figure 2.5-16. Correlations between pairs of pressure records. Upper panel: Correlations of 40-day low-pass filtered pressures plotted as a function of separation distance (open blue triangles) and binned every 10 km (black diamonds). A 70-km Gaussian function is plotted in red. Lower panel: Correlations of 40-day high-pass filtered pressures plotted as a function of separation distance (open blue triangles) and binned every 10 km (black diamonds). A 65-km Gaussian function is plotted in red. The common mode has been removed from the records in both panels.

2.5.7 Mooring Comparisons

This section compares mooring measurements of temperature and current to PIES-derived estimates. The comparison is not strictly a validation of the PIES methodology because the design of the array does not lend itself to strict verification: point measurements differ intrinsically from mapped geostrophic estimates. Nine tall moorings embedded in the middle of the array provided measurements to evaluate the PIES-derived fields of temperature and velocity.

The comparison of temperatures is most directly done between measured and estimated $T(t, p(t))$. The measurement depth $p_m(t)$ varied with time, because the moored temperatures were measured as the mooring was drawn deeper by the drag of strong currents. Detailed temperature comparisons were conducted at nine nominal depths between 150 and 1100 m. The upper level was chosen to be deeper than the influence of the seasonal cycle, and below 1100 m the temperature variance is small (standard deviation $\sim 0.14^\circ\text{C}$). PIES temperatures mapped to the mooring locations were vertically interpolated at each time step to the $p(t)$ record for each respective moored temperature sensor. Figure 2.5-17 shows the comparison between PIES and mooring for four depths at A4 (yellow dot in the right panel; other mooring locations are red, PIES locations blue). A summary of temperature comparisons for all nine tall moorings at all nine nominal levels is shown in Figure 2.5-18. Correlation coefficients are greater than 0.92 at all depths, and are greater than 0.975 at all sites for depths between 250 and 750 m, indicating that the PIES capture more than 95% of variance. The rms differences are small compared to the signal size as measured by the standard deviations.

Figure 2.5-19 shows the differences between measured and PIES-estimated temperature (squares) as well as predicted differences. Differences derive from instrument errors (both mooring and PIES), the GEM parameterization, mapping uncertainty, and uncertainty in the absolute pressure of the mooring measurements. The diamonds are the PIES error defined as the rms in the GEM table plus the error in the GEM table look-up due to τ uncertainty ($\tau_{\text{error}} * dT/d\tau$). τ_{error} includes both instrument and mapping uncertainty. Mapping uncertainty is determined in the same manner as Donohue et al. (2010). The mapping procedure (Bertherton et al. 1976) provides a percent variance error. This is dimensionalized by multiplying the estimated mapping error by the measured $\tau(100-1500)$ variance. Note that the tall moorings experienced some vertical motion when ocean currents caused the moorings to blow over or draw down. We assumed that the absolute sensor depths are known within 10 m. Our inability to determine the absolute pressure of the sensors can lead to discrepancies. For example, a thermocline temperature gradient of $0.035^\circ\text{C dbar}^{-1}$ combined with a 10 dbar uncertainty leads to a 0.35° difference between PIES estimated and measured temperature. Adding the impact of the uncertainty in absolute mooring sensor pressure ($P_{\text{error}} * dT/dp$ where $P_{\text{error}} = 10$ dbar) and an error of 0.1°C in current meter temperature to the PIES error yields the circles in Figure 2.5-19. Observed rms differences agree well with predicted differences.

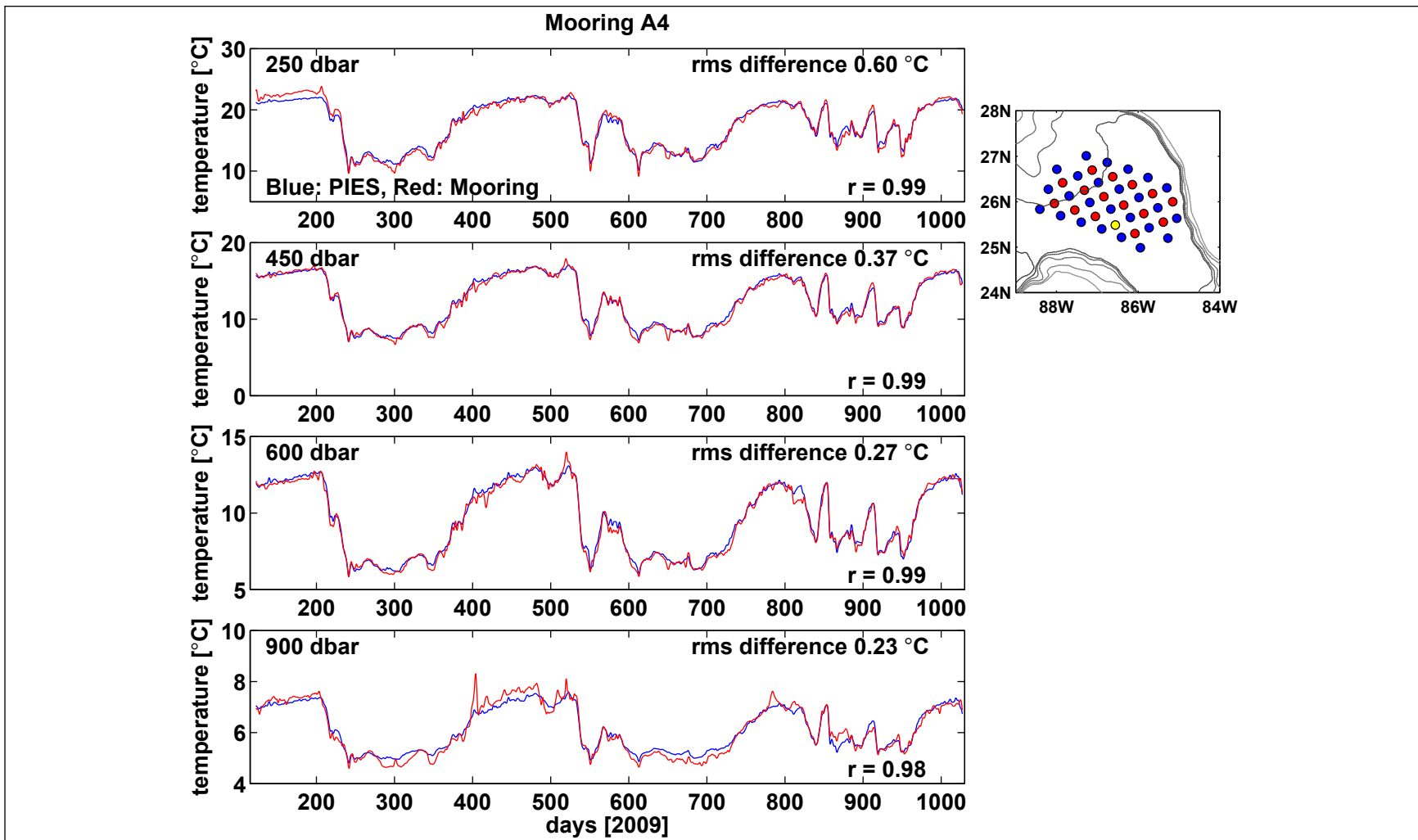


Figure 2.5-17. Comparison between the A4 mooring (red) and PIES-derived (blue) temperature. The nominal depth is noted in the left-hand corner of each panel. The rms difference and the correlation coefficient between PIES and the A4 mooring are noted in the right-hand corner of each panel. The right-most panel shows the location of the mooring (yellow). Other mooring locations are red; PIES locations blue. Bathymetry contoured every 500 m depth.

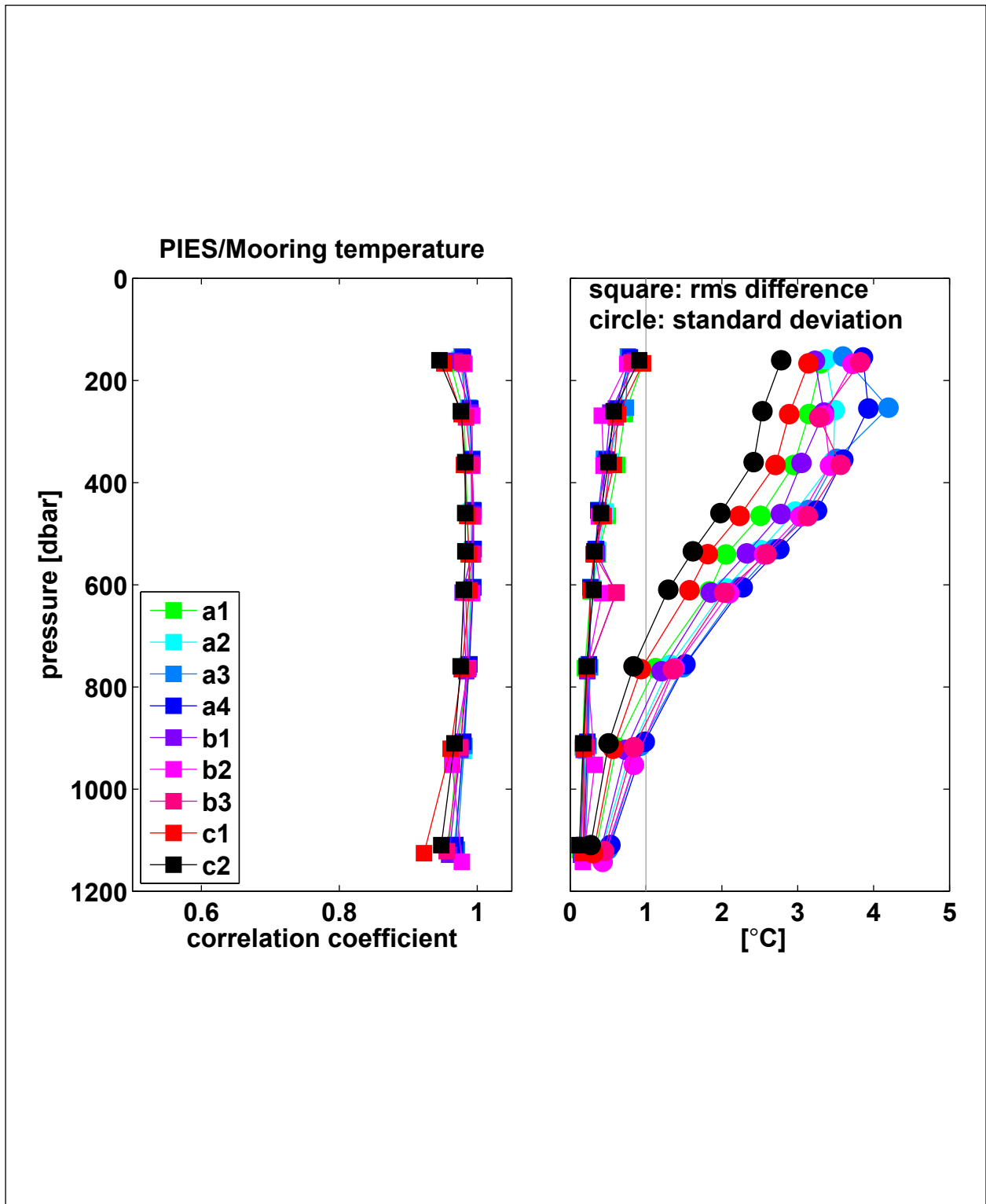


Figure 2.5-18. Summary of the temperature comparisons. Left panel: Correlation coefficients as a function of mooring and pressure level. Right panel: rms differences (squares) and standard deviation (circles). Rms differences are less than 1°C (grey vertical line).

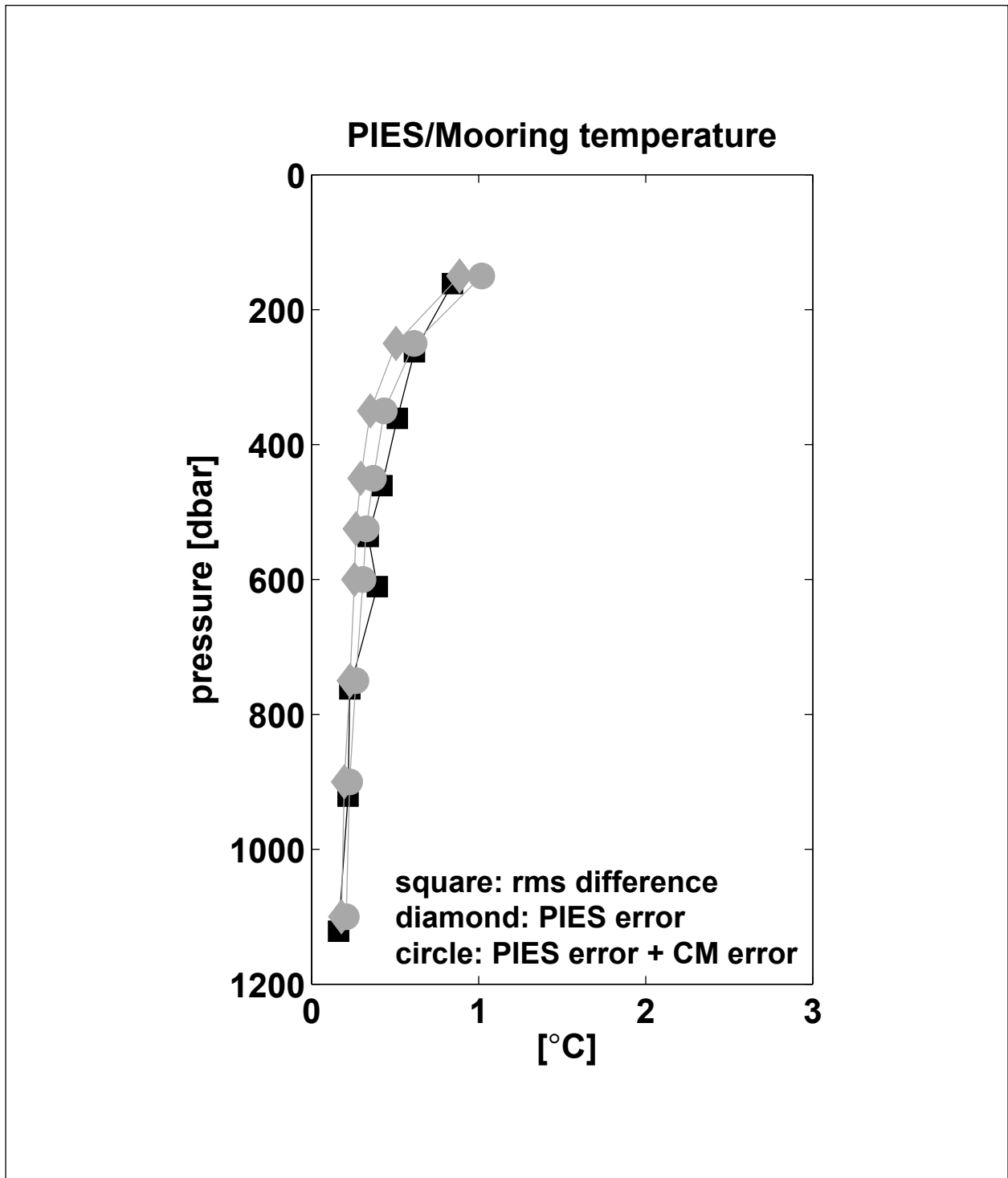


Figure 2.5-19. Observed rms and predicted differences between measured and PIES-estimated temperature. Squares are the mean rms differences at the nine nominal depths. Diamonds show the PIES uncertainty in temperature, including PIES mapping error and the error in the GEM table look-up due to τ uncertainty. Circles include the impact of the uncertainty in absolute mooring sensor pressure and current meter temperature sensor uncertainty.

PIES-mapped currents were compared to mooring currents at six nominal depths. Shown here are the comparisons for mooring A4 (Figure 2.5-20a through Figure 2.5-20c). The series track each other well, with correlation coefficients above 0.89, especially within the thermocline. The rms differences are less than 10 cm s^{-1} everywhere and reflect instrument errors (both mooring and PIES), errors associated with the GEM parameterization and the intrinsic difference between a point measurement and a mapped geostrophic estimate. Ageostrophic motion, such as high vertical wavenumber inertial currents, will not be reproduced in the maps of geostrophic velocity. The A4 comparisons are representative of all the other moorings. Summaries of velocity comparisons for all nine tall moorings are shown in Figures 2.5-21 and 2.5-22. Note that the signal (standard deviation) exceeds the noise (rms difference) by a factor of three to ten for all comparisons, and for each mooring the correlation coefficients are lowest at mid-depth. (The 900 and 1300-m depth current-meter records had prolonged periods of rotor stalls during the first deployment, therefore, for these depths, PIES-mooring comparison statistics are determined for only the second deployment period.). While it has not been determined as to the reason for the poorer comparisons at the A2 and A3 moorings, one cannot discount measurement errors in the current-meter measurements or uncertainty in the absolute pressure at the current-meter mooring. Figure 2.5-23 shows the differences between measured and PIES-estimated velocities (squares) as well as predicted differences (diamonds). Mapping uncertainty is determined in the same manner as Donohue et al. (2010). The mapping procedure (Bertherton et al. 1976) provides a percent variance error, which is dimensionalized by multiplying the estimated mapping error by the mapped eddy kinetic energy. The observed rms differences agree well with the predicted differences in the upper and lower water column, but are larger than predicted in the thermocline. The errors in baroclinic shear estimates contribute the most to geostrophic velocity error estimates.

In the Kuroshio Extension, Bishop et al. (2012) and Park et al. (2012) found that the ref mode was better represented by a vertically trapped mode proportional to $\cosh(z/b)$, where the vertical decay scale $b = 8 \text{ km}$ to 12 km . The terminology “ref mode” refers to the dominant vertical mode structure associated with the reference-level velocity fluctuations. In this experiment, frequency domain empirical orthogonal functions calculated from the current meter moorings (discussed further in Section 3.4.2) indicate that two modes capture most of the variance in the measured velocities: one mode is nearly depth independent and the second mode is a shear mode that represents the strong surface-intensified current. Here, the intent was to investigate whether or not one could determine a depth-dependent scale function $\gamma(z)$ that would suit the reference velocity mode based on the mooring comparisons and also fit the altimeter-PIES SSH comparisons. Specifically, the best fit between measured velocity and scaled mapped PIES velocities was determined (e.g., $u_{\text{pies}}(x,y,z,t) = u_{\text{bcb}}(x,y,z,t) + \gamma(z)u_{\text{ref}}(x,y,t)$), as was the best fit between along-track altimeter SSH and scaled PIES SSH (e.g., $\text{SSH}_{\text{pies}}(x,y,t) = \text{SSH}_{\text{bcb}}(x,y,t) + \gamma(z=0)\text{SSH}_{\text{ref}}(x,y,t)$).

Altimetric SSH anomaly data from alongtrack Jason-2 data were compared with PIES-derived estimates of total SSH anomaly. Just as for mapped SSH, absolute sea-surface heights were determined for seven PIES sites (P51-P53 and P70-P73) along Jason-2 groundtracks. The two SSH estimates compare well (Figure 2.5-24). The number of passes available for comparison varies by location and the number of passes coincident with PIES SSH is listed in the upper left of the figure. Rms differences are near 6 cm at all sites and correlation coefficients are 0.98 at

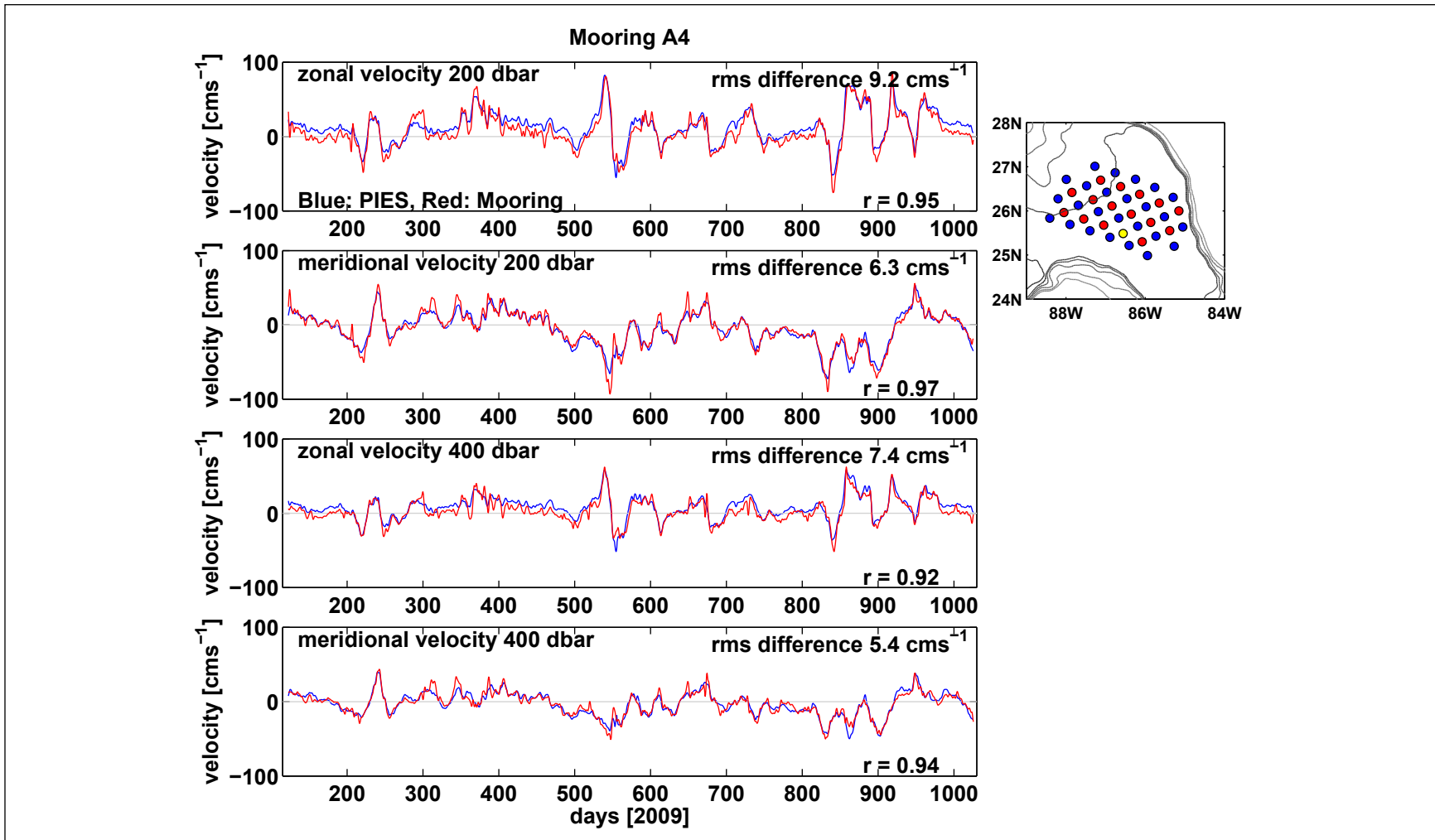


Figure 2.5-20a. Comparison between the A4 mooring (red) and PIES-derived (blue) zonal and meridional velocities. The nominal depths (200 and 400 dbars) are noted in the left-hand corner of each panel. The rms difference and the correlation coefficient between PIES and the A4 mooring are noted in the right-hand corner of each panel. The right-most panel shows the location of the mooring (yellow). Other mooring locations are red; PIES locations blue. Bathymetry contoured every 500 m depth.

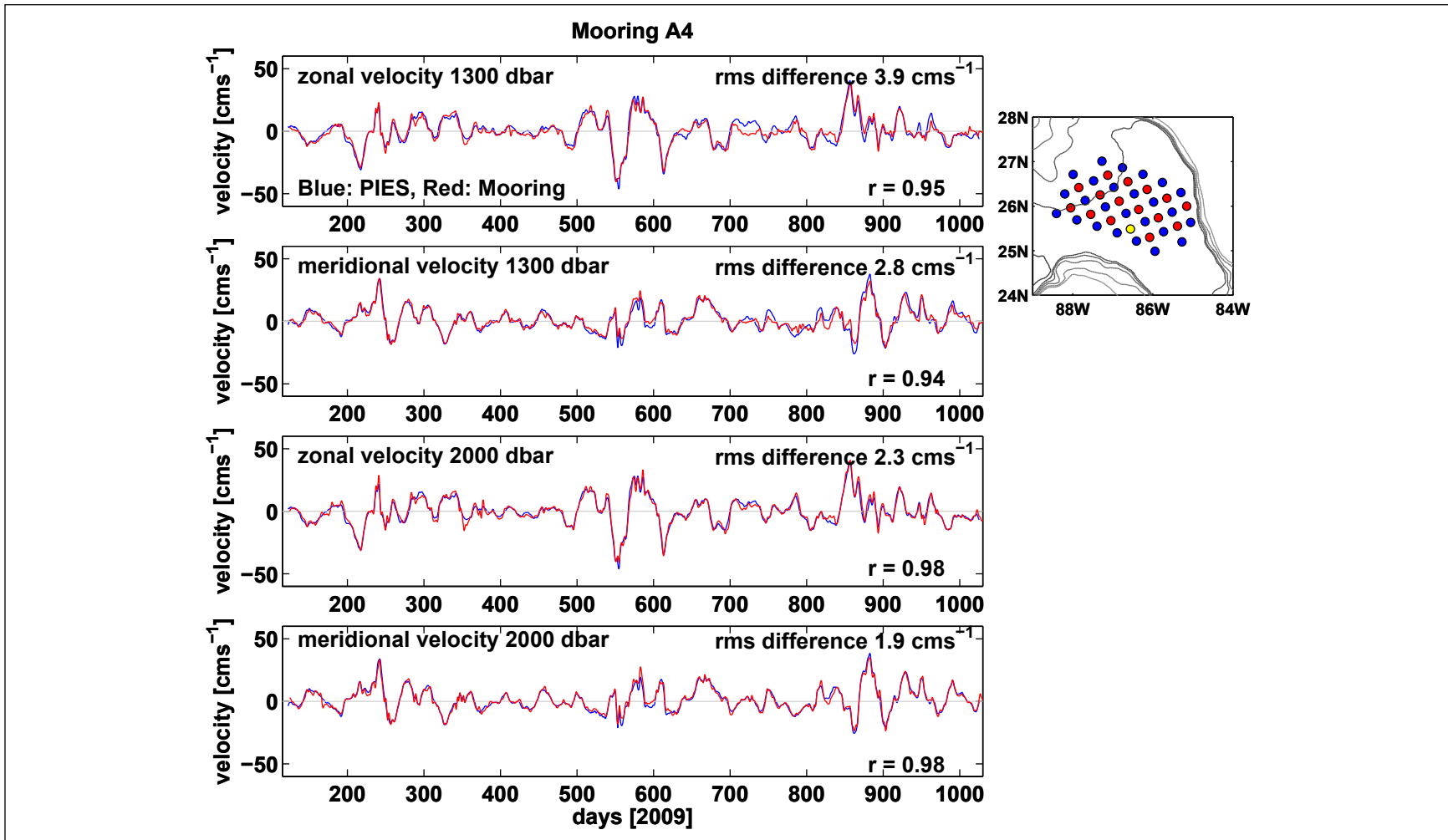


Figure 2.5-20c. Comparison between the A4 mooring (red) and PIES-derived (blue) zonal and meridional velocities. The nominal depths (1300 and 2000 dbars) are noted in the left-hand corner of each panel. The rms difference and the correlation coefficient between PIES and the A4 mooring are noted in the right-hand corner of each panel. The right-most panel shows the location of the mooring (yellow). Other mooring locations are red; PIES locations blue. Bathymetry contoured every 500 m depth.

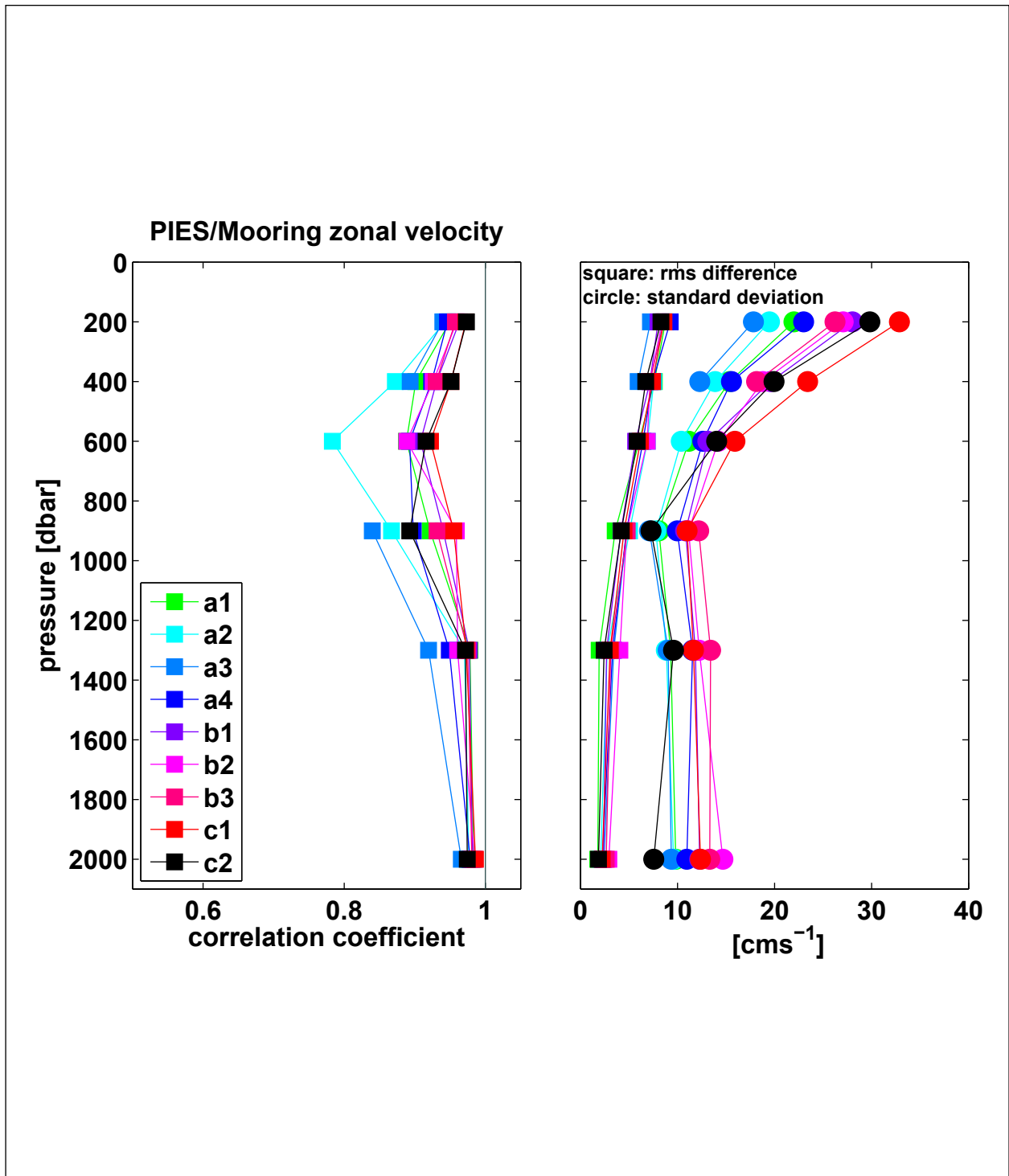


Figure 2.5-21. Summary of the zonal velocity comparisons. Correlation coefficients as a function of mooring and pressure level are plotted in the left panel. The rms differences (squares) and standard deviations (circles) are plotted in the right panel. Note A3 and B3 do not include the 600 dbar level. The data from the S-4 current meters at that level during the second deployment were noted as noisy during data processing.

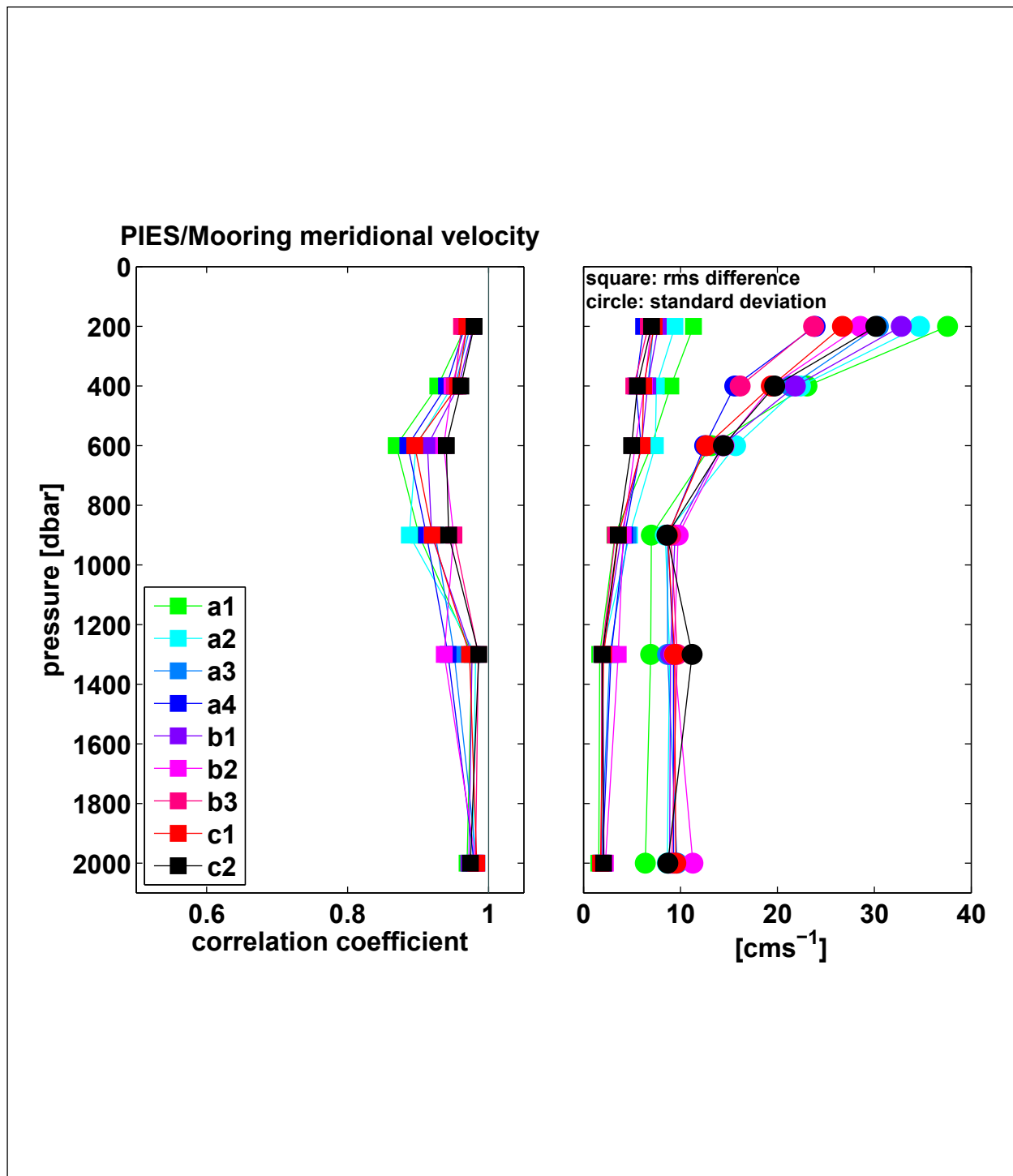


Figure 2.5-22. Summary of the meridional velocity comparisons. Correlation coefficients as a function of mooring and pressure level are plotted in the left panel. The rms differences (squares) and standard deviations (circles) are plotted in the right panel. Note A3 and B3 do not include the 600 dbar level. The data from the S-4 current meters at that level during the second deployment were noted as noisy during data processing.

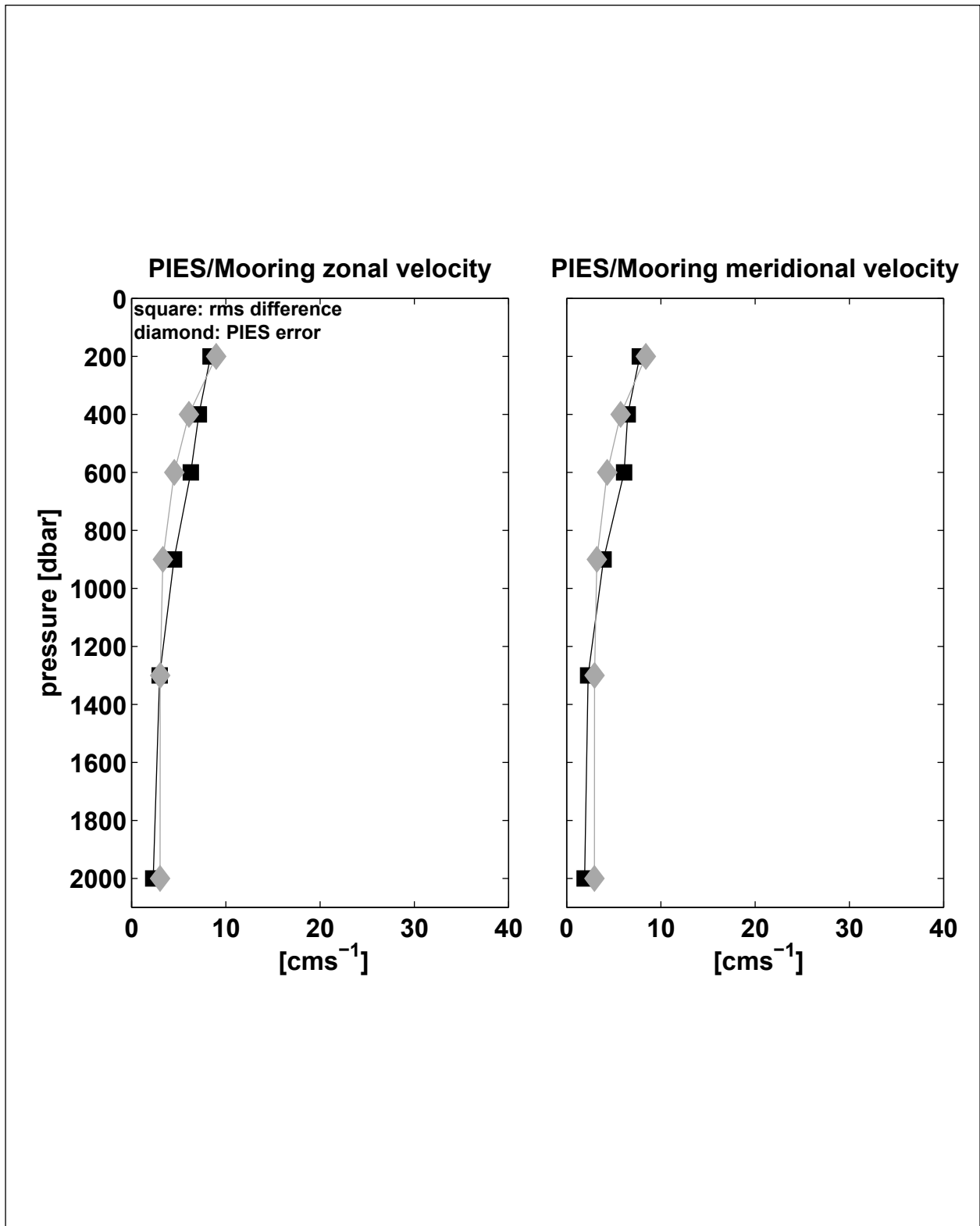


Figure 2.5-23. Rms and predicted differences between measured and PIES-estimated zonal (left) and meridional (right) velocities. Squares are the mean rms differences at the six nominal depths. Diamonds are PIES mapping error.

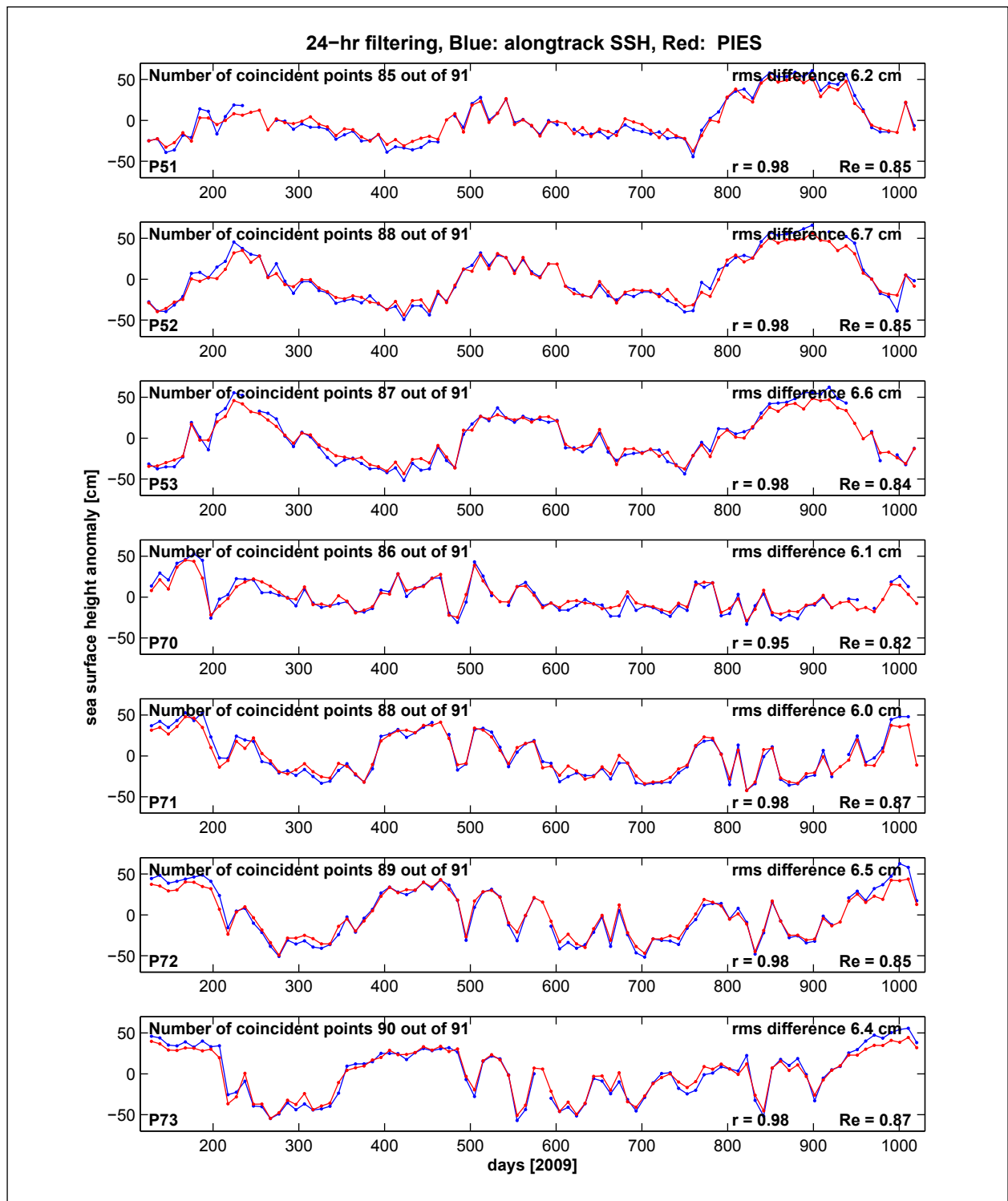


Figure 2.5-24. PIES-estimated total SSH anomaly (red) and Jason SSH anomaly (blue) for the seven PIES sites along groundtracks. PIES site is listed in the lower left, rms difference in the upper right, and correlation coefficient (r) and regression coefficient (Re) in the lower right. PIES data have been interpolated to the Jason-2 measurement times.

six of the seven sites. The regression coefficients are all less than one, near 0.85 at all sites, indicating that the PIES SSH overestimates altimeter SSH. The correlations are improved by applying the above fit with $\gamma < 1$; the minimum overall rms differences are found for $\gamma = 0.75$ (Figure 2.5-25).

Figure 2.5-26 shows the estimate of $\gamma(z)$. γ is near 1.0 at 3000 and 2000-m depth, and decays to near 0.85 in the upper 500 meters. The suite of cosh (z/b) curves shown in Figure 2.5-26 indicate that a vertically trapped structure, with long length scale ($b \sim 6000$ m) compared to the total depth of the ocean, might be appropriate. In subsequent analysis, because the vertical structure implies a correction factor $\gamma(z) = (1 - \epsilon(z))$ with $\epsilon(z)$ less than 15%, $\gamma(z)$ has not been applied to PIES mapped velocities. Further study would be necessary to fully resolve the vertical structure of the ref mode as well as any possible temporal or wavenumber variability in $\gamma(z)$.

2.6 REMOTE SENSING

The remote sensing component of the Dynamics of the Loop Current (LC) program acquired remotely sensed satellite data in the Gulf of Mexico (GOM), northwest Caribbean and the North Atlantic southeast of the U.S. east coast to aid in the interpretation of in-situ data collected in the study area. A combination of satellite observing systems has been used. To carry out this task, the Colorado Center for Astrodynamic Research (CCAR) collected and processed a complementary suite of satellite observations from satellite altimeter and radiometer remote sensing systems. This suite incorporates sea-surface-height (SSH) data with high-resolution sea-surface-temperature (SST) and ocean-color imagery. Satellite altimetry provides the all-weather multi-satellite monitoring capability required to map mesoscale circulation variability of the Loop Current in the eastern GOM and to monitor seasonal, annual, and interannual to decadal SSH variability in the region. During cloud-free conditions, multi-channel radiometry is used to supplement the altimetric sampling by providing high-resolution synoptic SST and ocean-color imagery for monitoring the rapidly evolving Loop Current and its associated eddies including small-scale frontal features in and around the study region.

2.6.1 Satellite Altimetry

Satellite altimeter data used in the LC Study program is the 20-year record of near real-time and archival altimeter data streams available from the ERS-1, TOPEX/Poseidon (TOP/POS), ERS-2, Geosat Follow-on (GFO), Jason-1, OSTM/Jason-2, and Envisat satellite missions spanning the time period from 1993 through 2012. Processing of the SSH data is based on near real-time mesoscale analysis techniques designed to exploit the multi-satellite altimetric sampling (Leben et al. 2002). This method has been used to operationally monitor the GOM since November 1995.

Altimeter data from a total of three operational satellites were available during the program time period from April 2009 through November 2011. Basic information on each of the missions is given in Table 2.6-1. The ground-track coverage provided by these satellites in the study region is shown in Figure 2.6-1 for the time period until 22 October 2010 when Envisat was in its nominal 35-day repeat orbit. Also included is the 17-day repeat ground track for GFO in the plot

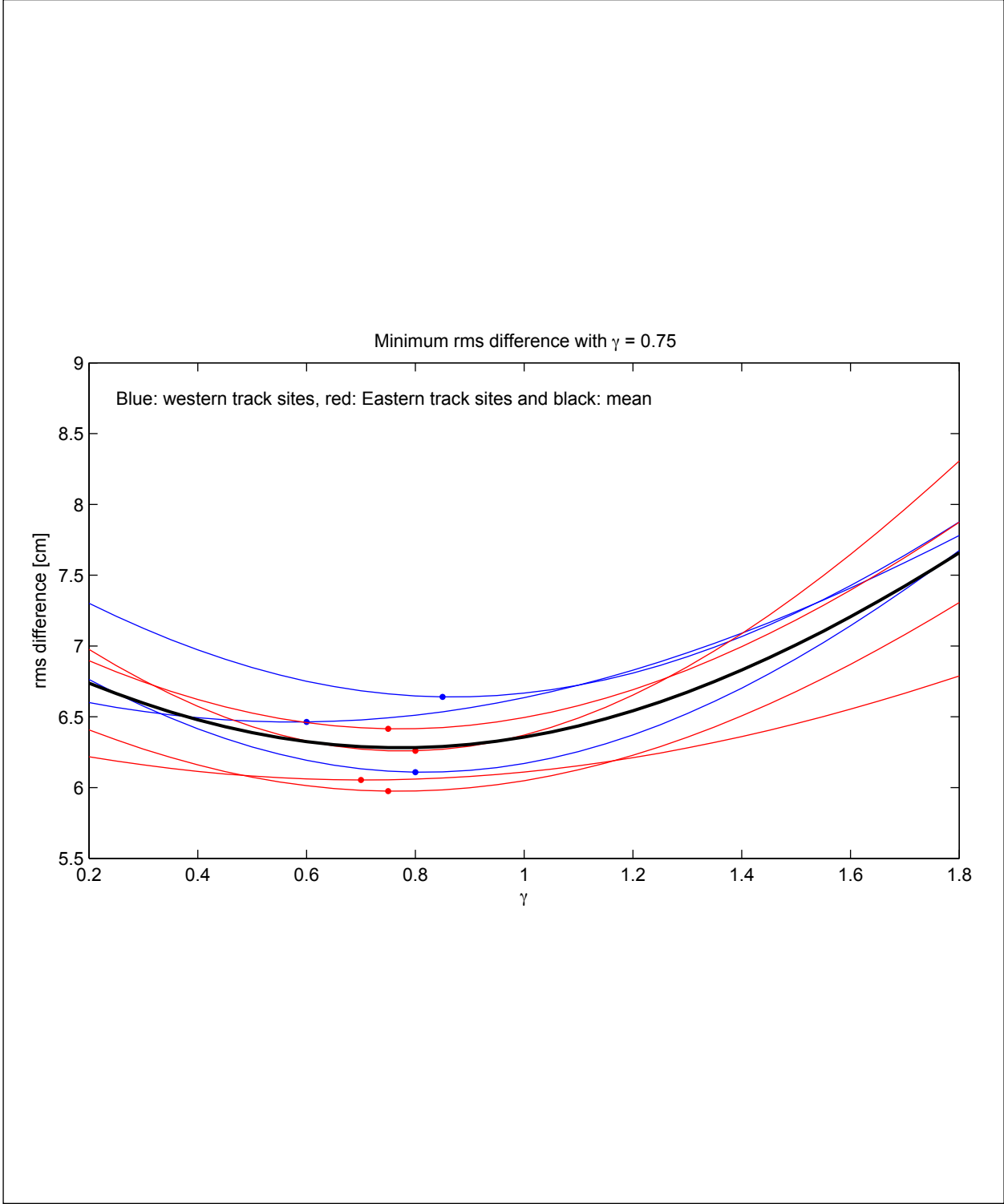


Figure 2.5-25. Rms differences between altimeter SSH anomaly and PIES-estimated total SSH anomaly as a function of γ . Thin curves are rms differences at seven PIES sites located along the Jason satellite tracks. The minimum value for each curve is denoted by a dot. Thick curve is the mean rms difference of the seven PIES sites. The mean rms differences minimum value is $\gamma = 0.75$.

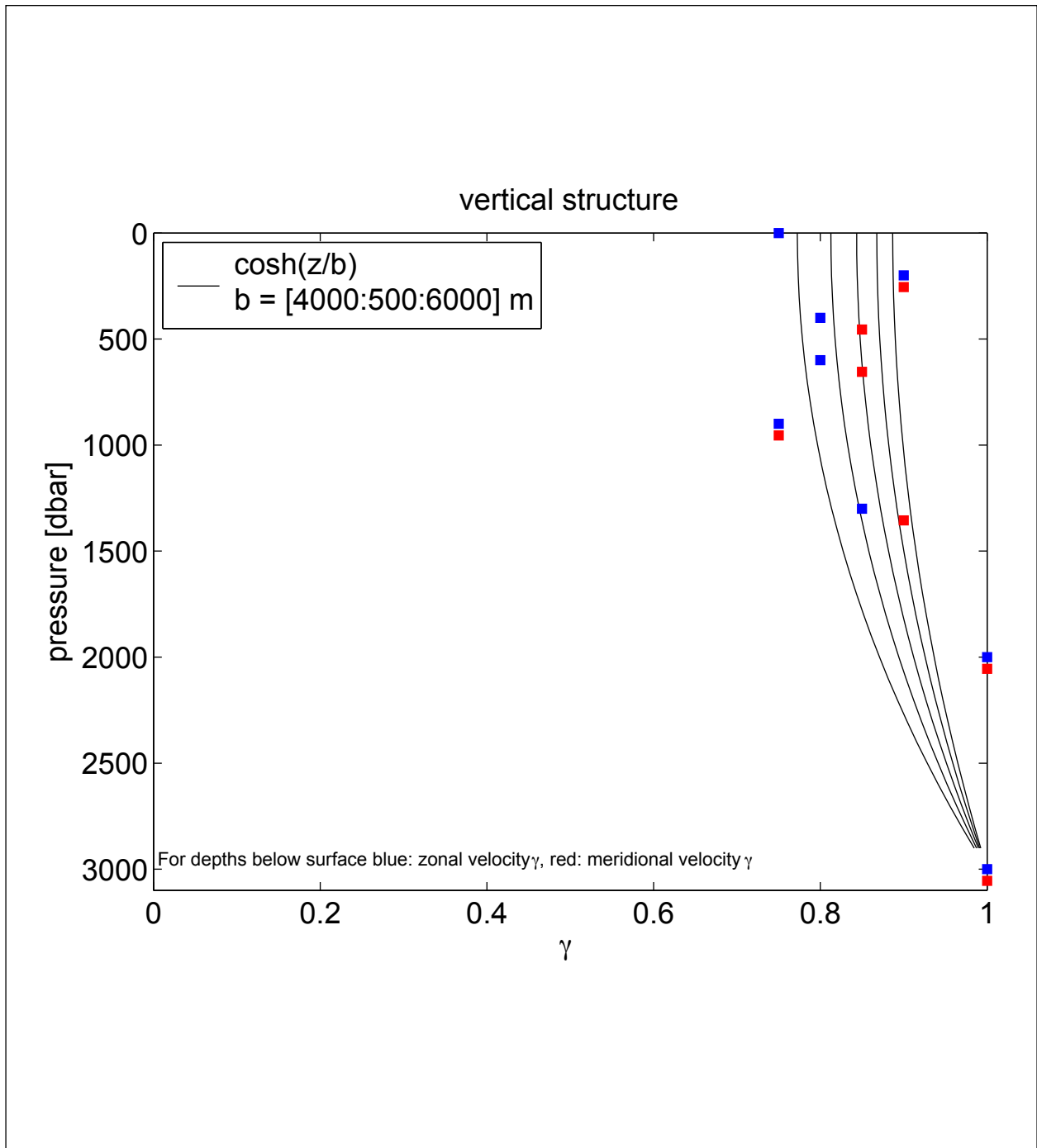


Figure 2.5-26. Multiplicative factor, γ , applied to the reference SSH (velocity) which when added to the baroclinic SSH (velocity) referenced to the bottom produces the lowest rms between measured and PIES-estimated quantities. Separate values for γ are calculated for zonal (blue) and meridional (red) velocities denoted by filled squares for the mean γ . The mean γ is computed from all available current meter records at each level. Black curves show $y = \cosh(z/b)$ for b values ranging from 4000 to 6000 m every 500 m. Note that the vertical trapping decreases for increasing values of b .

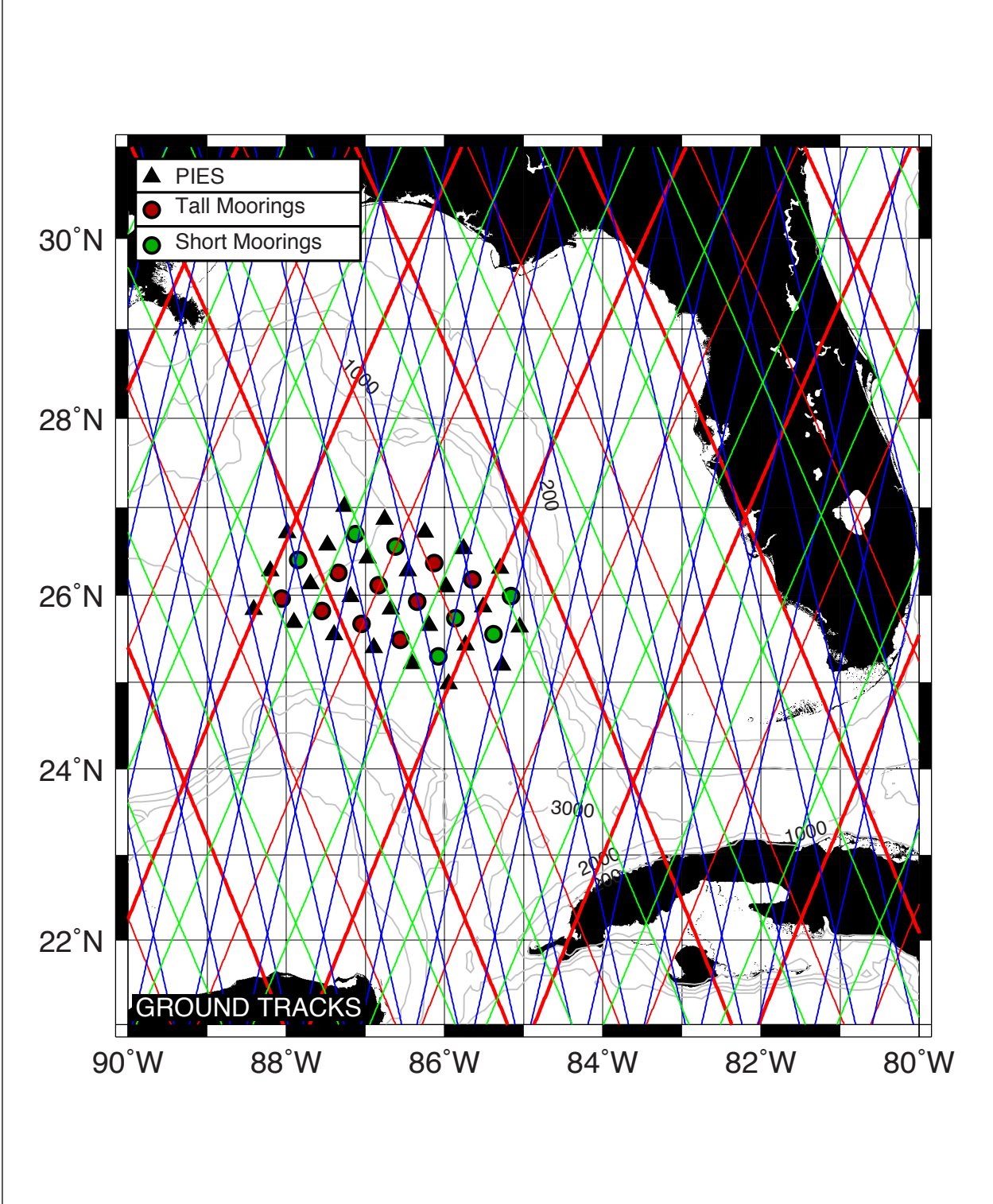


Figure 2.6-1. Satellite altimeter exact repeat groundtrack coverage in study region. Jason-1 (thin red), OSTM/Jason-2 (thick red), and Envisat (blue) are shown with a schematic of the instrument array. The 17-day repeat ground track for GFO (green) is also shown.

Table 2.6-1. Satellite Altimeter Missions Active During the LC Study Program

Satellite	Launch Date	Agency	Repeat Period (days)	Cross track Spacing	
				Degrees of Longitude	km*
Jason-1	18 Dec 1999	NASA/CNES	10	2.83	278
Envisat	1 Mar 2002	ESA	35	0.72	71
Envisat Extended Mission (started on 02 Nov 2010)			30	0.84	82
OSTM/Jason-2	20 Jun 2008	NASA/CNES	10	2.83	278
*at 28°N					
OSTM/Jason-2 and Jason-1 Tandem/Interleaved Mission: Jan 2009 to 12 Apr 2012					
TOPEX/Poseidon/Jason-1 Interleaved			10	1.42	140

to show the spatial sampling afforded by operational satellites in all four exact-repeat orbits occupied historically for mapping of ocean SSH variability.

Note that during the study program, the OSTM/Jason-2 & Jason-1 satellites were in tandem orbits with interleaved ground tracks. NASA/CNES scientists selected this configuration to improve the sampling of mesoscale ocean circulation by precision altimeters (Dibarboure et al. 2011), as was done during the original tandem altimeter mission flown by Jason-1 and TOP/POS (Fu et al. 2003). The space/time sampling provided from a single satellite in the original 10-day repeat orbit of the TOP/POS satellite, which was selected to map the ocean topography associated with large-scale variations in SSH, is not sufficient for monitoring mesoscale variability. This is because of the large distance between neighboring ascending or descending tracks on the 10-day repeat ground track. In the GOM, this spacing is 2.83° of longitude or about 278 km at 28°N, which is also the distance between crossover points between ascending and descending tracks. Moving a second satellite onto a parallel ground track that is midway between two adjacent ground tracks of the original TOP/POS orbit reduced this distance by half to a cross-track spacing of 140 km at 28°N. At latitudes midway between intra- and inter-satellite crossover points, the ascending/descending ground-track sampling improves by another factor of two to a cross-track spacing of just 71 km. Thus, the average cross-track sampling from the tandem mission data alone is 70 to 140 km within the study region.

The addition of Envisat data augments this spatial sampling, but at irregular sampling times. During the study program, Envisat was in the nominal 35-day repeat orbit until 22 October 2010, when maneuvers were initiated to place the satellite in the drifting 30-day repeat cycle Envisat extended mission orbit. A data gap of 35 days occurred between the last cycle of the nominal mission and first cycle of the extended. The Envisat 35-day exact repeat orbit (501 orbits per cycle) cross track spacing is 0.72° of longitude or about 71 km at 28°N. The Envisat 30-day repeat orbit (431 orbits per cycle) cross-track spacing is approximately 0.84° of longitude or about 82 km at 28°N.

GFO was not available during the study program, but historically provided cross-track sampling along its ground track at a spacing of 1.47° of longitude or about 144 km at 28°N. Tandem mission sampling from the OSTM/Jason-2 and Jason-1 orbits was more optimal than the original

TOP/POS since the orbits are interleaved in both space and time. For this second interleaved tandem mission, advantage was taken of Jason-1's still healthy propulsion system to put it into a much different position than TOP/POS was during the original tandem mission. In that mission TOP/POS remained so close to Jason-1 that the two spacecraft were flying almost simultaneously over the same region even though the ground tracks were offset by 1.42 degrees of longitude. In the OSTM/Jason-2 and Jason-1 tandem mission, Jason-1 was in the interleaved orbit, but much further away from OSTM/Jason-2, about five days behind and on the other side of Earth. Nevertheless, its ground track still falls mid-way between those of OSTM/Jason-2 in the interleaved ground-track sampling pattern with the interleaved Jason-1 track located next to Jason-2 with an apparent 5-day shift. There are three advantages to this configuration: 1) it is slightly better in terms of global aliasing, but is not the optimal 3.5-day offset tandem mission configuration described by Tai (2009), 2) it is slightly westwards propagating, and 3) it is slightly more efficient in terms of near-real-time (NRT) observation as measurements from the same dates are as far away as possible (Dibarboure et al. 2011).

Intuitively, mapping of SSH should improve if along-track altimeter data from multiple satellites are combined using objective analysis. SSH fields produced by combining multi-mission altimetry, however, may not be better than those constructed from Jason-1 or Jason-2 data alone, if uniform errors and wavelength/frequency resolution satisfying the Nyquist criteria are required of the space/time gridded product (Tai 2009), as has been proposed by Greenslade et al. (1997). While these constraints may be reasonable for large-scale eddy sampling studies (Chelton et al. 2011) or mission design, the constraints are too limiting for mesoscale mapping in general. Operational multiple-satellite objective mapping of the mesoscale circulation must therefore rely on suboptimal smoothing to resolve eddy-scale wavelength, albeit with the commensurate errors caused by non-uniform sampling and aliasing. This is true of both formal "optimal" interpolation and suboptimal objective analysis schemes. Nevertheless, the efficacy of the interpolated fields can be evaluated by comparing the interpolated altimetry with coincident in-situ data to quantitatively assess the processing and gridding strategies. PIES data are an ideal in-situ measurement type for these comparisons, and instrument sites were selected along altimeter ground tracks where possible to allow accurate assessment of not only the space/time gridded products, but the along-track data as well.

2.6.1.1 Along-Track Altimeter Data

Along-track altimeter data were collected from the Radar Altimeter Database System (RADS) hosted by the Delft Institute of Earth Observation and Space Systems at the Delft University of Technology in the Netherlands. RADS (Naeije et al. 2008; Naeije et al. 2000) is an online database that contains validated and verified altimeter data and correction data products for most of the historical and operational satellite altimeter missions. Standard corrections from RADS were applied to the along-track data including inverted barometer (MOG2D; Carrère and Lyard 2003), sea state bias (CLS), ionosphere (smoothed dual-frequency correction for Jason-1 and OSTM/Jason-2; JPL Global Ionosphere Maps (GIM) for Envisat), wet troposphere (on board radiometers) and dry troposphere (ECMWF) corrections. The data were further corrected for pole and solid-earth tides and the GOT 4.8 tide model (an update to Ray 1999) was used to remove ocean and load tides. Finally, the CNES CLS 2011 Global Mean Sea-Surface height (Schaeffer et al. 2012) at the location of each once-per-second sub-satellite point was subtracted from the corrected range measurement to produce along-track corrected SSH anomaly (SSHA).

In order to simplify further processing and analysis, collinear along-track SSHA datasets were created for each satellite when they were in an exact repeat orbit by interpolating the sub-satellite along-track data to reference ground tracks. Each 10-day exact repeat cycle of OSTM/Jason-2 and Jason-1 along-track SSHA data and each 35-day repeat cycle of Envisat SSHA data were linearly interpolated to reference ground tracks based on precision orbit determination ephemerides for each satellite at once-per-second along-track spacing. The OSTM/Jason-2 reference track used the computed ground track for TOP/POS cycle 18. The Jason-1 interleaved mission reference ground track was the same ground track with an offset in longitude corresponding to the nominal interleaved orbit. The Envisat 35-day reference ground track is based on repeat cycle 6 of the ERS-1 Multidisciplinary 1 Mission. Along-track data from the 30-day Envisat extended-mission orbit was stored and processed as non-repeat data as described for ERS-1 Geodetic Mission data in Leben et al. (2002).

Data coverage was very good from all three satellites along the exact-repeat reference ground tracks, although a gap of 35 days occurred when the Envisat orbit was changed in late October 2010. Along-track interpolated 1-Hz SSHA data coverage along the collinear ground-track points in water deeper than 200m in the Gulf was 94% for Jason-1 and 88% for OSTM/Jason-2 during the time period of the study program. Coverage during the Envisat nominal mission was 92%. We didn't attempt to calculate a similar statistic for data coverage from the drifting Envisat extended-mission orbit, but analysis of the data sampling used by objective mapping to be discussed later in this report suggests that the coverage was comparable.

2.6.1.2 Mesoscale Analysis

The processing of the altimeter data is designed to retain mesoscale signals while filtering out longer wavelength altimetric errors. This filtering, however, also removes long wavelength oceanographic signals. A detailed description of this processing and its implementation and validation in the GOM can be found in Leben et al. (2002). The procedure incorporates data from all of the available satellites, treating each data set in a consistent fashion as follows:

1. All along-track satellite data are referenced to an independent gridded-mean sea surface by subtracting the mean-sea-surface value at the sub-satellite point from each observation.
2. Along-track loess filtering is used to remove residual orbit and environmental correction errors. The loess filter removes a running least-squares fit of a tilt plus bias within a sliding window from the along-track data. The window width is approximately 15° of latitude (200 once-per-second along-track data points).
3. A multigrid preconditioned Cressman analysis with temporal weighting is used to objectively interpolate the along-track data to a $1/4^\circ$ grid.
4. A model-mean SSH field is added to the mapped SSH anomaly field to provide an estimate of the total SSH in the GOM.

2.6.1.3 Mean-Reference Surface and Model-Mean SSH

All along-track data are referenced to an existing altimetric-mean sea surface. The data are treated as non-repeating ground tracks and are referenced directly to the mean sea surface by interpolating the mean sea-surface value to the sub-satellite point (the point directly below the

satellite) and subtracting it from the sea- surface height. This applies an implicit cross-track geoid gradient correction to the along-track data before interpolation to the reference ground tracks.

The CNES CLS 2011 Global Mean Sea Surface (CLS11MSS) was used as the reference surface for the altimetry. The CLS11MSS was calculated from seven satellite missions: TOP/POS, ERS-1 GM, ERS-2, Jason-1, TOP/POS interleaved mission, GFO, and Envisat. Jason-2 data were not included because the altimetry data set used to determine this mean sea surface was based on work done in 2009 using data validated up to and through 2008 (Schaeffer et al. 2012). Although the data spans the time period from 1993 to late 2008, the data were processed to obtain a mean sea surface referenced to the time period from 1993–1999. This was done by preprocessing the altimetry so that the data would be homogeneous in terms of corrections and less contaminated by the oceanic seasonal variability. The interannual signals were then removed to obtain a mean sea surface referenced to the 7-year time period, 1993 through 1999.

To calculate the synthetic SSH estimates, we used the model-mean sea-surface height computed for the time period 1993-1999 from a data assimilation hindcast experiment performed by Drs. Lakshmi Kantha and Jei Choi for the MMS Deepwater Physical Oceanography Reanalysis and Synthesis Program (Nowlin et al. 2001). The data assimilation experiment used the University of Colorado-Princeton Ocean Model (CUPOM) and assimilated along-track TOPEX and ERS-1&2 sea-surface-height anomalies into CUPOM on a track-by-track basis as subsurface temperature anomalies (Kantha et al. 2005). Before adding the model mean to the gridded SSH- anomaly fields, we averaged the 1993-1999 SSH-anomaly fields and removed the residual anomalous altimetric mean over the time period. This references the SSH-anomaly fields to a mean spanning the same time period as determined from the CUPOM hindcast data assimilation experiment. The anomalous altimetric mean reflects the difference between the mean circulation contained in the CLS11 mean sea surface and the 1993-1999 data-assimilation mean. More discussion of these differences is found in Section 2.7.4 of this report.

2.6.1.4 Objective Mapping

Daily analysis maps of height anomaly relative to the mean sea surface were estimated using an objective analysis procedure (Cressman 1959) to interpolate the along-track data to a $1/4^\circ$ spatial grid. The method uses an iterative difference-correction scheme to update an initial-guess field and converge to a final gridded map. A multigrid procedure provides the initial guess. Five iterations were used with radii of influences of 200, 175, 150, 125, and 100 km while employing a 100-km spatial decorrelation length scale in the isotropic Cressman weighting function. The data were weighted in time using a 12-day decorrelation time scale relative to the analysis date using a ± 10 day window for the TOP/POS, Jason-1 and OSTM/Jason-2 data and a ± 17 day window for the ERS-1&2, Envisat, and GFO data. The details of the space and time-weighted version of the multigrid preconditioned Cressman analysis is described next and is based on the space-weighting-only technique described in Hendricks et al. (1996).

During the program time period, altimeter data were available from only the OSTM/Jason-2, Jason-1 and Envisat satellites. Figure 2.6-2 shows the availability and usage of data from each satellite over the time period from April 2009 through November 2011. In the plot, “actual” shows the satellites contributing data to the gridded product for any given day. The “available”

plot shows the days when there are valid data for a particular satellite. The “windowed” plot shows when there is no valid data on the actual day, but there are data within the window used for gridding. The “used” plot shows the days from which satellites could be chosen to be in the data product, but does not indicate valid data is available in a specific region. “Actual” is computed by forming a logical .AND. operation between “used” and the union of “available” and “windowed”.

2.6.1.5 Objective-Analysis Procedure

An objective-analysis (OA) procedure is used to interpolate the along-track sea-surface-height anomalies onto a regularly spaced $1/4^\circ$ global grid. The OA algorithm is based on the iterative difference-correction scheme of Cressman (1959). The initial guess field for the Cressman algorithm is supplied by an efficient multigrid procedure.

A rough estimate of the $1/4^\circ$ field is created by collecting the along-track SSH-anomaly data into $1/4^\circ$ grid cells. In grid cells where at least one SSH measurement is available, the average of all measurements within the cell is computed. Some of the grid cells may not contain data depending on the spacing of ground tracks. The OA procedure is designed to fill in these data gaps by creating an SSH-anomaly field that is consistent with the along-track measurements.

The $1/4^\circ$ -binned data can be used as an initial guess in the Cressman algorithm; however, having initial values in the empty grid cells can enhance the efficiency of the iteration procedure. A simple multigrid procedure is used to estimate values in cells where no altimeter measurements are available. Multigrid methods (Briggs 1987) rapidly solve a set of equations by working at several grid resolutions. In this case, if the along-track data are binned into 1° or 2° grid cells, there would be fewer or even no empty ocean-grid cells. Using a multigrid interpolation strategy to efficiently compute the means, a set of progressively coarser grids ($1/2^\circ$, 1° , 2° , ...) are created from the global $1/4^\circ$ grid, and the average SSH is computed at all coarser grid resolutions in each cell containing data. The mean values are transferred back to the original $1/4^\circ$ grid from the finest-scale grid containing a mean value coincident with that location. Finally, a fast red-black smoothing operator (e.g., see Press et al. 1992) is used on the $1/4^\circ$ initial guess field to smooth high-frequency noise introduced by the multigrid interpolation.

Cressman objective analysis uses an iterative-difference corrections scheme in which a new estimate of the SSH value for a given grid cell is equal to the sum of the previously estimated SSH at that location and a correction term. The correction term is forced by the difference between the estimated heights and the original data values over all grid cells within a specified radius of influence. A weight based on the number of original measurements within a grid cell is included in the correction term, as is a weight, based on the distance of a grid cell from the point being updated.

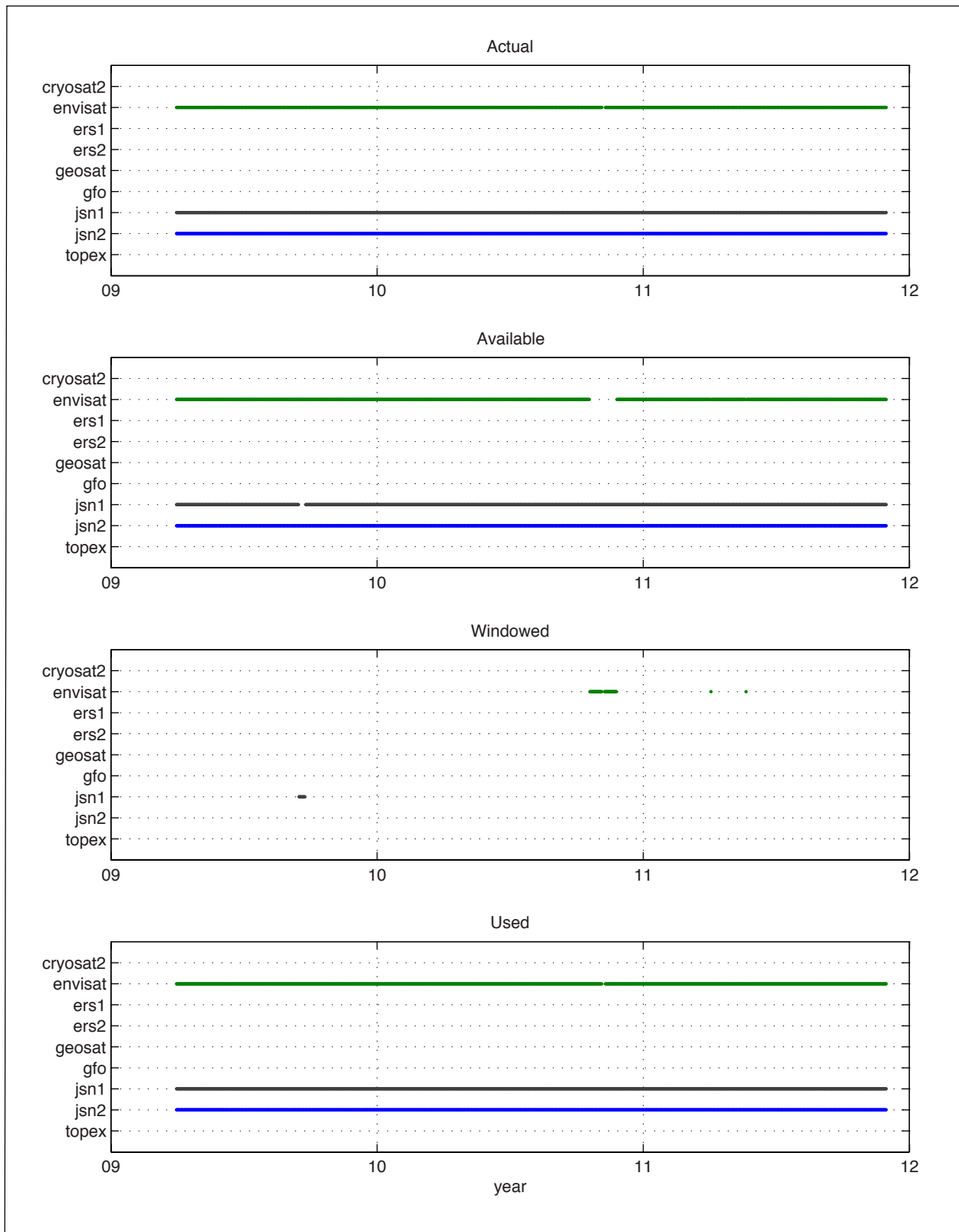


Figure 2.6-2. Plot showing daily “actual”, “available”, “windowed”, and “used” data from operational altimeter satellites during the study program.

The n th iteration for the SSH at grid cell i is computed using:

$$h_i^n = h_i^{n-1} + \frac{\sum w_m n_m^* (h_m^* - h_m^{n-1})}{\sum w_m n_m^*} \quad (2.6.1)$$

where the sums are taken over all m grid cells within the specified radius of influence R from the grid cell i being updated. The variables in (Eq. 1) are defined as:

- h_i^n n th iteration of SSH at grid cell i ;
- h_i^{n-1} the $(n-1)$ th iteration of SSH at grid cell i ;
- h_m^* average height at grid cell m based on the original data;
- h_m^{n-1} $(n-1)$ th iteration of SSH at grid cell m .
- n_m^* number of original measurements within grid cell m .

The weights in the correction term are defined by:

$$w_m = \exp(-ar_m^2 / R^2) \text{ for } r \leq R; \quad (2.6.2)$$

$$w_m = 0 \quad \text{for } r > R;$$

where r_m is the distance between grid cell m and the grid cell being updated and R is the maximum radius of influence. The parameter a is an adjustable weighting factor that scales the exponential spatial weighting of the data.

To incorporate weighting of the data in time, the data and the number of original measurements within a grid cell are each scaled by the weighting function:

$$w_t = \exp(-b\Delta t_m^2 / T^2) \text{ for } \Delta t \leq T; \quad (2.6.3)$$

$$w_t = 0 \quad \text{for } \Delta t > T;$$

where Δt_m is the difference between the measurement time and the time corresponding to the analyzed field. The parameter b is the time weighting factor, and T is the maximum time window of influence.

The empirical weighting parameters, a and b , are selected to map the mesoscale structure within the limitation of the scales resolvable by the cross-track altimeter sampling. The mesoscale analysis uses $a = 4$ and $b = 2$, which correspond to decorrelation space and time scales of 100 km and 12 days, respectively, for $R = 200$ km and $T = 17$ days. The maximum radius of influence, R , is decreased between the Cressman iterations to allow smaller scales to converge more quickly and to increase resolution when along-track sampling is available. For this study, R

is decreased from 200 to 100 km over five iterations giving a decorrelation length scale of 50 km on the final Cressman iteration.

2.6.2 Satellite Radiometry

Multi-channel satellite radiometry was used to complement altimeter sampling to provide high-resolution synoptic images for monitoring the LC and its associated eddies during cloud-free observing conditions. Radiometry from NASA's Moderate Resolution Imaging Spectroradiometer (MODIS) instrument onboard the Aqua satellite was the primary radiometry data set acquired and processed by CCAR for use by the project team. Several ancillary SST data sets were also acquired for use during the study program and in preparation of this report.

MODIS Ocean Color and SST

MODIS ocean color and SST data were downloaded from the Ocean Biology Processing Group (OBPG c2012) web and ftp sites at the NASA Goddard Space Flight Center (GSFC). All of the MODIS SST and ocean-color data were processed on or before January 19, 2012, and so are based on the MODIS data version R2010.0 reprocessing completed in June 2011. All of the CCAR processing for this study program used level 2 (L2) swath data.

Ocean-color data were processed by OBPG into chlorophyll-a (CHL-a) concentration using the empirical chlorophyll algorithm OC3 (O'Reilly et al. 2000), which uses measured radiances at 443, 488 and 551 nm to calculate the individual chlorophyll fields from each satellite image. The only editing flags applied were the processing flags and masks used by OBPG (Franz 2006). The OBPG generates two SST products from MODIS: short-wave (4 μ m) and long-wave (11 μ m). The L2 long-wave SST product generated from bands 31 and 32 located at 11 and 12 μ m, respectively, were used. The L2 SST hierarchical data format (HDF) files are generated by the Multi-Sensor L1 to L2 processing code (MSL12; OBPG 2010). For SST, the OBPG processing generates a quality level flag from a series of quality tests. The level flag ranges from 0 (best) to 4 (failure). We determined, by visual inspection, that a quality flag of 0 or 1 produced images of sufficient quality in the study region and applied that editing criteria to all the L2 SST data downloaded. This editing of the data is less stringent than that used by the OBPG in their production of L3 image products, where all values where the quality flag is nonzero are flagged. The OBPG editing might be preferred for high-accuracy quantitative analysis of SST data; however, the less stringent editing provided better coverage and accurate enough data for qualitative monitoring in the study region.

Both the MODIS L2 SST and ocean-color data come as individual HDF files per swath. These files contain the derived SST and CHL-a data at 1-km resolution. The geophysical values for each pixel are derived from the L1A raw radiance counts by applying the sensor calibration, atmospheric corrections, and various retrieval algorithms. Typically the data for one day in the GOM are split up across multiple swath files, some of which may overlap. The processing scripts read in all of the swaths files covering the GOM for one day, apply any editing masks (none for the CHL and only the quality flag for the SST), bin the data into a grid and write the gridded data out to a single netCDF file for a given day. The binning process averages data where there is an overlap (rare) and forms a grid of approximately 4-km resolution cells. In addition to the individual daily images, a moving average of the daily values is used to form 7-day composite daily images by averaging all of the valid data points within each 4-km cell.

2.6.3 Ancillary Satellite Altimeter Datasets

A 20-year dataset of Delayed Time (DT) mapped satellite altimeter analyses spanning the time period from 1993 through 2012 was downloaded from the Centre National d'Etudes Spatiales (CNES) Archiving, Validation, and Interpretation of Satellite Oceanographic (AVISO) data ftp site. The complete weekly DT-mapped time series through December 26, 2012 was released on June 4, 2013. This altimeter product was produced by SSALTO/DUACS and distributed by AVISO with support from the French Space Agency CNES. The multi-mission mapping of sea-level anomaly (SLA), which is another name for SSHA, is based on an optimal interpolation derived from Le Traon et al. 1998, with various improvements (e.g., Ducet et al. 2000, Le Traon et al. 2003, Dibarboure et al. 2011). Weekly Maps of Absolute Dynamic Topography (MADT) were downloaded on a $\frac{1}{4}$ degree Cartesian grid based on the sum of the interpolated maps of SLA and the Mean Dynamic Topography CNES/CLS 2009 (Rio and Larnicol 2010).

2.6.4 Ancillary SST Datasets

Three fully processed ancillary SST datasets were collected to use in the study program. Dr. Nan Walker at the LSU Earth Scan Laboratory provided one of the datasets and the other two were downloaded from the NASA/JPL Physical Oceanography Distributed Active Archive Center (PO.DAAC).

Dr. Nan Walker provided Geostationary Operational Environmental Satellite (GOES) Channel 2 brightness temperatures for the 3-year time period, 2009 through 2011, spanning the study program. The GOES GVAR image sensors provide high frequency repeat coverage that improves the potential for retrieving ocean temperature information over short time-scales and has been used successfully for tracking Loop Current frontal eddies (Walker et al. 2003, Walker et al. 2009).

The datasets downloaded from PO.DAAC were the 24 hour gridded 6-km GOES NRT L3 SST (GOES3 c2009) and the daily 0.011° Group for High Resolution Sea-Surface Temperature (GHRSSST) L4 Multi-scale Ultra-high Resolution (MUR) SST (GHRSSST [unknown date]). The GOES NRT L3 dataset is provided to PO.DAAC by NOAA/NESDIS. The GHRSSST MUR SST is produced by the NASA JPL MUR MEaSUREs Project and hosted by PO.DAAC (Chin [unknown date]).

2.7 PIES AND ALTIMETRY EVALUATION AND COMPARISON

PIES and satellite altimetry are complementary data types. Although the two measurement systems measure completely different physical quantities, they both yield an estimate of the height of the ocean surface relative to some datum, which is commonly referred to as sea-surface height (SSH).

In this section, the altimeter SSH measurement system is evaluated using PIES data as a benchmark for theoretical analyses and for comparison of PIES SSH directly to the coincident altimeter-derived SSH collected during the Dynamics of the Loop Current program. This is the fourth opportunity for these types of analyses and comparisons in the GOM, supplementing the results in the central, western, and northeastern GOM reported in the technical reports of the Exploratory, Northwestern, and Eastern surveys of deepwater currents (Donohue et al. 2006;

Donohue et al. 2008; Cox et al. 2010). Some of the statistics prepared for those reports will be presented again here and will be discussed in light of the results obtained in this program. These types of analyses and comparisons have the potential to identify problems in current datasets and to develop and test improvements in the altimeter data processing techniques used to produce future data products. This will facilitate the synthesis of altimetry data and PIES data from current and future arrays deployed in the deepwater GOM, which will improve observing and understanding of deepwater circulation patterns and dynamics throughout the water column and the Gulf.

2.7.1 Altimetric Sampling and Aliasing

Satellite altimeters provide discrete SSH measurements at sub-satellite points spaced approximately 5–7 km along ground tracks with exact repeats approximately every 10 or 35 days for the satellites used during the study program (Table 2.7-1). Orbital dynamics determine the space/time sampling pattern achieved on orbit, and there is a trade-off between spatial and temporal resolution when selecting an orbit during the mission-design phase of a satellite program. As an example, see the discussion of the TOP/POS mission in Parke et al. (1987). For single satellite sampling, high spatial resolution using a nadir pointing altimeter is achieved only at the expense of less frequent sampling of the sea surface in time, and vice versa.

Table 2.7-1. Satellite Altimeter Mission Exact-Repeat Periods and Periods Associated with the Nyquist Sampling Frequency

Satellite	Approximate Repeat	Repeat Period (days)	Nyquist Sampling Period (days)
TOPEX/Poseidon	10-day	9.9156	19.8313
ERS-2	35-day	35	70
Geosat Follow-On	17-day	17.0505	34.1010
Jason-1	10-day	9.9156	19.8313
OSTM/Jason-2	10-day	9.9156	19.8313
Envisat	35-day	35	70
Envisat Extended	30-day	30	60

Unlike ground-based instruments, where the sampling rate can be selected to satisfy a specific Nyquist criterion, satellite-based measurement systems in non-geosynchronous orbits have a temporal sampling rate imposed by the period at which a point on the Earth’s surface is sampled from orbit. Increasing the temporal sampling rate for a nadir-pointing altimeter, therefore, requires either the placing of the satellite in a shorter-repeat-period orbit, resulting in a loss of spatial sampling density, or by the addition of more satellites in the same repeat orbit and keeping the same spatial sampling density. Neither option can usually be justified from an economic, scientific, or operational perspective. Anecdotally, when additional sampling became available from TOP/POS after the commissioning phase of the TOP/POS and Jason-1 tandem mission, the decision was made to increase the spatial sampling density (Fu et al. 2003) and, by default, accept the existing level of temporal aliasing (i.e., aliasing caused by repeat sampling in time of the same spatial points) of the 10-day repeat sampling. A similar decision was made after the commissioning phase of OSTM/Jason-2, although the sampling and aliasing characteristics

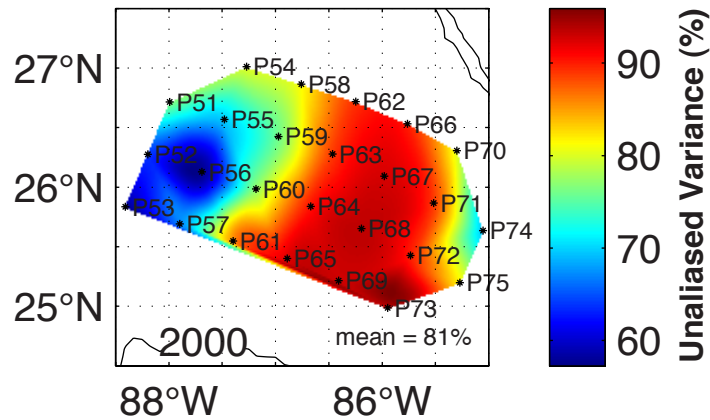
of the combined measurements of this tandem mission were more optimal (Dibarboure et al. 2011). A number of studies have addressed spatial/temporal aliasing issues (Schlax and Chelton 1994, Parke et al. 1998) including assessment of the aliasing of well known periodic signals such as tides; however, recently a few theoretical studies have assessed the SSH variance associated with the aliased signal from under-sampled SSH ocean measurements (Tai 2009).

The temporal aliasing of ocean signals by satellite-altimeter sampling can be addressed using the high-rate in-situ SSH data provided by PIES measurements. Hendry et al. (2002) performed the first study along these lines using PIES data collected within the North Atlantic Current in the Newfoundland Basin. They found that the time scales of motion observed in the region are such that 86-95% of the subinertial-period SSH variability was not aliased by the approximately 10-day TOP/POS repeat-period sampling. Gille and Hughes (2001) performed an earlier study of sampling using only bottom-pressure records; however, that type of study would not be appropriate in the GOM where the time scales associated with the bottom-pressure variability are not representative of the time scales of the SSH variability.

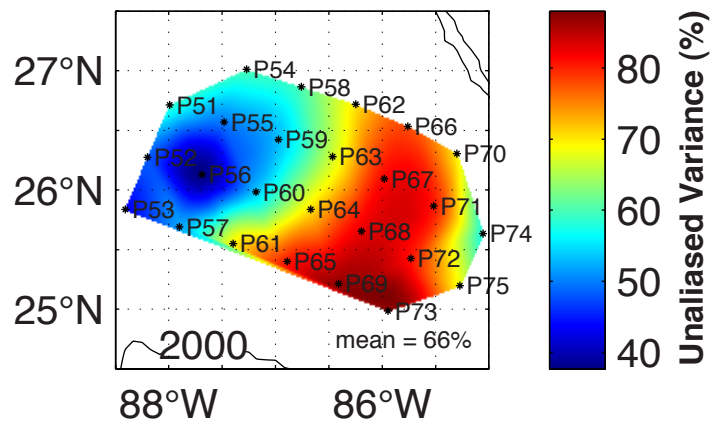
Following the methodology of Hendry et al. (2002), assessments were made of the SSH signal in the Exploratory, Northwestern, and Eastern Gulf Study regions in the central, northwestern, and eastern Gulf, respectively (Donohue et al. 2006, Donohue et al. 2008, Cox et al. 2010), and now report similar analyses for the Loop Current study array for the approximately 10-day, 17-day, and 35-day exact-repeat-period sampling historically available from the satellite altimeter missions. Power spectra were computed for each of the SSH time series – barotropic, baroclinic, and combined – and the percentage of cumulative power in the spectra up to each of the Nyquist frequencies associated with the 10-day, 17-day, and 35-day repeat sampling periods were calculated. The periods corresponding to the Nyquist frequency for each of the altimeter satellites are tabulated in Table 2.7-1. Figures 2.7-1, 2.7-2 and 2.7-3 show maps of the unaliased variance (i.e., from a signal measured at a sufficiently high sampling rate so that any aliased signal is negligible) associated with 10-day, 17-day, and 35-day repeat sampling periods in the study region for the current altimeter missions from the barotropic, baroclinic, and combined SSH signals, respectively. These study summary statistics are tabulated in Table 2.7-2 along with the statistics from the Exploratory, Northwestern, and Eastern Gulf PIES arrays. Tabulated values for each of the Loop Current PIES stations are listed in Table 2.7-3.

The aliasing of the barotropic SSH signal is the most severe of the three signals because of the shorter time scales associated with that signal in the GOM when compared with the baroclinic SSH or total SSH signals. When averaged over the Loop Current PIES array, the mean value of the 10-day sampling period unaliased barotropic variance is 81%, much higher than the mean values of 59%, 62%, and 63% estimated from the Exploratory Program, Northwestern and Eastern Gulf PIES arrays, respectively. The Loop Current array individual station results range from a minimum of 57% at PIES 53 to a maximum of 93% at PIES 67, 68, 69 and 73, which is a greater range than the 56% to 72% and the 44% to 77% ranges found for the Northwestern Gulf and the Exploratory program arrays, respectively. The spatial pattern of aliasing is similar for 17-day and 35-day sampling, with more aliasing in the northwestern half of the array and the least amount in the southeastern half. The mean values of the unaliased variance, however, decreased significantly to 66% and 45% for 17-day and 35-day sampling, respectively. This significant

Barotropic: 10-day Sampling



Barotropic: 17-day Sampling



Barotropic: 35-day Sampling

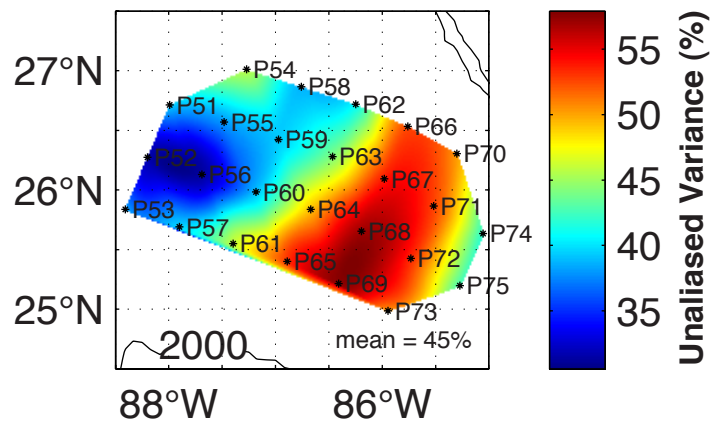


Figure 2.7-1. Maps of PIES barotropic unalised variance for 10-day, 17-day, and 35-day sampling.

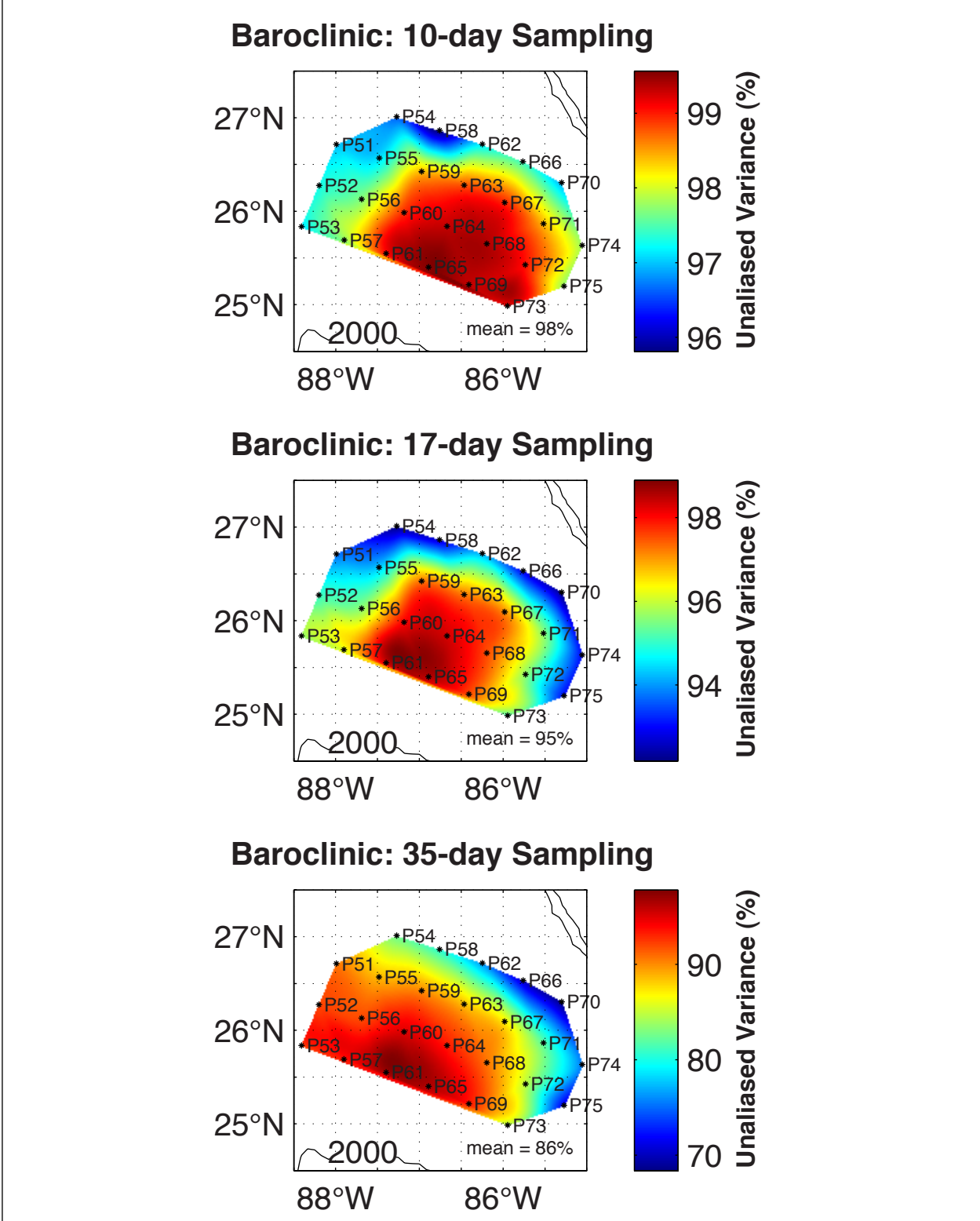


Figure 2.7-2. Maps of PIES baroclinic unalised variance for 10-day, 17-day, and 35-day sampling.

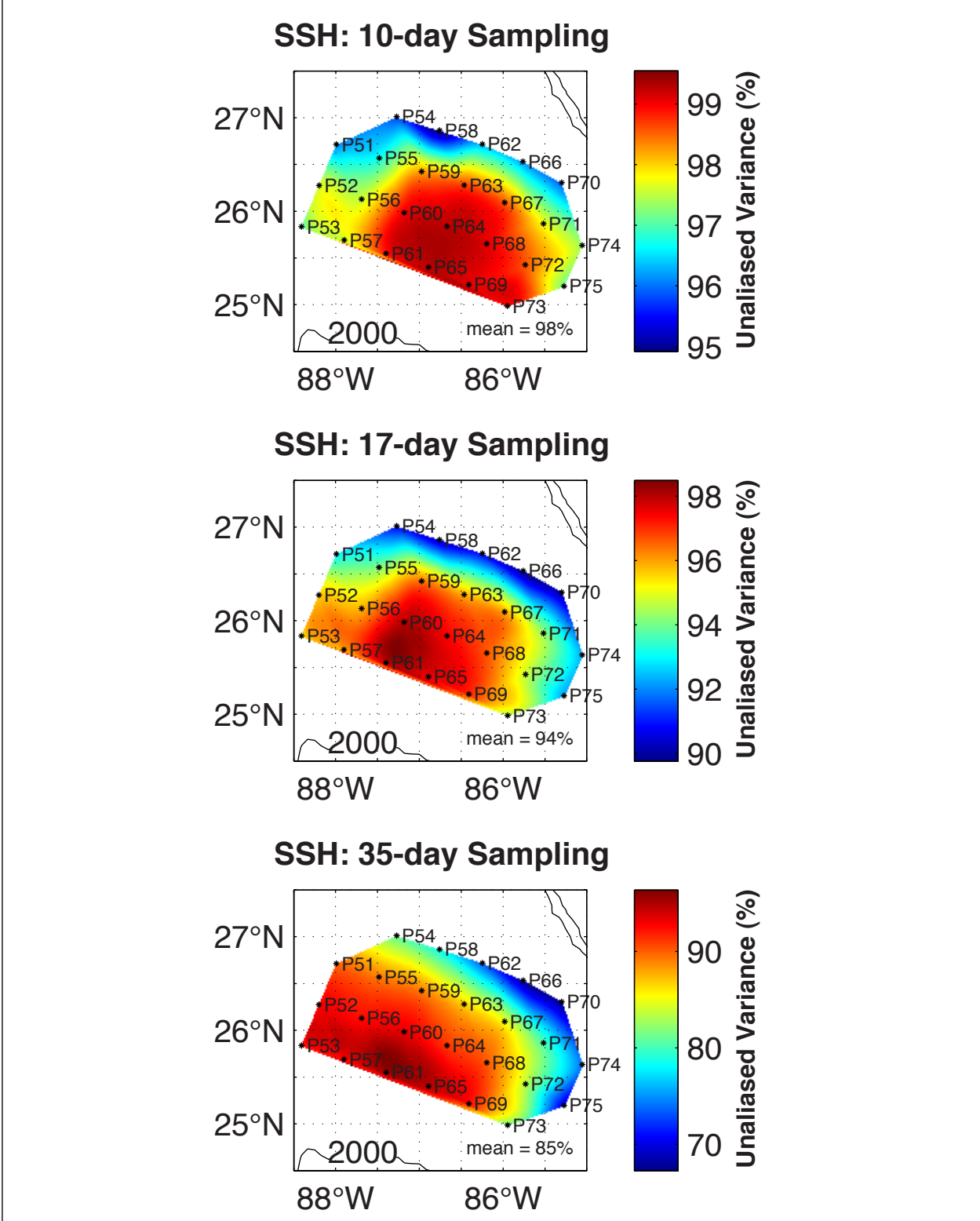


Figure 2.7-3. Maps of PIES SSH unalised variance for 10-day, 17-day, and 35-day sampling.

Table 2.7-2. Unaliased Variance Statistics for 10-day, 17-day, and 35-day Exact-Repeat Sampling of the PIES Barotropic, Baroclinic, and Combined SSH Signals

Stations	Barotropic Signal Mean (%)			Baroclinic Signal Mean (%)			Total SSH Signal Mean (%)			
	Repeat:	10-day	17-day	35-day	10-day	17-day	35-day	10-day	17-day	35-day
Loop Current Program										
all stations		81	66	45	98	95	86	98	94	85
Eastern Gulf Program										
all stations		63	49	35	93	89	76	92	88	75
Northwestern Gulf Program										
all stations		62	53	42	97	92	76	94	89	75
Exploratory Program										
all stations		59	47	37	97	93	78	95	92	78
above escarpment		56	45	39	96	93	75	94	91	75
below escarpment		61	49	36	97	93	80	96	93	79
Stations	Barotropic Signal Maximum (%)			Baroclinic Signal Maximum (%)			Total SSH Signal Maximum (%)			
	Repeat:	10-day	17-day	35-day	10-day	17-day	35-day	10-day	17-day	35-day
Loop Current Program										
all stations		93	87	57	100	99	97	99	98	95
Eastern Gulf Program										
all stations		70	55	39	97	92	85	97	93	83
Northwestern Gulf Program										
all stations		72	64	47	99	97	90	98	95	87
Exploratory Program										
all stations		77	60	45	99	98	93	99	98	93
above escarpment		60	50	42	99	98	90	97	96	90
below escarpment		77	60	45	99	98	93	99	98	93
Stations	Barotropic Signal Minimum (%)			Baroclinic Signal Minimum (%)			Total SSH Signal Minimum (%)			
	Repeat:	10-day	17-day	35-day	10-day	17-day	35-day	10-day	17-day	35-day
Loop Current Program										
all stations		57	38	31	96	92	68	95	90	67
Eastern Gulf Program										
all stations		59	44	31	84	79	68	84	80	67
Northwestern Gulf Program										
all stations		56	47	36	93	86	52	84	79	53
Exploratory Program										
all stations		44	38	29	92	86	54	87	82	54
above escarpment		51	42	36	92	86	54	87	82	54
below escarpment		44	38	29	93	87	56	92	85	56

Table 2.7-3. PIES SSH, Baroclinic, and Barotropic Statistics and Percent of Unaliased Variance Measured by Satellites in 10-day, 17-day, and 35-day Exact-Repeat Orbits

PIES ID#	Signal	Length (days)	Std (cm)	T _{0.5} (days)	Unaliased Variance (%)		
					10-day	17-day	35-day
P51	SSH	903.5	22.4	341	96	93	90
	Baroclinic		22.0	341	97	94	91
	Barotropic		4.2	32	77	59	39
P52	SSH	903.5	25.3	341	98	96	93
	Baroclinic		25.2	341	97	95	92
	Barotropic		4.0	23	64	48	32
P53	SSH	903.5	25.7	341	97	95	91
	Baroclinic		25.6	341	97	95	92
	Barotropic		3.3	18	57	43	39
P54	SSH	903.5	18.5	205	96	91	81
	Baroclinic		18.1	228	97	92	82
	Barotropic		4.6	35	80	60	46
P55	SSH	903.5	23.8	341	97	94	89
	Baroclinic		23.4	341	97	94	89
	Barotropic		4.5	26	70	50	38
P56	SSH	903.5	26.3	341	98	96	92
	Baroclinic		26.8	341	98	96	92
	Barotropic		4.0	19	58	38	31
P57	SSH	903.5	26.7	341	98	96	92
	Baroclinic		27.4	341	98	96	93
	Barotropic		3.6	24	67	52	40
P58	SSH	903.5	19.2	171	95	90	78
	Baroclinic		19.4	186	96	93	81
	Barotropic		4.5	35	81	60	39
P59	SSH	903.5	25.4	341	98	96	89
	Baroclinic		25.3	341	98	97	90
	Barotropic		4.5	31	76	53	39
P60	SSH	903.5	28.3	341	99	98	93
	Baroclinic		28.6	341	99	98	95
	Barotropic		4.5	32	77	54	39
P61	SSH	903.5	28.0	341	99	98	95
	Baroclinic		29.0	341	99	98	97
	Barotropic		4.7	46	85	69	46
P62	SSH	903.5	19.3	158	96	91	73
	Baroclinic		19.3	171	97	94	76
	Barotropic		5.2	47	89	70	41

Table 2.7-3. (continued)

PIES ID#	Signal	Length (days)	Std (cm)	T _{0.5} (days)	Unaliased Variance (%)		
					10-day	17-day	35-day
P63	SSH	903.5	26.9	293	99	96	88
	Baroclinic		26.5	341	99	97	89
	Barotropic		5.4	46	89	67	44
P64	SSH	903.5	30.3	341	99	97	91
	Baroclinic		30.0	341	99	98	93
	Barotropic		5.8	51	90	71	49
P65	SSH	903.5	29.3	341	99	98	95
	Baroclinic		30.1	341	100	99	97
	Barotropic		5.8	62	92	80	53
P66	SSH	903.5	17.9	137	96	90	68
	Baroclinic		17.8	137	97	93	70
	Barotropic		4.7	57	90	78	52
P67	SSH	903.5	25.7	293	99	96	85
	Baroclinic		25.4	341	99	97	87
	Barotropic		5.9	59	93	82	54
P68	SSH	903.5	28.9	341	99	97	90
	Baroclinic		28.8	341	99	98	91
	Barotropic		6.2	66	93	83	57
P69	SSH	903.5	28.8	341	99	97	92
	Baroclinic		29.3	341	99	98	93
	Barotropic		5.8	68	93	87	57
P70	SSH	903.5	16.0	89	96	90	67
	Baroclinic		16.0	89	97	92	68
	Barotropic		3.0	46	80	69	50
P71	SSH	903.5	22.9	256	98	94	80
	Baroclinic		23.2	293	98	96	82
	Barotropic		4.3	55	89	80	53
P72	SSH	903.5	25.4	341	99	95	83
	Baroclinic		25.9	341	99	96	85
	Barotropic		4.6	57	90	81	53
P73	SSH	903.5	27.0	341	99	94	81
	Baroclinic		26.9	341	99	95	84
	Barotropic		5.5	66	93	86	50
P74	SSH	903.5	19.1	108	97	92	74
	Baroclinic		19.1	120	98	93	75
	Barotropic		2.3	29	69	57	42
P75	SSH	903.5	22.0	114	97	92	70
	Baroclinic		21.8	146	98	93	71
	Barotropic		3.2	45	81	68	42

aliasing of the barotropic signal by the 17-day and 35-day sampling in the northwestern half of the Loop Current array is comparable to barotropic signal aliasing seen in the other Gulf study programs. The significantly reduced aliasing exhibited by the 10-day sampling of the barotropic signal suggests that the signals with periods less than the 20 days in the Loop Current region do not contribute as much to the total barotropic variability as they do in the other study regions. One gulf-wide source of aliased barotropic signal is the 16-day common mode that has been observed by both the Exploratory and Loop Current PIES arrays.

The unaliased variance of the baroclinic and total SSH signal is much higher than the barotropic-only case because of the longer-period baroclinic signals associated with the Loop Current and the dominance of the extremely energetic Loop Current baroclinic signal on the total SSH. Still, there are large differences between the 10-day and 35-day patterns, while the 10-day and 17-day patterns are more similar. For a 10-day sampling period of the baroclinic signal in the Loop Current array, the unaliased-variance-mean value over the array is 98% and ranges from a minimum of 96% at PIES 58 to a maximum of nearly 100% at PIES 65. The 35-day sampling mean value is only 86% and ranges from a minimum of 68% at PIES 70 to a maximum of 97% at PIES 61. The total combined baroclinic and barotropic SSH signal shows similar patterns. The SSH 10-day period unaliased-variance-mean value over the array is 98% and ranges from a minimum of 95% at PIES 58 to a maximum of 99% at PIES 63, 64 and 65. The 35-day sampling mean value decreased to 85% and ranged from a minimum of 67% at PIES 70 to a maximum of 95% at PIES 61 and 65. These overall averages and ranges are comparable to those found in our analyses of the Eastern, NW Gulf and Exploratory PIES, further confirming the similarity of the baroclinic and total SSH signals in the GOM deepwater even over separate and distinct observational time periods.

In summary, 95% to 98%, 84% to 97%, 84% to 98%, and 87% to 99% of the sub-inertial period SSH variability in the Loop Current, Eastern Gulf, Northwestern Gulf, and Exploratory Study regions, respectively, are unaliased by the TOP/POS 10-day repeat-period sampling. This is comparable to the 86% to 95% estimated from the Newfoundland Basin array by Hendry et al. (2002). The results for the 17-day and 35-day repeat sampling show, however, that there can be aliasing of GOM SSH signals in satellite altimetry, even with the dominance of the longer-period baroclinic signals associated with the LC and LC eddies in the GOM deepwater. The degree to which this affects the space/time-interpolated maps of altimetric SSH needs to be investigated in more detail. Also, the presence of the ubiquitous common mode needs to be considered when processing sea-surface-height data. In most cases, this signal will be removed by standard altimetric processing techniques, and the aliasing will be mitigated. However, the signal may be retained as more sophisticated processing and higher-frequency corrections are applied to the data.

2.7.2 Signal-to-Noise

A useful metric for assessing the accuracy of altimeter-derived estimates of SSH is the ratio of the unaliased variance to the aliased variance of the SSH signal, which is an estimate of the signal-to-noise ratio (SNR) of a perfect on-orbit measurement system. The amount of aliasing is also a function of the repeat-sampling period of the satellite altimeter as can be seen in Figure 2.7-4. Note that we do not consider the barotropic and baroclinic components separately because they cannot be distinguished from on-orbit measurements alone. Also, the “noise” in the

unaliaised-to-aliasd SNR is colored noise associated with under-sampled geophysical signals that are very difficult to remove without excessive smoothing or filtering of the along-track data before interpolation. This is the primary reason that the requirement of uniform errors and wavelength/frequency resolution satisfying the Nyquist criteria, as proposed by Greenslade et al. (1997) for gridded altimeter products, is unrealistic in practice.

Table 2.7-4 shows a summary of the SNR statistics estimated from the Loop Current, Eastern Gulf, NW Gulf, and Exploratory PIES data. In all cases, the Loop Current SNR is equal to or higher than the Eastern, NW Gulf, and Exploratory Program statistics for all three sampling scenarios. Nevertheless, the SNR in all of the study regions was very good for 10-day and 17-day altimetric sampling. The 35-day sampling is more problematic. The 35-day sampling spatial map (lower panel of Figure 2.7-4) shows SNR ratios in the low single digits on the outer edge of the Loop Current study array, which would make it difficult to distinguish between signal and aliased signal at that sampling frequency from a single-point measurement. Similar low SNR was found with 35-day repeat sampling of the PIES measurements from the other program arrays.

Table 2.7-4. Signal-to-Noise Ratio (SNR) Statistics for 10-day, 17-day, and 35-day Exact-Repeat Sampling of the PIES Barotropic, Baroclinic and Combined SSH Signals

Stations	Mean SNR			Minimum SNR			Maximum SNR		
	Repeat:	10-day	17-day	35-day	10-day	17-day	35-day	10-day	17-day
Loop Current Program									
all stations	58	22	8	19	9	2	136	49	20
Eastern Gulf Program									
all stations	16	8	3	5	4	2	32	13	5
NW Gulf Program									
all stations	22	11	4	5	4	1	49	19	7
Exploratory Program									
all stations	28	16	5	7	5	1	99	49	13
above escarpment	20	13	4	7	5	1	32	24	9
below escarpment	33	19	5	12	6	1	99	49	13

2.7.3 Sea-Surface-Height Time Scales

Following the methodology of Hendry et al. (2002), the period corresponding to the frequency at which the cumulative power spectrum reaches 50% of the total variance – the half-power period, $T_{0.5}$ – was determined from the spectral analysis of each of the PIES SSH anomaly time series. $T_{0.5}$ is a more robust measure of time scale than the temporal autocorrelation zero crossing, T_0 , and is the preferred scale to be used to define the effective degrees of freedom of a time series (Fofonoff and Hendry 1985). This robustness is due, in large part, to the global and integral nature of the $T_{0.5}$ metric, which is less sensitive to competing time scales within the time series. In contrast, the calculation of T_0 is a less robust measure because the first zero crossing of the temporal autocorrelation function is quite sensitive to the presence of multiple time scales and/or secular trends in the time series.

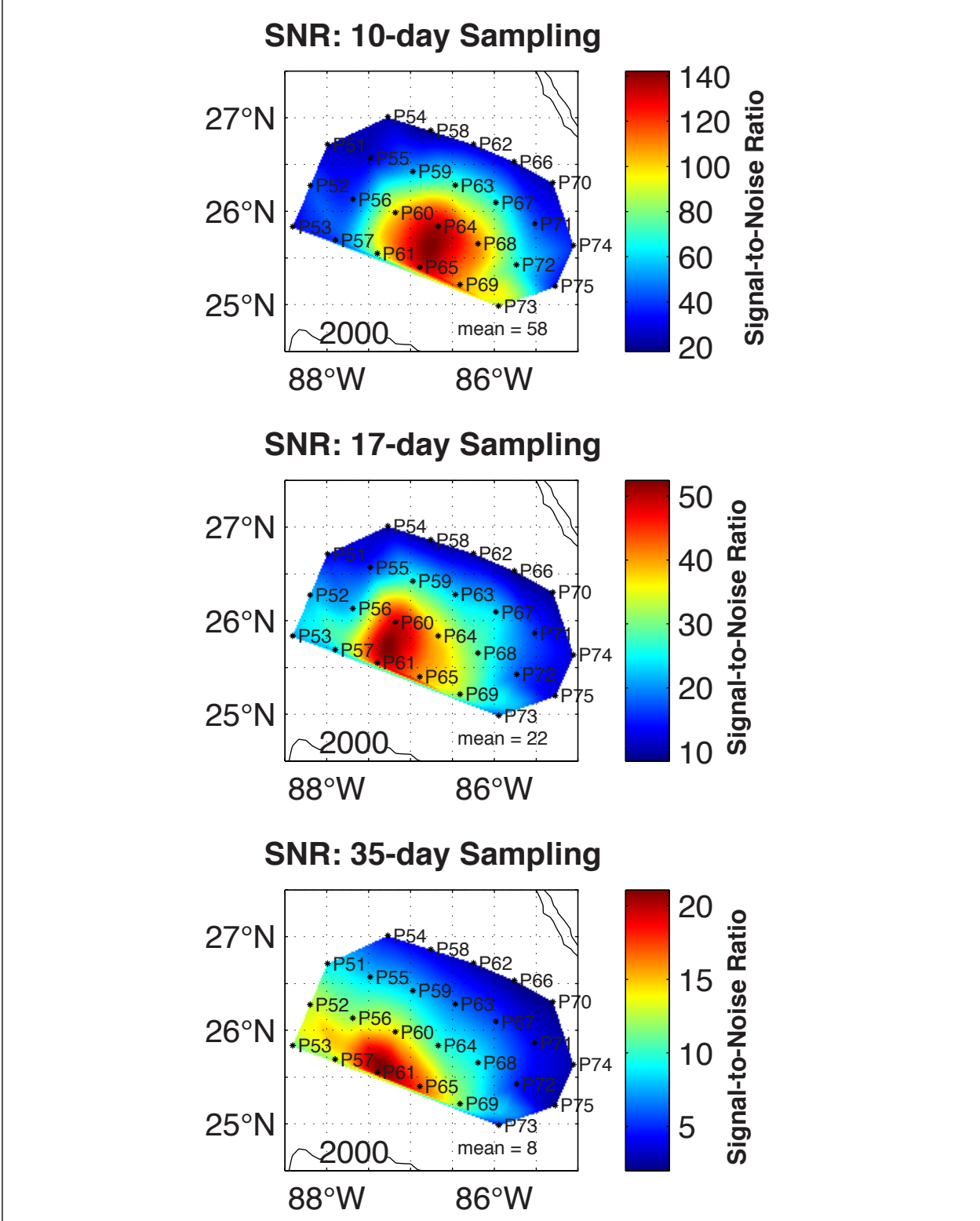


Figure 2.7-4. Maps of PIES SSH signal-to-noise ratio (SNR) for 10-day, 17-day, and 35-day sampling. SNR is estimated from the ratio of unaliased to aliased variance.

The half-power periods were computed from the 30-month Loop Current PIES barotropic, baroclinic, and SSH anomaly time series. Similar values were also computed from the 13-month Eastern Gulf, 9-month Northwestern Gulf, and 12-month Exploratory programs. Spatial maps of $T_{0.5}$ in the Loop Current study region for each of the three signals are shown in Figure 2.7-5. No effort was made to detrend the time series before calculating the spectra because of the relatively short duration of the earlier records. This allows estimation of the longer time scales of variability associated with the LC and LC eddies that occur in most of the records. Mean $T_{0.5}$ values are listed in Table 2.7-5 for each program, showing the average time scales for each of the signals at all PIES stations. The Exploratory Program averages for stations above and below the Sigsbee Escarpment are also shown.

Table 2.7-5. Half-Power Period of PIES Barotropic, Baroclinic, and Total SSH Signals

Stations	Barotropic Signal Half-Power Period (days)			Baroclinic Signal Half-Power Period (days)			Total SSH Signal Half-Power Period (days)		
	mean	max	min	mean	max	min	mean	max	min
Loop Current Program									
all stations	43	68	18	287	341	89	278	341	89
Eastern Gulf Program									
all stations	20	25	16	121	158	102	121	158	102
NW Gulf Program									
all stations	21	47	14	155	293	66	148	293	66
Exploratory Program									
all stations	19	34	12	230	34	12	232	512	60
above escarpment	16	18	14	188	18	14	195	341	64
below escarpment	21	34	12	262	34	12	260	512	60

The mean half-power periods of the barotropic signals are quite similar in all the regions and are dominated by the ubiquitous Gulf-wide common mode. The spatial distributions, however, are notably different between the east/central and western Gulf. In the Loop Current study region, the longer period barotropic signals are located in the southeastern half of the study array in the deepest water, as was the case in the Eastern Gulf study array. This pattern in the eastern Gulf is similar to the central Gulf where the longer-period signals are in the south-central part of the Exploratory array in the deepwater below the Sigsbee Escarpment. In contrast to the eastern and central Gulf results, the longer period barotropic signals in the NW Gulf are on the upper slope.

The time scales of the baroclinic and combined-barotropic-and-baroclinic SSH anomaly signals are very similar because of the small contribution by the barotropic mode to the total signal. The long half-power periods associated with these signals show the dominance of the low frequency LC and LC eddy variability observed in all four regions during the observational periods. In the Loop Current study, the 300-day and longer periods cover nearly the entire array, reflecting the low-frequency variability of the Loop Current that this study array was designed to monitor. The shortest half-power periods, less than 180 days, are found on the northeastern periphery of the

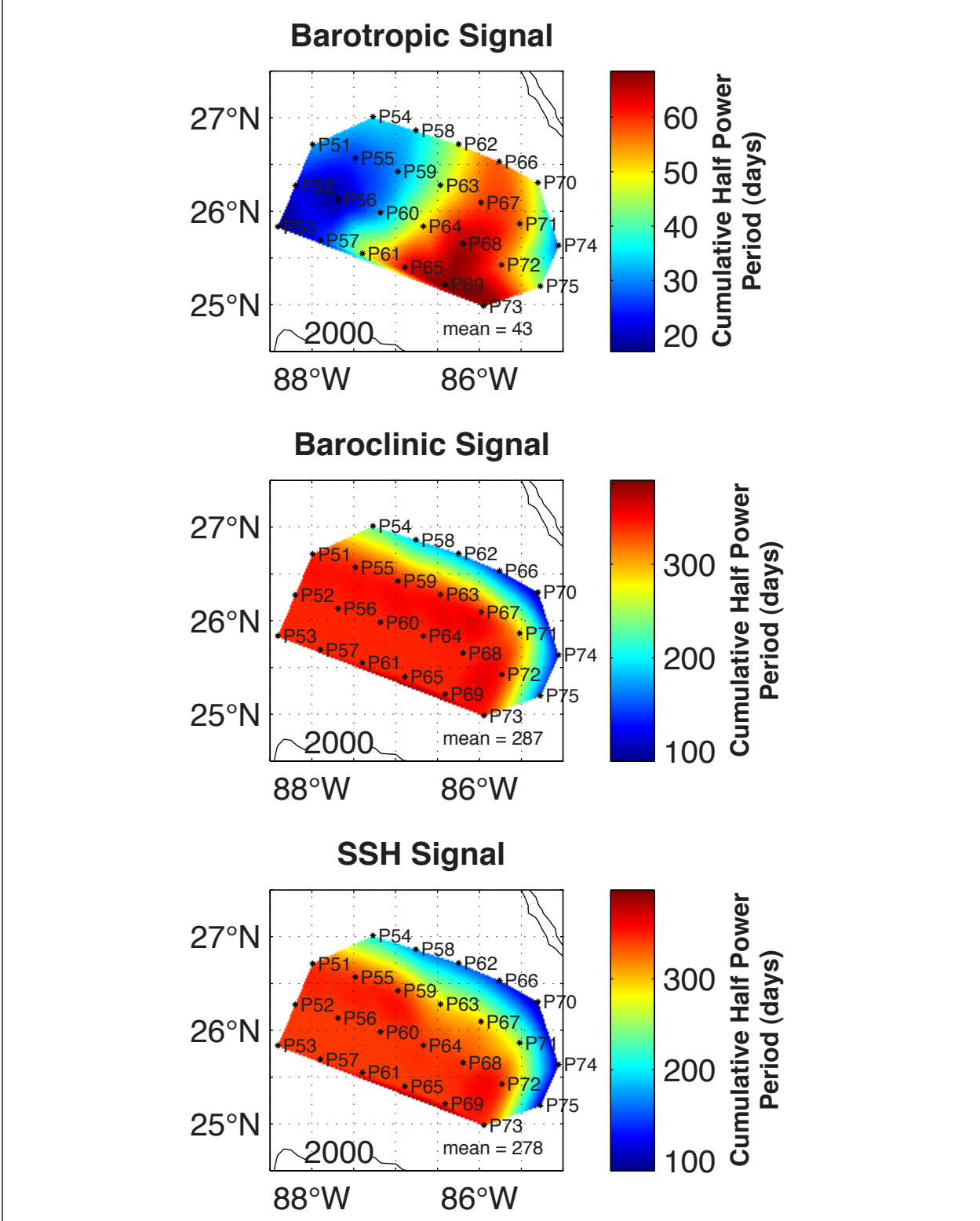


Figure 2.7-5. Spatial maps of the half-power period, $T_{0.5}$, computed from the PIES barotropic, baroclinic, and combined SSH anomaly time series. Mean values over all stations are also shown.

array. The higher-frequency signals, contributing these shorter periods, likely arise from the high-frequency SSH variability generated by Loop Current frontal meanders or cyclonic eddies along the northern and eastern margin of the array.

2.7.4 Comparison of CCAR Mesoscale, AVISO, and PIES Mapped Absolute SSH

The CCAR Mesoscale SSH-gridded-altimeter data product that was distributed and used for data synthesis activities in this report was evaluated by comparison with the maps of absolute SSH derived from the PIES measurements (see section 2.5.6). Comparisons were also made with the weekly AVISO maps coincident with the PIES records. Maps of the CCAR Mesoscale versus PIES SSH, and the AVISO versus PIES SSH temporal-correlation-coefficient maps are shown in Figure 2.7-6. The temporal correlation of the PIES-mapped SSH with the CCAR Mesoscale SSH is higher over the entire array than it is with the AVISO SSH; nevertheless, the correlation of the PIES-mapped SSH with both altimeter SSH data products is excellent. Differences in the correlation maps reflect the filtering and smoothing applied during the data processing and the spatial and temporal scales retained by each of the objective-mapping schemes. One difference in the data products is the seasonal steric signal, which is only retained by the processing employed for the AVISO product. For consistency, the seasonal steric signal was estimated and removed from each AVISO SSH map by subtracting the average of the SSH values from that map over all points in the Gulf deeper than 200 m, and then the correlation map was recalculated as shown in Figure 2.7-7. This improves the correlation of the AVISO product with the PIES data to levels nearly as high as those calculated with the CCAR Mesoscale product. The impact of the filtering and smoothing of the CCAR Mesoscale SSH processing can be seen by comparing the SSH standard deviation computed from each of the data products over the program time period (Figure 2.7-8). The SSH standard deviation is comparable between the PIES and AVISO-mapped SSH, but attenuated in the CCAR Mesoscale-mapped SSH product primarily because of the along-track filtering of the SSHA data before objective mapping.

The comparison of the CCAR Mesoscale and AVISO-mapped SSH to the PIES-mapped SSH shown in Figures 2.7-6, 2.7-7 and 2.7-8 are independent of the mean SSH height added to the altimeter-derived maps of SSHA to produce an estimate of the total SSH. The 30-month record of PIES SSH from the Loop Current study, however, provides the first opportunity to directly compare an accurate mean SSH, which spans a large area in the eastern Gulf dominated by the presence of the Loop Current, with the mean SSH fields used in the altimeter data products. To do this initial comparison, the different reference levels used in each of the mapped SSH datasets were accounted for. Then, each of the SSH fields was referenced so that the 17-cm contour would be consistent between the three datasets. This was done using the regressions shown in Figure 2.7-9. First, the 17-cm tracking contour in the PIES data set was estimated from the regression of the PIES daily-mean SSH values on to the CCAR daily-mean SSH values in the study region (upper panel of Figure 2.7-9). From this regression, the CCAR 17-cm tracking contour was estimated corresponding to the 259.6-cm PIES contour. Then, the 259.6-cm PIES contour, corresponding to the 12.1-cm AVISO SSH contour, was estimated using the regression of the PIES daily-mean SSH values on to the AVISO daily-mean SSH values in the study region using the AVISO weekly $\frac{1}{4}$ -degree SSH data product (lower panel of Figure 2.7-9). For consistency, the seasonal steric signal was removed from each AVISO SSH map as described

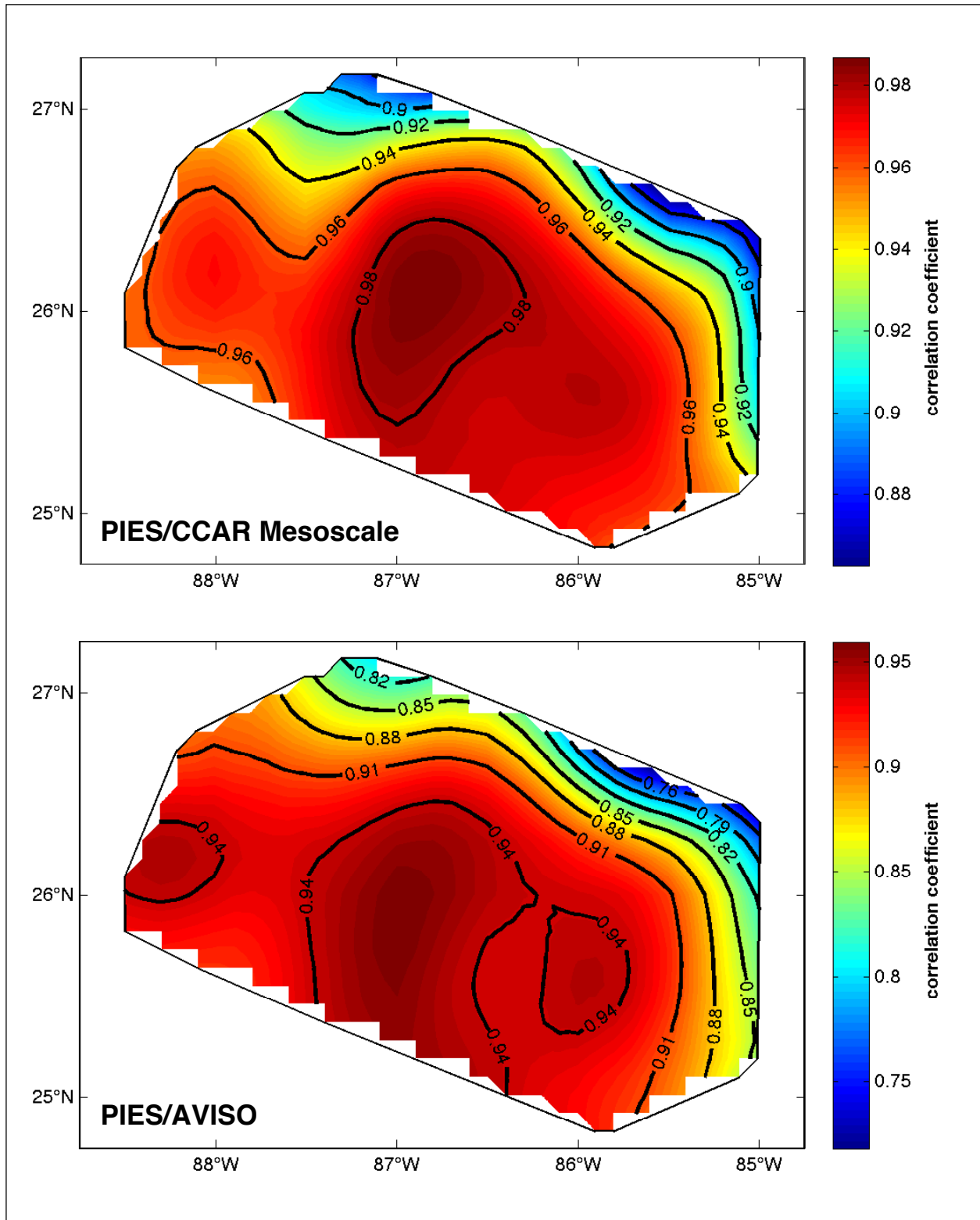


Figure 2.7-6. Spatial map of the temporal correlation between the PIES mapped SSH time series and the CCAR Mesoscale SSH (upper panel) and AVISO SSH (lower panel) time series coincident with the LC study.

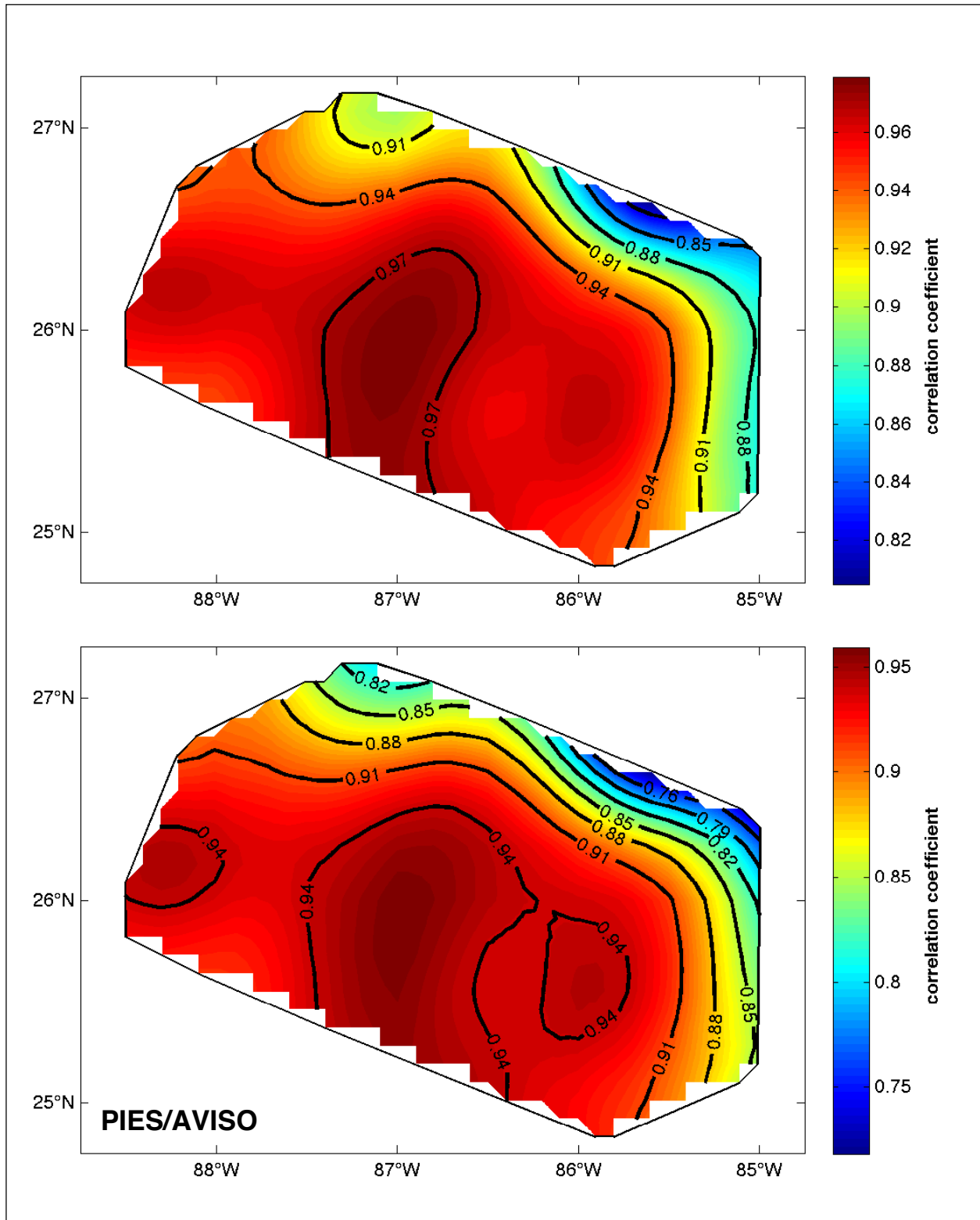


Figure 2.7-7. Spatial map of the temporal correlation between the PIES mapped SSH time series and the AVISO SSH time series with (upper panel) and without (lower panel) the seasonal steric signal removed.

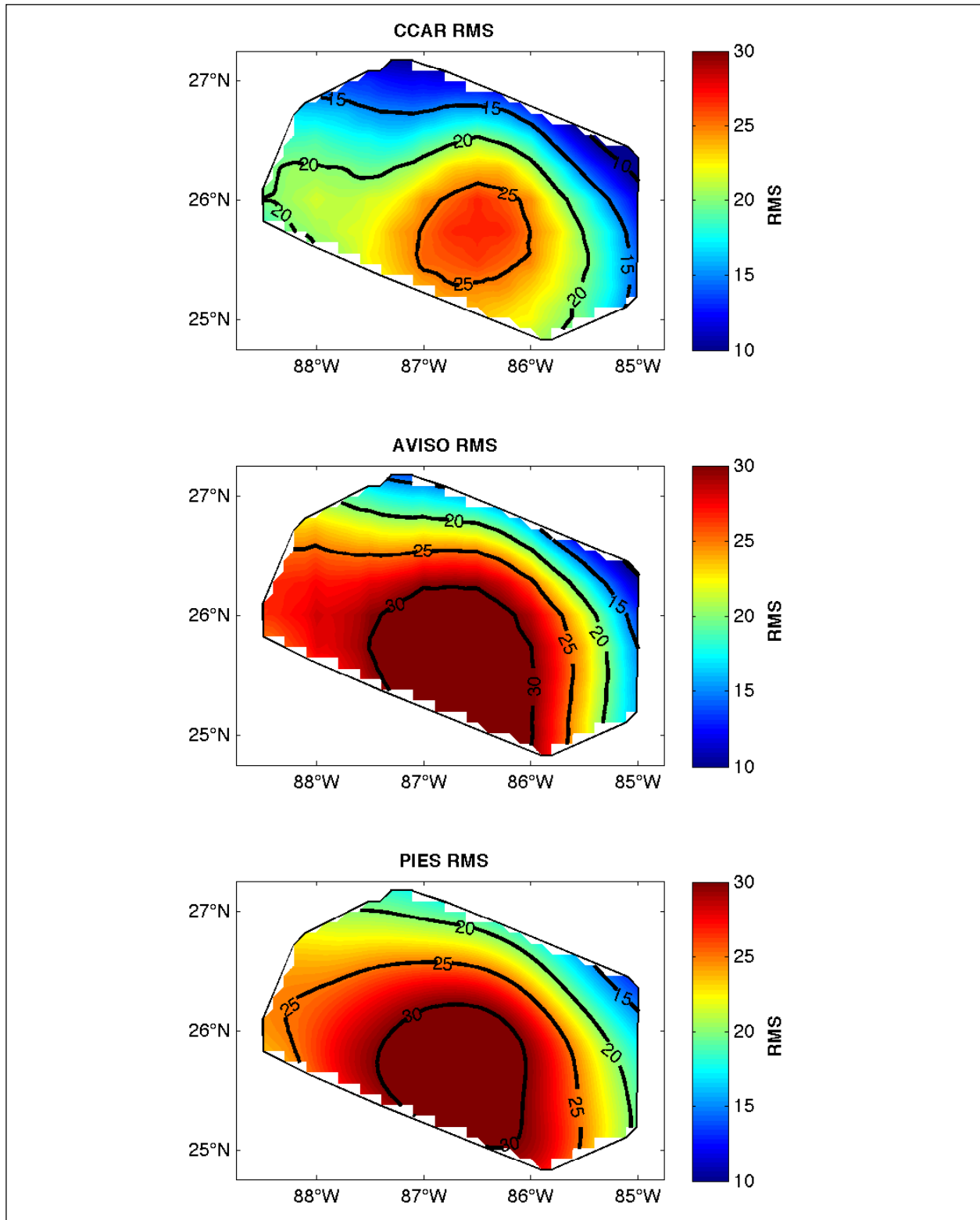


Figure 2.7-8. Rms SSHA (standard deviation about the mean) during the program time period of the CCAR Mesoscale (upper panel), AVISO (middle panel), and PIES mapped datasets.

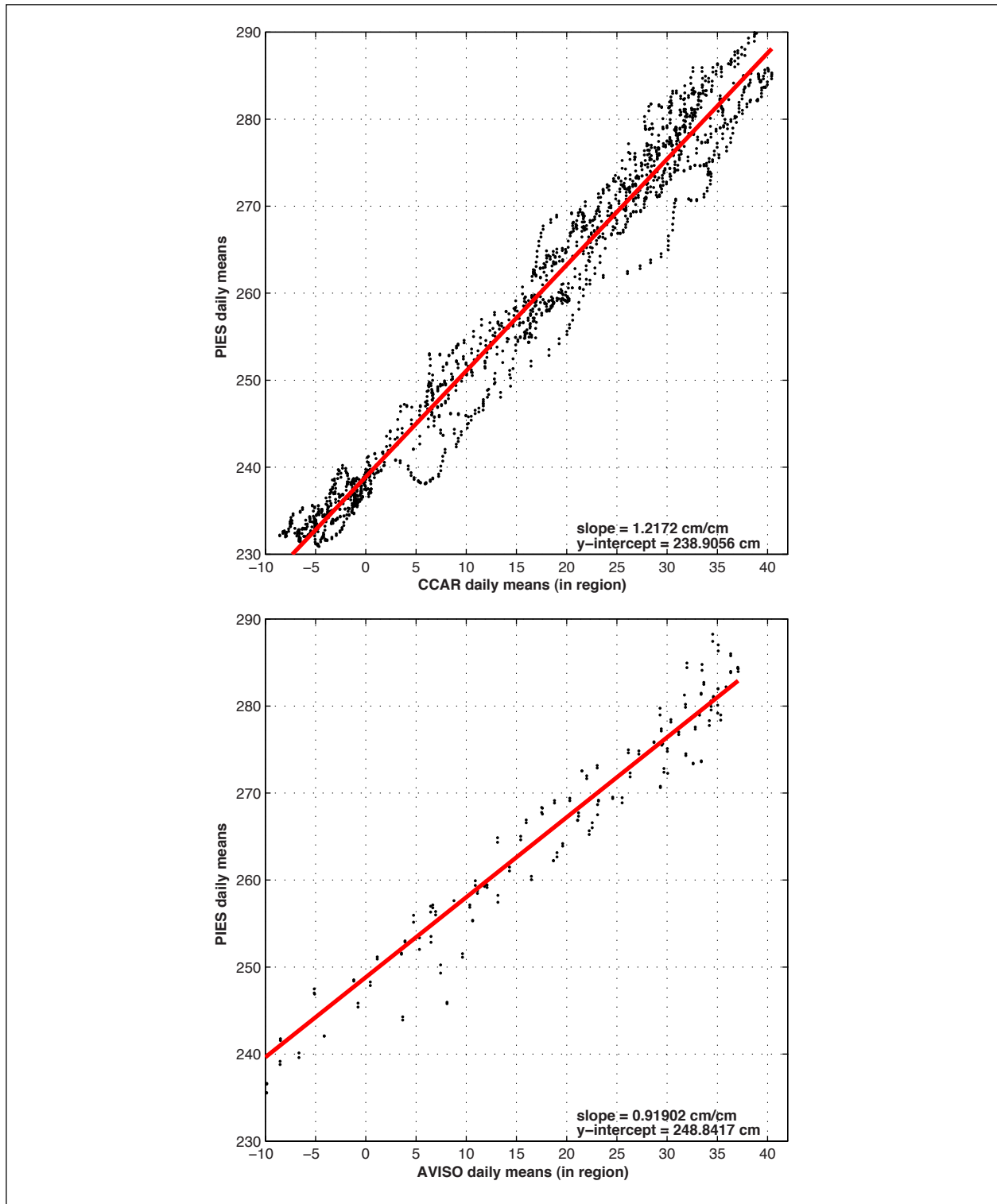


Figure 2.7-9. Regression of the daily means of the PIES mapped SSH on to the means of the CCAR Mesoscale (upper panel) and AVISO (lower panel) mapped SSH in the study region. Daily and weekly sampling were used to derive the CCAR and AVISO regressions, respectively.

previously for the correlation comparisons before making this estimate. Offsets were calculated to make the corresponding Loop Current tracking contours in all mean surfaces equal to 17 cm. This allows direct comparison of each of the altimetric SSH means to the PIES SSH mean during the study program, which are shown in the composite maps in Figure 2.7-10. Correspondence between the PIES mean SSH is better with the CCAR mean SSH than with the AVISO mean. There are significant differences in both the amplitude and spatial structure of the CCAR- and AVISO-mean SSH maps in the eastern Gulf, with the largest differences within the Loop Current near Cuba (Figure 2.7-11). Uncertainty in the mean SSH in the Gulf remains a significant challenge to remote sensing and modeling studies in the region. Fortunately, this is a deficiency that can be overcome in the Gulf by PIES SSH measurements of sufficient duration and density to directly estimate the mean.

2.8 NUMERICAL MODEL

The Princeton Regional Ocean Forecast System (PROFS) for the Gulf of Mexico is used for this study. This model system is based on the Princeton Ocean Model (POM) and has been extensively tested for (i) process studies to understand the Loop Current and eddy-shedding dynamics (e.g., Oey et al. 2003a and Chang and Oey 2011); (ii) comparison against observations (e.g., Wang et al. 2003, Fan et al. 2004, Oey et al. 2004, Lin et al. 2007); and (iii) hindcasts and forecasts (e.g., Oey et al. 2005, Yin and Oey 2007). The present version of the model has Message Passing Interface (MPI) directives implemented into POM by Dr. Toni Jordi (Jordi and Wang 2012) and achieves good (i.e., linear) scalability. Most of the original PROFS (and POM) features are retained. There are 25 terrain-following sigma levels with (logarithmically) finer resolutions near the surface and bottom, but a fourth-order pressure gradient scheme (Berntsen and Oey 2010) is used to reduce pressure-gradient errors. An orthogonal curvilinear grid is used in the horizontal with Δx and $\Delta y \sim 2$ -5 km in the Gulf of Mexico. Mellor and Yamada's (1982) turbulence closure scheme is used as modified by Craig and Banner (1994) to include input of turbulence energy due to breaking waves near the surface. Also, a Grant and Madsen (1979) type bottom-drag scheme is used in the bottom-boundary layer to empirically account for increased bottom roughness due to surface gravity waves; this is particularly effective over shallow shelves and under strong wind conditions. Finally, Smagorinsky's (1963) shear and grid-dependent horizontal viscosity is used with a nondimensional coefficient = 0.1, with the corresponding horizontal diffusivity made five times smaller. The sea-surface temperature (SST) is relaxed to AVHRR MCSST with an e-folding time constant of 1 day^{-1} (GCMD [unknown date]). However, tests (and previous experience – e.g., Yin and Oey 2007) indicate that the effects of SST boundary conditions on Loop Current dynamics are minor.

The model domain includes the northwest Atlantic Ocean west of 55°W and from 5°N to $\sim 55^\circ\text{N}$. The World Ocean Atlas data (i.e., "climatology") (NODC 2005) is used for boundary conditions along the eastern open boundary at 55°W . The topography was set up according to the NOAA/NGDC 2-minute Earth topography database (ETOPO2) and edited on shelves using NOS-digitized maps. The model is used in both a free mode, forced by external boundary conditions and surface forcing, and a data-assimilative mode where sea-surface temperature (SST) and sea-surface-height anomalies (SSHAs) are used to infer a three-dimensional analysis field on a daily basis. The analysis field was obtained for 19 years from 1993-2011, during which satellite sea-surface-height anomaly from AVISO (AVISO+ [date unknown]) is assimilated into the model using a statistical surface-to-subsurface projection method (see Yin and Oey 2007 for details and

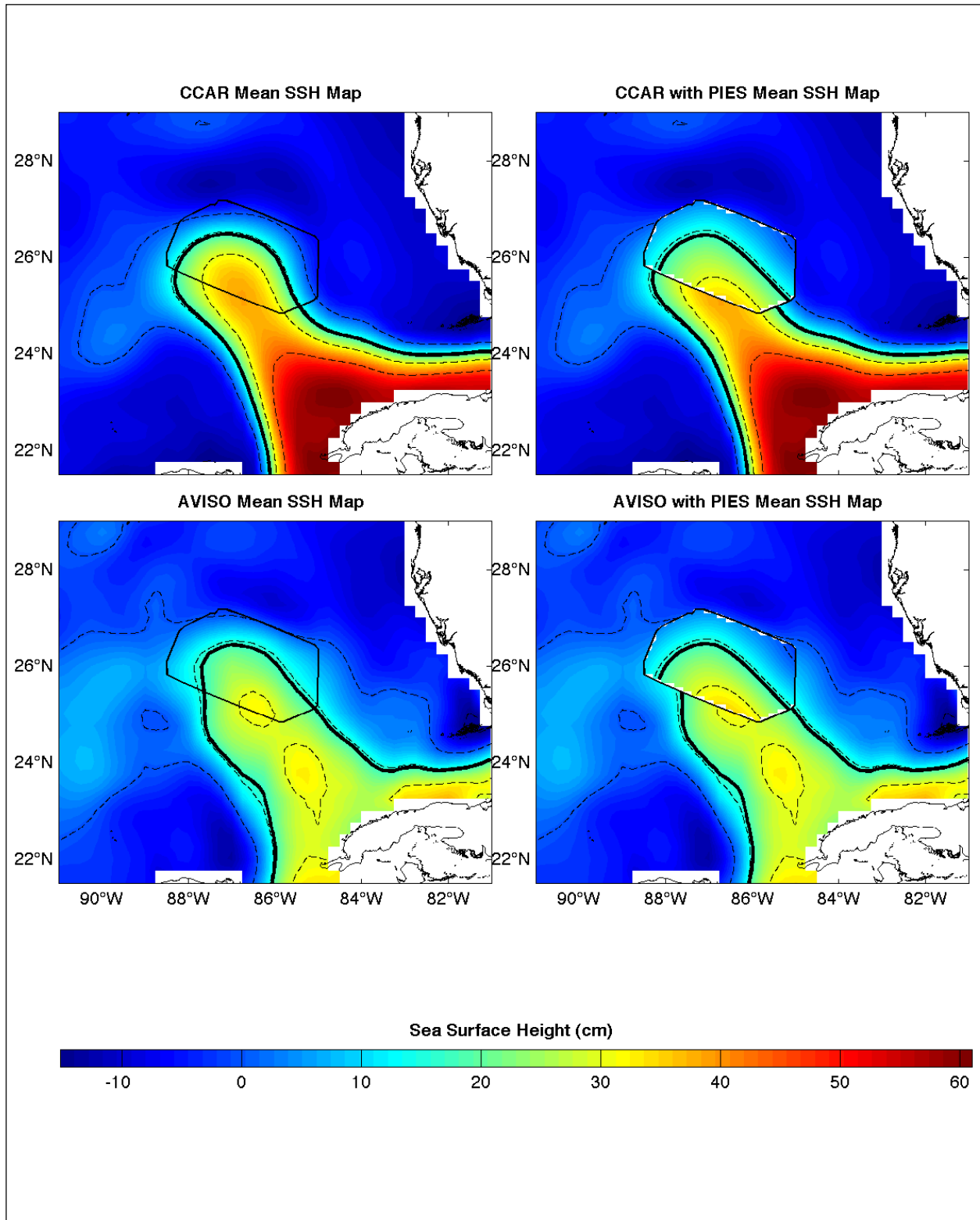


Figure 2.7-10. CCAR Mesoscale (upper panels) and AVISO (lower panels) mean SSH maps over the program time period with the PIES mean SSH inset in the panels on the right. The 17-cm LC tracking contour is shown by the thick line.

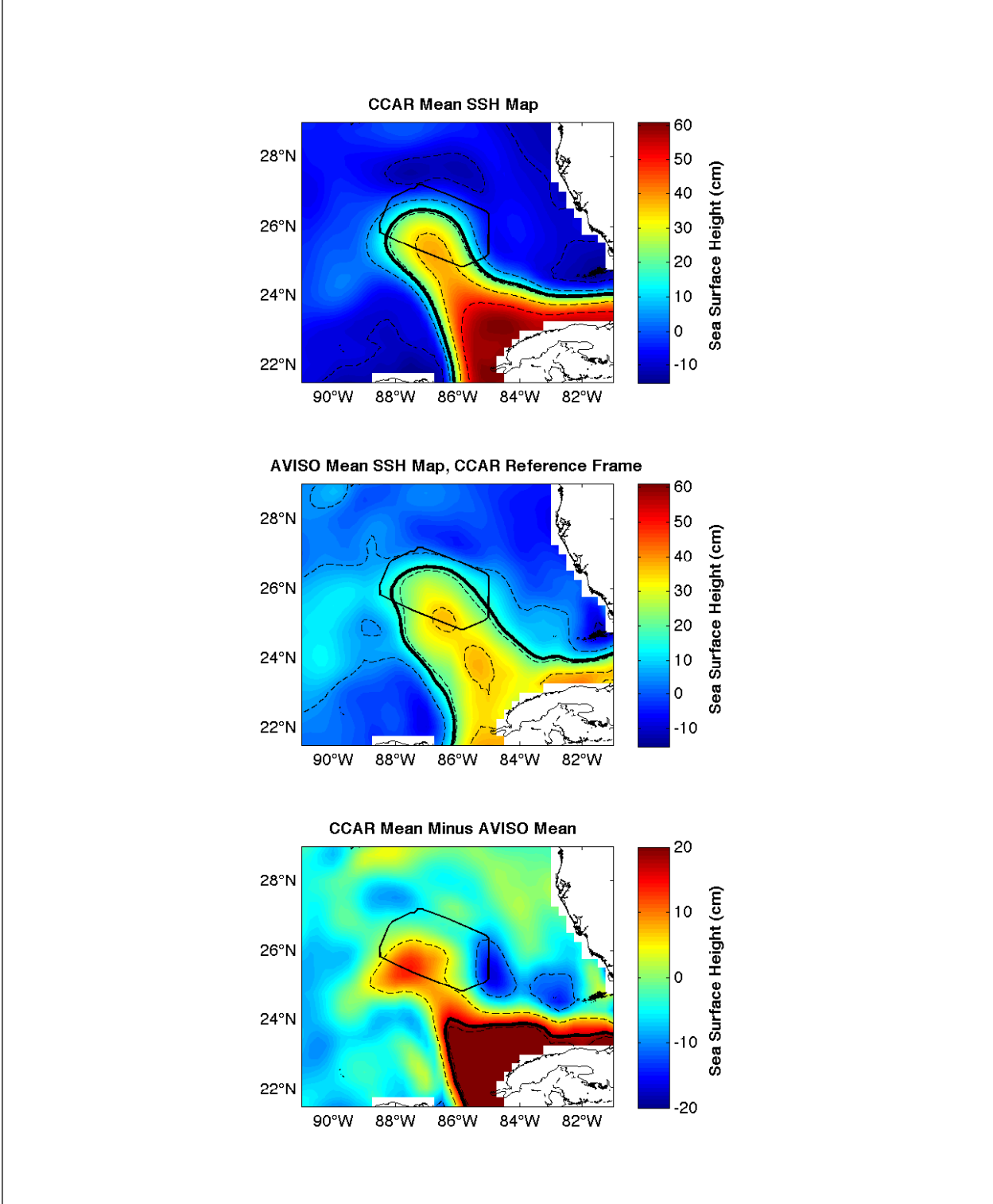


Figure 2.7-11. Comparison of the CCAR Mesoscale and AVISO mean SSH maps over the program time period. The mean maps of the CCAR Mesoscale (upper panel), AVISO (middle panel), and the difference of CCAR minus AVISO (lower panel) are shown. The thick black line is the 17-cm LC tracking contour.

references). The model is forced by six-hourly winds (1993-2009: 0.25° x 0.25° cross-calibrated multi-platform (CCMP), and 2009-2011: NCEP 0.5° x 0.5° Global Forecast System (GFS)), by M2, S2, K1 and O1 tides specified along the open boundary at 55°W, and by daily river discharge obtained from the U.S. Geological Survey at 51 locations along the U.S. coastline (34 rivers in the Gulf and 17 rivers along the eastern coast).

2.8.1 Model Skill Metrics for In-Situ Measurements

For the LC study, model simulations are compared with currents and temperatures from the nine full-depth moorings. Various metrics are used to measure model skill in reproducing *in-situ* observations. The complex or vector correlation “CC” between two velocity time series $\mathbf{u}_m = (u_m, v_m)$ for model and $\mathbf{u}_o = (u_o, v_o)$ for observation, is defined as (Lin et al. 2007, following Kundu and Allen 1976):

$$CC = \langle w_m w_o^* \rangle / [\langle w_m w_m^* \rangle^{1/2} \cdot \langle w_o w_o^* \rangle^{1/2}] \quad (2.8.1)$$

where $w_n = u_n + iv_n$, $n = m, o$, $i = (-1)^{1/2}$, the asterisk indicates the complex conjugate, and $\langle \cdot \rangle$ denotes time averaging. Thus CC ($= Re^{i\theta}$) measures how closely the model vector w_1 follows the observation vector w_2 in time. Small complex correlation angle θ ($|\theta| < 45^\circ$, say) and $R = |CC| \approx 1$ generally indicate good model skill.

Given model m_i and observation o_i time series, model skill is defined by Willmott (1981):

$$Skill = 1 - \langle (m_i - o_i)^2 \rangle / \langle (|m_i - \langle m \rangle| + |o_i - \langle o \rangle|)^2 \rangle \quad (2.8.2)$$

The *Skills* are computed separately for u and v, and then averaged ($= Skill_{uv}$). Other metrics include computing the ratios of model-to-observed standard deviations ($R_{std} = std_m / std_o$), speeds ($R_{spd} = spd_m / spd_o$), and the mean-velocity angles ($\alpha_{m-o} = \alpha_m - \alpha_o$).

2.9 METHODS

Prior sections have discussed methods used to process and, in some cases, statistically analyze various data types. This section collects together various time-series methodologies that are used in the following chapters. Some are small changes to standard methods of time-series analysis, such as EOFs, and others were developed for this study, such as calculating vertical velocities from mooring data.

2.9.1 Vertical Velocities

In highly energetic regions such as the LC, estimating vertical velocities from velocity and temperature observations has to take into account the variability of the depth of the instruments caused by mooring motion, which can produce depressions of several hundred meters from nominal depths. To accomplish this, the method separates horizontal from vertical displacements in the temperature conservation equation:

$$\frac{DT_A}{Dt} = 0 = T_A(t_0, x_0, z_0) - T_A\left(t_0 - \Delta t, x' = x_0 - \int_{t_0 - \Delta t}^{t_0} u dt, z'\right) \quad (2.9.1)$$

where the temperature anomaly, T_A , at depth z_θ is the difference between the observed temperature, T and an area averaged mean temperature profile. Thus,

$$T_A = T(t, x, z) - T_m(z) \quad (2.9.2)$$

For the LC study, T_m is the mean of 45 CTD casts taken during the course of the program to calibrate the deployed PIES (Figure 2.9-1). The depth of the temperature observation, z_0 , is also a function of t , and is estimated for the instruments by linear interpolation using the pressure records. Most of the moorings had pressure recording instruments at nominal depths of 150, 450, 750, 900, 1300, and 2000 m.

The basis of the method is to calculate the location of the water particle at time $t_0 - \Delta t$ that is advected to location x_θ in the horizontal plane ($z' = z_0$) by the horizontal velocity field $u(t, x, z_0)$. The semi-Lagrangian estimation of the horizontal displacement interpolates velocities using Kriging (Press et al. 2007) - Section 3.7.4), where each major time step, Δt , is split into a number of smaller increments. Four increments of six hours (the time step of the 40-HLP velocity records) were used for each major time step. The advantage of interpolation using Kriging is that an array of irregularly spaced observational nodes can be used in an optimal way. To estimate the vertical displacement required to satisfy Equation 2.9-1, the temperature anomaly at location (x', z_0) at time $t_0 - \Delta t$ is first estimated from interpolation by Kriging. The nominal depth, z_0 , also varies with time, and the estimated depth $z_0(t_0 - \Delta t, x')$ is also calculated by the Kriging method from the array of estimated pressure at the nominal depth. The next step is to find the depth, z' , where conservation is satisfied by a purely vertical displacement:

$$T_m(z') - T_m(z_0(t_0 - \Delta t, x')) = T_A(t_0, x_0, z_0) - T_A(t_0 - \Delta t, x', z_0) \quad (2.9.3)$$

The displacements are found by bracketing and bisection, and making use of the monotonically decreasing character of T_m , from the mean temperature profile, so that z' satisfies Equation 2.9-3. The use of a mean high-vertical-resolution temperature profile increases the precision over a temperature profile from widely vertically-spaced recorders on a mooring. From z' , the vertical velocity, w , is obtained by:

$$w = \frac{z' - z_0(t_0 - \Delta t, x')}{\Delta t} \quad (2.9.4)$$

By using temperature anomalies, and estimating the displacements required to satisfy Lagrangian temperature conservation in two separate steps, horizontal and then vertical, where the vertical takes into account the varying depths of the observations by interpolating onto a mean profile, a reasonably robust estimate of w (positive upwards) is generated at the locations of the tall moorings. For this study w was calculated for a nominal depth of 900 m, in the interface between upper and lower layers, where temperature and current records were largely complete over the observation interval. Estimates were calculated from the 40-HLP records, and then subsequently filtered with a 7-DLP Lanczos kernel to remove high frequency noise.

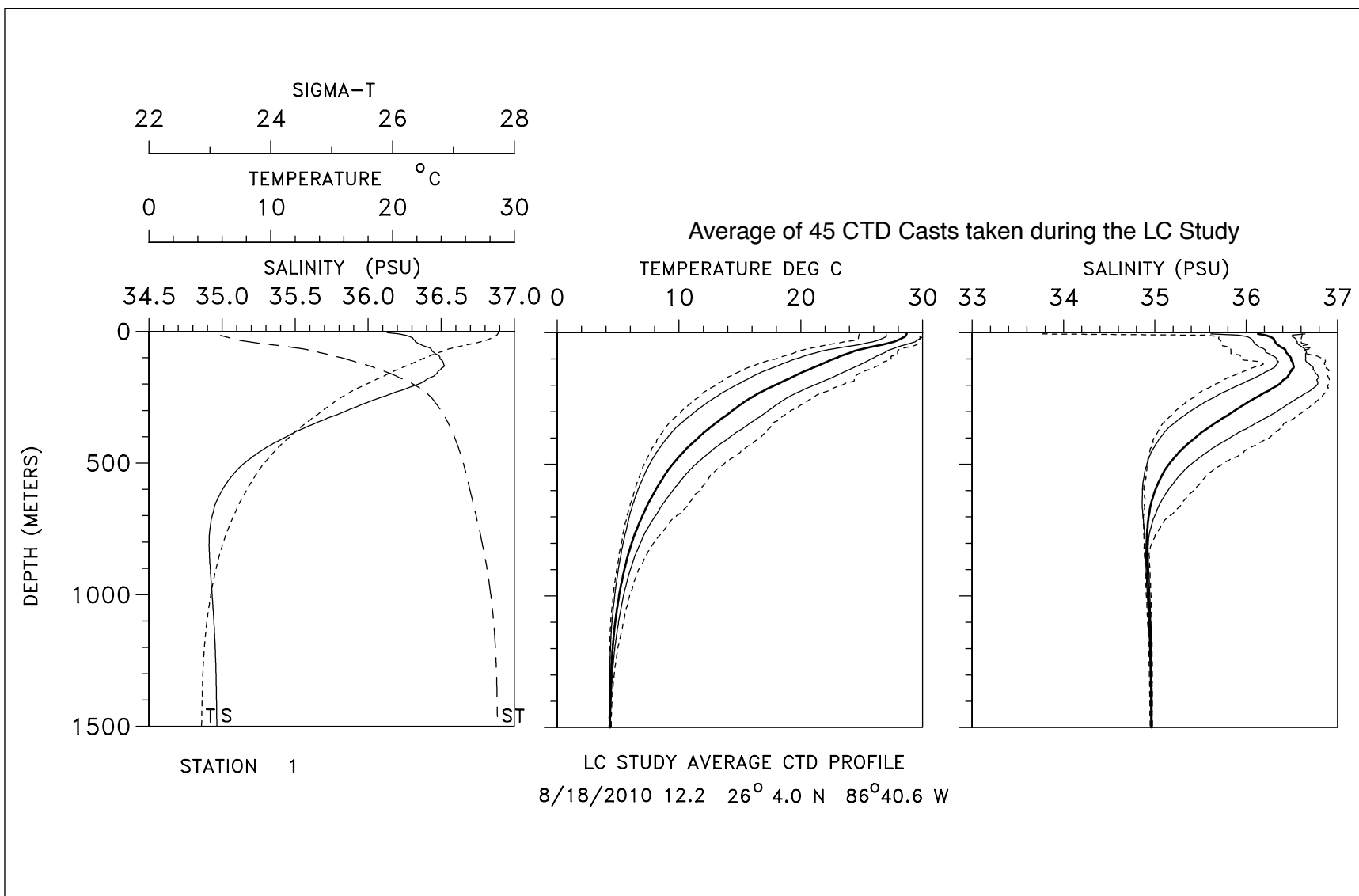


Figure 2.9-1. Average temperature, salinity and sigma-t profiles for CTD casts taken during the LC study. The RH panels show the standard deviations (light solid lines) and extrema (dashed lines) for the profiles.

Estimating errors in w is difficult because it depends on the accuracy of the semi-Lagrangian interpolations, which in turn depend on the spacing of the measurements. Also the mean vertical temperature gradients may not exactly represent the instantaneous temperature gradients. However, the results for 900 m have a reasonable correspondence (not shown) to w estimated from the $\partial\eta/\partial t$ where η is the depth of the 6 °C isotherm, which has a mean depth ~ 900 m. A very rough estimate of the error is $\sim 30\%$ of the magnitude of w .

2.9.2 Relative Vorticity

Because the observational moorings were laid out in an array, higher dynamical quantities can be calculated by fitting planes through groups of observations. Minimums of three locations (not co-linear) are required to estimate gradients of velocity using:

$$u(x, y, t) = u_0 + x \frac{\partial u}{\partial x} + y \frac{\partial u}{\partial y} + (\text{Higher} \cdot \text{Order} \cdot \text{Terms}) \quad (2.9.5)$$

with a similar equation for the v -component. When there are more than three locations, least-square fitting is used where the velocity components are weighted by their standard deviations. This is similar to the method given by (Chereskin et al. 2000). After the gradients are obtained, relative vorticity is given by:

$$\zeta = \frac{\partial v}{\partial x} - \frac{\partial u}{\partial y} \quad (2.9.6)$$

The relative vorticity locations for the array, divided into triangles and rectangles, are given in Figure 2.9-2. Because the lower-layer velocities have a larger array, the 100-mab relative vorticity locations (yellow dots) differ slightly from higher in the water column (grey dots) where only the nine tall moorings were available. Relative vorticity locations have IDs that reference the nearest PIES location number.

The CICESE moorings were deployed in transects, and so velocity gradients can only be estimated in the along-transect direction. However, for the majority of the time, transects N and E are dominated by LC flows along the Campeche slope, and ζ can be approximated by $\partial v/\partial x$, where v is the along-slope velocity component. On transect E, the 2009-2010 deployment included mooring EN which formed a triangle so that both gradient terms can be evaluated. A comparison of ζ using the triangle, and the two transect moorings is given in Figure 2.9-3, and it can be seen that the two calculations give very similar results as regards the fluctuations with some underestimation of peak amplitudes at the shallower depth. For the most part, relative vorticity is plotted normalized by the local Coriolis parameter.

2.9.3 Potential Vorticity

The Ertel potential vorticity (PV), $(f + \zeta)/h$ where h is the layer depth and the water column is divided up into isopycnal layers, is a conserved quantity following streamlines. In Eulerian terms, a normalized potential-vorticity anomaly (PVA) is defined as:

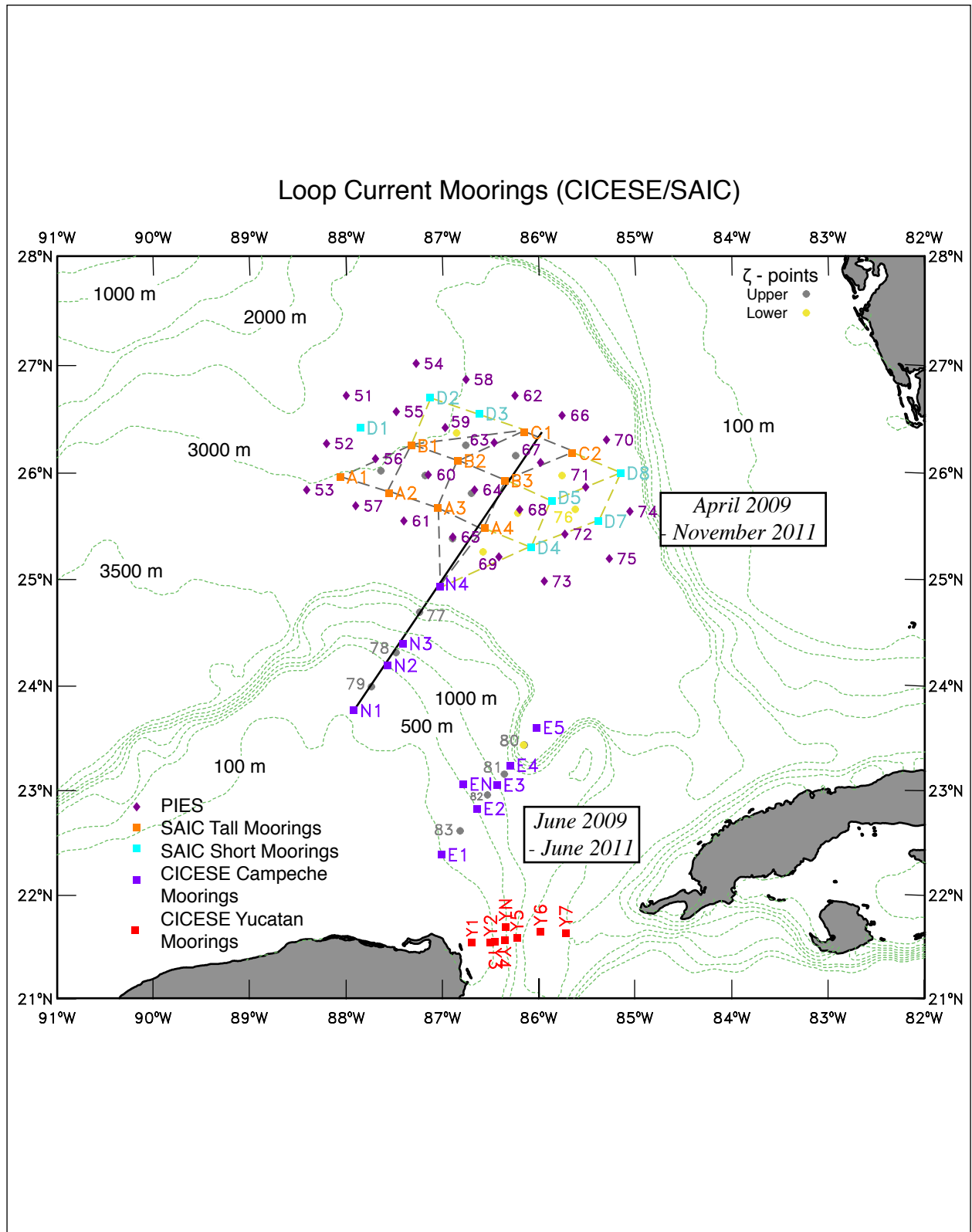


Figure 2.9-2. Mapping array and CICESE transects showing the locations of relative vorticity points (numbered grey and yellow dots) and their surrounding triangles and rectangles.

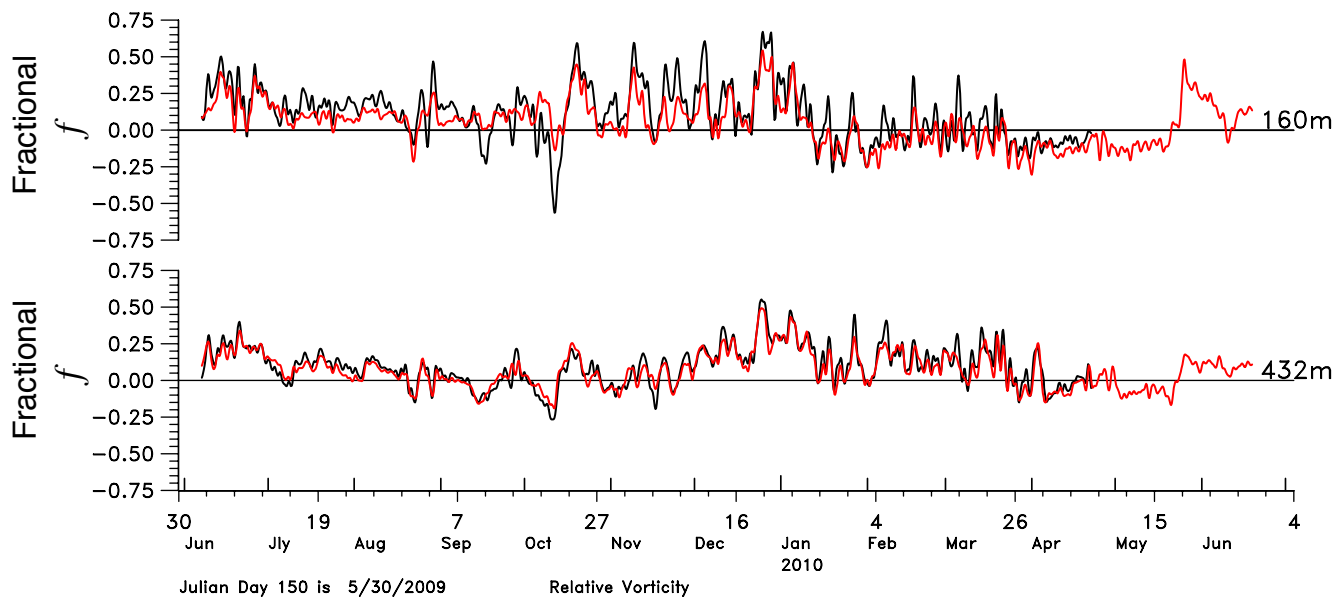


Figure 2.9-3. Comparison of relative vorticity at two depths for location 82 using the triangle E2-E3-EN (black line) and the E2-E3 pair (red line) to estimate velocity gradients.

$$PVA = \frac{H}{f} \left(\frac{f + \zeta}{h} - \frac{f}{H} \right) = \frac{H}{h} \left(\frac{\zeta}{f} \right) + \left(\frac{H}{h} - 1 \right) \quad (2.9.7)$$

where H is the mean depth of the layer. The first term on the right-hand-side (RHS) is essentially the layer-average relative vorticity and the second term is the layer stretching term, sometimes referred to as the Sverdrup PV . For the LC moorings, the depth of the 6 °C isotherm is used to divide upper and lower layers, and the mean relative vorticity between the surface and 6 °C, and 6 °C and the bottom is estimated by averaging the appropriate $\zeta(z,t)/f$ at available discrete depth levels (see above).

2.9.4 Streamlines and Velocity Potentials

Analysis often requires that observations be mapped onto a regular grid. For scalar variables, standard optimal or statistical interpolation is used with Gaussian autocorrelation functions. For the most part, this study uses the method of successive corrections for interpolation as given by Pedder (1993), with the length scale given by the average separation of the observations. However, for velocity vector data, it is useful to decompose currents into non-divergent geostrophic (streamfunction) and divergent (velocity potential) components:

$$u = -\frac{1}{f} \frac{\partial \phi}{\partial y} + \frac{\partial \chi}{\partial x}; v = \frac{1}{f} \frac{\partial \phi}{\partial x} + \frac{\partial \chi}{\partial y} \quad (2.9.8)$$

where ϕ is the geopotential (dynamic height) and also the streamfunction, and χ is the velocity potential, which gives the divergent-irrotational component that can be equated to ageostrophic flows. The streamfunction and velocity potential can be optimally determined by the universal co-Kriging (UCK) method of Pedder (1989), where ϕ and χ are assumed to be uncorrelated, and Gaussian functions are used to model the cross-covariance matrices. Standard least-square procedures are used to find the statistically-optimal solutions. Parameters of the method are the horizontal length scale for the Gaussian functions, determined by the average spacing of the data; fractional-geostrophic variance = 0.9; and thus, fractional-divergence variance = 0.1. The results are not particularly sensitive to these parameters. Wang et al. (2003) used the UCK method to produce daily maps of rotational and divergent velocity components from current-meter observations in the DeSoto canyon (Hamilton and Lee 2005), which were jointly analyzed with satellite altimetry and numerical model output.

Figure 2.9-4 shows the results of using the UCK method where the data are two-day averaged 40-HLP currents at 160 m. The geostrophic velocities align closely with the observations and clearly show the closed anticyclonic circulation during the formation of Hadal. The velocity-potential vectors indicate a divergence towards the northeast, and a convergence towards the southwest sides of the array, which roughly correspond to the upwelling and downwelling regions of vertical velocities at 900 m, respectively. This can be interpreted as illustrating the ageostrophic connection between upper and lower layers.

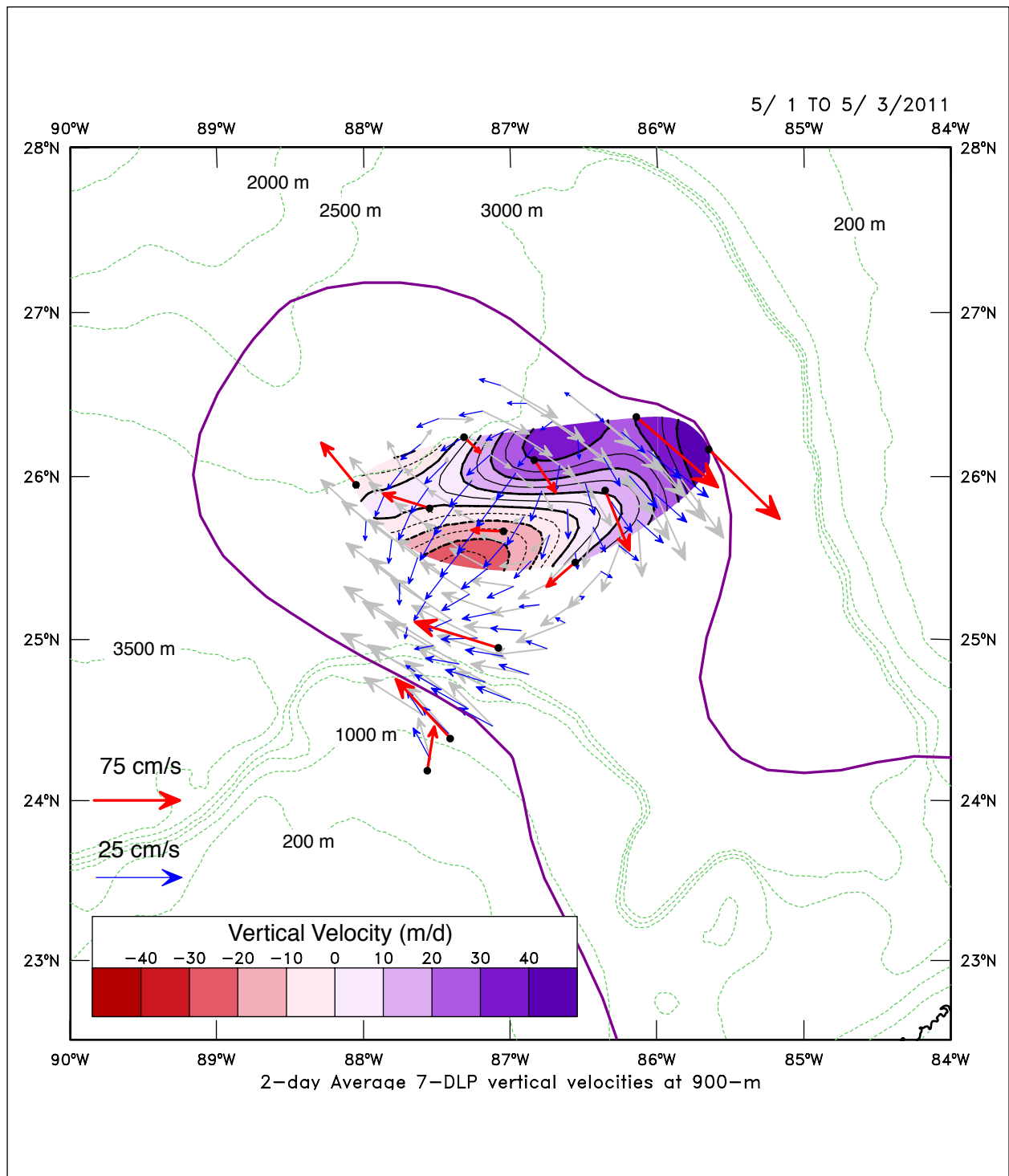


Figure 2.9-4. Geostrophic velocities from mapped geopotential (gray arrows), and observed 2-day averaged 40-HLP currents at 160 m (red arrows); both using the red scale arrow. Blue vectors are from the mapped velocity potential (note change in scale). Contours are the 2-day averaged vertical velocities at 900 m, and the solid purple line is the 17-cm SSH contour from satellite altimeter data showing the location of the LC front.

2.9.5 Wavelet Analysis

Wavelet analysis decomposes a time series into time and frequency space to determine the dominant modes of variability, and how those modes vary in time. This is particularly useful for event-dominated regimes such as LC variability, where oscillations can be seen in a clear way. For analysis purposes, the continuous wavelet, which is a function localized in time and space that scales with time, is more useful than the discrete wavelet. Following Torrence and Compo (1998), the Morlet-6 function is used for the transform, where the wavelet time scale is almost identical to the Fourier period. The wavelet transform is used to show the variability of the power of the input series as a function of time and the Fourier period. Edge effects can be significant at longer scales, and it is usual to define a “cone of influence” where such errors are negligible. The significance of the peaks can be estimated by determining a background spectrum and a significance level. Torrence and Compo (1998) use an autoregressive AR(1) process where the lag-1 autocorrelation, α , defines the background red spectrum and the significance level, and is determined from the input series (Allen and Smith 1996).

The common power, as a function of time and the Fourier period, between two time series is given by the cross-wavelet transform, which is discussed by Torrence and Compo (1998), and Grinsted et al. (2004). Local relative phase, represented as an angle between the two series in time and frequency space, can be estimated where common power is significant (Grinsted et al. 2004). There are a number of examples of the continuous-wavelet transform (CWT) and cross-wavelet transform (XWT) in the following analysis chapters.

2.9.6 Complex Demodulation

An earlier relative of the CWT is complex demodulation of a scalar time series. It is used when the object of the analysis is to find an estimate of the amplitude and phase of a signal with a well-defined period that is imbedded and prominent in the time series. Examples are semi-diurnal and diurnal tidal frequencies, and for this study, the inertial frequency f , where f is the Coriolis parameter. This is the dominant high frequency signal observed in deepwater currents. A time series of inertial amplitudes, A , and phases, θ , are obtained from:

$$A(\tau)e^{i\theta(\tau)} = \frac{1}{T} \int_{t-T}^{t+T} (u(t) - u_m(\tau)) e^{ift} dt \quad (2.9.9)$$

where T is the inertial period ($=2\pi/f$), and u_m is the running mean, i.e., $u_m(\tau) = \frac{1}{2T} \int_{\tau-T}^{\tau+T} u(t) dt$ of

the variable u . In practice, a 4-day low-pass (4DLP) filter to ensure adequate smoothing of the results replaces the integral in 2.9.9. The inertial period for the analysis is chosen to be an integral number of time steps to avoid filter edge effects. For highly time variable signals such as near inertial internal waves, the resulting amplitudes show when signals are large and how they change in time and space (see Chapter 6).

2.9.7 Notes on EOF Analysis

EOF analysis is a standard way of extracting coherent structures from a large number of simultaneous time series (Preisendorfer and Mobley 1988). EOF analysis is applied in this study

in both the time and frequency domains. For velocity data, complex EOFs (CEOFs) are used where $u(x,t) = u + iv$, and the eigenmodes are given by:

$$u(x,t) = \sum_n A_n(t) \bullet e_n(x) \quad (2.9.10)$$

where all quantities are complex and the mode amplitude, A_n , is normalized to unit variance (i.e., $\langle A_n^* A_n \rangle = 1$, where $\langle \rangle$ denotes time average). The record means of U are removed before the analysis. The mode amplitudes and eigenvectors, e_n , are orthogonal and ordered by variance explained, but their orientation is relative to an arbitrary reference (Kundu and Allen 1976). The usual practice (Merrifield and Winant 1989) is to rotate the spatial eigenvector into the frame of the semi-major principal axis of the corresponding amplitude time series.

Because EOF analysis maximizes the variance explained by the modes, data with large variations in variances by location can produce low numbered modes that are dominated by the high variance records, and so de-emphasize significant patterns in the data. For single mooring velocity records, the depth range that each velocity record represents is used to weight the record variances. Thus, $u_k(t, z_k)$ is weighted by $0.5 \cdot (z_{k+1} - z_{k-1})$ where z_k is the depth of the record for construction of the covariance matrix. The eigenvectors carry the units of the data, and are de-weighted before plotting. The de-weighted eigenvectors are also used to construct derived quantities such as depth-integrated eddy kinetic energy (Hamilton 2009):

$$EKE_H = \frac{1}{2} \langle \int_{z_1}^{z_2} u^* u dz \rangle \quad (2.9.11)$$

Frequency-domain EOFs are similar to time-domain EOFs where record spectra are used to construct the cross-spectral matrix for given frequency bands. This allows the analysis of propagating signals as phase differences between locations can be found from the eigenvectors.

CHAPTER 3: BASIC DESCRIPTIONS AND STATISTICS

3.1 INTRODUCTION

The purpose of this chapter is to give basic descriptions of the mesoscale variability of the LC, including the major detachments and eventual separations of Ekman, Franklin and Hadal, during the measurement program. This is followed by a detailed look at the statistics of the observations of currents, temperature and derived parameters from the PIES mapping array for the whole water column, and separately for the upper and lower layers. These discussions will serve as the background for a more detailed dynamical analysis in Chapter 4.

An overview of various observations and theories of LC eddy detachment processes is given in Section 1.4. To set the scene, Figures 3.1-1a-b shows the 40-HLP time series of velocities and temperatures from two moorings: A2 and C2 on the northwest and northeast sides, respectively, of the mean LC. The isotherm depths in the upper water column have been corrected for drawdown using available pressure records on the mooring, and the intervals for which the eddies were part of the LC extending into the Gulf, derived from the SSH maps using the 17-cm contour, are indicated by the solid green bar. The large-scale sequences of warm water encroaching on the array as the LC front extends to the north are clearly seen at both moorings. As the LC front moves across these moorings, velocities increase and decrease in the upper layer, generally northward at A2 and southward at C2, corresponding to the clockwise anticyclonic flow of this current. The upper-layer fluctuations are markedly different between moorings and LC eddies. For Ekman (May 2009) and Franklin (January-March 2010), the initial descent of the isotherms at A2 show very rapid, ~10-day fluctuations that correspond to similar periodicities in the velocity vectors. The latter do not reverse but have a “haystack” appearance that is characteristic of propagating cyclonic frontal eddies (Bane et al. 1981) which, in this context, are usually called LC-frontal eddies (LCFEs). For Hadal, these type fluctuations are hardly present or have longer periodicities and are short lived. At C2, the rapid fluctuations, during the same phase of LC growth, are also only weakly present, but just prior to the first detachments of Franklin (May-June 2010) and Hadal, and midway through Hadal’s growth (March-May 2011), large cold events intrude on the mooring. It will be shown later that these correspond to large-scale meanders (~ 300 km wavelengths) on the east side of an extended LC. Crests and troughs of a meander are defined as displacements of the front, defined by the 17-cm SSH contour, out from and towards the center of the eddy or LC, respectively. The cold events correspond to the cyclonic circulations in the troughs of the meanders that have periodicities of ~ 40 days. The long-wavelength, large-amplitude meanders are not present on the west side of the LC. The ~ 40-day periodicities are also present in the isotherm depths during the extensive cool intervals after the separations of Ekman and Franklin at both moorings, and this frequency band is prominent in the statistical analysis below.

Strong vertical shear characterizes the upper layer with velocity magnitudes decreasing with depth. In the lower layer, velocities have weak shears showing only small or no increases in magnitude, depending on location, from 1300 m to 2000 m, and then remaining constant to the top of the bottom boundary layer. Though the deepest levels, 100 mab, are not shown in Figure 3.1-1, the 40-HLP records are essentially identical to the 2000-m level. Bottom intensification is

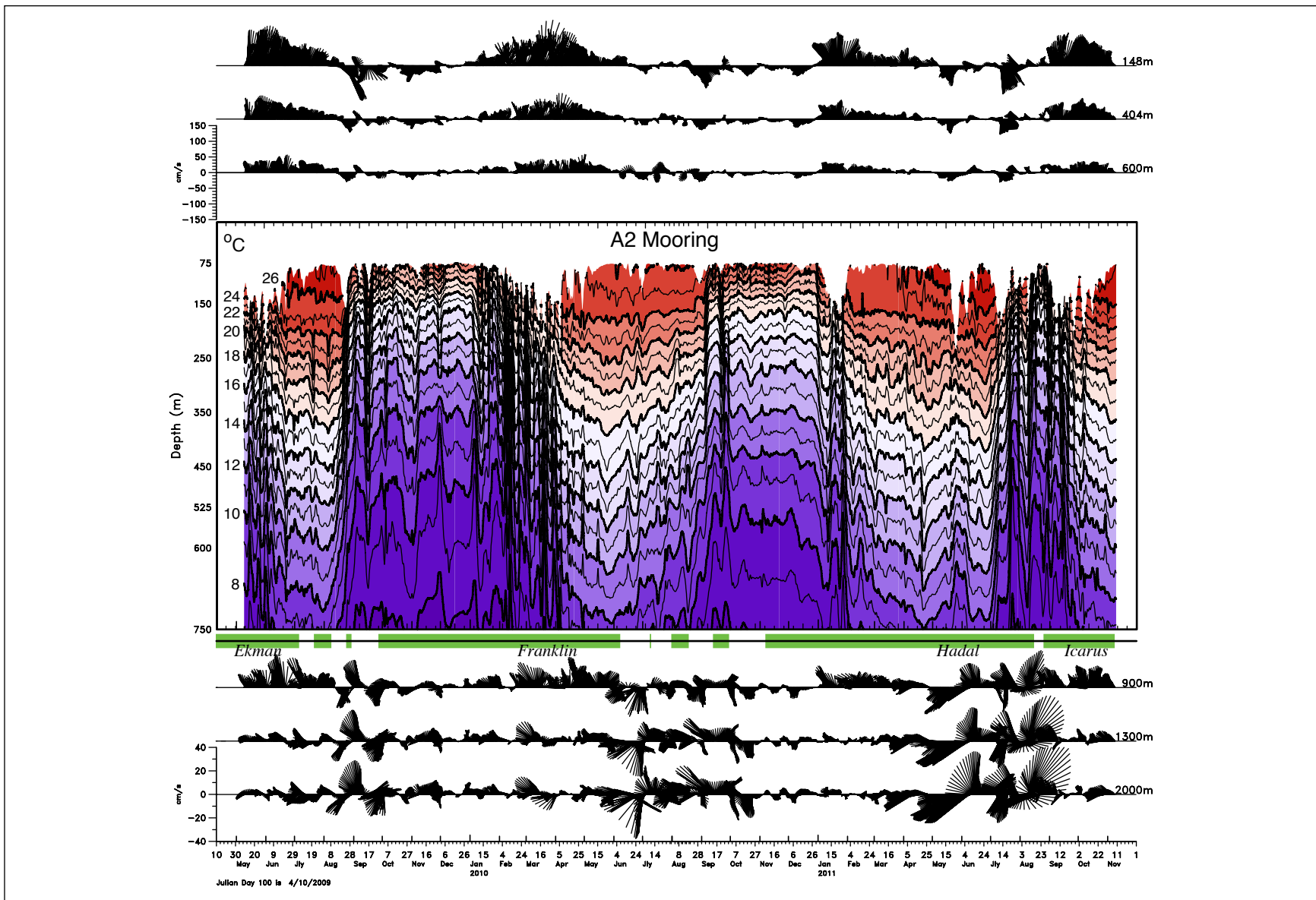


Figure 3.1-1a. 40-HLP temperature and velocity records from the A2 mooring at the indicated depths. Up is north direction.

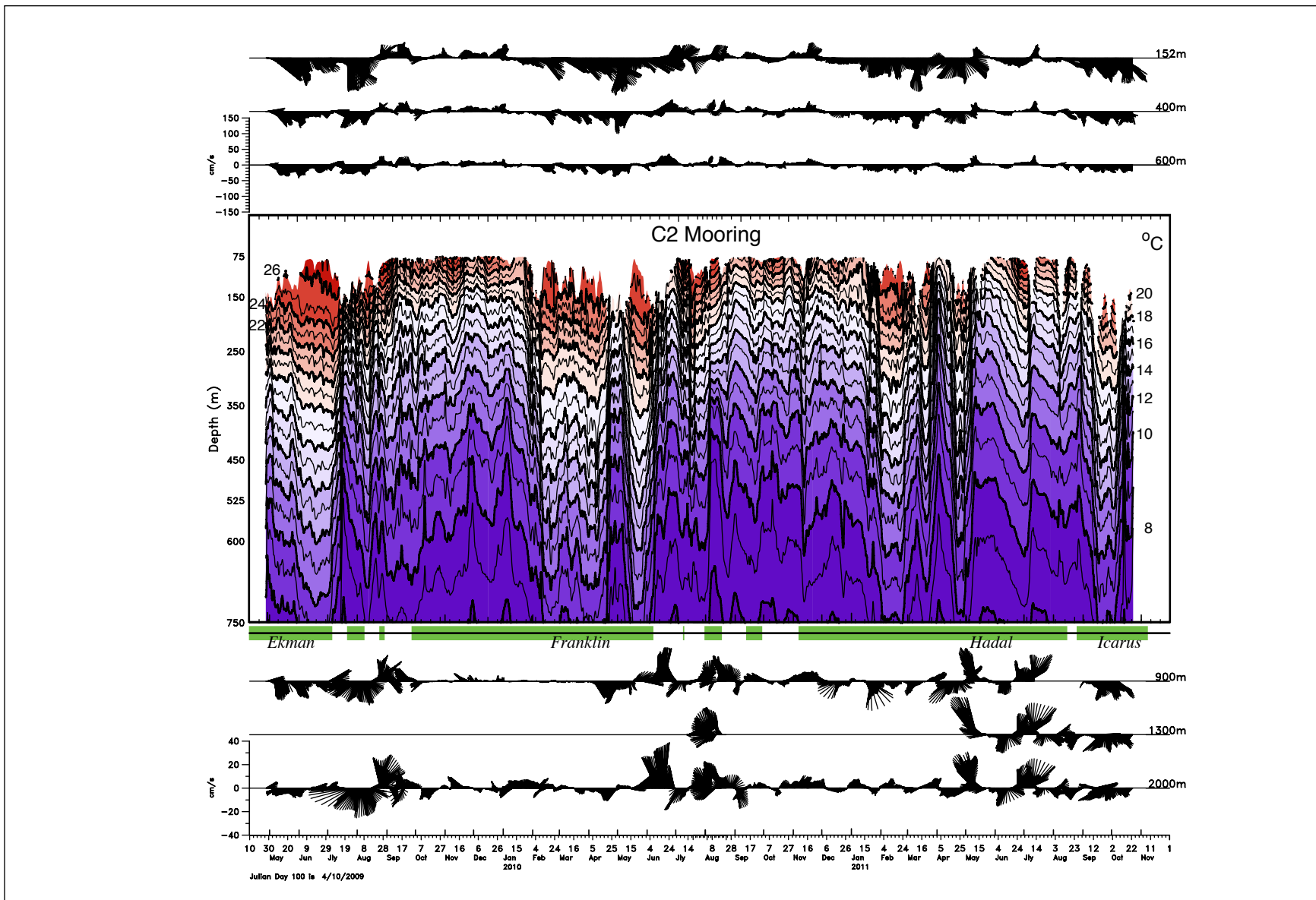


Figure 3.1-1b. 40-HLP temperature and velocity records from the C2 mooring at the indicated depths. Up is north direction.

a common characteristic of currents deeper than ~1000 m throughout most of the Gulf (Hamilton 2009) and has been associated with topographic Rossby waves (TRWs). However, for the LC array the lower-layer currents are much more depth independent than for observations made further west. Above 900 m, flows are visually coherent, and similarly below 1300 m. The 900-m level at both moorings shows some characteristics of both layers, with a tendency to look like the upper layer when the isotherms deepen, and the lower layer when the isotherms shoal. In general, variability in the upper layer is not the same as in the lower layer, though a number of events at both moorings seem to be present in both layers, e.g., the strong southward event at 2000 m ~ 24 June 2010 at A2 could be said to be present through the whole water column (Figure 3.1-1a). Lower layer fluctuation amplitudes (and thus eddy kinetic energy – EKE) also vary in time with large increases during the detachments and separations of Ekman and Franklin, and prior to the separation of Hadal. A mechanism for energy transfer from upper to lower layer is given in Chapter 4.

The locations of the CICESE N transect and the U.S. moorings A4, B3 and C1 (Figure 1.2-1) allow the definition of a SW to NE section across the LC from the shelf break on the Campeche bank to the deep water adjacent to the west Florida escarpment. The section is approximately normal to the mean direction at the N transect of the LC front over the Campeche slope, and therefore, the coordinate axes for the velocities have been rotated so that the v -component is directed 330 °T. The upper- and lower-layer currents for the section are given in Figures 3.1-2a-b, which also includes the depths of the 6°C isotherm and the location of the LC front relative to the N2 and C1 locations, where the front is defined by the 17-cm SSH contour from the daily altimeter maps discussed in Chapter 2.

The LC front over the Campeche slope has relatively little variability in location (the gaps in the time series are caused when a detached eddy does not intersect the N2-C1 section). This is consistent with the strongest currents being in the vicinity of N2 and N3, and N3 and N4 isotherm depths having lower variances (Figure 3.1-2a). The N2 mooring is generally on the cyclonic side of the front, and during the growth phase of Franklin, and to a lesser extent Hadal, the rapid fluctuations characteristic of LCFEs occasionally reverse prevailing LC northwesterly flows. These short period LCFE fluctuations are not resolved in the SSH maps. On the northeast side of the section, the LC front location has large displacements, and this is reflected in the large amplitude long-period fluctuation in the depths of the isotherms at C1 and B3. The southeastward flows at C1 and B3 are generally weaker than the equivalent flows at N2 and N3 even when the fronts are at similar distances from the moorings (e.g., February through April 2010 in Franklin). Similarly short period fluctuations are much weaker when present at C1 than at N2.

Representative deep currents (> 1000 m) across the section (Figure 3.1-2b) all show only slight bottom intensification of the 2000-m versus 1300-m levels. Essentially flows below 1300 m are depth independent with amplitudes of the fluctuations having similar magnitudes across the section. All locations show a high degree of changes in intensity corresponding to detachment events (Ekman and Franklin) or large scale meanders as shown by the C1 isotherm depths (Hadal). At some locations (e.g., B3 and A4), the variability resembles decaying wave trains triggered by these major upper-layer events.

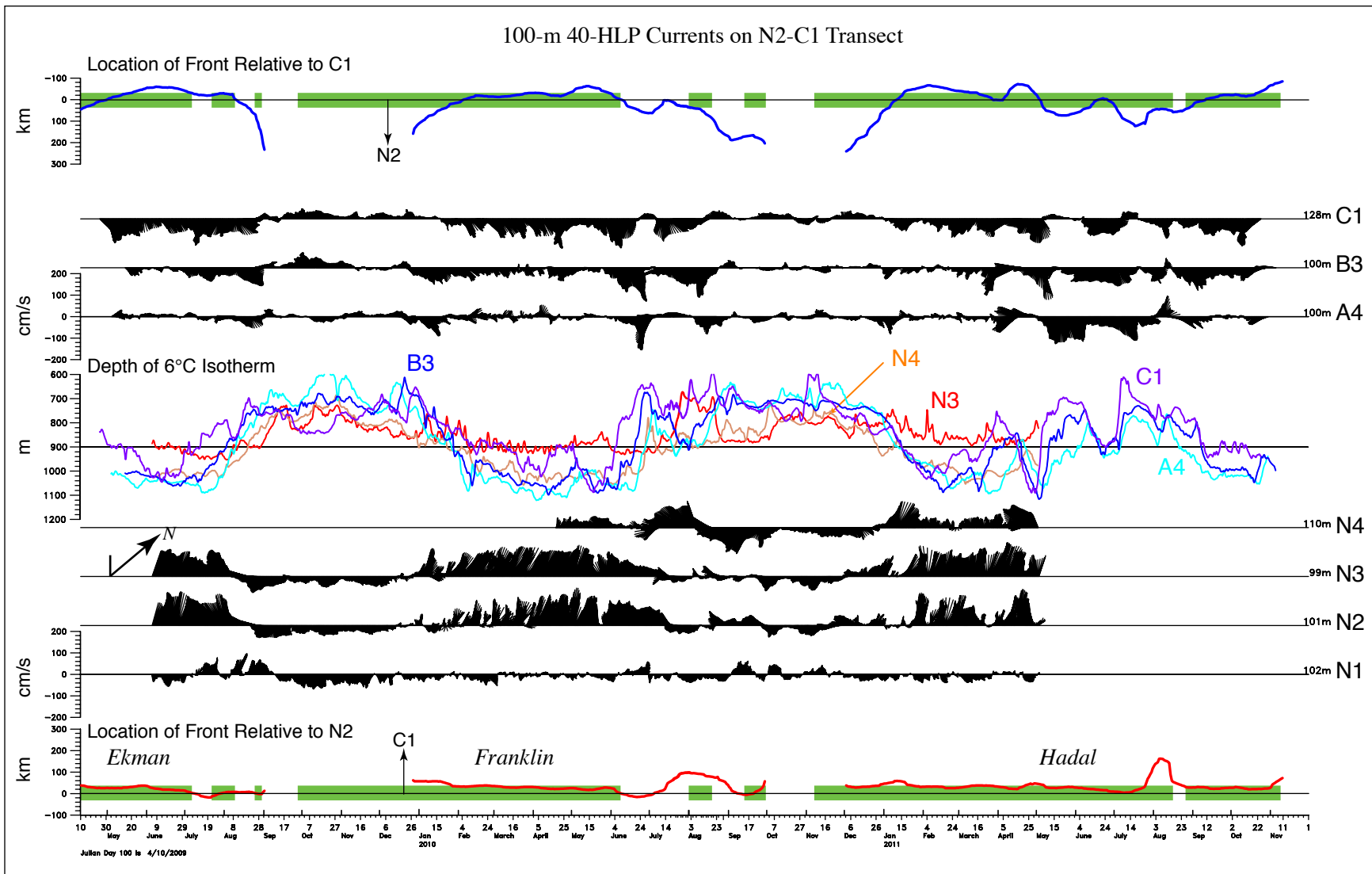


Figure 3.1-2a. Surface-layer (~ 100 m) currents on the N2 to C1 transect where up is normal to the transect (NW direction). The top and bottom panels show the distance along the transect of the 17-cm SSH contour from the respective end points, and the center panel shows the depths of the 6 °C isotherm at mooring locations.

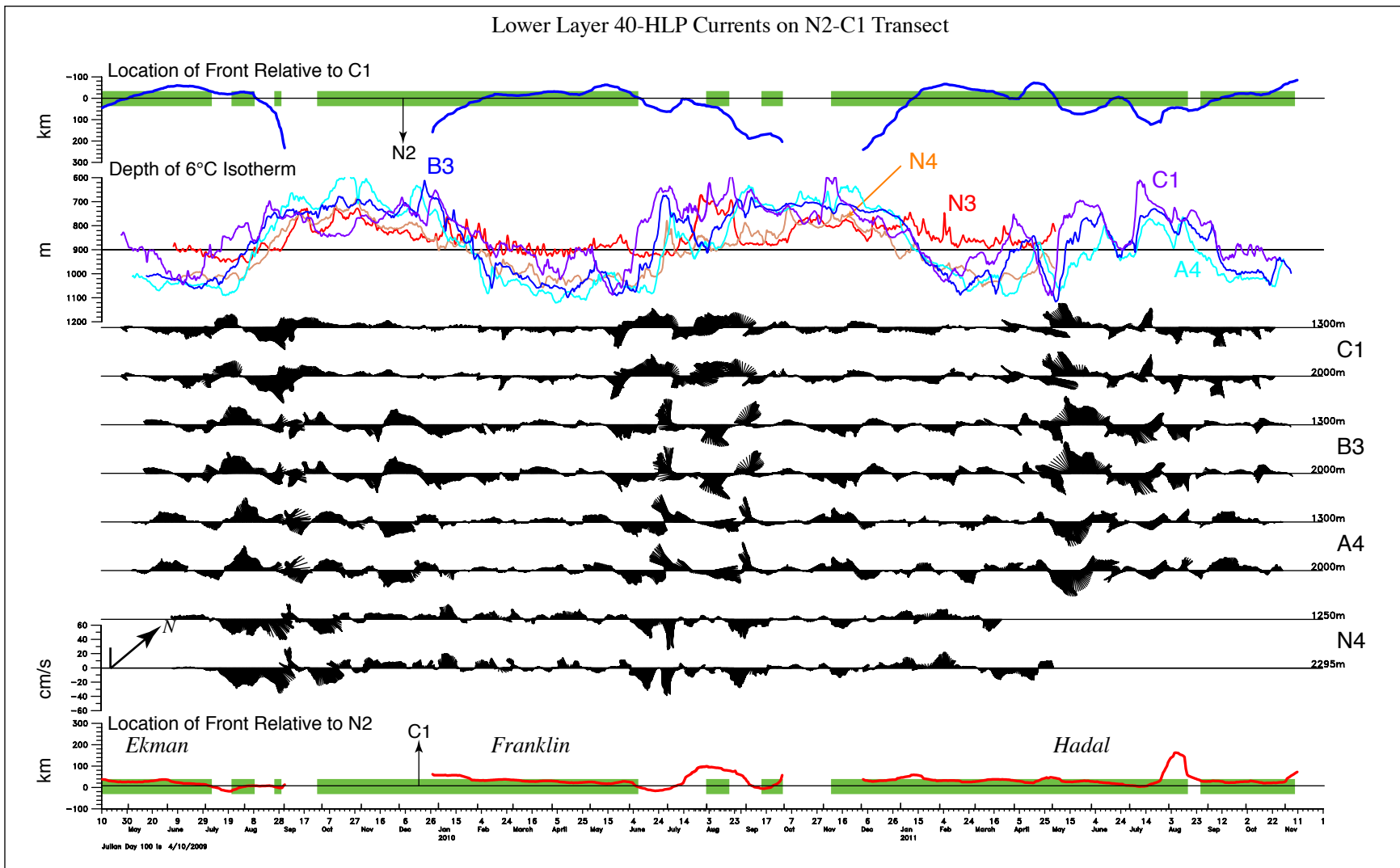


Figure 3.1-2b. Lower-layer currents at ~1300 and ~2000 m on the N2 to C1 transect where up is normal to the transect (NW direction). The top and bottom panels show the distance along the transect of the 17-cm SSH contour from the respective end points, and the next to top panel shows the depths of the 6 °C isotherm at mooring locations, repeated from the previous figure.

The overall view of the variability and the sequencing of the events given here are expanded in the following sections where the growth and detachments of Ekman, Franklin and Hadal are examined individually. Some common themes emerge, particularly the role of large-scale propagating meanders on the east side of an extended LC. However, each eddy separation has unique features, and therefore events and their statistics are described on an eddy-by-eddy basis in the following sections.

3.2 EDDY FORMATION AND SEPARATION

3.2.1 Ekman

The previous eddy to Ekman separated from the LC on 24 February 2009, two months prior to the start of the observational program. The separation point was quite far north (just southeast of A2), and the LC did not retreat southwards very far after the eddy departed into the western Gulf. The LC grew in area and northward extension in April 2009, and then remained constant in size, forming Ekman, until the first detachment on 6 July (see Figure 1.5-1). The detachment point was well to the south in the vicinity of E4 and E5. The detached Ekman remained roughly in the same place until a lobe of the eddy reconnected to the LC on 20 July. The reattached eddy also did not significantly change its area, but the LC bulged to the north, increasing the total area of the LC plus eddy. The second detachment took place on 9 August, with the detachment point further north than the previous time and the eddy starts to elongate in an east-west direction along the north side of the Campeche Bank, with the result that the center of Ekman moves slowly westward. Ekman briefly reattached its southeastern side to the LC on 23 August, but at this time a large meander trough was developing along the long northern side on the eddy that eventually cleaved the eddy in two along 87°W on 29 August, resulting in a larger western portion (Ekman) that moved into the western Gulf, and a small eastern anticyclone distinct from, but almost attached to, the LC that quickly dissipated.

This sequence is illustrated by the sequence of LC front locations, derived from SSH maps, given in Figure 3.2-1, where the interval between the fronts is 15 days. At the beginning of the sequence on 25 May the extended LC is regular, showing practically no frontal perturbations. The next three contours show a large scale meander (wavelength ~ 300 km) developing on the east side that increases in amplitude and also propagates southwards (compare successive locations of crests and troughs) such that by the 9 July contour a trough $\sim 24^{\circ}\text{N}$ separates Ekman from the LC. The trough then moves northward as the LC pushes into the Gulf even after reattachment so that the 9 August detachment takes place a degree further north than the initial one on 6 July. It might be expected that the 9 August detachment would be the cause of eddy separation. However, the elongation of the LC and eddy towards the west allows the development of large scale amplifying meanders on the north side of the extended northwest-southeast directed front, and it is the developing trough along the $\sim 87^{\circ}\text{W}$ meridian that finally separates Ekman and allows the eddy to move into the western Gulf. The Ekman separation sequences are the most complex of the three major eddies in the data. Two points should be noted: 1) the large amplitude and long wavelength meanders develop on the east or north side of an extended LC-eddy system and they occur over, and seem to require, deep water (> 2500 m); 2) the deepening meander troughs that cause detachment develop from the east or north side of the LC, and it is not necessary or even usual for a cyclone to be present on the Campeche slope

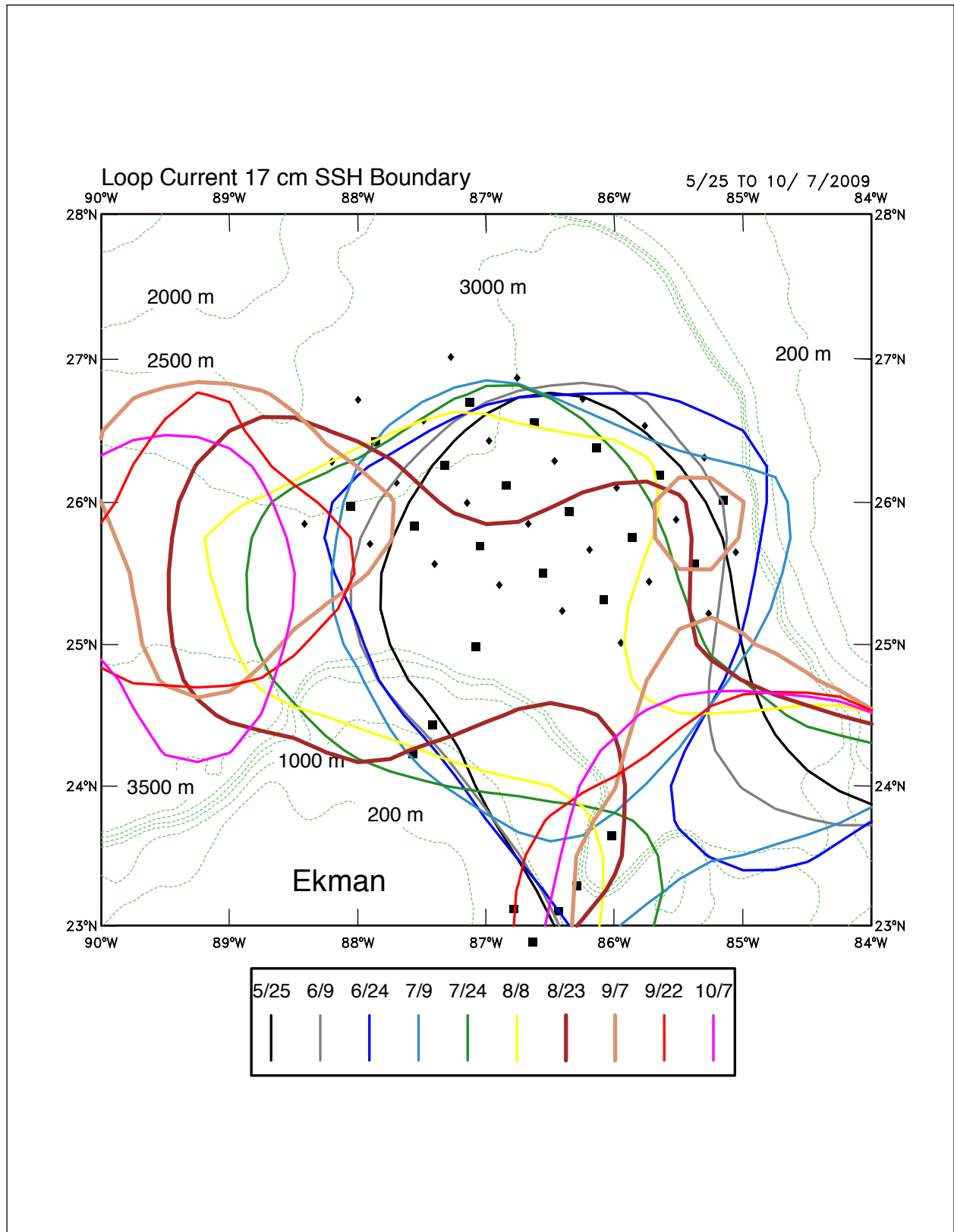


Figure 3.2-1. The growth and detachments of Ekman using the SSH 17-cm contour from altimeter maps at 15-day intervals.

for a detachment to occur, even though the 17-cm contour may suggest the presence of such a feature (e.g., 23 August in Figure 3.2-1). The latter will be discussed more thoroughly below, but the presence of an apparent Campeche slope cyclone, despite the presence of shallow water and a slope, has been previously advanced as a mechanism for detachment (Schmitz 2005).

Illustration of the upper- and lower-layer flows during Ekman's final detachment and separation are given in Figure 3.2-2. On the 22 August map, the lower-layer geopotential shows highs and lows displaced downstream from the crests and trough of the north side meander with both upper- and lower-layer currents west of 87°W flowing southwards or southeastwards, and east of 86.5°W flowing north or northeastward such that the lower-layer flows are reinforcing the developing trough along $\sim 87^{\circ}\text{W}$ and the crest at $\sim 85.5^{\circ}\text{W}$. By 29 August, the lower-layer highs and lows have strengthened and become more aligned with the surface layer crest and trough. By 1 September, the eastern lower-layer high is roughly aligned with the small, detached upper-layer anticyclone, and the low seems to be attached to the east side of the separating Ekman (it displaces westward between 29 August and 1 September) such that upper and lower layer flows are in a similar south or southwestward direction on the east side of Ekman. Only four days later, the small upper-layer eastern anticyclone has weakened, and will dissipate completely in another 10 to 15 days, but the lower-layer anticyclonic high remains strong and has translated westward with its companion low along with Ekman. On this 5 September map, Ekman is apparently contributing to the southward flow on the Campeche slope at N2 and N3, indicating that the eddy is interacting with the slope topography. The low SSH centered on the shelf break over the Campeche bank in late August is not consistent with the currents on the E and N transects. The surface-layer currents at E suggest entrainment from the southeastern Campeche shelf and slope into the LC, and a closed cyclonic flow is hard to discern. Except for E5, this is one of the few cases where measured upper layer currents are not roughly parallel to SSH contours.

3.2.2 Franklin

After the departure of Ekman, the LC remained south of 24.5°N until the end of November 2009, after which there is steady growth to the north through February 2010 (Figure 1.5-1), with the northern boundary reaching 26.5°N , and the extended LC having no major frontal perturbations. Figure 3.2-3 shows the 17-cm SSH contour at 15-day intervals from March through the middle of July. Up to the first detachment on 8 June, Franklin behaved very similarly to Ekman, had a similar area and location, with the detachment point being well to the south around section E at $\sim 23^{\circ}\text{N}$. Again the eastern boundary develops large-amplitude, long-wavelength meanders that increase in amplitude and propagate southwards (compare the crest and trough locations for successive fronts beginning 15 April in Figure 3.2-3). The trough between the LC and Franklin develops through June as the irregular shaped eddy rotates, developing a strong cyclonic "Tortugas" eddy by early July that promotes the southward advection of a southern lobe of Franklin to reattach briefly (9 July) to the LC. This southern lobe of Franklin is reabsorbed into the LC, reducing the area of the eddy. Franklin moves to the northwest and advects the trough cyclone through to the Campeche bank, where it intensifies and promotes the eastern LC front to move northwards and reattach to the eddy on 30 July. This next interaction with the LC lasts until 18 August, and results in a reduction in the area and maximum SSH of the Franklin portion. A third detachment point is $\sim 25^{\circ}\text{N}$, and even though an elliptical Franklin is clear of the northern Campeche bank slope, its small size (~ 150 km diameter) and possibly a blocking

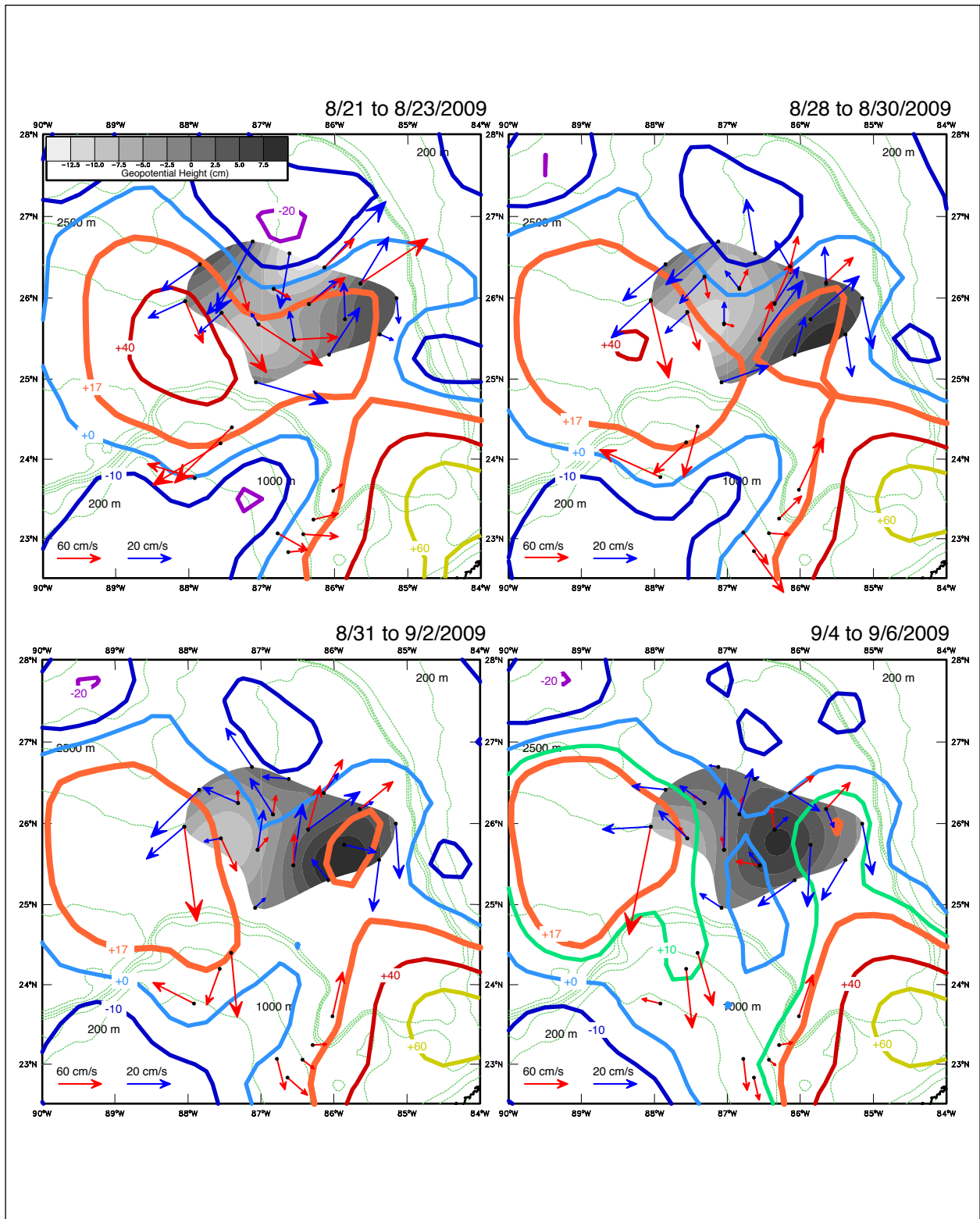


Figure 3.2-2. Maps of the separation of Ekman for the indicated dates showing 2-day mean currents at ~80-100 m (red) and 100 mab (blue), geopotential height for the bottom currents (gray shaded), and SSH contours (cm) from altimeter maps.

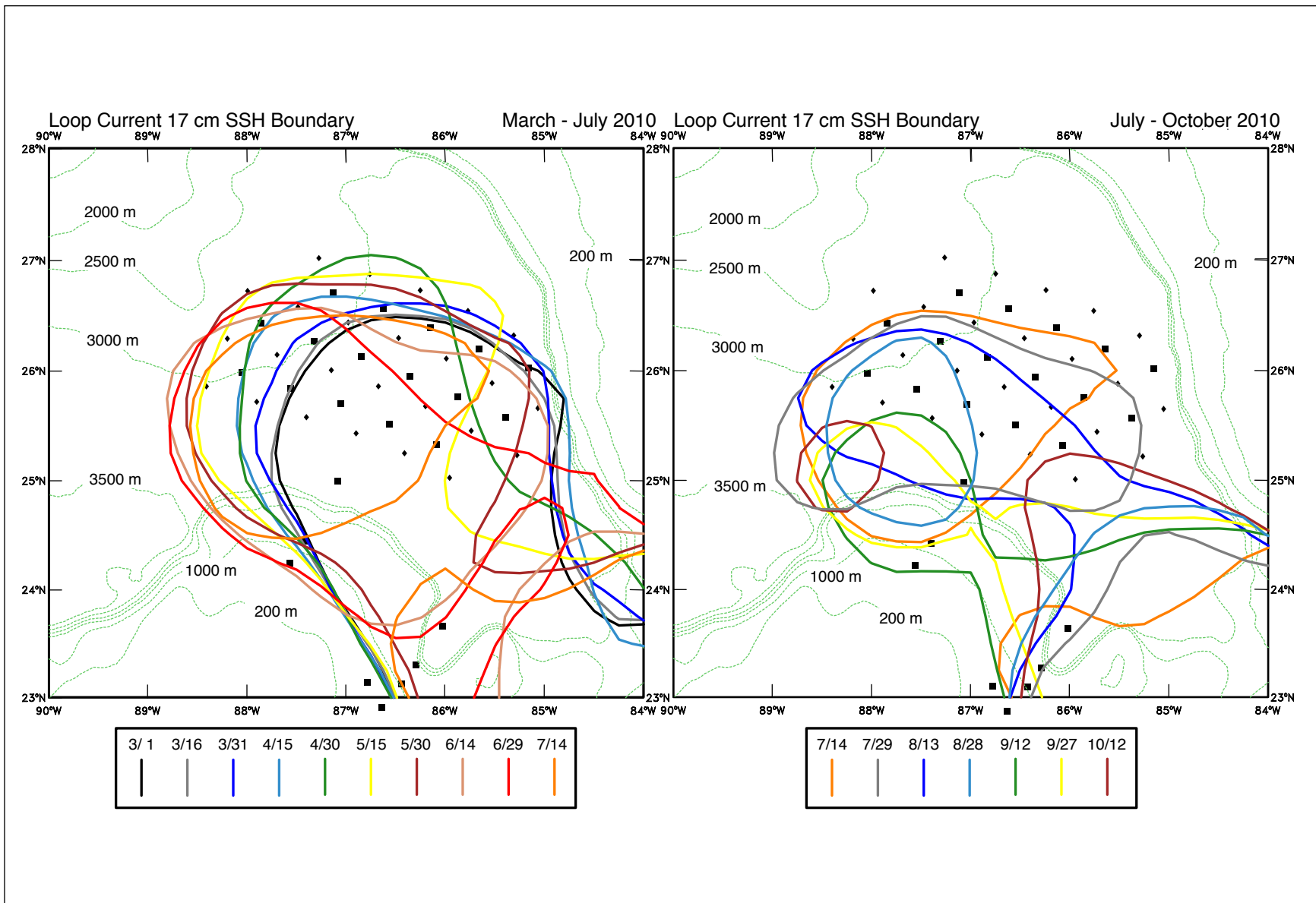


Figure 3.2-3. Loop Current 17-cm frontal boundaries from SSH altimeter maps for Franklin for the indicated dates.

anticyclone centered $\sim 24^{\circ}\text{N}$, 90°W seem to prevent it moving westward. Franklin weakens during this 3rd detachment (18 August 18 to 11 September), moves southward along the Campeche slope and reattaches for another time. Again, the LC absorbs most of the eddy leaving a small area of anticyclonic vorticity, which rapidly dissipates after the final separation on 28 September. Though the first detachment of Franklin is very similar to that of Ekman, the subsequent reattachments and detachments were very different in that they seem more to be chance encounters of lobes of Franklin with a highly variable LC front, mediated by cyclonic flows both on the east and west sides of the separation zone. Each encounter reduced the size (shown in the July to August sequence of front locations in the right hand panel of Figure 3.2-3) and vitality of the eddy until it is speculated that it was small and weak enough not to be able to move westward by the β -effect and self-advection (Nof, 1981).

The *Deepwater Horizon* (DWH) oil discharge occurred from April through July 2010 while the LC was extended to the north, Franklin was forming through the first detachment, and then remained in the eastern Gulf south of 27°N (Hamilton et al. 2011). During this interval, a large number of satellite-tracked GPS surface drifters were deployed both near the DWH spill site and in Franklin by USGS and USF (Liu et al. 2011a). Utilizing the drifters to estimate mean flows over the two-month May-June interval for selected $1^{\circ} \times 1^{\circ}$ squares (Figure 3.2-4) shows that a closed anticyclonic circulation was present even though Franklin did not detach completely until 8 June according to SSH contours. The drifter means agree well with means from the moorings for the same interval and the location of the mean 17-cm SSH frontal contour. The strong southwesterly flows in the southern part of Franklin are consistent with the elongating trough at $\sim 24^{\circ}\text{N}$ as indicated by the tracks of two drifters that leave the eddy and move into the LC. The drifter tracks also show a large cyclonic feature, centered at $\sim 27^{\circ}\text{N}$, 86°W (Walker et al. 2011) that produced northward currents over the northern west-Florida slope and outer shelf. Some of the drifter tracks also indicate the intrusion of a meander crest over the west-Florida slope between 25 and 26°N . Means exceed standard deviations in the southern and western parts of Franklin, but are comparable in the north and east where, in some cases, the principal axis of the standard deviation ellipses is directed across the front (Figure 3.2-4), indicating that it is the movement of a relatively constant current with lateral front displacements that causes variability at a fixed location.

The depth of the 6°C isotherm, calculated from both PIES temperature profiles and mooring temperature measurements, on the day (8 June) of the first detachment is given in Figure 3.2-5. It closely corresponds to the SSH contours as expected, but shows more clearly the large-scale meander troughs and crests along the northern and eastern sides that make the boundary of Franklin irregular. The 5-day upper-layer mean flows along transect E in the southwest are directed towards the Campeche slope and shelf, indicating that the development of the trough between the LC and Franklin should be having a strong influence on this shallow shelf.

The upper- and lower-layer flows just prior to the first detachment through the following reattachment are given in Figure 3.2-6. The lower-layer highs and lows are displaced downstream from their respective crests and troughs in the SSH, resulting in lower-layer flows that are at right angles or opposed to their respective upper-layer currents. The crests and troughs for 8 June, are more clearly seen in the 6°C isotherm surface in Figure 3.2-5 than in SSH. Over the six days between the first and second plot, the lower layer high-low pattern is

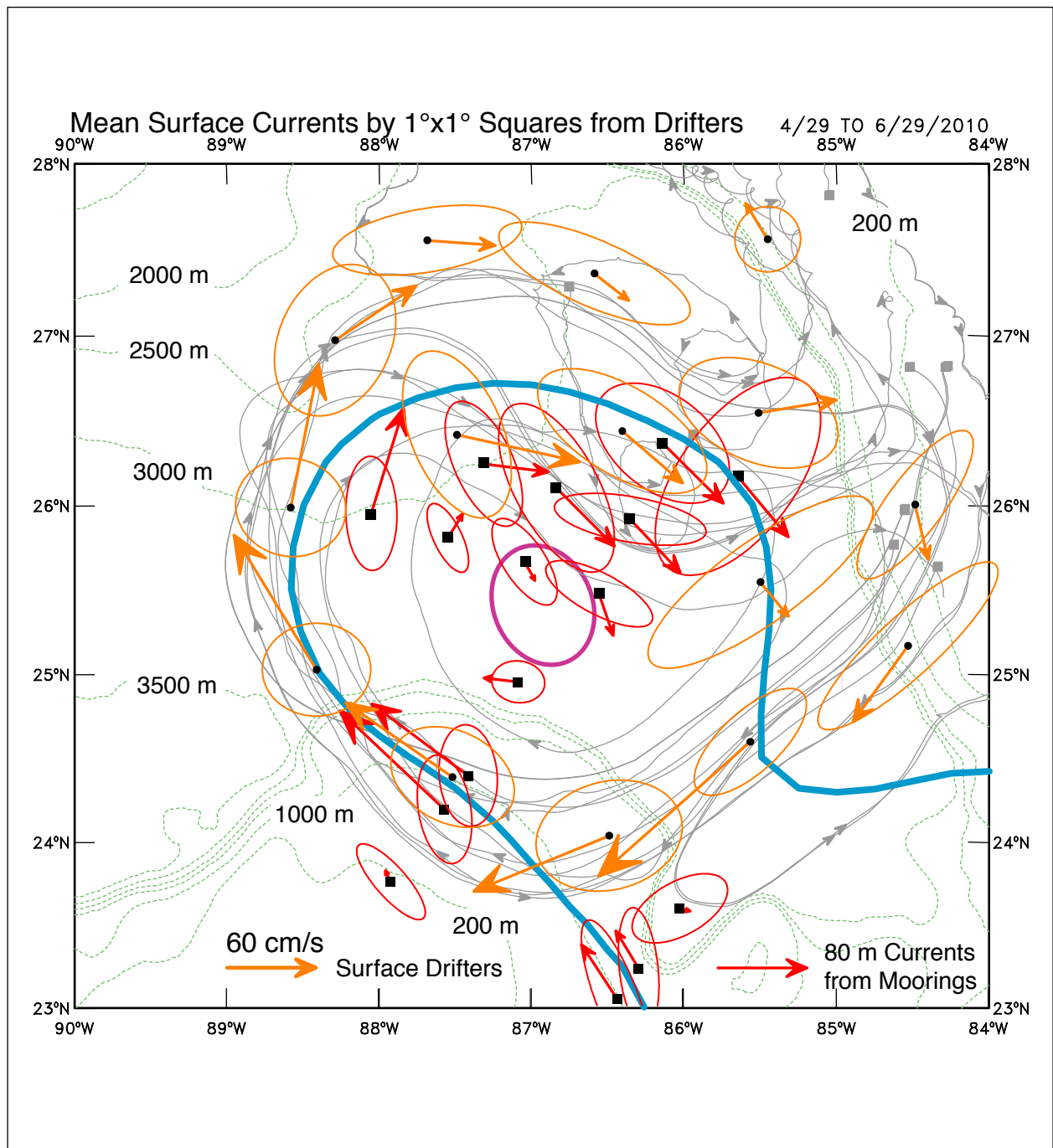


Figure 3.2-4. Mean surface velocities and standard deviation ellipses from drifter tracks (gray lines) for May and June 2010. The 1°x 1° squares are centered on the nearest one or half latitude or longitude degree. The calculated positions (round dots) are the average locations of the drifters passing through each square. The 80-m mean velocities and ellipses from the moorings (square dots) are given for the same interval. The mean location of the 17-cm SSH contour for May and June is given by the thick cyan line, and the location of the mean SSH high is given by the purple oval line.

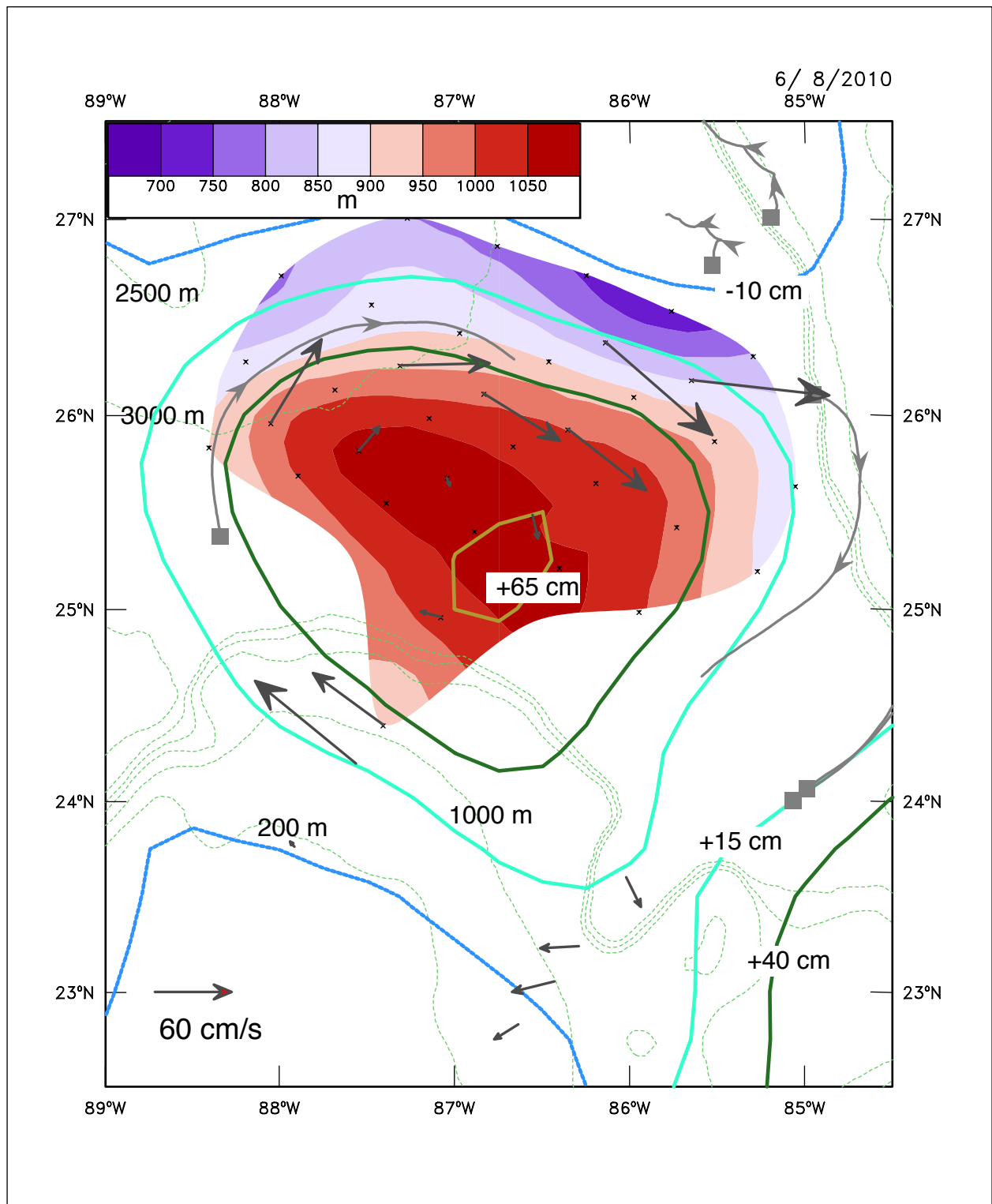


Figure 3.2-5. The first detachment of Franklin showing the depth of the 6 °C isotherm and 80 to 100-m velocity vectors from the moorings (5-day means). Three-day surface drifter tracks from USCG and USF with arrow heads every day, and altimeter SSH contours. All means and tracks are centered on 8 June 2010.

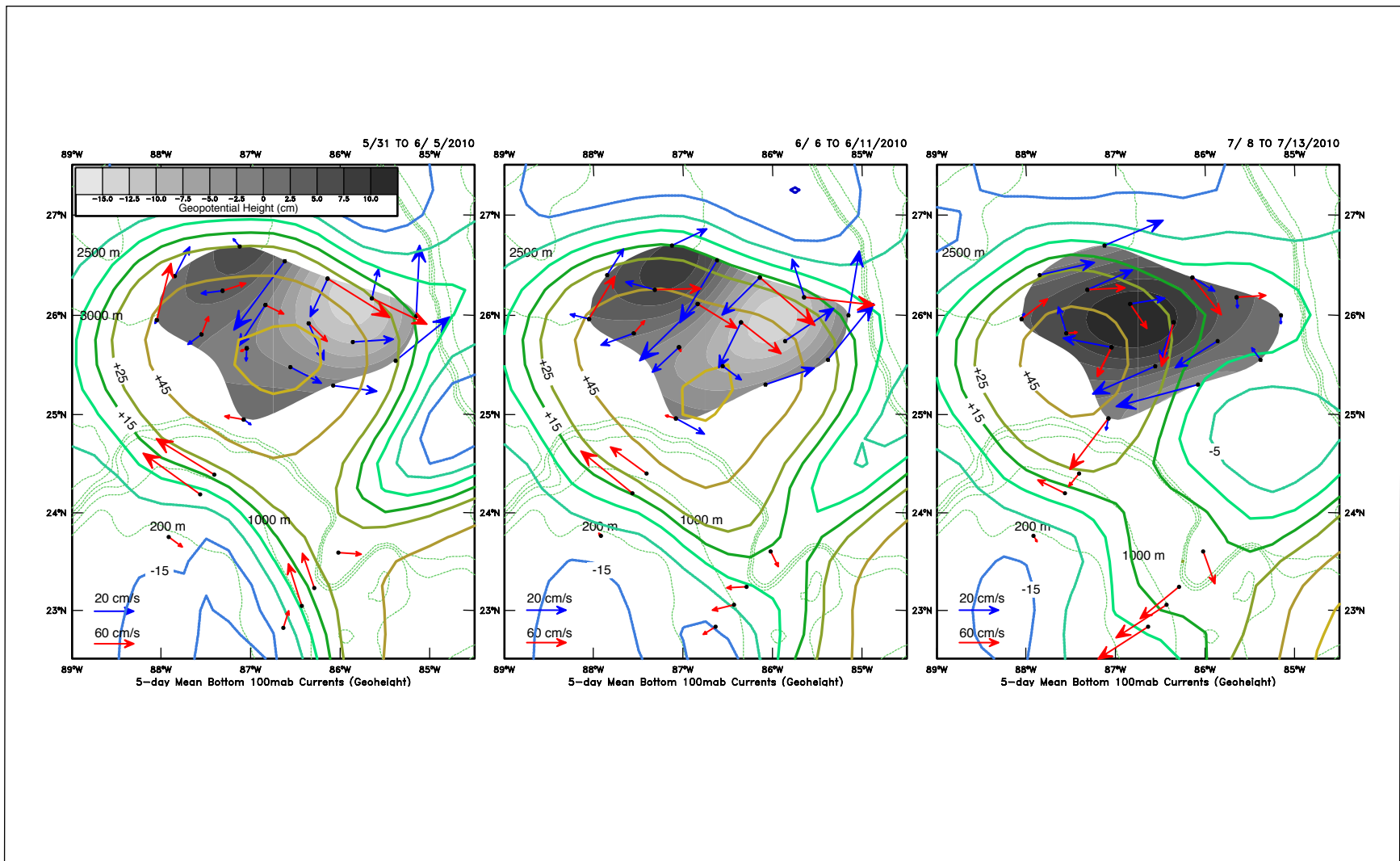


Figure 3.2-6. Franklin detachment 1: Upper and lower-layer circulation for indicated dates. Surface layer - SSH (cm) from altimeter with 5-day mean 40-HLP velocities (red arrows) at 80 to 120 m. Bottom layer - Geopotential (dynamic height, cm) from 5-day mean 40-HLP velocities 100 mab (blue arrows). SSH contour interval is 10 cm from -25 to +25, and 20 cm above +25 cm. Note differing scales for upper and lower layer velocities.

displaced eastward. During the reattachment a month later, an intense lower-layer high is situated under the east side of Franklin with the result that upper- and lower-layer flows are more coincident. The upper-layer circulation appears closed within the eddy, leaving the southern lobe, which was the eastern lobe on the 8 June map, to be advected towards the LC (velocities at E5 are southwards) by the cyclonic circulation of the Tortugas eddy. Similar to when the trough expanded at the first detachment, the E transect shows even stronger flows directly towards the Campeche slope and also normal to the SSH contours. This is similar to the first detachment of Ekman. The along- and across-isobath velocity components for section E, down to 1000 m, are shown for 10 July 2010 in Figure 3.2-7, which shows that the flow is towards the slope at all depths inshore of E4. This indicates there is no compensating flow at depth to the onshore surface flow so that there is a mean transport, during this detachment, onto the Campeche shelf. The along-isobath component shows weak flows at all depths, except at E5 where the flow is southward. Flow over shoaling depths should produce an anticyclonic circulation through the conservation of potential vorticity. If this exists, it is not resolved by the spacing of the E and N transects.

3.2.3 Hadal

After the final separation and fading away of Franklin in late September 2010, the LC did not retreat, and remained moderately extended with the northern boundary at $\sim 25^\circ\text{N}$ through October and early November. Some long wavelength meanders develop on the east-west directed section of the front during late November and December that propagate eastward through the Florida Straits. The LC begins to extend northwestward in December, favoring the Campeche slope. The LC east-west extent is less than for Franklin and Ekman at a similar stage of development (Compare 2 January 2011 front in Figure 3.2-8 with 1 March 2010 (Figure 3.2-3), and 25 May 2009 (Figure 3.2-1)). The LC extends northwestwards through January and February with increasing area (Figure 1.5-1) that plateaus in March 2011. During this phase, large amplitude, long wavelength, southward propagating meanders develop on the eastern boundary, similar to Ekman and Franklin. The meanders have maximum amplitudes in late February and early March, and then begin to decrease so that by early April, the LC has regular, fairly straight eastern and western boundaries, and occupies a larger area than at the beginning of January (Figure 3.2-8). During the next growth phase in April 2011, the LC again develops large meanders on the eastern boundary that also decay when the areal growth again plateaus in May-June (see Figure 1.5-1). The main difference with the earlier meanders is that the longer length of the eastern boundary allows two crests and troughs to develop (see 2 May in Figure 3.2-8), instead of one crest and trough. At the end of this sequence in early June, the Hadal part of the LC bulges out to the west along 28°N . This western lobe moves northward and becomes the northwestern part of developing meanders propagating southeastward along the very long eastern boundary of the combined LC and Hadal. This northwestern lobe detaches a very small eddy (named Galileo, even though it was not a true LC anticyclone, on 27 June 2011. However, by mid to late July a meander trough on the eastern boundary, situated in the middle of the array at $\sim 26^\circ\text{N}$, 87°W began to amplify and nearly caused a detachment on 26 July when some of the cyclonic vorticity was squirted through to the western side of the LC (compare 16 and 31 July boundaries in Figure 3.2-8). This event will be discussed in more detail below and resulted in a strong cyclone being spun up between the northern side of the Campeche bank and an already westward-extended Hadal. This Campeche cyclone further assists the westward movement of Hadal, which was large enough and unimpeded by topography for westward translation by β to

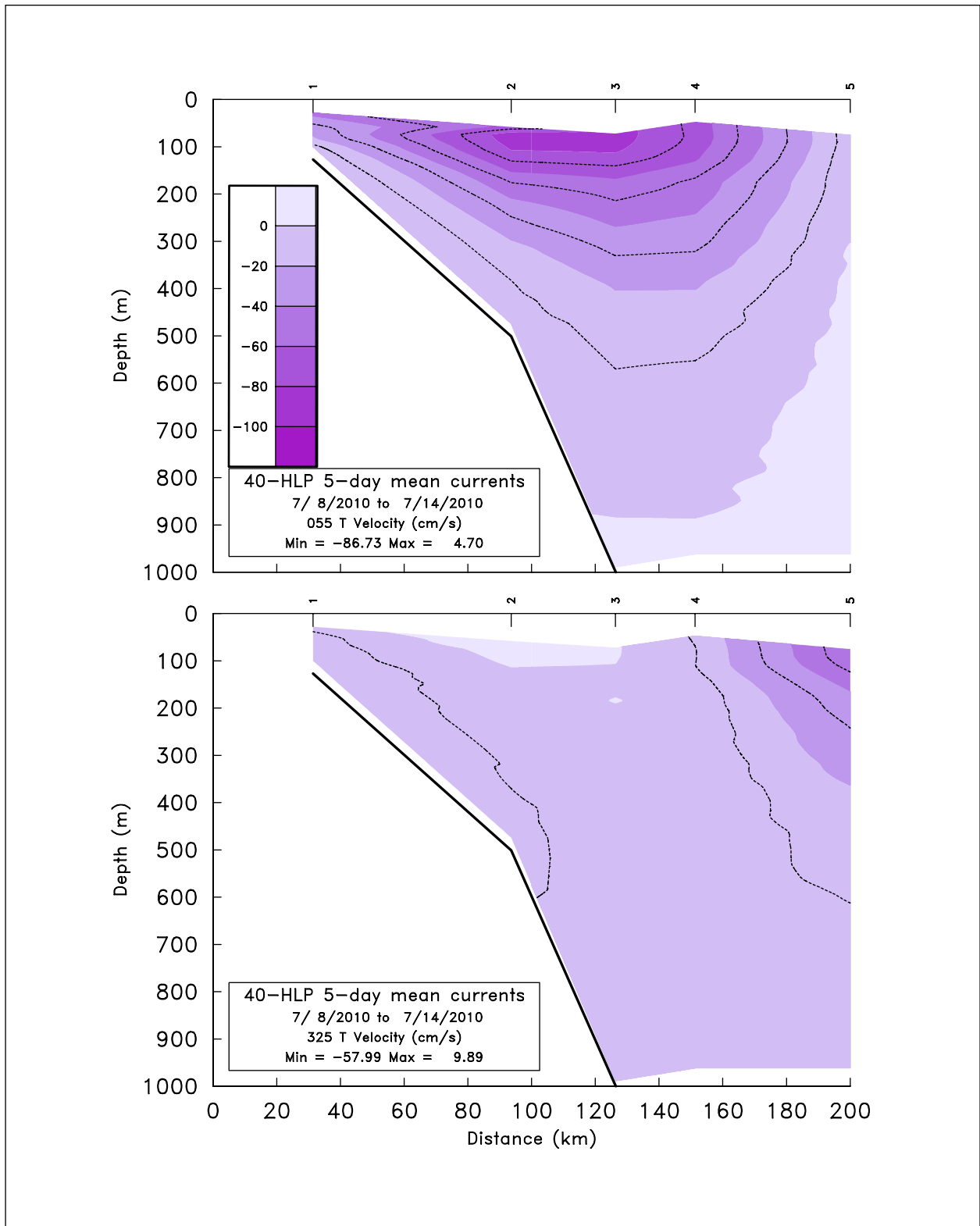


Figure 3.2-7. Five-day average velocity components for transect E moorings (E1 to E5). Upper panel: cross-isobath component (+ve directed 055°T). Lower panel: along-isobath component (+ve directed 325°T).

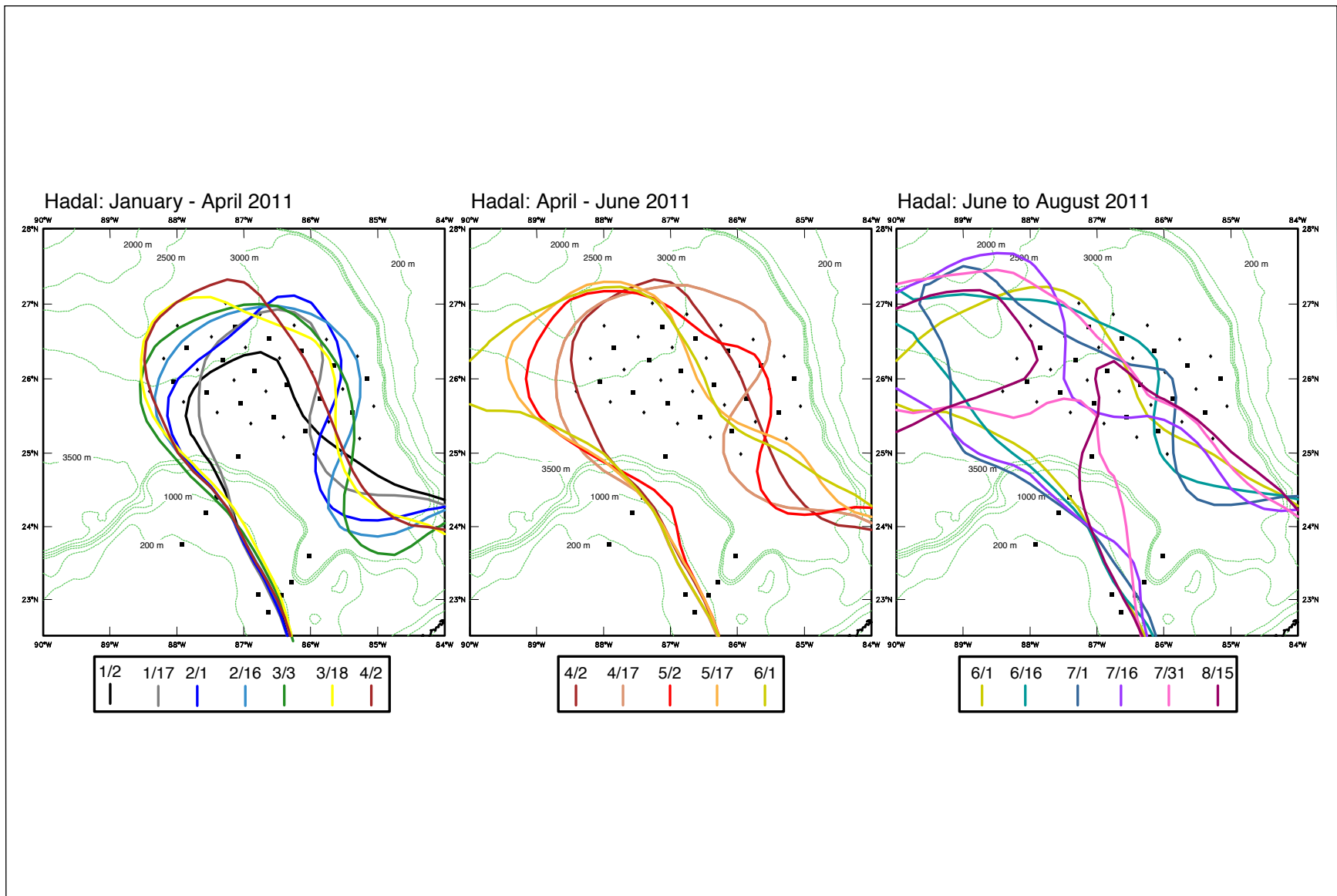


Figure 3.2-8. Loop Current 17-cm frontal boundaries from SSH altimeter maps for Hadal for the indicated dates.

be effective. This results in an eventual final separation on 15 August. The LC remained extended and began to increase in size almost immediately after Hadal's separation, again developing meanders on the eastern boundary that led to the first detachment of Icarus on 8 November 2011 (see Figure 1.5-1) immediately prior to the end of the field program.

The sequence showing the depth of the 6 °C isotherm surface in relation to SSH is shown in the top panels of Figure 3.2-9 for late July through 12 August, just prior to the final separation. Between 25 and 31 July, the cold-meander trough on the east side of the LC is advected through to the west side by the south and southwestward flows on the east side of Hadal. This causes the 17-cm SSH contour on the east side of the LC/Hadal configuration to be deflected northeastward, but this apparent developing trough is directly a result of the cold cyclonic vorticity being squirted through the neck from the east side of the system. Over the next 15 days, the cold cyclone strengthens over the north Campeche slope, and seems to play a role in the movement of Hadal westward that stretches the narrow neck in the SSH leading to separation on 15 August. The lower panels of Figure 3.2-9 show the lower-layer circulation, and on 25 July on the west side of the array, there are a high and low displaced southward from the corresponding surface-layer high and low (warm and cold, respectively). There is also a lower-layer high on the east side of the array that is only slightly displaced from the corresponding warm northern lobe of the LC. The two lower-layer highs merge into a ridge that is maintained and increases as Hadal and the LC draw apart. On the 12 August map, the lower-layer flows on the west side of the ridge are northward, acting as if to further narrow the neck. The southeastward flows on the east side of the ridge parallel the LC SSH contours, and thus the similar southeastward surface-layer flows. These lower-layer circulation patterns are quite different from the meander-mediated separation of Ekman (Figure 3.2-2), which occurred in a similar location and was also caught by the array.

The surface chlorophyll map for 12 August (Figure 3.2-10) shows the more productive waters stretching across the neck in the direction of the flows on the east side of Hadal, in contrast to low productivity waters of both the LC and Hadal. The Campeche cyclone, centered at ~25°N, 88°W, is also clearly advecting low productivity water from the south side of Hadal onto the northern part of the Campeche bank. The higher productivity (green color in Figure 3.2-10) that intrudes southwards at ~26.5°N on the east side of Hadal originates from the shelf around the Mississippi delta, being advected off the shelf by Hadal's swirl currents. This intrusion is consistent with the southward flow at A1, and indicates that circulation is almost closed within Hadal event though the 17-cm contour shows a connection.

In summary, the three major LC eddy separations in this dataset are quite different, though there are features in common. Common features are:

- The development of long-wavelength, large-amplitude meanders on the eastern side of an extended LC that propagate southwards is common to all three separations.
- Detachments occurred when a growing meander trough stretched across the neck of the LC.
- Deep cyclones and anticyclones traversed the separation zone in a southwestward or westward direction, and seem to play a role in the detachment.

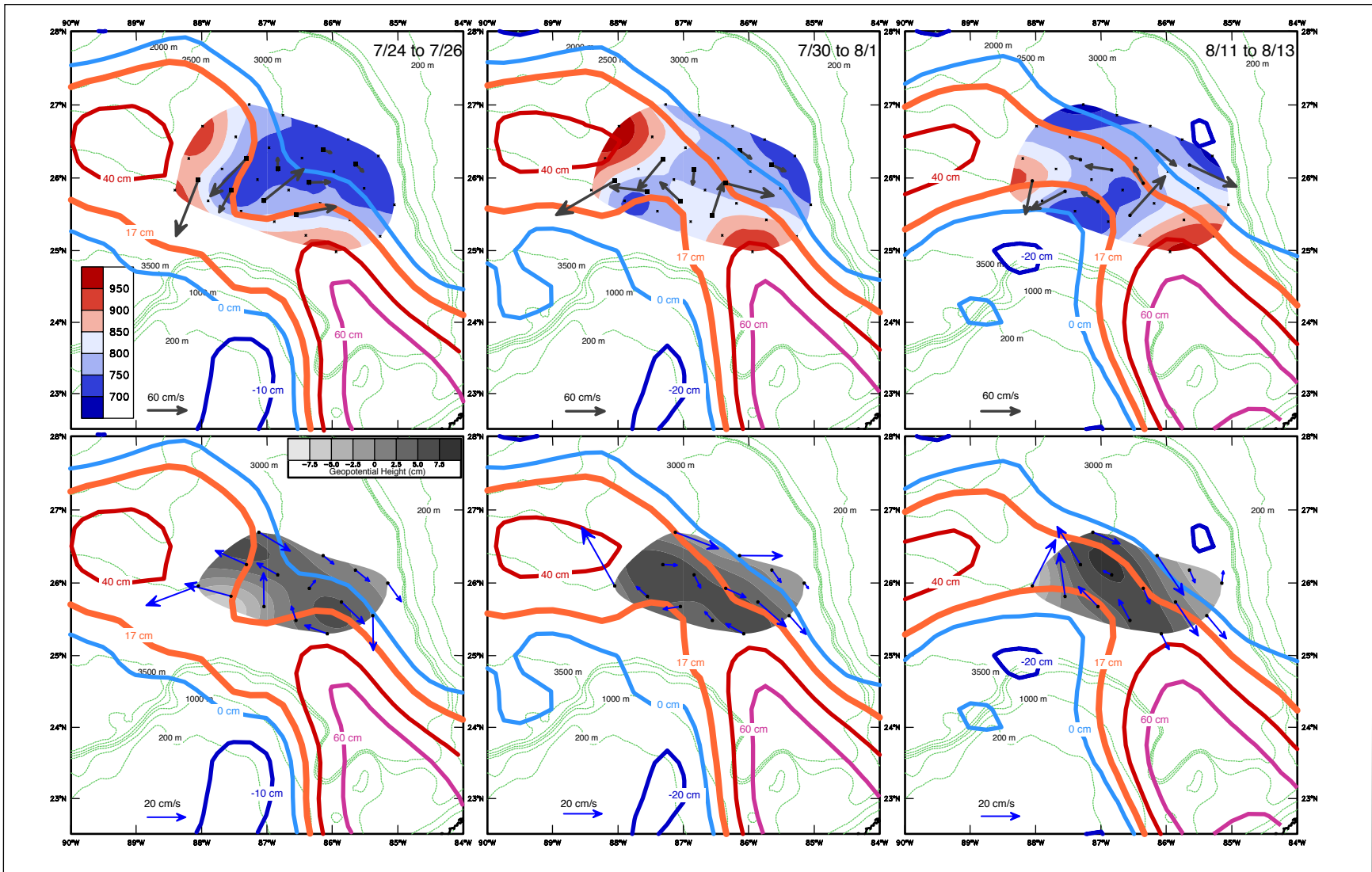


Figure 3.2-9. Maps of the separation of Hadal for the indicated dates in 2011 showing upper (top row) and lower-layer (bottom row) circulations. Parameters are 2-day mean currents at ~80-100 m (gray) and 100 mab (blue), geopotential height for the bottom currents (gray shaded), SSH contours (cm) from altimeter maps, and depth of the 6 °C isotherm (color shaded).

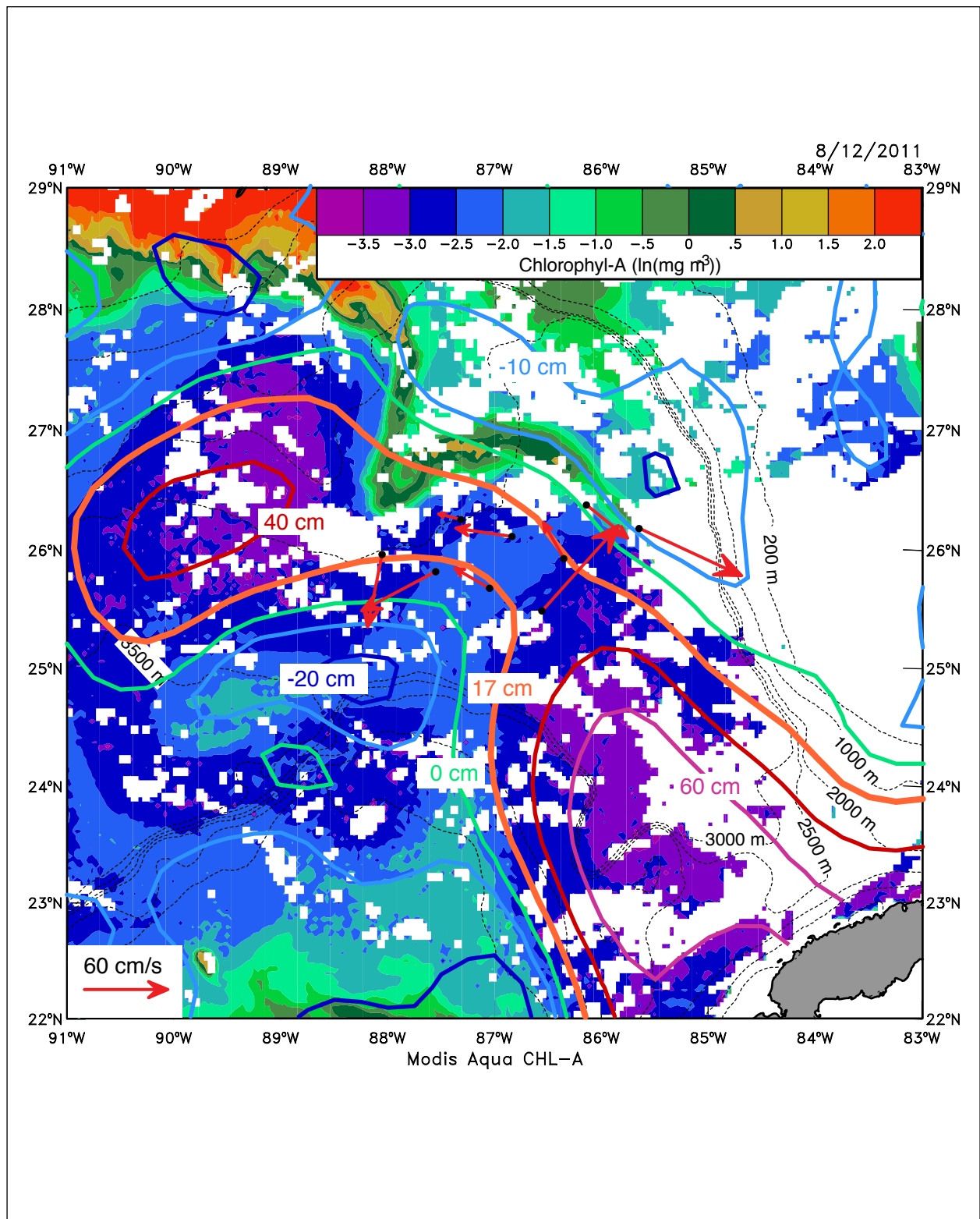


Figure 3.2-10. Surface Chlorophyll-A from Modis Aqua overlaid with SSH from altimeter maps for 12 August 2011. Two-day average 40-HLP velocity vectors at 80 to 120 m (thick red arrows) are shown for the moorings.

Notable differences are:

- Hadal had a greater the extension and hence the length of the eastern boundary with more crests and troughs than Ekman or Franklin. This suggests a preferred wavelength.
- Areal growth of Hadal had plateaus when eastside meanders seem to shutdown. Similar plateaus in growth did not apply for Ekman and Franklin.
- After Franklin's initial detachment, multiple reattachments with the LC essentially drained mass from the eddy, and though a separation was eventually achieved, it rapidly dissipated.
- Hadal's separation was for an eddy that was well extended into the deep Gulf, and was large enough for β -driven westward translation to take over (see next section), though the initial partial detachment by the meander trough seemed to be a precondition, and the development of the Campeche bank cyclone from this trough also seems to assist the westward push of the eddy.
- Hadal's lower-layer circulation consisted of a ridge of high pressure linking the LC and was quite different from Ekman.

3.3 NUMERICAL MODELING OF HADAL'S SEPARATION

3.3.1 Introduction

One way the shedding of Loop Current eddies can be understood is as a competing imbalance between the mass influx through the Yucatan Channel, which grows the Loop, and a westward Rossby wave that tends to 'peel' an eddy from the Loop; this will be referred to as the Pichevin-Nof mechanism (Nof 2005; Pichevin and Nof 1997). According to Chang and Oey (2013a) and Xu et al. (2013b), the Loop Current grows larger and deeper with mass influx from the Yucatan Channel. When its Rossby radius, R_0 (based on the Loop's upper-layer depth), reaches a certain size, the variation of the Coriolis parameter (f) becomes significant (β effects), and the westward eddy's speed (which is proportional to long Rossby wave velocity $\sim \beta R_0^2$) exceeds the LC growth rate due to the mass influx. At this point, the Loop Current eddy begins to detach. The idea may be extended to the case when the mass influx (i.e., Yucatan channel transport) varies slowly in time (longer than 1~2 months), so that eddy shedding may also depend on this variation. Oey et al. (2003b) show that models forced by time-dependent winds produce strong Yucatan transport fluctuations, of the order of a few Sverdrups ($1 \text{ Sv} = 10^6 \text{ m}^3\text{s}^{-1}$) and larger, which in turn also influence the shedding periods. Chang and Oey (2013a) identify biannual preferences of LC eddy shedding in summer and winter by analyzing long-term observational data and numerical model results. This will be discussed further in Chapter 5. They found a strong dependence of eddy shedding on Yucatan transport. The biannual variation in the trade winds forces a corresponding biannual transport through the Yucatan Channel; as a consequence, the LC has a tendency to shed eddies as the wind weakens from summer to fall, and also from winter to spring. In Chapter 5 and Chang and Oey (2013a), the process is studied in the simplest possible setting using a reduced-gravity model forced by idealized, biannually-varying winds. The simple model suggests that the biannual signal is produced by vorticity and transport fluctuations in the Yucatan Channel due to the piling-up and retreat of warm water in the northwestern Caribbean Sea (forced by the trade winds). The LC grows and expands with increased northward velocity and cyclonic vorticity of the Yucatan Current, and eddies are shed when these are near minima. These findings agree with the prediction based on the Pichevin-Nof mechanism and Reid's (1972) theory.

Chang and Oey (2013a) also suggest that, while other factors such as baroclinic instability and upper-lower layer coupling do not determine eddy shedding, they can modify it, by accelerating the timing when eddies are shed. Oey (2008) showed that the region north of the Campeche Bank is a fertile ground for baroclinic instability, which can generate deep cyclones below 1000m. In Chapter 4, these baroclinic instabilities will be analyzed using the present study observations. These cyclones may accelerate the upper-layer LC eddy shedding. In the initial stages of shedding an eddy, the westward-extended LC forces a deep return flow into the eastern Gulf where the upper layer then becomes divergent while the lower layer becomes convergent. The resulting strong upwelling in the eastern Gulf may also accelerate shedding.

This section uses the free-running version of the model to investigate the separation of Hadal in late July 2011. The model is validated against AVISO SSHA fields, and AVISO maps determined that the separation occurred on 25 July, which, according to the CCAR analysis that is the basis of the observational description above, was a partial but not quite complete detachment. The hindcast analysis run (described in Section 2.8), which assimilates AVISO SSHA, is used as initial conditions for two free-running experiments to study Hadal's eddy-shedding dynamics. One experiment is initialized from the 1 July 2011 hindcast field (Exp.Jul01) and another experiment initialized from the 15 May 2011 hindcast (Exp.May15). The rationale for these initialization dates will become clear. For these free-running experiments, neither the AVISO SSHA, nor the MCSST data were used; other forcings are the same as in the hindcast analysis run. For convenience, these experiments will be called "forecasts" even though, strictly-speaking, they really are not, since winds (and other forcings) are used. For each experiment, daily-averaged fields are used for analyses. The majority of the material in this section was originally published in Xu et al. (2013b).

3.3.2 Model Forecast Skill

Exp.Jul01 predicts a LC eddy shedding during the last week of July in agreement with the AVISO satellite sea-surface-height (SSH) data (Figure 3.3-1). The hindcast analysis and AVISO both show for 1 July (Figure 3.3-1) a northwestward-extended Loop Current, although the AVISO zero-SSH contour is some 50 km more extended. Ten days later (on 11 July) the forecast LC intrudes northwestward, which compares well with AVISO. On 21 July, both AVISO and the model LC developed a thin neck, typical of the situation at incipient eddy shedding (Oey 1996; Oey 2008; Schmitz 2005; Schmitz et al. 2005). The forecast shows that a large eddy was shed shortly thereafter on July 25 in agreement with AVISO. Exp.May15 produces an eddy shedding on 8 July, 2-3 weeks earlier than observed with AVISO, and predicted by Exp.Jul01. This eddy shedding date is 7-8 weeks into the forecast horizon, which is near the limit of modeled LC predictability (Yin and Oey 2007). Exp.May15 will be used in Chapter 4 to investigate LC separations as influenced by Yucatan transport, vorticity, and Caribbean winds.

Model Skill Assessment Against SSH Observations

To evaluate forecast skill, time series of the spatial correlation coefficient and root-mean-square errors between the model and AVISO SSH anomalies are calculated and compared against persistence for the open-ocean region of the Gulf: north of 23°N and west of 84°W, in water depths deeper than 500m (Figure 3.3-2). The correlation, R , is ≈ 0.8 on 1 July for the initial

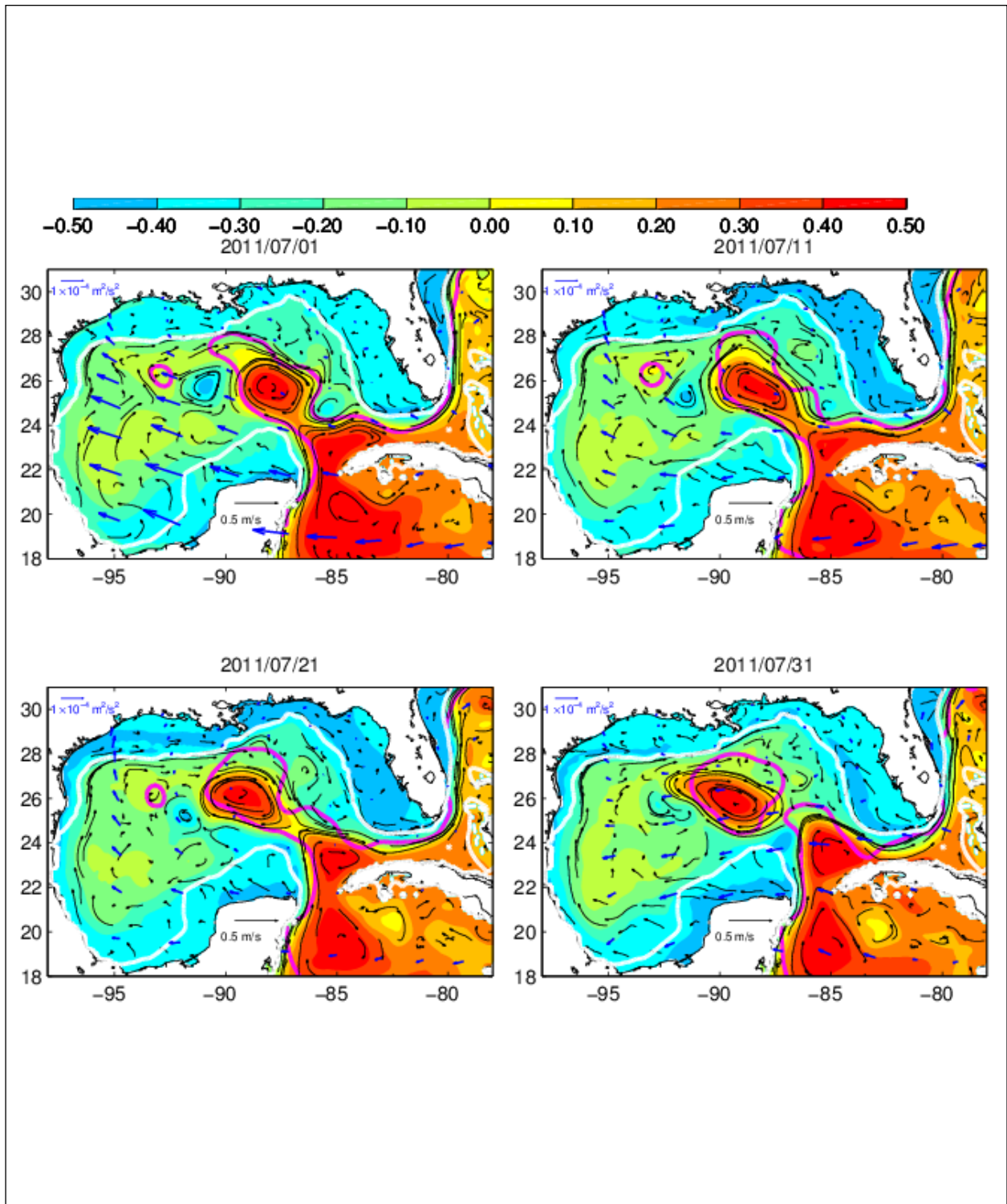


Figure 3.3-1. Daily averaged SSH (colors in m) and surface currents (squiggly black lines with scale shown) for every 10 days of the forecast simulation, starting from 1 July 2011 (Exp.Jul01). Blue vectors are wind stresses with scale shown. White contour indicates the 200-m isobath. The magenta line indicates the SSH=0 from AVISO for comparison with the model.

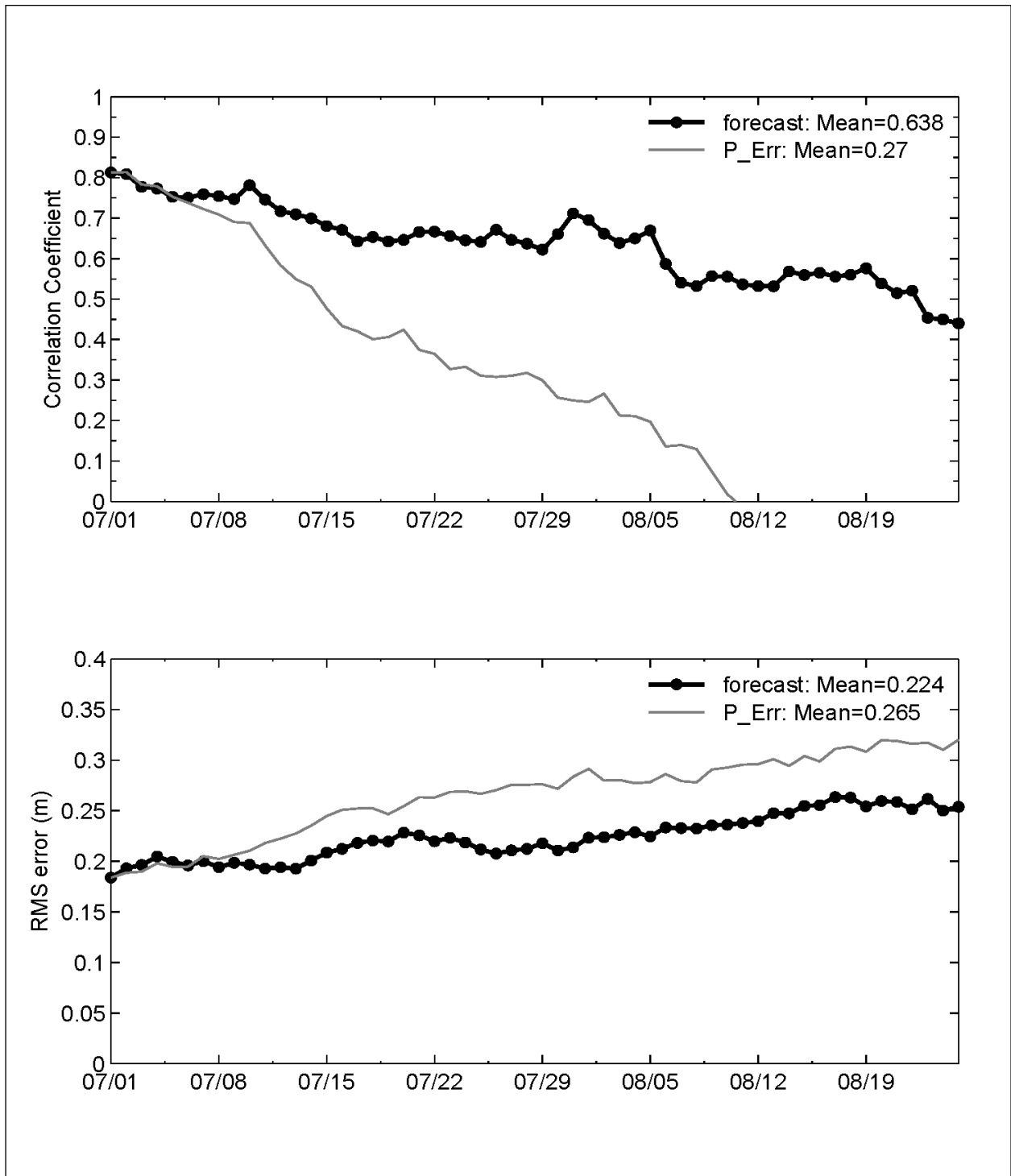


Figure 3.3-2. Comparison between AVISO and forecast (exp Jul01) SSHA. Top: the spatial correlation coefficient between the model and AVISO SSHAs in the region north of 23°N and west of 84°W, over water regions deeper than 500 m in the Gulf of Mexico (for eight weeks from 1 July to 26 August 2011). Bottom: the corresponding RMS error for the same region. Black dotted lines are forecast and grey lines are persistence.

hindcast value. It remains above 0.65 during the first five weeks of the forecast consistent with Yin and Oey (2007) who concluded, based on bred-vector analyses, that the LC and eddy forecast horizon in the Gulf of Mexico is four to six weeks before the model skill deteriorates. At week six, the correlation drops to approximately 0.5 but it remains above this value from weeks six to seven before degrading further to about 0.45 at the end of week eight. The RMS errors increased from 0.18 to 0.23 over the first eight weeks. For both measures, the model forecast beats persistence.

Model Skill Assessment Against In-Situ Observations

Both the model hindcast and forecast skills are calculated for the nine full-depth moorings in the U.S. array using the metrics given in Section 2.8.1. Figure 3.3-3a shows the nine mooring locations superimposed on the color map of modeled SSH averaged over July 2011, and Figure 3.3-3b plots the depth-averaged R and $|\theta|$ at each mooring. Relatively large errors at moorings A1 and A2 are due to the highly variable flow as the main portion of the Loop passed these locations during the eddy-shedding process. On the other hand, the relatively large error at mooring C2 is caused by the weak altimetry signal there, and data assimilation becomes ineffective. At other moorings, the R s are generally higher than 0.5 and $|\theta|$ s are less than 50° . As can be expected, the nowcast (i.e., the SSHA data are assimilated through July) is generally more accurate than the forecast. These general inferences are also seen from the vertical distributions of R , θ and other metrics (Figure 3.3-4). Near the surface, the modeled currents generally agree with those observed, with $R \approx 0.7$ (forecast) ~ 0.8 (nowcast) and $|\theta|$ less than 45° (Figure 3.3-4a,b). These values degrade in the deep levels (where the model is basically prognostic with no assimilation), but the model retains some skills with $R > 0.5$ for nowcast and ≈ 0.45 for forecast, and $|\theta| < 50^\circ$ with the forecast $|\theta|$ being actually slightly smaller. The model generally underestimates the current fluctuations, by as much as 50% near the surface for the forecast ($R_{std} \approx 0.5$; Figure 3.3-4c), while it overestimates the current fluctuations ($R_{std} > 1$) just above the main thermocline at the base of the LC and eddy. This behavior in R_{std} also shows up in the mean speeds, as indicated by the R_{spd} plots in Figure 3.3-4e. Thus the modeled currents generally have weaker vertical shears in the upper layer (plots not shown). The $Skill_{uv}$ near the surface is high, but it degrades substantially to a minimum of about 0.52 (nowcast), and ≈ 0.6 (forecast) at $z \approx -400$ m. The large errors are due to the lower $Skill(u)$ for the zonal velocities at most of the moorings in the upper layer. During the comparison period in July 2011, most of the moorings were, based on AVISO, to the east of the LC in a region of cyclonic recirculation (Figure 3.3-3a) where ADCPs measured generally eastward currents near the surface. In contrast, in the model, the cyclonic edge of the Loop was biased southward compared with AVISO (Figure 3.3-3a), and the observed moorings were mostly in the region where the modeled eastward currents were weak. This apparent slight misalignment of the edge of the LC leads to poor $Skill(u)$ in the upper 500-m layer. This large discrepancy near $z = -400$ m also shows up in the mean velocity angles between model and observation, α_{m-o} , in Figure 3.3-4f. On the other hand, the directions of the modeled deep currents are quite well simulated.

Table 3.3-1 summarizes the average skill metrics for the model-ADCP comparisons (i.e., above 500 m). While there can exist large discrepancies due to misalignment of the modeled and observed LC fronts during the eddy-shedding event in July 2011, the model possesses some skills, as shown by the generally good complex correlations, which indicate that modeled currents co-vary reasonably well with those observed. Given the emphasis on east-side meanders

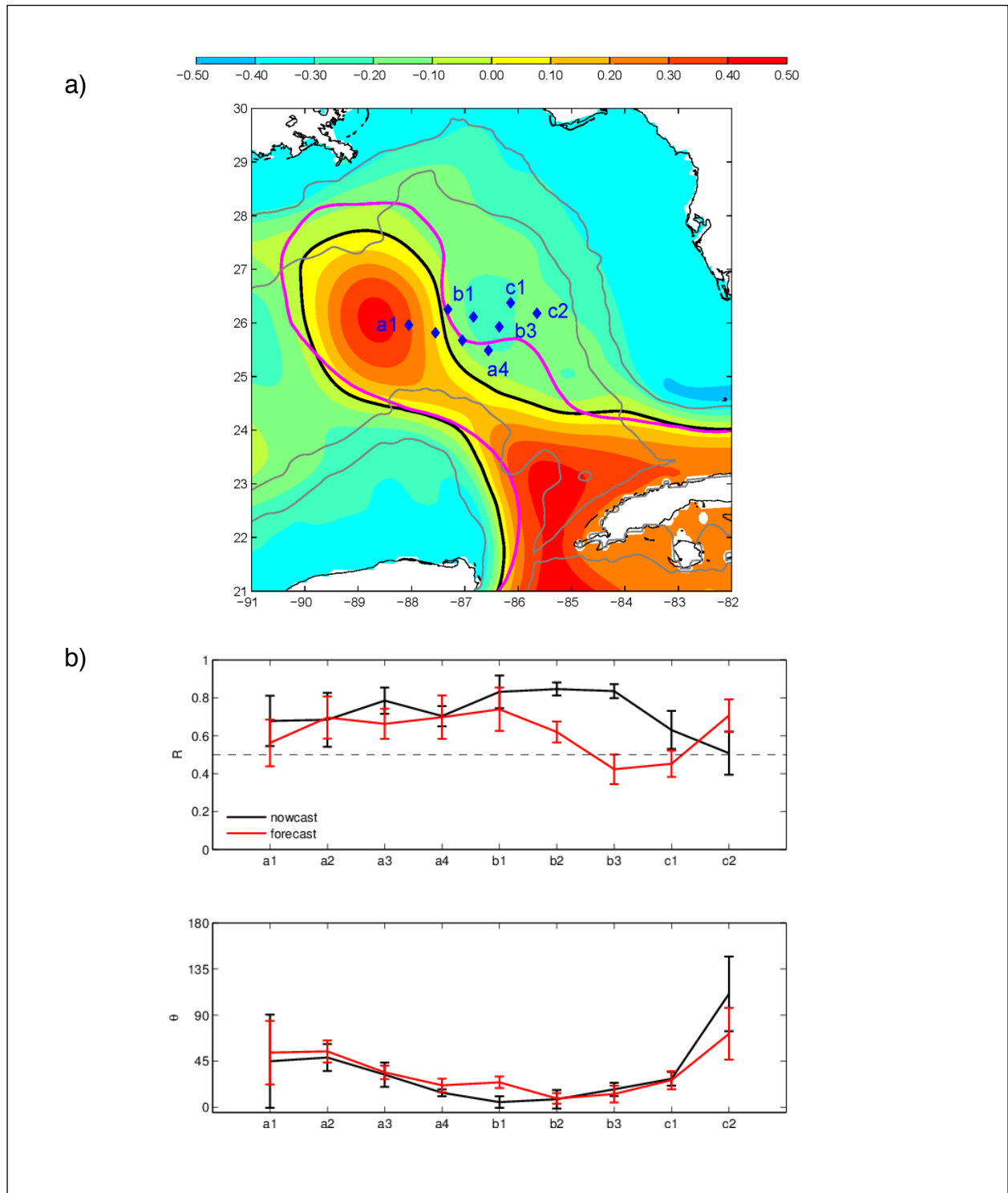


Figure 3.3-3. (a) Full-depth ADCP mooring (a1a4, b1b3 and c1c2) locations from the U.S. array superimposed on the July mean model forecast SSH (color with the zero contour in black, in meters). The purple contour is the zero contour of AVISO SSH. (b) Complex correlation R s and $|q|$ s averaged over depths at each of the nine tall moorings (i.e., horizontal distribution).

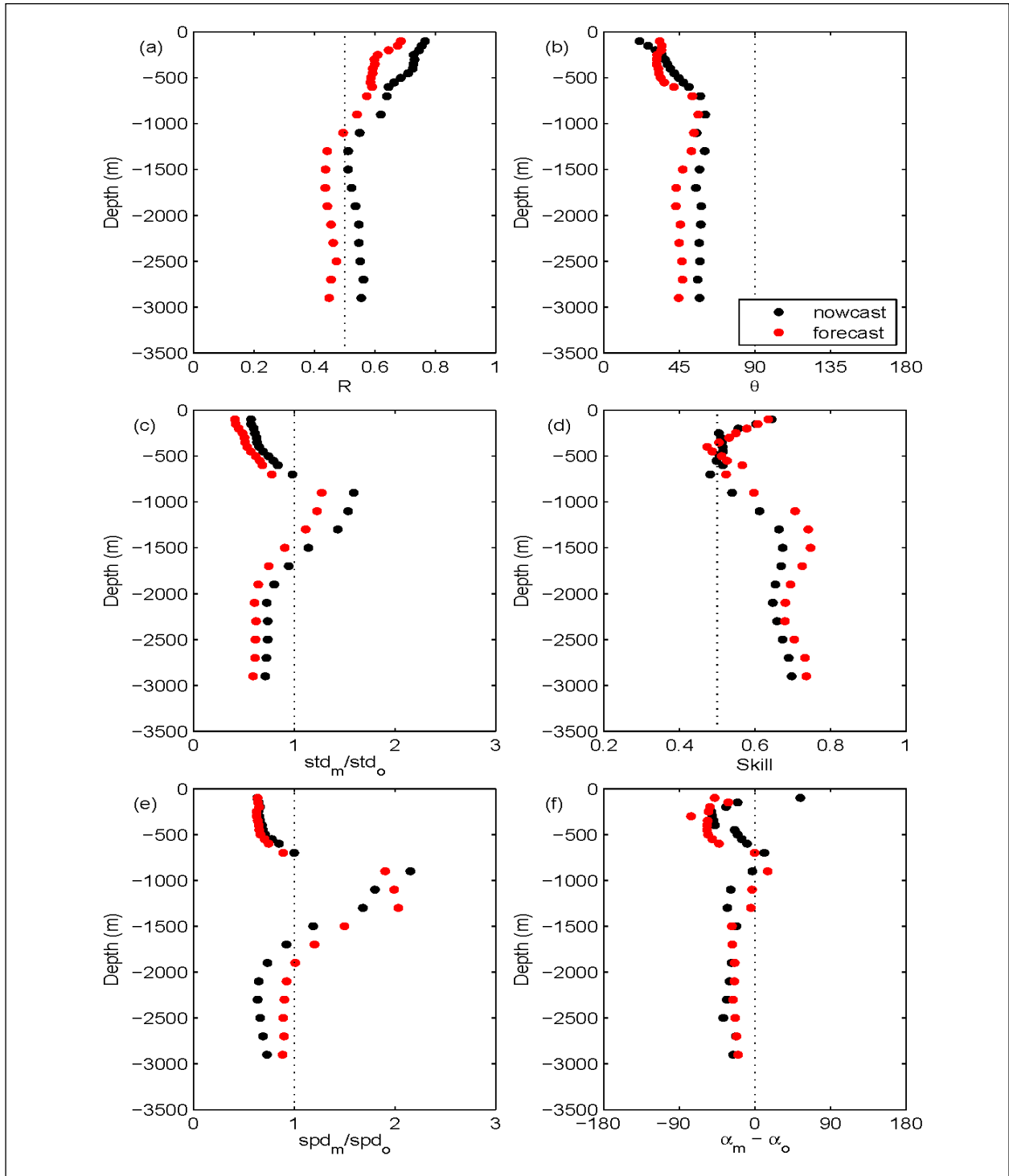


Figure 3.3-4. Vertical profiles (i.e., averaged over all nine moorings at each horizontal level) of: (a) & (b) complex correlation R s and Q s; (c) ratio of model-to-observed standard deviations (R_{std}); (d) Skill ($=[\text{Skill}(u)+\text{Skill}(v)]/2$); (e) ratio of model-to-observed mean speeds (R_{spd}) and (f) angle of modeled observed mean velocity, in degrees, negative if model is clockwise w.r.t observation (α_{m-o}). Black (red) symbols are nowcast (forecast).

and their consequences in the observational sections of this report, it is noteworthy that the model hindcast underestimates their amplitudes (Figure 3.3-1 and 3.3-3).

Model skills in simulating deep currents are quite high (Figure 3.3-4d), despite the fact that deep currents tend to be dominated by highly dispersive topographic Rossby waves (Hamilton 1990; Oey and Lee 2002) and are therefore more difficult to model. The magnitudes of the deep current fluctuations and means are underestimated and deviation angles are not zero ($\approx 30^\circ$; Figures 3.3-4c,e,f). However, this represents a major improvement over the earlier, coarser-resolution model (Oey et al. 2003a) in which the deep energy was very weak, by almost an order of magnitude, when compared with observations.

Table 3.3-1. A Summary of Various Skill Metrics Computed Using Currents from the Model and ADCP Measurements from Moorings A1 to C2

Model	R	θ	Skill		Mean		Std. Dev R_{std}
			u	v	Ratio R_{spd}	α_{m-o}	
Hindcast	0.63	28°	0.41	0.88	0.71	20°	0.84
Forecast	0.54	34°	0.55	0.75	0.73	-33°	0.68

3.4 STATISTICS

3.4.1 Mean Flows

Mean velocities are calculated from 40-HLP data for the two-year common interval to both U.S. and Mexican field studies. Comparisons with mean velocities from the 2.5-year study show little significant differences for the U.S. moorings. The results for all valid measurements are shown in a pseudo-3D view in Figure 3.4-1. The largest means occur on the west side along the Campeche Bank, reducing somewhat over the deeper water of the north and west side of the LC. Upper-layer mean flows are highly sheared, reducing in depth to low values at 750 to 1000 m, which is most of the water column in the vicinity of the mean LC front over the Campeche slope. Below 1000 m, the mean flows are nearly depth-independent to the lowest level (100 mab). Both upper- and lower-layer flows have uniform but generally different directions with a transition occurring between ~ 900 m and 1300 m. Upper-layer currents align with the mean LC front (represented by the 15-cm contour in Figure 3.4-1), and the bowl-shaped 6°C isotherm surface matches nicely the area of the mean LC and indicates that the center is between N4, A4 and A3. It is noted that near-surface flows are slightly divergent on the west side, and slightly convergent on the north and east sides of the array. The mean low in SSH north of the LC has previously been noted as a quasi-permanent cyclonic flow in the eastern Gulf.

The lower-layer means suggest both anticyclonic and cyclonic flow, with high and low geopotential heights, respectively, of flows under the northwestern and northeastern parts of the mean LC. This is more evident if the first year (5/2009 to 6/2010) means are used because complete near bottom records are available (Figure 3.4-2). The lower-layer mean anticyclonic flow, centered on B2, is well defined, but the trailing cyclone to the east is a little more ambiguous. An explanation is that as the LC extends into the Gulf it moves over the shoaling depths of the Mississippi Fan with the net result that the lower layer will be compressed, and by

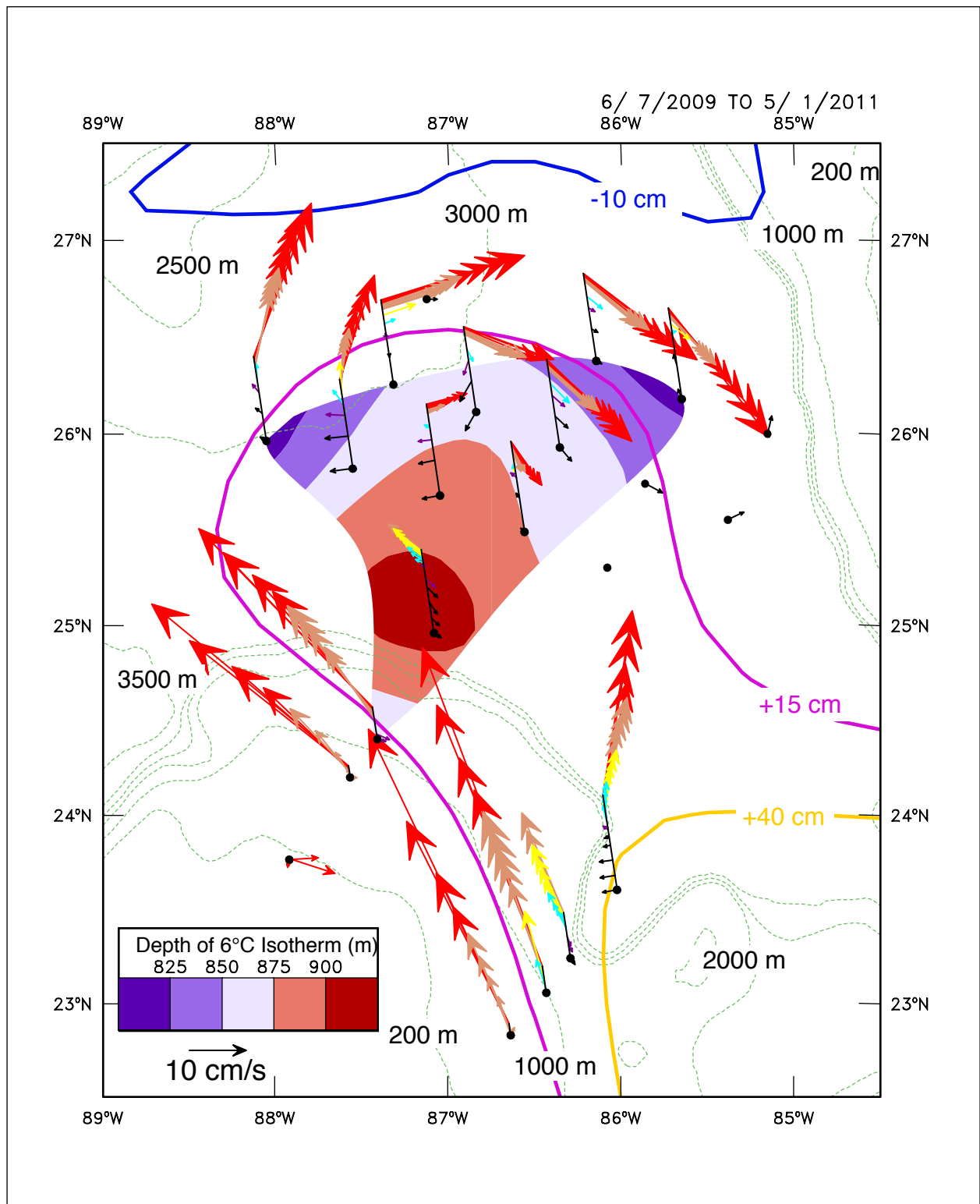


Figure 3.4-1. Mean 40-HLP currents for all moorings overlaid with mean SSH (contours) and mean depths of the 6 °C isotherm (color shaded). Vector depths are color coded: red 0-250 m, tan 250-500 m, yellow 500-750 m, cyan 750-1000 m, purple 1000-1500 m, and black > 1500 m.

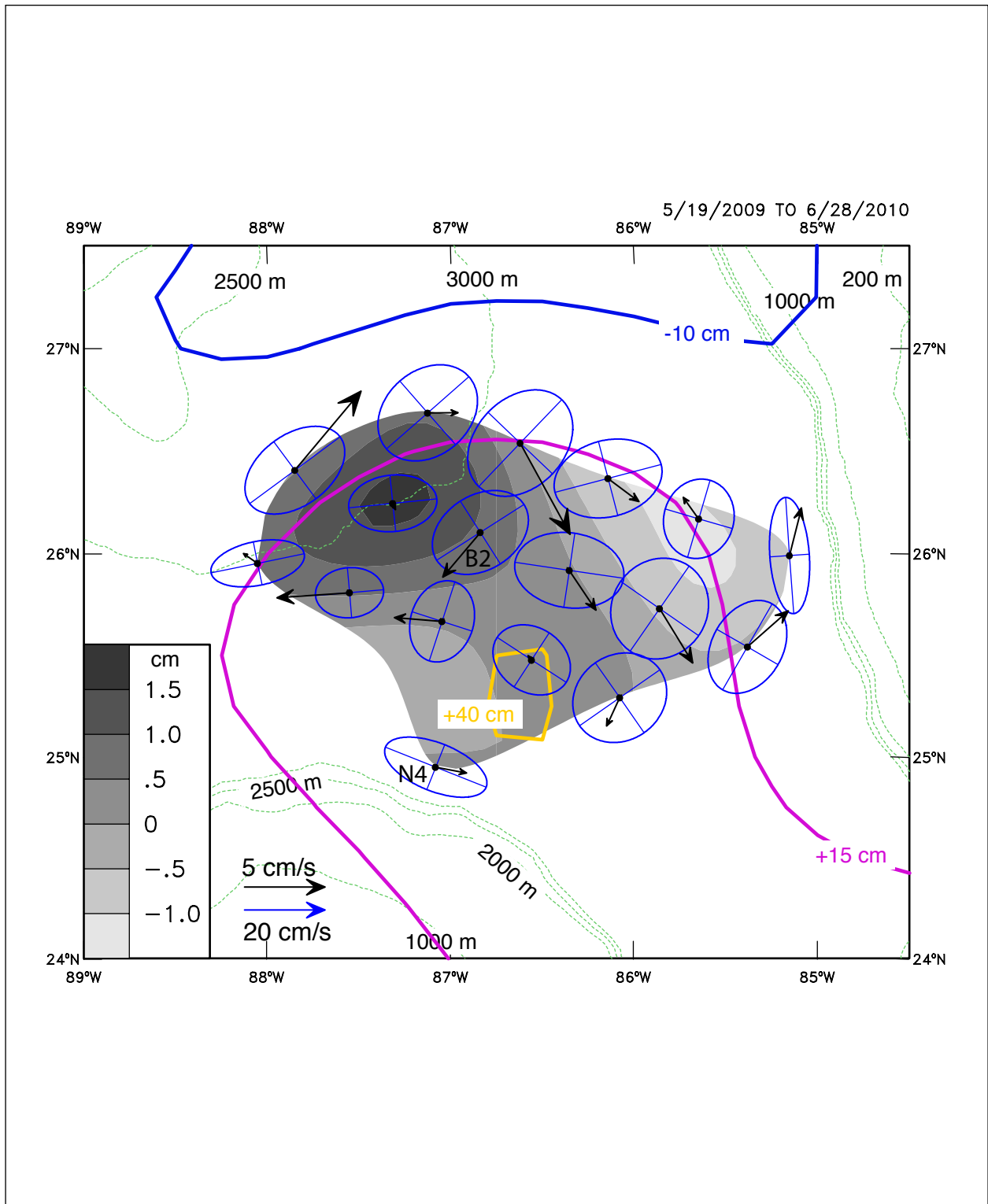


Figure 3.4-2. Mean near-bottom 40-HLP currents (black scale) and standard deviation ellipses (blue scale) for the indicated interval. The mean SSH (cm) contours, and the geopotential height (gray shaded; dynamic cm) corresponding to the mean velocities for the same interval are also shown.

conservation of potential vorticity generates anticyclonic (negative) relative vorticity anomalies. Similarly, because an extended LC tends to move westward, due to the Pichevin-Nof mechanism and the β -effect, the lower water column on the northeastern side is stretched as the upper-layer shoals, generating cyclonic (positive) relative vorticity anomalies.

The mean flow at the base of the Campeche slope (N4) is to the east in both the one and two-year results. This could be consistent with being part of the deep-return current of the basin-wide deep-mean cyclonic circulation that runs westward along the Sigsbee escarpment and southward along the base of the western Mexican slope (the Perdido escarpment) as observed by Lagrangian floats and moorings (Hamilton 2009) and discussed by DeHaan and Sturges (2005).

The variability, as represented by the standard deviation ellipses, is much larger than the mean near-bottom currents (Figure 3.4-2) and is quite inhomogeneous. The amplitudes tend to be smaller and larger on the southeastern and north and northwestern sides of the array, respectively. Lower-layer variances will be explored in more detail in the next section.

3.4.2 Depth Variability of Velocities

The mean flow shows that the water column in the deep eastern Gulf may be divided into two layers. For much of the analysis, a good analogue of the division between upper and lower water columns is the depth of the 6 °C isotherm which represents the lower boundary of the LC (Bunge et al. 2002), and roughly corresponds to the bottom depth of the Florida Straits (800 m). Analysis of the variability through the water column also shows markedly differing characteristics in both space and time of flows above and below the 900 m to 1100 m transition between the two layers. To show this, depth-weighted CEOF analysis is performed on the 40-HLP currents, after means have been removed, for each full-depth mooring separately. Again the two-year common interval is used and the results show only minor differences if the full 2.5-year interval is used for the U.S. moorings alone. In general, over 90% (and often over 95%) of the total variability of the currents through the water column at a given mooring can be accounted for by two CEOF modes.

Typical depth CEOF modes are given in Figure 3.4-3, and show a relatively depth independent dominant mode 1 and a surface intensified mode 2 above 1000 m that has more than twice the amplitude of mode 1 at the shallowest depth level. Together, they account for > 97% of the total depth range weighted variance of the low-frequency currents in the water column at this location. Mode 2 has essentially zero contributions from records below 1000 m, but near-surface flows do have a contribution from the nearly depth-independent mode 1, even though its R^2 with the observed record is low. Flows below 1000 m are almost entirely accounted for by mode 1 that shows almost constant amplitudes between 1300 m and 100 mab. Mode 2 is unidirectional, but mode 1 has a small change in direction between upper and lower layers. Given these characteristics, the nearly depth-independent mode is named “quasi-barotropic” -QB, and mode 2, though at some locations on the Campeche slope it will be mode 1, is “surface intensified” – SI. The QB mode implies that some of the surface layer flow is coupled to the lower layer. Even though CEOFs are purely statistical constructs, there is a correspondence to barotropic and first baroclinic dynamic modes for a stratified water column in a flat-bottomed ocean.

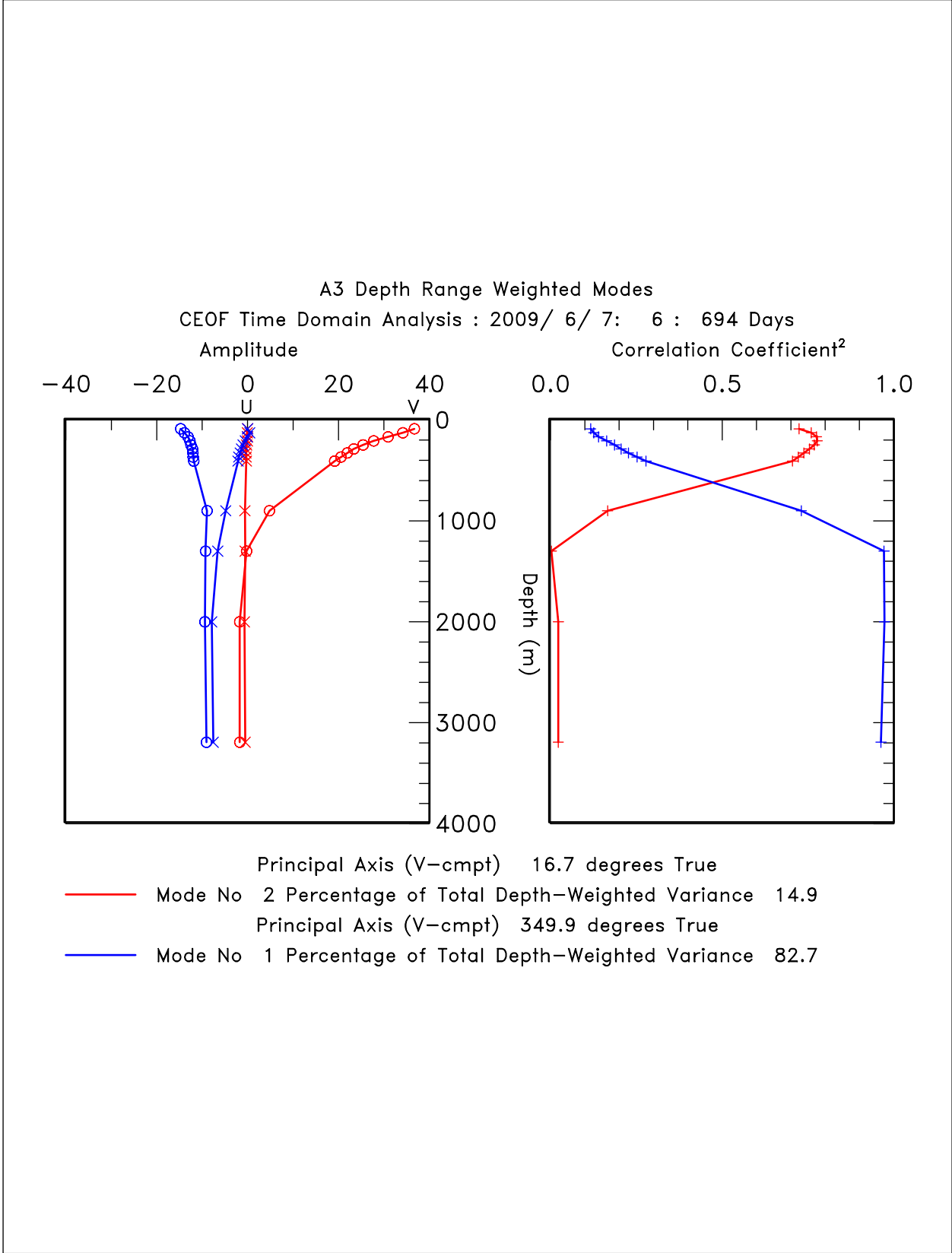


Figure 3.4-3. Depth range weighted CEOF modes for mooring A3.

The CEOF modes for all the moorings (Figure 3.4-4) all show similar characteristics. The SI mode is roughly aligned with the mean LC front, and is the only mode over the Campeche slope where amplitudes are much larger than further downstream. The QB mode shows only weak bottom intensification in the lower layer and the principal axis direction is often normal to the SI mode, particularly in the vicinity of the mean front. The principal axis directions for the QB mode are roughly in the same direction across the deep water U.S. array. The variances accounted for by these two modes are given in Table 3.4-1. The QB mode dominates in terms of variance explained at locations with water depths > 2000 m, even though amplitudes are less than the SI mode. This is because the SI mode decreases rapidly with depth and is only significant in the upper 1000 m, whereas the QB mode has significant amplitudes through the whole water column which is often > 3000 m deep. In terms of ratios of QB/SI variances, the QB mode has lower significance in the northwest (A1 & A2), and most significance in the north and center (B2, B3 and A4). The N4 mooring lacked a complete two-year record in the upper 500 m, and so the results are a little different from the profiles observed at the other deep sites.

Table 3.4-1. Percent Variance Accounted for by Depth-Range Weighted CEOF Modes (7 June 2009 to 1 May 2011)

Location	QB	SI	Total	Location	QB	SI	Total
A1	67.7	29.2	96.9	B1	81.8	15.6	97.4
A2	75.5	20.9	96.4	B2	83.8	14.0	97.8
A3	82.7	14.9	97.6	B3	86.8	11.4	98.2
A4	88.8	8.4	97.2	C1	81.0	17.4	98.4
				C2	79.7	16.8	96.5
E2		91.7	91.7	N2	8.4	88.6	97.0
E3	9.7	85.1	94.8	N3		90.1	90.1
E4		93.2	93.2	N4	71.5	26.7	98.2
E5	56.3	32.6	88.9				

The normalized CEOF-mode amplitude time series for each location (Figure 3.4-5) essentially show the complete time history of the velocity field over the 2-year interval. The SI modes show the long-term fluctuations through the growth phases of Franklin and Hadal, particularly on the LC west side, but also showing the ~ monthly fluctuations on the east side (e.g., C1 & C2), associated with large-scale meanders. Rapid, ~ weekly, fluctuations associated with LC frontal cyclones are seen at N3, N4, A1 and A2 during the growth phase of Franklin (January - April 2010), but are largely absent further downstream at C1 and C2. Similar fluctuations are only weakly observed along the LC-Campeche slope front for the similar growth phase of Hadal, a year later. The most prominent features of the QB-mode fluctuations that dominate the lower layer are the marked increases in amplitude during the detachments of Ekman and Franklin, and differing periodicities compared with the SI modes that dominate the upper layer. The responses are not uniform either in amplitude or timing for the two separation events. For example, the Ekman detachment events trigger a strong response resembling a wave train at A1, but for Franklin the periodicities are shorter and less intense. These characteristics are reversed for A4 and N4.

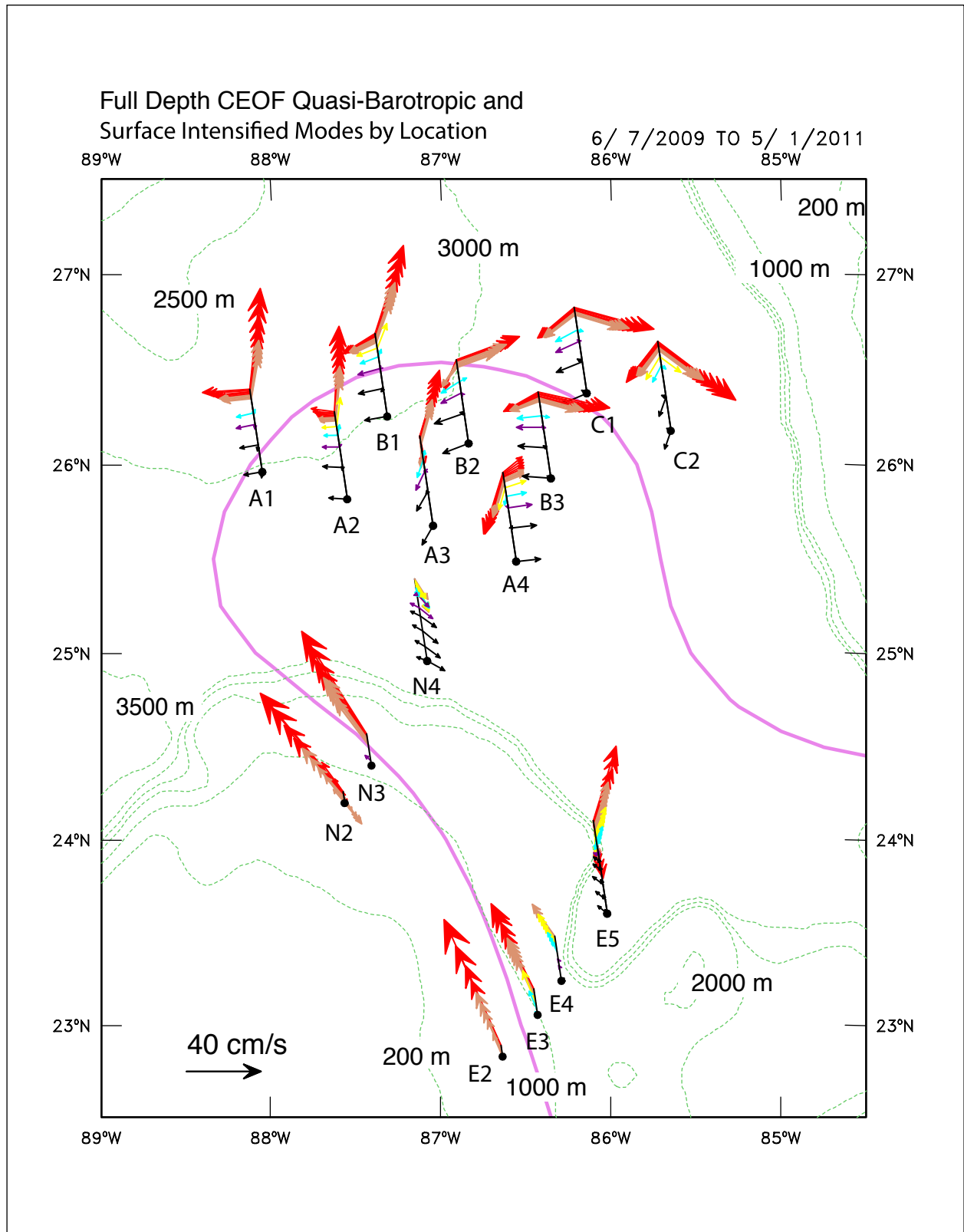


Figure 3.4-4. CEOF modes for the 2-year common interval. Both QB and SI modes are given. Depth dependent colors are the same as for Figure 3.4-1.

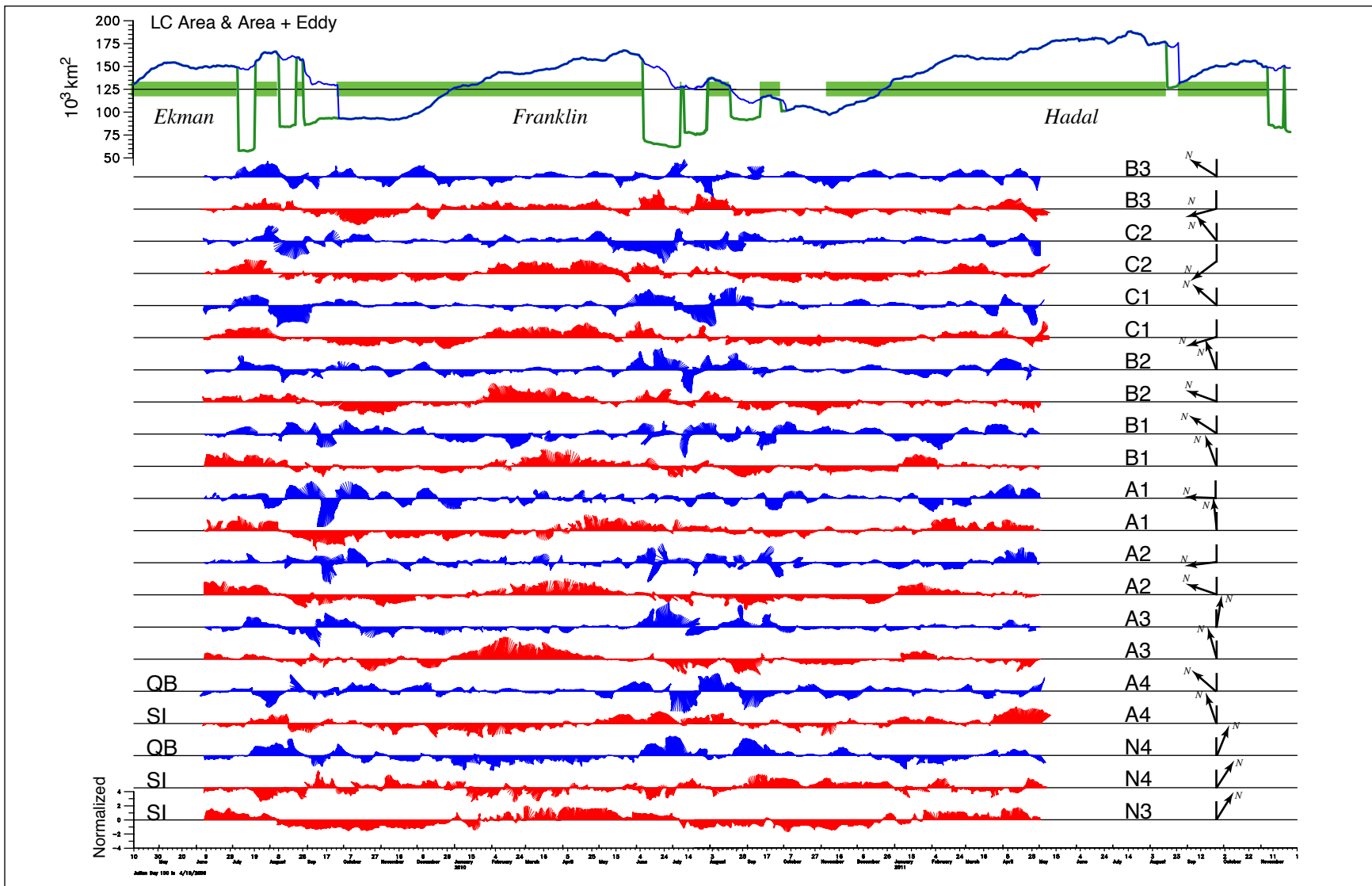


Figure 3.4-5. Normalized mode amplitudes for CEOFs by mooring for the 2-year interval. Red and blue vectors correspond to the surface-intensified and quasi-barotropic modes, respectively. The direction of the principal major axis w.r.t. north for each mode is given on the RHS of each ordinate axis.

The EKE spectra of selected normalized amplitude time series are shown in Figure 3.4-6. Because the time series are normalized, the apparent differences in power between locations are not significant, but the relative variance levels between frequency bands at a single location show which periodicities dominate the velocity records. The upper-layer or surface-intensified mode shows that long period (> 100 -day) fluctuations have the highest variance and are associated with the large-scale growth, retreat and eddy shedding of the LC. At shorter periods, the variance level changes with location along the mean LC front. Over the Campeche slope (N2 and N3), there are peaks in EKE at less than 10 days, but at 20 to 40 days there is relatively little activity. The A1, the SI mode shows more variance at periodicities longer than 20 days, and also peaks at ~ 15 days and at 10 days or less. On the east side, at C1, the 40-100 day periodicities dominate and there is less variance than for the west-side records at short periods. The QB-mode EKE spectra are quite different and can be considered as characterizing the lower-layer fluctuations. For periods > 100 days, variances are small, and the spectra are dominated by peaks in the 20- to 100-day band with only A1 showing a secondary peak at ~ 15 days that corresponds to the upper layer at A1. The A4 and C1 EKE have the strongest peak in the 40- to 100-day band. The spatial variability of the important frequency bands in the upper and lower layers is explored in the next two sections using the PIES mapping array data.

The QB and SI CEOFs are used to calculate the depth-integrated total EKE, at each location, as outlined in Chapter 2 and also given in Hamilton (2009). Figure 3.4-7 shows the cumulative depth-integrated KE from the mean flow and the two CEOF modes. Along the Campeche slope, the SI mode dominates, but the mean flow KE is a substantial fraction of the total. The mean-flow KE fraction of the total reduces from about a half to a third between E3 and N3, indicating that along the front, fluctuations are extracting energy from the mean. Once over deep water, both mean flow and SI-KE fractions decrease and the QB-mode EKE is the most important. The mean flow KE and the SI-EKE magnitudes, though less than over the Campeche slope, remain approximately constant along the path of the mean LC front over the deep basin. The QB EKE, however, tends to increase from the NW to the NE side of the LC, implying that transferring EKE to the lower layer is occurring all along the northern front after the LC leaves the Campeche slope. Total depth-integrated KE is less over deep water than over the slope where the totals at E3 and N3 are almost equal. However, the maximum total KE over the deep water is at C1 and is about the same as at N3, though the EKE has been transformed from SI to strongly QB. Thus, transfer of EKE from SI, and to a lesser extent KE from the mean flow, over the Campeche slope to a nearly depth-independent QB mode over deep water, is of major importance to the Gulf deepwater circulation processes. It has been observed that deep fluctuations that seem to originate from the LC can propagate towards the Sigsbee escarpment and the western Gulf in the form of TRWs (Hamilton 2007; Hamilton 2009; Oey and Lee 2002).

3.4.3 Horizontal Variability in the Upper Layer

The above CEOF analysis of the tall-mooring velocities indicates that most of the variance of the mooring velocities can be explained by two modes, one surface-intensified, and the other nearly depth-independent. In the following analysis, the statistics of these modes are characterized with the two components of PIES-mapped sea surface height (SSH). The surface-intensified (SI) mode is represented by the baroclinic SSH referenced to the bottom (SSH_bcb). Recall from Chapter 2 that SSH_bcb is surface geopotential referenced to 3000 dbar and converted to a height equivalent (geopotential divided by gravity). The nearly depth-independent (QB) mode is

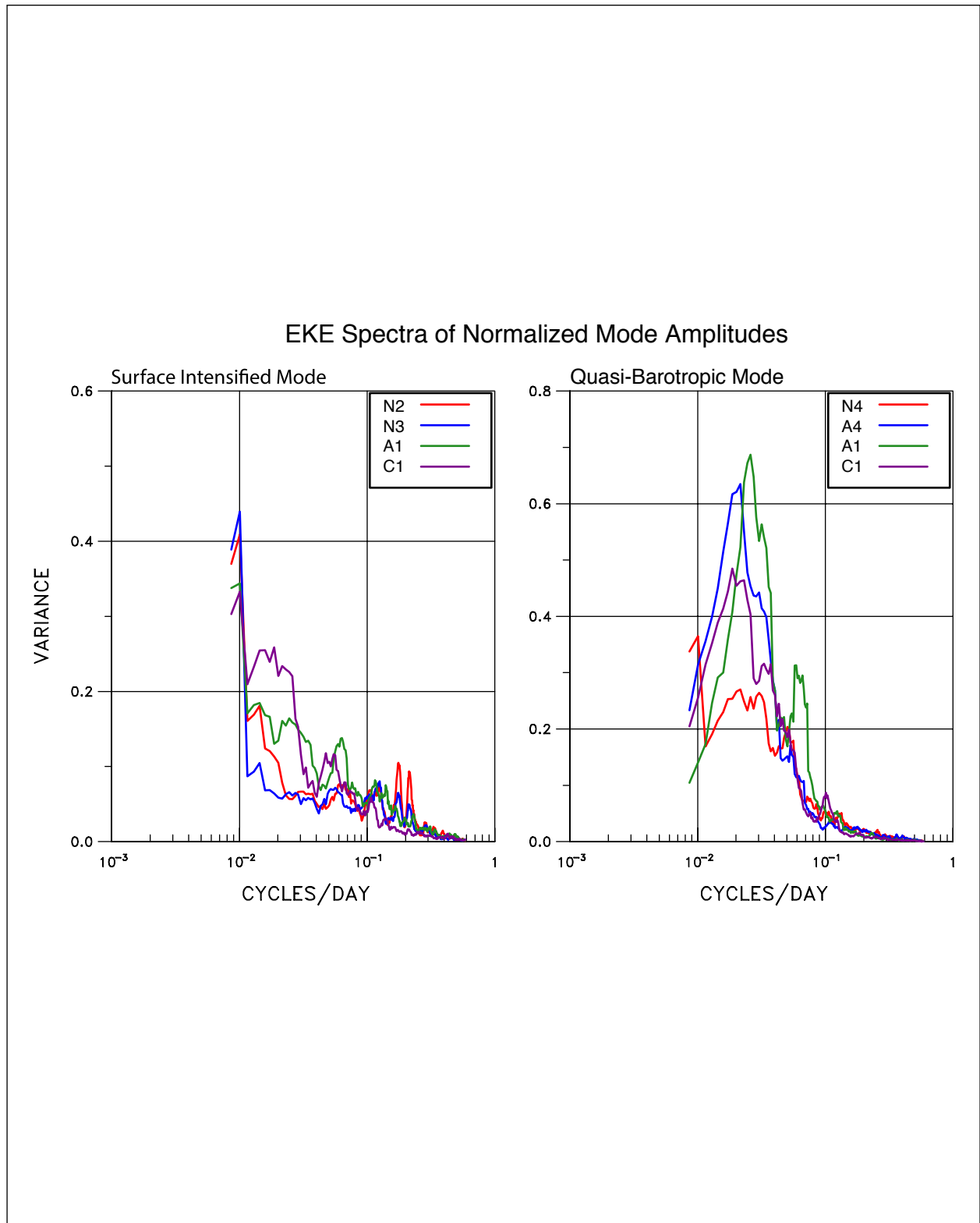


Figure 3.4-6. EKE spectra in variance preserving form of selected normalized mode amplitudes shown in Figure 3.4-5. LH and RH panels are for surface-intensified and quasi-barotropic modes, respectively.

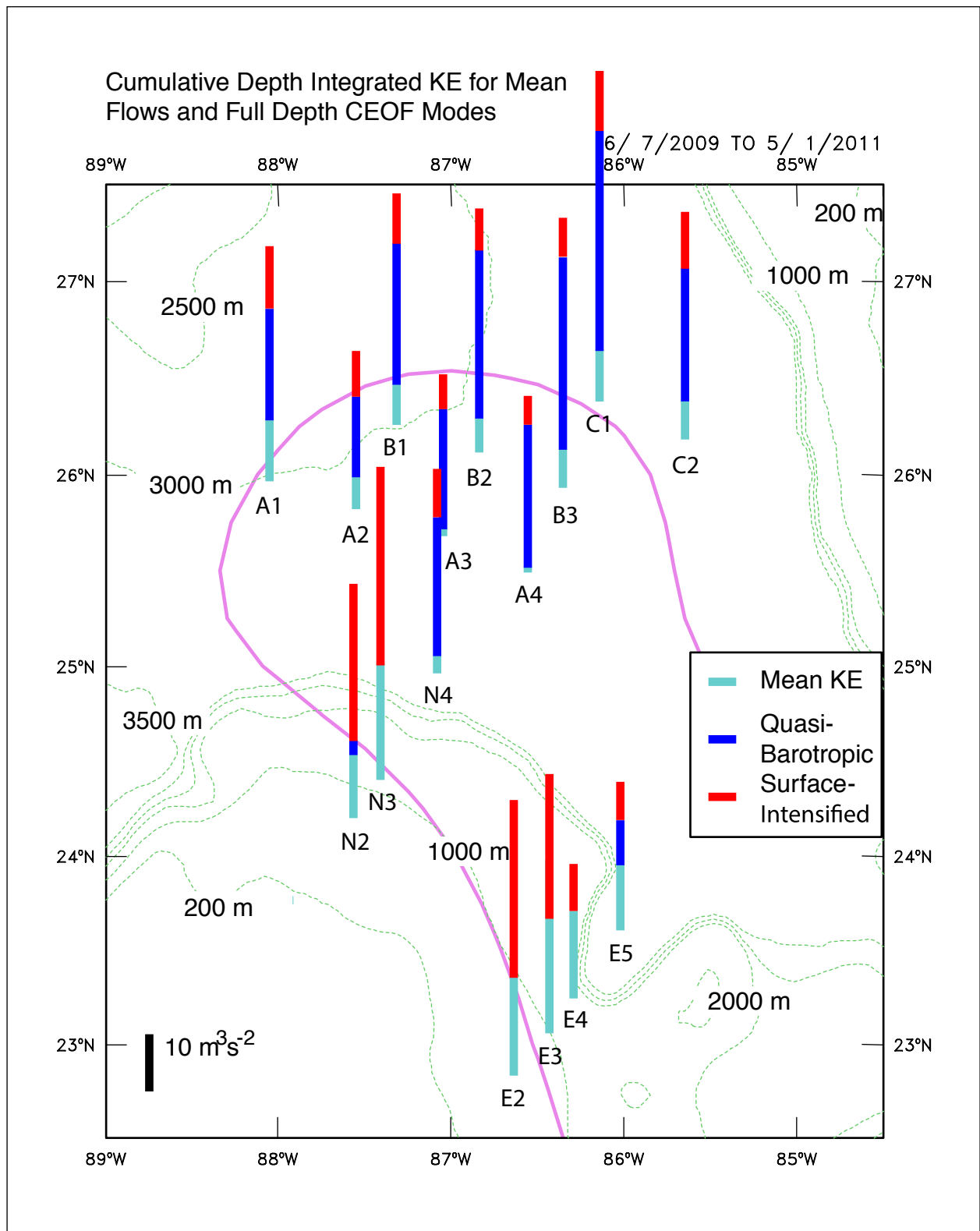


Figure 3.4-7. Cumulative depth-integrated KE for mean flow, and the QB and SI CEOF modes. The height of the bars represents the total KE with color coding showing the division between the three components.

represented by SSH_ref, which is 3000-dbar pressure converted to a height equivalent (pressure divided by gravity and density).

Loop Current meanders are major contributions to variability at periods shorter than 100 days. This section characterizes the statistics of their spatial distribution of energy, frequency, wavenumber, and phase speed.

Figure 3.4-8 shows the near-surface, time-mean velocities and mean EKE over the 30-month duration of the U.S. mapping array. Mean near-surface (200-m depth) currents are anticyclonic with mean speeds near 15 cm s^{-1} , maximum speed near 25 cm s^{-1} . This broad-scale circulation results from the repeated advance and retreat of the LC during LC eddy shedding events. EKE is elevated along a swath centered on the mean LC position. Standard-deviation ellipses are slightly elongated in the along-path direction in the western portion (moorings A1, A2, and A3), and they are mainly isotropic elsewhere. EKE is modulated in time, with levels tending to be low and increase as the LC moves into the array (Figure 3.4-8b). Elevated EKE levels tend to occur during the three LC-eddy-shedding events (Ekman, Franklin, Hadal). Close examination indicates that the peak EKE within each individual LC-eddy-separation event can occur just after (Ekman), during (Franklin) or prior to (Hadal), a separation. This is likely due to the relative positions of the LC and LC eddies within the array, which vary event to event. Multiple time scales of variability are present in the EKE time series. For example, there is high-frequency variability during February to April 2010, in the buildup prior to Franklin formation that is also seen in the individual CEOF vertical modes (Figure 3.4-5). Lower-frequency variability dominates from May through September 2010 during and following Franklin detachment and separation.

Figure 3.4-9 shows the spatial distribution of SSH_bcb variance where standard deviation, with units of cm, is plotted rather than variance. Total SSH_bcb variance is dominated by the LC advance and retreat (Figure 3.4-9a), and this is most evident for periods longer than 100 days. To investigate spatial patterns of higher frequency signals, SSH_bcb is band passed using four frequency bands, 100 to 40 days, 40 to 20 days, 20 to 10 days and 10 to 3 days. The frequency range choices were guided by PIES SSH_bcb spectra (not shown, but are similar to the EKE velocity spectra given in Figure 3.4-6) that have peaks near 60, 30, and 15 days. The spectrum is red: a large fraction, 86% of the total SSH_bcb variance occurs at frequencies greater than 100 days. Within the 100 to 3-day mesoscale band, variance is distributed as follows: 72% within 100 to 40 days, 19% within 40 to 20 days, 7% within 20 to 10 days and 2% within 10 to 3 days.

The spatial patterns of variability change systematically with frequency band, as shown in Figure 3.4-9b-e. As frequency increases, the location of maximum variance transitions from central and eastern portions of the array to the northwest corner. Analysis will show that high-frequency variability, less than 20 days, occurs along the western side of the array and often occurs well in advance of LC eddy shedding. Whether these high-frequency meanders propagate along the full length of the LC may depend on the location of the LC front within the eastern Gulf. Low frequency variability, 40 to 20 days, propagates clockwise along the LC periphery, intensifying either over the Mississippi Fan or in the southeastern portion of the array during LC eddy detachments. The lowest frequency variability, 100 to 40 days, peaks during detachment events, is confined eastward of the Mississippi Fan, and propagates southwards along the LC front.

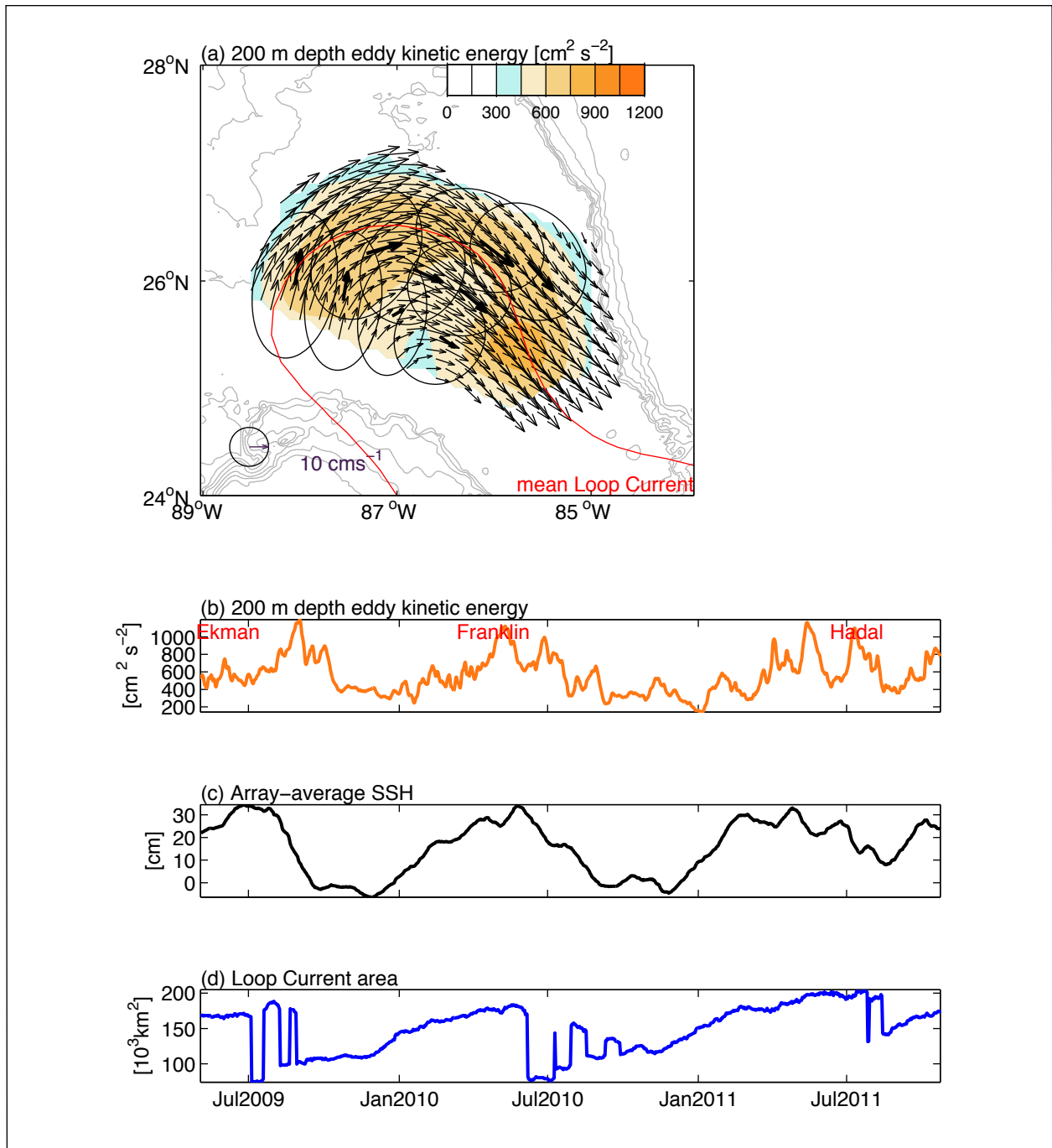


Figure 3.4-8. Upper panel (a): 200-m depth mapped and measured mean current vectors (bold) and standard deviation ellipses superimposed on the time-mean 200-m depth eddy kinetic energy. Red line denotes the mean Loop Current position defined by the CCAR SSH 17-cm contour. Bathymetry plotted with gray contours every 500-m depth. Time mean is taken over the 30-month experiment duration from 3 May 2009 through 23 October 2011. Panel b: Time series of array-averaged 200-m depth eddy kinetic energy. Panel c: Time series of array-average SSH. Panel d: Loop Current area.

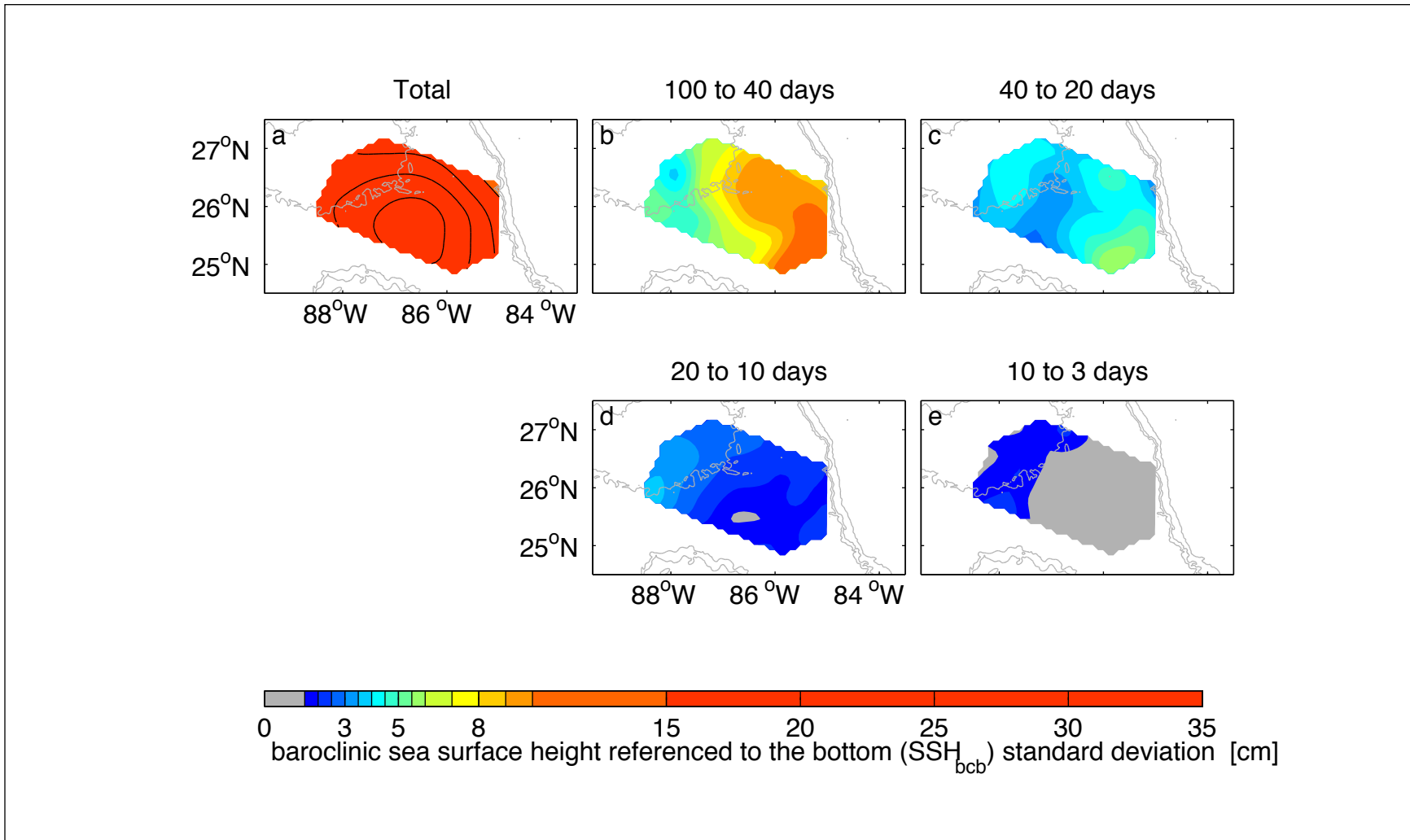


Figure 3.4-9. Standard deviation of baroclinic sea-surface height referenced to the bottom (SSH_{bcb}) as a function of frequency band. Upper left (a): Total variance. Note all mapped values exceed 10 cm; standard deviation is contoured every 5 cm. Maximum (minimum) values are 32 (13) cm. Four right panels (b-e): Standard deviation in four frequency bands noted in the title of each panel. Bathymetry contoured in grey every 500-m depth. Note that the contour interval is not uniform.

(Propagation direction and speed associated with each frequency band is determined by complex empirical orthogonal analysis presented later in this section.)

To illustrate how SSH_bcb variance compares among LC-eddy detachments, Figure 3.4-10 shows the time series of SSH_bcb variance as a function of frequency band. To provide a broader context, the LC-area index (Figure 3.4-10a), indicating times of detachments and reattachments, and the array-mean SSH (Figure 3.4-10b), indicating the presence of the LC within the array, are shown. Clearly, variance is elevated during the LC-eddy events while the LC is within the array, yet levels and sequencing vary among these events. Hadal appears as the strongest, and Ekman as the weakest event. The timing of peak variance within the frequency bands varies between eddies: during Ekman and Franklin, peak variance within each band occurs at successively later times as frequency decreases. Elevated variance in the 20- to 10-day band is a precursor to all three separations. Interestingly, very little variance in the 10- to 3-day band appears prior to Hadal formation. Figure 3.4-10 reinforces that each LC-eddy shedding event is best treated individually, not only because the basin or regional statistics of each LC-eddy shedding event could be different, but also because the array provides a limited spatial window into the mesoscale variability associated with each LC eddy.

Ultimately, Figure 3.4-10 is used to identify time intervals for further diagnoses. CEOFs are calculated during time intervals that capture enhanced levels of SSH_bcb variance. Interest is in the spatial structure of the upper-ocean variability within the mesoscale band with an emphasis on amplitude and phase propagation. Four time intervals are analyzed (gray shaded boxes in the lower four panels of Figure 3.4-10). We label these time intervals Ekman, Franklin, Hadal and Icarus in the following CEOF case studies. In addition, CEOFs are calculated in a broader region using the CCAR SSH altimeter data band-passed between 100 and 40 days. The CCAR SSH analysis is restricted to the lowest frequency band because for periods 40 days and shorter, the altimeter sampling leads to spatial and temporal aliasing.

Figure 3.4-11 shows the weekly and time-mean position of the LC front during the four time intervals. The CCAR SSH analysis provides a basin context for the mesoscale variability. CEOF results are shown in Figures 3.4-12 through 3.4-15. The second mode of each CEOF is shown only if it explains 30% or more of the total variance with the band. For each individual LC-eddy event labeled above, results for the four frequency bands will be discussed. Because in each event the high-frequency variance builds up first (as was shown above), followed by progressively lower-frequency variance, the CEOF discussions will also proceed from high to low frequency. Following that, all the CEOF phase information will be summarized together to examine wavenumbers and phase speeds and relate them to previous studies in the Gulf Stream.

Ekman CEOFs

The highest frequency band (10 to 3 days) spatial pattern has its highest amplitudes along the western and northern portions of the study area. Mode-1, accounting for 70% of the variance in this band, shows phase propagation to the northwest turning in an anticyclonic sense. The mode spatial amplitude (left column) remains high to approximately 86.5°W, beyond which it decreases rapidly (Figure 3.4-12b). The temporal amplitude peaks in May, about a month before the first Ekman separation and earlier than the other frequency bands.

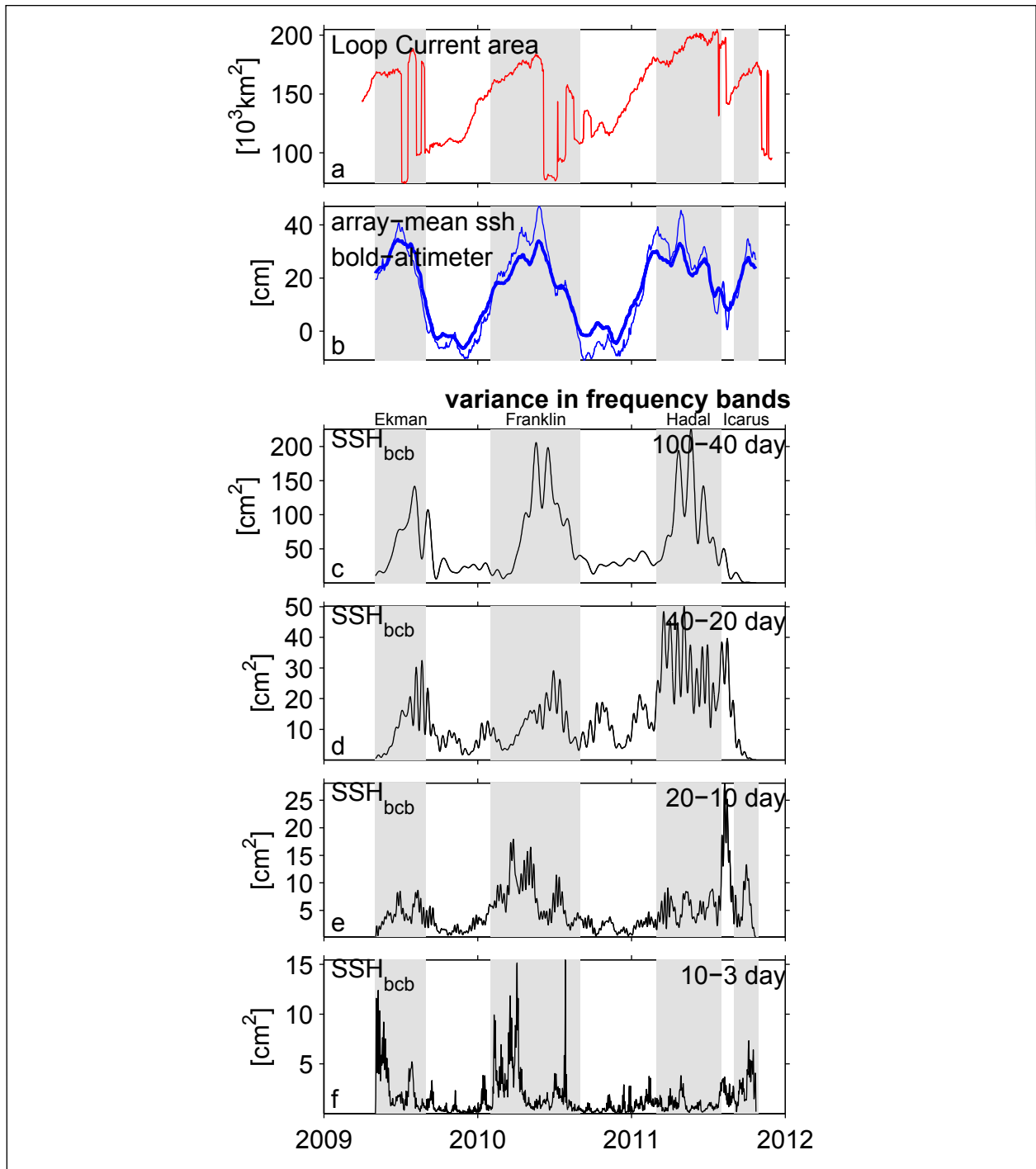


Figure 3.4-10. (a) Loop Current area. (b) Array mean baroclinic sea-surface height referenced to the bottom, SSH_bcb (CCAR sea-surface height in bold). The mean of the baroclinic sea-surface height referenced to the bottom has been adjusted to match the CCAR sea-surface height. (c - f) Variance of array-averaged baroclinic sea-surface height referenced to the bottom, SSH_bcb. Frequency band noted in the title of each panel. Gray filled boxes in panels c through d correspond to the time period over which complex empirical orthogonal functions have been calculated.

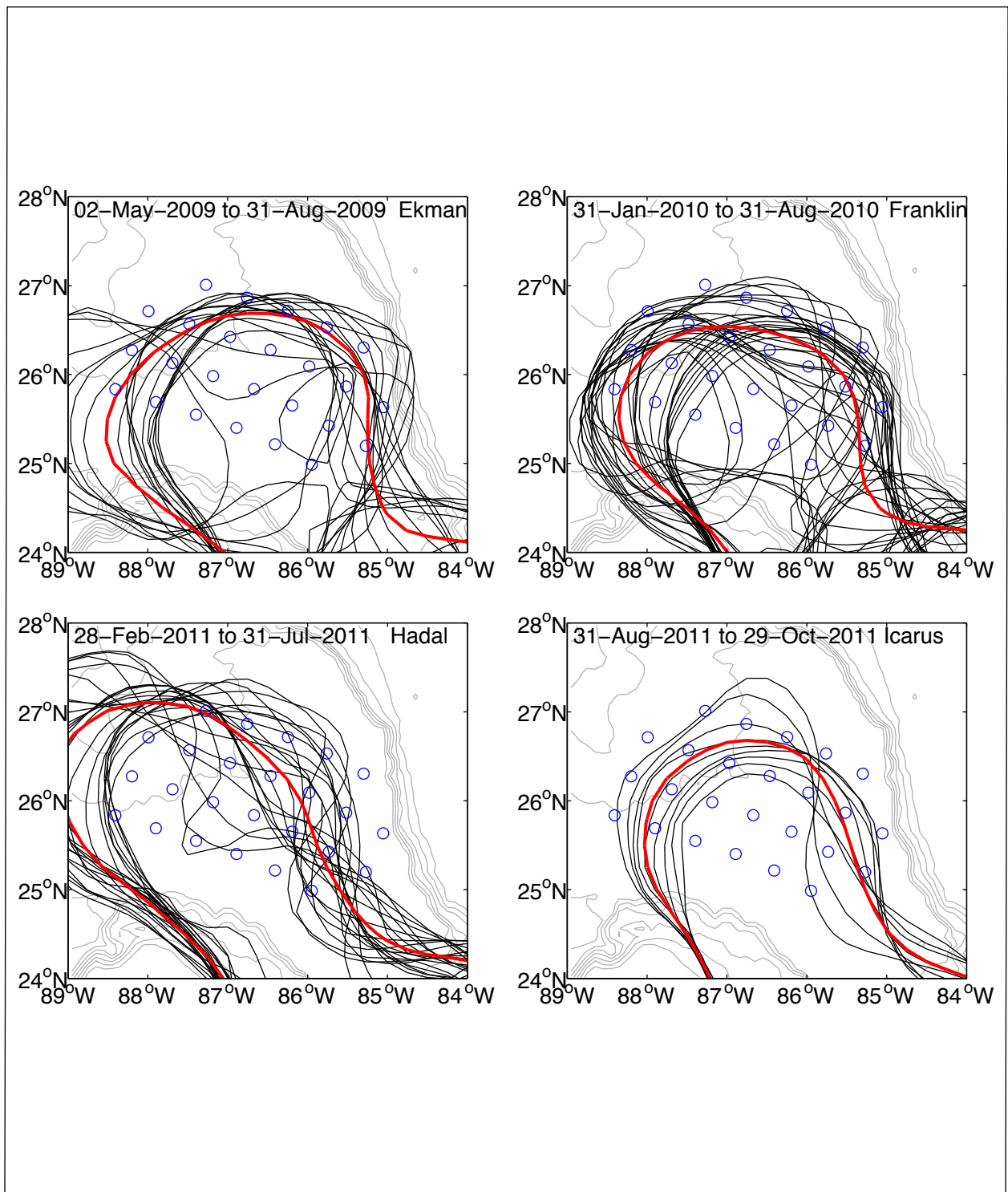


Figure 3.4-11. CCAR SSH determined Loop Current positions during CEOF time periods. For each panel, the position of the 17-cm contour is plotted every seven days during the interval noted in the upper edge of the plot. Location of the PIES represented by open blue circles. The mean Loop Current position is shown by the bold red line. Bathymetry interval is 500 meters.

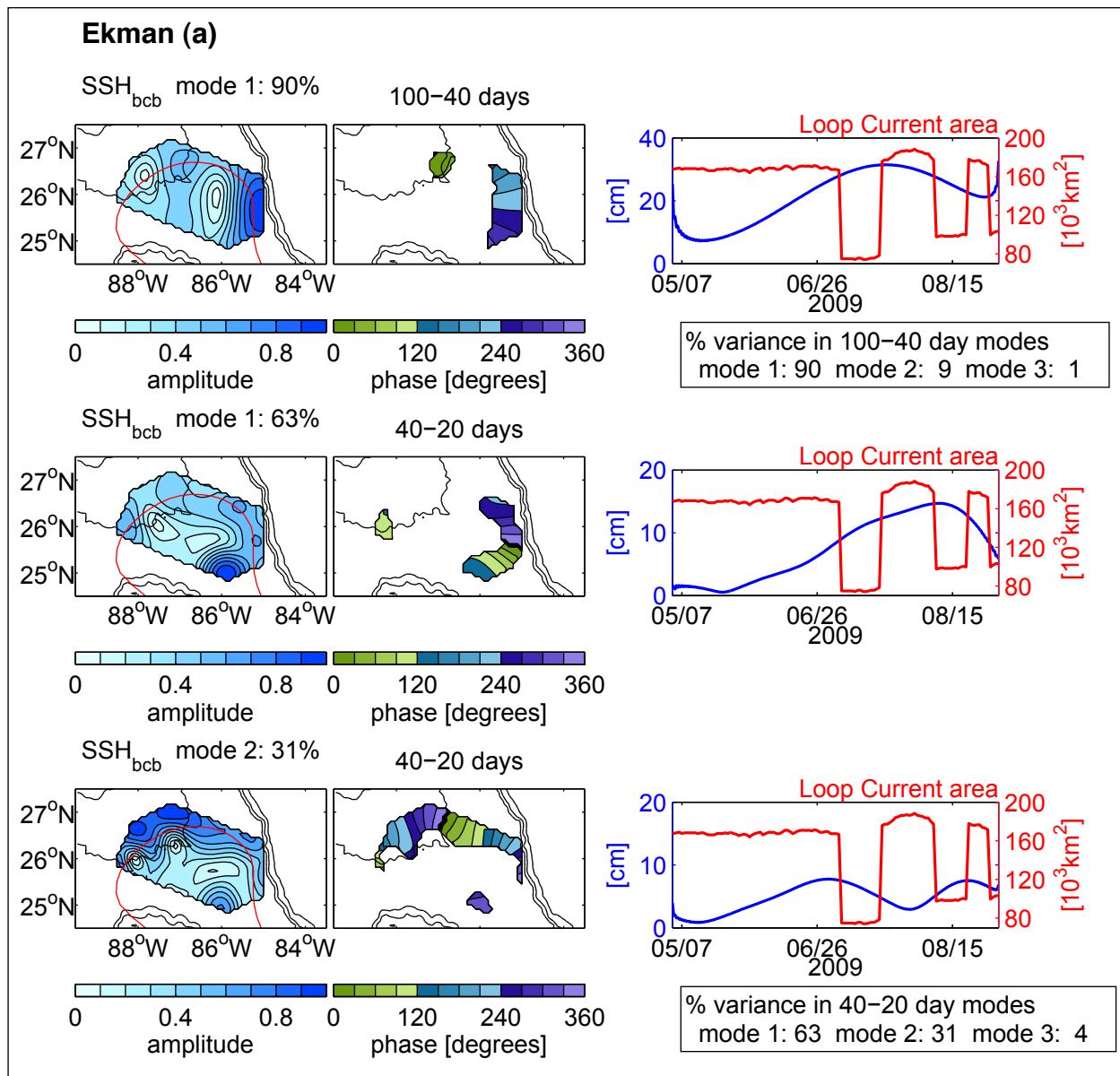


Figure 3.4-12a. CEOfs determined from band-passed baroclinic sea-surface height referenced to the bottom, SSH_{bcb}, during the Ekman time period. Two frequency bands are shown: 100 to 40 days (Mode 1), and 40 to 20 days (Modes 1 and 2). For each CEOf, the left panel shows normalized spatial amplitude, the middle panel shows phase in degrees, and the right panel shows amplitude time series in cm. In the left panel, the mode number and percent explained by the mode is noted in the title. In addition to the mode time series (blue), the mean position of the Loop Current (17-cm contour) during the time interval of the CEOf is represented by the red line. In the middle panel, the phase is plotted for regions where the spatial amplitude exceeds 0.5. Propagation is in the direction of increasing phase. Bathymetry is contoured every 1000 m depth. In the right panel, the mode time series is blue; Loop Current area is red.

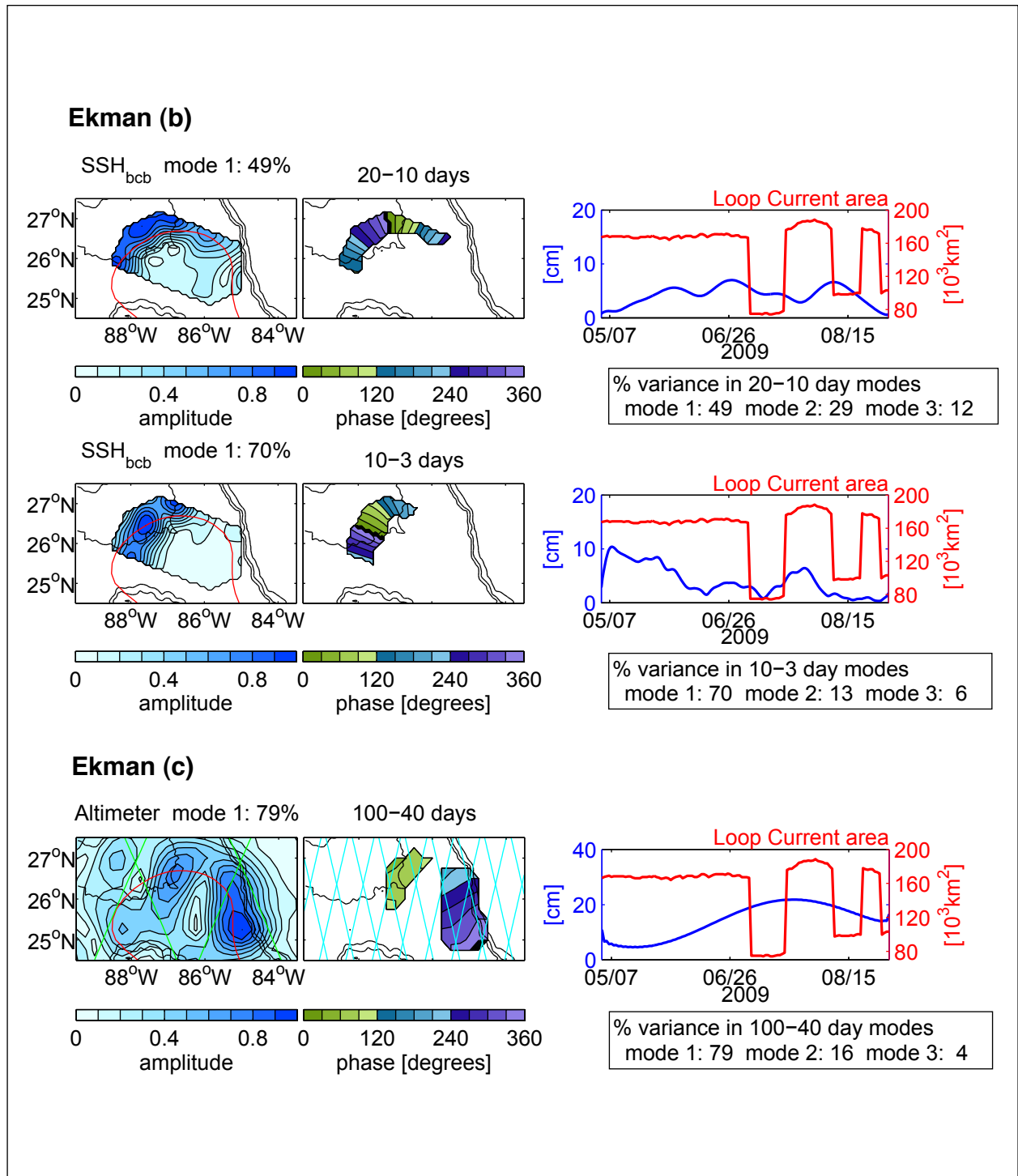


Figure 3.4-12b-c. (b) CEOFs determined from band-passed baroclinic sea-surface height referenced to the bottom, SSH_{bcb} during the Ekman time period. Two frequency bands are shown in the upper panels: 20 to 10 days (Mode 1) and 10 to 3 days (Mode 1). (c) CEOFs determined from 100 to 40 day band-passed CCAR sea-surface height (cm) during the Ekman time period using the same conventions as in Figure 3.4-12a with Envisat ground tracks plotted with cyan lines.

The low-frequency CEOF mode for the 100- to 40-day band accounts for 90% of the variance. It reaches peak amplitude during Ekman's first detachment (Figure 3.4-12a). Highest amplitudes are found along the eastern side of the array with approximately due-south propagation along the LC.

The comparison between the Ekman PIES and CCAR-SSH CEOFs (Figure 3.4-12c) is excellent in the 100- to 40-day band. Both show the same spatial pattern, phase propagation and timing although the CCAR-SSH phase propagation appears slightly faster.

Franklin CEOFs

Franklin CEOFs (Figures 3.4-13a,b) share several characteristics of the Ekman CEOFs and again the LC mean path is well contained by the array during this event. Within the two high-frequency bands (<20 days), mode amplitudes are high only along the northwest portion of the array, and phase propagation is anticyclonic (downstream). Their temporal amplitudes grow to a peak prior to detachment.

Within the 40- to 20-day band, the spatial amplitude is largest near the Mississippi Fan, propagation is anticyclonic along the LC, and amplitudes peak during Franklin's first detachment. This mode resembles the sum of modes 1 and 2 for Ekman CEOFs in the 40- to 20-day band, and the phase propagation is downstream along the LC. Relative to eddy detachments, the temporal amplitude builds and peaks with very similar timing to Ekman CEOFs.

Within the 100- to 40-day band, the spatial amplitude is largest along the eastern side of the LC, propagating south during Franklin's first detachment. The CCAR-SSH 100- to 40-day CEOF (Figure 3.4-13c) demonstrates, for this larger region, that meanders in this frequency band are confined east of the Mississippi fan along the southward-flowing portion of the LC.

Hadal CEOFs

During the Hadal time interval, the mean position of the LC differs from the Ekman and Franklin time intervals. It is further west, and the array captures only the eastern side of the LC (Figure 3.4-11). The CEOF spatial amplitudes are generally highest along this encompassed portion of the LC. The mode-1 CEOFs for all four frequency-bands propagate downstream along the LC (southeastward and southward) (Figures 3.4-14a,b). An interesting exception is the meander mode in the 10- to 3-day band (Figure 3.4-14b), which only partially follows the full length of the mean LC and then turn eastwards near 26°N to encounter the Florida shelf break. The CCAR-SSH CEOFs (Figure 3.4-14c) in the 100- to 40-day band are remarkably similar to the PIES. Like the Ekman and Franklin case studies, they indicate that the 100- to 40-day meanders are mainly located east of the Mississippi Fan.

Icarus CEOFs

The LC mean position during the Icarus time interval resembles the Ekman and Franklin time intervals. During short interval of the formation of Icarus, variability for periods longer than 20 days is weak. Consequently CEOF modes are shown only for periods < 20 days (Figures 3.4-15). Again, the highest frequency band (10 to 3 days) mode is strongest along the western side of the array, decaying in amplitude as the mode propagates clockwise along the LC. The 20- to

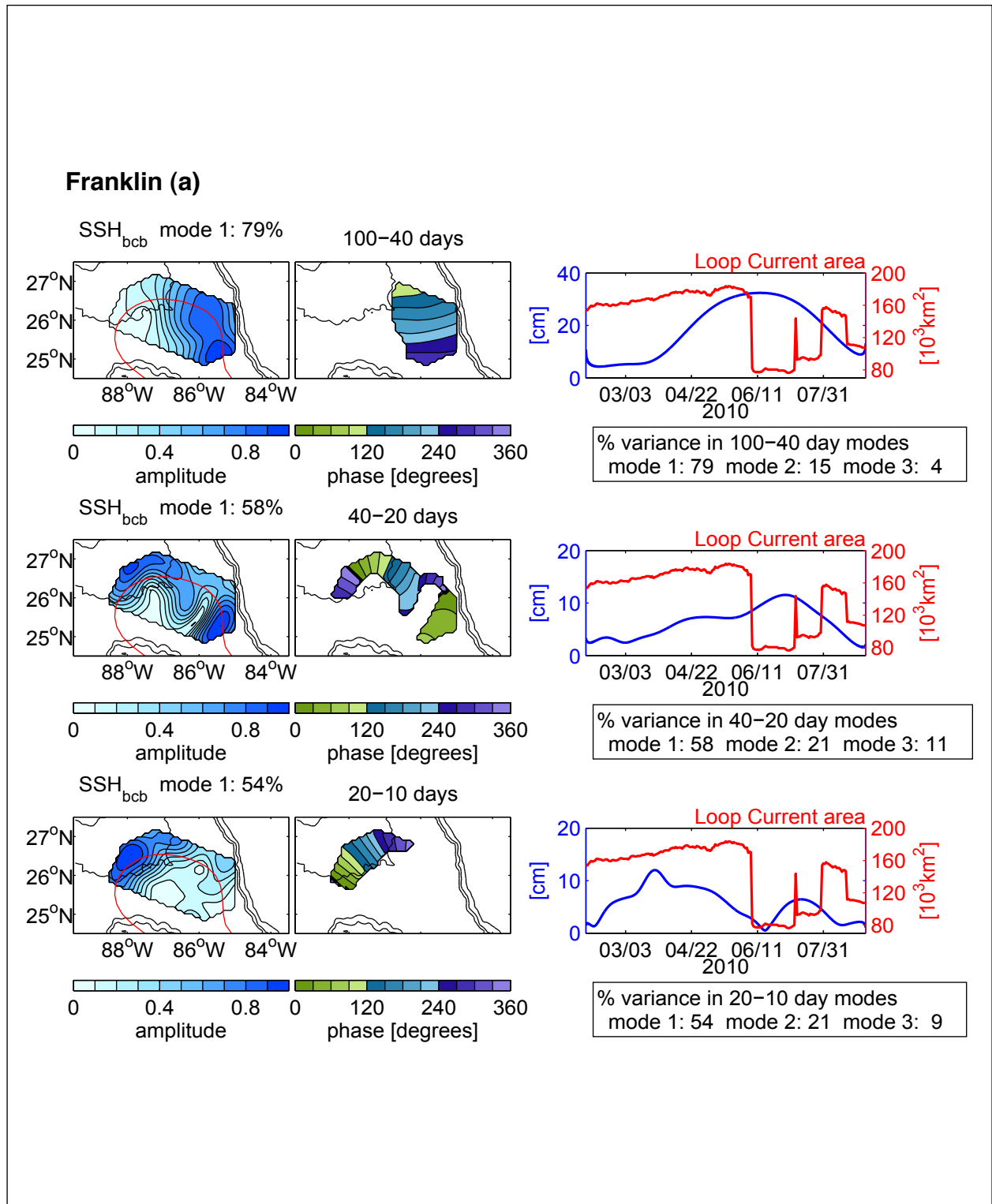


Figure 3.4-13a. CEOfs determined from band-passed baroclinic sea-surface height referenced to the bottom, SSH_{bcb}, during the Franklin time period. Three frequency bands are shown, 100 to 40 days, 40 to 20 days, and 20 to 10 days. Conventions same as in Figure 3.4-12a.

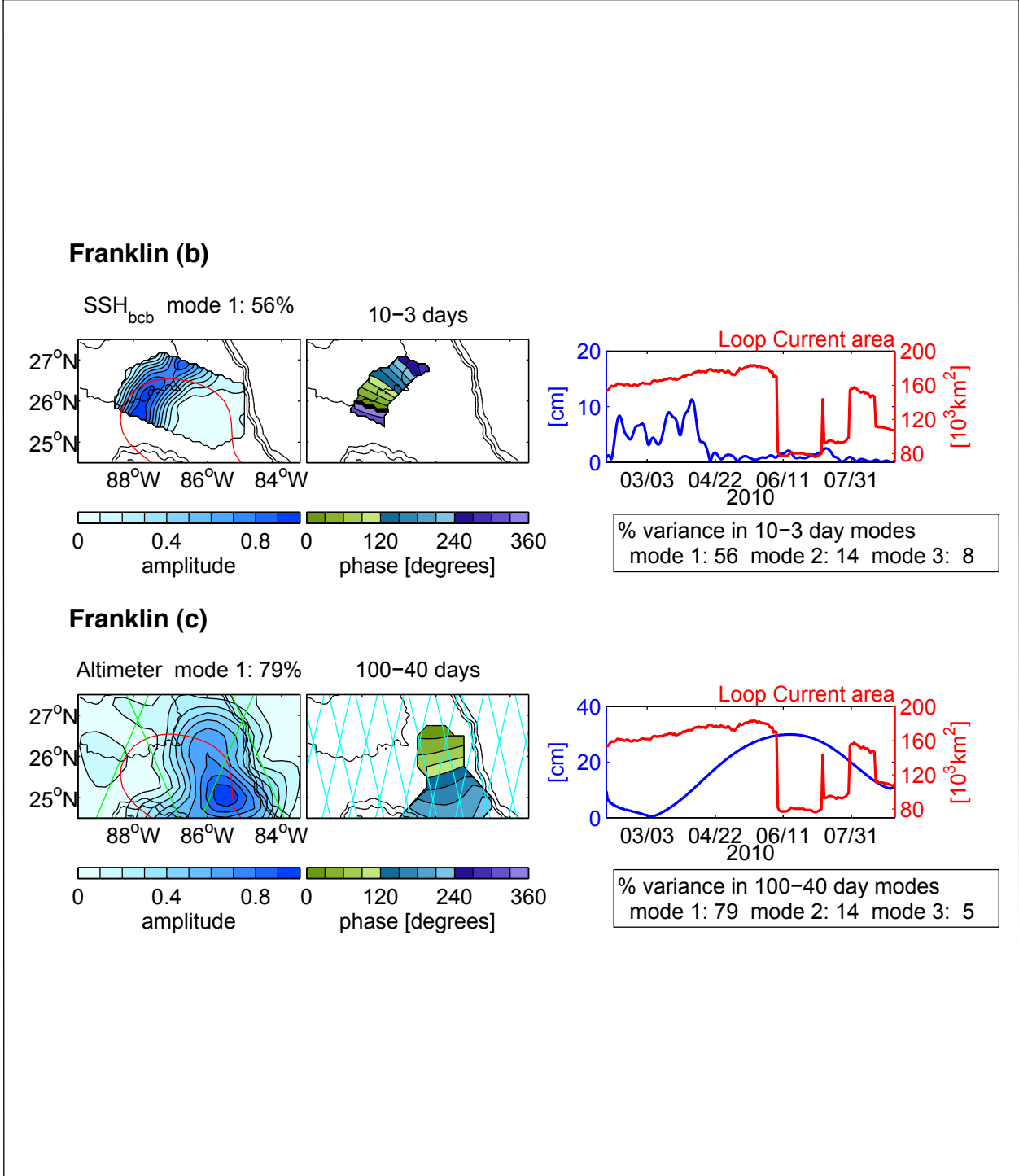


Figure 3.4-13b-c. (b) CEOFs determined from band-passed baroclinic sea-surface height referenced to the bottom, SSH_{bc} during the Franklin time period. One frequency band is shown in the upper panel: 10 to 3 days (Mode 1). (c) CEOFs determined from 100 to 40 day band-passed CCAR sea-surface height (cm) during the Franklin time period using the same conventions as in Figure 3-4-12a with Envisat ground tracks plotted with cyan lines.

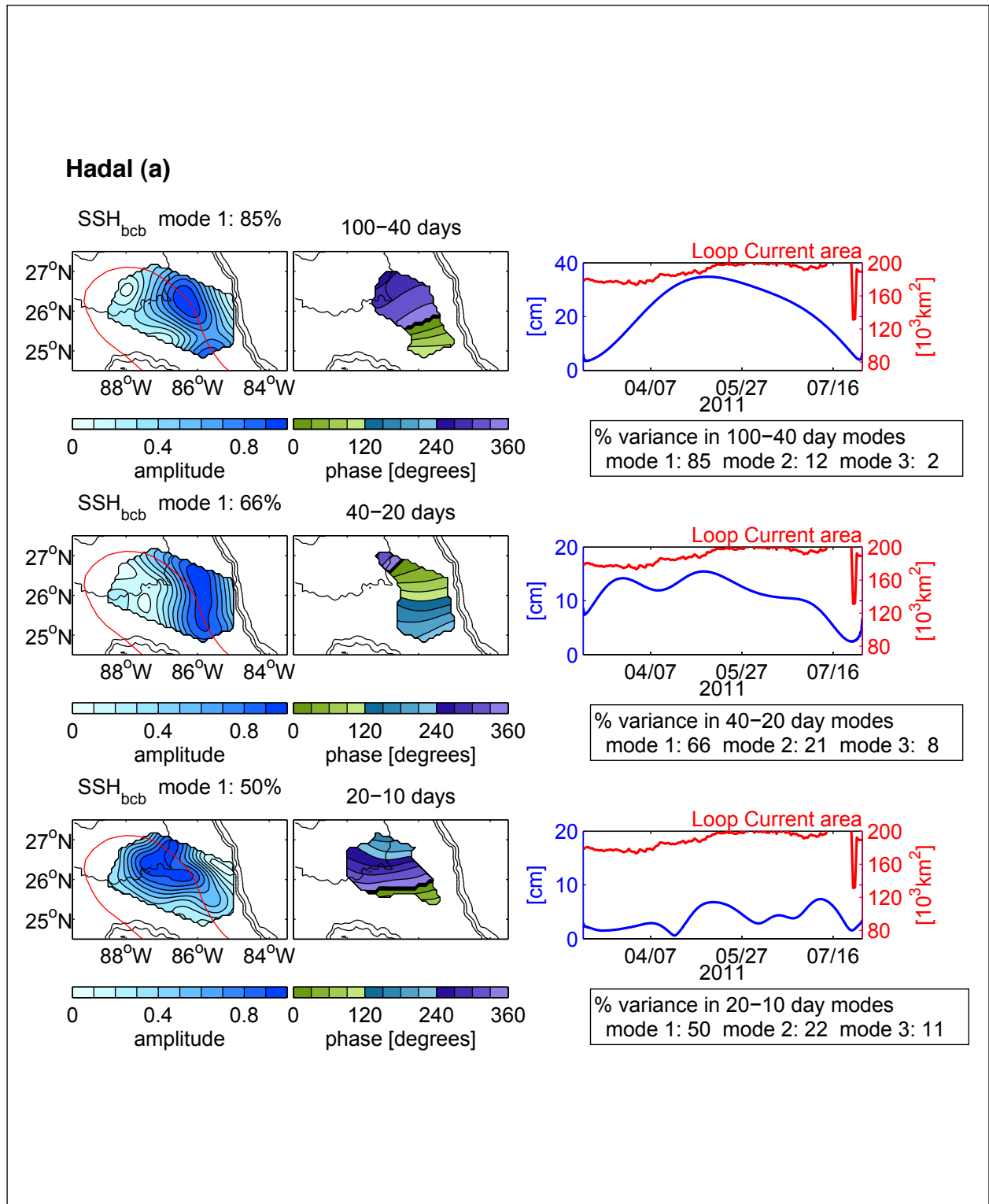


Figure 3.4-14a. CEOFs determined from band-passed baroclinic sea-surface height referenced to the bottom, SSH_{bcb}, during the Hadal time period. Three frequency bands are shown, 100 to 40 days, 40 to 20 days, and 20 to 10 days. Conventions same as in Figure 3.4-12a.

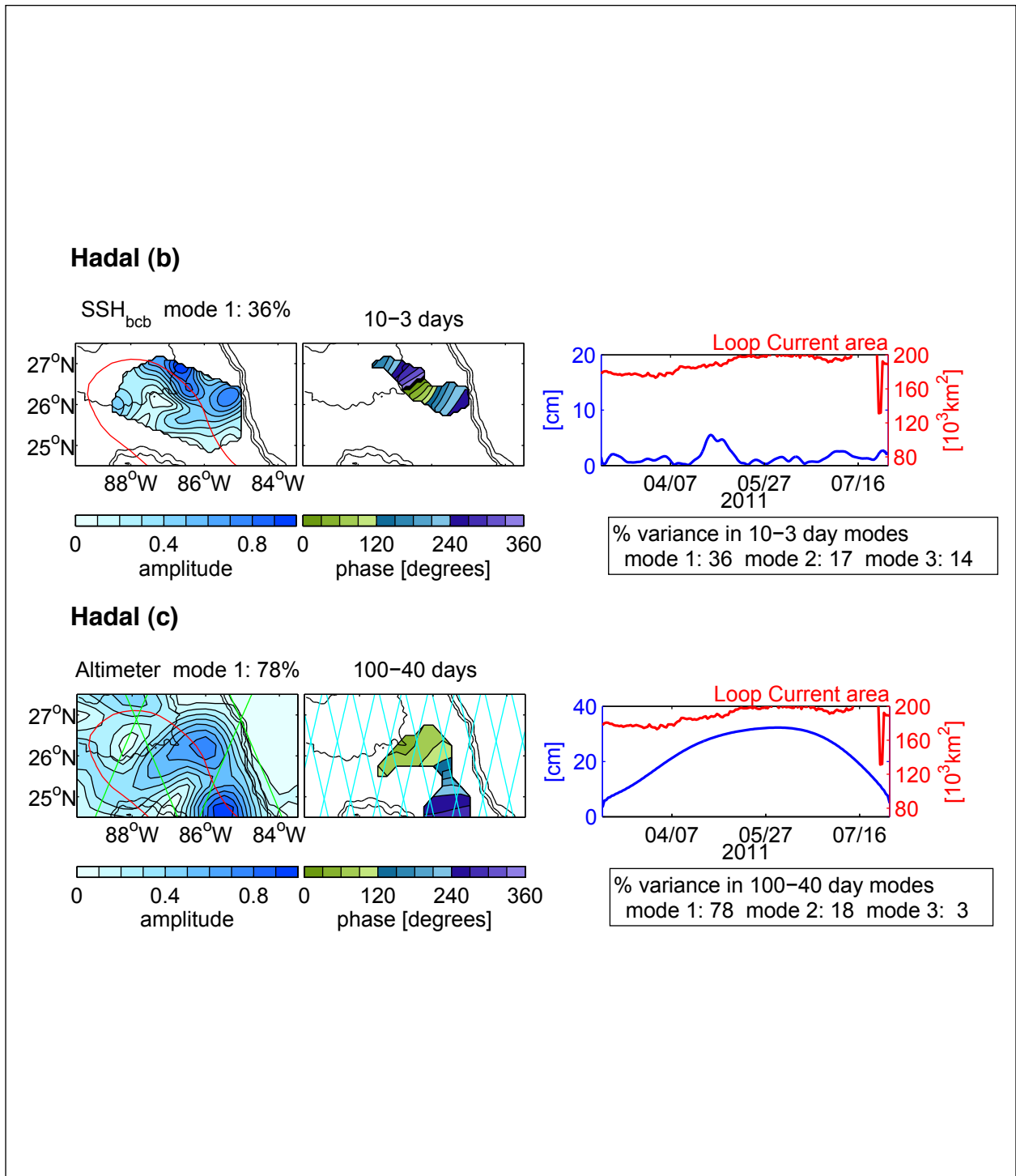


Figure 3.4-14b-c. (b) CEOFs determined from band-passed baroclinic sea-surface height referenced to the bottom, SSH_{bcb} during the Hadal time period. One frequency band is shown in the upper panel: 10 to 3 days (Mode 1). (c) CEOFs determined from 100 to 40 day band-passed CCAR sea-surface height (cm) during the Hadal time period using the same conventions as in Figure 3.4-12a with Envisat ground tracks plotted with cyan lines.

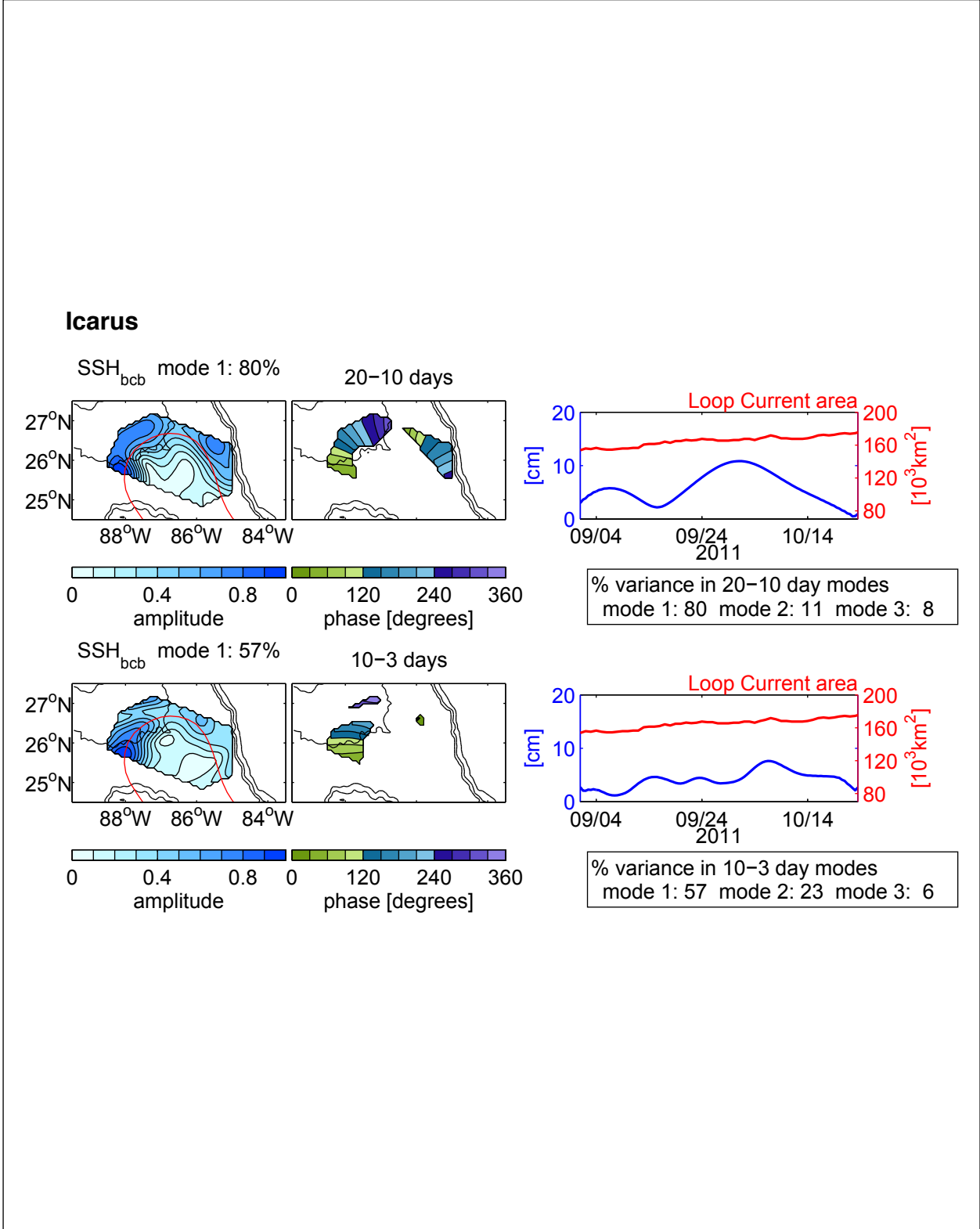


Figure 3.4-15. CEOFs determined from band-passed baroclinic sea-surface height referenced to the bottom, SSH_{bcb}, during the Icarus time period. Two frequency bands are shown, 20 to 10 days, and 10 to 3 days. Conventions same as in Figure 3.4-12a.

10-day mode has a swath of elevated amplitude along the LC propagating anti-cyclonically. It has a slight minimum just downstream of the Mississippi Fan, and branches off to the east rather than accompany the LC southward.

CEOF Spatio-Temporal Summary

The strongest variability is in the 100- to 40-day band. The peak amplitudes coincide temporally with and persist for a cycle or two after eddy detachment and separation. Spatially these 100- to 40-day modes are restricted to east of the Mississippi Fan, growing and propagating downstream along the eastern portion of the LC. There is excellent agreement between PIES-mapped and CCAR-SSH regarding the 10- to 40-day CEOF spatio-temporal structure. The CCAR-SSH amplitudes are slightly weaker and their wavelengths (and hence phase speeds) are slightly larger.

Meanders between 40 and 20 days propagate along the full, encompassed length of the LC. Their temporal amplitudes peak at the time of eddy detachment and separation. Meanders with shorter periods than 20 days grow in amplitude during the one or two month interval preceding eddy detachment. Judging from the difference in spatial amplitudes among the above cases, it is speculated that their ability to propagate along the full length of the LC may depend on the location of the LC. If the Loop Current is positioned to the east, flowing close to the Florida Shelf, then these short period (20 to 10, and 10 to 3 day) waves do not propagate southward along the eastern edge of the LC. But when the LC forms slightly farther to the west, the 20-10 day meanders can follow its entire mean path.

The highest frequency bands (20 to 10 day, and 10 to 3 day) CEOFs suggest several interesting scientific questions. Why don't the high frequency meanders (< 20 days) propagate along the entire length of the LC? Do they slow down as they approach the northern tip of the LC? Do they undergo a non-linear eddy rectification process? Do the high frequency meanders feed the downstream growth of lower frequency meanders, which peak later during the eddy detachment and separation process?

CEOF Phases – Meander Wavenumbers and Phase Speeds

Figure 3.4-16 and Table 3.4-2 show the wavenumber and phase speed estimates from the CEOF analysis. Wavenumber is determined by calculating the amplitude of the spatial phase gradient ($\delta\phi/\delta s$, where ϕ is phase and s is distance). For each CEOF, the spatial phase gradient is calculated for regions where the corresponding spatial amplitude is greater than 0.5. Phase speed is determined by $2\pi\omega$ ($\delta s/\delta\phi$) where ω is the central frequency of the band-passed frequency. The wavenumber-speed dispersion relationship for Loop Current meanders agrees particularly well at wavelengths longer than 300 km with that for Gulf Stream (GS) meanders in the region northeast of Cape Hatteras (Kontoyiannis and Watts 1994; Lee and Cornillon 1996). The short-period (10 to 3 day) LC meanders have somewhat longer wavelengths and higher phase speeds than their counterparts in the GS. In both regions, the dispersion relation resembles a parabolic shape, $c = Ak^2 - B$, as is consistent with a simple 1/2 layer analytical thin-jet prediction by Cushman-Rosin et al. (1993). The constant B is similar for the LC and GS cases, governed mainly by the beta effect. The constant A for the LC appears to be somewhat larger than for the GS, and this would be consistent with the lower latitude and smaller cross-stream change in

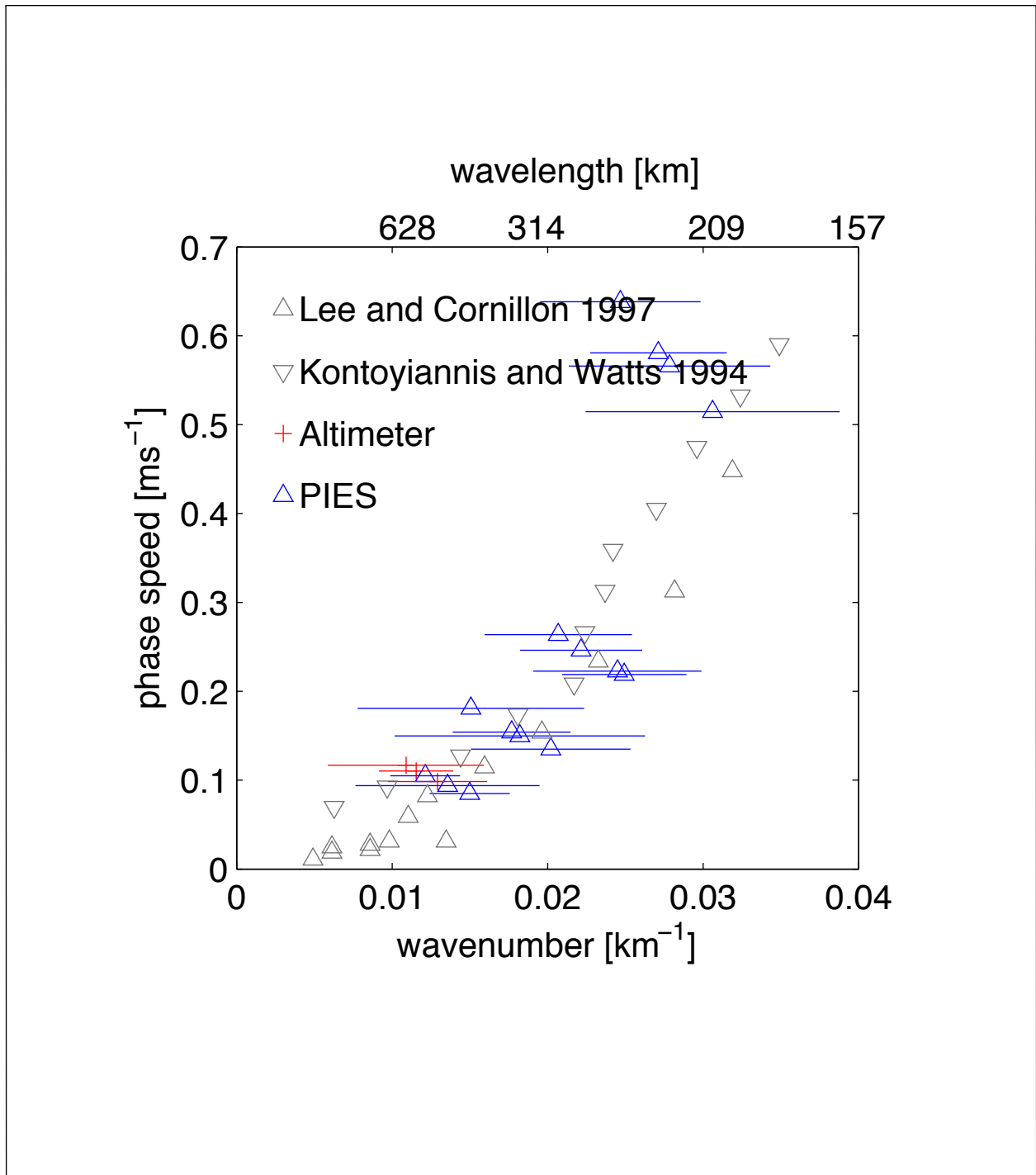


Figure 3.4-16. Wavenumber (km^{-1}) versus phase speed (ms^{-1}). Values are determined from the phase information in the CEOFS (Figures 3.4-12 through 3.4-15). Wavelengths are noted along the upper edge of the plot. PIES mapped SSH_bcb estimates (CCAR sea-surface height) shown by blue triangles (red plusses). Horizontal lines indicate standard deviation. Estimates from Lee and Cornillon (1996) and Kontoyiannis and Watts (1994) for the Gulf Stream (gray triangles) are also included.

thermocline depth in the LC than in the GS. Altimeter estimates produce slightly longer wavelengths and correspondingly faster phase speeds than from the PIES maps.

Table 3.4-2. Average Propagation Speeds Determined from the CEOF Analysis

Period (days)	Wavenumber (rad km ⁻¹)	Wavelength (km)	Phase Speed (km day ⁻¹)
57.14 PIES	0.0121	518	9.1
	0.0150	419	7.3
	0.0136	463	8.1
57.14 CCAR-ALT	0.0115	544	9.5
	0.0129	486	8.5
	0.0109	576	10.1
26.67	0.0182	345	12.9
	0.0151	417	15.6
	0.0177	355	13.3
	0.0202	311	11.7
13.33	0.0245	257	19.2
	0.0249	252	18.9
	0.0222	284	21.3
	0.0207	304	22.8
4.62	0.0278	226	48.9
	0.0271	232	50.2
	0.0306	205	44.5
	0.0247	255	55.2

3.4.4 Horizontal Variability in the Lower Layer

In contrast to the broad anticyclonic mean flow observed in the upper ocean, the mean deep circulation exhibits more structure (Figure 3.4-17). Along the western side of the array, an anticyclonic gyre with ~200 km lateral extent is centered near B1 (26.3°N, 87.3°W) with mean speeds near 6 cm s⁻¹. To the east, a weaker cyclonic gyre, speeds near 3 cm s⁻¹, is centered near C2 (26.2°N, 85.7°W). These gyres were discussed in Section 3.4.1 using means from the lower-layer current meters. Along the southern boundary of the array, mean flow is to the northwest. Standard deviation ellipses are mainly isotropic with a tendency for more elongated ellipses along the West Florida Shelf (D2: 26.4°N, 87.9°W).

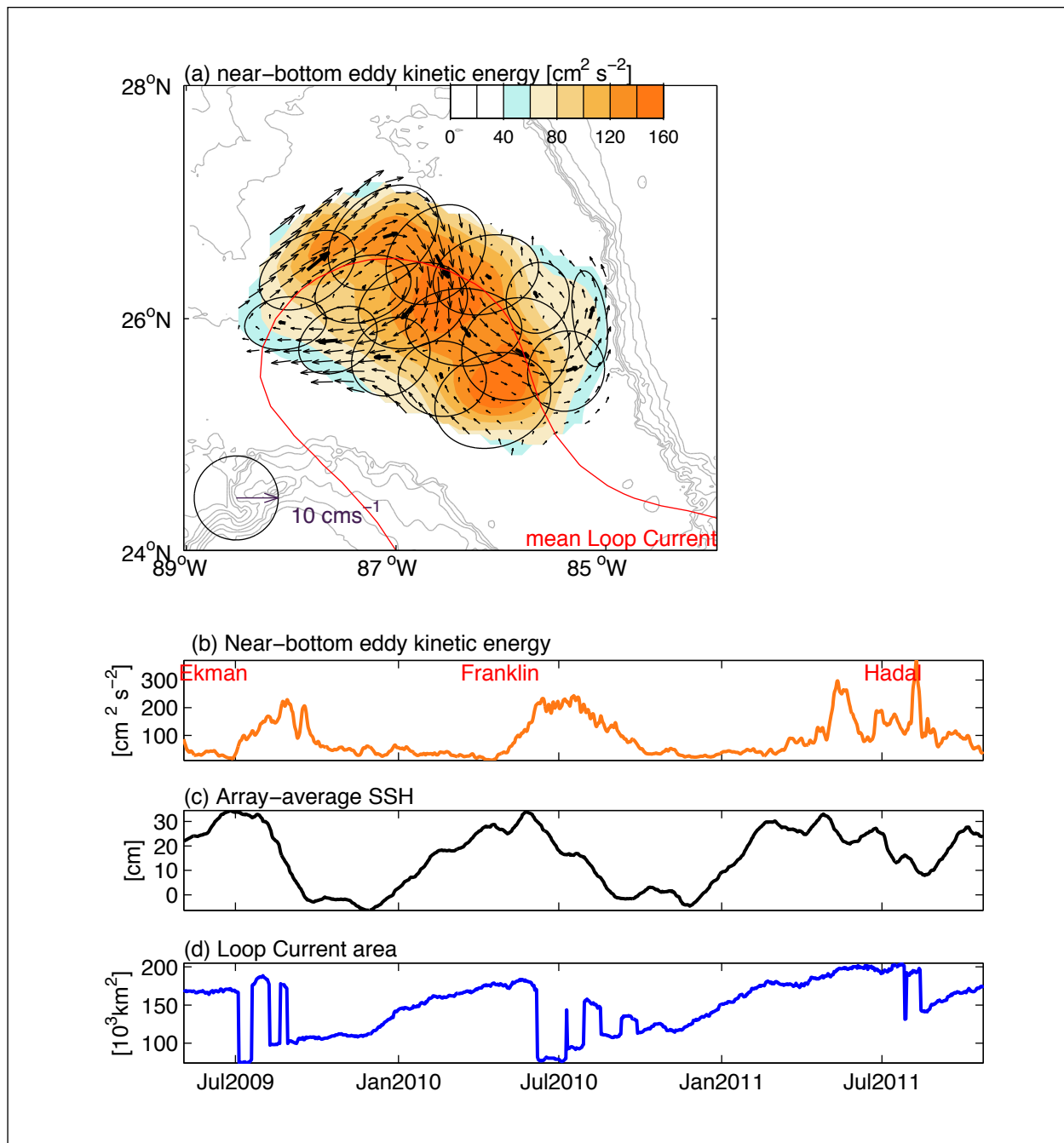


Figure 3.4-17. (a) Near-bottom mapped and directly-measured mean currents (thin and bold vectors, respectively). Standard-deviation ellipses superimposed on the time-mean near-bottom eddy kinetic energy (color-bar). Scale for vectors and ellipses shown in lower left corner. Red line denotes the mean Loop Current position defined by the CCAR SSH 17-cm contour. Bathymetry plotted with gray contours every 500-m depth. Time mean is taken over the 30-month experiment duration from 3 May 2009 through 23 October 2011. (b) Time series of array-averaged near-bottom eddy kinetic energy. (c) Time series of array-average CCAR SSH. (d) Loop Current area.

Elevated time-mean EKE is found beneath the mean position of the LC (Figure 3.4-17). This swath of high EKE can be traced from the Mississippi Fan, where it is offset slightly to the north of the mean LC position, across the array to the southeast where the EKE maxima lies slightly westward of the LC. Highest-mean EKE values occur in the central portion of the array (26.2°N, 86.5°W) and the southeast corner (25.3°N, 86.0°W). Array-averaged EKE also shows the influence of the LC. Values are enhanced during LC-eddy-shedding events (Figure 3.4-17). During Ekman, Franklin, and Hadal peak EKE occurs at or near the first eddy detachment. An additional EKE peak occurs in June 2011 – during this time, the LC necks down but does not form a LC eddy.

In contrast to the upper ocean, there is proportionally more energy in the high-frequency bands (Figure 3.4-18): 72 % of the variance is in periods shorter than 100 days. Within the 100- to 3-day mesoscale band, variance is distributed as follows: 57% within 100 to 40 day, 24% within 40 to 25 day, 12% within 25 to 16 day and 7% within 16 to 3 day. By casting the upper and deep circulation in terms of sea surface height, one can compare the relative contributions of upper and deep variance to total sea surface height. Deep, SSH_ref, variance is only 2% of the upper SSH_bcb variance. This proportionality increases slightly to 10% for periods shorter than 100 days. However, the CEOF depth analysis of the velocities in Section 3.4.2 indicates that the lower water column below ~ 1000 m may have higher total depth-integrated EKE because of the greater thickness of the lower water column and the lack of depth variability of the currents.

Similar to the upper ocean, the spatial structure of the variance changes as a function of frequency band (Figure 3.4-18). Within the highest frequency band, 16 to 3 days, elevated values occur along the base of the Mississippi Fan in the northwest portion of the array. As frequency decreases, this ridge of high variance shifts to the southeast within the array. In the lowest frequency band, 100 to 40 days, the spatial pattern resembles the time-mean EKE (Figure 3.4-17).

Figure 3.4-19 shows the time series of SSH_ref variance as a function of frequency band. Similar to the array-average EKE shown in Figure 3.4-17, variance is also elevated during LC eddy events within each band. During each LC eddy event, peak variance tends to occur at successively later times as the frequency band increases. This contrasts the upper ocean where high-frequency variability preceded low-frequency variability. Because the juxtaposition of the LC, LC eddies, and the array, dictate the timing of observed elevated deep energy, a case-based CEOF analysis was performed. The focus of the CEOF analysis is on three time intervals that span the peaks in the four frequency bands that are designated, Ekman_deep, Franklin_deep and Hadal_deep to distinguish them from the time intervals used in the LC meander results. Loop current positions during these time intervals are shown in Figures 3.4-20, 3.4-21, and 3.4-22. Corresponding CEOF results are shown in Figures 3.4-23, 3.4-24 and 3.4-25, respectively. Ekman_deep and Franklin_deep CEOF case studies are remarkably similar in their spatial structure, phase speeds and propagation as well as timing relative to LC eddy detachments (Figures 3.4-23 and 3.4-24).

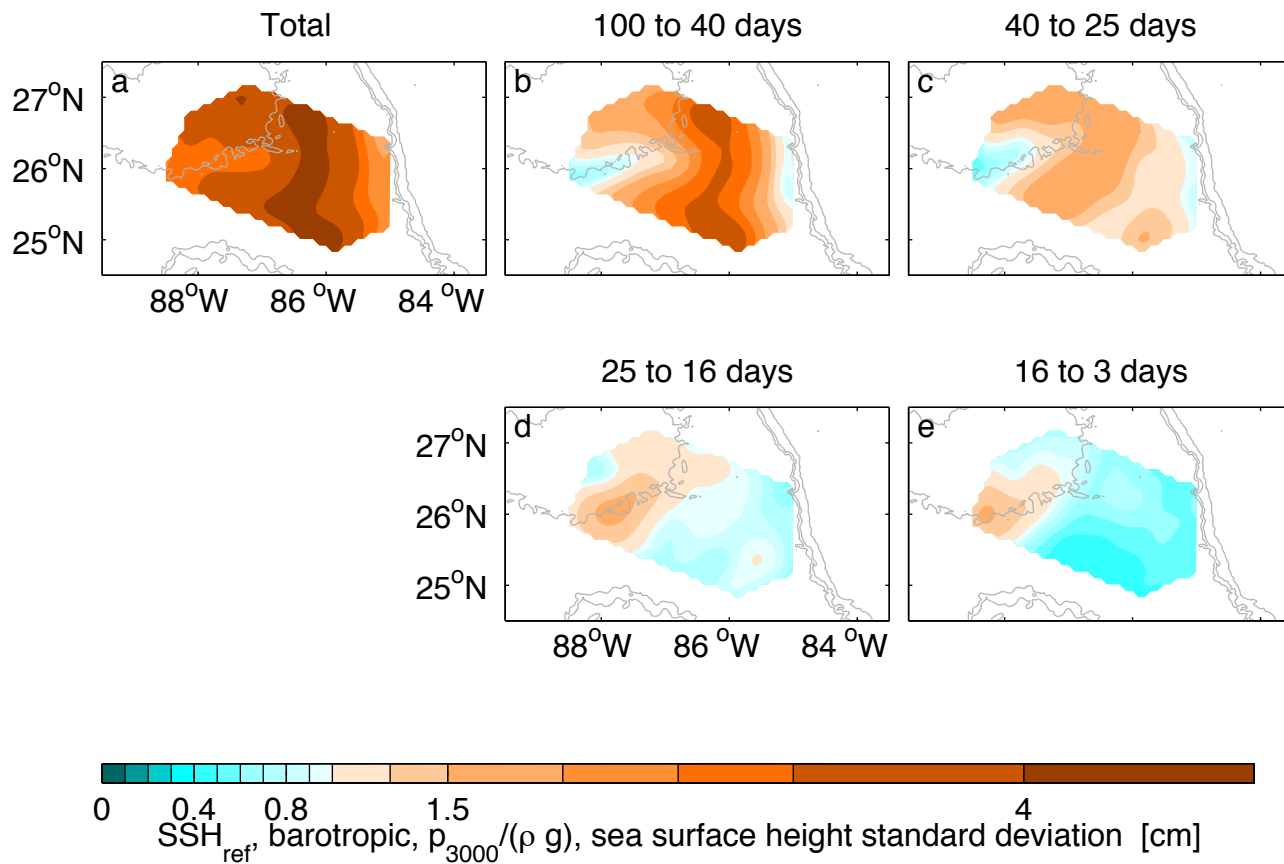


Figure 3.4-18. Standard deviation of reference sea-surface height (SSH_{ref}) as a function of frequency band. SSH_{ref} is the 3000-dbar pressure converted to a height equivalent (pressure anomaly divided by gravity and density). Upper left (a): Total variance. Four right panels (b-e): Standard deviation in four frequency bands noted in the title of each panel. Bathymetry contoured in grey every 500-m depth. Note that the color contour interval is not uniform.

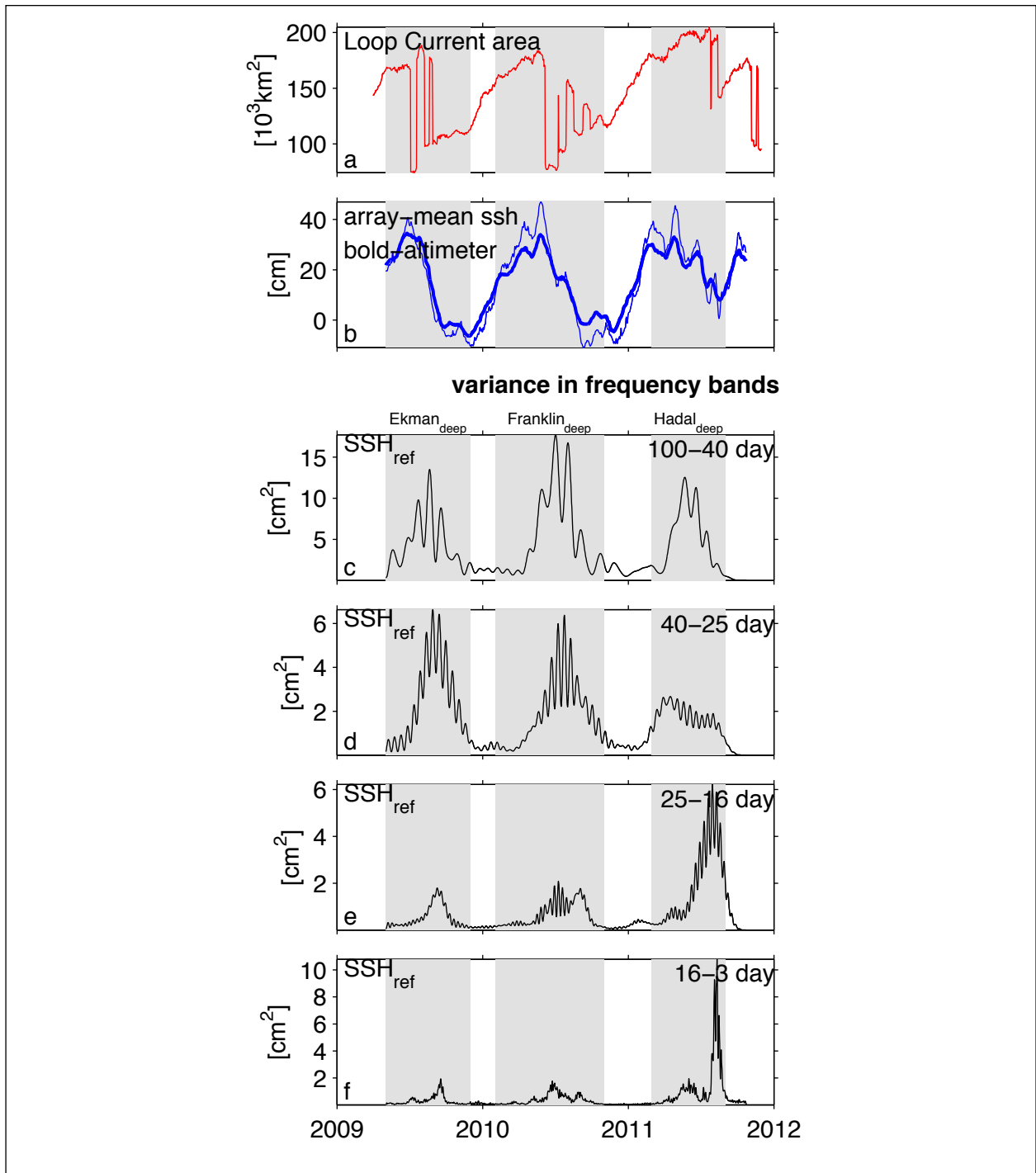


Figure 3.4-19. (a) Loop Current area. (b) Array-mean baroclinic sea-surface height referenced to the bottom, SSH_{bcb} (thin line) and CCAR sea-surface height (bold line). The mean of the baroclinic sea-surface height referenced to the bottom has been adjusted to match the CCAR sea-surface height. (c-f) Variance of array-averaged reference sea-surface height, SSH_{ref}, within frequency bands, as noted in the title of each panel. Grey-filled boxes correspond to the time period over which complex empirical orthogonal functions have been calculated.

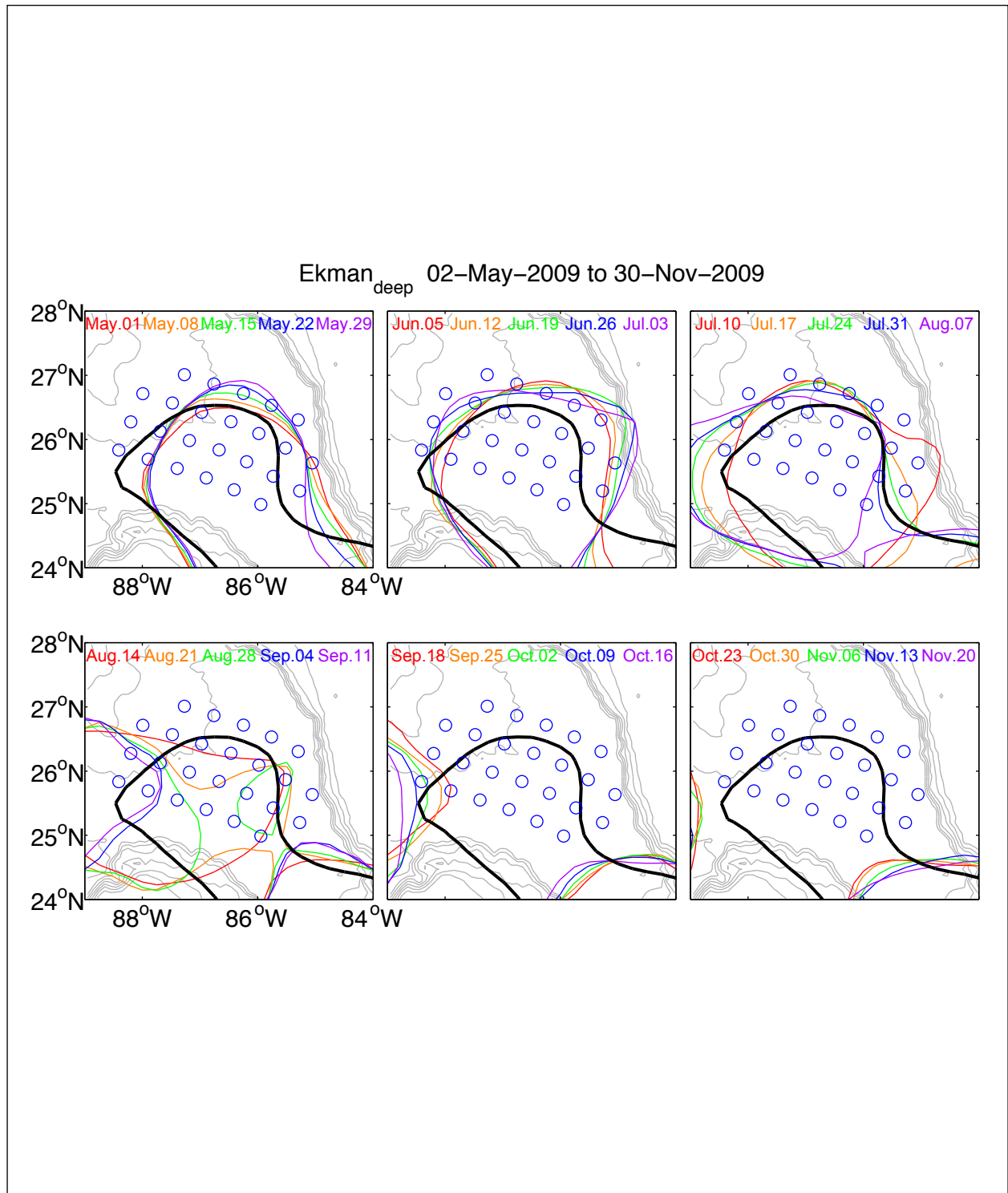


Figure 3.4-20. CCAR SSH-determined Loop Current positions during Ekman_{deep} CEOF time period. For each panel, the position of the 17-cm contour is plotted every seven days and color coded by date, as noted at top of each panel. Location of the PIES represented by open blue circles. The mean Loop Current position is shown by the bold black line. Bathymetry contoured every 500-m depth.

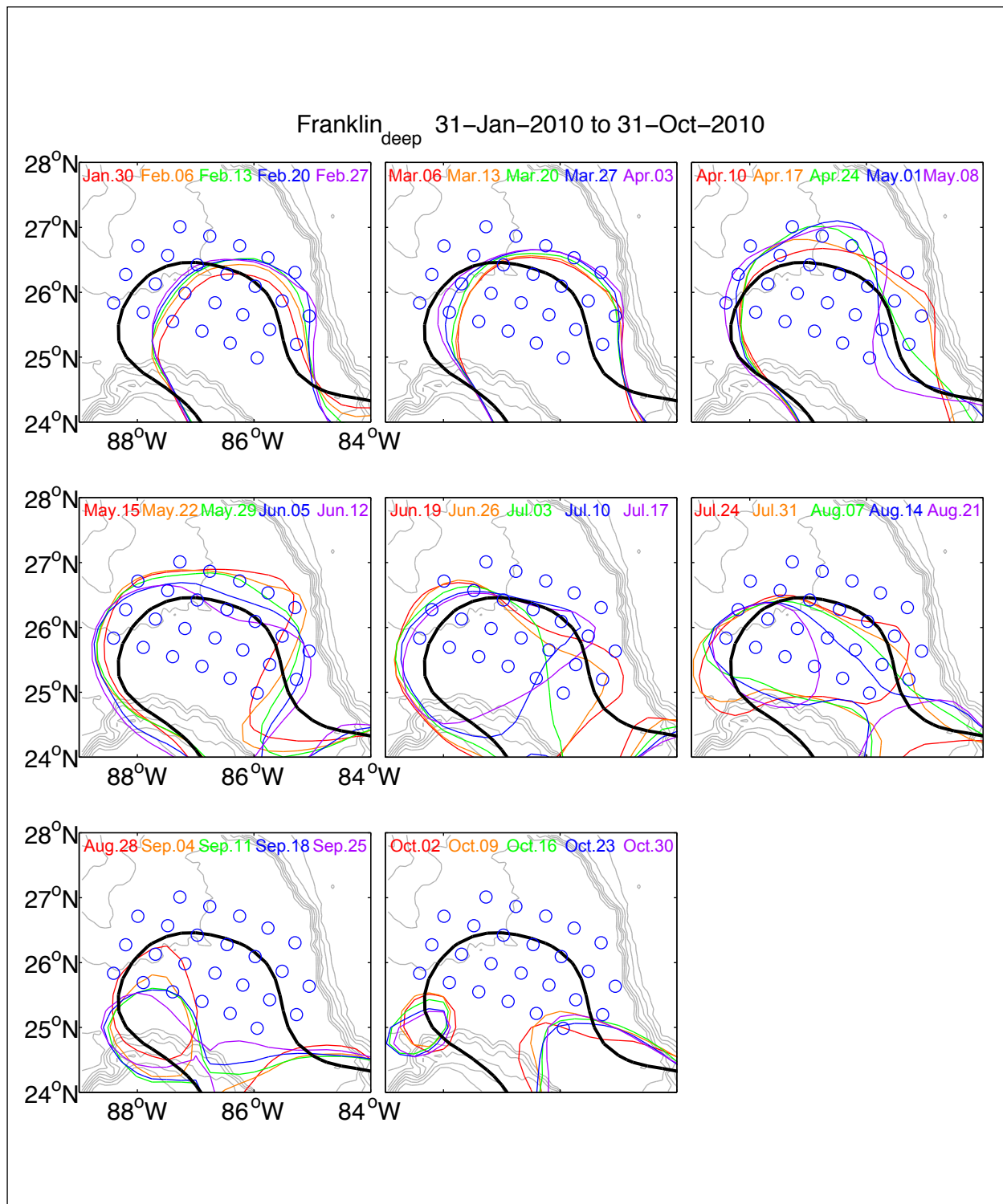


Figure 3.4-21. CCAR SSH-determined Loop Current positions during Franklin_{deep} CEOF time period. For each panel, the position of the 17-cm contour is plotted every seven days and color coded by date, as noted at top of each panel. Location of the PIES represented by open blue circles. The mean Loop Current position is shown by the bold black line. Bathymetry contoured every 500-m depth.

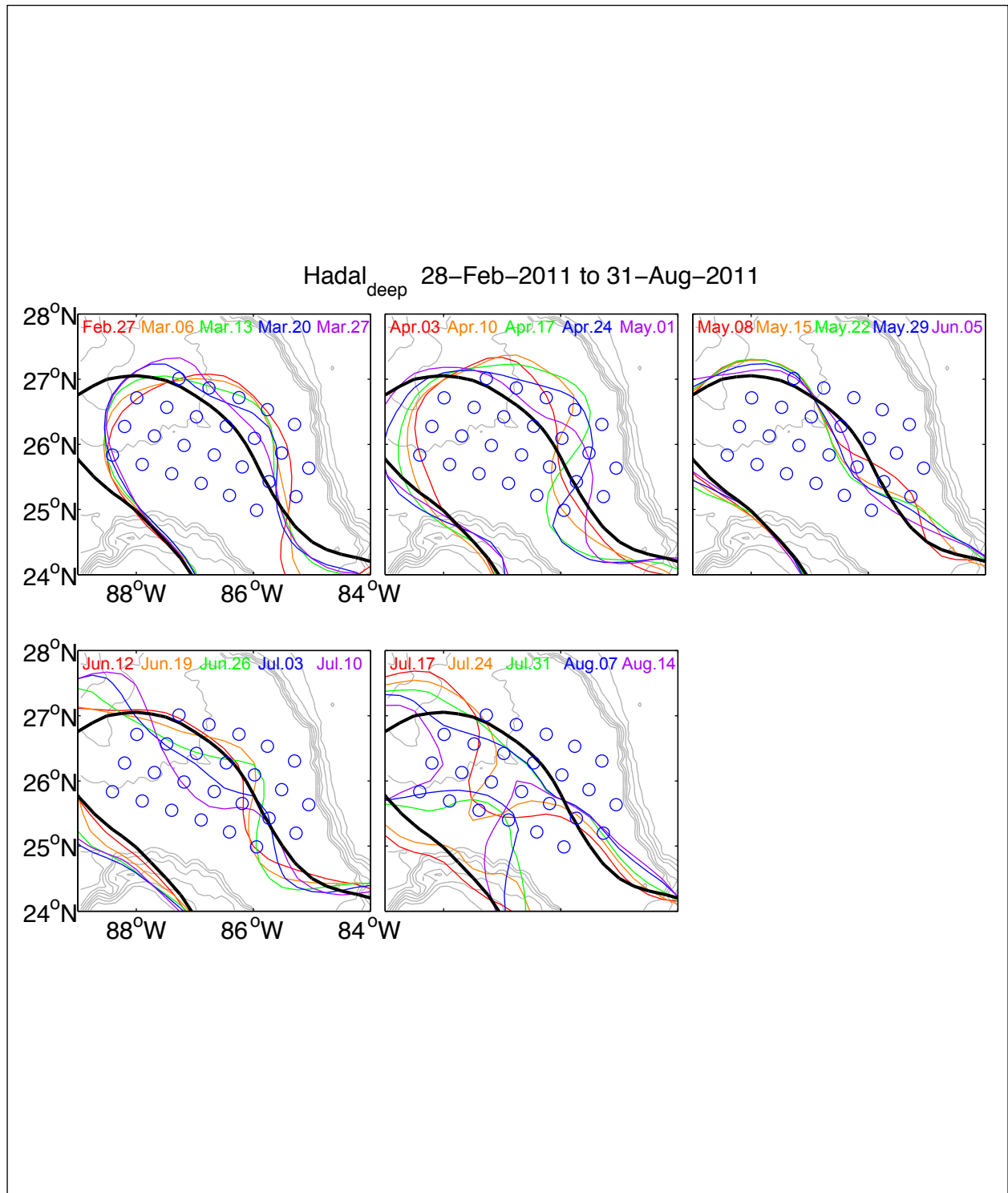


Figure 3.4-22. CCAR SSH-determined Loop Current positions during Hadal_{deep} CEOF time period. For each panel, the position of the 17-cm contour is plotted every seven days and color coded by date, as noted at top of each panel. Location of the PIES represented by open blue circles. The mean Loop Current position is shown by the bold black line. Bathymetry contoured every 500-m depth.

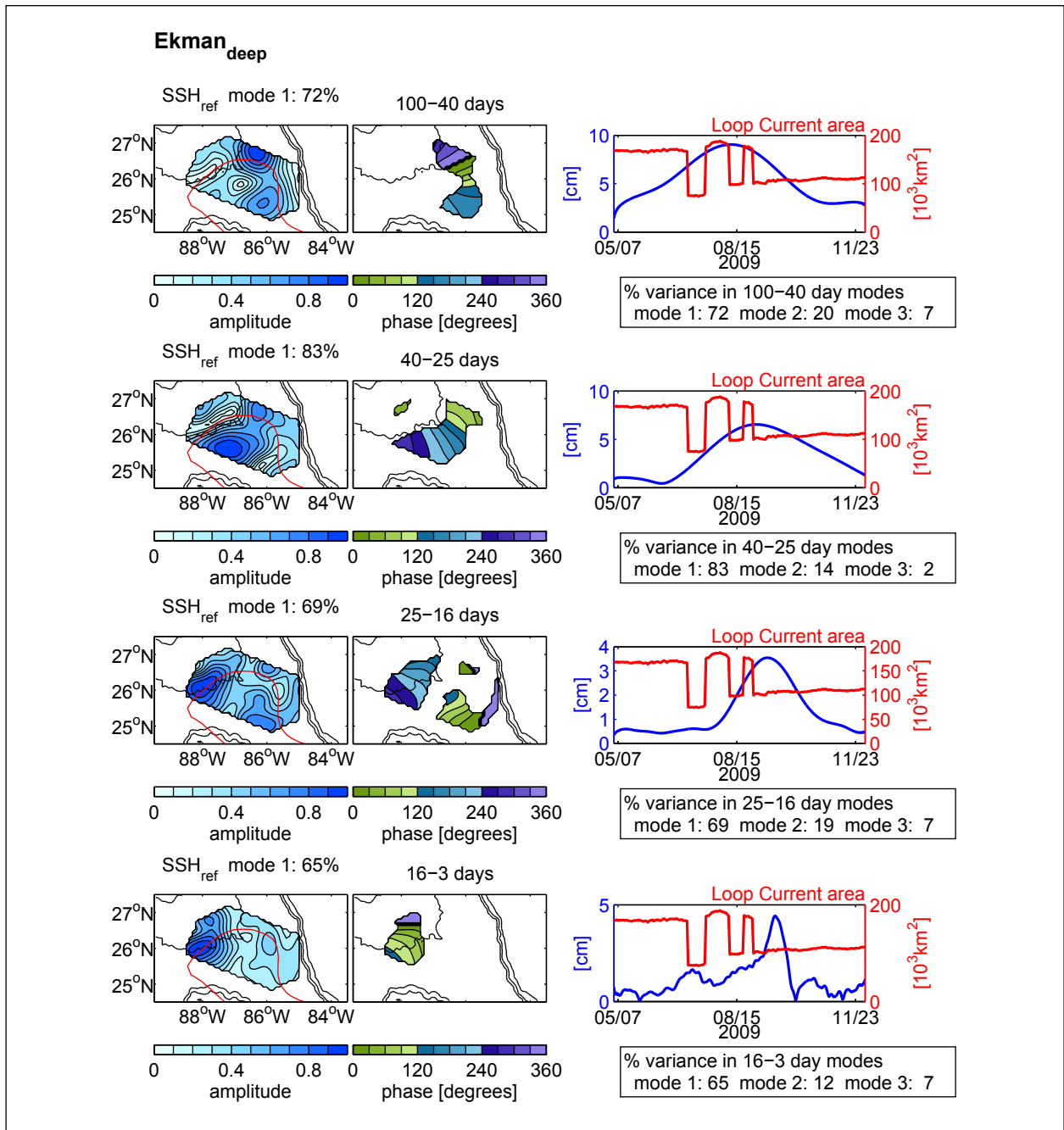


Figure 3.4-23. CEOFs determined from band-passed deep reference sea-surface height, SSH_{ref}, during the Ekman_{deep} time period. Four frequency bands are shown. For each CEOF, left panel: normalized spatial amplitude, middle panel: phase in degrees, right panel: amplitude time series in cm. In the left panel, in addition to the mode amplitudes (blue), the mean position of the LC (17-cm contour) during the time interval of the CEOF is represented by the red line. In the middle panel, phase is plotted for regions where the spatial amplitude exceeds 0.5. Propagation is in the direction of increasing phase. Bathymetry is contoured every 1000-m depth. In the right panel, mode time series is blue; Loop Current area is red.

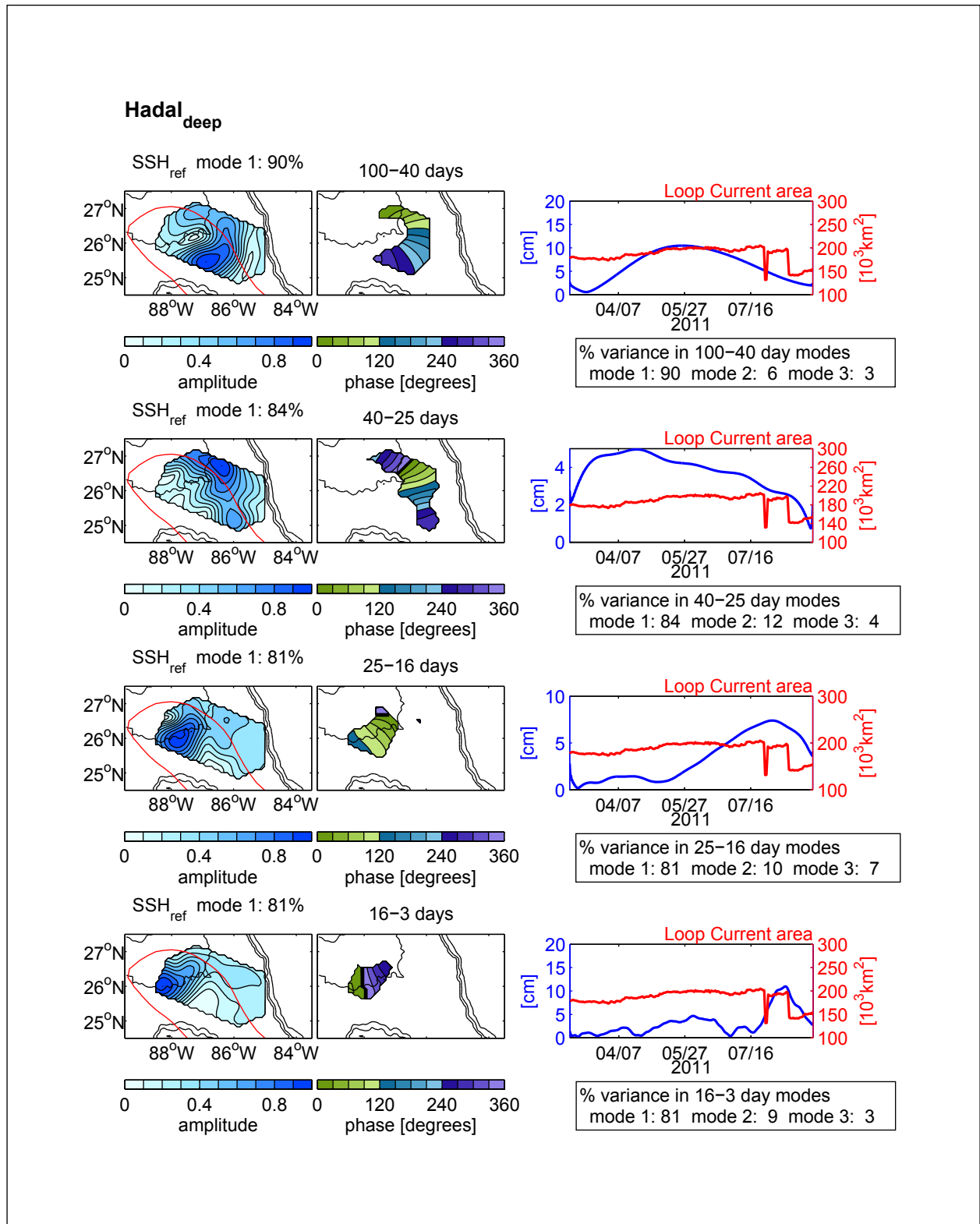


Figure 3.4-25. CEOFs determined from band-passed deep reference sea-surface height, SSH_{ref}, during the Hadal_{deep} time period. Conventions are the same as in Figure 3.4-23.

Ekman_Deep and Franklin_Deep 100 to 40 Day Band

Ekman_deep and Franklin_deep CEOF-mode amplitudes grow to maxima during detachments. The spatial modes reveal a high amplitude ridge extending north-to-south along the eastern side of the array. These modes propagate anticyclonically with phase speeds near 7 km day^{-1} , and wave number near 0.015 km^{-1} . A noticeable phase speed increase is apparent in the southeast near where the LC necks down.

Ekman_Deep and Franklin_Deep 40 to 25 Day Band

The 40- to 25-day CEOF mode also peaks during the LC eddy detachments, but at a slightly later time than the 100- to 40-day band. This mode propagates anticyclonically within the array. Phase speeds are near 10 km day^{-1} , and wave number near 0.02 km^{-1} . The 100- to 40- and 40- to 25-day band-passed SSH_ref data are separately mapped every seven days for the time intervals when these modes have high amplitudes within the Franklin_deep time interval (Figures 3.4-26 and 3.4-27). These map sequences are next examined together with the CEOF analysis to elucidate the close relationship between the nearly depth-independent mode and the eddy-formation process in the LC.

Prior to the first detachment, a deep anticyclone-cyclone pair propagates along the LC. As they move southward, both features intensify jointly with a growing upper meander crest and trough along the eastern edge of the LC. On 9 July 2010, the deep strong cyclone is positioned at the southernmost extent of the array, near 25.3°N , 86.0°W . While the ultimate fate of this feature is unknown, due to the array's limited spatial extent, it is speculated that this deep cyclone facilitates Franklin's first detachment and the trailing deep anticyclone aids the subsequent reattachment that occurs 1 August 2010. During this same Franklin_deep time interval, in the 40- to 25-day band, several cyclones and anticyclones move successively along the LC from the northwest corner to the central portion of the array, and they continue on an anticyclonic path southwestward to cross the LC. The passage of the strong anticyclone-cyclone pair occurs 8 August to 7 September 2010, just prior to and during the final separation of eddy Franklin.

Ekman_Deep and Franklin_Deep 25 to 16 Day Band

These mode amplitudes peak after LC eddy separation. The spatial structure is slightly different between the Ekman_deep and Franklin_deep. The Ekman_deep pattern has two maxima, one along the Mississippi Fan propagating slightly down-slope and another along the southern portion of the array propagating northwestward. The Franklin_deep pattern also has two maxima, one along the Mississippi Fan and another extending from the southern portion with northwestward propagation. The Franklin_deep amplitude is slightly greater in the array interior compared to Ekman_deep, revealing connected propagation across the array. Phase speeds in this band are near 20 km day^{-1} , and wave number = 0.016 km^{-1} .

Ekman_Deep and Franklin_Deep 16 to 3 Day Band

In this highest-frequency band, both Ekman_deep and Franklin_deep have their largest mode amplitudes along the Mississippi Fan with southwest along-slope propagation. Phase speeds are rapid, near 60 km day^{-1} , and wave numbers are between 0.016 and 0.020 km^{-1} . As noted in Hogg (2000), while shorter-wavelength ($<100 \text{ km}$) topographic Rossby waves would have a

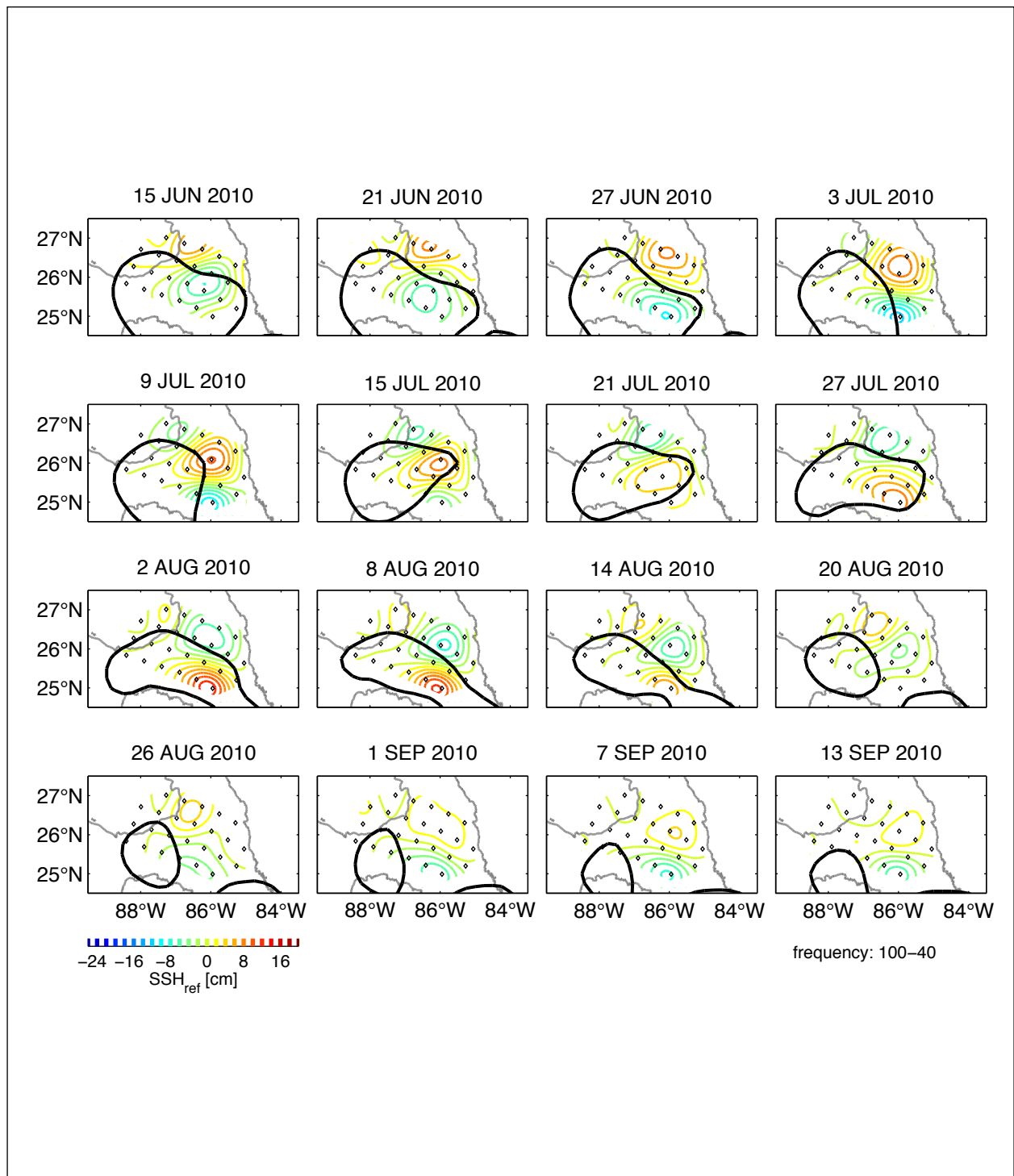


Figure 3.4-26. Snapshots of 100 to 40 day band-passed deep reference sea-surface height (SSH_{ref}) for a portion of the Franklin_deep time interval. The date of each snapshot is given in each panel title. In each panel, the location of the CCAR SSH 17-cm contour is plotted with a bold black line. Color bar in the lower left corner notes the SSH_{ref} contour interval in cm. The 3000-m depth isobath is shown by the grey contour.

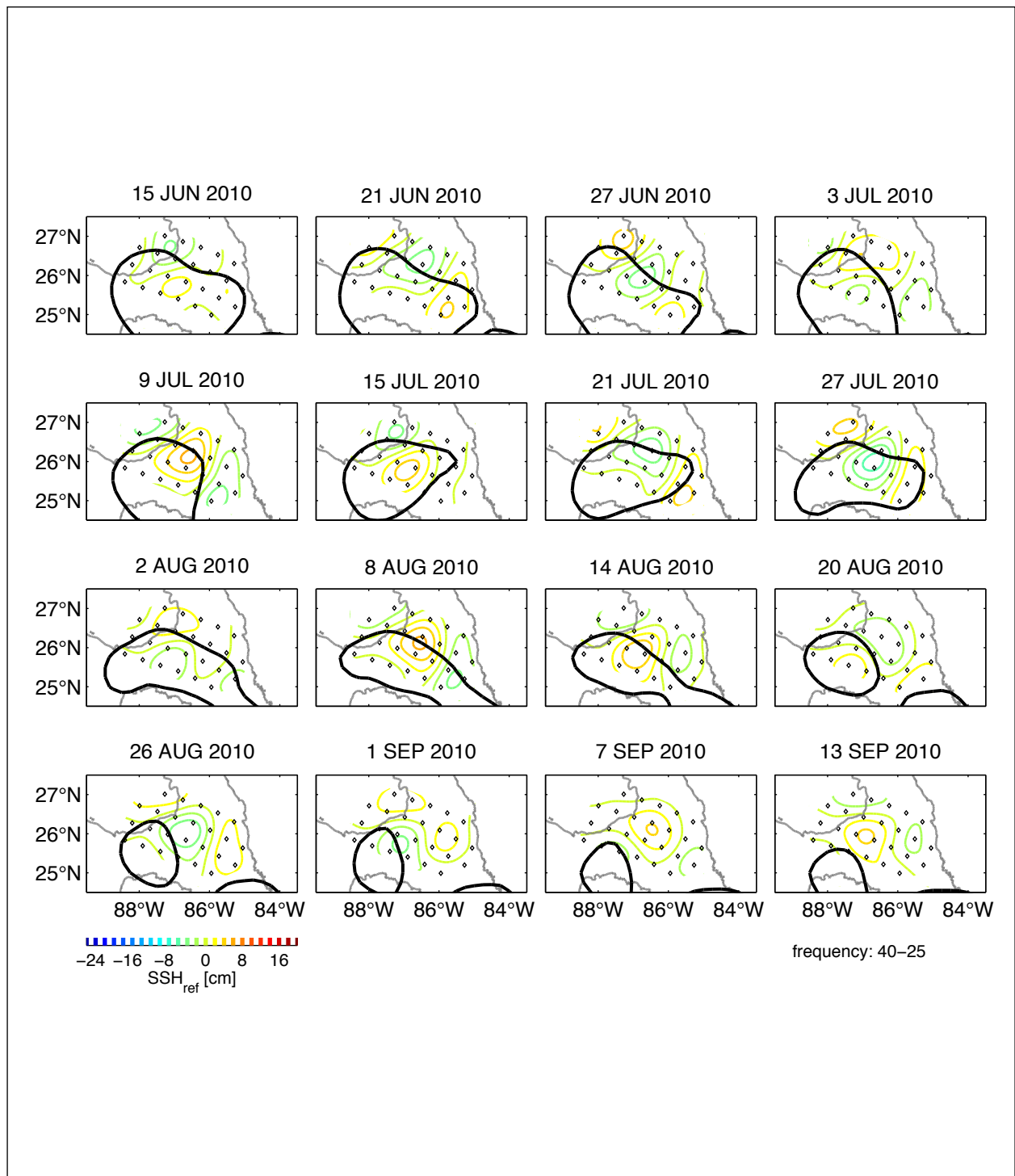


Figure 3.4-27. Snapshots of 40 to 25 day band-passed deep reference sea-surface height (SSH_{ref}) for a portion of the Franklin_{deep} time interval. The date of each snapshot is given in each panel title. In each panel, the location of the CCAR SSH 17-cm contour is plotted with a bold black line. Color bar in the lower left corner notes the SSH_{ref} contour interval in cm. The 3000-m depth isobath is shown by the grey contour.

high-frequency cutoff around a 30-day period in this region, these longer-wavelength features (~300 to 400 km) are only weakly bottom trapped and resemble barotropic-topographic Rossby waves, which can support much shorter period variability.

It is worth noting that in both high-frequency bands, the upper-ocean (SSH_bcb) and nearly depth-independent mode (SSH_ref) signals are strongest along the northwest corner of the array, along the Mississippi Fan, yet the phase propagation is in the opposite sense: northeastward in the SSH_bcb fields; southwestward in the SSH_ref fields.

Hadal_Deep 100 to 40 Day Band

Hadal_deep 100- to 40-day spatial mode shows anticyclonic propagation (Figure 3.4-25). Phase speeds and wavenumbers are similar to Ekman_deep and Franklin_deep. Also similar to Ekman_deep and Franklin_deep is the slight increase in phase speed where the LC necks down near 25.5°N, 87.0°W. The temporal amplitudes peak about a month prior to Hadal separation. The sequence of mapped SSH_ref for this frequency band (Figure 3.4-28) shows that as cyclones and anticyclones move off the Mississippi Fan, they further intensify. These long-period deep cyclones interact with and jointly intensify with an upper-layer trough in the LC. For example, the LC develops a steep trough as the cyclones move through the array during 15 to 22 May 2011 and 10 to 24 July 2011, however, no LC eddy detachment occurs during these two LC neck-downs.

Hadal_Deep 40 to 25 Day Band

The 40- to 25-day variability exhibits the signature of baroclinic instability, as exemplified by deep cyclones leading upper troughs on 1 to 15 May 2011 and 10 to 24 July 2011, and by a deep anticyclone leading an upper crest on 10 to 24 July 2011 (Figure 3.4-29). These features jointly intensify in the region just downstream of the Mississippi Fan. Nevertheless, the amount of steepening in these cases was not sufficient to close the LC neck and cause a LC eddy detachment. The mode amplitude peaks well in advance of Hadal detachments, propagation is anticyclonic and mainly along or very close to the mean path of the LC during this time interval (Figure 3.4-25).

Hadal_Deep 25 to 16 Day and 16 to 3 Day Band

In several respects, the 25- to 16-day and 16- to 3-day CEOFs for the Hadal_deep time interval closely resemble Ekman_deep and Franklin_deep: spatial amplitudes and phases indicate southwestward propagation along the base of the Mississippi Fan (Figure 3.4-25). In several other respects, these frequency bands differ from Ekman_deep and Franklin_deep: the Hadal_deep amplitudes are larger (see also bottom two panels of Figure 3.4-19), and in the 25- to 16-day band the CEOF maximum amplitude coincides in time and space with Hadal's separation. This is clearly shown in Figure 3.4-30, for 26 June 2011 through 14 August 2011. Note that as the deep cyclones and anticyclones propagate along the Mississippi Fan, they intensify and after the passage of a strong cyclone on 7 August 2011, Hadal separates.

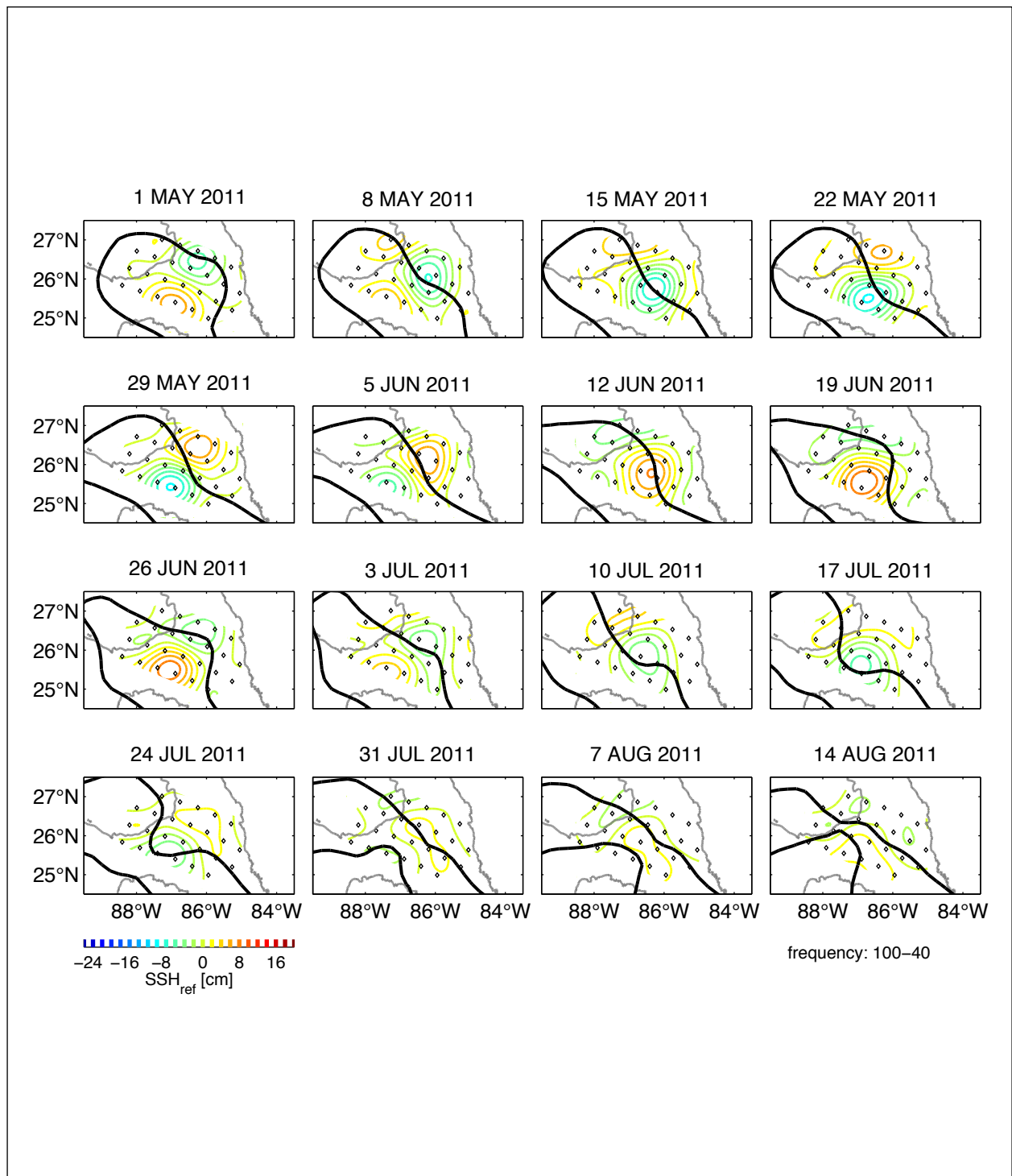


Figure 3.4-28. Snapshots of 100 to 40 day band-passed deep reference sea-surface height (SSH_{ref}) for a portion of the Hadal_deep time interval. The date of each snapshot is given in each panel title. In each panel, the location of the CCAR SSH 17-cm contour is plotted with a bold black line. Color bar in the lower left corner notes the SSH_{ref} contour interval in cm. The 3000-m depth isobath is shown by the grey contour.

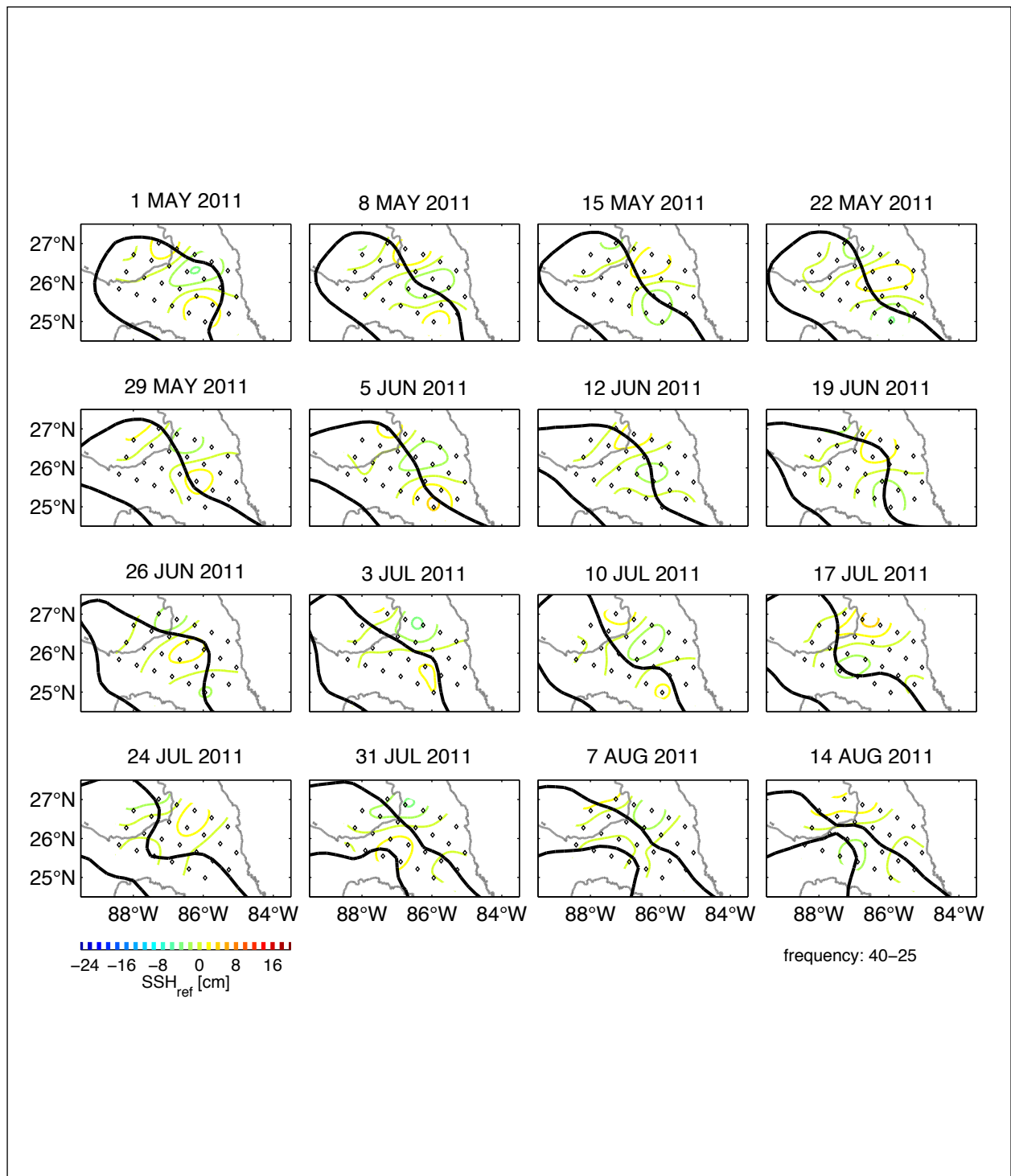


Figure 3.4-29. Snapshots of 40 to 25 day band-passed deep reference sea-surface height (SSH_ref) for a portion of the Hadal_deep time interval. The date of each snapshot is given in each panel title. In each panel, the location of the CCAR SSH 17-cm contour is plotted with a bold black line. Color bar in the lower left corner notes the SSH_ref contour interval in cm. The 3000-m depth isobath is shown by the grey contour.

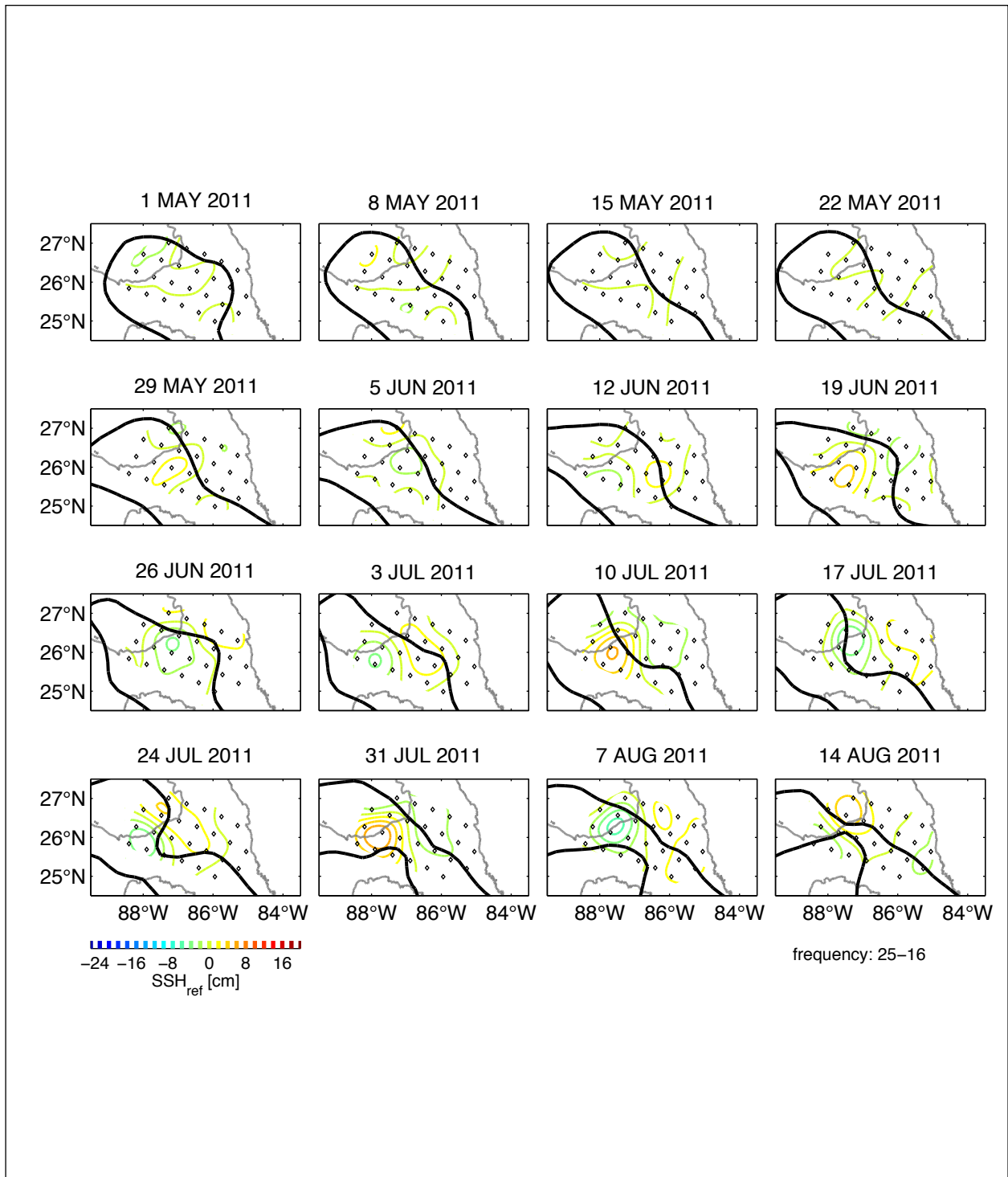


Figure 3.4-30. Snapshots of 25 to 16 day band-passed deep reference sea-surface height (SSH_{ref}) for a portion of the Hadal_{deep} time interval. The date of each snapshot is given in each panel title. In each panel, the location of the CCAR SSH 17-cm contour is plotted with a bold black line. Color bar in the lower left corner notes the SSH_{ref} contour interval in cm. The 3000-m depth isobath is shown by the grey contour.

CHAPTER 4: DYNAMICS

4.1 INTRODUCTION

This chapter investigates LC physical processes, including frontal cyclones, the development of large-scale meanders, deep eddies and topographic Rossby waves (TRWs), and attempts to relate their generation mechanisms such as baroclinic instabilities. The role of topography is important both as a constraint on the flows, but also through topographic slopes, the generation of lower-layer eddies and waves. The emphasis will be on meso-scale variability that is resolved by the arrays. Discussion of longer time scales than 1-2 years, and the role of external influences from the Caribbean and Atlantic is given in Chapter 5. As before, the interface between the upper and lower layers is taken to be the depth of the 6 °C isotherm (Bunge et al. 2002), and much of the analysis will make use of vertical relative vorticity (ζ) fields. The calculation of ζ from plane fits to 40-HLP velocity components, at a given depth level, is given in Chapter 2, and the locations of the ζ -points were given earlier in Figure 2.9-2 where they are similar, and similarly numbered, to the equivalent PIES position. Because the CICESE N-transect plus A4, B3 and C1 tall moorings span the LC from the Campeche Bank almost to the west Florida escarpment, it allows simultaneous examination of processes on both the east and west sides of an extended LC. This section will be referred to as the N1-C1 transect.

4.2 RELATIVE VORTICITY, UPWELLING AND LC EDDY SEPARATIONS

The array area-averaged EKE, deviations of ζ from the mean at 200 m and 100 mab, and vertical velocity at 900 m, are given in Figure 4.2-1. The EKE time series are equivalent to the baroclinic and barotropic variability discussed in Chapter 3 and show marked increases in EKE for the lower layer during eddy detachments (as for Ekman and Franklin) or just prior to eddy detachments (as for Hadal). There are also increases in lower-layer ζ' fluctuations for these events with periodicities ~ 40 to 60 days. Whereas the bottom EKE decreases rapidly to a low level after separation, the ζ' fluctuations decay more slowly. In the upper layer, ζ' is bi-modal, being negative (anticyclonic) during the later growth stages where the LC is over the array, with an abrupt shift to cyclonic when an eddy detaches. Again Hadal differs from the previous two eddies in that the large pulses of positive ζ' , and increases in lower-layer EKE occur before the separation and roughly correspond to episodes of large east-side meander activity discussed in the previous chapter. At 200 m, intervals of positive and negative ζ' have similar magnitudes ($\sim 0.1f$), indicating that when the LC or LC eddy is not present, cyclonic flows predominate, even though they have lower velocities and EKE than the LC. This implies that when the LC is absent, smaller scale (compared to the LC) cyclonic eddies predominate. It is noteworthy that for Franklin and Hadal, the first switch from negative to positive ζ' at 200 m corresponds to a positive pulse of ζ' in the lower layer and a large increase in lower-layer EKE and to some extent an increase in upper-layer EKE, indicating that stronger layer coupling occurs or is initiated at these times. Something similar happens for Ekman except that the positive ζ' pulse and less abrupt increase in EKE in the lower layer precede the upper layer switch to positive ζ' .

Chang and Oey (2010b) derive a canonical eddy-separation scenario and its coupling with the deep flows by using the numerical model in a free running mode with no surface forcing and invariant boundary conditions. In this mode, the model sheds eddies at regular intervals of 8.1

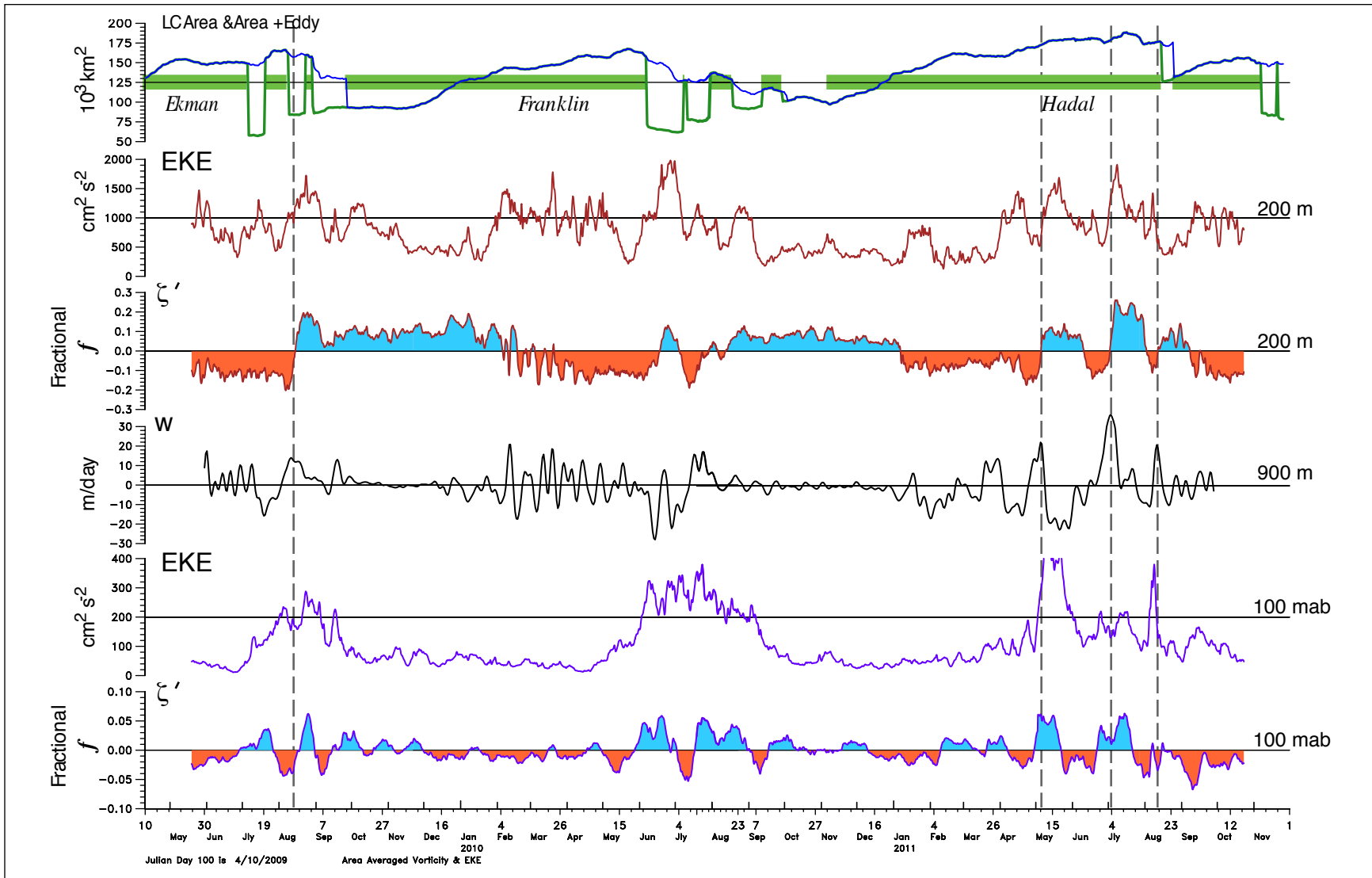


Figure 4.2-1. Array averaged relative vorticity anomaly (ζ'), eddy kinetic energy (EKE) at 200 m and 100 mab, with area averaged 7-DLP vertical velocities (w) at 900 m. LC area (green) and LC+Eddy area (blue) are given in the top panel to show LC growth and eddy deatchments.

months and a total of 12 shedding events were combined for the analysis. Chang and Oey (2011) use a control volume approach with an interface between the upper and lower layers at 1000 m, and a division between the east and west basins of the Gulf at 90°W. Transports through these interfaces, including the upper and lower layers at the Yucatan Channel, were generated from the model outputs. The LC cycle was divided into three stages. Stage A is “Loop-reforming” with downward flux and deep divergence under the LC. Stage B is “incipient-shedding” with strong upward flux and deep convergence. Stage C is “eddy-migration” with waning upward flux and deep through flow from the western Gulf into the Yucatan Channel. Because of the strong deep coupling between the eastern and western Gulf, the LC expansion is poorly correlated with deep flows through the Yucatan Channel. This pattern of transports is sketched in Figure 4.2-2. The mean vertical flux due to the Loop Current Cycle is downward, so that since the net circulation around the abyssal basin is zero, the deep Gulf’s gyre must be cyclonic. Observations indicate that the deep circulation in the western Gulf is cyclonic (DeHaan and Sturges 2005; Hamilton 2009). The gyre’s strength is strongest when the LC is reforming, and weakest after an eddy is shed. The numerical study suggests that the LC Cycle can force a surprisingly strong, low frequency (shedding periods) abyssal oscillation in the Gulf of Mexico.

Examination of the average vertical velocity for the array at 900 m gives some support to Chang and Oey’s (2011) results for stage B. Both Ekman and Hadal show intervals of upwelling when the eddy or the extended LC moves off to the west. For Ekman, August-September 2009 has sustained upward velocities that slightly precede the upper-layer ζ' switching from negative to positive (marked by dashed event lines in Figure 4.2-1). Similarly for Hadal, the three large upwelling events, beginning in the middle of April 2011, also correspond to positive ζ' pulses that in turn correspond to Hadal events that extend the LC to the northwest and away from the array, and thus towards or into the western Gulf. The third upwelling event in August 2011 corresponds to the separation of Hadal. Because Franklin essentially faded away after separation, the Chang and Oey (2011) scenario does not apply and any upwelling flux would be weak and is not definitively observed in the vertical velocity (w) time series. The mean of w over the 2.5 years is $-0.52 \pm 0.7 \text{ m d}^{-1}$, which corresponds to a net downwelling under the LC for the experimental period. Moreover, for the intervals during Franklin and Hadal where the area average relative vorticity is negative (Figure 4.2-1), the calculated average w ’s are also negative (-0.5 ± 1.4 and $-3.7 \pm 2.0 \text{ m d}^{-1}$, respectively), lending support to the idea that the extending LC generates a downward mass flux to the lower layer of the Gulf.

4.3 LOOP CURRENT FRONTAL VARIABILITY

The east-west excursions of the front, as given by the 17-cm SSH contour, were found to differ in amplitude and characteristic wavelengths between the east and west side of an extended LC. The discussion in the previous chapter centered on detachments and separations of the three eddies. In general, when the LC is extended into the Gulf, the front along the Campeche Bank shows only small displacements until a separation event occurs, but the east side often develops large scale (~ 300 km wavelength), large amplitude meanders with periods of ~ 40 to 60 days that propagate south or southeastwards towards the Florida Straits. The consistency of the wavelength and periods of the east-side meanders for the three eddy shedding events do not have an explanation at this time, though vortex instabilities are a possible process. This section examines the variability along the extended LC front in more detail.

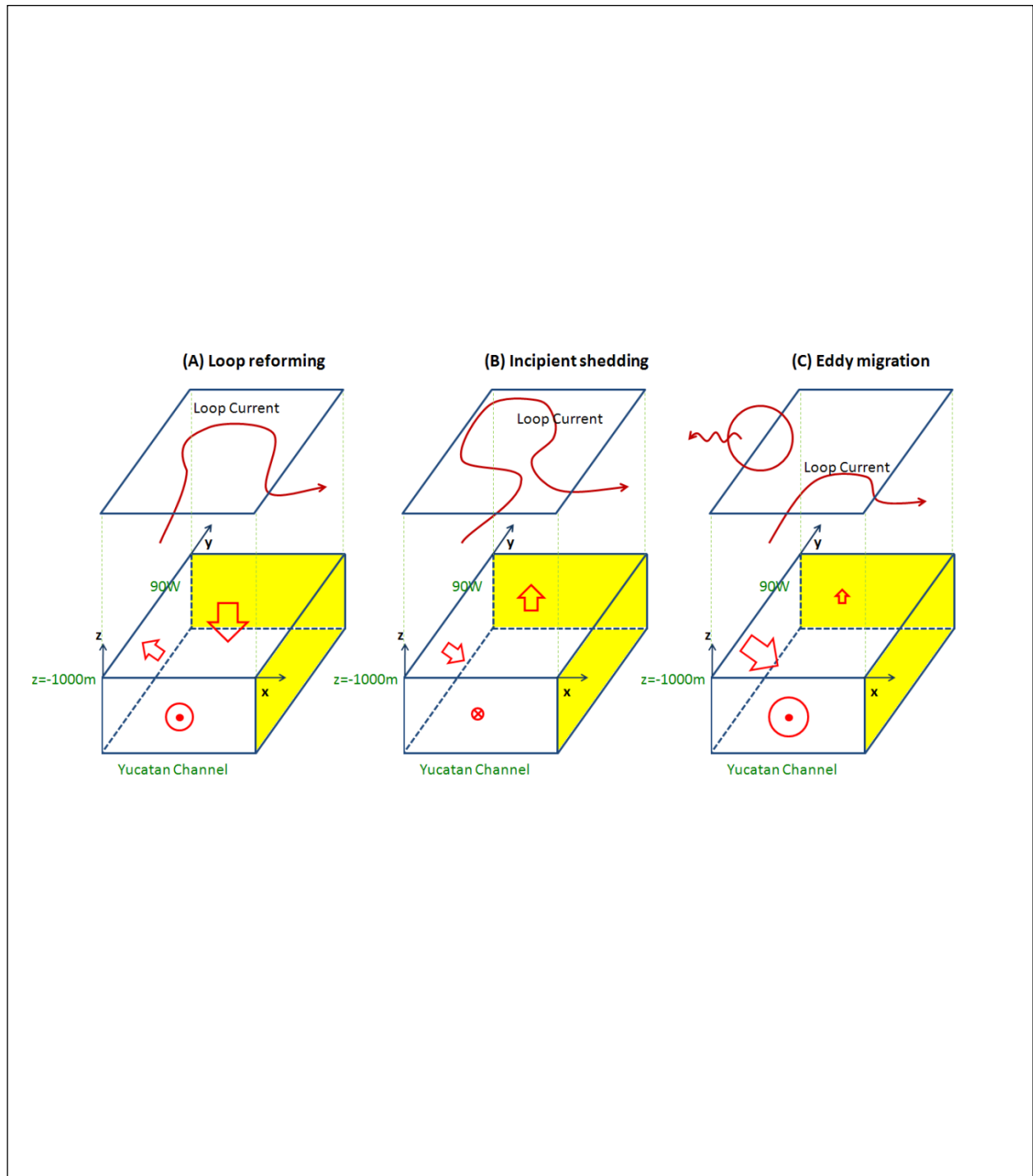


Figure 4.2-2. A schematic illustration of the three stages of the LC cycle. Lower box shows the mass balance in the deep control volume bounded by 90°W , the Yucatan Channel, and the depth of $z = -1000\text{ m}$. Arrows and symbol circles indicate the directions and (approximate) magnitudes of the transports. Yellow shading indicates a closed boundary. Projected upper layer shows the condition of the LC during stage (A) Loop reforming, (B) incipient eddy-shedding, and (C) westward eddy migration across 90°W (from Chang and Oey 2011).

The depth of the 6 °C isotherm along the N1-C1 transect is given in Figure 4.3-1. The location of fronts along the transect are overlaid and show a close correspondence with the 800-850 m isotherm depth contour. The isotherm depths are constructed from both the moorings and the PIES temperature profiles to increase the horizontal resolution, and because the PIES locations are not exactly on the transect, and differences in vertical resolution between mooring-based temperature sensors and acoustic travel-time-derived temperature profiles, there are some bulls eyes in the plot. However, the major features are well observed and include a clear northeast to southwest propagation of isotherm depth signal during the warm intervals when the LC is present. The periodicity of these fluctuations is about 40 days and the propagation time from C1 to N4 is around one to two months. Water depth increases from C1 to N4 by about 250 m, and thus phase propagation along the depth gradient could suggest TRWs with group velocities towards the northwest. Hamilton (2009), using data from a long-term mooring (L7) deployed near A4, showed that the lower-layer fluctuations were compatible with TRWs with periods of 40 to 70 days. However, the apparent southwestward propagation could also be a consequence of the southward propagation of east-side meander crests and troughs. Fluctuations of ~ 40-60 days are also present during the cold intervals when the LC or LC eddy is not present in the transect. However, the propagation of the signal along the transect is not clear and where events seem to propagate (e.g., between Franklin and Hadal), they are much slower than when the eddy is present.

The velocity component normal to the N1-C1 transect, which is approximately parallel to the mean LC front on the western side, is shown in Figure 4.3-2. Magnitudes on the western side are a maximum near the front location and show rapid fluctuations that are associated with cyclonic LCFEs (note that the SSH contour does not resolve fluctuations with time scales < ~10 to 20 days, and length scales < ~50 to 100 km). For the purposes of this analysis LCFEs are defined as having along-front length scales of 50-100 km and periodicities of < 20 days. These rapid fluctuations are also observed in the isotherm depths (Figure 4.3-1), and are most strongly present when the front is between N2 and N3 (e.g., June 2009 for Ekman, March through June 2010 for Franklin, and February through May 2011 for Hadal). When the front moves closer and away from the Campeche bank, the intensity of the fluctuations decreases indicating that the relative location of the western front to the shelf break influences the development and propagation of the LCFEs. On the eastern side of the transect, the oppositely directed current fluctuations have smaller magnitudes, and generally occur inside the front location. The fluctuations have longer periodicities and less amplitude than on the western side (Figure 4.3-2). The same high-frequency fluctuations, but with less magnitude, are observed at E2 and E3 on transect E when the front is in the vicinity of these stations (not shown).

The velocities at 120 m along the N1-C1, and E transects are interpolated to the front location and the coordinates rotated so that the v-component is directed along the front as defined by the 17-cm SSH contour, where it crosses the transects. The resulting vectors are denoted as along-front velocities, and approximately directed northwestward on the west and southeastward on the east side of the LC. They are given, along with the front displacements relative to E2, N2 and C1, in Figure 4.3-3. During the Franklin and Hadal intervals, the west-side front displacements relative to the 500 m (i.e., N2 and E2) isobaths are very similar. However, both the intensity of the fluctuations and the means are larger on the N1-C1 transect than the E transect. There is also

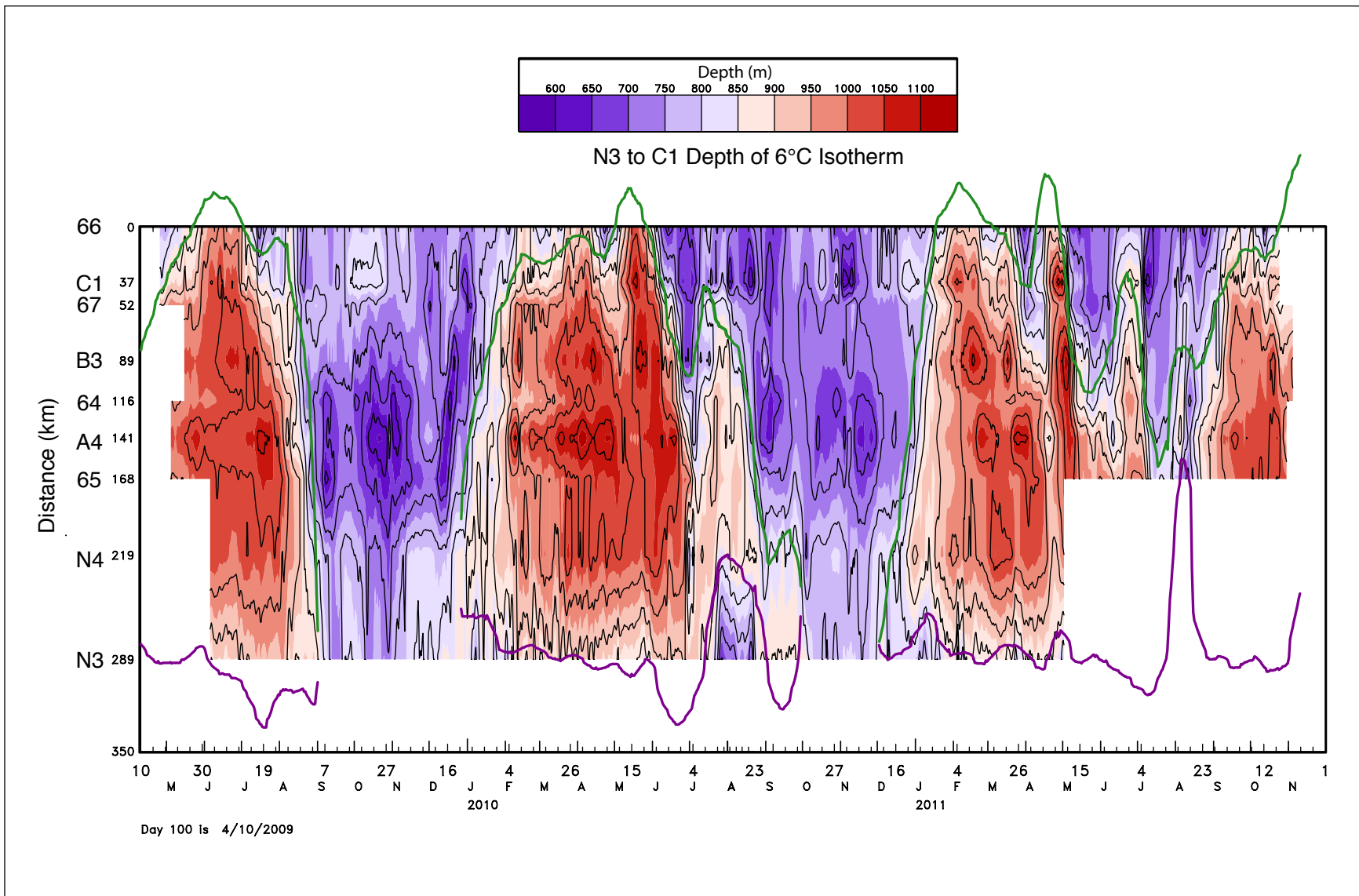


Figure 4.3-1. Depth of the 6 °C isotherm along the N3-C1 transect. The locations of the SSH 17-cm contour on the transect are given by the thick lines for the east (green) and west (purple) sides, respectively.

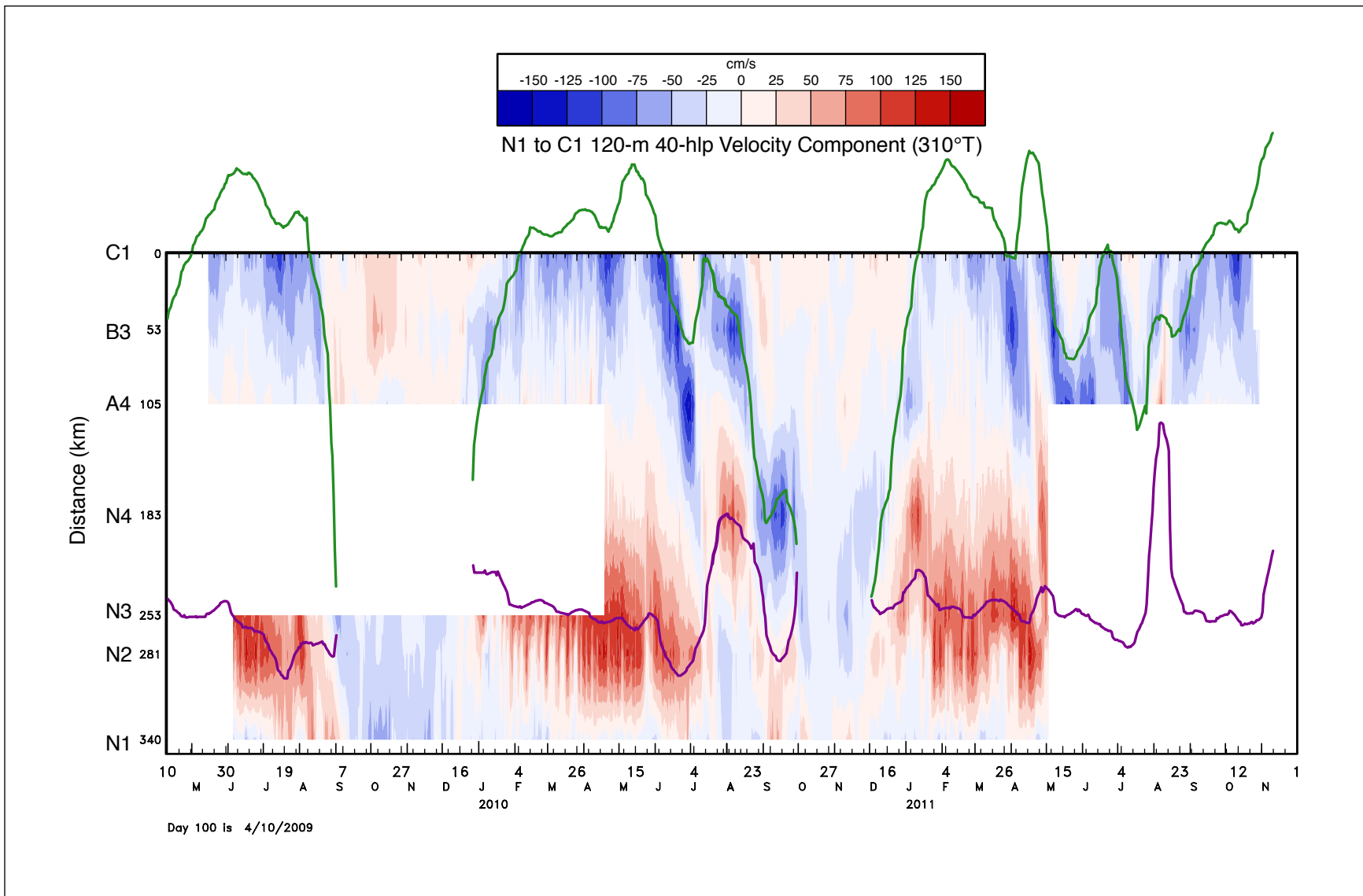


Figure 4.3-2. Velocity components, directed 310°T, at 120 m for moorings along the N1-C1 transect. The locations of the SSH 17-cm contour on the transect are given by the thick lines for the east (green) and west (purple) sides, respectively.

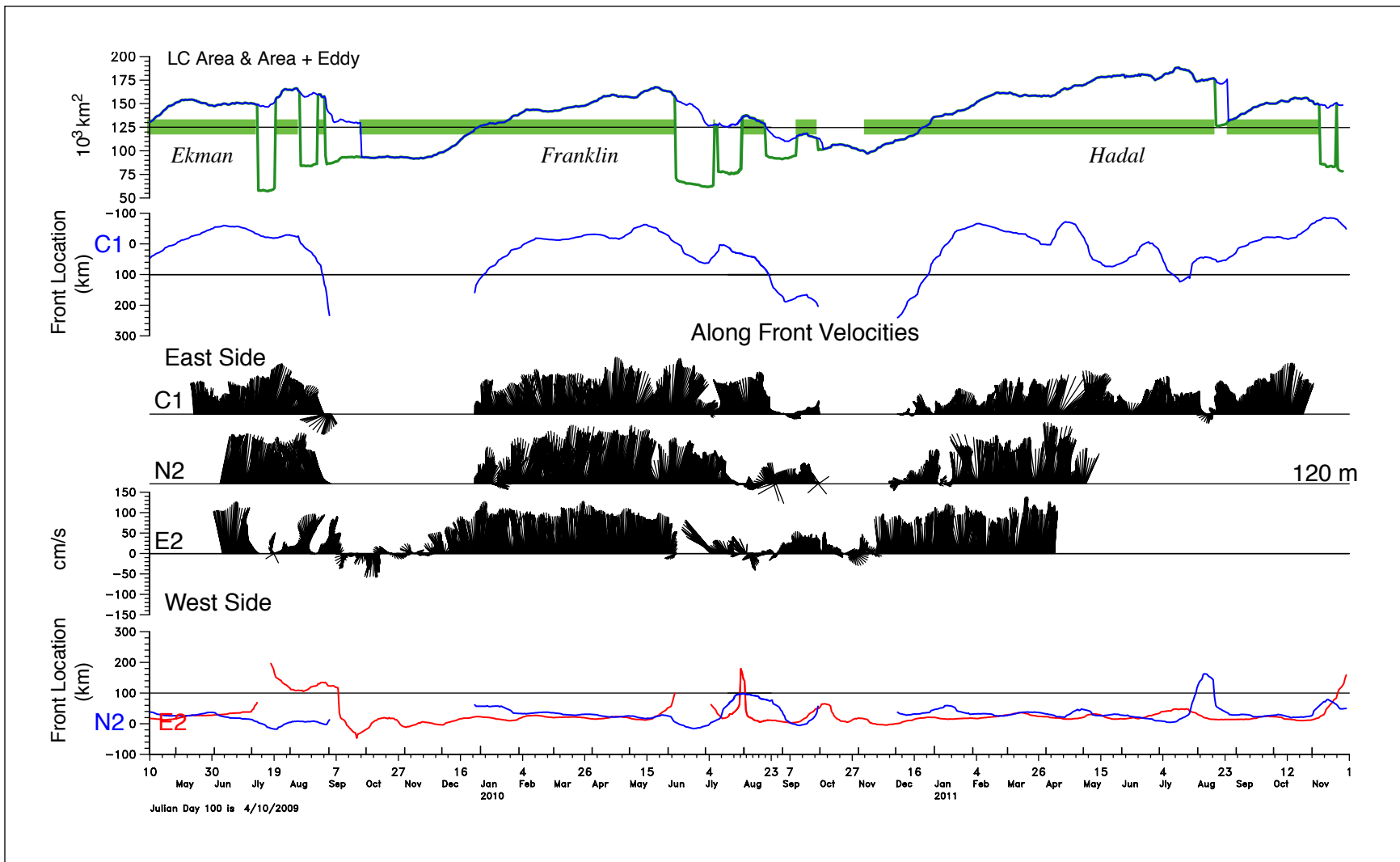


Figure 4.3-3. Along-front velocity vectors for the E and N1-C1 transects for the west (E2 and N2) and east (C1) sides, respectively. Lower panel gives the displacement relative to the 500-m isobath of the 17-cm SSH contour along the E (red) and N1-C1 (blue) transects where positive is towards the northeast. The top panel is the displacement of the front on the N1-C1 transect relative to C1 where positive is towards the southwest along the transect.

a reduction in mean flow on the east side of the N1-C1 transect compared with the west side, however, the fluctuations are larger and generally of longer periodicities.

The variability of the fluctuation EKE is analyzed through spectra of the along-front velocities in the vicinity of E2, N2 and C1 for the Franklin and Hadal intervals, when the western fronts were close to the slope and LCFE activity is evident (Figure 4.3-4). The increase in EKE from the E to N1-C1 transects is clear in both eddy intervals (the spectra are variance preserving with equal areas under the curve representing equal variances), implying that small perturbations in the front north of the Yucatan, grow as the current flows north along the Campeche slope. The mechanism is most likely the mixed instability analyzed by Luther and Bane (1985) for the analogous Gulf Stream flowing along the slope of the South Atlantic Bight (SAB). The EKE energy for the frontal velocities near N2 has peaks at 5-7 days and ~10 days, most prominently for the Franklin interval. These periodicities are characteristic of propagating cyclonic frontal eddies, as is the characteristic “haystack” configuration of the stick vectors in Figure 4.3-3 (Lee and Atkinson 1983). Transects E and N1-C1 are too far apart to definitively track propagating signals (this may also be a consequence of displacements of the jet core when the mooring spacing is relatively coarse), and sequences of clear sky satellite SST images are rare, but previous work has established along-front length scales of ~100 km (Walker et al. 2009). For the northeast LC front, the along-front velocity EKE show little energy at periods shorter than 10 days, and relatively more EKE variance at longer periods than near N2 (Figure 4.3-4). This implies either that short-period cyclonic frontal eddies decay after the main current leaves the slope, and/or there is non-linear transformation to longer-period fluctuations. The latter could be consistent with the observed merging of LCFEs in satellite imagery along the northern boundary of an extended LC (Walker et al. 2011). There is an analogy with the Gulf Stream leaving the slope and flowing into deep water at Cape Hatteras, which also occurs for the northward-flowing branch of the extended LC that leaves the slope at the northeast corner of the Campeche Bank. The Gulf Stream downstream of Cape Hatteras develops long-period meanders and the frontal-eddy perturbations, prominent in the SAB, are not observed.

4.4 RELATIVE VORTICITY

The Hadal interval (January to May 2011) mean upper-layer cross-sectional vorticity and velocity component, normal to the section, are given for the N1-C1 and E transects in Figure 4.4-1. On the cyclonic side of the LC jet, ζ has a strong horizontal gradient and is fairly depth independent down to 500 to 900 m. The jet is centered around N3 and between E2 and E3, and is slightly wider on the northern section, which reflects the greater movement of the front because of LCFE activity. On the anticyclonic side of the front, i.e., within the LC, ζ is nearly constant horizontally but decreases in depth. This is consistent with solid body rotation with speeds that decrease with depth, and is, not surprisingly, similar to the solid body rotation found in detached eddies (Hamilton et al. 2003). For the N1-C1 transect, the center of the solid body rotation is between N4 and A4. Thus, the isolines of speed spread out with increasing depth on the anticyclonic side, but remain parallel, constrained by slope of the bottom on the cyclonic side.

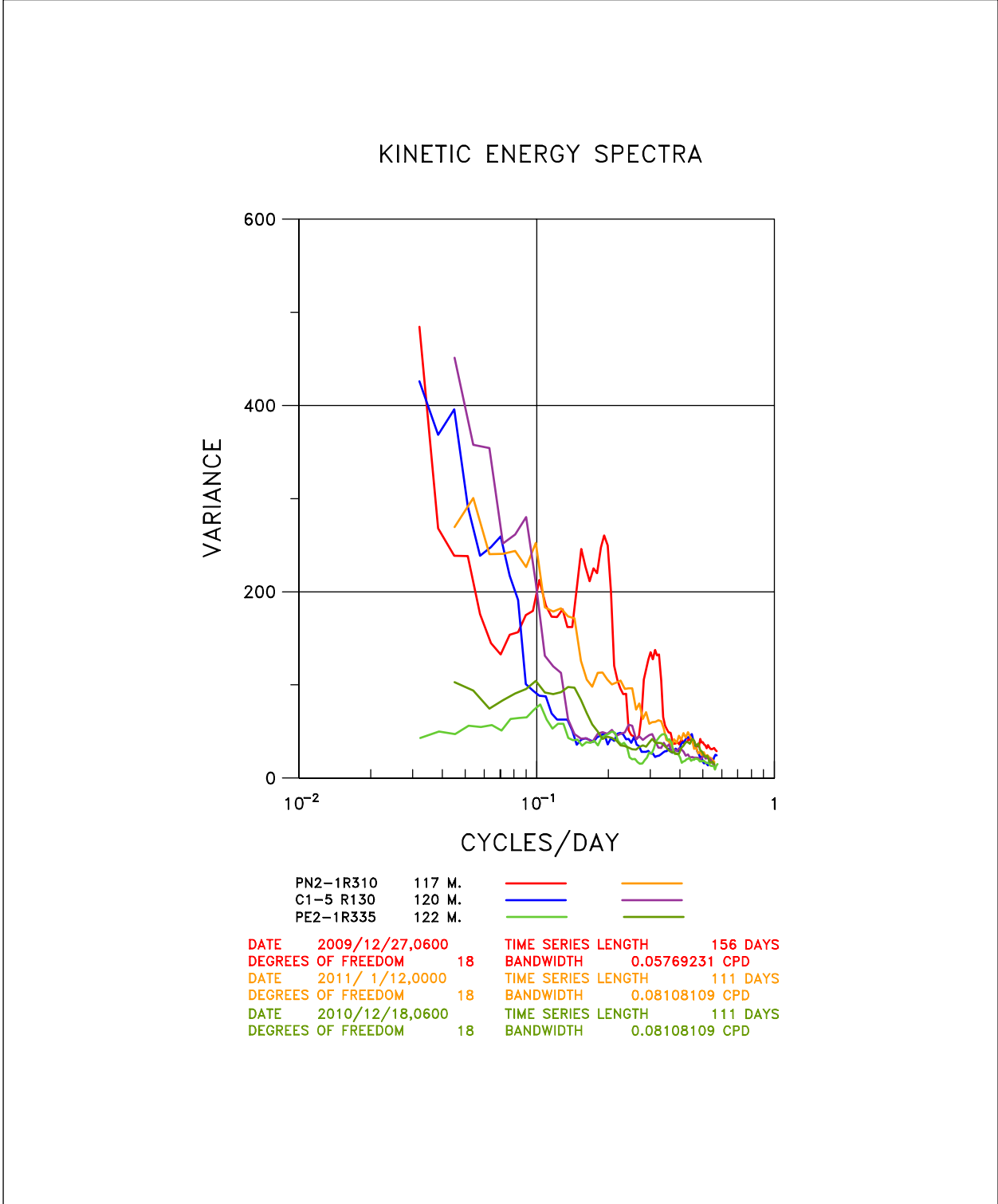


Figure 4.3-4. EKE Spectra of the along-front interpolated velocities on the N2-C1 and E transects. Western LC front spectra are red and yellow (N2-C1), and green and dark green (E) and the Eastern LC front spectra are blue and magenta, for the Franklin and Hadal intervals, respectively. The Hadal interval differs slightly between the E and N2-C1 transects.

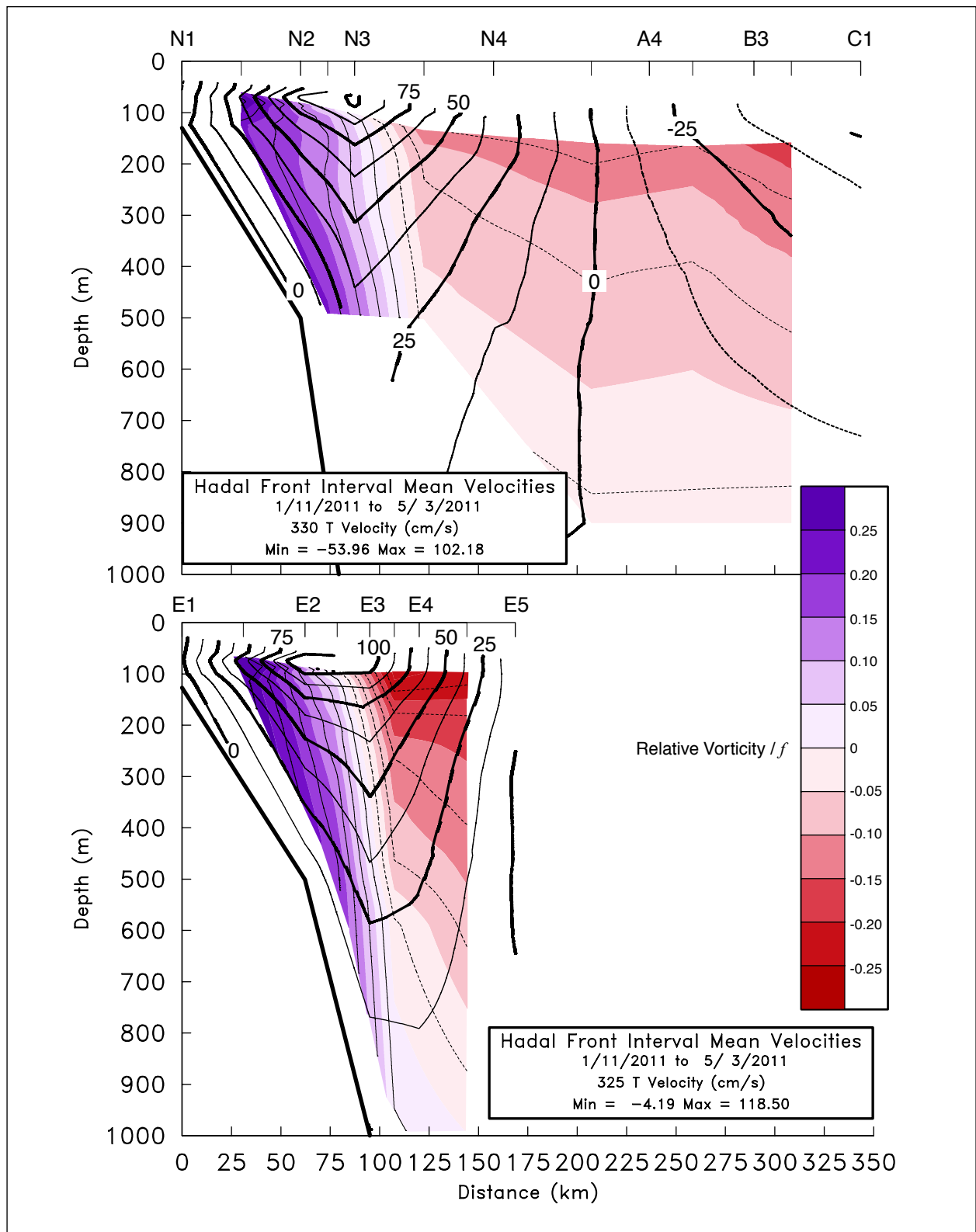


Figure 4.4-1. Mean along-front velocities (cm s^{-1}) and relative vorticity (fraction of f) for the indicated interval and sections across the Campeche slope during the LC formation of Hadal.

The variation of ζ through the water column is given in Figures 4.4-2 for ζ locations 78 and 82 (derived from moorings N2 and N3, and E2, E3 and EN, respectively; see Figure 2.9-2). The vertical fluctuations are consistent with the means (Figure 4.4-1) in that cyclonic (positive) ζ does not have much depth attenuation, and anticyclonic (negative) ζ events are attenuated with depth. At 78, for Ekman (June-July 2009) and Franklin (April-May 2010), the greater seaward slope with depth of the location of maximum velocity (e.g., Figure 4.4-1) creates intervals where the upper water column is anticyclonic, and the lower water column is cyclonic. Moving down stream from N2 into deeper water, the depth distribution of ζ is given for location 56 (derived from moorings A1, A2 and B1) in Figure 4.4-3. At 56, ζ is predominantly anticyclonic, being within the LC or a LC eddy most of the time. The mean location of the 17-cm contour is 20 km northwest of A1. The dominance of negative ζ extends to the lower layer where anticyclonic fluctuations are larger and longer lasting than cyclonic pulses. A mean anticyclonic ζ is consistent with the mean lower-layer anticyclone given by the mean velocities (see Section 3.4) for the west side of the LC, and attributed to weakly shoaling topography, and the tendency of LC/LC eddies to move westward under the influence of β that leads to compression of the lower water column. The lower-layer ζ is relatively depth independent with some anticyclonic events showing evidence of weak bottom trapping during intervals when the LC is advancing to the north.

There are visual indications in Figure 4.4-3 that the upper and lower layer have coherent events, and this is analyzed using frequency domain EOFs, where the ζ s are depth-range weighted, and the frequency bands (100-40, 40-20, 20-10, and 10-3 days) are the same as used for quasi-barotropic and baroclinic analysis using the PIES array in Section 3.4. The EOF modes for location 56 are given in Figure 4.4-4, where for 100-40 days there is a strong connection between lower-layer and upper-layer fluctuations with a 90° phase lead of bottom ζ with the upper layer. The lowest frequency band has a significant surface-intensified mode 2 with little expression in the lower layer that accounts for upper-layer fluctuations associated with the northwest part of the LC. With increasing frequency bands, the mode 1 fluctuations become more bottom trapped with much weaker connections to the surface layer, and are typical (high coherence and in-phase) of TRWs. Highest bottom amplitudes occur for the 20-10 day period band, and the lowest for the 10-3 day band. The shortest period band has a significant second mode that is surface trapped, indicating that short-period motions of less than 20 days, associated with LCFEs propagating along the front, are not extending into the lower layer.

Further downstream at location 67, ζ (from velocities at B2, B3, C1 and C2) is given in Figure 4.4-5. Lower-layer fluctuations have large amplitude, longer periods, and more dominant cyclonic pulses, when compared with 56 (Figure 4.4-3) on the northwest side of the LC. Similar characteristics are seen in the upper layer, except for some relatively weak higher-frequency fluctuations in the Franklin (January-April 2010) growth interval. The EOF modes for location 67 (Figure 4.4-4) show that periods longer than 40 days have a strong connection between layers with only small ($< 90^\circ$) phase leads of the lower over the upper, with the longer periods having larger amplitudes, which are about twice those of the equivalent modes at 56. Mode 1 for this lowest frequency band combines the near-surface intensification with the barotropic mode.

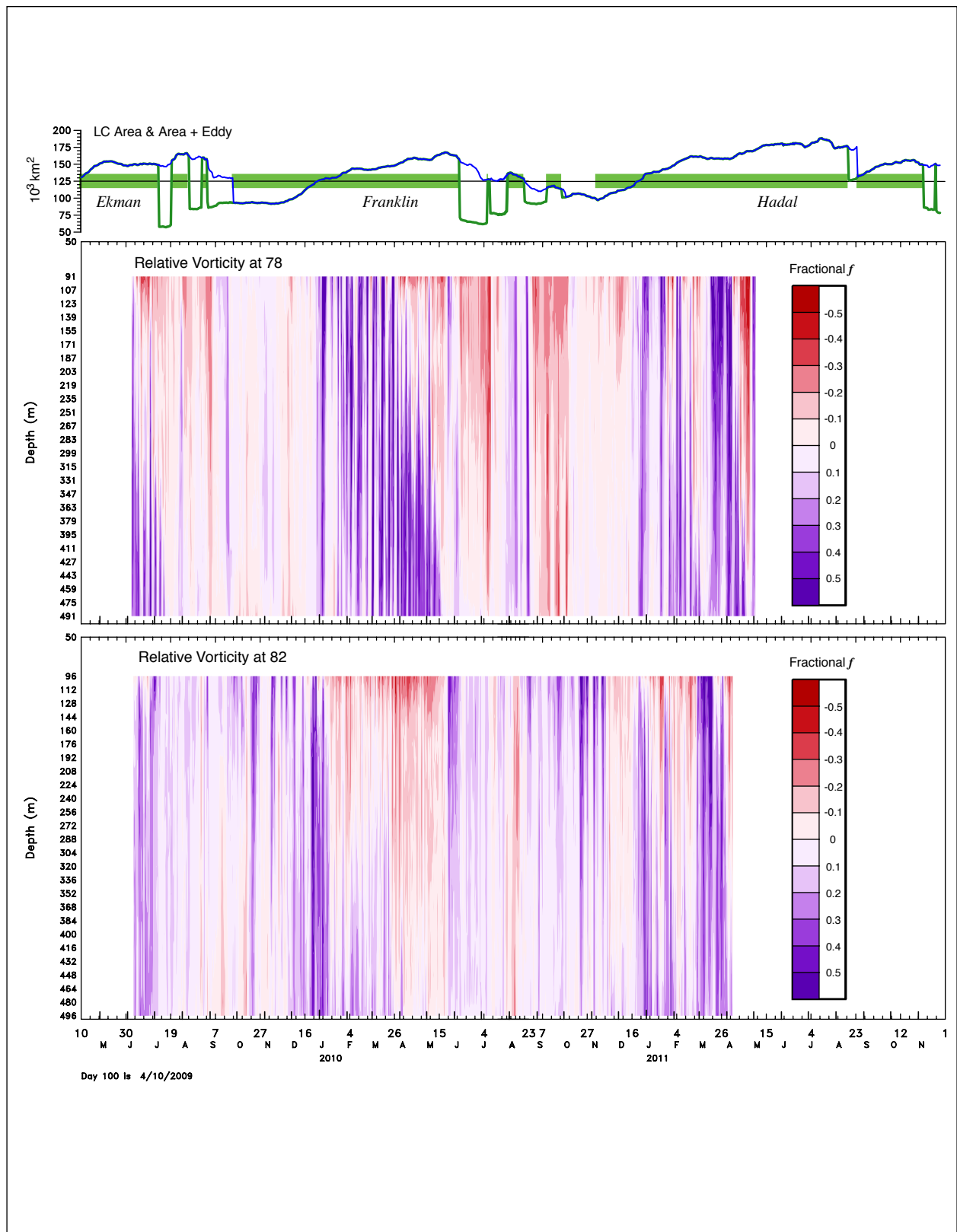


Figure 4.4-2. Time series of relative vorticity (normalized by f) for locations 78 (from N2 and N3 velocities), and 82 (from E2, E3 and EN velocities) as a function of depth.

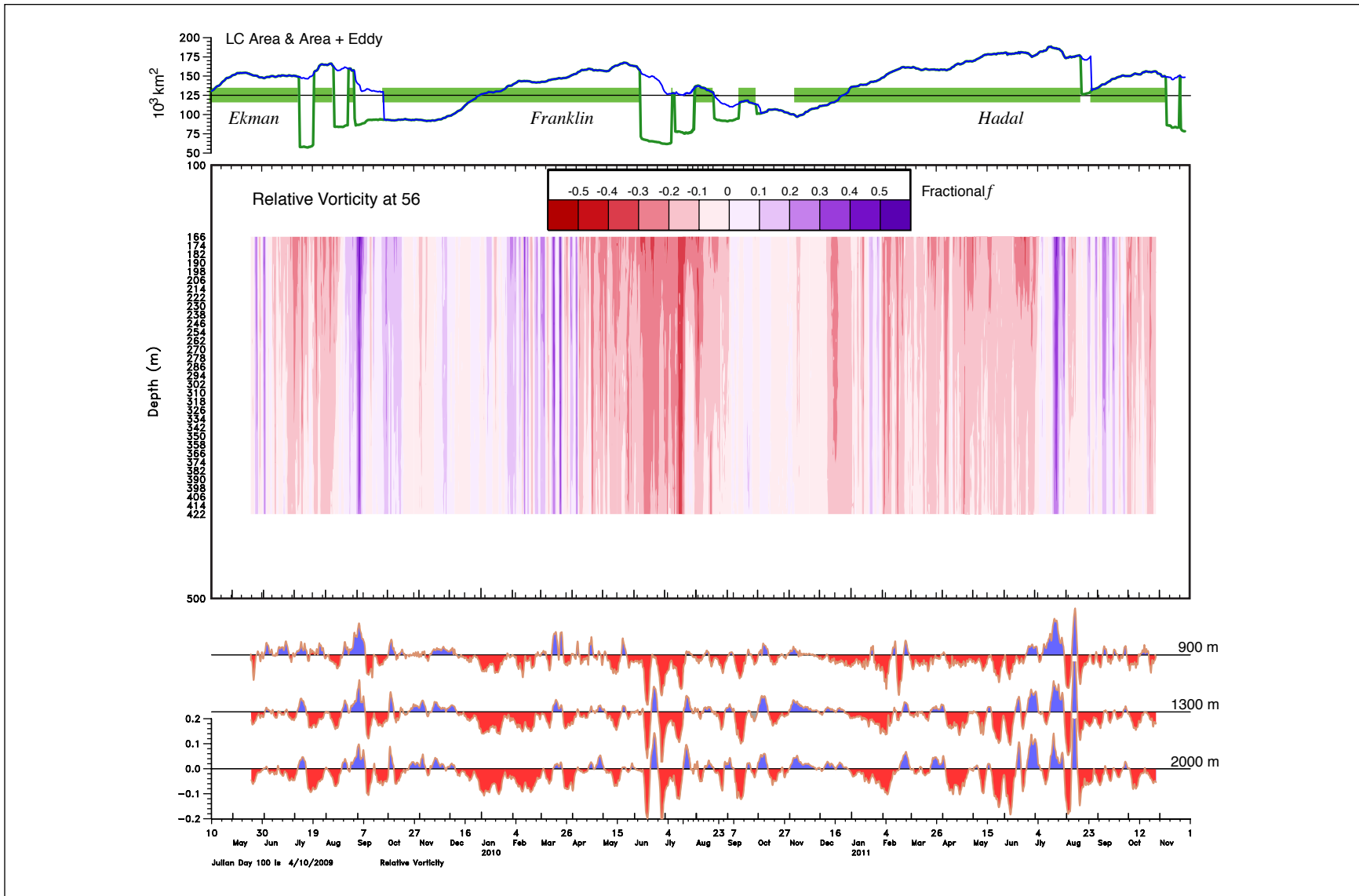


Figure 4.4-3. Time series of relative vorticity (normalized by f) for location 56 (from A1, A2 and B1 velocities), as a function of depth.

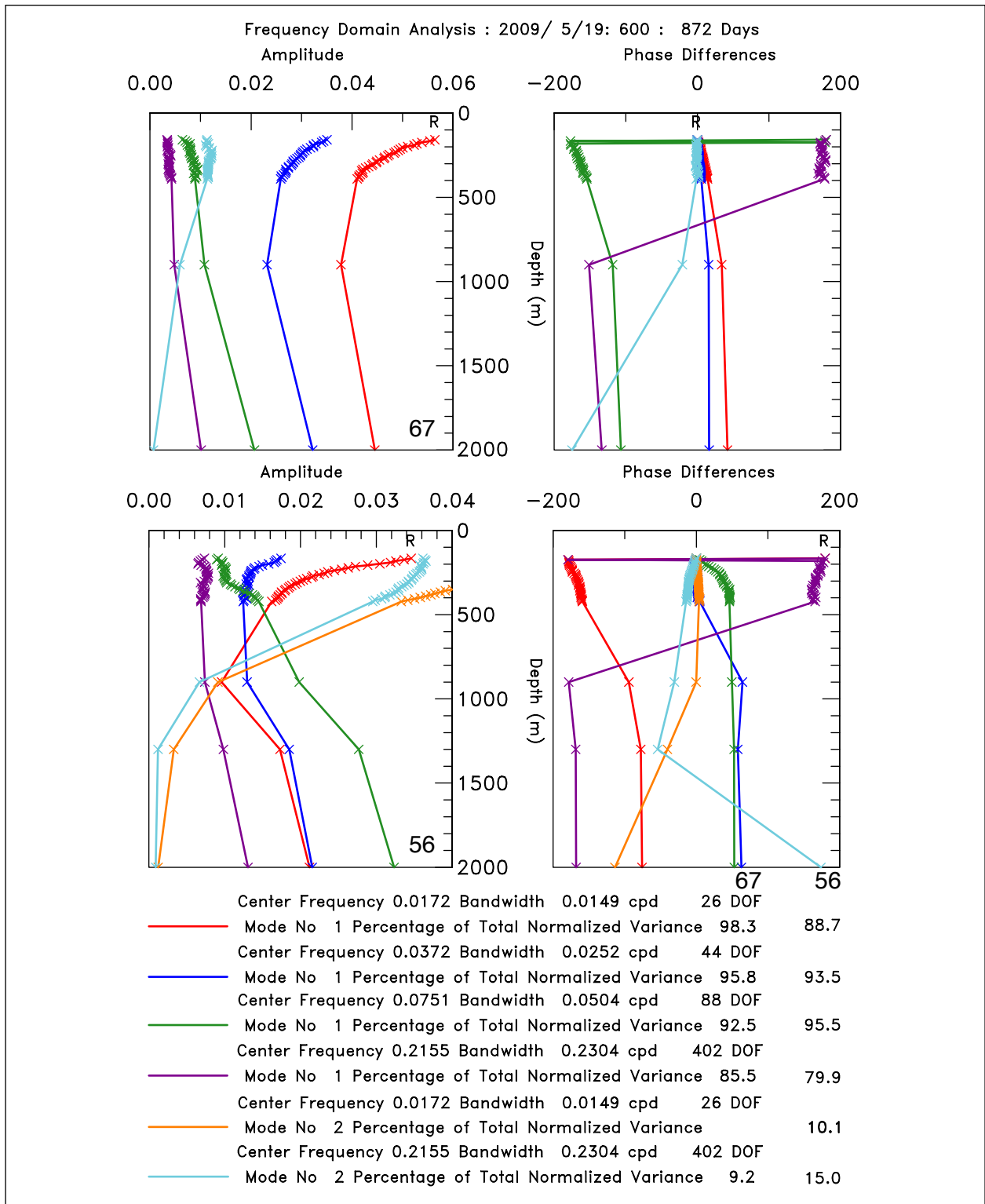


Figure 4.4-4. Frequency domain EOFs of vertical profiles of relative vorticity (units τ^{-1}) at locations 56 and 67. Frequency bands are 100-40 days (red: mode 1, orange: mode 2), 40-20 days (blue), 20-10 days (green: mode 1), and 10-3 days (purple: mode 1, cyan: mode 2).

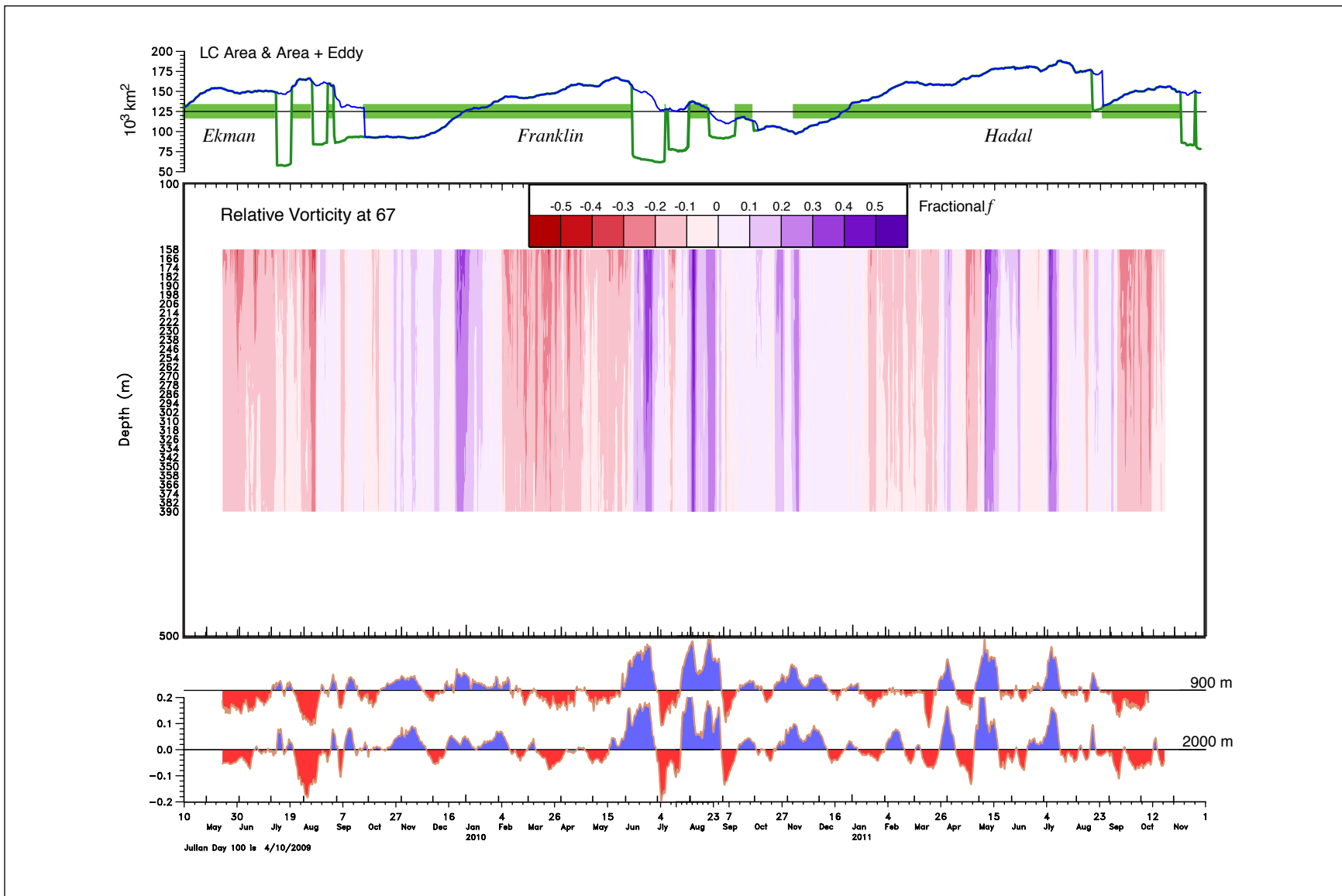


Figure 4.4-5. Time series of relative vorticity (normalized by f) for location 67 (from C1, C2, B2 and B3 velocities), as a function of depth.

Unlike at 56, a separate upper-layer mode is not present. The significant high-frequency mode 2, for the 10-3 day band, is again surface trapped with these fluctuations having smaller amplitudes than at 56. Thus, ζ profiles on the east side of the LC are more barotropic, energetic, and have longer periods than further upstream along the front. This is consistent with motions being dominated by large-scale meanders (i.e., ~ 300 km wavelength with periods of 40 to 60 days) that are strongly connected to the lower layer.

To further illustrate the along-front and eddy-event changes in ζ fluctuations from transect E through N around to the west Florida slope at C1, wavelet power and cross-power have been calculated for locations 82, 78, 56 and 67, respectively. Wavelet analysis for the two Campeche slope locations (Figure 4.4-6) at 82 on transect E, show that short-period fluctuations, < 8 days, are weak and do not rise above the 95% significance level, estimated as in Torrence and Compo (1998). Ten-to-twenty-day power is significant during the earlier growth stages of Franklin and Hadal, but signals longer than 30 days, particularly for Hadal, resulting from longer-scale variations of the LC front, tend to dominate. Further downstream, at section N, the shorter period LCFEs are prominent for Franklin; less so for Hadal. At longer periods, 16-32 days, there are events during the growth phase and first detachment of Franklin and in the early growth phase of Hadal. However, they are not coincident, even allowing for 1-2 weeks propagation lag times, with the events on transect E. This is consistent with the spectral analysis (Figure 4.3-4) and indicates that short-period LCFEs undergo growth between the Yucatan and the northern part of the Campeche slope. It has been speculated from numerical modeling studies that similar period wind forcing, acting through a coastal-trapped wave, could be the trigger for these short period instabilities on the LC front on the Campeche slope (Sheinbaum, personal communication).

Moving into deeper water, the connections between upper layer and lower layer are investigated using cross-wavelet power (Figure 4.4-7). At 56 there is little connection between layers at periods less than 10 days, and between 10 and 20 days the most significant connection occurs for Hadal just before the separation, where the phase angles indicate a 90° phase lag of upper against lower layer ζ (Grinsted et al. 2004). At periods longer than 30 days, where cross power is significant, the lower layer tends to lead by $\sim 90^\circ$, which is consistent with baroclinic instability, except for detachment and separation intervals where the layers tend to be in phase or in anti-phase. On the east side of the LC, at 67, all the significant cross power is at longer than 20 days. Phase leads of the lower layer are generally less than 90° , as was indicated by the EOFs in Figure 4.4-5.

The main conclusions from this section on relative vorticity are that short-period, upper-layer frontal eddies grow along the Campeche slope north of the Yucatan. When they transition to deep water, growth stops and decreases in amplitude are seen from the northwest to the east side of the extended LC. In the northwest, periodicities tend to be shorter than in the northeast, consistent with evidence of baroclinic instabilities at periods longer than 20 days. Short period cyclones have little or no signal in the lower layer. In the northeast, periods longer than 30-40 days dominate with larger amplitudes than in the northwest, with less evidence of baroclinic instability, but still strong connections at these longer periods between the layers.

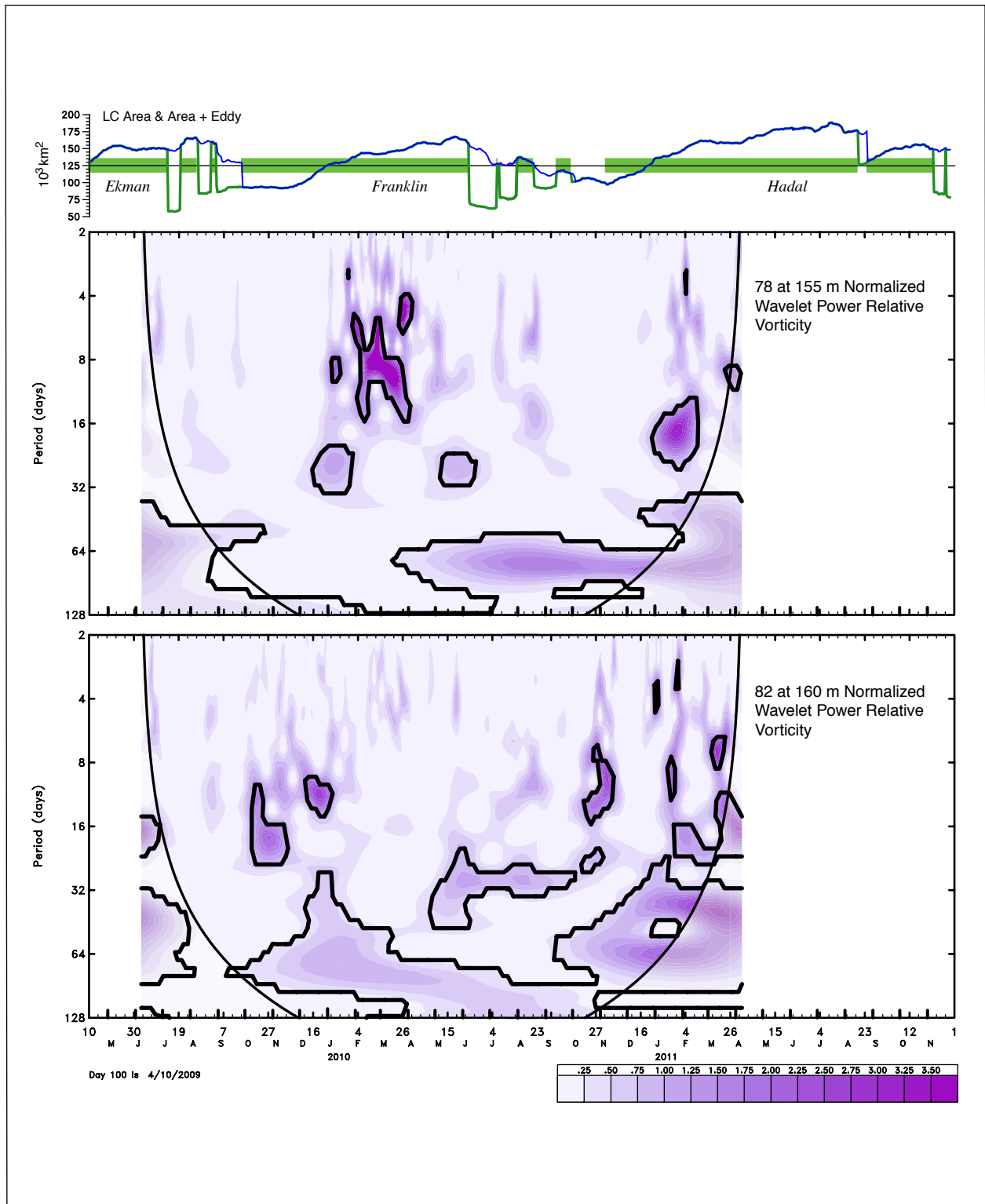


Figure 4.4-6. Normalized wavelet power for relative vorticity at 160 m at locations 82 (transect E), and 78 (transect N) using the Morlet wavelet. The thick solid contours encloses regions of greater than 5% significance against a red-noise process. The lighter shades indicate the “cone of influence” where edge effects are important.

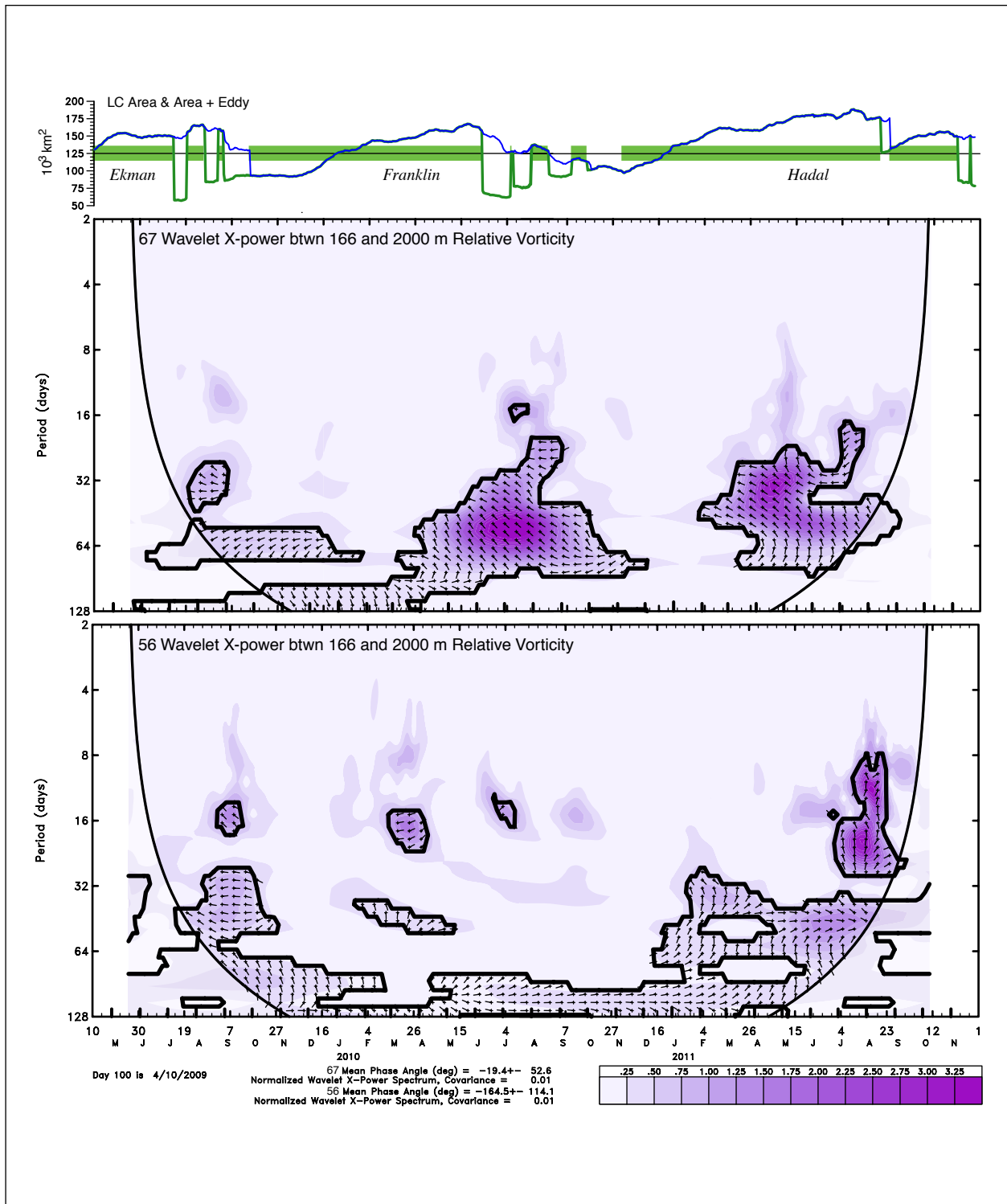


Figure 4.4-7. Cross-wavelet normalized power between 166 and 2000 m at locations 56 and 67. The 5% significance level against red noise is shown as a thick contour. The relative phase relationship is shown as sticks emanating from the crosses (with in-phase pointing right, anti-phase pointing left, and lower leading upper by 90° pointing straight down).

4.5 BAROCLINIC INSTABILITY ANALYSIS

During LC eddy detachment and separation events, a marked increase in lower-layer eddy kinetic energy occurred coincident with the development of a large-scale meander along the northern and eastern parts of the LC (Figure 4.5-1). In this section, it is shown that these lower-layer eddies gain their high-energy levels in a pattern consistent with developing baroclinic instability (Cushman-Roisin and Beckers 2011; McWilliams 2006). Coherence estimates and case studies reveal that the deep streamfunction perturbations lead corresponding perturbations in the upper streamfunction, as they jointly intensify. This baroclinic instability is intrinsically a whole-water-column process, and the interaction between the upper and lower water column is quantified by evaluating the mean-eddy potential-energy budget. Within that budget, as will be treated in this section, the baroclinic energy conversion term, represented by down-gradient eddy heat fluxes, is found to be largest along the eastern side of the LC. In those peak conversion regions there is a near balance between horizontal down-gradient eddy heat fluxes (baroclinic conversion rate) and vertical down-gradient eddy heat fluxes, indicating that eddies extract available potential energy from the mean baroclinic field and further convert that eddy potential energy to eddy kinetic energy.

A signature of growing baroclinic instability events is a vertical phase tilt; along the direction of propagation, deep leads upper. Consequently, at a fixed location, deep leads upper in time also. Here we illustrate that characteristic phase tilt, as was done in Donohue et al. (2006). More comprehensive discussions are presented in ocean-atmosphere texts such as Cushman-Roisin (1994) and Cushman-Roisin and Beckers (2011). The schematic in Figure 4.5-2 presents an eastward jet with a meander crest and trough in the pattern conducive to baroclinic instability. A deep anticyclone (high-pressure center) leads the anticyclonic crest in the upper jet; a deep cyclone (low-pressure center) leads the upper cyclonic trough. In this configuration the upper baroclinic jet can intensify the deep eddies as follows. As the upper crest intensifies and shifts its sloped thermocline structure northward, this squashes the lower water column, adding anticyclonic vorticity to the deep eddy. As the upper trough intensifies and shifts southward, the rising sloped thermocline stretches the lower water column, adding cyclonic vorticity to the deep eddy. Complementing this, the deep eddies can also intensify the upper meander under this illustrated phase shift. Consider a water parcel translating along the upper jet from crest to trough. The deep eddy contribution to this circulation draws the parcel across the baroclinic front deeper into the trough. This stretches the upper water column and adds cyclonic vorticity, tending to grow the trough. Cold advection due to cyclonic turning with height further intensifies the upper trough. Correspondingly, an upper-layer water parcel, passing from trough to crest, is drawn by the deep eddy to move higher into the crest; this squashes the upper column and adds anticyclonic vorticity, and the upper crest grows. Warm advection due to the anticyclonic turning with height intensifies the upper crest. The consequence of this vertical phase tilt is joint growth and development of upper meanders and deep eddies acting upon each other, where this configuration allows them to draw upon the mean potential energy in the sloped thermocline of the baroclinic jet.

To investigate vertical coupling, coherences and phases between upper and deep streamfunctions (SSH_bcb and SSH_ref, respectively) were estimated using the averaged periodogram method of Welch (1967) (256-day length segment with 50% overlap). Upper and deep streamfunctions are coherent over large portions of the array for frequencies between $1/64 \text{ d}^{-1}$ and $1/32 \text{ d}^{-1}$. Figure

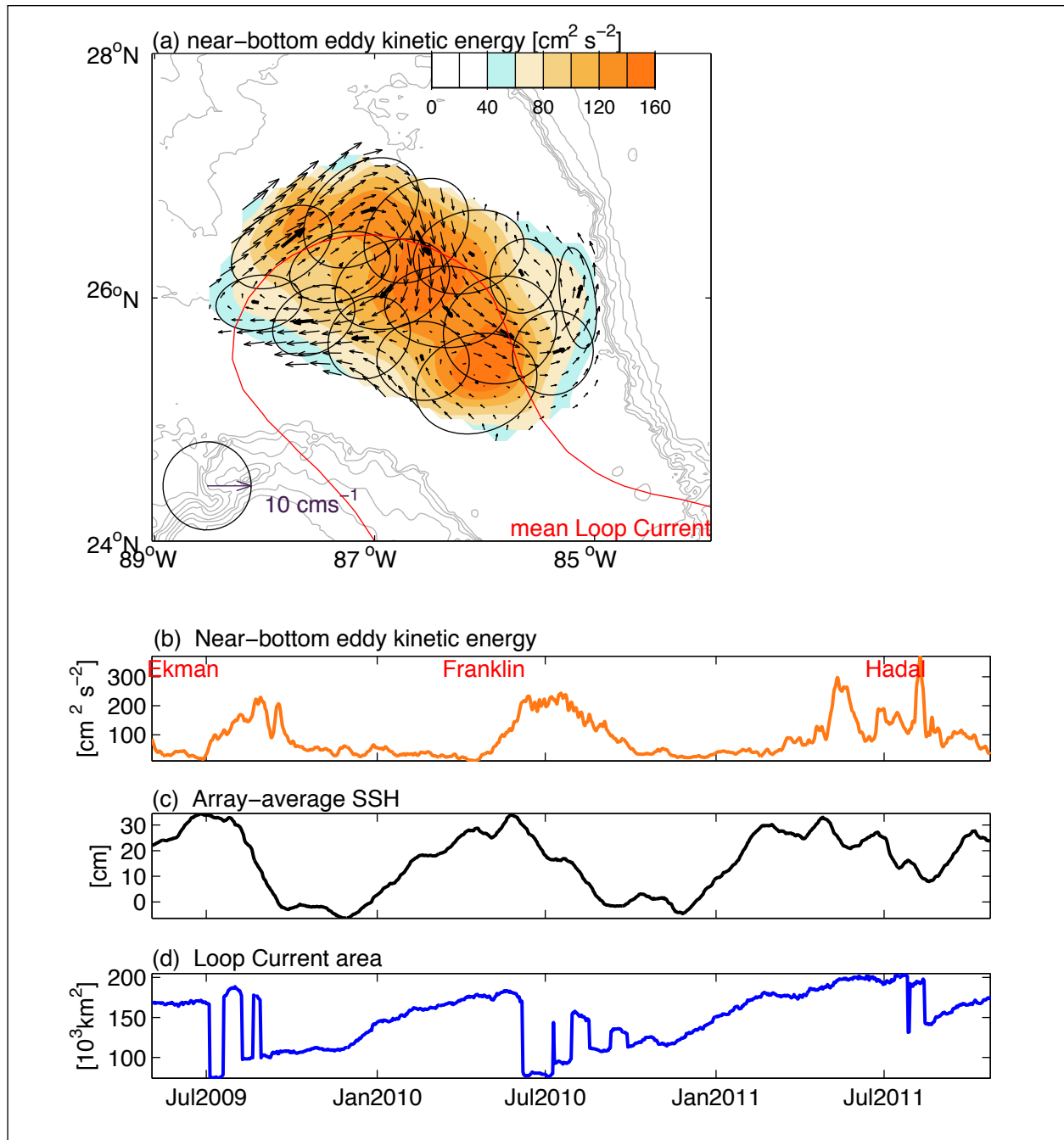


Figure 4.5-1. (a): Near-bottom mapped and directly measured mean currents (thin and bold vectors, respectively). Standard deviation ellipses superimposed on the time-mean near-bottom eddy kinetic energy (color-bar, $\text{cm}^2 \text{s}^{-2}$). Scale for vectors and ellipses shown in lower left corner. Red line denotes the mean Loop Current position defined by the CCAR-SSH 17-cm contour. Bathymetry plotted with gray contours every 500 m depth. Time mean is taken over the 30-month experiment duration from 3 May 2009 through 23 October 2011. (b): Time series of array-averaged near-bottom eddy kinetic energy ($\text{cm}^2 \text{s}^{-2}$). (c): Time series of array-averaged CCAR-SSH. (d): Loop Current area in units of 10^3 km^2 .

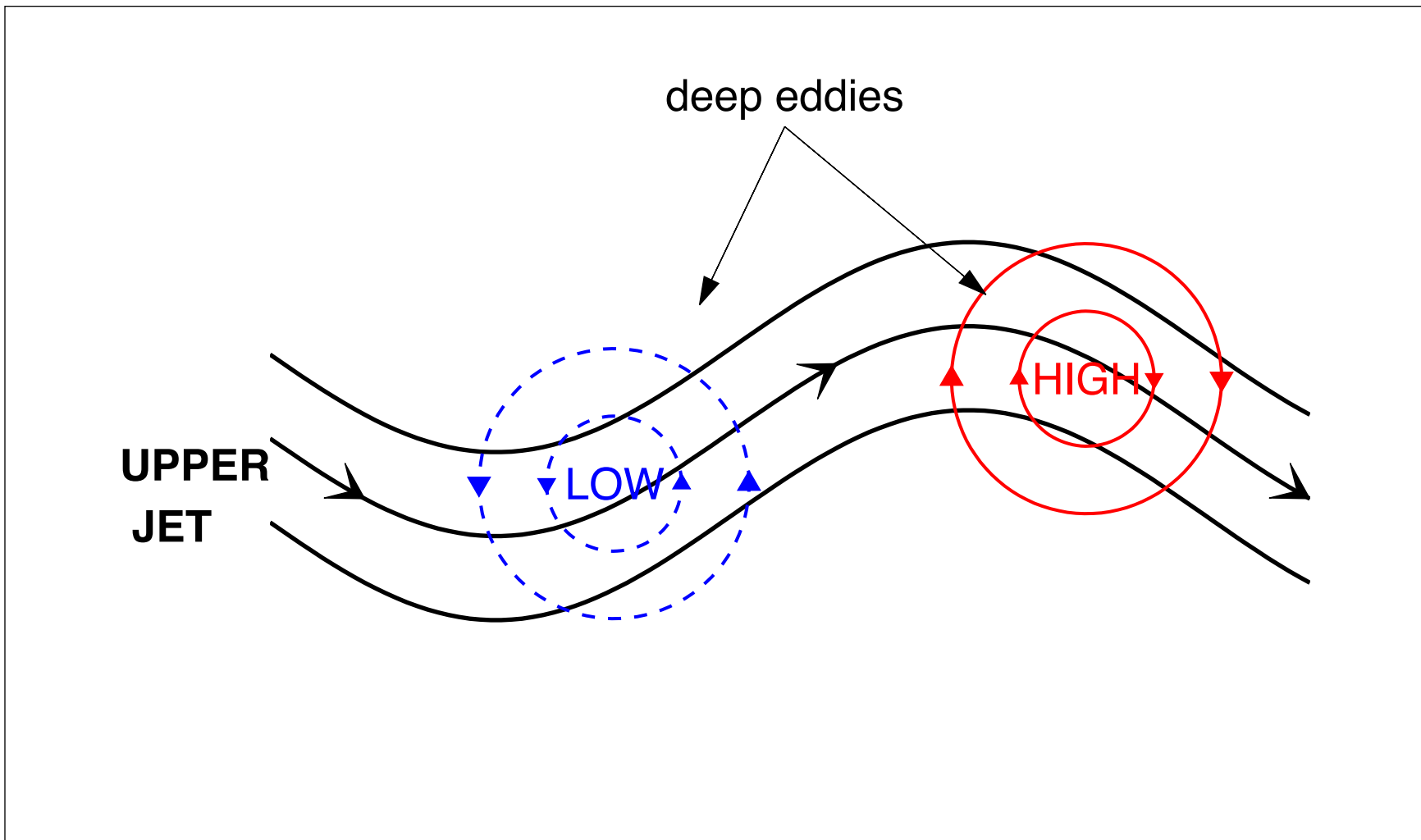


Figure 4.5-2. Schematic representation of the characteristic phase offset between upper and lower-layer cyclonic or anticyclonic perturbations that favor baroclinic instability. A meander trough and crest propagate east along the upper eastward baroclinic jet (bold black contours). Leading the upper trough is a deep cyclone (thin dashed blue contours); leading the upper crest is a deep anticyclone (thin red contours). The phase offset (vertical tilt of the low-pressure centers and the high-pressure centers, respectively) would favor meander growth. Reproduced from Donohue et al. (2006).

4.5-3 shows the spatial pattern of coherence and phase for three frequencies within this band. A tongue of high coherence extends from the northeast trending south-southwest toward the central portion of the array. Two additional peaks occur, one near the base of the Mississippi Fan and another in the southeastern corner. Where statistically coherent, the phase offset is such that the deep leads the upper. Phase estimates range between 60 and 150 degrees. Frequencies outside the band $1/64 \text{ d}^{-1}$ and $1/32 \text{ d}^{-1}$ do not show statistically significant coherence between upper and deep. This spectral approach characterizes the overall mean statistics, yet each LC eddy shedding event differs, e.g., location of final separation, number of brief detachments that precede the separation, location of the LC within the Gulf and within the array. In the remainder of the discussion, the focus is on each LC eddy shedding event separately, as case studies.

To illustrate the evolution of LC eddy-shedding events and the relationship between upper and deep, maps of upper and deep streamfunction were plotted with a five-day interval. In each plot, mapped baroclinic SSH referenced to the bottom (SSH_bcb, filled colored contours) is embedded within altimetric SSH that covers the broader region. The 17-cm contour denotes the location of the LC and LC-eddy fronts. The deep-pressure fields (deep ref streamfunction) are expressed in centimeters of water height as SSH_ref, so that relative strengths of the upper (bcb) and deep (ref) fields are evident. Mapped SSH_ref reveals the presence of deep cyclones (blue contours) and deep anticyclones (red contours). Two sets are provided for each shedding event: full frequency (3-day low pass quasigeostrophic), and 100 to 40-day band pass fields (Figures 4.5-4a-d for Ekman, 4.5-5a-d for Franklin and 4.5-6a-d for Hadal). The following discussion focuses upon the 100 to 40 day band where coherence between upper and deep was found to be high.

Eddy Ekman: 3 May to 31 August 2009

A long-wavelength meander developed along the northern edge of the LC in early July (Figure 4.5-4b). The 3 July map depicts two deep eddies labeled as cyclone A and anticyclone B. These two deep eddies are positioned on this date such that the deep anticyclone B leads an upper high and the deep cyclone A slightly leads an upper low. This classic pattern associated with baroclinic instability remains with varying vertical phase-tilt as the meander and deep eddies propagate together anticyclonically along the LC periphery from 3 July to 27 August. While the amplitude of deep cyclone A remains nearly constant during this interval, deep anticyclone B's strength modulates. Anticyclone B intensifies from 8 to 18 July, remains constant in strength until 28 July, then weakens over the next 10 days. A slight re-amplification occurs 27 August. On 23 July (Figure 4.5-4d), another deep cyclone labeled C, located on the Mississippi Fan, begins to develop. It is positioned slightly downstream of a developing upper trough. This trough and deep cyclone C jointly intensify 23 July through 22 August. During this interval, the trough deepens to nearly pinch off the neck of the LC, and the vertical phase tilt gets smaller as deep cyclone C becomes nearly vertically aligned under the trough. By 27 August, the phasing of deep leading upper no longer exists, Eddy Ekman is nearly separated, and deep cyclone C has weakened and subsequently propagates southwestward out of the array.

Eddy Franklin: 15 February to 14 September 2010

Similar to Eddy Ekman, during the formation of Eddy Franklin, the signature vertical phase tilts of baroclinic instability are present. This case study includes upper and deep events leading to an

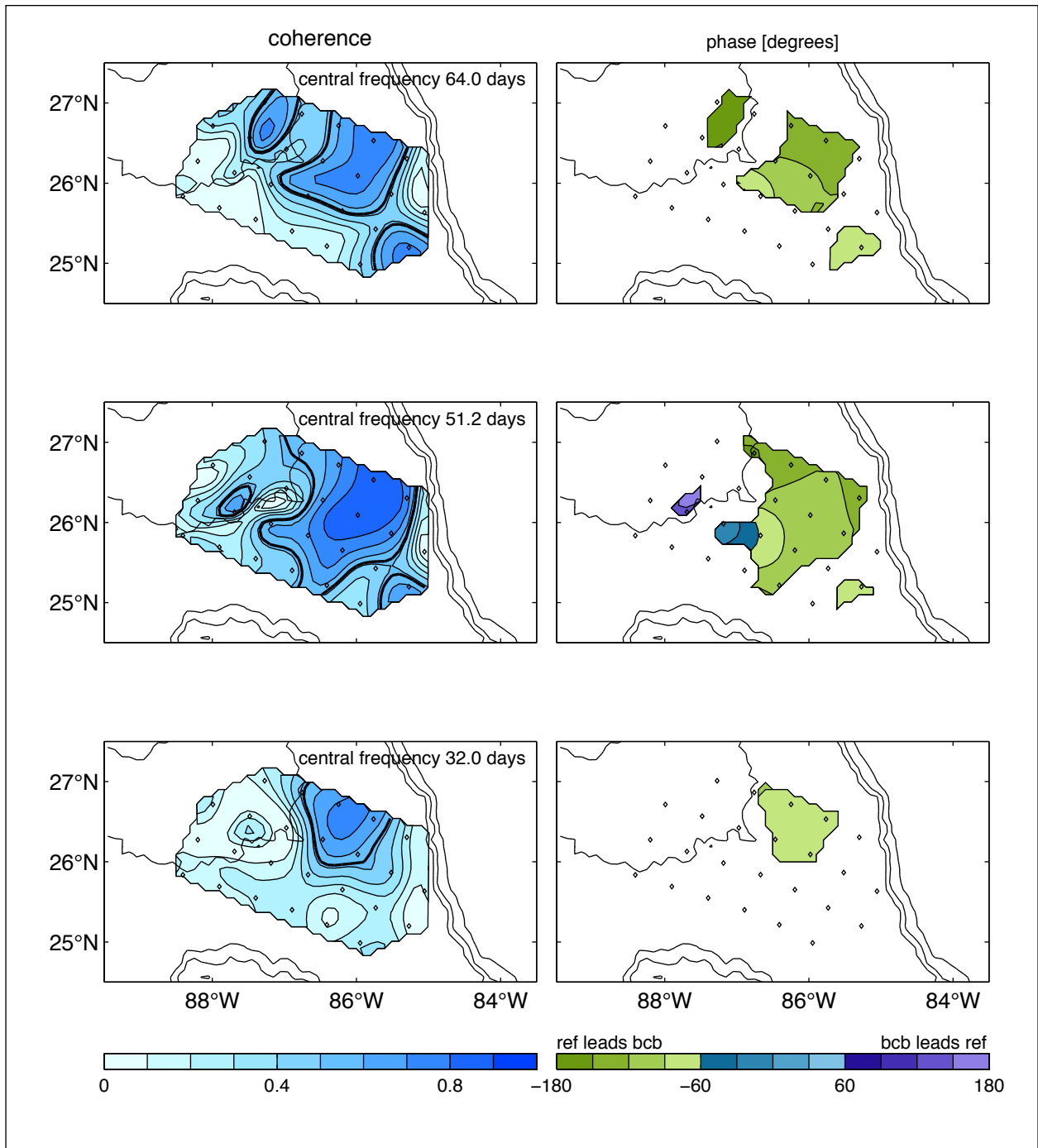


Figure 4.5-3. Coherence (left) and phase (right) between upper, SSH_bcb, and lower, SSH_ref, streamfunction for three frequency bands: top ($1/64 \text{ d}^{-1}$), middle ($1/51.2 \text{ d}^{-1}$), and bottom ($1/32 \text{ d}^{-1}$), estimated using the averaged periodogram method of Welch (1967) (256-day length segment with 50% overlap). Phase (in degrees) contoured where coherence exceeds 95% confidence limits denoted by the thick black contour in the coherence maps. Negative phase indicates that deep leads upper. PIES locations shown by black diamonds. Bathymetry (thin black line) contoured every 1000-m depth.

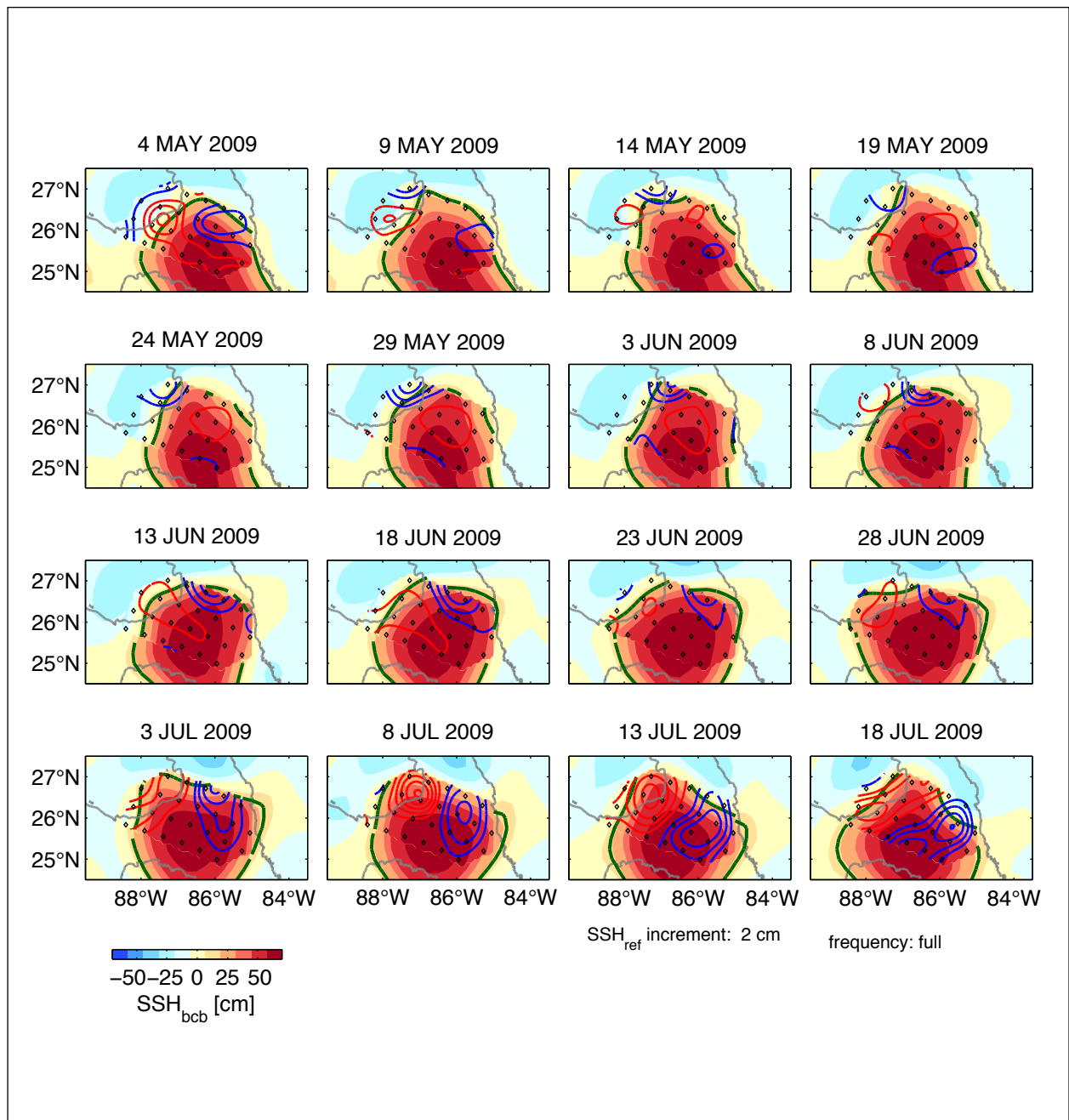


Figure 4.5-4a. Loop Current eddy-shedding event Ekman, 4 May through 18 July 2009. Maps of baroclinic SSH referenced to the bottom (SSH_{bc_b}) embedded within altimetric SSH (filled color contours; colorbar and contour interval on the bottom left). Maps shown sequentially left to right, top to bottom at 5-day intervals. The 17-cm contour (green, SSH_{bc_b} within array, altimetric SSH outside array) denotes the location of the Loop Current. Mapped reference level SSH (SSH_{ref}) reveals the presence of deep cyclones (blue contours) and deep anticyclones (red contours) contoured every 2 cm. Diamonds denote PIES sites. Grey lines denote the 3000-m depth contour. The frequency band of the SSH data is listed below the bottom right panel.

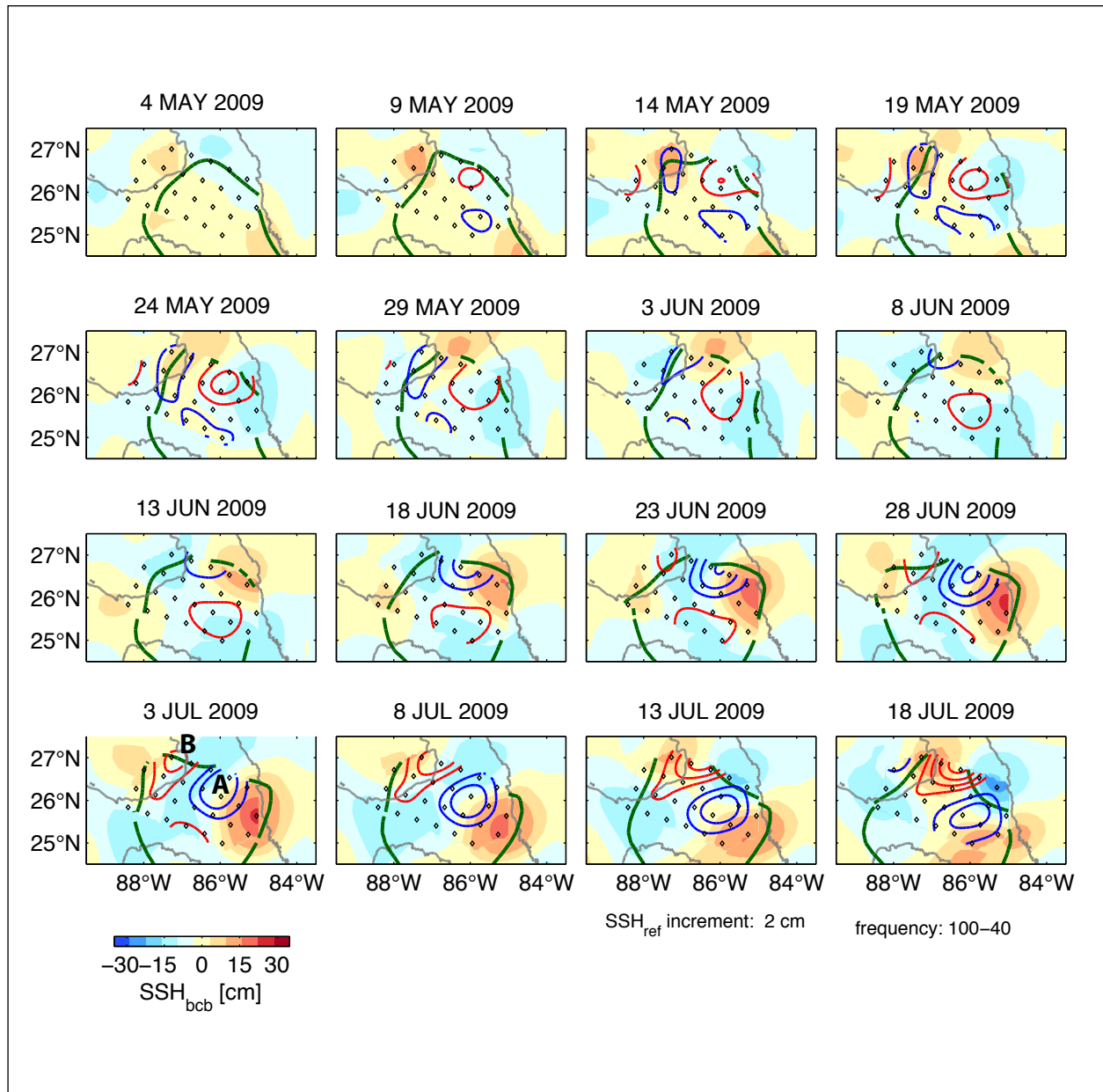


Figure 4.5-4b. Loop Current eddy-shedding event Ekman, 4 May through 18 July 2009. Maps of 100-40 day band-passed baroclinic SSH referenced to the bottom (SSH_{bcb}) embedded within altimetric SSH (filled color contours; colorbar and contour interval on bottom left). Maps shown sequentially left to right, top to bottom at 5-day intervals. The 17-cm contour (green, SSH_{bcb} within array, altimetric SSH outside array) denotes the location of the Loop Current. Mapped 100-40 day band-passed reference level SSH (SSH_{ref}) reveals the presence of deep cyclones (blue contours) and deep anticyclones (red contours) contoured every 2 cm. Diamonds denote PIES sites. Grey lines denote the 3000-m depth contour. The frequency band of the SSH data is listed below the bottom right panel. The 3 July map indicates deep cyclone A and deep anticyclone B, discussed in the text.

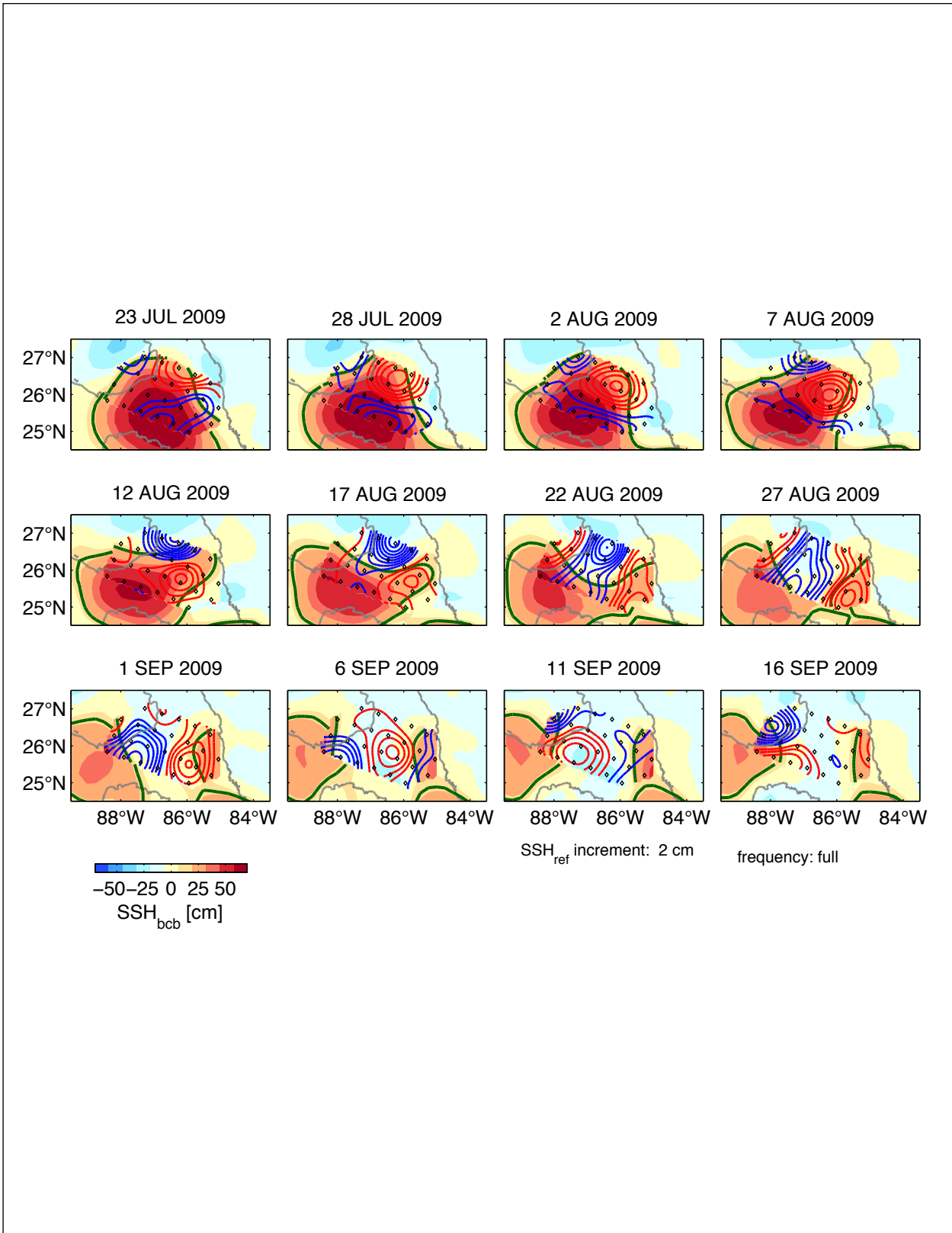


Figure 4.5-4c. Loop Current eddy-shedding event Ekman, 23 July through 16 September 2009. (full frequency as in Figure 4.5-4a).

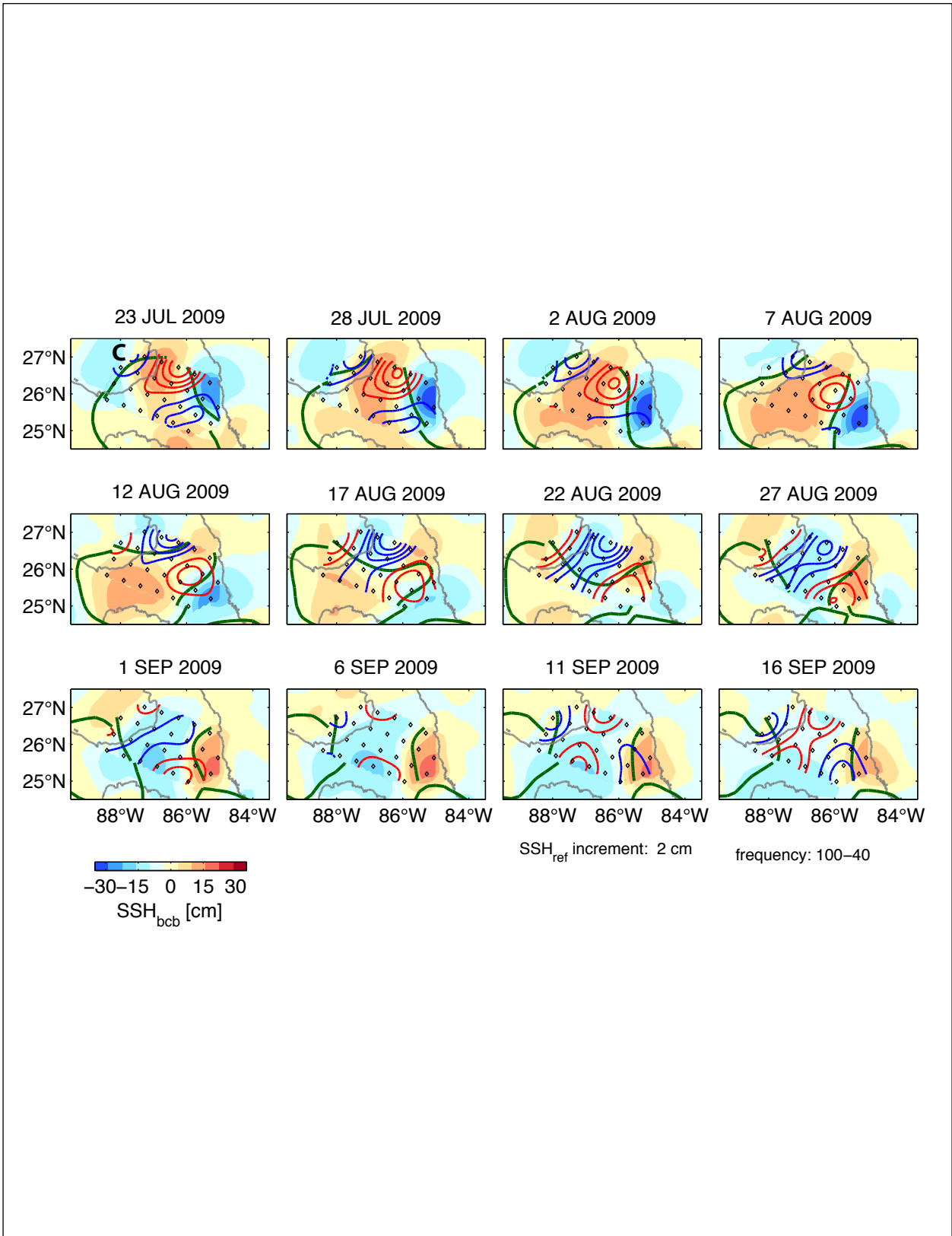


Figure 4.5-4d. Loop Current eddy-shedding event Ekman, 23 July through 16 September 2009 (100-40 days frequency as in Figure 4.5-4b).

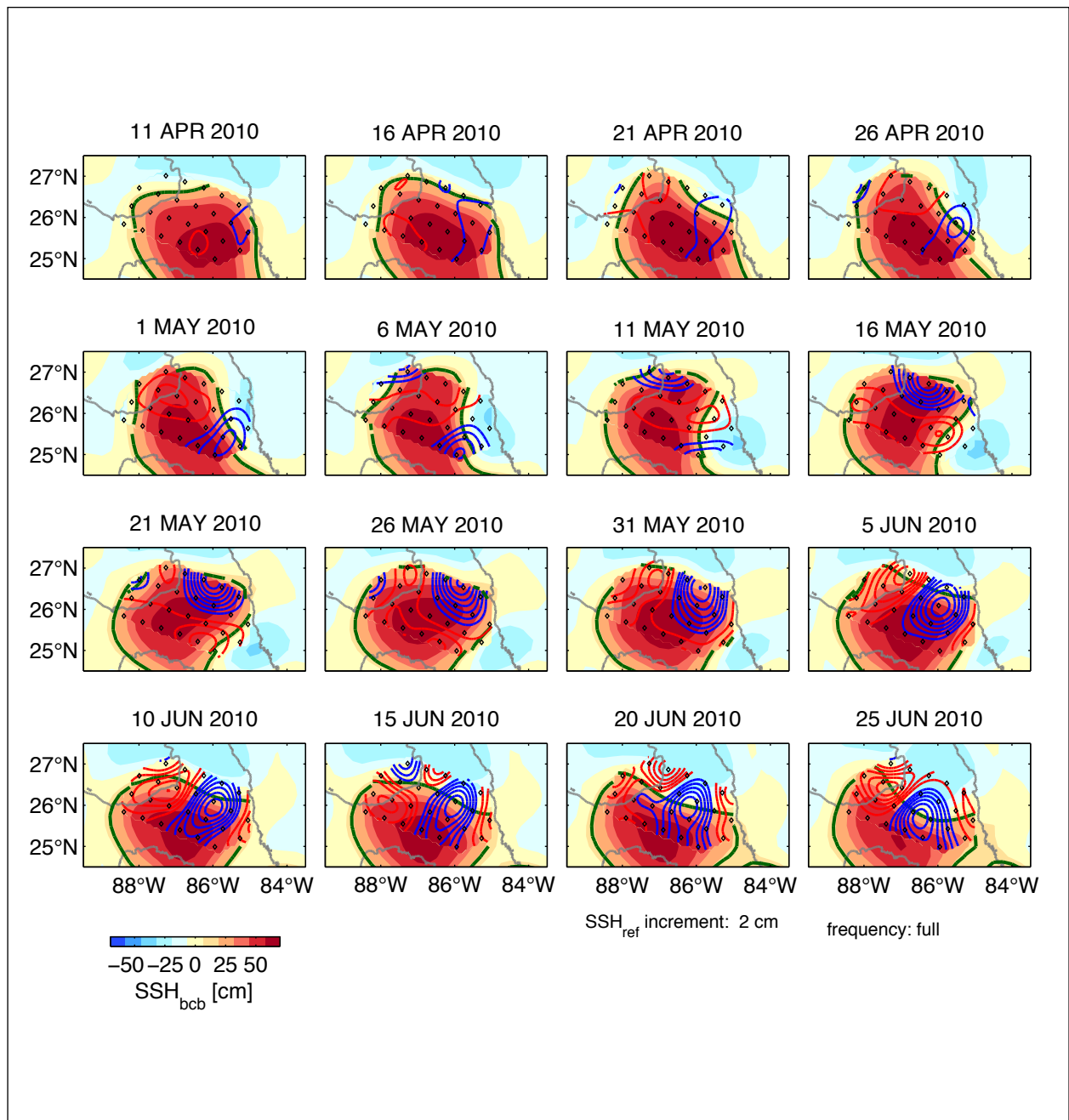


Figure 4.5-5a. Loop Current eddy-shedding event Franklin, 11 April through 25 June 2010. Maps of baroclinic SSH referenced to the bottom (SSH_{bcb}) embedded within altimetric SSH (filled color contours; colorbar and contour interval on bottom left). Maps shown sequentially left to right, top to bottom at 5-day intervals. The 17-cm contour (green, SSH_{bcb} within array, altimetric SSH outside array) denotes the location of the Loop Current. Mapped reference level SSH (SSH_{ref}) reveals the presence of deep cyclones (blue contours) and deep anticyclones (red contours) contoured every 2 cm. Diamonds denote PIES sites. Grey lines denote the 3000-m depth contour. The frequency band of the SSH data is listed below the bottom right panel.

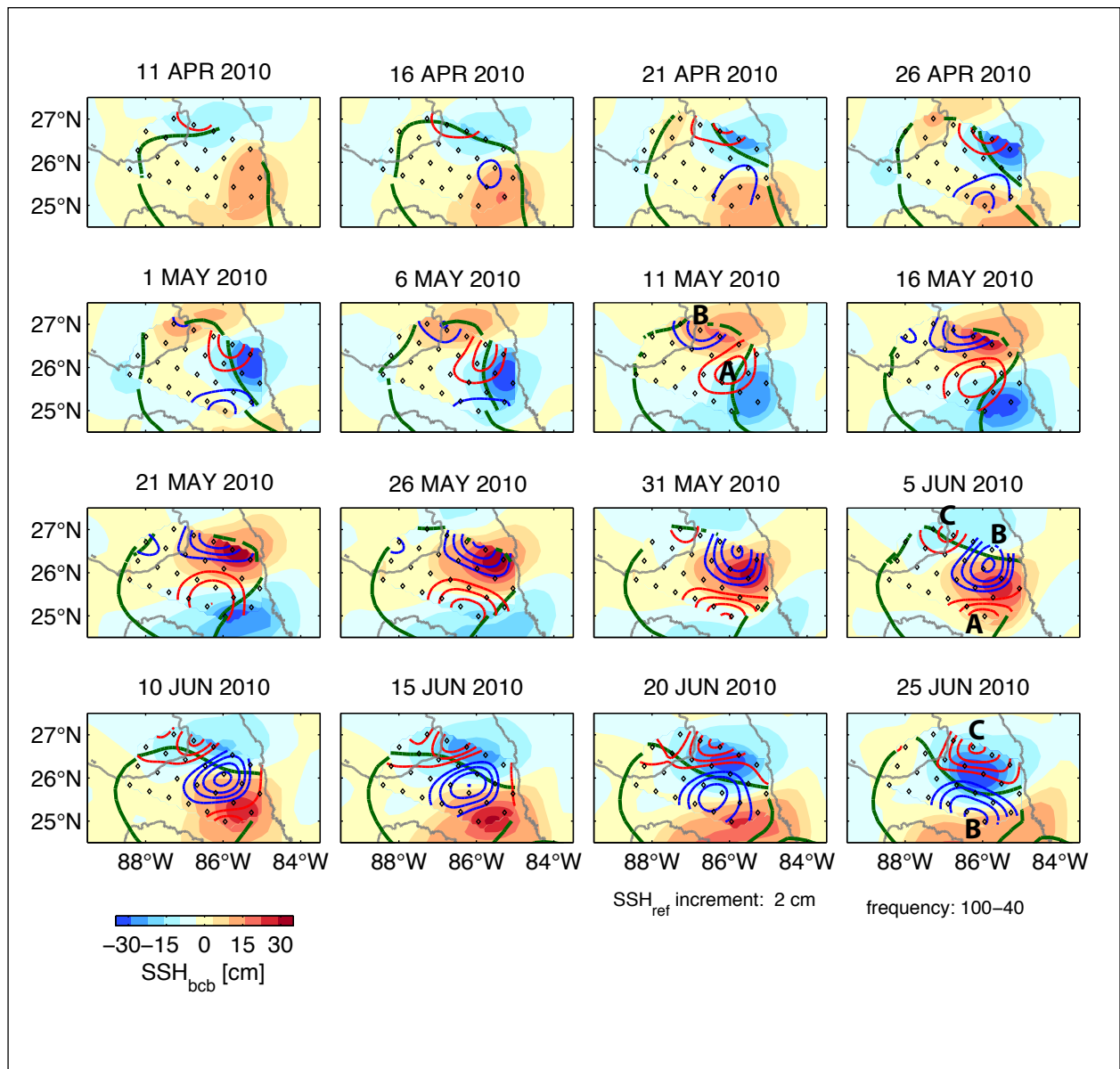


Figure 4.5-5b. Loop Current eddy-shedding event Franklin, 11 April through 25 June 2010. Maps of 100-40 day band-passed baroclinic SSH referenced to the bottom (SSH_bcb) embedded within altimetric SSH (filled color contours; colorbar and contour interval on bottom left). Maps shown sequentially left to right, top to bottom at 5-day intervals. The 17-cm contour (green, SSH_bcb within array, altimetric SSH outside array) denotes the location of the Loop Current. Mapped 100-40 day band-passed reference level SSH (SSH_ref) reveals the presence of deep cyclones (blue contours) and deep anticyclones (red contours) contoured every 2 cm. Diamonds denote PIES sites. Grey lines denote the 3000-m depth contour. The frequency band of the SSH data is listed below the bottom right panel. The 11 May map indicates deep anticyclone A and deep cyclone B discussed in the text. The 5 June map indicates deep anticyclone C discussed in the text.

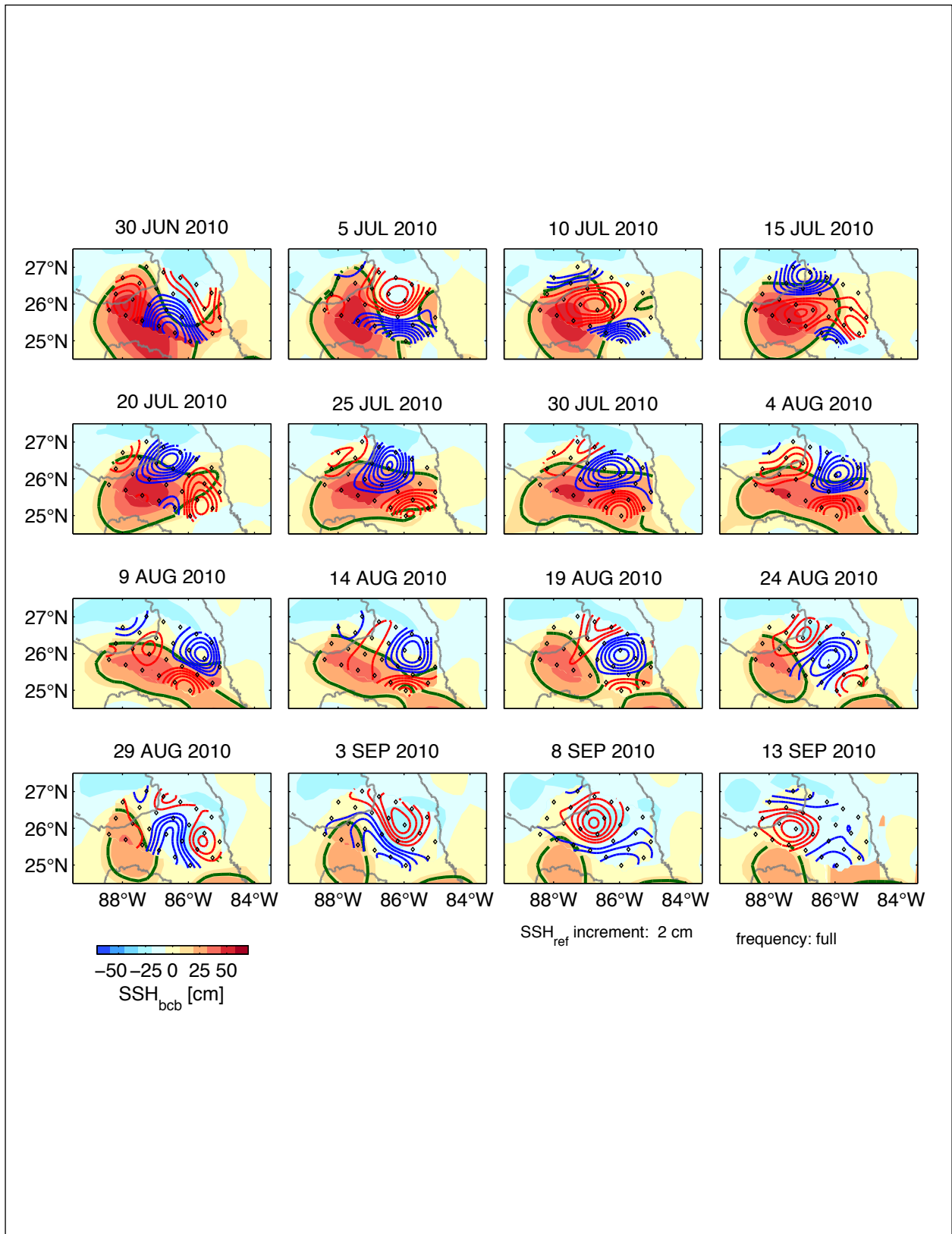


Figure 4.5-5c. Loop Current eddy-shedding event Franklin, 30 June through 13 September 2010 (full frequency as in Figure 4.5-5a).

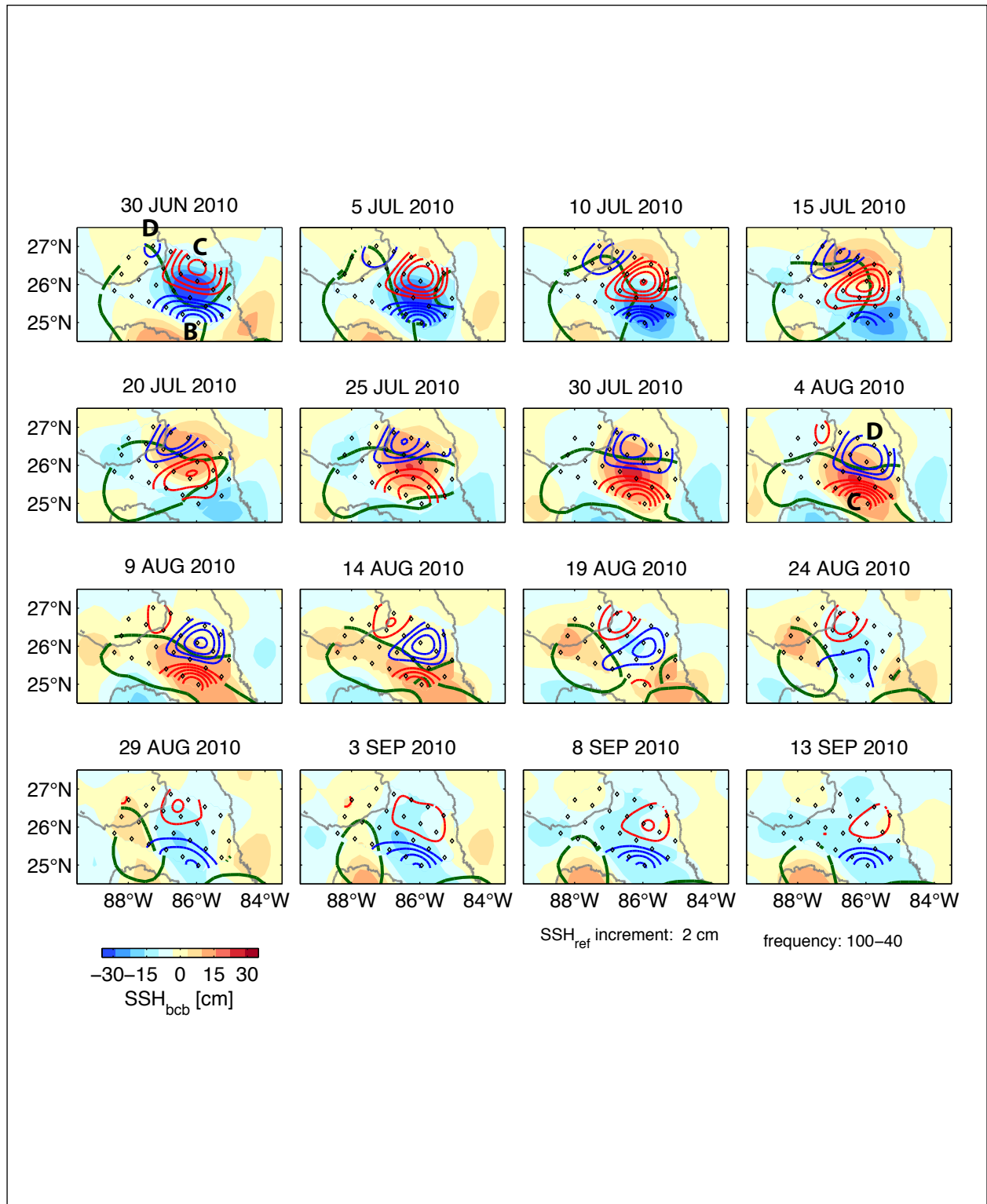


Figure 4.5-5d. Loop Current eddy-shedding event Franklin, 30 June through 13 September 2010. The 30 June map indicates deep cyclones B, D and deep anticyclone C discussed in the text. The 4 August map also indicates deep cyclone D and deep anticyclone C (100-40 day frequency as in Figure 4.5-5b).

eddy detachment in early July 2010 and final separation in early August 2010. Consider the large-scale LC meander that is developing in early May 2010. The 11 May map (Figure 4.5-5b) shows two deep eddies, anticyclone A and cyclone B. They are positioned such that the deep anticyclone resides downstream of and leads the upper crest. The deep cyclone B resides upstream of that upper crest, and in subsequent days (5 June to 25 June) cyclone B intensifies as it leads a developing upper trough within the array. Anticyclone C comes into view 5 June with an upper crest following close behind it. During June, the B and C deep eddies and their slightly trailing upper meander trough and crest propagate downstream around the Loop. The trough and deep eddy B jointly intensify, and by early July (Figure 4.5-5d) the LC neck pinches off into a short-lived detachment. The 30 June map shows three deep eddies; a deep cyclone, labeled D, appears near the Mississippi Fan. The northern limit of the array leaves the question open as to whether these deep eddies (A, B, C or D) initially propagate into the array from further north, or whether they originate upstream along the LC front. During July, deep eddies C and D and their slightly trailing upper meander crest and trough propagate downstream around the LC. For example, on 10 and 15 July 2010, the vertical phase tilt is evident, and the features jointly intensify. Eventually, the trough ‘necks down’ again, and eddy separation occurs in August. The recurrent structure observed in these map sequences is that as deep eddies propagate through the array they lead their upper counterpart. For example, from 5 June to 10 July (Figures 4.5-5b and 4.5-5d), deep cyclone B leads an upper cyclone (trough); from 15 July to 4 August, deep anticyclone C leads an upper anticyclone. Finally, we note that during the Franklin event, the largest amplitude deep eddies occur during the early to mid-July detachment, prior to the final separation of a relatively small LC eddy in August.

Eddy Hadal: 1 March to 14 September 2011

Upper-deep coupling with the vertical phase tilt of baroclinic instability also characterizes the Hadal shedding cycle. Figures 4.5-6b and 4.5-6d show that during Hadal, long-wavelength meanders develop along the eastern side of an extended LC. The eastern side of the LC runs through the middle of the array during much of this time, and the associated deep eddies are relatively well centered within the observational window. This case study will follow a sequence of four deep eddies, anticyclones A and C, and cyclones B and D. Their propagation starts southward and downstream along the LC, and as they intensify they turn southwestward across the neck of the LC. As seen in our Ekman and Franklin case studies, while these deep eddies translate along the LC, they lead their upper counterpart as they jointly develop and tend to constrict the neck. For example, on 13 April, deep anticyclone A sits just downstream of an upper crest (high SSH_bcb), and during the subsequent 15 days the upper and deep highs jointly intensify. Shortly after that, on 3 May deep cyclone B leads an upper trough (low SSH_bcb), and both intensify during the subsequent 20 days. Immediately following that, on 23 May, the deep anticyclone C leads an upper crest downstream, intensifying during the next 20-30 days to about 22 June. Deep-cyclone D follows this train of upper-deep coupling interactions. From 22 June to 17 July 2011 deep-cyclone D leads and jointly develops with an upper low SSH_bcb and trough, constricting the LC neck greatly. Shortly afterward Hadal separates. Limits to the growth phase of the upper and deep perturbations appears to occur where the deep eddy trajectory turns to the southwest, not following the downstream path of the upper jet. Subsequently, their vertical phase tilt becomes non-conducive to baroclinic instability, and they jointly decay. Deep-cyclone B decays after 28 May together with its upper-strong low. Analogously deep-anticyclone C decays after 22 June together with its upper strong high. Similar

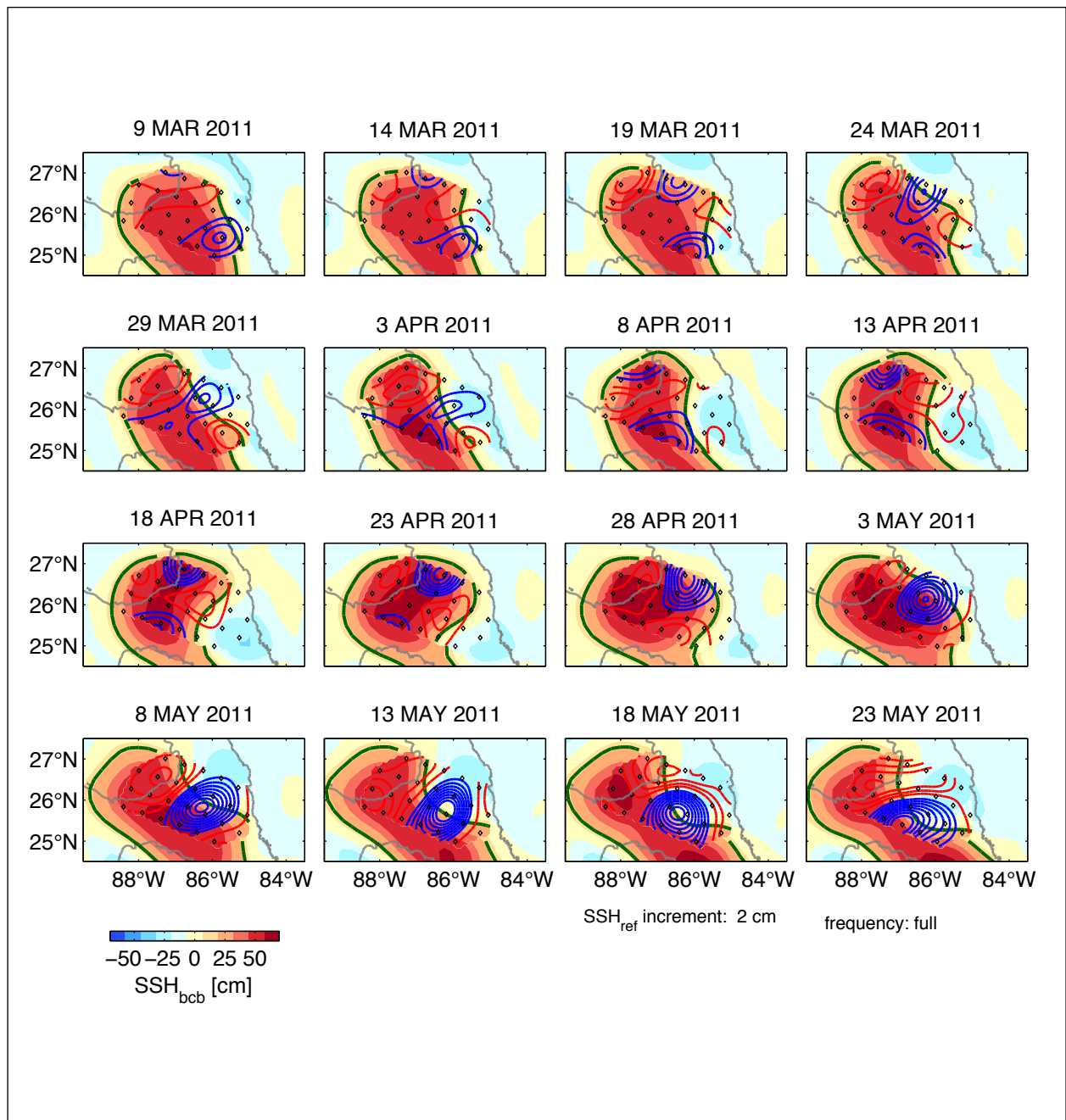


Figure 4.5-6a. Loop Current eddy-shedding event Hadal, 9 March through 23 May 2011. Maps of baroclinic SSH referenced to the bottom (SSH_{bc}) embedded within altimetric SSH (filled color contours; colorbar and contour interval on bottom left). Maps shown sequentially left to right, top to bottom at 5-day intervals. The 17-cm contour (green, SSH_{bc} within array, altimetric SSH outside array) denotes the location of the Loop Current. Mapped reference level SSH (SSH_{ref}) reveals the presence of deep cyclones (blue contours) and deep anticyclones (red contours) contoured every 2 cm. Diamonds denote PIES sites. Grey lines denote the 3000-m depth contour. The frequency band of the SSH data is listed below the bottom right panel.

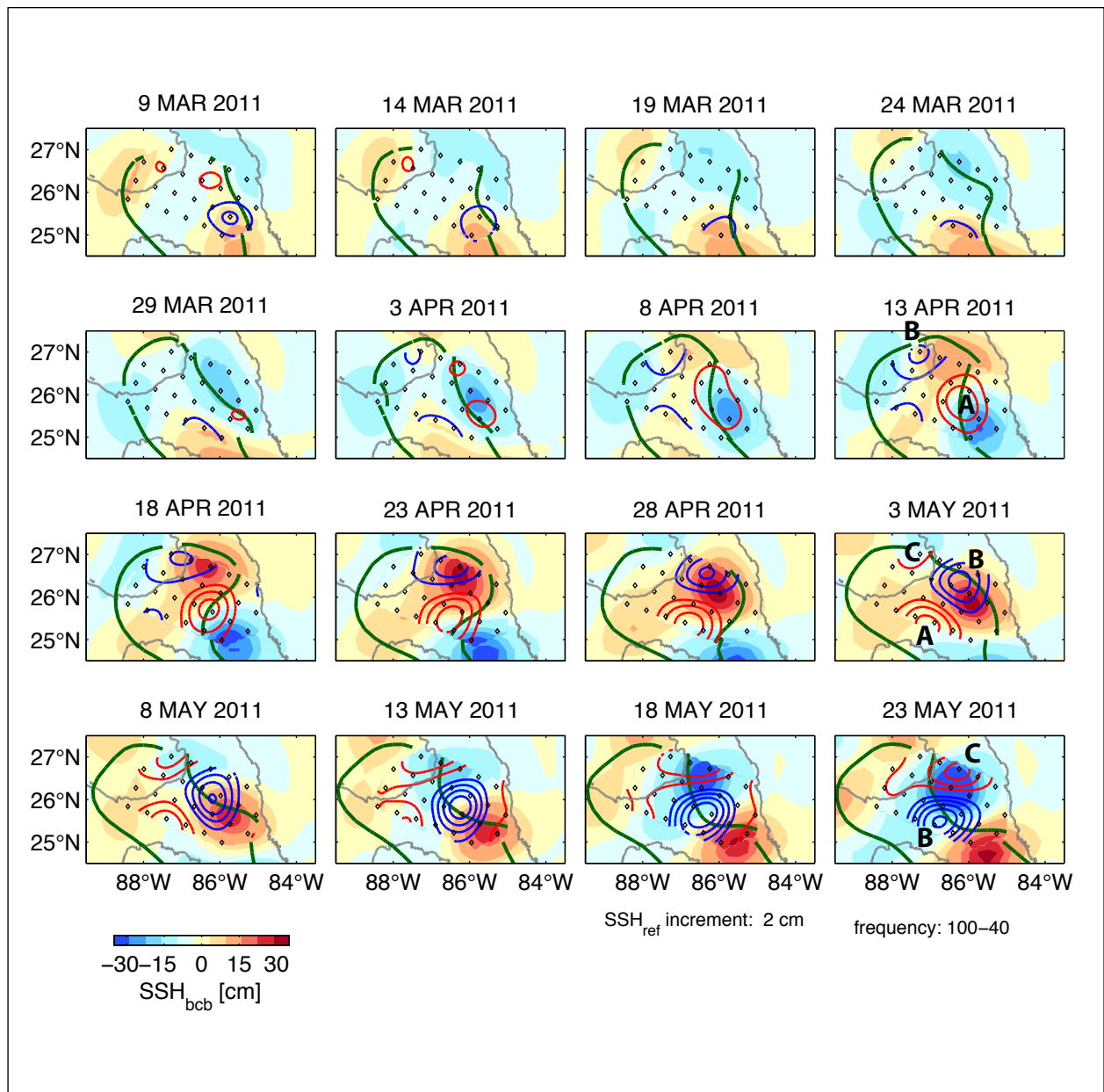


Figure 4.5-6b. Loop Current eddy-shedding event Hadal, 9 March through 23 May 2011. Maps of 100-40 day band-passed baroclinic SSH referenced to the bottom (SSH_{bc}) embedded within altimetric SSH (filled color contours; colorbar and contour interval on bottom left). Maps shown sequentially left to right, top to bottom at 5-day intervals. The 17-cm contour (green, SSH_{bc} within array, altimetric SSH outside array) denotes the location of the Loop Current. Mapped 100-40 day band-passed reference level SSH (SSH_{ref}) reveals the presence of deep cyclones (blue contours) and deep anticyclones (red contours) contoured every 2 cm. Diamonds denote PIES sites. Grey lines denote the 3000-m depth contour. The frequency band of the SSH data is listed below the bottom right panel. The 13 April, 3 May and 23 May maps indicate deep anticyclone A, deep cyclone B, and deep anticyclone C, respectively.

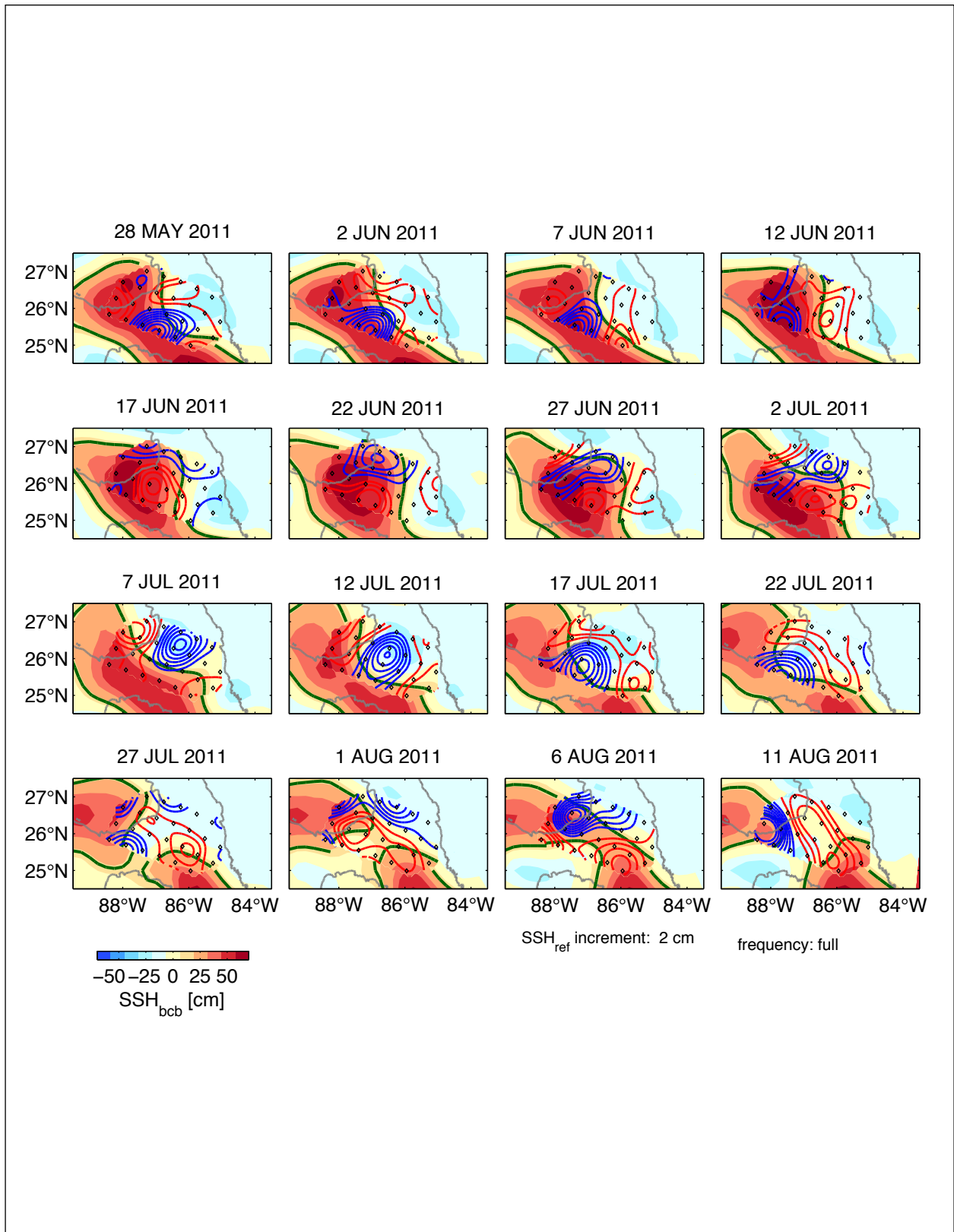


Figure 4.5-6c. Loop Current eddy-shedding event Hadal, 28 May through 11 August 2011 (full frequency as in Figure 4.5-6a).

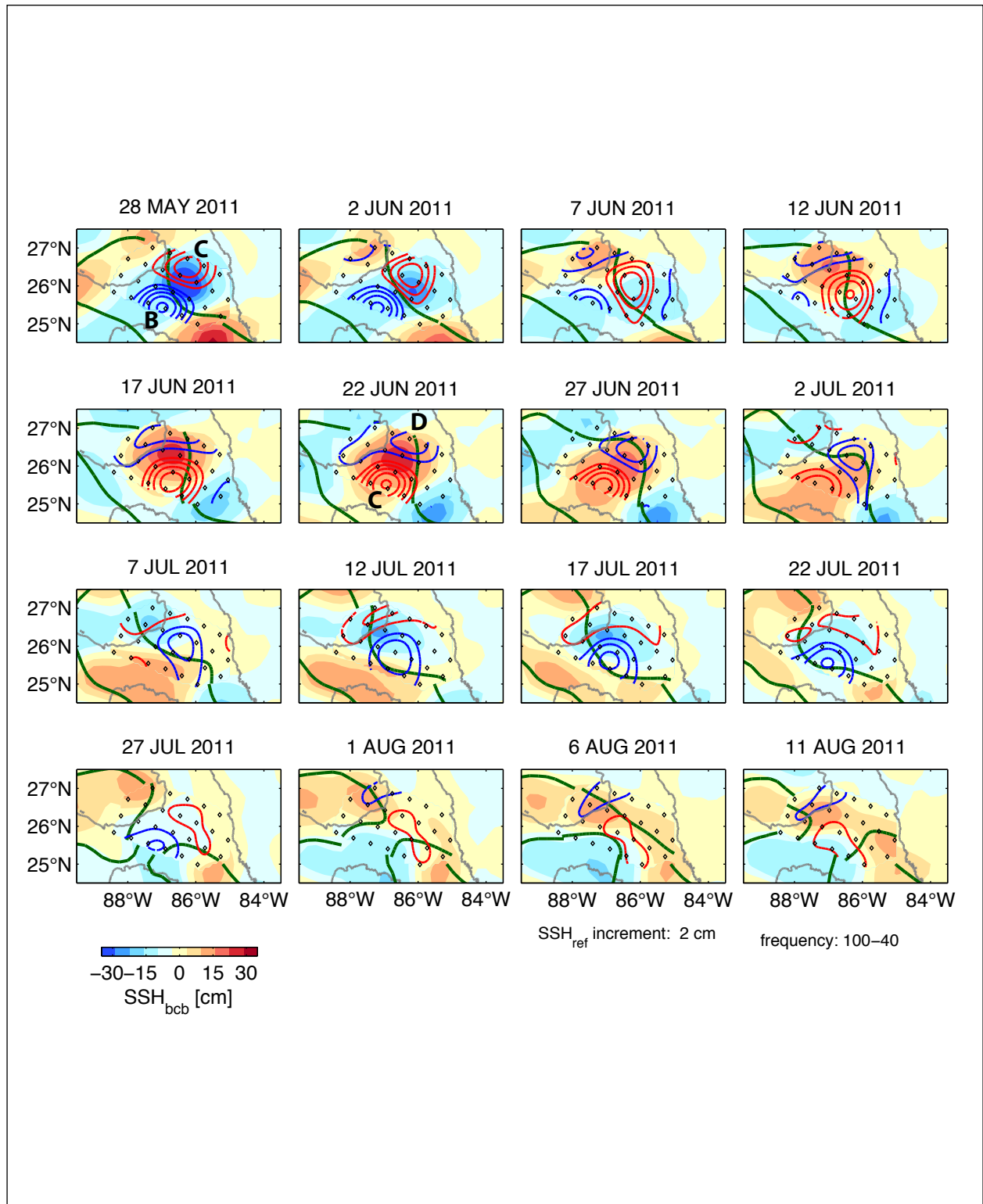


Figure 4.5-6d. Loop Current eddy-shedding event Hadal, 28 May through 11 August 2011. The 28 May map indicates deep cyclone B and deep anticyclone C discussed in the text. The 22 June map indicates deep cyclone D discussed in the text (100-40 day frequency as in Figure 4.5-6b).

to the Franklin event, large amplitude deep eddies and joint intensification (mid-April through late June) occur prior to the final eddy separation (mid-August).

In summary, our case studies of upper and deep coupling reveal several interesting aspects of upper-deep coupling:

- Joint intensification is intermittent, lasting only tens of days while the vertical phase tilt is optimal for baroclinic growth.
- Due to the limited spatial domain of the array, we cannot unambiguously distinguish between locally generated deep eddies and external deep eddies that may enter and intensify when they encounter favorable phasing with the upper thermocline waters.
- Strongest upper-deep interaction and the most energetic deep eddies can occur well in advance of the final eddy separation. A train of upper-deep eddy interactions precedes each eddy separation.

4.5.1 Eddy Potential Energy

The terms in the time-mean eddy potential-energy budget are evaluated so as to diagnose the role of eddies in the system. The goal is to show that eddies extract potential energy from the mean field (stored in the sloping isopycnals of the LC) and ultimately convert that energy to eddy kinetic energy.

Following Cronin and Watts (1996), a quasigeostrophic framework (small Rossby number) is assumed to be valid for our diagnostics. Temperature will be a proxy for density: $\rho = \rho_o(1 - \alpha T)$, where α is an effective thermal expansion coefficient ($10^{-4} \text{ }^\circ\text{C}^{-1}$). Potential energy budget terms are evaluated near 400 m depth. This avoids the near-surface depth of Subtropical Underwater where otherwise the role of salinity would have to be independently included when calculating density.

In a Boussinesq incompressible fluid, the temperature equation is:

$$\overline{\mathbf{u}} \cdot \nabla \overline{T} = -\overline{w} \theta_z - \nabla \cdot \overline{\mathbf{u}'T'}, \quad (4.5.1)$$

where $\mathbf{u}=(u,v)$ is geostrophic velocity, T is temperature, w is vertical velocity and θ_z is the regional background vertical temperature gradient. Overbars indicate a time mean and primes indicate deviation from the mean. In the following discussion, $\mathbf{u}'T'$ is referred to as ‘eddy heat flux’ since eddy temperature flux multiplied by density and specific heat at constant pressure ($\rho_o C_p$) is a heat flux. Equation 4.5.1 states that mean horizontal advection is balanced by mean vertical advection and the divergence of horizontal eddy heat flux. Note that the dynamically important part of the eddy heat flux term is the divergent component of eddy heat flux:

$$\mathbf{u}' \cdot \nabla T' = \nabla \cdot \mathbf{u}'T'. \quad (4.5.2)$$

Eddy heat flux can be decomposed into rotational and divergent components by Helmholtz' theorem. The rotational component merely recirculates heat whereas the divergent component provides the net lateral heat flux that transfers potential (baroclinic) energy into eddies. It is a challenge, numerically and observationally to isolate these divergent eddy heat fluxes from the total eddy heat flux (see Griesel et al. (2009) for a recent discussion).

The approach will be to take advantage of the velocity vector decomposition, expressed as the baroclinic velocity relative to the bottom plus a bottom reference velocity, $\mathbf{u} = \mathbf{u}_{\text{bc}} + \mathbf{u}_{\text{ref}}$. Mean ψ_{bc} streamlines are nearly parallel to mean temperature contours and therefore do not advect mean temperature. Figure 4.5-7 shows the linear relationship between mean ψ_{bc} and mean T at 400 m within our array. The divergent component of the heat flux arises from the nearly depth-uniform reference current of which a component can cross the time-varying baroclinic LC front. The dynamically important heat flux is entirely contained in $\mathbf{u}'_{\text{ref}}T'$. Figure 4.5-8 shows the mean eddy heat fluxes for the three LC eddy-shedding events superimposed on temperature variance. Eddy heat flux is calculated three ways for this illustration, using the total eddy velocity ($\mathbf{u}'T'$), baroclinic eddy velocity ($\mathbf{u}'_{\text{bc}}T'$), and reference eddy velocity ($\mathbf{u}'_{\text{ref}}T'$). For each eddy event, $\mathbf{u}'T'$ has the largest magnitudes. As expected $\mathbf{u}'_{\text{bc}}T'$ circulates around temperature variance. $\mathbf{u}'_{\text{ref}}T'$ shows downgradient heat fluxes in all events with strongest fluxes along the eastern side of the LC.

The eddy potential energy budget in steady state is determined by multiplying the temperature equation by $g\alpha T'/\theta_z$,

$$0 = -\bar{\mathbf{u}} \cdot \nabla \frac{g\alpha}{2\theta_z} \overline{T'^2} - \overline{\nabla \cdot \mathbf{u}' \frac{g\alpha}{2\theta_z} T'^2} - \frac{g\alpha}{\theta_z} \overline{\mathbf{u}'T'} \cdot \nabla \bar{T} - g\alpha \overline{T'w'}. \quad (4.5.3)$$

where eddy potential energy is defined as

$$EPE = \frac{g\alpha}{2\theta_z} \overline{T'^2}. \quad (4.5.4)$$

Dividing by $\alpha g/\theta_z$ and rearranging yields,

$$\underbrace{\bar{\mathbf{u}} \cdot \nabla \frac{1}{2} \overline{T'^2}}_{MAP} + \underbrace{\nabla \cdot \mathbf{u}' \frac{1}{2} \overline{T'^2}}_{EAP} + \underbrace{\theta_z \overline{T'w'}}_{PKC} = \underbrace{-\overline{\mathbf{u}'T'} \cdot \nabla \bar{T}}_{BC}. \quad (4.5.5)$$

Equation 4.5.5 states that the horizontal down-gradient eddy heat flux (BC) is balanced by the mean advection of eddy potential energy (MAP), eddy advection of eddy potential energy (EAP) and the vertical down-gradient heat flux (PKC). In baroclinic instability, the eddy conversion term (BC) of mean potential energy to eddy potential energy is balanced by the eddy conversion of eddy potential to eddy kinetic energy (PKC).

If we decompose our velocity field as described above into the baroclinic-referenced-to-the-bottom and reference components, we can rewrite the eddy energy budget:

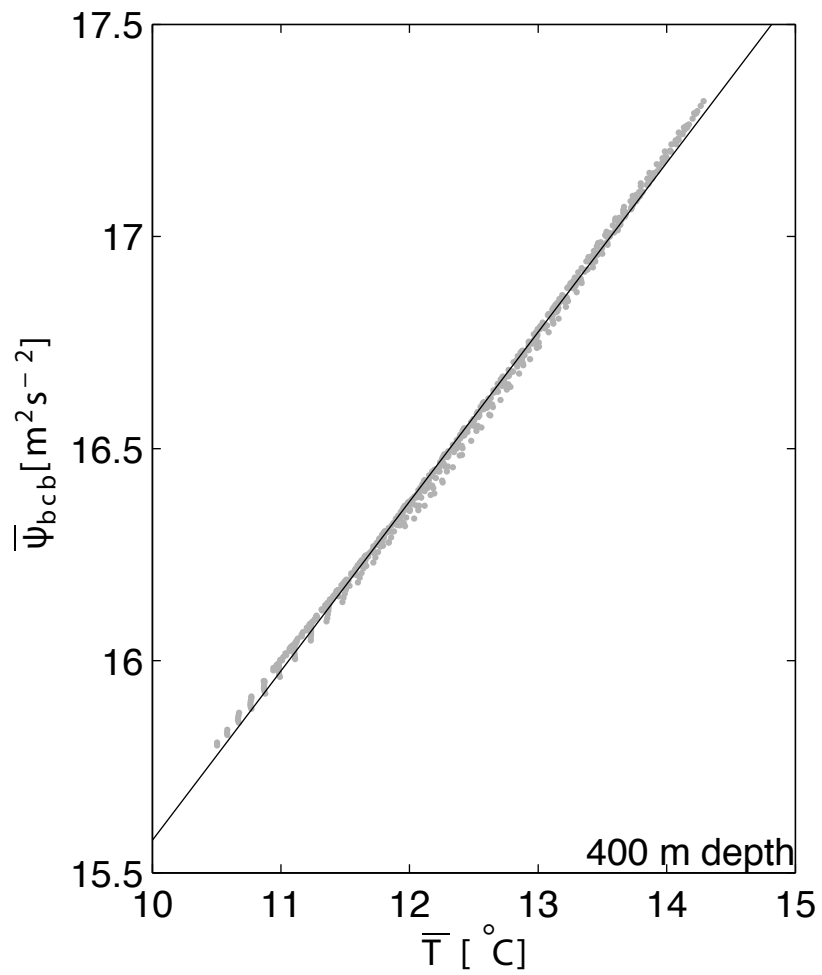


Figure 4.5-7. A linear relationship (black line) exists between mean ψ_{bcb} and mean T at 400 m (grey dots).

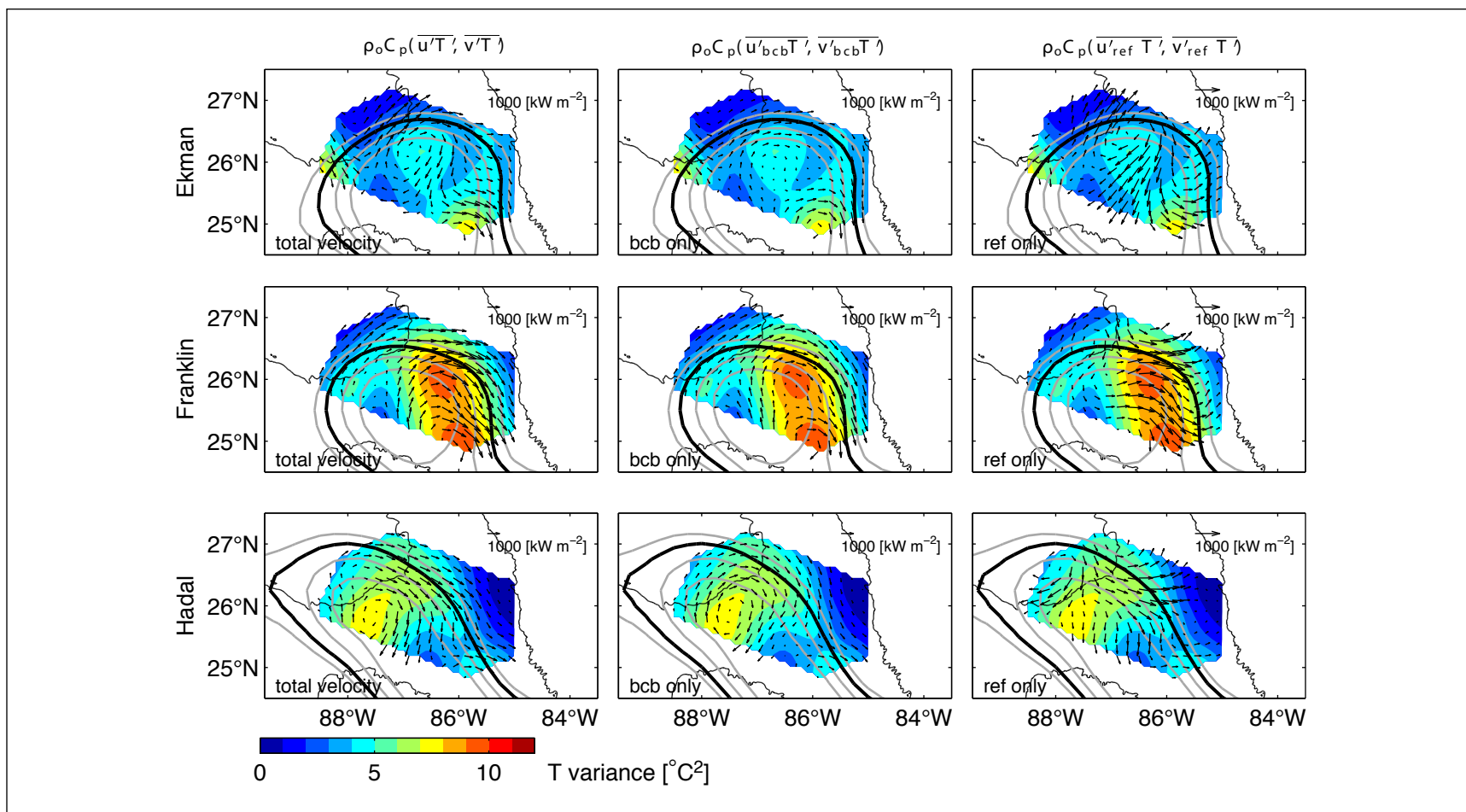


Figure 4.5-8. Eddy heat flux vectors at 400-m depth for the three LC eddy-shedding events superimposed on the 400-m depth temperature variance. Rows correspond to the LC eddy-shedding events: Ekman, 3 May through 31 August 2009 (top); Franklin, 15 February through 14 September 2010 (middle); Hadal, 1 March through 14 September 2011 (bottom). Columns correspond to the perturbation velocity used in the eddy heat flux calculation: total (left), baroclinic-referenced-to-the-bottom (center), reference (right). The bold black line denotes the mean position of the 17-cm altimeter-mapped SSH contour; grey contours indicate the 10, 17, 27, and 37-cm contour. The 3000-m isobath contoured with thin black line.

$$\underbrace{\overline{\mathbf{u}_{bc b}} \cdot \nabla \frac{1}{2} \overline{T'^2}}_{MAP_{bc b}} + \underbrace{\overline{\mathbf{u}_{ref}} \cdot \nabla \frac{1}{2} \overline{T'^2}}_{MAP_{ref}} + \underbrace{\overline{\nabla \cdot \mathbf{u}'_{bc b} \frac{1}{2} T'^2}}_{EAP_{bc b}} + \underbrace{\overline{\nabla \cdot \mathbf{u}'_{ref} \frac{1}{2} T'^2}}_{EAP_{ref}} + \underbrace{\overline{\theta_z T' w'}}_{PKC} = \underbrace{\overline{-\mathbf{u}'_{bc b} T' \cdot \nabla \overline{T}}}_{BC_{bc b}} + \underbrace{\overline{-\mathbf{u}'_{ref} T' \cdot \nabla \overline{T}}}_{BC_{ref}}. \quad (4.5.6)$$

Because the baroclinic-referenced-to-bottom velocities flow along mean temperature contours, there is a relationship between mean temperature and velocity:

$$f \overline{\mathbf{u}}_{bc b} = 2\gamma \mathbf{k} \times \nabla \overline{T} \quad (4.5.7)$$

where γ is an empirical constant,

$$\gamma = \frac{1}{2} \frac{d\psi_{bc b}}{d\overline{T}}. \quad (4.5.8)$$

Equations 4.5.7 and 4.5.8 state that the baroclinic-referenced-to-the-bottom field is aligned vertically with the front (“equivalent barotropic”), which is a good approximation in our array (Figure 4.5-7). With this decomposition, the following relationships hold:

$$\underbrace{\overline{\mathbf{u}_{bc b}} \cdot \nabla \frac{1}{2} \overline{T'^2}}_{MAP_{bc b}} = \underbrace{\overline{-\mathbf{u}'_{bc b} T' \cdot \nabla \overline{T}}}_{BC_{bc b}} \quad (4.5.9)$$

and

$$\underbrace{\overline{\nabla \cdot \mathbf{u}'_{bc b} \frac{1}{2} T'^2}}_{EAP_{bc b}} = 0, \quad (4.5.10)$$

Therefore, the mean eddy potential energy budget can be reduced to the following:

$$\underbrace{\overline{\mathbf{u}_{ref}} \cdot \nabla \frac{1}{2} \overline{T'^2}}_{MAP_{ref}} + \underbrace{\overline{\nabla \cdot \mathbf{u}'_{ref} \frac{1}{2} T'^2}}_{EAP_{ref}} + \underbrace{\overline{\theta_z T' w'}}_{PKC} = \underbrace{\overline{-\mathbf{u}'_{ref} T' \cdot \nabla \overline{T}}}_{BC_{ref}}. \quad (4.5.11)$$

Hereafter the subscript ref will be dropped from Equation 4.5.11.

To calculate these terms, one needs to determine vertical velocity w and mean θ_z . θ_z is determined by the mean stratification within the array and at 400 m depth has a value of 0.023 °C.m⁻¹. Following Lindstrom and Watts (1994) and Howden (2000), vertical velocity is estimated near the base of the thermocline from the depth of the 6° isotherm (Z_6)

$$w = \frac{\partial Z_6}{\partial t} + \mathbf{u} \cdot \nabla Z_6. \quad (4.5.12)$$

Z_6 is negative and becomes increasingly negative with depth.

Figures in the following eddy-specific discussions show the results of calculating the terms in the mean eddy potential energy budget (Eqn. 4.5.11), and it is noted that the energetics for the three shedding events share the following characteristics:

- The magnitude of eddy advection of eddy potential energy, EAP, a triple-correlation term which has often been assumed small, must in fact be included in the budget, because it is of the same order as the baroclinic conversion (BC) and vertical down-gradient heat flux (PKC). The mean advection of eddy potential energy (MAP) by the ref field is small compared to the other four terms. The spatial pattern and magnitude of the combined PKC+EAP+MAP terms is very similar to the BC term.
- At any particular location, the time series that contribute to the terms in the eddy energy budget are event-like in the LC, often with only a few events dominating the mean. The maps summarize the energy conversion rates over the time interval of each respective case study. They are not individually intended as statistical studies, but there is obviously a strong similarity amongst them. Conversion of eddy potential energy to eddy kinetic energy occurs primarily along the eastern edge of the LC.

Eddy Ekman

The BC term nearly balances the sum of the PKC, EAP and MAP terms (Figure 4.5-9). The BC term is positive (indicating down-gradient fluxes) along the northwestern corner near the Mississippi Fan and along the eastern side of the LC. Overall, the pattern in the PKC term corresponds well to the BC term, although the maxima and minima are slightly displaced from one another. Time series of the BC' and PKC' terms in three regions where both terms are strong and positive are shown in Figure 4.5-10. Here BC' is defined as $-\mathbf{u}'_{ref}T' \cdot \nabla \bar{T}$ and PKC' is defined as $\theta_z T' w'$. Time series track each other well and are positively correlated with one another, with correlation coefficients (r) ranging from 0.51 to 0.74. The peaks in the time series can be traced back to dates when the deep eddies and upper SSH_{bcb} 40-to-100 day band passed fields jointly intensify. For the three time series shown here, located at the correspondingly color-coded stars on the map at the top of the figure, the peaks are associated with times when deep cyclone A intensifies as it propagates along the LC periphery: near the Mississippi Fan (magenta star in Figure 4.5-10) in mid-July, at the northeast corner (blue star) in late July and in the southeast corner (cyan star) in early August.

Eddy Franklin

Similar to Ekman, during the Franklin event, the BC term nearly balances the sum of the PKC, EAP and MAP terms (Figure 4.5-11). The BC term is positive (indicating down-gradient fluxes) near the base of the Mississippi Fan, along the eastern side of the LC as well as in the central portion of the array. Overall, the pattern in the PKC term corresponds well to the BC term, although the maxima and minima are slightly displaced from one another. Additionally, the range of PKC values is larger than the BC range, particularly in the central array. Time series of the BC' and PKC' terms in three regions where both terms are strong and positive are shown in Figure 4.5-12. Note the vertical scale extends to higher rates than for the other two eddy separation case studies discussed here. Time series track each other well and are positively

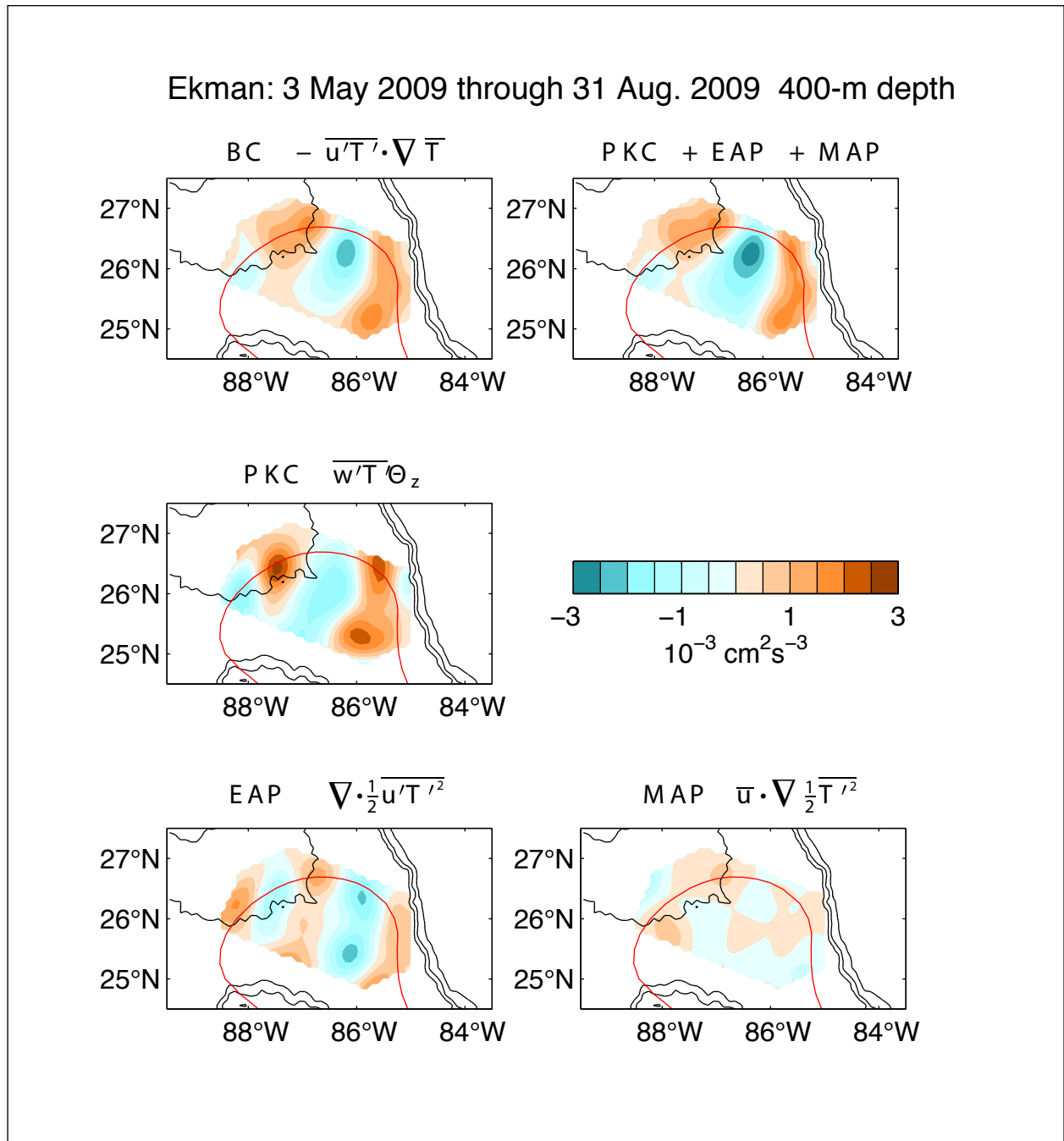


Figure 4.5-9. Four terms in the steady eddy potential-energy budget (Equation 4.5.5) determined for the Ekman event, 3 May through 31 August 2009 at 400-m depth (contour interval is $0.5 \times 10^{-3} \text{ cm}^2 \text{ s}^{-3}$; colorbar indicates that blue hues are negative and orange hues are positive). The horizontal down-gradient eddy heat flux (BC) is balanced by the mean advection of eddy potential energy (MAP), eddy advection of eddy potential energy (EAP) and the vertical down-gradient heat flux (PKC). Top right panel shows the sum of the PKC, EAP and MAP terms. The red line denotes the mean position of the 17-centimeter-mapped SSH contour. Bathymetry (black lines) contoured every 1000-m depth.

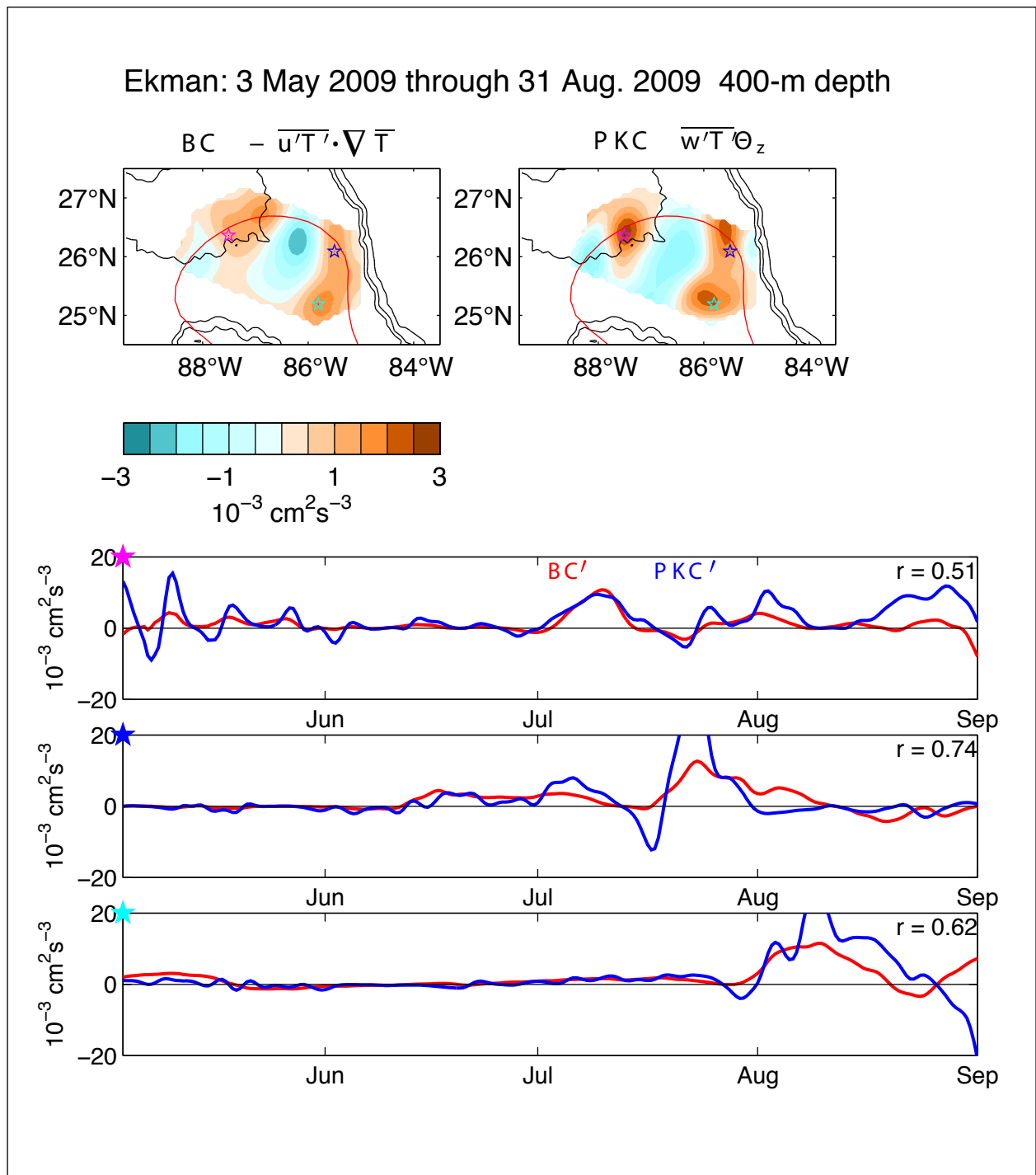


Figure 4.5-10. Top panels: BC (left) and PKC (right) at 400-m depth determined for the Ekman event (contour interval is $0.5 \times 10^{-3} \text{ cm}^2 \text{ s}^{-3}$; colorbar indicates that blue hues are negative and orange hues are positive). The red line denotes the mean position of the 17-cm altimeter-mapped SSH contour. Bathymetry (black lines) contoured every 1000-m depth. Bottom three panels: time series of BC' (red) and PKC' (blue) at locations indicated by colored stars in the mapped energetic terms (top panels) and denoted on the top left corner of each time series plot.

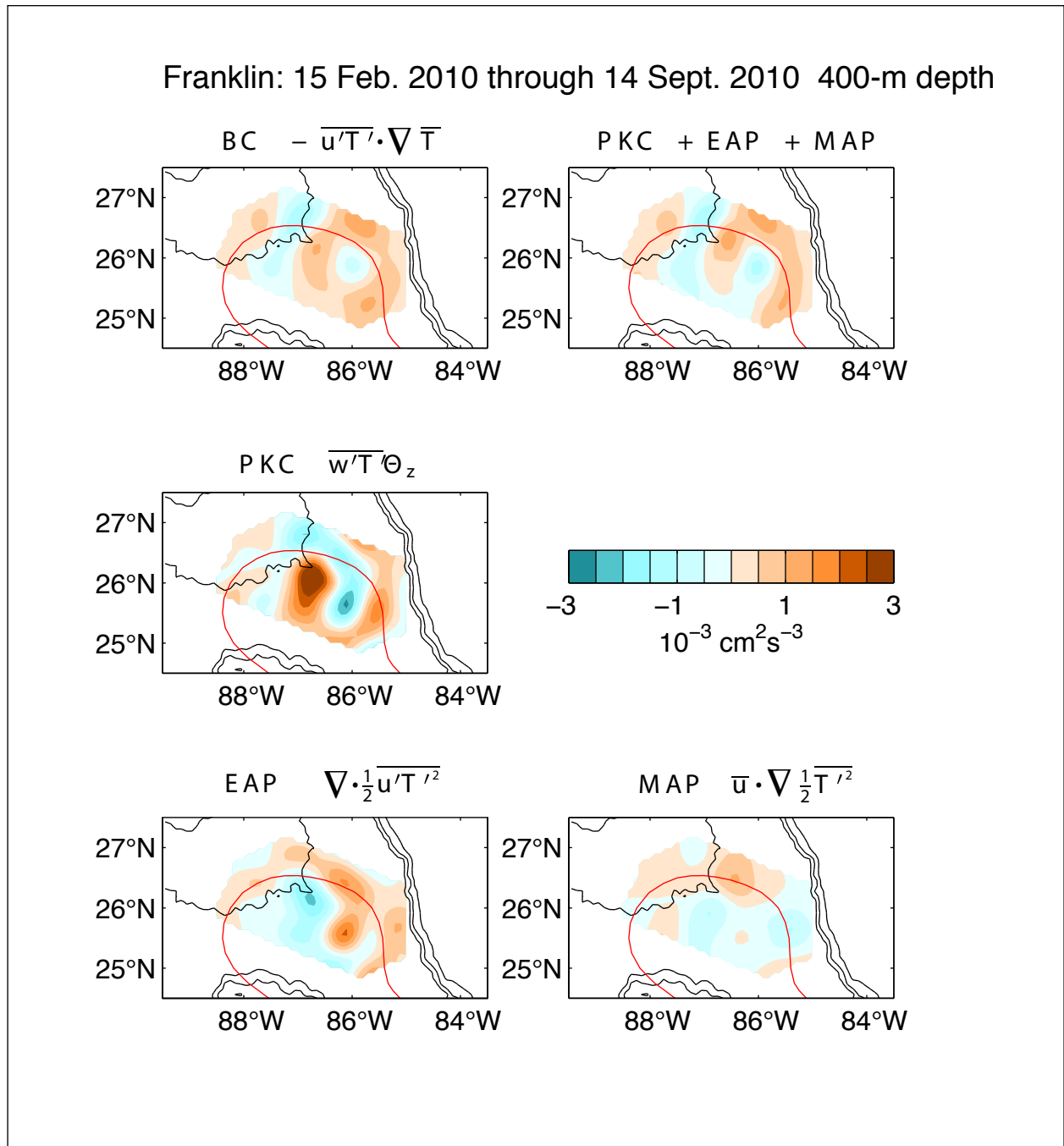


Figure 4.5-11. Four terms in the steady eddy potential-energy budget (Equation 4.5.5) determined for the Franklin event, 15 February through 14 September 2010 at 400-m depth (contour interval is $0.5 \times 10^{-3} \text{ cm}^2 \text{ s}^{-3}$; colorbar indicates that blue hues are negative and orange hues are positive). The horizontal down-gradient eddy heat flux (BC) is balanced by the mean advection of eddy potential energy (MAP), eddy advection of eddy potential energy (EAP) and the vertical down-gradient heat flux (PKC). Top right panel shows the sum of the PKC, EAP and MAP terms. The red line denotes the mean position of the 17-cm altimeter-mapped SSH contour. Bathymetry (black lines) contoured every 1000-m depth.

Franklin: 15 Feb. 2010 through 14 Sept. 2010 400-m depth

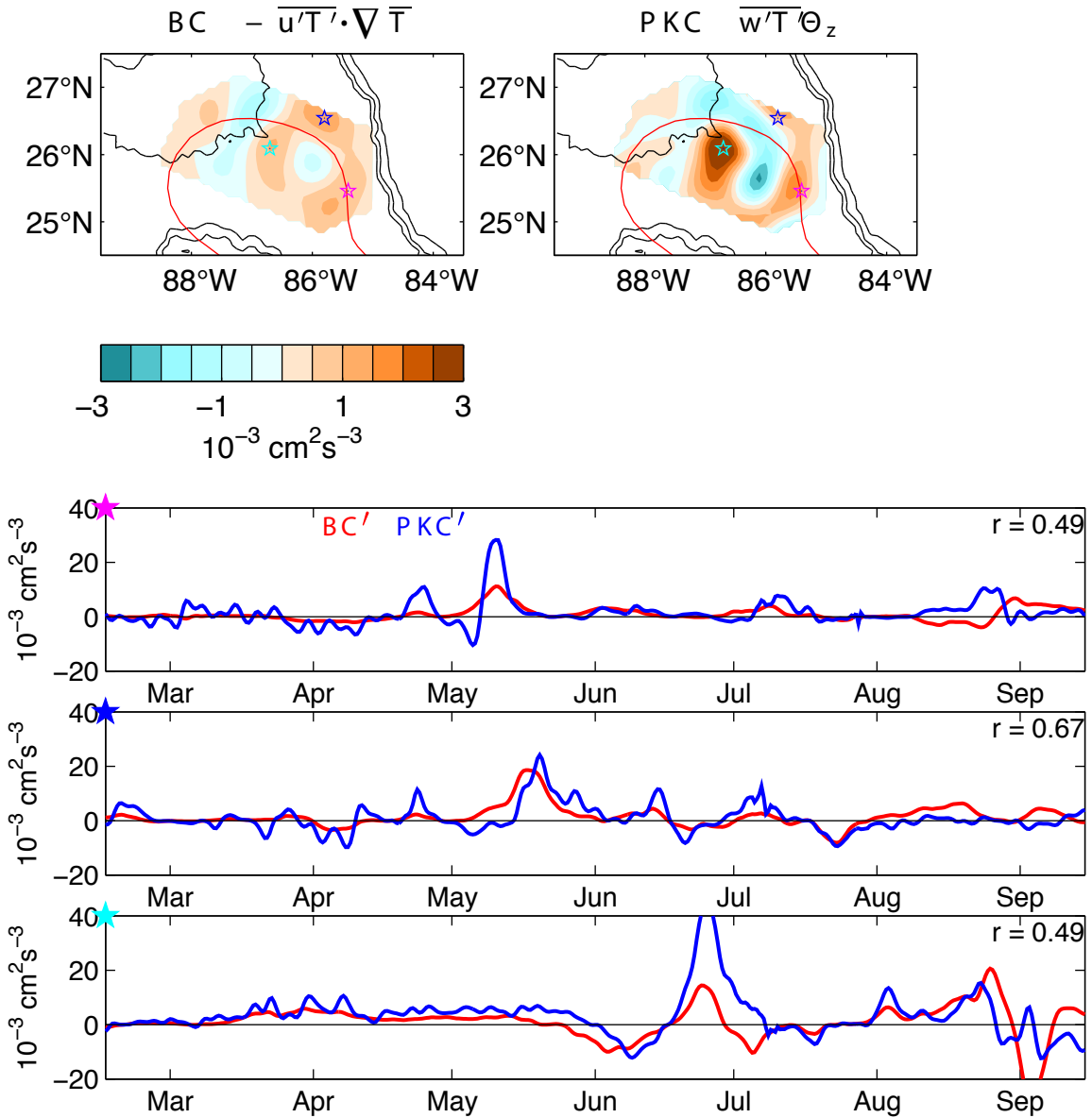


Figure 4.5-12. Top panels: BC (left) and PKC (right) at 400-m depth determined for the Franklin event (contour interval is $0.5 \times 10^{-3} \text{ cm}^2 \text{ s}^{-3}$; colorbar indicates that blue hues are negative and orange hues are positive). The red line denotes the mean position of the 17-cm altimeter-mapped SSH contour. Bathymetry (black lines) contoured every 1000-m depth. Bottom three panels: time series of BC' (red) and PKC' (blue) at locations indicated by colored stars in the mapped energetic terms (top panels) and denoted on the top left corner of each time series plot.

correlated with one another, with correlation coefficients (r) ranging from 0.49 to 0.67. Positive BC and PKC peaks along the eastern side of the LC coincide with the propagation of several deep eddies. In the southeast (magenta star in Figure 4.5-12), peaks are due to the intensification of deep anticyclone A (Figure 4.5-5b) in early May. Along the northeast (blue star in Figure 4.5-12) the peak is due to the intensification of deep cyclone B. In the central array (cyan star), the mid-June BC and PKC peaks occur when deep anticyclone C is intensified.

Eddy Hadal

Just as for the Ekman and Franklin case studies, the BC term nearly balances the sum of the PKC, EAP and MAP terms (Figure 4.5-13). The BC term has a maximum just downstream of the Mississippi Fan near 26.2°N , 86.2°W . The PKC term is also high here, indicating that eddies gain potential energy from the mean LC and convert that energy to eddy kinetic energy. An additional maximum occurs in the PKC field, near 26.2°N , 87.5°W , and here the balance is mainly between PKC and EAP. Figure 4.5-14 shows the time series of BC' and PKC' centered on a location where both terms sum to a strong positive peak. Again, the time series track each other well; the correlation coefficient is 0.86. The two large peaks in the time series, late April and mid-May, coincide with the intensification of deep cyclone B and deep anticyclone C, respectively (Figure 4.5-6b).

4.6 TOPOGRAPHIC ROSSBY WAVES

In a review of lower-layer current observations in the Gulf, Hamilton (2009) showed that bottom-trapped low frequency motions were consistent with TRWs in almost all deep water regions. He speculated that the LC could generate TRWs that would propagate towards the Sigsbee escarpment where high-speed near-bottom currents had been observed (Hamilton and Lugo-Fernandez 2001). Moreover, the variation of the frequency bands of the dominant EKE along the Sigsbee, from ~ 10 days in the east to ~ 60 days in the west, could be explained by the dispersion of TRWs of different periodicities having different paths to the slope. Using a high-resolution numerical model, Oey (2008) proposed a mechanism where the growth of LCFEs along the western and northern parts of the LC front generated corresponding deep eddies that detached from the LC and translated to the west. The decay of these westward translating deep eddies generated the TRWs that radiated towards the northern slope. As discussed above, there is little evidence of a direct generation of deep eddies by LCFEs over this part of the LC front. A more direct generation mechanism that is consistent with the models of Malanotte-Rizzoli et al. (1987) is that as the LC advances to the northwest over shoaling topography, there is compression of the water column, which leads to the observed mean anticyclonic deep circulation, but would also radiate broad band TRWs. Because TRW motions have a high-frequency cut off proportional to the bottom slope, above which propagating waves are not supported (Rhines 1970), short-period waves would only be generated over the steeper topography of the Mississippi Fan, and the relatively gentle abyssal slopes under the LC would favor the longer periods of 40 to 60 days that are prominent in the velocity records. LaCasee (1998) discusses the stability of geostrophic vortices over a slope, and in many cases both an initially barotropic and a surface-intensified vortex will radiate TRWs and still maintain a stable upper-layer vortex. This seems possible for the barotropic modes under the LC, but would also be true for a separated westward-translating LC eddy (also pointed out by Oey and Lee (2002)). So it is unclear, from theoretical arguments, whether the barotropic modes of the LC or the

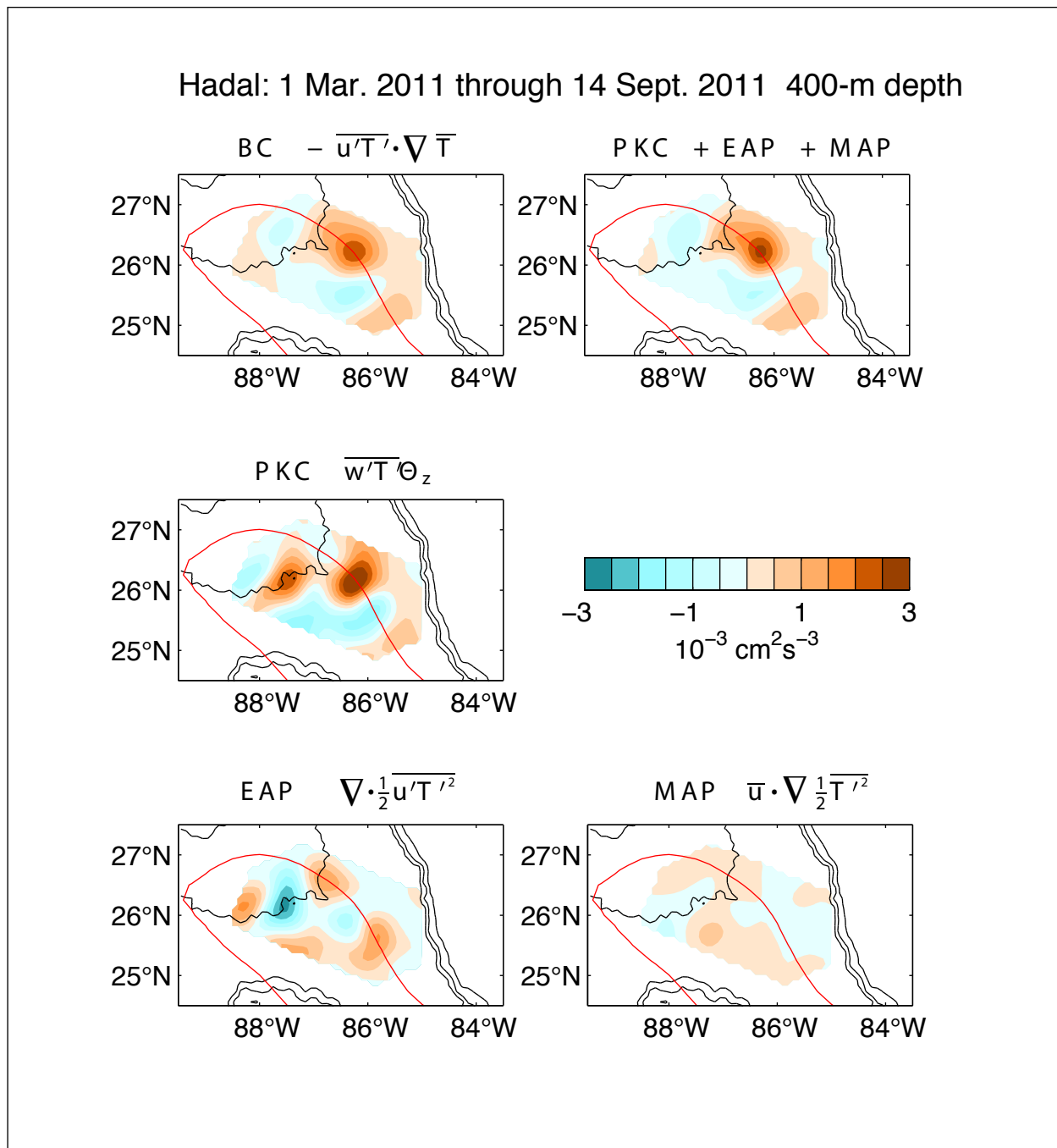


Figure 4.5-13. Four terms in the steady eddy potential-energy budget (Equation 4.5.5) determined for the Hadal event, 1 March through 14 September 2011, at 400-m depth (contour interval is $0.5 \times 10^{-3} \text{ cm}^2 \text{ s}^{-3}$; colorbar indicates that blue hues are negative and orange hues are positive). The horizontal down-gradient eddy heat flux (BC) is balanced by the mean advection of eddy potential energy (MAP), eddy advection of eddy potential energy (EAP) and the vertical down-gradient heat flux (PKC). Top right panel shows the sum of the PKC, EAP and MAP terms. The red line denotes the mean position of the 17-cm altimeter-mapped SSH contour. Bathymetry (black lines) contoured every 1000-m depth.

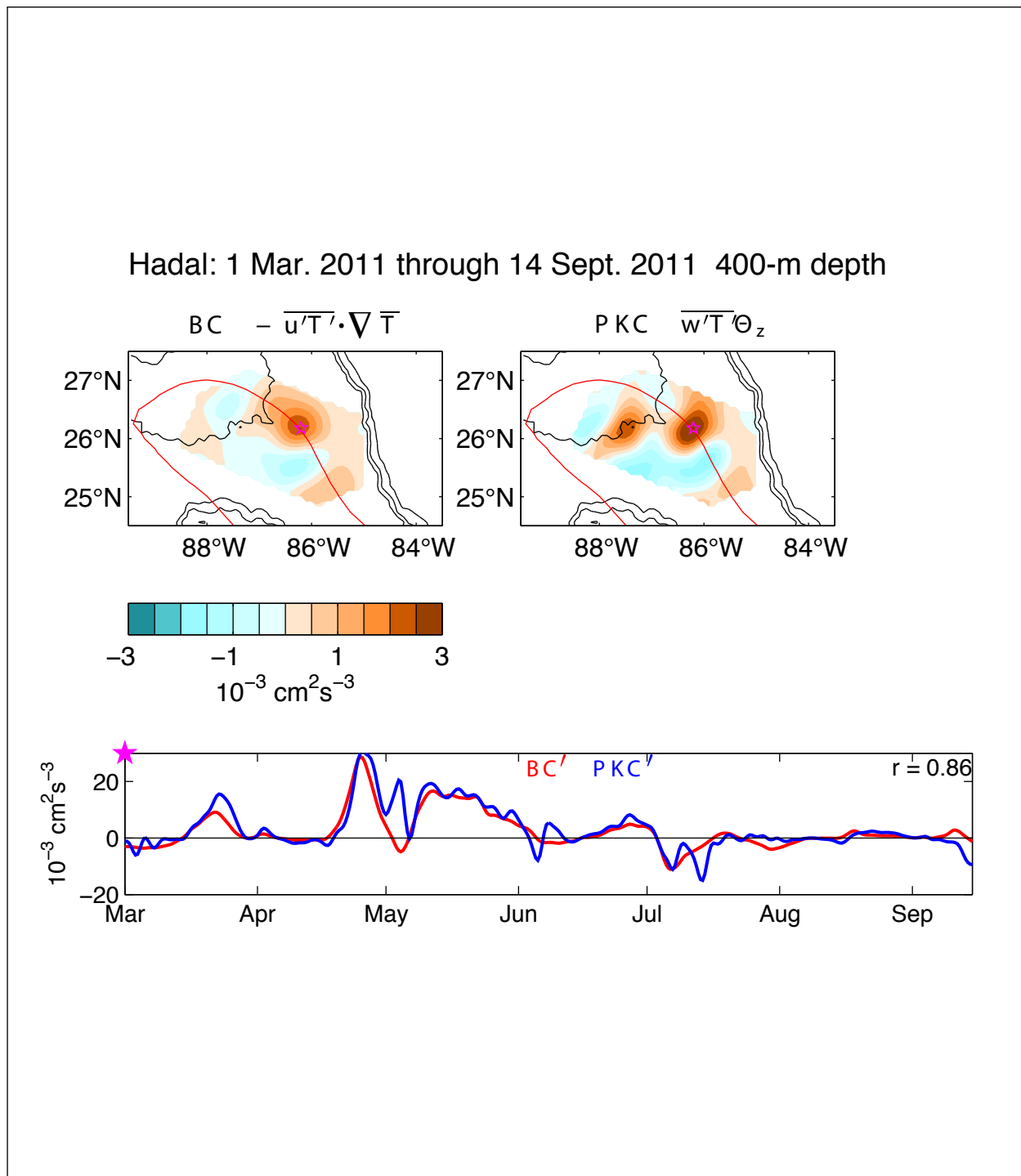


Figure 4.5-14. Top panels: BC (left) and PKC (right) at 400-m depth determined for the Hadal event (contour interval is $0.5 \times 10^{-3} \text{ cm}^2 \text{ s}^{-3}$; colorbar indicates that blue hues are negative and orange hues are positive). The red line denotes the mean position of the 17-cm altimeter-mapped SSH contour. Bathymetry (black lines) contoured every 1000-m depth. Bottom panel: time series of BC' (red) and PKC' (blue) at location indicated by colored star in the mapped energetic terms (top panels) and denoted on the top left corner of the time series plot.

surface-intensified large (relative to the Rossby deformation radius) LC eddies are more efficient at generating the TRWs that impinge on the lower-northern slope.

To investigate whether TRWs are supported by deep-current fluctuations under the LC, a wavenumber analysis was performed for the interval during the detachments of Franklin when deep EKE and relative vorticity fluctuations increase in magnitude (Figure 4.2-1). This interval was defined to be from 15 March to 15 October 2010. Using the velocity records at 100 mab in subsets of three or four locations surrounding a PIES location, frequency domain EOF modes were calculated for the 100 to 20-day band. This is consistent with the periodicities chosen for the PIES baroclinic instability analysis given in the previous section. The velocity stations used for each nominal PIES location are exactly the same as for the relative vorticity calculations (see Section 2.9). In most cases two EOF modes were significant, and using a least square fit to the phase angles, east and north wave numbers were estimated as in Hamilton (1990; 2009). The direction of the local isobaths at each PIES location was determined from a least square plane fit to the latest version (13) of the Smith and Sandwell (1997) global topography data base, where the one minute resolution topography was smoothed with a 25 km median filter. Where the wavenumber was directed into the second or third quadrant in the local isobath coordinate frame where the shallower water is to the left of the along-isobath coordinate, the mode was considered a candidate for being a TRW. Thus, the along-isobath wavenumber component (k) is negative in the isobaths coordinate frame, as is required by the theory (Rhines 1970). The cross-isobath wavenumber component (l) usually dominates and may be directed up or down slope. The group velocity is perpendicular to the phase velocity and also directed into the 2nd or 3rd quadrants, and for long-period waves, this is a small angle to the negative along-isobath direction. The results are given in Figure 4.6-1 where the size of the dot gives the variance of the mode divided by the number of velocity locations (three or four). Under the east side of the LC, amplitudes are small or non-existent (locations 71 and 76), with the largest amplitudes in a north-south band between 86.5 and 87°W. Most of the wavenumbers are directed up slope, but are nearly parallel to the across-isobath axes. This indicates that the TRWs would propagate along the isobaths to the west. Wavenumber magnitudes indicate wavelengths ranging from ~50 to 200 km, which is typical of short wavelength TRWs in the Gulf (Hamilton 2009). Conclusions are that lower-layer currents have some characteristics of TRWs under the LC, but only in the north and central part of the array. Amplitudes may be small (maximum of ~7 cm s⁻¹), but would involve the whole of the ~3000-m water column as the mode is barotropic. The western side of the LC front, over deep water where measurements were not made (Figure 4.6-1), is also a candidate for a source region for TRWs.

4.7 NUMERICAL MODELING

Numerical modeling studies were largely devoted to understanding LC variability and its effects on the Gulf basin, particularly looking at the intra-annual variability and its relation to large-scale wind systems including those over the Caribbean. In addition, research was made into more efficient assimilation schemes that produce more skillful forecasts and hindcasts. The latter has been published (Xu et al. 2013a) and shows that a local ensemble transform Kalman filter was better than optimal interpolation and persistence of AVISO SSHA in forecasting the location, size, and slow separation velocity of Franklin in 2010. This was particularly challenging because Franklin's separation speed, caused by its small size and weak circulation after August 2010, was not determined by Rossby wave propagation, as is more usual. The

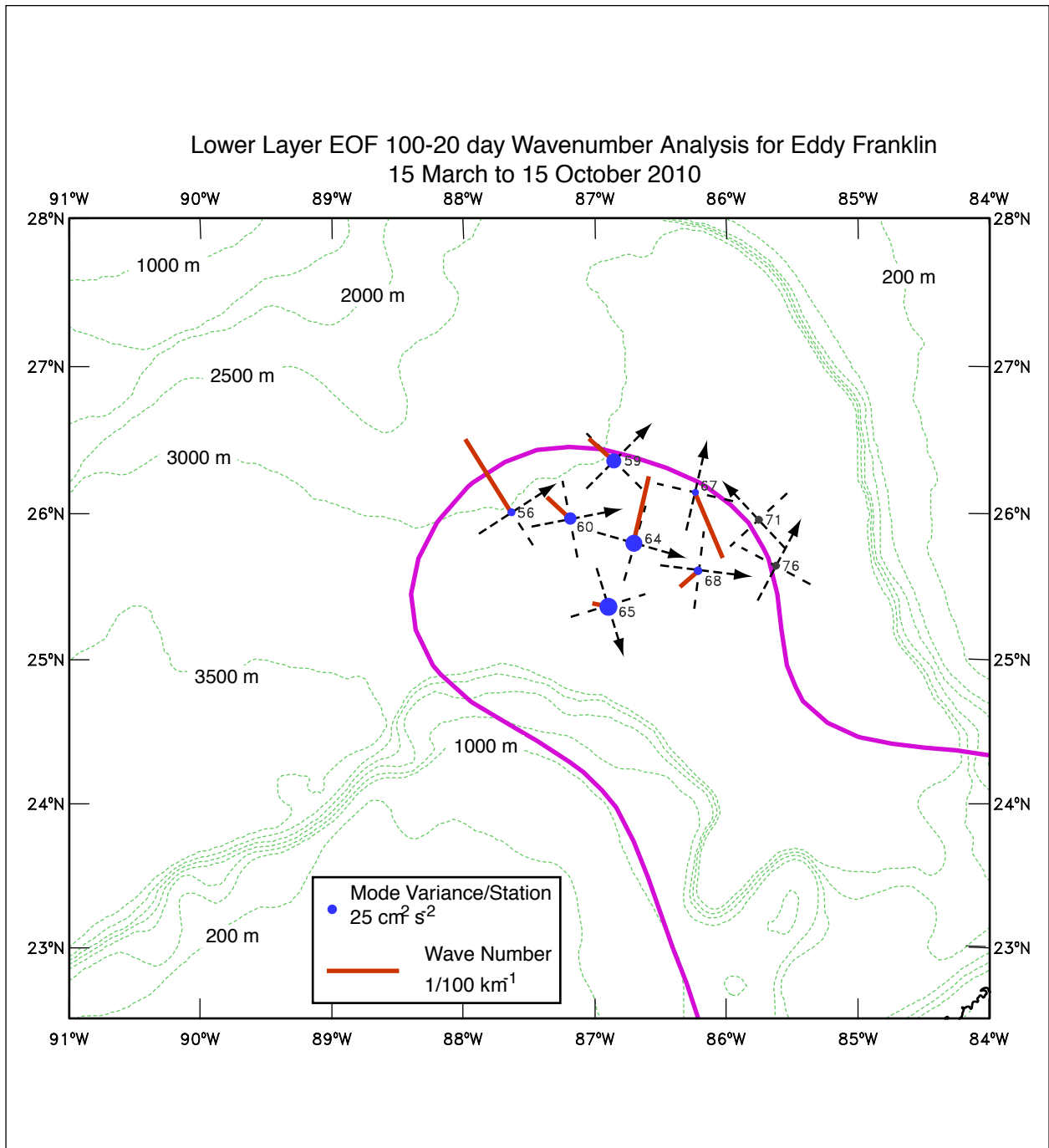


Figure 4.6-1. Wavenumbers from 100 to 20-day EOFs for the 100-mab currents for Franklin where the propagation is compatible with TRWs. The wavenumber and direction is given by the red lines, and the total variance (normalized by the number of stations (three or four) in the EOF mode) by the diameter of the blue dot. Isobath coordinate axes are given by the dashed lines where the arrowhead denotes the direction of the local isobaths, where the shallower water is to the left. The mean location of the 17-cm SSH contour for the analysis period is given by the purple line.

reader is referred to the paper for details of the techniques and comparisons, which will not be repeated here.

In section 4.2, tentative observational support was given, in terms of array-averaged vertical velocity, for Chang and Oey's (2011) modeling study of canonical LC growth and separation, driving large-scale upwelling and downwelling. The translation of a model LC eddy to the west drives deep exchanges between the western and eastern basins. The phasing of these transports provides an explanation of why deep counter flows in the Yucatan Channel do not directly relate to LC growth and retreat. Chang and Oey (2011) give dynamical arguments that, because of essentially closed topographic contours in the lower layer, a cyclonic gyre must exist in the western Gulf as a compensation of the net downward flux imposed by the LC in the eastern basin. Observations support (DeHaan and Sturges 2005; Hamilton 2009), at least in the northern abyssal Gulf, a cyclonic deep gyre. They predict that the gyre strength is modulated by the LC cycle such that it is strongest when the LC is reforming, and weakest when an eddy separates and translates into the western basin. At present, there are not enough long-term observations to confirm this prediction.

Chang and Oey (2010a) discuss the effect of large-scale wind fields over the Gulf on the shedding of eddies. They postulate that LC eddy shedding is largely mediated by the Pichevin-Nof mechanism, and thus does not involve the lower layer. An eddy separation occurs when the westward translation of the eddy, as a Rossby wave, exceeds the growth of the LC from upper-layer volume transport imbalances between the Yucatan Channel and the Florida Straits. Note that the Pichevin-Nof theory (Pichevin and Nof 1997) per-se does not predict that eddies will separate, but merely accounts for an extended LC to bend and stretch towards the west. The results from this program's observations indicate that baroclinic instabilities involving the upper and lower layers act as the main agent for eddy detachments. Further discussion of these points is reserved for Chapter 7. However, it is noted that after an eddy has separated, it will translate westwards at Rossby wave speeds if the western basin upper layer is quiescent. Chang and Oey (2010a) apply a spatially uniform, constant, westward wind over the Gulf (i.e., excluding model regions external to the Gulf) that mimics the trades. They find, compared to the no wind case, that substantial westward transports are forced on the northern (Louisiana and Texas) and southern (Campeche Bank) shelf regions. The compensating eastward upper-layer transport occurs mainly in the center of the basin that opposes the westward translation of LC eddies, and therefore would impede an eddy attempting to detach from a fully extended LC. A recent study by Sturges and Bozec (2013), using historical databases of ship drift and surface-layer drifters from many decades of observations, show that there are substantial westward mean flows over the northern and southern shelves, but these westward drifts are not compensated by mid-basin eastward surface mean flows. Indeed, the mean flow in mid basin from their calculations is still westward. Sturges and Bozec (2013) compare their surface-transport results with a couple of numerical-model calculated means, and find that the model results approximately obey continuity with westward and eastward transports in balance. This model-data discrepancy has yet to be resolved, but has profound implications for mean circulations. If the surface transport is westward across the 91°W meridian, as indicated by Sturges and Bozec's (2013) calculations, then the compensating return flow must occur at depth and involve downwelling in the western part of the Gulf. If the eastward return flow is at a shallow depth, then the Chang and Oey (2010a) mechanism for delaying LC eddy shedding may be valid. Observations are too sparse

below the surface layer to resolve this dilemma. When more realistic but still idealized winds are used, as in Chang and Oey (2013a), the delaying effect of westward winds over the Gulf is less apparent. This is discussed in more detail in Chapter 5 where the historical record of eddy separations is subjected to a rigorous analysis, and suggests that westward winds over the Gulf do not play a significant role.

Chapter 5 discusses the historical record of LC eddy shedding, and establishes that there is an annual signal in average LC metrics, with maxima in the spring, minima in the fall and early winter. This leads to higher and lower probabilities for eddy shedding in these respective seasons. A number of reduced-gravity model experiments were performed to establish possible mechanisms behind these seasonal preferences. These experiments are reported in Chang and Oey (2013a). In a single-layer reduced gravity model, eddy separation is attributed to the Pichevin-Nof mechanism where the Rossby wave westward translation of the northern part of an extended LC exceeds the growth of the LC. Thus, this mechanism does not involve the lower layer, and Xu et al. (2013b) indicate that in their fully 3D model, wind effects and baroclinic instability modify the timing of separations, but the Pichevin-Nof mechanism is the fundamental process. This differs from the observational analysis of Section 4.5 where baroclinic instability has a much more prominent role.

Nevertheless, the numerical experiments established a relation with the biannual signal of the Caribbean trade winds, which have westward component maxima in June-July and December, with minima in April-May and September-October. The biannual wind cycle is not symmetric, but was approximated by a biannual sinusoidal modulation, which (in the model) drives a biannual northward transport anomaly in the Yucatan Channel. The flow patterns and biannual cycles of wind and Caribbean transports are shown in Figure 4.7-1 (taken from Chang and Oey (2013a); their Figures 7 and 9). The YC northward transport anomaly promotes LC growth when it is positive, and promotes a shedding event by the Pichevin-Nof mechanism when it is negative, if the LC is well extended. The SSHA monthly composite in the northwest Caribbean (from the model) is compared to the equivalent AVISO-derived signal in Figure 4.7-1f. If the model leads by one month, the correlation (R) is 0.66, with a 95% significance level of 0.52. The reanalysis of the historical SSH altimeter record is performed in Chapter 5, where the significance of the Caribbean anomalies is discussed, and an alternate mechanism involving coastal-trapped waves that perturb the LC within the Gulf, rather than winds in the northwest Caribbean, is proposed and analyzed. These somewhat contradictory investigations indicate that several processes that still need more study may be the causes of the complex variability of the LC.

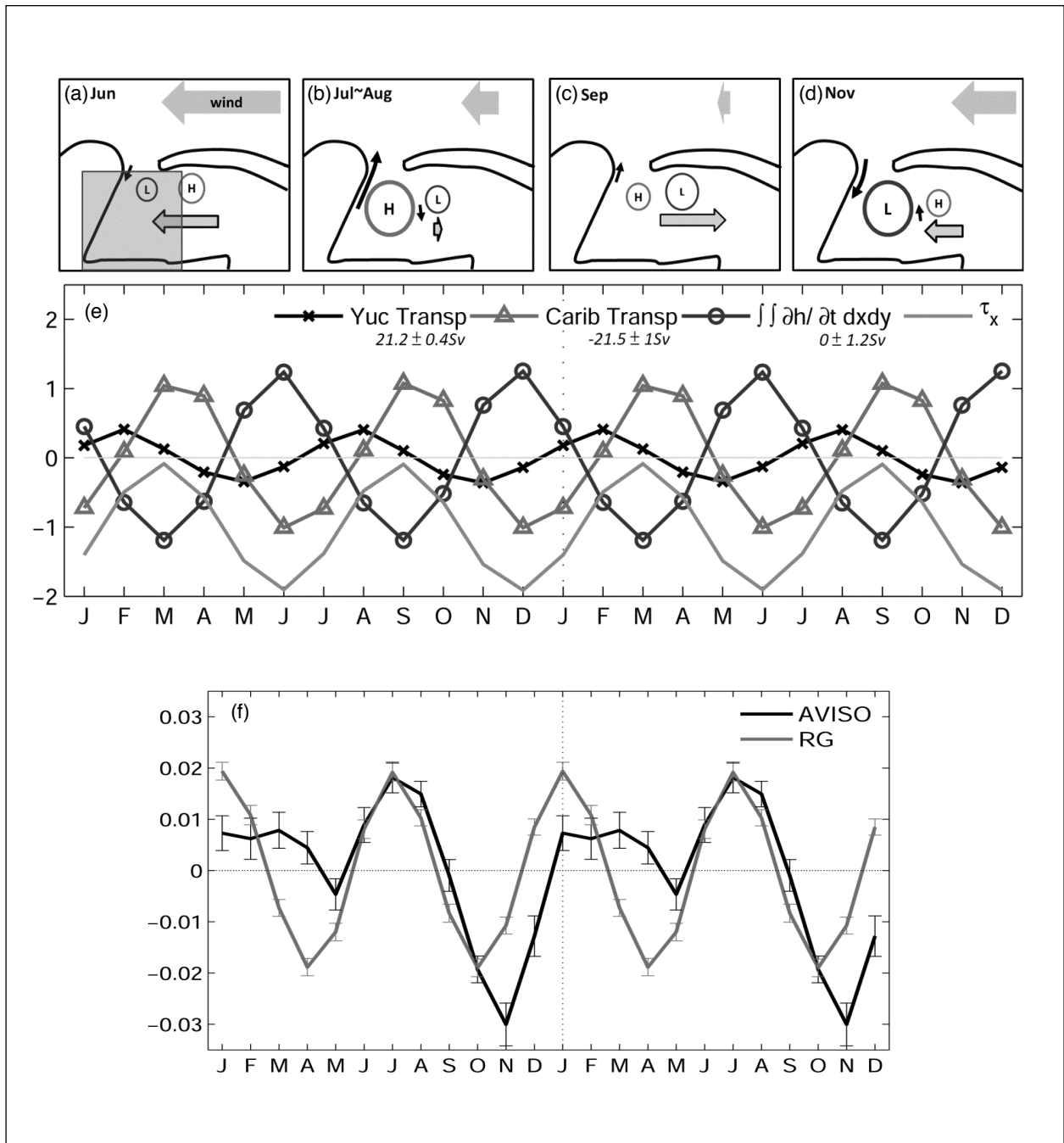


Figure 4.7-1. (a)-(d): Schematic illustrations of the dominant flow anomalies in the northwestern Caribbean Sea for the indicated months based on monthly composites derived from EOF analysis of model SSH; grey vector shows total (i.e., not anomaly) wind. (e) 12-year composite of monthly transport anomalies ($\text{Sv} = 10^6 \text{ m}^3\text{s}^{-1}$) in the control volume shown in the rectangle in (a). The mean \pm fluctuation (in Sv) for each term is shown. Grey curve is the specified zonal wind stress in m^2s^{-2} . (f) Monthly AVISO SSHA and scaled reduced gravity (RG) model SSH averaged over $17.5^\circ\text{-}22.5^\circ\text{N}$; $87^\circ\text{-}80^\circ\text{W}$ in the northwestern Caribbean Sea with standard error bars. Plots are repeated for two years (from Chang and Oey 2013a).

CHAPTER 5: LONG TERM AND SEASONAL VARIABILITY

5.1 INTRODUCTION

Continuous monitoring of the LC is required to accurately identify LC eddy separation events, since eddies frequently detach and re-attach before ultimately separating, and separation may occur at any time of the year. Multi-satellite altimetric mapping of the ocean mesoscale afforded by the ERS-1 and TOPEX/Poseidon missions, and later follow-on missions, provided the satellite sampling required to achieve this monitoring capability in the early 1990s. Continuous multi-satellite altimetric mapping has remained to the present day.

Before the advent of satellite altimetry, a number of observational technologies were exploited for LC monitoring. Studies of LC intrusion and eddy separation in the 1970s relied on a variety of data sources, including in-situ and satellite data to identify separation events, and were subject to periods of poor sampling. The earliest studies were based on upper-ocean temperature sections along shipboard survey cruise transects (Leipper 1970; Maul 1977; Behringer et al. 1977). Most of these observations were made during the spring, summer and fall. In those studies an annual cycle of LC intrusion was hypothesized based on earlier observations of an annual cycle in Yucatan Current inflow, with maximum currents in May and June and a minimum in October and November (Cochrane 1965). Leipper (1970) proposed an annual cycle of LC intrusion in the spring followed by either a deeply intruded LC in the fall or a separated eddy and retreated LC. That study was based on in-situ data collected primarily during 1965 and 1966. Maul (1977) found a similar cycle in 1972 and 1973, and was able to track the frontal position of the LC over 14 months. Thus, by the mid-1970s the emerging consensus was that the LC exhibited a mean annual cycle, with significant deviations due to highly variable eddy-separation events. Separation periods had been observed to range from as short as eight months to as long as 17 months (Behringer et al. 1977). During an average annual cycle, the LC intruded northward into the Gulf in the spring, followed by maximum intrusion with probable eddy separation during summer and fall, and retreat to the south during winter, since the few winter observations over this time period did not show a LC intrusion north of 26°N.

In the mid-1970s, satellite radiometry imagery became available at sufficient resolution and precision to observe synoptic-scale and mesoscale fronts in the Gulf. Maul (1975) demonstrated that satellite imagery could be used to detect the western margin of the LC during winter. Legeckis (1976) reported the first wintertime deep intrusion and eddy separation determined from direct observations during the winter of 1974 and 1975. Later, Molinari et al. (1977) used both satellite and in-situ data to identify intrusions of the LC north of 26° N from 1974 through 1977, and LC eddy separation events in both winter and spring. They concluded that, since the earlier observational dataset was limited during the wintertime, it was not clear whether winter intrusions occurred before the mid-1970s. Their work provided the first evidence, however, that eddy separation could occur in any season.

By the late 1970s, “monthly” sea-surface temperature (SST) frontal analyses in the Gulf were being made from the very high-resolution radiometer (VHRR) instruments onboard polar orbiting NOAA satellites (Vukovich et al. 1979). These analyses were typically based only on a few clear-sky SST images and could not be made throughout the year. From June through

October, the LC and LC eddy fronts could not be distinguished in the SST imagery when the warm seasonal surface mixed layer developed in the Gulf. In May, when the seasonal mixed layer was developing, intense image enhancement of some of the imagery was needed to identify the fronts. For this reason, there were times when the accuracy of some features in May frontal analyses were questioned and earlier analyses were used instead. In the time periods when LC and LC eddy SST thermal fronts were masked by the mixed layer, information on the LC and warm rings were also obtained from MMS, Navy, NSF, NOAA, and the various oil companies that sponsored ship surveys in the Gulf. That information was supplemented with available Coastal Zone Color Scanner (CZCS) data to estimate the LC and LC eddy positions, the position of the northern boundary of the LC, the diameter of the ring, etc. Though frontal analyses could not be created from those data, they were entered into an unpublished database maintained by Dr. Fred Vukovich (Vukovich 2012).

Infrared images from the Geostationary Operational Environmental Satellite (GOES) were also used for LC monitoring in the late 1970s. Imagery processed by the NOAA Miami Satellite Field Services Station was geo-registered using photographic techniques and animated in order to attempt to map daily locations of the LC front (Maul et al. 1978). The 24-hour coverage provided by GOES geostationary sampling reduced data outages associated with cloud cover, and oceanic fronts in the Gulf Stream system could be mapped about half of the days (Maul et al. 1984).

Several significant technological advancements in satellite oceanography occurred in the 1970s that contributed to the development of operational satellite monitoring of the LC and LC eddies. These advancements included the first successful tests of satellite-tracked drifting buoys, satellite altimetry, and satellite ocean-color radiometry. Satellite-tracked drifting ocean buoys were developed using data collected by the NASA Nimbus-6 satellite, which carried a Tracking and Data Relay experiment that was used to determine drifting buoy positions using Doppler tracking (Kirwan et al. 1976). Nimbus-6 was launched on 12 June 1975 and operated until 29 March 1983. This research mission led to the development of the Advanced Research Global Observation Satellite (ARGOS) system, which collects, processes, and disseminates data from fixed and mobile platforms using polar orbiting NOAA satellites to the present day. Kirwan et al. (1984) documented the first use of satellite-based tracking of drifting buoys within a LC eddy. Three satellite-tracked drifting buoys were air deployed in November 1980 by the NOAA Data Buoy Center into a fall-separated LC eddy and permitted satellite tracking of the LC eddy into the western Gulf, well into spring 1981. The drifters were undrogued, but had 200-m thermistor cables attached. It is noteworthy that this is the only mention of a LC eddy separation event in the fall of 1980 reported in the peer-reviewed literature. This event does not appear in published LC eddy separation event censuses (Vukovich 1988; Sturges 1994) or their re-publication (Sturges and Leben 2000; Leben 2005; Vukovich 2012). In the late 1970s, the first ocean-altimetry and ocean-color satellite missions were flown by NASA. Seasat, launched on 27 June 1978, carried the first satellite altimeter capable of measuring ocean-surface topography with the accuracy required to resolve ocean-mesoscale signals (Cheney et al. 1983). The first instrument devoted to the measurement of ocean color, the CZCS, was launched aboard the Nimbus-7 satellite on 24 October 1978. These were experimental missions and little of these data made it into the general user community for use in operational ocean monitoring or into the published LC eddy separation censuses. Later, Müller-Karger et al. (1991) demonstrated that the combined

use of CZCS ocean-color and Advanced Very High Resolution Radiometer (AVHRR) SST images permits year-round monitoring of LC intrusion and eddy separation. The LC eddy separation event in the fall of 1980, mentioned above, can be seen clearly in the August and September ocean-color images shown in Plate 1b of that paper.

In the early 1980s, the hypothesis that the LC sheds eddies in response to annual variations in the inflow through the Yucatan Channel was challenged by a study of LC intrusion and eddy shedding using a numerical ocean model (Hurlburt and Thompson 1980). They found that a modeled LC could penetrate into the Gulf, bend westward, and shed realistic LC eddies at a quasi-annual natural shedding frequency with steady inflow. The quasi-annual period was about 290 days. This was the first numerical model of the Gulf that was integrated to statistical equilibrium and simulated the basic repetitive features of the LC eddy shedding (Hurlburt and Thomson 1982). They also found that realistic time varying upper-layer inflow could significantly influence the eddy separation. Nevertheless, the eddy shedding was dominated by the natural period, not the period of forcing in the model experiments. At about the same time, Sturges and Evans (1983) speculated that there were wind-forced annual variations in the north-south position of the LC. They relied on hydrographic data to determine the northernmost position of the LC. Difficulties were noted in reconciling the in-situ estimates of the LC position with surface observations determined from satellite images, so only in-situ data were used in their analyses. Thus, the basic hypotheses determined from modeling and observational studies were at odds with each other, with the state-of-the-art modeling studies indicating a natural shedding period (a quasi-annual period of about 10 to 11 months) and some unidentified external forcing contributing to the limited observational evidence of a true annual cycle. Given that the annual signal amplitude in the northern LC boundary was only 1.7 degrees, it seemed reasonable that the annual signal detected in observations was just an artifact of under sampling and averaging over the observed highly variable LC eddy shedding cycles.

All subsequent analyses of the LC annual cycle and LC eddy separation periods published in the late 1980s and early 1990s relied heavily on monitoring of the LC using SST imagery (Vukovich 1988; Maul and Vukovich 1993; Sturges 1992; 1993; 1994) and were affected by outages due to seasonal heating of the mixed layer and the lack of consistent sampling. There was also limited access to satellite altimetry, satellite ocean color, and industry monitoring. This led to inaccuracies in the published record and misrepresentation of the annual cycle in the pre-altimetric record when SST imagery was relied on too heavily for LC monitoring, as will be shown in this chapter. Thus, the general consensus from the 1980s and through the 1990s was that the LC exhibited little or no annual cycle.

Late in the 1990s and into the new century, satellite altimetric and industry monitoring made tracking of the LC and its associated eddies fully operational. Nevertheless, the seasonality of LC eddy separation only became apparent over time as the length of the continuous record of altimetric monitoring of the LC and LC eddies increased enough to resolve the seasonal signal, independent of the earlier historical and published records. Industry concerns, about the joint probability of eddy-hurricane events in the Gulf (Cooper and Stear 2009) and the potential impact of LC seasonality on the joint probability, motivated a preliminary re-analysis of the pre-altimetric and altimetric record of LC intrusion and eddy shedding.

The following sections in this chapter describe the detailed observational analyses that were performed using the available historical and satellite records, and what has been learned about the dynamics contributing to LC seasonality and eddy separation. Section 5.2 describes the re-analysis of the pre-altimetric LC record; Section 5.3 provides comparisons of the re-analysis with previously published separation dates; Section 5.4 describes the 20-year-long altimetric LC record; and Section 5.5 presents a detailed statistical analysis of LC seasonality. Section 5.6 presents the present study's investigation of the dynamics contributing to LC seasonality and identifies the dominant signal contributing to the observed LC seasonality and annual cycle.

5.2 RE-ANALYSIS OF THE “PRE-ALTIMETRIC” LOOP CURRENT RECORD

Continuous multi-satellite altimetric sampling required for accurate mapping of the SSH associated with mesoscale circulation in the Gulf and monitoring of the LC and LC eddies did not exist prior to late 1992. NASA Seasat altimetry, NASA CZCS ocean color, AVHRR SST, and ESA ERS-1 satellite altimetry data were used to perform a re-analysis of the separation events during the “pre-altimetric” LC record before 1993. LC and LC eddy positions determined from Horizon Marine Inc. (HMI) EddyWatch™ reports and the Climatology and Simulation of Eddies/Eddy Joint Industry Project (CASE/EJIP) Gulf Eddy Model (GEM) analyses were used to supplement the satellite observations. Table 5.2-1 lists the dates of all 20 identified separation events in the record along with HMI industry names (if available), separation periods, and retreat latitudes. The separation period is the length of time between separation events. Retreat latitude is the maximum latitude of the LC immediately following separation of a LC eddy (Leben 2005). The mean separation period over this time period is 270.5 days and the mean retreat latitude is 25.7°N.

Seasat along-track altimetry data are available from July through October 1978 from the NASA Ocean Altimeter Pathfinder program (Koblinsky et al. 1998). The data were processed as non-repeat track data similar to the processing described for ERS-1 geodetic mission data in Leben et al. (2002). CZCS data are available from November 1978 into June 1986 from the NASA Ocean Color Webpage (CZCS 2008). Level-3 chlorophyll-a concentration 8-day composite images at 4-km resolution were used in the re-analysis (downloaded 10 July 2008). AVHRR data, described in Casey et al. (2010), are available from the National Ocean Data Center (NODC) Pathfinder SST Program website (Casey et al. 2010 [Internet]). The September 1981 through January 1985 Pathfinder SST data were first released on 13 April 2009 by NODC, which was the first time that these data had been available in the nearly 20-year history of the AVHRR Pathfinder program. The weekly-averaged 4-km resolution SST product, Version 5.1, was used (downloaded in May and September of 2009 and February 2010). Example images of the LC from CZCS ocean-color and AVHRR SST images, in the time period before industry analyses from HMI became available in 1984, are shown in Figure 5.2-1. The CZCS ocean-color image shown is an 8-day composite from 13-20 August 1979. The AVHRR SST image is the weekly mean from 19-25 February 1982. Along-track 35-day repeat ERS-1 altimeter data, from the multidisciplinary mission phase (14 April 1992 through 21 December 1993), were extracted from the Radar Altimeter Database System (RADS) and were processed as described in Leben et al. (2002) and Section 2.6.1 of this report.

Table 5.2-1. Eddy separation events with the corresponding retreat latitudes and separation periods from July 1978 through December 1992

No.	Year-Letter	Industry Name	Separation Date	Best Available Imagery/Chart	Retreat Latitude (°N)	Separation Period (days)
1	1978	-	15 Jul 1978	*†SSH	24.7§	-
2	1980a	-	18 Feb 1980	*Chlorophyll-a	26.2	583
3	1980b	-	16 May 1980	*Chlorophyll-a	26.4	88
4	1980c	-	04 Aug 1980	*Chlorophyll-a	26.0	80
5	1981a	-	04 Jul 1981	Chlorophyll-a	25.5	334
6	1981b	-	24 Oct 1981	*Chlorophyll-a	26.4	112
7	1982	-	21 Aug 1982	*Chlorophyll-a	26.0	301
8	1983a	-	08 Mar 1983	*SST	26.8	199
9	1983b	-	23 Aug 1983	*†SST	26.0	168
10	1984a	-	25 Jan 1984	*SST	25.8	155
11	1984b	Arnold	28 Aug 1984	Chlorophyll-a	25.6	216
12	1985	Fast	18 Jul 1985	*†EddyWatch™	25.6	324
13	1986a	Hot Core	18 Jan 1986	SST	25.7	184
14	1986b	Instant	12 Sep 1986	*†SST	25.7	237
15	1987	Kathleen	08 Nov 1987	SST	25.6	422
16	1988	Murphy	25 Apr 1988	*SST	24.5	169
17	1989	Nelson	01 Sep 1989	*†EddyWatch™	25.3	494
18	1990	Quiet	14 Sep 1990	*†EddyWatch™	25.0	378
19	1991	Triton	01 Nov 1991	*SST	26.4	413
20	1992	Unchained	10 Aug 1992	SSH	24.7§	283
Mean					25.7	270.5

* GEM P&C analyses (Evans Hamilton 1992) were available to verify separation date estimate.

† GEM P&C analyses determined separation date estimate.

§ An offset of 0.36° must be added to SSH-derived retreat latitudes to make them consistent with values estimated from satellite SST and ocean-color frontal analyses. The offset was applied when calculating the mean.

The HMI EddyWatch™ reports, used in the re-analysis to help identify both LC eddy separation and LC retreat latitude, span the time period from 4 September 1984 through 31 December 1992. However, there were several time spans when the weekly reports were not published: 30 August 1986 through 5 February 1987, 15 August 1987 through 30 March 1988, 12 November 1988 through 16 February 1989, and 1 April 1992 through 3 September 1992. The available reports were digitized from hardcopies provided by CASE/EJIP for the development of a statistical LC hindcast model (Forristall et al. 2010). An EddyWatch™ report is shown in Figure 5.2-2 for LC eddy “Hot Core”, which separated from the LC on 18 January 1986. This is a representative example of the type of information provided in the EddyWatch™ reports used in the re-analysis to help identify both LC eddy separation and LC retreat latitude. Although the GEOSAT Geodetic and Exact Repeat Missions (ERM) spanned many of the time periods when EddyWatch™ reports were not published, GEOSAT altimeter data were not used in the re-analysis because of the frequent data outages in the eastern Gulf during this mission. These

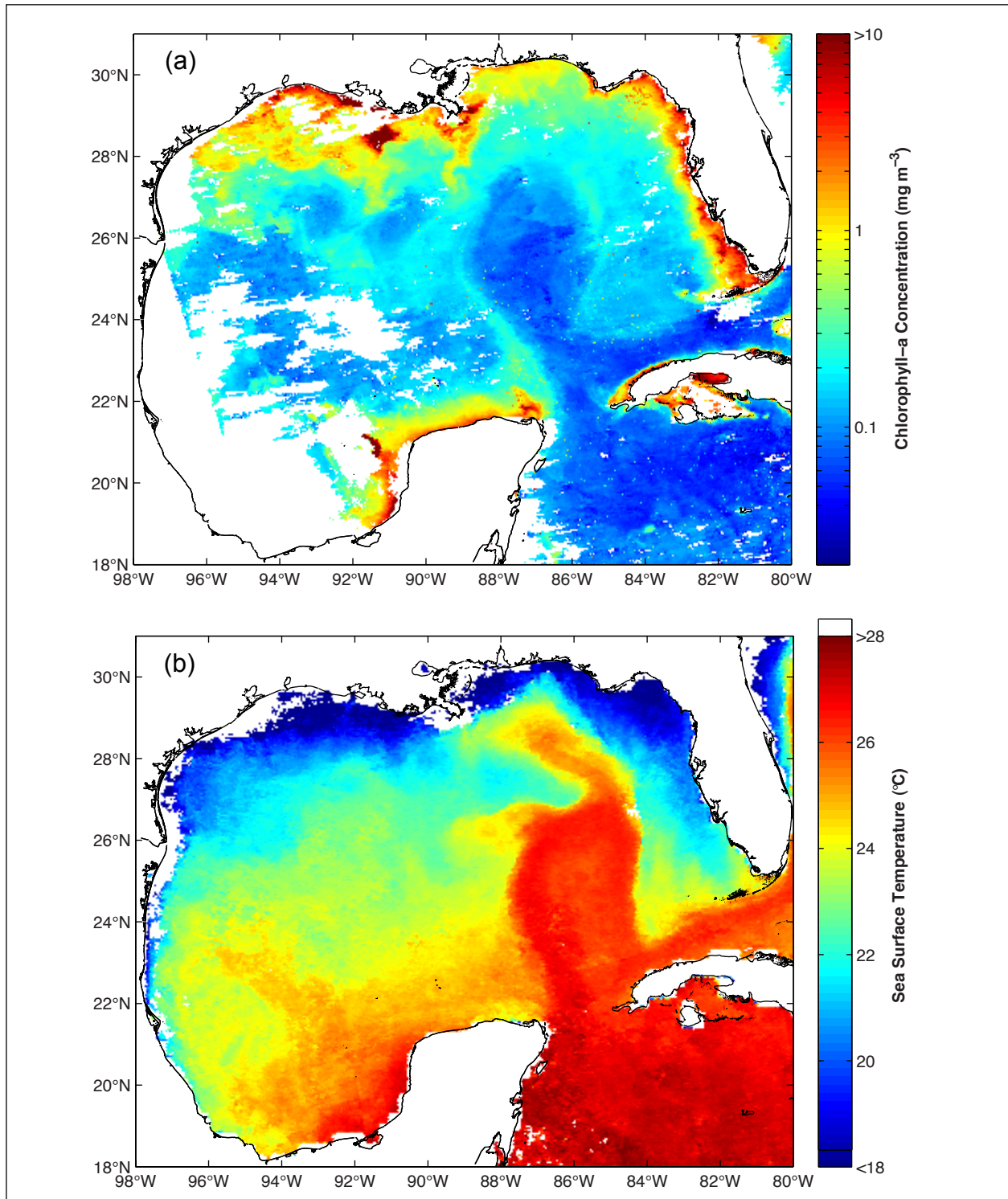


Figure 5.2-1. Examples of the “best” LC images from (a) CZCS ocean color and (b) AVHRR SST in the time period before EddyWatch analyses from Horizon Marine, Inc. became available in 1984 (see Figure 5.2-2). The CZCS ocean-color image is an 8-day composite from 13-20 August 1979. The AVHRR SST image is a weekly mean from 19-25 February 1982.

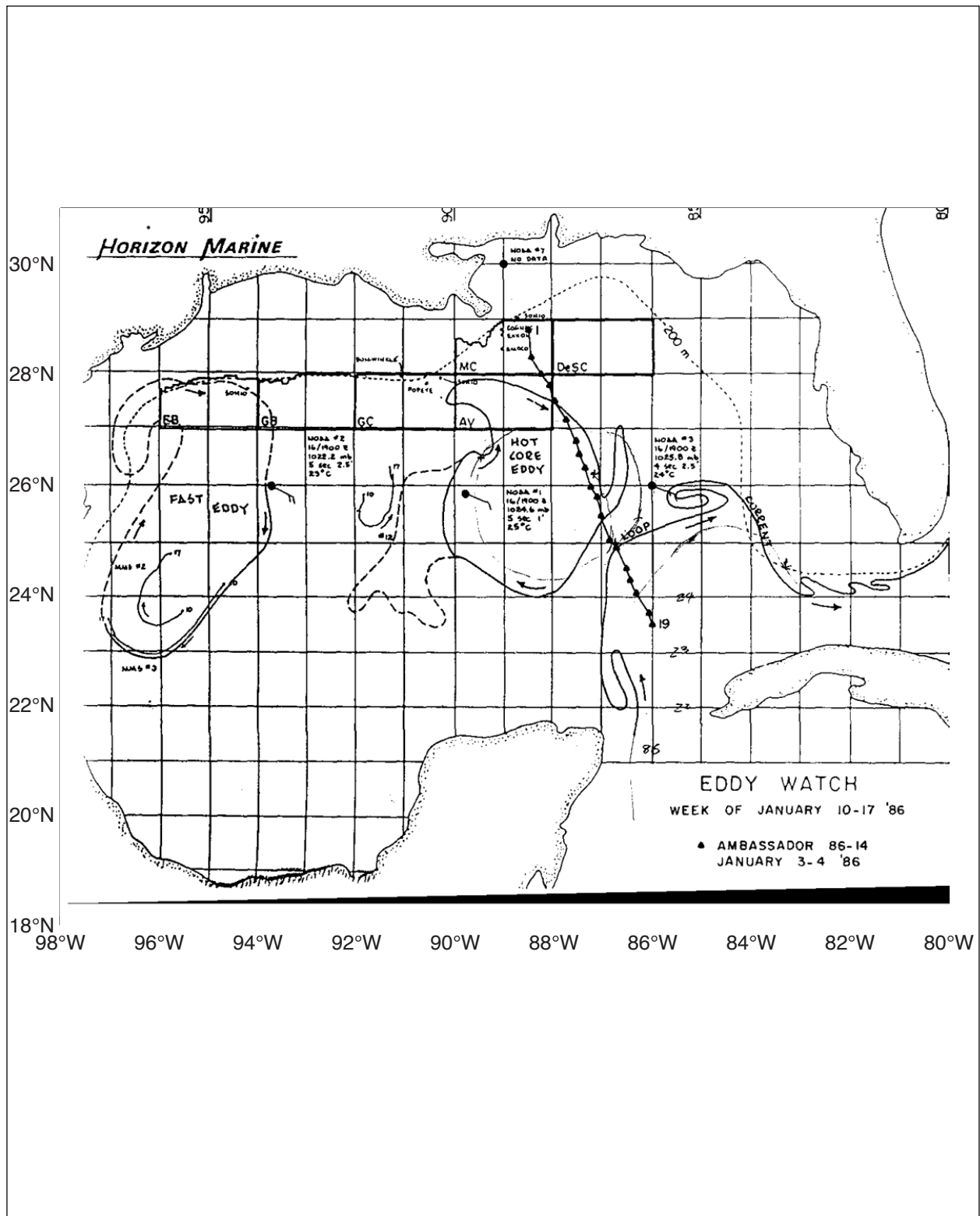


Figure 5.2-2. Sample HMI EddyWatch map from week of 10-17 January 1986 showing frontal analysis of “Fast Eddy”, “Hot Core Eddy”, and the Loop Current based on satellite-tracked drifters, SST, and a ship-of-opportunity transect.

outages occurred whenever the passive-gravity gradient stabilization system allowed the satellite to point too far off nadir, which caused the on-board tracker to fail to regain lock on the returned waveform over the ocean when coming off of land (Sandwell and McAdoo 1988). Continuous satellite altimetry from 35-day repeat sampling during the ERS-1 multidisciplinary phase, however, provided altimetric coverage during the time period in 1992 when EddyWatch™ reports were not published. This was fortunate because no ocean-color data were available during the summer of 1992 for monitoring of the LC and LC eddy fronts.

GEM Path and Configuration (P&C) daily analyses (Evans Hamilton 1992) were also used in the re-analysis to help determine LC eddy separation dates. GEM is both a model and a database and is the standard industry tool for hindcasting LC and LC eddy currents. Gulf metocean engineering designs rely on hindcasts from the model to provide a database for the location of the LC and LC eddies and the associated currents (Forristall et al. 2010). GEM is based on the feature model developed by Glenn et al. (1990) to support exploratory deepwater-drilling operations off the U.S. east coast. The model fits an idealized isolated translating elliptical paraboloid with a swirl velocity to: surface fronts in satellite imagery, expendable bathythermograph survey data, and satellite-tracked drifting-buoy data associated with anticyclonic recirculation embedded within the intruding LC and LC eddies, both separating from and propagating away from the LC. GEM eddy tracks from 1966 to 1991, including the initial portion of the track that corresponds to LC eddies embedded in the intruding LC, are shown in Figure 3 of Kantha et al. (2005).

Animations of the combined time series of color maps, SST images, HMI EddyWatch™ charts, and GEM P&C analyses were used to identify LC eddy separation and LC retreat following separation, supplemented with satellite altimetry maps from Seasat and ERS-1. CZCS images and GEM analyses showed conclusively that there were no LC eddy separation events from November 1978 through 1979. The one separation event reported in the literature during this time period, in April 1979 (Vukovich 1988; Vukovich 2012), was identified in the reanalysis as an eddy detachment, not an eddy separation. The first LC eddy separation event was identified using GEM analyses and occurred in July 1978, after which a continuous record of separation events and LC retreats following separation could be derived using the satellite and industry data records. Remarkably, the short-lived NASA Seasat Mission sampled this initial LC eddy separation event with both the Seasat satellite altimeter and the Seasat Synthetic-Aperture Radar (SAR) (Fu and Holt 1982), confirming the industry observations of a separation event. Figure 5.2-3 shows Gulf SSH calculated by adding Seasat SSH anomaly to the CUPOM model mean. The Seasat altimetric sampling allows an estimate of the LC retreat latitude, which was one of the most southern retreats observed in the historical record. Consistent with the far southern retreat of the LC after the first LC eddy separation, the second LC eddy separation event was detected in color images in February 1980, approximately 19 months later, which is the longest LC eddy separation period observed in the entire 35-year record from 1978 through 2012.

The retreat latitudes of the LC following LC eddy separation derived from SSH are not equivalent to retreat latitudes derived from SST or ocean-color fronts. In Forristall et al. (2010) the edge of the LC, as defined by the 17-cm SSH tracking contour used to track the LC in the CCAR Mesoscale SSH data products, was estimated to lie inside the surface thermal or ocean-color front by about 40 km. This offset is 0.36° along the northern edge of the LC front, which

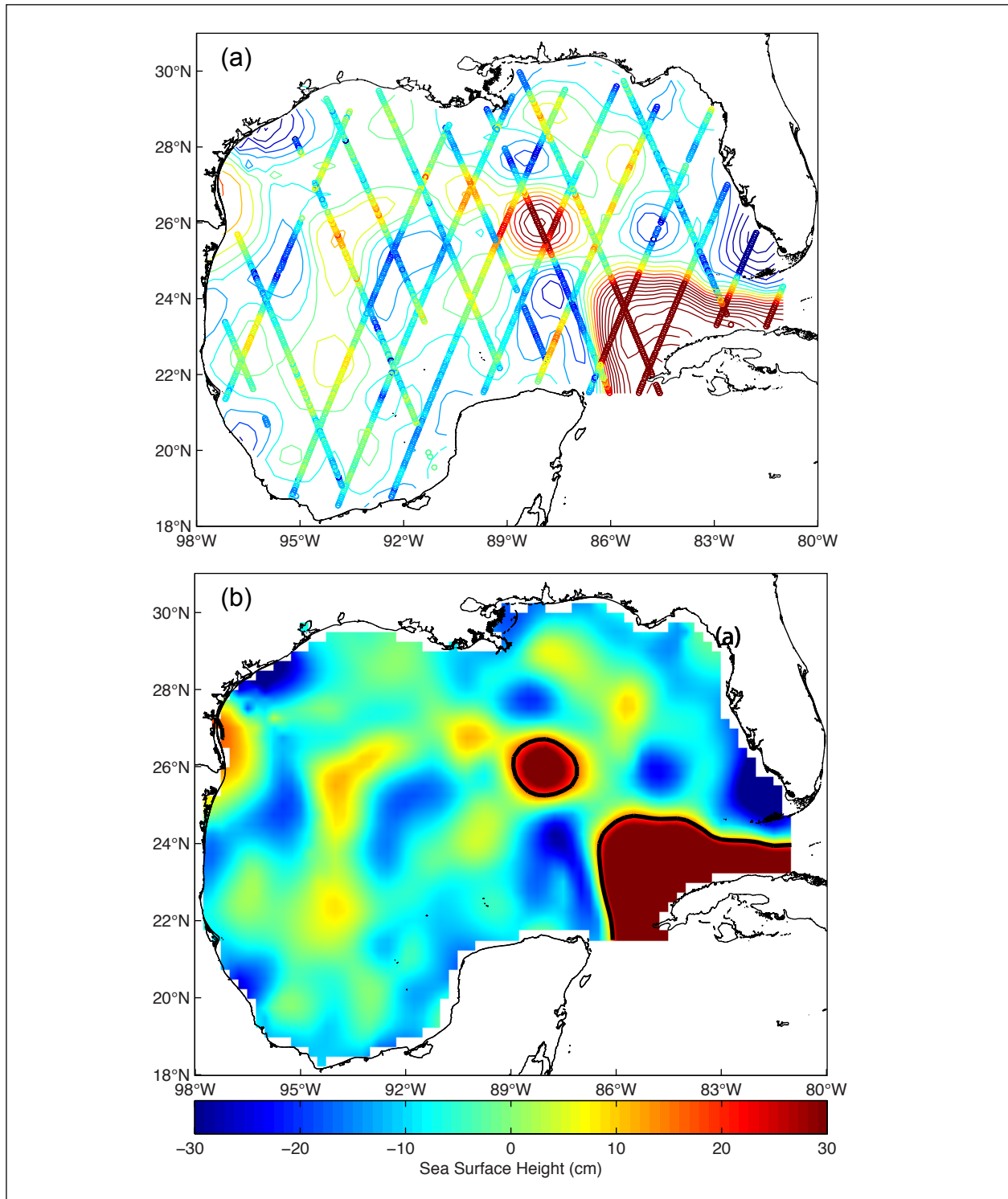


Figure 5.2-3. LC eddy 1978 as observed by Seosat approximately two weeks after eddy separation. Shown (a) as color-mapped along-track data overlaid on a contour plot of the objectively-mapped SSH (contour increment = 5 cm), and (b) as a SSH color image with the 17-cm LC tracking contour overlaid. Along-track data are from 16 July through 9 August 1978. The analysis date of the mapped data is 28 July 1978.

must be added to each SSH-derived retreat latitude value to allow consistent analyses of the LC retreat latitudes when combining the altimetric estimates with non-altimetric estimates. The two retreat latitudes derived from altimetry during the pre-altimetry time period, shown in Table 5.2-1, do not incorporate the offset, but the offset was applied before calculation of the mean.

Figures 5.2-4, 5.2-5 and 5.2-6 show imagery of all pre-altimetric eddies with exception of the two SSH-derived events shown in Figures 5.2-3 and 5.2-7, respectively, for the separation events detected using Seasat and ERS-1 altimetry. The black dashed lines show the derived LC retreat latitudes. Each eddy in Table 5.2-1 has been given a year or year-letter designation since multiple LC eddies were shed in some years. Note that the EddyWatch™ chart in Figure 5.2-6 (q) shows a deeply retreated Loop Current, although the SST data for the respective date suggest that the LC maximum latitude was further north. Two eddy separation events, LC eddy 1984b (#11, 28 August 1984) and LC eddy 1986b (#14, 12 September 1986), do not fall within the date range of the corresponding image/chart. For those events, images have been provided where the LC and LC eddy can be most clearly seen, although the movie sequences of satellite imagery and GEM P&C analyses suggest that separation happened a week to a month before the images shown in Figure 5.2-5 (j) and Figure 5.2-6 (m). Table 5.2-2 gives the data type and date range for the data used to create each image in Figures 5.2-4, 5.2-5 and 5.2-6. For the most part, the dataset used to create each image was also used to determine the respective separation date. The exceptions used GEM P&C analyses to set the separation date and are marked by a “†” symbol in Table 5.2-2. These include two SST images, #9 and 14, and all three EddyWatch™ maps, #12, 17, and 18. Otherwise, for the event dates derived from composite chlorophyll-a images, the first date of the corresponding image-date range was selected as the separation date. The date of the earliest image swath within the composite, providing evidence of LC eddy separation, was not identified, so the first date in the date range used to form the composite image was used for convenience. The separation dates derived from weekly SST images were set to mid-week.

The goal of the re-analysis was to derive a pre-altimetric LC record as consistent as possible with the LC eddy separation record derived from satellite altimetry, using the automated LC tracking procedure based on tracking the 17-cm LC contour in CCAR SSH maps (Leben 2005). Since altimetry well-resolves only the dominant Gulf mesoscale ocean circulation, small anticyclonic eddies generated near the periphery of the LC are typically not detected at the 17-cm level in the gridded CCAR SSH data products. SST imagery, however, may show warm surface features on the periphery of the LC that are not LC eddies per se because the subsurface waters below these features are not warm Caribbean water comprising the LC and LC eddies. These features are usually smaller in diameter and exhibit a weaker surface thermal expression than LC eddies. They may also be associated with cyclonic circulation that can be identified by the time-evolution of the SST pattern. Nevertheless, SST signatures of some of the smallest LC eddies in the 20-year altimetry record (i.e., Zapp, Walker, Brazos, etc.) were compared with the signatures of the pre-altimetry eddies to ensure that all eddies identified in the pre-altimetric record were large enough to be counted as LC eddies. Since all of the LC eddies in the altimetry record are “verified” – that is, all LC eddies appearing in the SST during the altimetry time period have been confirmed by the corresponding altimetry – eddies in the pre-altimetry record are considered LC eddies as long as their surface areas or surface thermal signatures are comparable or larger than the smallest LC eddies observed during the altimetry period. All the pre-altimetry LC eddies identified in the reanalysis meet this criterion. Neither was a minimum lifetime nor

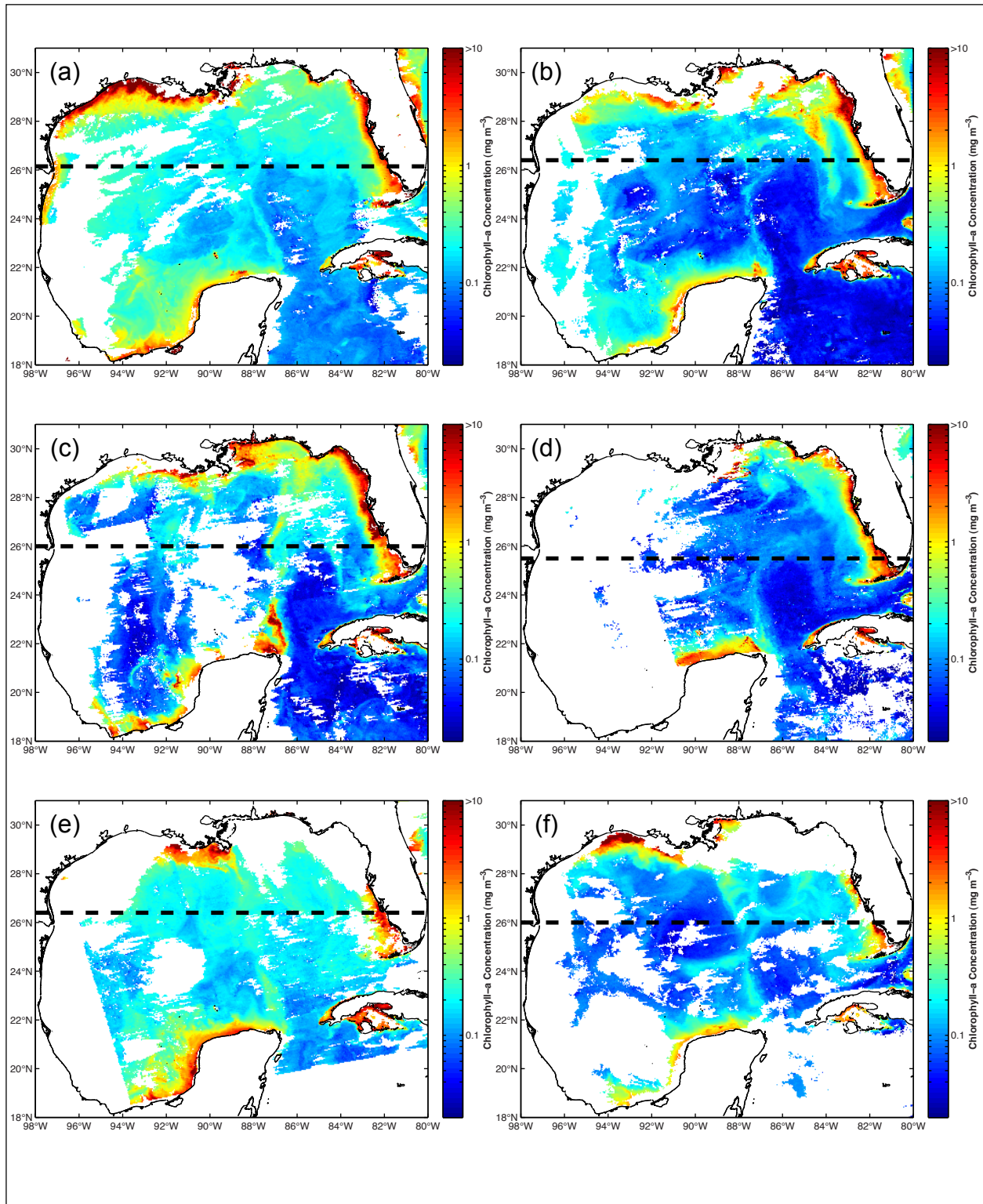


Figure 5.2-4. LC eddy separation events with LC retreat latitude following separation shown by dashed black lines. Date ranges for which the plots are valid are given in Table 5.2-2. LC eddy separation date: (a) 18 February 1980; (b) 16 May 1980; (c) 4 August 1980; (d) 4 July 1981; (e) 24 October 1981; (f) 21 August 1982.

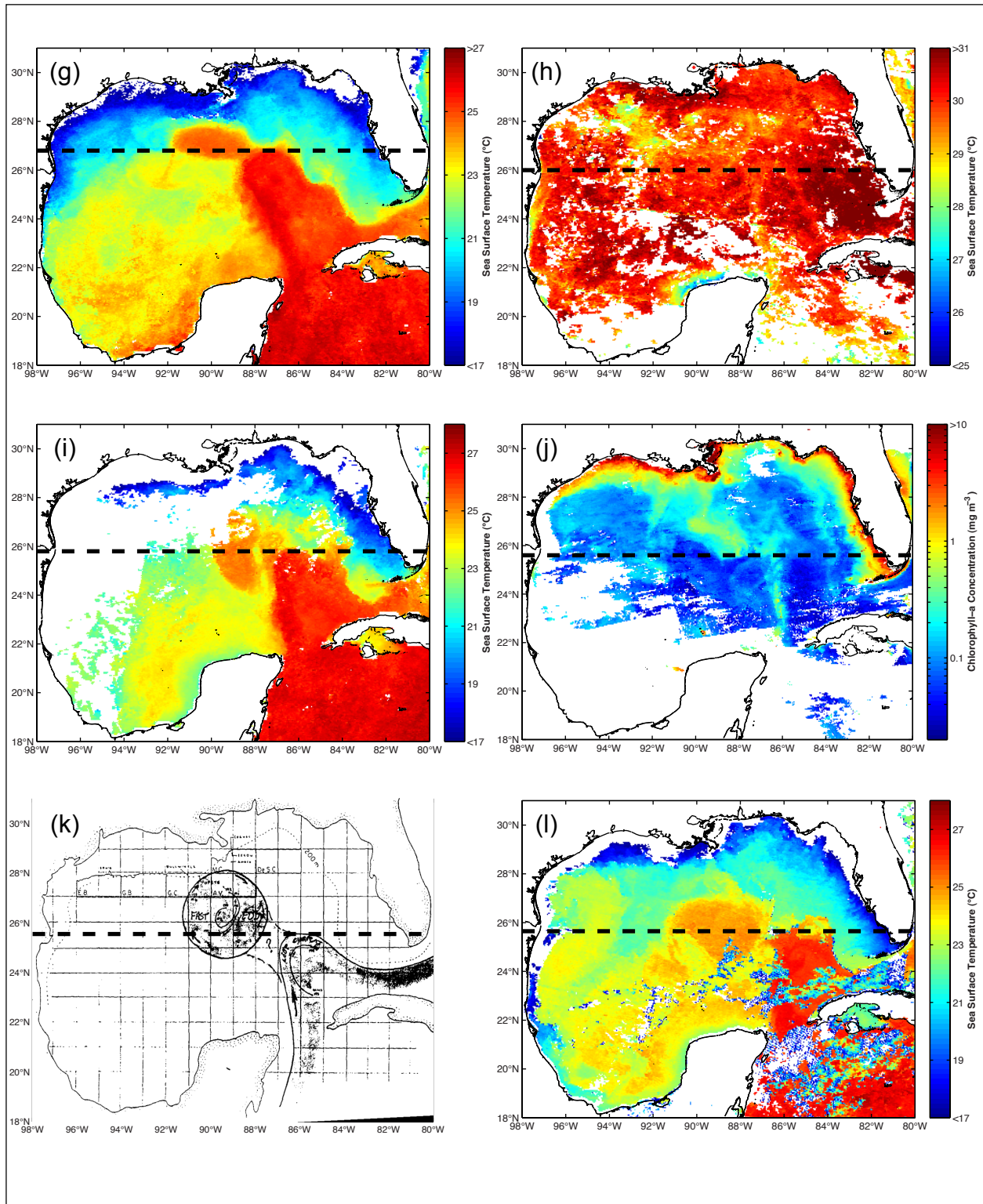


Figure 5.2-5. LC eddy separation events with LC retreat latitude following separation shown by dashed black lines. Date ranges for which the plots are valid are given in Table 5.2-2. LC eddy separation date: (g) 8 March 1983; (h) 23 August 1983; (i) 25 January 1984; (j) 28 August 1984; (k) 18 July 1985; (l) 18 January 1986.

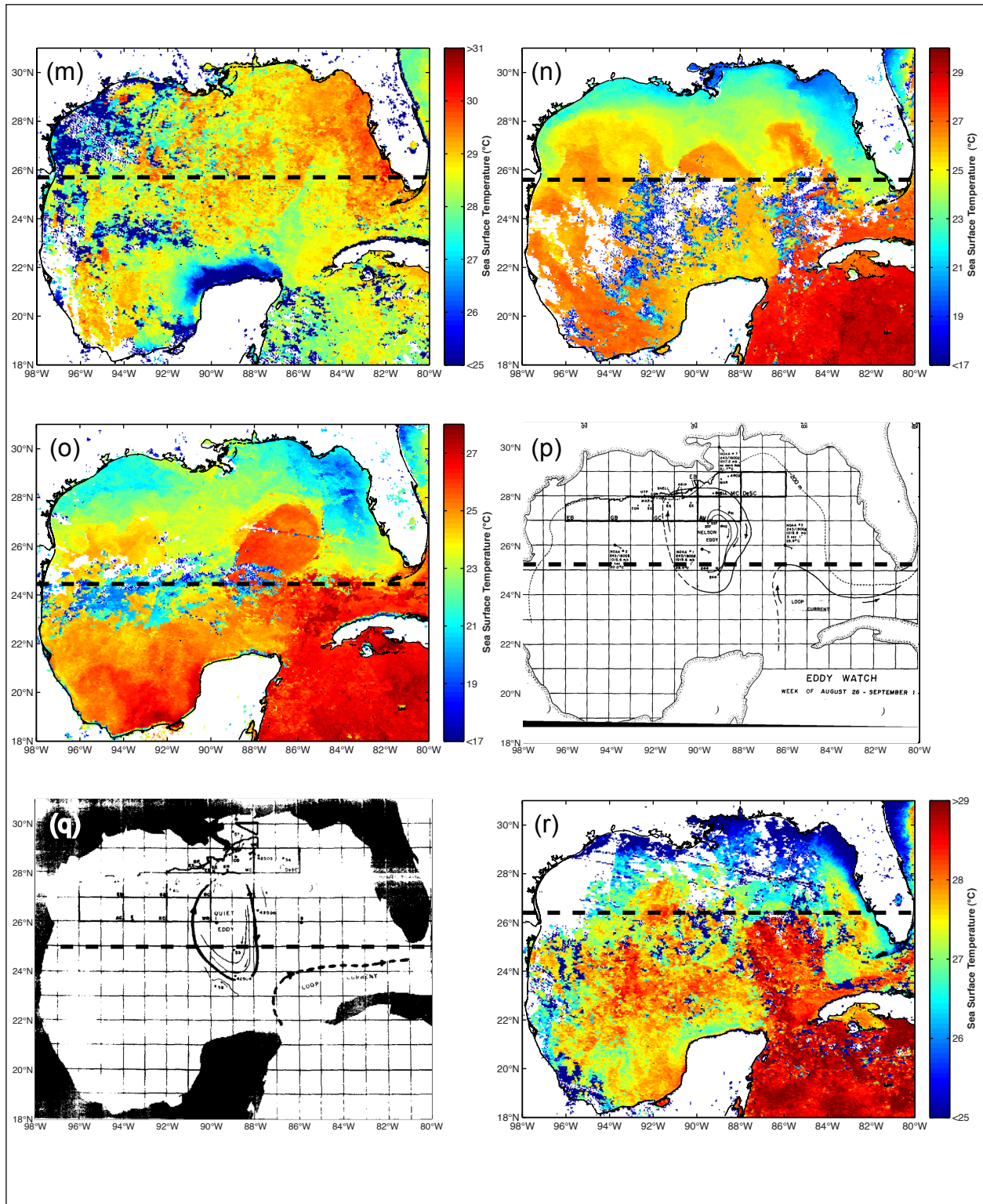


Figure 5.2-6. LC eddy separation events with LC retreat latitude following separation shown by dashed black lines. Date ranges for which the plots are valid are given in Table 5.2-2. LC eddy separation date: (m) 12 September 1986; (n) 8 November 1987; (o) 25 April 1988; (p) 1 September 1989; (q) 14 September 1990; (r) 1 November 1991.

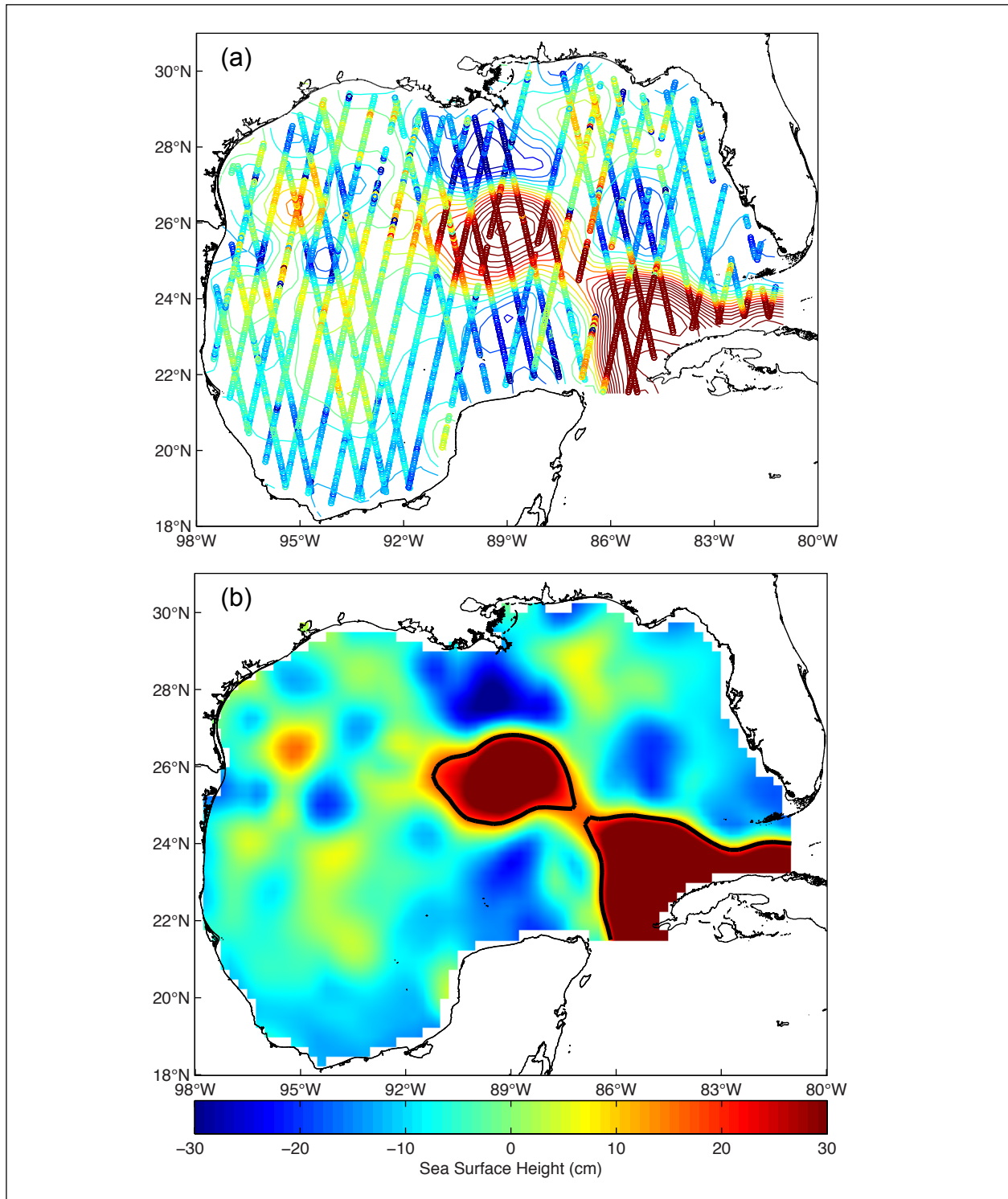


Figure 5.2-7. LC eddy 1992 "Unchained" as observed by ERS-1 on the date of separation, 10 August 1992. Shown (a) as color-mapped along-track data overlaid on a contour plot of the objectively-mapped SSH (contour increment = 5cm), and (b) as a SSH color image with the 17-cm LC tracking contour overlaid. Data are from 24 July through 27 August 1992.

Table 5.2-2. Date ranges for LC eddy separation events shown in Figures 5.2-4, 5.2-5 and 5.2-6

No.	Fig. No.	Separation Date	Best Available Imagery/Chart	Date Range for Data in the Image/Chart
2	5.2-4 (a)	18 Feb 1980	*Chlorophyll-a	18 Feb 1980 – 25 Feb 1980
3	5.2-4 (b)	16 May 1980	*Chlorophyll-a	16 May 1980 – 23 May 1980
4	5.2-4 (c)	04 Aug 1980	*Chlorophyll-a	04 Aug 1980 – 11 Aug 1980
5	5.2-4 (d)	04 Jul 1981	Chlorophyll-a	04 Jul 1981 – 11 Jul 1981
6	5.2-4 (e)	24 Oct 1981	*Chlorophyll-a	24 Oct 1981 – 31 Oct 1981
7	5.2-4 (f)	21 Aug 1982	*Chlorophyll-a	21 Aug 1982 – 28 Aug 1982
8	5.2-5 (g)	08 Mar 1983	*SST	05 Mar 1983 – 11 Mar 1983
9	5.2-5(h)	23 Aug 1983	*†SST	20 Aug 1983 – 26 Aug 1983
10	5.2-5 (i)	25 Jan 1984	*SST	22 Jan 1984 – 28 Jan 1984
11	5.2-5 (j)	28 Aug 1984	Chlorophyll-a	05 Sep 1984 – 12 Sep 1984§
12	5.2-5 (k)	18 Jul 1985	*†EddyWatch™	12 Jul 1985 – 19 Jul 1985
13	5.2-5 (l)	18 Jan 1986	SST	15 Jan 1986 – 21 Jan 1986
14	5.2-6 (m)	12 Sep 1986	*†SST	01 Oct 1986 – 07 Oct 1986§
15	5.2-6 (n)	08 Nov 1987	SST	05 Nov 1987 – 11 Nov 1987
16	5.2-6 (o)	25 Apr 1988	*SST	22 Apr 1988 – 28 Apr 1988
17	5.2-6 (p)	01 Sep 1989	*†EddyWatch™	26 Aug 1989 – 01 Sep 1989
18	5.2-6 (q)	14 Sep 1990	*†EddyWatch™	07 Sep 1990 – 14 Sep 1990
19	5.2-6 (r)	01 Nov 1991	*SST	29 Oct 1991 – 04 Nov 1991

* GEM P&C analyses (Evans Hamilton 1992) were available to verify separation date estimate.

† GEM P&C analyses determined separation date estimate.

§ Images shown in Figure 5.2-5 (j) and Figure 5.2-6 (m) do not depict the official separation dates but do show the LC eddy more clearly separated than the corresponding images.

minimum separation interval required of the LC eddies counted in the re-analysis. Beyond these caveats, the guidelines used for counting events were necessarily subjective: cohesive masses of water separating from the LC and causing significant change in LC area were deemed to be LC eddies provided they did not reattach to the LC at a later date.

Each LC eddy in the altimetry record was assigned a discrete date marking the completion of the eddy-separation process, objectively derived using the continuous sampling afforded by the multi-satellite altimetry and the breaking of the LC-tracking contour. Yet, eddy separation is a slow, continuous process that happens over the entire depth of the LC water column and can take months to complete. The estimated uncertainty in objective altimetric estimates, when compared with coincident subjective estimates, is ± 1 month (Leben 2005). SST and ocean-color sampling, however, are frequently interrupted by cloud-cover, often preventing clear views of ongoing separation processes. Therefore, LC and LC eddy signatures in SST and ocean-color imagery can be difficult to identify. Complex surface flows may obscure the northern boundary of the LC and the connectivity of the LC with a separating LC eddy. GEM analyses also may show large changes in LC eddy diameters and large variations in LC eddy positions. These uncertainties impact retreat latitude and separation-date estimates in the pre-altimetric record. As such, the

separation dates derived in the reanalysis are probably accurate to only ± 1.5 months, and the retreat latitudes to only $\pm 0.25^\circ$, at best.

5.3 COMPARISONS OF PREVIOUSLY PUBLISHED SEPARATION DATES WITH THE RE-ANALYSIS

Various versions of the LC eddy separation record over the pre-altimetry time period have been published and republished in the peer-reviewed literature (Vukovich 1988; Sturges 1993; Sturges 1994; Sturges and Leben 2000; Leben 2005) with the most recent being Vukovich (2012). Present comparisons and discussion focus on Vukovich (2012), since that work replicates and extends the pre-1988 separation record published in Vukovich (1988) and provides more information on the sampling available during the pre-altimetry time period. The other studies cited above, and recent publications supported by this study program (Chang and Oey 2012; Chang and Oey 2013a; 2013b), relied on the record published in Vukovich (1988). Therefore, it is important to review these early records of LC eddy separation and compare them with the reanalysis included in this report.

Table 5.3-1 shows the LC eddy separation dates from the re-analysis (Table 5.2-1) and corresponding dates in Vukovich (2012). For the pre-altimetry time period (1978-1992), Vukovich (2012) employed NASA CZCS ocean-color (or chlorophyll-a) data from 1979 through 1985, “ship-of-opportunity” data, and SST data to identify LC eddy separations. SST data came primarily from NOAA AVHRR instruments, though SST data from NOAA VHRR, GOES, Seasat, and the Heat Capacity Mapping Mission (HCMM) were also used. Vukovich (2012) relied heavily on NOAA VHRR SST to derive dates from 1972 through 1978, but does not specify which SST data source was used to identify specific separation events. The last usable VHRR data were collected on 1 March 1979 (NOAA 5 satellite), before the second LC eddy separation event in early 1980 (Table 5.3-1). AVHRR coverage began with the launch of the first four-channel AVHRR instrument (TIROS-N satellite) on 13 October 1978. The AVHRR instrument was later enhanced to include five channels and was then put into operational use onboard NOAA 7 on 23 June 1981 (Casey et al. 2010; Kramer 2002; Schnapf 1981). AVHRR coverage lasted through the end of the pre-altimetry time period and beyond. VHRR LC monthly-frontal analyses, including copies of the original SST maps over the time period from 1972 through 1977, are found in Vukovich et al. (1978) and Vukovich et al. (1979). Other AVHRR SST monthly-frontal analyses and imagery are found in Vukovich (1986), Vukovich and Maul (1985), Vukovich and Crissman (1986), Vukovich (1988), Vukovich (2007), and Vukovich (2012). GOES SST may have been used for any number of events, but were minimally used according to the description in Vukovich (2012). Seasat recorded both microwave and infrared SST, although these data were only available from July to October 1978, after the first and before the second Vukovich (2012) LC eddy separation found in Table 5.3-1. No separation events could have been directly observed with the Seasat data, given the identified separation dates. Additionally, Table 5 of Vukovich (2012) indicates that no usable data were available in the Gulf during the entire lifetime of Seasat. The HCMM satellite was launched in April 1978 and was decommissioned in August 1980, so it could only have been used to help identify the first three of the Vukovich (2012) separation events listed in Table 5.3-1 (Kramer 2002). Table 4 of Vukovich (2012) indicates which data type – ocean color, SST, or ship-of-opportunity – was used to derive each of the LC eddy separation dates.

Table 5.3-1. Comparison of re-analysis LC eddy separation dates with those from Vukovich (2012)

No.	Year-Letter	Industry Name	Re-analysis	*Vukovich (2012)	†Difference (days)
1	1978	-	15 Jul 1978	Jun 1978	30
-	-	-	-	Apr 1979	-
2	1980a	-	18 Feb 1980	Jan 1980	34
3	1980b	-	16 May 1980	-	-
4	1980c	-	04 Aug 1980	-	-
5	1981a	-	04 Jul 1981	Mar 1981	111
6	1981b	-	24 Oct 1981	-	-
7	1982	-	21 Aug 1982	May 1982	98
8	1983a	-	08 Mar 1983	Mar 1983	-7
9	1983b	-	23 Aug 1983	-	-
10	1984a	-	25 Jan 1984	Feb 1984	-21
11	1984b	Arnold	28 Aug 1984	-	-
12	1985	Fast	18 Jul 1985	Jul 1985	3
13	1986a	Hot Core	18 Jan 1986	Jan 1986	3
14	1986b	Instant	12 Sep 1986	Oct 1986	-33
15	1987	Kathleen	08 Nov 1987	Nov 1987	-7
16	1988	Murphy	25 Apr 1988	May 1988	-20
17	1989	Nelson	01 Sep 1989	May 1989	109
18	1990	Quiet	14 Sep 1990	Sep 1990	-1
19	1991	Triton	01 Nov 1991	Sep 1991	47
20	1992	Unchained	10 Aug 1992	Jul 1992	26
Mean					24.8
RMS					52.1
Mean without #5, 7, and 17					4.5
RMS without #5, 7, and 17					24.1

* Dates for LC eddy separation events that occurred in the 1970s and after 1992 are listed in Vukovich (2012).

† Differences assumed that all Vukovich (2012) separation events occurred on the 15th of the given month.

All available information on ocean features was integrated into monthly frontal-analysis maps indicating the location of LC and LC eddy fronts (e.g., Vukovich (2012), Figure 1). As noted in the preceding discussion, satellite SST data played a major role in the development of these analyses. In the time periods 1972 through 1978, and 1986 through 1991, only satellite SST data were available to develop the frontal analyses. (Details in Vukovich (2012) describing events preceding 1978 are largely omitted from this chapter since online data archives do not exist for satellite data from that time period.) Information provided in Table 5 of Vukovich (2012) indicates that satellite data were insufficient to map LC and LC eddy fronts during June through October every year from 1978 through 1983 and for two to five months every summer and fall for the years 1984 through 1991. This is because the LC and LC eddy fronts could not be detected in SST imagery when the warm seasonal mixed layer masked the surface thermal

signature of the fronts. According to Vukovich (1988), there were generally only five to nine clear-sky images during the months from November through May, and only occasionally were images in late October and early June usable. When SST frontal analyses were insufficient for LC tracking, Vukovich (2012) used ship-of-opportunity data. Specifically, ship-of-opportunity data were used to identify LC eddy separations #1, 12, 18, 19, and 20 in Table 5.3-1 (ship-of-opportunity data were used exclusively to derive #18, 19, and 20). According to Table 5 of Vukovich (2012), there were no data available during the time periods when LC eddy separation events #1, 12, 14, 18, and 19 occurred, and LC eddy #20 was ambiguously reported to have “missing” data. Five of these six LC eddy separation events were derived with ship-of-opportunity data. However, since there was either missing or no data at the actual times of separation for the five events, the ship-of-opportunity data may not have provided much useful information. Therefore, it is difficult to evaluate the efficacy of the LC or LC eddy monitoring during these time periods or to confirm the reported results.

The criteria met by each LC eddy separation listed in Vukovich (2012) are the following: only LC eddy separation events shedding eddies with a diameter of ~300 km or greater at the time of separation, that persisted for five months or more, and propagated into the western Gulf were counted. There are significant differences between the re-analysis dates and the Vukovich (2012) dates in Table 5.3-1. Vukovich (2012) identified one separation event in April 1979 that GEM analyses and CZCS imagery showed was an eddy detachment since the eddy later reattached to the LC. As a result, that event was ignored in the re-analysis. Five eddies detected in the re-analysis do not appear in Vukovich (2012) (#3, 4, 6, 9, and 11 in Table 5.3-1), four of which relied primarily on chlorophyll-a data. Three of the five eddies (#4, 6, and 9) separated in time periods when Vukovich (2012) reported no data were available. This includes the event that was identified using SST imagery (#9). The other two (#3 and 11) may have been undetected in the chlorophyll-a or failed to meet LC eddy diameter criteria. Diameter approximation using chlorophyll-a or SST imagery is a subjective process since cloud cover, meanders, surface-layer masking, and peripheral cyclones frequently conceal full-eddy areal coverage. Vukovich (2012) may have estimated that the diameters of these two LC eddies were less than 300 km. These eddies may also have been ignored because they could not be tracked for five months into the western Gulf. In the re-analysis, LC eddies were often impossible to track systematically beyond about three months after separation unless trajectory information from GEM P&C analyses were available. In SST and chlorophyll-a images, LC eddy surface signatures typically fade into the background less than five months after eddy separation. If the five-month eddy lifetime requirement had been strictly enforced in the re-analysis, many of the early LC eddy events including eddy #3 and #11 would have been eliminated.

Beyond differences in the number of LC eddy separations listed in Table 5.3-1, there are also some differences between the separation dates in the re-analysis and those in Vukovich (2012) for the events that were identified in both studies. Assuming that each date in Vukovich (2012) corresponds to the 15th day of the respective month, nine separation dates differ by one month or less (#1, 8, 10, 12, 13, 15, 16, 18, and 20) and three events (#2, 14, and 19) differ by between one and two months. These twelve events show good agreement (mean = 4.5 days, RMS = 24.1 days), comparable to uncertainty estimates of LC eddy separation dates found between subjective tracking by an expert and automated-altimetric tracking in Leben (2005) (mean = 3 days, RMS = 28 days). The three other events, however, differ by more than three months (#5, 7,

and 17) and degrade uncertainty estimates substantially (mean = 24.8 days, RMS = 52.1 days). The re-analysis separation dates for these separation events fell in summer, when Vukovich (2012) reported that no satellite data were available.

Satellite data and industry analyses used in the re-analysis were significantly different than the data used in Vukovich (2012). Pathfinder AVHRR SST data (August 1981-1992) were employed extensively in the re-analysis. The Pathfinder SST program began in the early 1990s and is a NASA/NOAA/NODC joint effort to produce a long, accurate, and consistent AVHRR data record. Newly reprocessed SST data from 1985 through 2001 were released by NODC in April 2003, and reprocessed SST data from 1981 through 1984 were released in April 2009 (Casey et al. 2010). AVHRR data prior to August 1981, VHRR, Seasat, HCMM, and GOES SST were not used at all in the re-analysis, though they were also minimally used by Vukovich (2012). CZCS ocean-color data were employed considerably more in the re-analysis. Table 4 in Vukovich (2012) shows that in no instance during the pre-altimetry time period was a separation event identified using exclusively ocean-color data, and there were only two instances (#7 and 12) for which ocean color was used. Conversely, the re-analysis used CZCS to derive seven event dates (#2, 3, 4, 5, 6, 7, and 11), two of them exclusively (#5 and 11). See Table 5.2-1. In the re-analysis, CZCS chlorophyll-a images were reliable from May through August and also at times during the months of February, March, April, September and October. Missing frontal analyses during the summer and fall of 1978 through 1985, listed in Table 5 of Vukovich (2012), indicate little or no reliance on CZCS ocean-color data for LC tracking. This may be an artifact of the CZCS data processing available at the time that the original published analyses in Vukovich (1988) were performed. The re-analysis reported here benefited greatly from the comprehensive reprocessing of the CZCS archive by NOAA and NASA (Gregg et al. 2002). Ship-of-opportunity data were not used in the re-analysis per se. However, 15 of the 20 pre-altimetry separation dates were covered by GEM analyses (see Table 5.2-1), which incorporate ship-survey data and offer additional kinematic information about LC eddy separation from satellite-tracked drifting-buoy trajectories. EddyWatchTM reports were also available, providing frontal analyses as well as ship surveys and satellite-tracked drifting-buoy tracks used by the offshore industry for operational monitoring of the LC. Seasat altimetry data were used to map SSH in the Gulf just after the separation of the first event counted in the re-analysis (LC eddy 1978). ERS-1 altimetry was used to derive event #20, LC eddy 1992 “Unchained”.

In summary, time periods were noted in both the re-analysis, and by Vukovich (2012) when satellite data quality was poor, with the eastern Gulf obscured by clouds or the LC masked by seasonal warming of the mixed layer. Subsequently, identification of LC and LC eddy fronts and LC eddy separation events during the summer and fall were difficult without ancillary information such as that provided from ship-board surveys and satellite-tracked drifting buoys. Nevertheless, in the re-analysis, more satellite coverage was found than was described in Vukovich (2012). Compared to the datasets used to estimate the separation dates in Vukovich (2012), the re-analysis included more satellite data during summer and late fall, and had access to supplementary information provided by the EddyWatchTM and GEM analyses. Thus, the separation dates in the re-analysis are likely more accurate and less affected by seasonal data outages than those reported in Vukovich (2012). Discussion of whether date discrepancies like those found in the data comparison shown in Table 5.3-1 prevented identification of a seasonal LC signal will be pursued in Section 5.5 of this report.

5.4 THE ALTIMETRIC LOOP CURRENT RECORD

The 20-year multi-satellite altimeter data record was used to investigate LC intrusion and LC eddy separation events over the time period from January 1993 through December 2012. Analyzed altimetry datasets included daily CCAR and AVISO SSH and a hybrid daily SSH based on AVISO SSHA added to the University of Colorado Princeton Ocean Model (CUPOM) mean (AVISO-CUPOM). The daily AVISO and AVISO-CUPOM datasets were created from the delayed-time weekly $\frac{1}{4}^\circ$ AVISO SSH (absolute dynamic topography) dataset, linearly interpolated to daily maps. AVISO and AVISO-CUPOM datasets were both demeaned in the deepwater by subtracting the daily-averaged values of SSH in water deeper than 200 m in the Gulf to remove the steric signal associated with seasonal heating of the mixed layer. The steric signal appears approximately as an annual sine wave with 5.8 cm amplitude in AVISO SSH, with the peak near 15 September and the trough near 16 March. The demeaning procedure was not applied to the CCAR SSH because the along-track altimeter data are de-trended before gridding of the CCAR SSH fields, which effectively removes the steric signal. Satellite altimeter missions that provided the sampling used in the CCAR SSH product are shown in Figure 5.4-1. Coincident satellite coverage, from different satellites, was available during nearly the entire record, except for three months in early 1994 when ERS-1 was placed into a 3-day exact repeat orbit for ice sheet mapping and only TOPEX/Poseidon altimeter data were available. Additional information about the CCAR SSH product is provided in Chapter 2. Specifics of satellite coverage used in the AVISO (and AVISO-CUPOM) dataset are not documented, but are likely comparable to that used in the CCAR dataset.

LC eddy separation dates and LC metrics (Leben 2005) were derived using a MATLAB® toolbox developed during this research program at CCAR called the Loop Current Toolbox (LCT). The LCT automatically identifies and tracks the LC and LC eddies in gridded SSH datasets. LC and LC eddy boundaries are defined by the location and breaking of the 17-cm tracking contour. CCAR separation dates are given in Table 5.4-1 along with the corresponding retreat latitudes and separation periods. Retreat latitude is defined as the maximum latitude of the LC immediately following separation of a LC eddy (Leben 2005). In the LCT, the retreat latitude is equal to the minimum value of the maximum latitude of the LC tracking contour observed in SSH maps during the first five days after LC eddy separation. In the CCAR SSH dataset, the mean separation period is 243.3 days, and the mean retreat latitude is 26.2° (with offset; see Section 5).

Table 5.4-2 compares the CCAR LC eddy separation dates with the corresponding dates derived from the AVISO and AVISO-CUPOM SSH datasets. Also, Tables 5.4-1 and 5.4-2 contain two anomalous events, LC eddies Zorro and Franklin, which were large anticyclonic eddies that formed after deep LC intrusions and yet exhibited little or no westward propagation away from the LC during their lifetimes. Zorro separated from the northwestern edge of the LC in June 2007 and dissipated in 10 weeks without any significant westward propagation. Satellite-tracked drifting buoys deployed in Zorro at the time of separation showed that the entire recirculation of the separated anticyclonic eddy was entrained along the outer edge of the LC and advected out of the Gulf (Coholan et al. 2008). This was the first time that the rapid and total dissipation of a major anticyclonic eddy in the Gulf had been observed. Franklin was one of the LC eddies observed during the study program, and its formation and ultimate separation is described in detail in Section 3.2.2. Franklin was a relatively large eddy when it initially detached from the

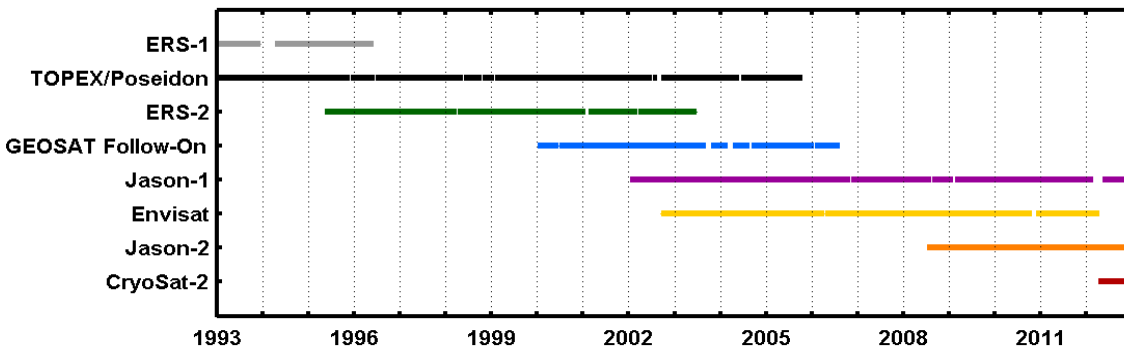


Figure 5.4-1. Satellite usage in the CCAR gridded altimeter dataset during the time period from 1993 through 2012.

LC in June 2010; however, the eddy became progressively smaller as repeated reattachment and detachment cycles reduced the size and intensity of the recirculation. The weakening of the eddy circulation resulted in little or no β -induced westward propagation, since the induced velocity is a function of eddy amplitude (Nof 1981). As a result, the eddy remained near the LC and continued to interact with the LC until early 2011.

Counting Zorro and Franklin, the number of LC eddy separation events identified in the CCAR, AVISO, and AVISO-CUPOM datasets over the 20-year satellite-altimeter record totaled 30, 28, and 30 events, respectively. The difference in the totals is because Quick and Zorro were not distinct events in the AVISO SSH record. According to the AVISO SSH maps, Pelagic and Quick were connected and appeared as one eddy at the 17-cm contour level when they separated from the LC and then later split into the two observed eddies. In the CCAR and AVISO-CUPOM SSH maps, Pelagic separates first from a deeply intruded LC followed quickly by the separation of Quick, hence the name. The difference in the order of eddy separation versus splitting in the two scenarios is a consequence of the means used to estimate the total SSH. As was discussed in Section 2.7.4, there are differences in both the amplitude and spatial structure of the CCAR and AVISO mean SSH maps in the eastern Gulf (Figure 2.7-11). When the two datasets have been referenced to the same level, the CCAR mean SSH, which depends on CUPOM for the unobserved stationary signal not observable by altimetry, is as much as 15 cm higher than the AVISO mean SSH in the central eastern Gulf where the LC tracking contour tends to break during LC eddy separation. Consequently, the CUPOM mean contributes SSH signal in the CCAR and AVISO-CUPOM SSH products that keeps Quick attached until after the separation of Pelagic, as was determined by Horizon Marine, Inc. (HMI) at the time these events occurred.

This is not the case for the AVISO SSH that is based on the CNES/CLS 2009 Mean Dynamic Topography (Rio and Larnicol 2010). In the case of Zorro, AVISO SSH shows a reattachment of the eddy to the LC at the 17-cm contour level that is not detected in the CCAR or AVISO-CUPOM datasets, which may also be attributed to the differences in the mean. In most cases, the separation dates of the CCAR and AVISO-CUPOM datasets are more similar, as is the case of Xtreme (two days apart) and Albert (1 day apart) – and both of them dissimilar to the corresponding AVISO product dates. For example, the separation dates of Xtreme and Albert are different by 20 and 18 days and 26 and 25 days, respectively, from the LC eddy separation dates determined from the CCAR and AVISO-CUPOM datasets.

Table 5.4-1. LC eddy separation event dates with the corresponding retreat latitudes and separation periods from January 1993 through December 2012, derived from CCAR SSH dataset

No.	Year-Letter	Industry Name*	Separation Date	Confirmation Dataset	Retreat Latitude (°)	Separation Period (days)
21	1993a	Whopper	10 Jul 1993	SSH	27.1	334
22	1993b	Xtra	11 Sep 1993	SSH	26.5	63
23	1994	Yucatan	26 Aug 1994	SSH	26.2	349
24	1995a	Zapp	19 Apr 1995	SSH	26.8	236
25	1995b	Aggie	07 Sep 1995	SSH	25.5	141
26	1996a	Biloxi	15 Mar 1996	SSH	26.2	190
27	1996b	Creole	25 Oct 1996	SSH	24.6	224
28	1997	El Dorado	30 Sep 1997	SSH	25.2	340
29	1998	Fourchon	22 Mar 1998	SSH	24.7	173
30	1999	Juggernaut	28 Sep 1999	SSH	25.2	555
31	2001	Millennium	10 Apr 2001	SSH	25.7	560
32	2002a	Pelagic	28 Feb 2002	SSH	27.3	324
33	2002b	Quick	13 Mar 2002	SSH	24.7	13
34	2003	Sargassum	05 Aug 2003	SSH	26.6	510
35	2004a	Titanic	08 Feb 2004	SSH	25.8	187
36	2004b	Ulysses	26 Aug 2004	SSH	25.0	200
37	2005	Vortex	13 Sep 2005	SSH	26.8	383
38	2006a	Walker	08 Feb 2006	SSH	27.3	148
39	2006b	Xtreme	04 Mar 2006	SSH	26.0	24
40	2006c	Yankee	26 Sep 2006	SSH	25.8	206
41	2007a	Zorro	07 Jun 2007	SSH	26.1	254
42	2007b	Albert	16 Nov 2007	SSH	26.2	162
43	2008a	Brazos	06 Mar 2008	SSH	26.3	111
44	2008b	Cameron	01 Jul 2008	SSH	26.0	117
45	2009a	Darwin	24 Feb 2009	SSH	25.4	238
46	2009b	Ekman	29 Aug 2009	SSH	24.9	186
47	2010	Franklin	01 Oct 2010	SSH	25.0	398
48	2011	Hadal	14 Aug 2011	SSH	25.9	317
49	2012a	Icarus	03 Feb 2012	SSH	25.9	173
50	2012b	Jumbo	04 Aug 2012	SSH	24.3	183
Mean					26.2†	243.3

* Using an earlier version of the CCAR SSH dataset, Leben (2005) identified HMI eddy Odessa/Nansen as a minor eddy. In the current CCAR SSH dataset Odessa/Nansen was completely insignificant and was excluded from further analysis.

† An offset of 0.36° must be added to SSH-derived retreat latitudes to make them consistent with the pre-altimetry retreat latitude values in Section 5.2 estimated from satellite SST and ocean color frontal analyses. The offset was not added to the retreat latitudes listed in the table, but was applied when calculating the mean. The mean of the values listed in the table is 25.8°.

Table 5.4-2. Comparison of LC eddy separation event dates derived from CCAR, AVISO, and AVISO-CUPOM SSH datasets from January 1993 through December 2012

No.	Industry Name	CCAR Separation Date	AVISO Separation Date	AVISO-CUPOM Separation Date
21	Whopper	10 Jul 1993	08 Jul 1993	08 Jul 1993
22	Xtra	11 Sep 1993	04 Sep 1993	06 Sep 1993
23	Yucatan	26 Aug 1994	19 Aug 1994	24 Aug 1994
24	Zapp	19 Apr 1995	17 Apr 1995	15 Apr 1995
25	Aggie	07 Sep 1995	01 Sep 1995	08 Sep 1995
26	Biloxi	15 Mar 1996	08 Mar 1996	15 Mar 1996
27	Creole	25 Oct 1996	20 Jul 1996	17 Aug 1996
28	El Dorado	30 Sep 1997	25 Sep 1997	29 Sep 1997
29	Fourchon	22 Mar 1998	12 Feb 1998	20 Feb 1998
30	Juggernaut	28 Sep 1999	28 Sep 1999	05 Oct 1999
31	Millennium	10 Apr 2001	29 Mar 2001	07 Apr 2001
32	Pelagic	28 Feb 2002	24 Feb 2002	26 Feb 2002
33	Quick	13 Mar 2002	*	02 Mar 2002
34	Sargassum	05 Aug 2003	11 Aug 2003	11 Aug 2003
35	Titanic	08 Feb 2004	20 Dec 2003	24 Dec 2003
36	Ulysses	26 Aug 2004	19 Aug 2004	21 Aug 2004
37	Vortex	13 Sep 2005	11 Sep 2005	10 Sep 2005
38	Walker	08 Feb 2006	06 Feb 2006	03 Feb 2006
39	Xtreme	04 Mar 2006	12 Feb 2006	02 Mar 2006
40	Yankee	26 Sep 2006	15 Sep 2006	18 Sep 2006
41	Zorro	07 Jun 2007	†	09 Jun 2007
42	Albert	16 Nov 2007	21 Oct 2007	15 Nov 2007
43	Brazos	06 Mar 2008	02 Mar 2008	04 Mar 2008
44	Cameron	01 Jul 2008	27 Jun 2008	30 Jun 2008
45	Darwin	24 Feb 2009	14 Feb 2009	23 Feb 2009
46	Ekman	29 Aug 2009	22 Jun 2009	03 Jul 2009
47	Franklin	01 Oct 2010	27 Jun 2010	04 Jun 2010
48	Hadal	14 Aug 2011	22 Jul 2011	28 Jul 2011
49	Icarus	03 Feb 2012	05 Nov 2011	11 Nov 2011
50	Jumbo	04 Aug 2012	28 May 2012	16 Jun 2012

* In the AVISO product, Pelagic and Quick separate from the LC as one eddy, though they split from each other only days after separation.

† Zorro appears as a detachment event in the AVISO product.

Direct comparison of the LC eddy separation dates derived from each of the datasets shows that separation occurs later in the CCAR SSH dataset than the other two datasets for the majority of the events, sometimes even months later. Of the 28 LC eddy separation events identified in all three datasets at the 17-cm level, a total of 24 separation dates were later in the CCAR dataset versus those derived from the datasets based on AVISO SSHA. Thus, the “delay” is likely caused by differences in smoothing applied during objective analysis of the CCAR and AVISO SSHA datasets rather than differences in mean SSH used to produce the synthetic SSH. Several specific examples implicating the smoothing are the CCAR separation dates for Titanic, Franklin, and Icarus, which are one month, three months, and two months later, respectively, than the corresponding AVISO and AVISO-CUPOM dates even though the CCAR and AVISO-CUPOM datasets are both based on the CUPOM model mean.

In addition to LC eddy separation detection, the LCT uses the breaking of the 17-cm LC tracking contour for detachment detection and continuously tracks each detached LC eddy contour until reattachment to the LC. Dates of LC eddy detachment detected in the CCAR, AVISO, and AVISO-CUPOM datasets are listed in Table 5.4-3. Although separation events can be matched up relatively well between the three datasets, finding correspondence between detachment events is more difficult since the eddy typically remains detached from the LC for less than one month. The number of detachment events detected in the CCAR, AVISO, and AVISO-CUPOM datasets totaled 30, 27, and 13, respectively. The CCAR and AVISO datasets have approximately the same number of detachment events as separation events. The detachment event count for AVISO-CUPOM, however, is significantly less, indicating that when the smoother, higher amplitude AVISO SSHA is combined with the higher amplitude mean SSH field from CUPOM fewer detachments are detected.

Detachment events were matched up by assuming that LC eddy detachments detected in the datasets correspond to the same event when the dates differ by less than one month. The number of detachment events separated by less than one month occurred 12 times in the CCAR and AVISO datasets, nine times in the CCAR and AVISO-CUPOM datasets, and 12 times in the AVISO and AVISO-CUPOM datasets. There were eight times that all three datasets showed detachment events separated by less than one month. AVISO and AVISO-CUPOM show the best agreement since all but one of the AVISO-CUPOM dates were within one month of an AVISO-derived date. Even so, AVISO-CUPOM did not match AVISO 15 times. Overall the results for LC eddy detachment events agree less than LC eddy separation events indicating that detachment is sensitive to both differences in the smoothing and differences in the mean between the three datasets.

Monthly histograms of LC eddy separation and detachment dates from Table 5.4-2 and 5.4-3 respectively, are shown in Figure 5.4-2. The histograms from all three datasets show peaks in the February/March and August/September time periods. The CCAR dataset histogram peaks are the most sharply defined, while AVISO-CUPOM peaks are least distinct. Seasonality of LC eddy separation will be discussed in greater detail in Section 5.5. The seasonal distribution of detachment events is inconsistent among the datasets. CCAR detachments peak strongly in July – September. AVISO dates show two small peaks, one in January and one in May. The AVISO-CUPOM annual monthly distribution is close to uniform, with a minor peak in July. Detachment events are complex processes that merit further exploration in the future.

Table 5.4-3. Comparison of LC eddy detachment event dates derived from CCAR, AVISO, and AVISO-CUPOM SSH datasets from January 1993 through December 2012. The HMI industry name of the LC eddy separation event following each date is also listed

No.	Impending Event/ Industry Name	CCAR Detachment Date	AVISO Detachment Date	AVISO-CUPOM Detachment Date
1	Whopper	28 May 1993	24 May 1993	27 May 1993
2	Xtra		15 Aug 1993	22 Aug 1993
3	Zapp	11 Mar 1995	06 Mar 1995	12 Mar 1995
4	Biloxi		25 Jan 1996	04 Feb 1996
5	Creole	20 Aug 1996		
6	Creole	12 Sep 1996		
7	Creole	14 Oct 1996		
8	El Dorado		26 Jul 1997	
9	Fourchon	*30 Sep 1997		
10	Fourchon	02 Mar 1998		
11	Juggernaut	28 May 1999	20 Jun 1999	19 Jun 1999
12	Millennium		20 Jan 2000	
13	Millennium		27 Oct 2000	
14	Millennium	24 Jan 2001	27 Jan 2001	
15	Pelagic	10 Sep 2001		
16	Pelagic		26 Nov 2001	10 Dec 2001
17	Sargassum		26 May 2003	
18	Sargassum	14 Jul 2003	08 Jul 2003	12 Jul 2003
19	Titanic	26 Sep 2003	19 Sep 2003	25 Sep 2003
20	Titanic	31 Dec 2003		
21	Ulysses		24 May 2004	
22	Vortex	25 Feb 2005	20 Feb 2005	28 Feb 2005
23	Vortex	22 Jun 2005	17 Jun 2005	
24	Vortex	04 Aug 2005		23 Jul 2005
25	Walker		24 Sep 2005	
26	Yankee		*12 Feb 2006	
27	Yankee	11 Jul 2006	08 Jul 2006	16 Jul 2006
28	Yankee		19 Aug 2006	
29	Zorro	10 Apr 2007	02 Apr 2007	08 Apr 2007
30	Albert		06 Jun 2007	
31	†Albert/Brazos	27 Sep 2007	*21 Oct 2007	
32	Brazos		30 Jan 2008	

Table 5.4-3 (Continued)

No.	Impending Event/ Industry Name	CCAR Detachment Date	AVISO Detachment Date	AVISO-CUPOM Detachment Date
33	Cameron		21 May 2008	
34	Darwin		06 Nov 2008	29 Nov 2008
35	Ekman	05 Jul 2009		
36	Ekman	10 Aug 2009		
37	Franklin	07 Jun 2010	23 May 2010	
38	Franklin	11 Jul 2010		
39	Franklin	18 Aug 2010		
40	Hadal	27 Jul 2011		
41	Icarus	07 Nov 2011		
42	Icarus	23 Nov 2011		
43	Icarus	25 Dec 2011		
44	Jumbo	20 Jun 2012		
45	Jumbo	13 Jul 2012		

* Detachment occurred on same date as a separation event. See Table 5.4-2. Detachment event was associated with the following separation event, not the separation event occurring on the same day.

† CCAR detachment date is associated with Albert. AVISO detachment date is associated with Brazos.

Figure 5.4-3 shows LC metrics computed from the CCAR dataset: area, volume, anticyclonic circulation, westernmost longitude, and northernmost latitude. The metrics are shown both as time series and as histogram distributions over the 20-year record. Red dashed lines on the time series plots identify separation events. Identical statistics were computed for AVISO and AVISO-CUPOM datasets. Figure 5.4-4 shows monthly composite annual cycles (CACs) calculated from all three datasets for each of the metrics given above. The CAC of LC area plus the area of detached LC eddies are also shown. The 95% confidence intervals show that monthly means in February are statistically different than means in either October or November or both for all three data types and all six metrics. The metrics from all three datasets largely follow the same trends: a maximum in February (there are a few exceptions) and a minimum in October or November. AVISO data show the lowest values per month for all metrics with the exception of latitude; latitude CACs are similar among all three datasets. Though the AVISO dataset mean is weaker than CUPOM overall, it is comparable to the CUPOM mean on the northern boundary of the LC. CCAR data show the highest magnitudes for area, area including detachments, volume, and longitude metrics. AVISO-CUPOM has the highest in anticyclonic circulation, indicating that the AVISO SSHA objective analyses have higher geostrophic speeds parallel to the 17-cm contour when combined with the CUPOM model mean SSH.

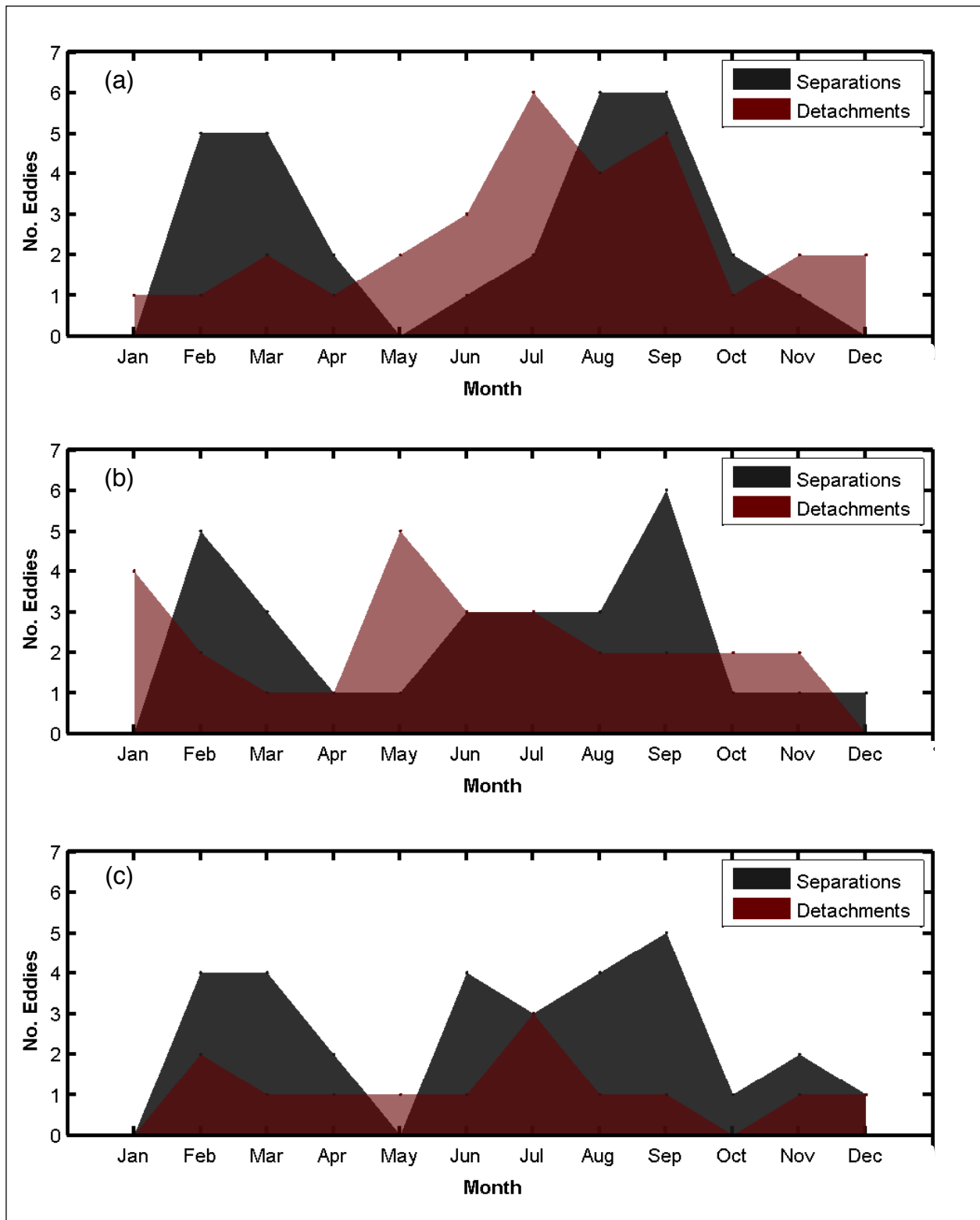


Figure 5.4-2. Monthly histograms of separation and detachment dates (Tables 5.4-2 and 5.4-3) determined from the (a) CCAR, (b) AVISO, and (c) AVISO-CUPOM SSH datasets by automated tracking of the 17-cm SSH contour.

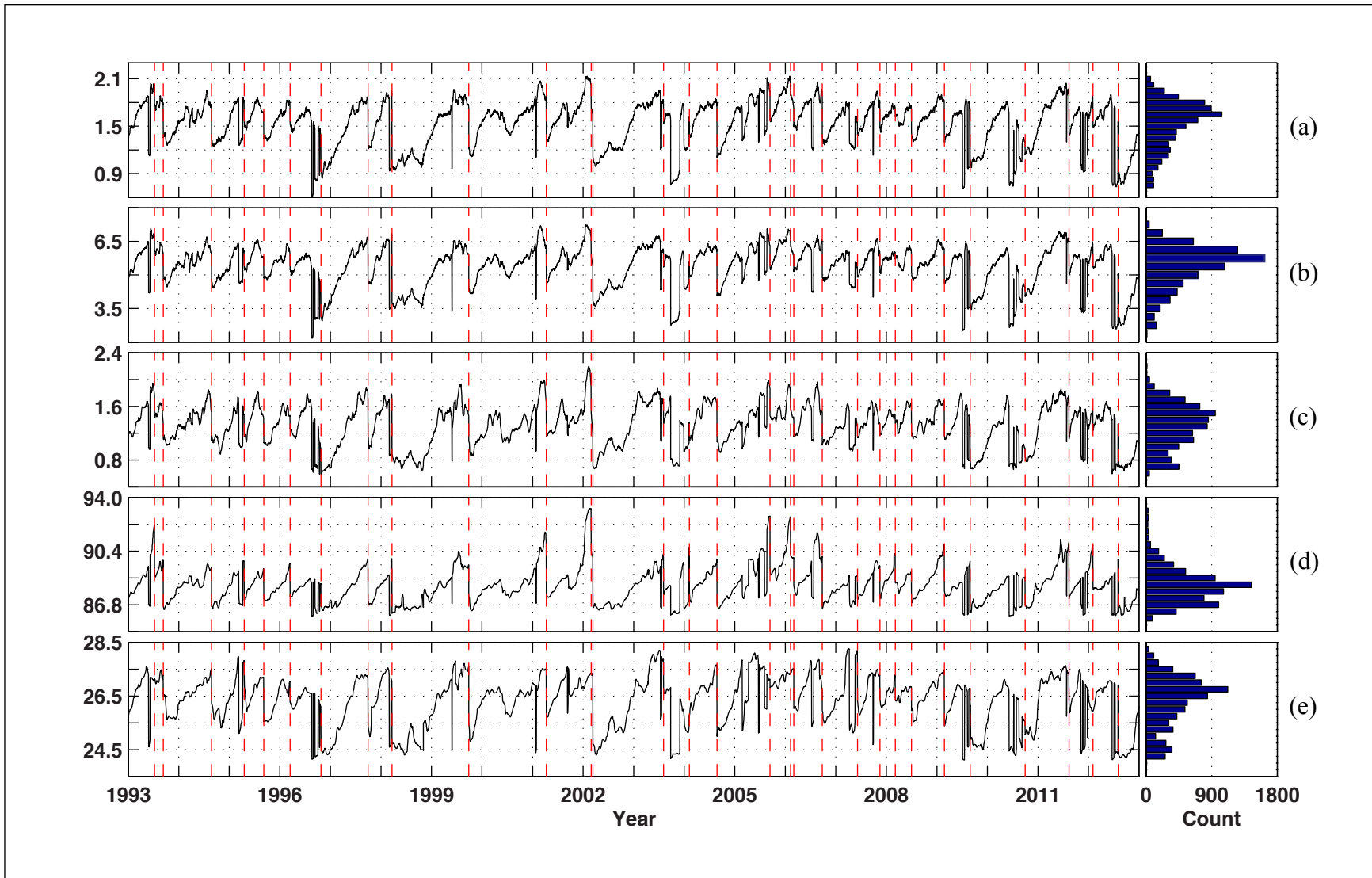


Figure 5.4-3. Daily LC (a) area ($\times 10^5 \text{ km}^2$), (b) volume ($\times 10^4 \text{ km}^3$), (c) anticyclonic circulation ($\times 10^6 \text{ m}^2\text{s}^{-1}$), (d) westernmost longitude ($^\circ\text{W}$), and (e) northernmost latitude ($^\circ\text{N}$) time series and corresponding histograms, derived from CCAR SSH data.

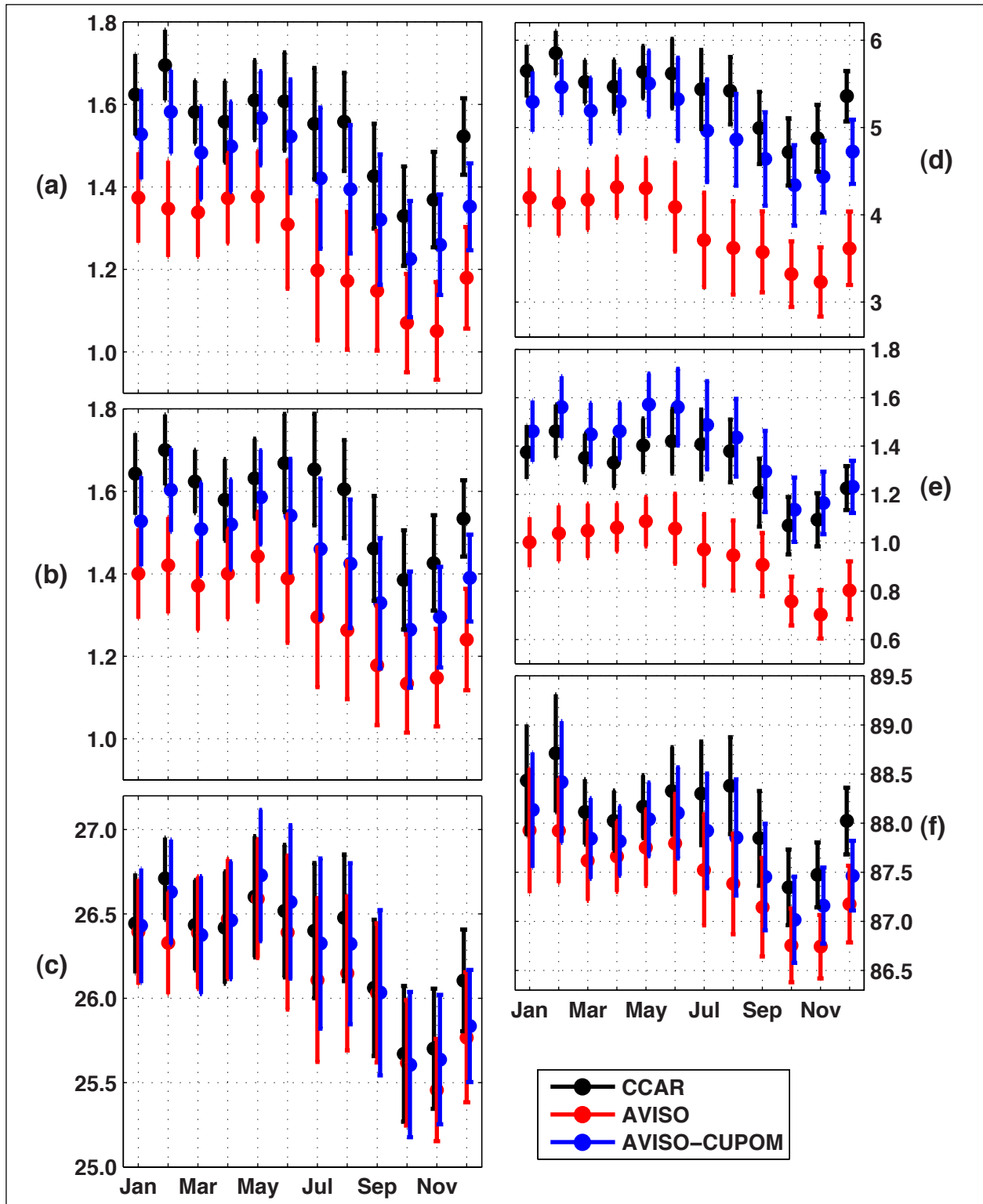


Figure 5.4-4. Monthly mean plots of LC (a) area ($\times 10^5 \text{ km}^2$), (b) area including detachments ($\times 10^5 \text{ km}^2$), (c) northernmost latitude ($^\circ\text{N}$), (d) volume ($\times 10^4 \text{ km}^3$), (e) anticyclonic circulation ($\times 10^6 \text{ m}^2 \text{ s}^{-1}$), and (f) westernmost longitude ($^\circ\text{W}$) statistics, derived from the CCAR, AVISO, and AVISO-CUPOM SSH datasets.

To highlight the effects of different tracking methods on derived separation dates, Table 5.4-4 compares the AVISO re-analysis LC eddy separation dates given in Table 5.4-2 with LC Eddy separation dates published in Chang and Oey (2013b), Vukovich (2012), and Lindo-Atichati et al. (2013). All LC eddy separation dates listed in Table 5.4-4 were derived from altimetry data; however, only Vukovich (2012) used CCAR SSH. The AVISO dataset re-analysis dates were used in the Table 5.4-4 comparison instead of CCAR or AVISO-CUPOM re-analysis dates because two of the three publications compared, Chang and Oey (2013b) and Lindo-Atichati et al. (2013), used AVISO datasets to derive separation dates. As described previously in this report, the AVISO re-analysis used $1/4^\circ$ daily AVISO SSH (interpolated from the weekly AVISO delayed-time product), which was demeaned in water deeper than 200 m to remove the steric signal (see Section 2.7.4). Tracking of separation events was performed using the LCT.

Analyses of LC eddy separation dates derived from AVISO SSH data were presented in both Chang and Oey (2012) and Chang and Oey (2013b). Chang and Oey (2012) derived a set of monthly LC eddy separation dates from 1993 through 2009, but did not publish the actual dates. Instead, the analyzed dates were presented in the form of a monthly histogram (Figure 1(a) in Chang and Oey (2012)), from which the actual year and month of each event cannot be determined. However, Chang and Oey (2013b) showed separation dates plotted as month versus year. LC eddy separation months were determined by manually tracking the 1.65 m SSH contour in an animation of AVISO SSH. The animation was based on the release of AVISO data just prior to that used in the preparation of this report. Comparison of the event dates from 1993 through 2009 in Chang and Oey (2013b) with the annual monthly histogram in Chang and Oey (2012) shows that the Chang and Oey (2013b) dates have one more March separation event and one less June separation event. Since the two papers use different altimeter-derived separation dates, the two datasets will be treated independently throughout the statistical discussion of LC eddy separation presented in Section 5.5. In the remainder of this section, only the dates given graphically in Chang and Oey (2013b) will be used.

Vukovich (2012) used SST, ocean color, and in-situ data from various sources in addition to satellite altimetry to derive LC eddy separation events. Altimeter data from TOPEX/Poseidon, JASON, and ERS missions were mentioned specifically, and altimeter data from the CCAR website were cited in the acknowledgments. Lindo-Atichati et al. (2013) used a weekly $1/4^\circ$ AVISO SSH dataset, which was based on the Rio and Hernandez (2004) mean dynamic topography.

For quantification of the differences in the derived LC eddy separation dates in Table 5.4-4, only month and year (without day-of-month, if given) were considered for each event. The numbered events that do not have dates from all four sources (event #22, 33, 39, 41, 43, 47, 48, 49, and 50) and all the unnumbered events (Odessa/Nansen, “unnamed1”, “unnamed2”, and “unnamed3”) are ignored because one or more of the date list sources would be otherwise unrepresented. This leaves 21 “ubiquitous” LC eddies. Of those events, all dates agreed for two events (#25 and 34); there were no events where no dates agreed; the difference between the earliest and latest dates was one month for 15 events (#21, 23, 24, 26, 28, 29, 30, 31, 32, 35, 36, 37, 38, 42, and 45); and the difference was two months for four events (#27, 40, 44, and 46). Table 5.4-5 shows how many times each eddy separation analysis had the earliest or latest eddy separation date. For example, AVISO re-analysis dates (first row of table) were earlier than all respective dates from

Table 5.4-4. Comparison of altimetry record LC eddy separation dates from AVISO re-analysis (from Table 5.4-2), Chang and Oey (2013b), Vukovich (2012), and Lindo-Atichati et al. (2013)

No.	Industry Name	AVISO Re-analysis	Chang and Oey (2013b)	Vukovich (2012)	Lindo-Atichati et al. (2013)
21	Whopper	08 Jul 1993	Jul 1993	Jun 1993	21 Jul 1993
22	Xtra	04 Sep 1993	*	*	08 Sep 1993
23	Yucatan	19 Aug 1994	Aug 1994	Sep 1994	31 Aug 1994
24	Zapp	17 Apr 1995	Apr 1995	Mar 1995	26 Apr 1995
25	Aggie	01 Sep 1995	Sep 1995	Sep 1995	13 Sep 1995
26	Biloxi	08 Mar 1996	Mar 1996	Feb 1996	20 Mar 1996
27	Creole	20 Jul 1996	Oct 1996	Aug 1996	21 Aug 1996
28	El Dorado	25 Sep 1997	Sep 1997	Oct 1997	24 Sep 1997
29	Fourchon	12 Feb 1998	Mar 1998	Mar 1998	04 Mar 1998
30	Juggernaut	28 Sep 1999	Oct 1999	Oct 1999	29 Sep 1999
31	Millennium	29 Mar 2001	Apr 2001	Apr 2001	11 Apr 2001
	Odessa/Nansen	†	Sep 2001	†	21 Sep 2001
32	Pelagic	24 Feb 2002	Feb 2002	Mar 2002	13 Mar 2002
33	Quick	§	§	Mar 2002	17 Apr 2002
34	Sargassum	11 Aug 2003	Aug 2003	Aug 2003	20 Aug 2003
⌘	(unnamed1)				24 Sep 2003
35	Titanic	20 Dec 2003	Jan 2004	Jan 2004	24 Dec 2003
36	Ulysses	19 Aug 2004	Sep 2004	Sep 2004	01 Sep 2004
37	Vortex	11 Sep 2005	Sep 2005	Sep 2005	03 Aug 2005
38	Walker	06 Feb 2006	Mar 2006	Feb 2006	08 Mar 2006
39	Xtreme	12 Feb 2006	∅	∅	19 Apr 2006
⌘	(unnamed2)			Jun 2006	
40	Yankee	15 Sep 2006	Aug 2006	Oct 2006	27 Sep 2006
41	Zorro	◇	May 2007	◇	11 Apr 2007
42	Albert	21 Oct 2007	Oct 2007	Nov 2007	14 Nov 2007
43	Brazos	02 Mar 2008	Mar 2008	Mar 2008	∇
44	Cameron	27 Jun 2008	Jul 2008	Aug 2008	02 Jul 2008
⌘	(unnamed3)				03 Dec 2008
45	Darwin	14 Feb 2009	Mar 2009	Mar 2009	04 Mar 2009
46	Ekman	22 Jun 2009	Jul 2009	Jul 2009	02 Sep 2009
47	Franklin	27 Jun 2010		Aug 2010	
48	Hadal	22 Jul 2011			
49	Icarus	05 Nov 2011			
50	Jumbo	28 May 2012			

* Chang and Oey (2012) considered Whopper and Xtra to be one event because they separated less than two months apart and reported the separation date of the first eddy only. Vukovich (2012) may have also identified Whopper and Xtra as one event.

† Odessa/Nansen dissipates in less than a month in the AVISO re-analysis with little westward propagation and is, therefore, not considered a separation event. Vukovich (2012) provides no specific information on the LC or LC eddies during this time period.

§ Pelagic and Quick appear as a single separation event in the AVISO re-analysis, but the eddy splits into two pieces less than a week after separation. Since the two eddies separate less than two months apart, Chang and Oey (2012) considered the two eddies to be one event and reported the date of the first eddy only.

⋈ The eddy appears as a detachment event in the re-analysis AVISO dates, not a separation. Reasons for why the eddy is not a separation event in the other publications are unknown.

⊘ Chang and Oey (2012) do not mention a short-period separation (less than two months) to have occurred in 2006. Due to how the SSH data were processed, Walker and Xtreme may have appeared as one eddy originally such that combining the two was not necessary. Similarly, Vukovich (2012) may have also identified Walker and Xtreme as one event.

◇ Zorro appears as a detachment event in the AVISO re-analysis. Vukovich (2012) provides no specific information on the LC or LC eddies during this time period.

∇ The objective tracking technique in Lindo-Atichati et al. (2013) missed this event.

the other three sources (e.g., event #27) for seven events. For another seven events, the AVISO re-analysis shared the earliest separation dates with one or two of the other sources, but at least one source had a later date (e.g., event #23). For four events, the AVISO re-analysis shared the latest separation dates with one or two of the other sources, but at least one source had an earlier date (e.g., event #21). The AVISO re-analysis dates were never later than all of the respective dates from the three other sources. The three other LC eddy separation date sources listed in the second, third, and fourth rows of Table 5.4-5 can be interpreted similarly. The two events where all dates agreed (#25 and 34) were excluded from the counts in the table.

“Earliest” and “latest” sum columns are also given. The AVISO re-analysis provided the earliest separation date 14 times, far greater than the other three sources. Likewise, the AVISO re-analysis provided the latest separation date four times, far less than the others. Chang and Oey (2013b), Vukovich (2012), and Lindo-Atichati et al. (2013) all seem to be very comparable.

Table 5.4-5. LC eddy separation timing of the 19 events where each source – the AVISO re-analysis (from Table 5.4-2), Chang and Oey (2013b), Vukovich (2012), and Lindo-Atichati et al. (2013) – reported a separation event, excluding events #25 and 34

Analysis	Earliest Alone	Earliest Shared	Sum of Earliest	Latest Shared	Latest Alone	Sum of Latest
AVISO Re-analysis	7	7	14	4	0	4
Chang and Oey (2013a)	1	4	5	11	1	12
Vukovich (2012)	3	1	4	9	4	13
Lindo-Atichati et al. (2013)	1	4	5	10	1	11

Tracking procedures in all four sources were different. As discussed previously, for the AVISO re-analysis, the LC and LC eddies were defined by the 17-cm contour in deepwater-demeaned AVISO SSH fields to derive the dates. Breaking of the 17-cm contour objectively established

each date. Chang and Oey (2012) also identified LC eddies by tracking on a fixed contour level in AVISO data. However, the steric signal was retained in the data, eddy-separation periods less than or equal to two months were ignored, and each separation date may have been somewhat determined based on expert opinion. Testing suggests that retention of the steric signal would have had the affect of advancing separation events in winter and spring and delaying separation events in summer and fall in comparison to the same event dates derived without the steric signal.

To perform the tests, separation dates were objectively derived using the AVISO re-analysis dataset with (steric) and without the steric signal (nosteric) at the 13-cm level for both. (Combining AVISO mean SSH with the steric signal caused several persistent LC and LC eddy tracking issues in winter and spring months at the 17-cm level that made a 17-cm level comparison invalid.) Table 5.4-6 contains reprinted AVISO re-analysis 17-cm nosteric separation dates with 13-cm nosteric dates and 13-cm steric dates for comparison. The 13-cm nosteric dates were subtracted from the 13-cm steric dates to yield delay (last column in Table 5.4-6). To interpret the delays, the events were separated into two groups, the group where events should be delayed and the group where events should be advanced. Based on the annual peak and trough of the steric signal (15 September and 16 March, respectively), steric signal sinusoidal inflection points were estimated to be 15 June and 15 December. Between 15 June and 15 December, separation events were expected to be delayed by the steric signal. Between 15 December and 15 June, events were expected to be advanced. Expected-delayed events are highlighted in red in Table 5.4-6, while expected-advanced events are highlighted in blue. Events that behaved as expected are highlighted in green in the last column. (Event #26 was disregarded since no separation event occurred in the 13-cm steric AVISO data.) Only events #27, 49, and 50 did not behave as expected. Events #49 and 50 were both near an inflection point. Steric heating in the Gulf has some inter-annual variation, and so the actual inflection points can fluctuate from year-to-year about the estimates. If the events whose nosteric separation dates occurred within plus or minus ten days (arbitrary) of the estimated inflection points are ignored (#35, 46, 49, and 50), the RMS of the remaining date differences is 3.2 days. Delays are between zero and four days. Advances are between three and eight days. Notice that event #46, eliminated in the calculation, is an outlier (42 days), showing that delays (and maybe advances) caused by the steric signal can be upwards of a month. However, it seems more likely that the effect of the steric signal on events will usually be less than one week, though this result is dependent on tracking contour level. Thus, the effect of the steric signal could be to shift the separation month in Chang and Oey (2013b) by one month, depending on the day of the month the separation occurred. However the separation day-of-month is critical information in assessing the impact on individual events. Even so, for the 21 ubiquitous events mentioned previously, based on month only, re-analysis dates are just as early or earlier than the corresponding Chang and Oey (2013b) dates for all events but one (#40). This one event has a summer/fall date, thus, contradicting the expected trend. If one assumes that each Chang and Oey (2013b) date in Table 5.4-4 corresponds to the fifteenth day of the given month, the mean delay of the 21 events between the Chang and Oey (2013b) dates and the re-analysis is 13 days. Using the ten-day window about the inflection points, events expected to be delayed have an average delay of 10.6 days. Events expected to be advanced are actually also delayed on average by an even larger value, 13.8 days. These results are not consistent, and the source of the discrepancy is unknown.

Table 5.4-6. Comparison of LC eddy separation events

No.	Industry Name	(1) AVISO 17-cm No Steric	(2) AVISO 13-cm No Steric	(3) AVISO 13-cm Steric	(2) - (1) Days	(3) - (2) Days
21	Whopper	08 Jul 1993	11 Jul 1993	13 Jul 1993	3	2
22	Xtra	04 Sep 1993	05 Sep 1993	07 Sep 1993	1	2
23	Yucatan	19 Aug 1994	21 Aug 1994	22 Aug 1994	2	1
24	Zapp	17 Apr 1995	18 Apr 1995	15 Apr 1995	1	-3
25	Aggie	01 Sep 1995	03 Sep 1995	04 Sep 1995	2	1
26	Biloxi	08 Mar 1996	11 Mar 1996	*	3	
27	Creole	20 Jul 1996	24 Jul 1996	24 Jul 1996	4	0
28	El Dorado	25 Sep 1997	27 Sep 1997	29 Sep 1997	2	2
29	Fourchon	12 Feb 1998	16 Feb 1998	12 Feb 1998	4	-4
30	Juggernaut	28 Sep 1999	30 Sep 1999	04 Oct 1999	2	4
31	Millennium	29 Mar 2001	31 Mar 2001	27 Mar 2001	2	-4
32	Pelagic	24 Feb 2002	25 Feb 2002	24 Feb 2002	1	-1
33	Quick	†	†	†		
34	Sargassum	11 Aug 2003	13 Aug 2003	16 Aug 2003	2	3
35	Titanic	20 Dec 2003	22 Dec 2003	21 Dec 2003	2	-1
36	Ulysses	19 Aug 2004	20 Aug 2004	22 Aug 2004	1	2
37	Vortex	11 Sep 2005	12 Sep 2005	14 Sep 2005	1	2
38	Walker	06 Feb 2006	09 Feb 2006	05 Feb 2006	3	-4
39	Xtreme	12 Feb 2006	15 Feb 2006	11 Feb 2006	3	-4
40	Yankee	15 Sep 2006	17 Sep 2006	19 Sep 2006	2	2
41	Zorro	§	§	§		
42	Albert	21 Oct 2007	09 Nov 2007	11 Nov 2007	19	2
43	Brazos	02 Mar 2008	09 Mar 2008	01 Mar 2008	7	-8
44	Cameron	27 Jun 2008	28 Jun 2008	30 Jun 2008	1	2
45	Darwin	14 Feb 2009	17 Feb 2009	14 Feb 2009	3	-3
46	Ekman	22 Jun 2009	25 Jun 2009	06 Aug 2009	3	42
47	Franklin	27 Jun 2010	09 Aug 2010	13 Aug 2010	43	4
48	Hadal	22 Jul 2011	23 Jul 2011	26 Jul 2011	1	3
49	Icarus	05 Nov 2011	17 Dec 2011	18 Dec 2011	42	1
50	Jumbo	28 May 2012	07 Jun 2012	13 Jun 2012	10	6

* A very small eddy separates from the LC for this event on 4 March 1996, too small to be considered a LC eddy.

† In all three versions of the AVISO data, Pelagic and Quick separate from the LC as one eddy, though they split from each other days after separation.

§ Zorro appears as a detachment event in all three versions of the AVISO data.

If the AVISO re-analysis had been performed on a lower-tracking contour than 17 cm throughout, it could have had the effect of delaying all separation event dates. The second to last column in Table 5.4-6 shows that tracking the LC at the 13-cm level in nosteric AVISO data delayed every separation event, compared to tracking at the 17-cm level. Delays ranged from one to 43 days. The mean delay is 6.1 days, and the median is two days. Four delays were greater than one week (#42, 47, 49 & 50). Two delays were greater than one month (#47 & 49). Unfortunately, effects of changing contour level are unpredictable and event-dependent. Even so, re-derived event dates from lower-contour tracking may be more consistent with Chang and Oey (2013b) dates.

Comparison of Loop Current eddy separation events derived from AVISO SSH without steric signal at the 17-cm level, without steric signal at the 13-cm level, and with steric signal at the 13-cm level, from January 1993 through December 2012, is presented in Table 5.4-6. The last two columns show resulting event separation delay (in days) when changing the tracking contour from 17-cm to 13-cm and when changing from data without the steric signal to data with the steric signal. The 13-cm events that were expected to be delayed by the steric signal are highlighted in red, while events that were expected to be advanced are highlighted in blue. Events that behaved as expected for either case are highlighted in green in the last column.

Vukovich (2012) provided no explicit information as to how LC eddies were tracked, although specified lifetime and diameter criteria were mentioned, as discussed in Section 5.3. Given that GOES SST, SeaWiFS and MODIS ocean color, and CCAR altimetry were used in combination, event dates may have been derived entirely subjectively. Vukovich (2012) dates were later than re-analysis dates for 14 events and earlier for only three events. Lindo-Atichati et al. (2013) used maximum gradient in AVISO SSH fields to determine the boundaries of the LC and LC eddies. Removing the steric signal would have had no affect on separation dates since a constant offset applied to a SSH field would not affect the gradient calculation. Lindo-Atichati et al. (2013) dates were later than re-analysis dates for ten events and earlier for only one event. Combinations of the contour level and SSH gradient techniques described are likely to yield similar results. For instance, Dukhovskoy et al. (in preparation) tracked the LC and LC eddies in HYbrid Coordinate Ocean Model (HYCOM) data using a predictor-corrector method in which SSH contour level defined the first estimation of LC and LC eddy boundaries and SSH gradient improved the first estimation. Separation dates derived using the predictor-corrector routine were only slightly later than dates found using SSH contour level alone, as implemented in the LCT.

Tracking techniques applied in the LCT, in Chang and Oey (2012) and Lindo-Atichati et al. (2013) are Eulerian approaches to separation detection. The techniques use SSH or SSH gradient at specified grid points to track LC and LC eddy positions at every time-step following streamlines or the instantaneous velocity field. Because ocean flows are quasi-geostrophic, they evolve slowly enough that streamlines well-approximate path lines of the flow field, and since the flow is unsteady, path lines do cross streamlines, and the fluid contained within a closed streamline is not conserved. Nevertheless, tracking of a SSH contour or velocity fronts can identify separation dates relatively accurately. It could be argued that the Vukovich (2012) tracking technique, although subjective, is Lagrangian through the use of time-evolving SST and ocean-color patterns in satellite images as a Lagrangian tracer. However, neither SST nor chlorophyll concentrations are conserved quantities, so a subjective technique based on satellite

imagery is, at best, a mixed Eulerian/Lagrangian approach that relies heavily on expert judgment. In contrast, explicit Lagrangian tracking focuses on specific fluid parcels moving with the flow rather than Eulerian flow-field variables specified at fixed points in space. For example, Andrade-Canto et al. (2013) presented a method for finding manifolds – Lagrangian coherent structures (LCSs) – in velocity fields using finite-time Lyapunov exponents. These LCSs are material boundaries that follow parcel path lines through a flow. In the case of the LC, LCSs can show whether the main circulation coming into the Gulf through the Yucatan Channel is flowing northward around a presently detached LC eddy or is cutting immediately east to exit through the Florida Straits. A northward flow typically means that the detached LC eddy will re-attach, but an eastward flow means that the LC eddy is separated. Euclidean methods often require more than a month of data beyond separation of a LC eddy to confirm that the LC eddy is truly separated and not just detached from the LC. The technique given in Andrade-Canto et al. (2013) confirms separation more promptly. Even so, separation dates derived using this Lagrangian technique, which is significantly more complicated to implement, are comparable to dates derived from Eulerian tracking techniques.

In conclusion, dates of LC eddy separation (and detachment) events are affected by two main factors: data processing and tracking technique. Original CCAR, AVISO, and AVISO-CUPOM datasets were all derived from similar along-track altimetric sampling (SSHA), were free of steric heating and cooling affects, and were used to identify LC eddy separation events by the breaking of the 17-cm contour. Yet, corresponding LC eddy separation dates derived from the three datasets (Table 5.4-2) were usually different, sometimes by more than a month. Date differences were as much caused by differences in SSHA smoothing as they were caused by differences in mean SSH. In-depth testing of the AVISO dataset showed that steric heating of the Gulf can have the effect of delaying separation of LC eddies in summer and fall seasons and advancing separation in winter and spring seasons, relative to the same events in nosteric data (RMS of 3.2 days). Aside from data processing, the tracking technique employed can also affect LC eddy separation event results in significant ways. Variations in the application of a specific tracking technique can impact all derived separation dates. For example, decreasing the tracking-contour level in nosteric AVISO data, from 17 cm to 13 cm, delayed the separation time for all events in the altimeter record by an average of 6.1 days (Table 5.4-6). Different Eulerian tracking techniques, whether objective (Lindo-Atichati et al. 2013), semi-objective (Chang and Oey 2012), or subjective (Vukovich 2012), all yield different results (Table 5.4-4). Just as in the pre-altimetry era, separation dates derived from altimetry data are very much analyst dependent, in spite of the fact that most use similar altimetry products.

The pre-altimetry and altimetry time periods were compared to determine in which time period LC eddy separation dates were more consistent. Revisiting the Table 5.3-1 pre-altimetry dates, 29% (six) of the 21 listed events (both numbered and unnumbered events) were only recognized by one date list, the re-analysis or Vukovich (2012), not both. Similarly, 30% (nine) of the 30 listed altimetry events in Table 5.4-4 occurring from 1993 through 2009 (both numbered and unnumbered events) were unacknowledged by at least one of the date lists. This means that uniformity of LC eddy separation event identification has remained a problem regardless of Gulf data used. In the pre-altimetry time period, LC eddy counts were misrepresented due to poor data quality and seasonal satellite data outages. Now, with higher-quality altimetry data, LC eddy counts still differ among authors due to application of different eddy size, lifetime, and

propagation criteria, allowance of short-period events, and ambiguity of separation status (detachment or separation). Of the 15 ubiquitous pre-altimetry events, re-analysis and Vukovich (2012) dates differed by a month or less for 73% (11) of the events (ignoring day-of-month, as in the present section). Slightly better, 81% (17) of the 21 ubiquitous altimetry events in Table 5.4-4 differed by one month or less. Lastly, 20% (three) of the ubiquitous pre-altimetry dates and 0% of the ubiquitous altimetry dates differed by three months or greater. These results indicate that the altimetry dates have better agreement overall than the pre-altimetry dates, especially since a total of four altimetry date lists exhibited more consistency than only two pre-altimetry date lists. With full consideration of the various tracking techniques compared, the SSH contour-tracking technique used in the CCAR LCT to identify LC eddy separation events in this report is relatively simple to apply, although the 17-cm level would need to be decreased to make derived separation dates more comparable to dates derived by the other analyses. Changing the tracking contour level is a user-selectable option within the LCT to allow general use of the LCT on Gulf observational and modeling data. As the use of more accurate SSH data improves, in combination with objective tracking techniques, LC eddy separation dates will likely become more consistent in the future.

Although the LCT was used only by the remote sensing component of this study, the tool has been used in other studies. For example, the LCT was used extensively to test the sensitivity of LC eddy separation event dates to changes in Gulf satellite-altimetric sampling. SSHA fields from a Gulf 54-year high-resolution HYCOM run were sub-sampled along four different satellite (TOPEX/Poseidon, TOPEX/Poseidon interleaved, Geosat, and Envisat) ground tracks to generate simulated along-track data. The simulated along-track data were then smoothed and gridded using the CCAR altimetry-processing procedures described in Section 2.6 and combined with the HYCOM mean SSH to create seven different 54-year synthetic SSH time series. The objective 17-cm tracking employed in the LCT made counting of LC eddies fast and unbiased. The effects of the various satellite sampling were then compared systematically. This suite of sensitivity tests revealed relatively weak sensitivity of the probability distribution of the LC eddy shedding to uncertainties and biases related to the derivation of the SSH fields from altimetric sampling (Dukhovskoy et al., in preparation).

5.5 STATISTICAL ANALYSIS OF LOOP CURRENT SEASONALITY

Several recent studies have suggested that the LC may exhibit seasonality in the timing of LC eddy separation. Alvera-Azcárate et al. (2009) found 21 LC eddies in a survey of altimetry data from October 1992 into February 2006, 12 of which separated in the months of July, August, or September. Leben and Hall (2010) presented monthly-binned histograms of pre-altimetry and CCAR altimetry LC eddy separation dates as additional observational evidence that separation timing has a seasonal preference. Chang and Oey (2012) similarly suggested that pre-altimetry separation dates in past literature combined with altimetry dates derived from an AVISO product also support seasonality. More rigorously, Lindo-Atichati et al. (2013) calculated the mean annual cycle of the northern boundary of the LC with error bars, and concluded that northern penetration at some times of the year is statistically different than at other times. The 95% confidence intervals in Figure 5.4-4 of this report similarly support that there are two distinct LC seasons, one of maximums and one of minimums, though the extents of the two are not clearly defined. In the current study, a number of pre-altimetry, altimetry, and combined (both pre-

altimetry and altimetry) datasets were compared to assess seasonality and the statistical significance and boundaries of seasons where LC eddy separation is most likely.

Statistical χ^2 tests were performed on the re-analysis pre-altimetry dates (N=20) shown in Table 5.3-1 to assess the null hypothesis that LC eddy separation dates come from a uniform distribution. Since expected bin counts using monthly binning would be too low to test for statistical significance, the data were binned quarterly (not shown) to increase expected counts in each three-month bin to five. Bins larger than three months (e.g., four months or six months) can begin to conceal seasonality and are, therefore, undesirable. Quarterly binning proceeded in three different ways: first with the bins Feb-Apr, May-Jul, Aug-Oct, and Nov-Jan (binning1), second with the bins Jan-Mar, Apr-Jun, Jul-Sep, and Oct-Dec (binning2), and third with the bins Mar-May, Jun-Aug, Sep-Nov, and Dec-Feb (binning3). Results from the χ^2 tests indicate that at the 95% confidence level, the null hypothesis is rejected for binning1 and binning2 (Ott and Longnecker 2001), implying that separation timing is seasonal. The tests of binning3 did not yield statistical significance at the 95% confidence level. Statistical significance can be a function of bin boundaries and size; therefore, suppression of seasonality in at least one of the three-month binning schemes is expected. There are too few pre-altimetry dates from Vukovich (2012) in Table 5.3-1 (N=16) to statistically determine whether the separation dates are from a uniform distribution. The χ^2 distribution is not well approximated whenever 20% or more of the bins have expected values less than five (Ott and Longnecker 2001). Vukovich (2012) LC eddy separation dates fail this requirement since all four bins have an expected value of four. However, Table 5.3-1 contains only a portion of the pre-altimetry dates given in Vukovich (2012) from 1978 through 1992. If all pre-altimetry separation dates from Vukovich (2012), from 1972 through 1992, are tested (N=23), the expected bin counts are sufficient, but none of the three sets of bins show statistical significance of seasonality.

Monthly-binned histograms of the pre-altimetry re-analysis dates and the pre-altimetry dates from Vukovich (2012) listed in Table 5.3-1 are shown in Figures 5.5-1a and 5.5-1b, respectively. The blue dashed line in each subplot represents the average number of LC eddies to separate per month, per year. Randomization tests were performed on both datasets to determine which peaks in the histograms, if any, were significant. Re-analysis LC eddy separation event testing proceeded as follows: The events were randomly reordered 100,000 times, forming 100,000 separation date sequences. Each sequence used each original separation event exactly once (selection without replacement) so that every sequence had exactly 20 events, just as the original sequence, and the separation periods and duration of the record were preserved. The initial day of the year to start each sequence was also randomized. Then all 100,000 sequences were binned by month to produce a distribution of LC eddy separation counts for each month. Significance was determined from the random outcomes. For example, if there were no seasonal signal in the original re-analysis LC eddy separation sequence, then each of the 12 monthly counts represented by bars in the original histogram (Figure 5.5-1a) would be frequently replicated among the 100,000 random sequences. However, Figure 5.5-1a shows that the count in August is significant. The value 1.7% above the bar means that of all 100,000 sequences, only 1.7%, or 1,700, of the randomized sequences contained, in this case, five or more separation events in August. Any count with a value of 5% or less was considered significant at the 95% confidence level. The only significant month of separation in the re-analysis dates is August. Even so, one month is enough to indicate that there is some seasonal preference in the re-analysis pre-

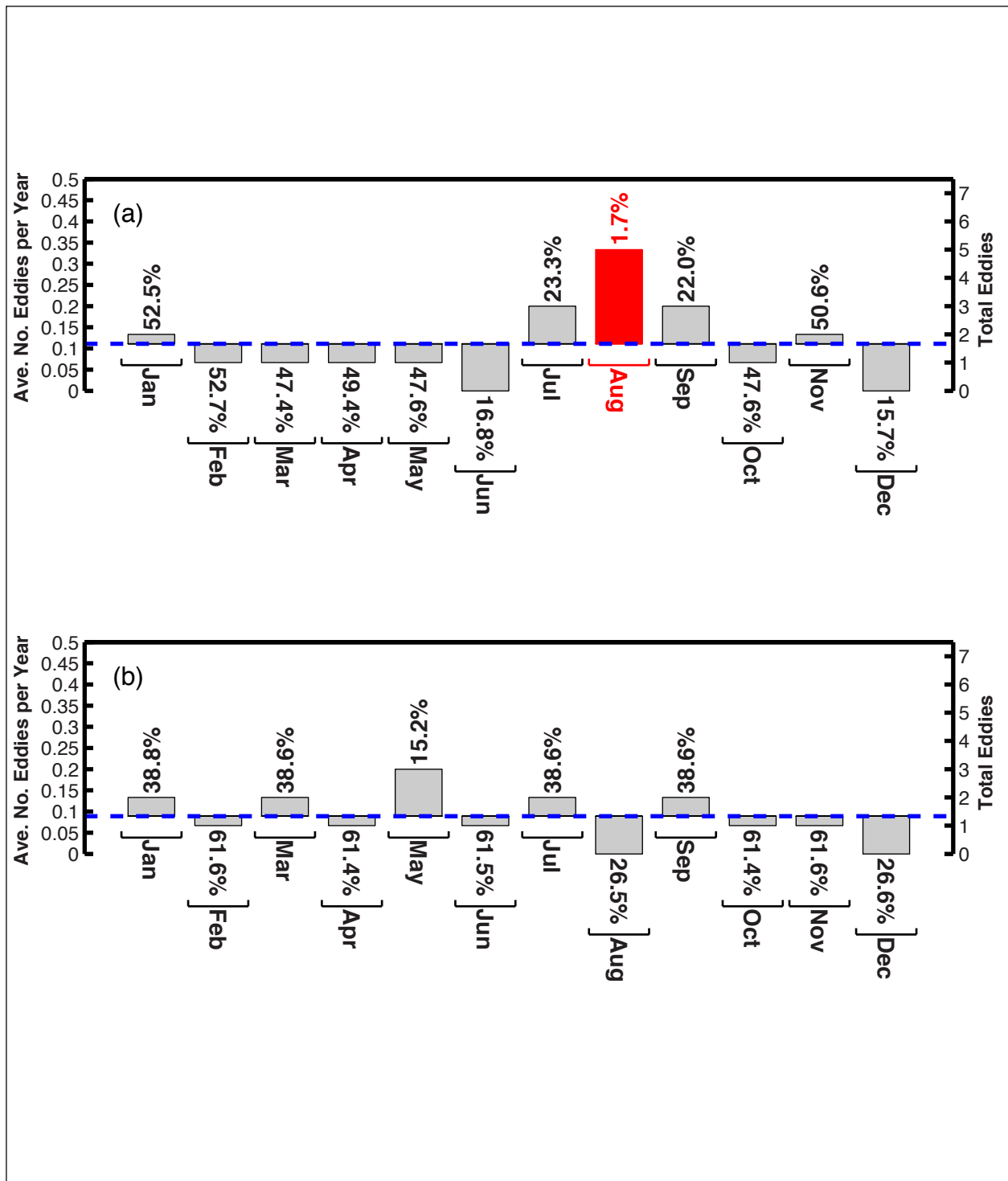


Figure 5.5-1. LC eddy separation dates (Table 5.3-1) binned monthly from (a) reanalysis and (b) Vukovich (2012) pre-altimetry (1978-1992). Blue dashed lines show the average number of LC eddies to separate per month, per year. The percent likelihood of observing an LC eddy count as extreme or more extreme by chance is displayed for each monthly bar. All bars at 5% or less are considered significant at the 95% confidence level and colored red.

altimetry dates. The same randomization testing was performed on the pre-altimetry Vukovich (2012) dates in Figure 5.5-1b and on the complete pre-altimetry record from 1972 through 1992 in Vukovich (2012) (not plotted as histogram). There were no significant months found, indicating no seasonality in the Vukovich (2012) pre-altimetry dates. Traditional histograms of Figures 5.5-1a and 5.5-1b are shown in Figures 5.5-2a and 5.5-2b for comparison.

These two types of statistical tests, χ^2 and randomization, complement each other. The χ^2 test indicates whether a distribution of LC eddy separation dates exhibits statistically significant seasonality; if the dates are not from a uniform distribution, then the distribution exhibits seasonality. However, the χ^2 test does not indicate in which month or season LC eddy separation is more likely or less likely to occur. Conversely, if the randomization test shows any months as being significant, the test not only indicates that the respective dates exhibit seasonality, but also provides information on the seasonal preference. If no months are significant, then the randomization test is a null result, and no information on seasonality is obtained. Table 5.5-1 summarizes results of the χ^2 and randomization tests on the pre-altimetry re-analysis and Vukovich (2012) datasets along with results of the same tests performed on additional datasets. Of all pre-altimetry datasets shown, the re-analysis LC eddy separation date list is the only one to show a statistically significant peak and is one of two lists to show significant χ^2 test results. The other list with a significant χ^2 test is given in Sturges (1994). Sturges (1993), Sturges (1994), and Vukovich (2012) dates were all based on dates in Vukovich (1988), which had too few events to make the χ^2 test valid. Vukovich (2012) continued the list presented in Vukovich (1988) through the pre-altimetry time period. Note that the dates in Vukovich (2012) over the longer time period from 1972 through 1992 exhibited no statistically significant seasonality by either test. Because seasonality was not evident in Vukovich (1988), seasonality was indiscernible until the altimetry record became sufficiently long to overcome the lack of seasonality in these earlier published pre-altimetry LC eddy separation dates.

Figures 5.5-3a, 5.5-3b and 5.5-3c display, respectively, the CCAR (N=30), AVISO (N=28), and AVISO-CUPOM (N=30) altimetry separation dates from Table 5.4-2, binned monthly. (The same separation date lists are plotted as traditional histograms in Figures 5.5-2c, 5.5-2d, and 5.5-2e, respectively.) All three histograms have bimodal distributions. The CCAR histogram is strongly bimodal, while the AVISO-CUPOM shows weak bimodality, with one peak in the late winter/early spring (February/March) and the other in late summer/early fall (August/September). Henceforth, these peaks will be called the “spring” and “fall” seasons since they represent time periods of preferred LC eddy separation and reach maximums near the spring and fall equinoxes. Randomization tests performed on the three datasets show that August and September are significant months in the CCAR dataset, and August is significant in the AVISO dataset. None of the other months’ eddy counts in any of the three histograms are significantly different from the mean. There are no significant months in the AVISO-CUPOM dataset. These results indicate that the spring peak is not significant; although, it may become significant with a longer satellite altimeter-derived time series based on more observations of separation events if the statistics remain stationary. The fall peak is likely significant; however, Figure 5.5-3c demonstrates that different versions of SSHA and mean SSH do affect the significance of the fall peak. Although CCAR and AVISO-CUPOM datasets both use the same mean SSH, the fall

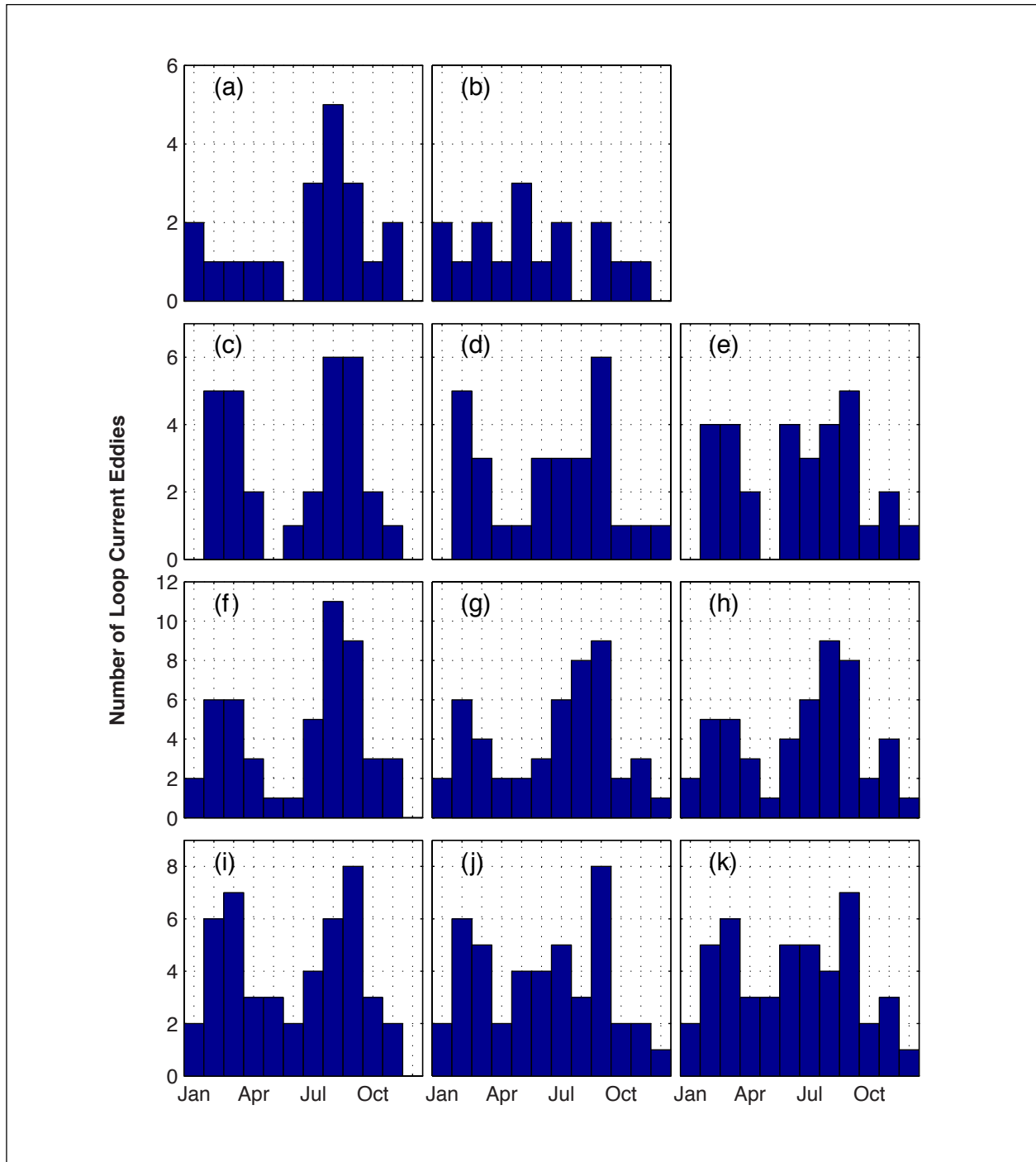


Figure 5.5-2. Monthly-binned histograms of pre-altimetry, altimetry, and combined LC eddy separation date datasets. First row: (a) reanalysis and (b) Vukovich (2012) pre-altimetry separation dates (1978-1992) from Table 5.3-1. Second row: (c) CCAR, (d) AVISO, and (e) AVISO-CUPOM altimetry (1993-2012) from Table 5.4-2. Third row: reanalysis pre-altimetry (1978-1992) and (f) CCAR, (g) AVISO, and (h) AVISO-CUPOM altimetry (1993-2012) combined. Fourth row: Vukovich (2012) pre-altimetry (1978-1992) and (i) CCAR, (j) AVISO, and (k) AVISO-CUPOM altimetry (1993-2012) combined.

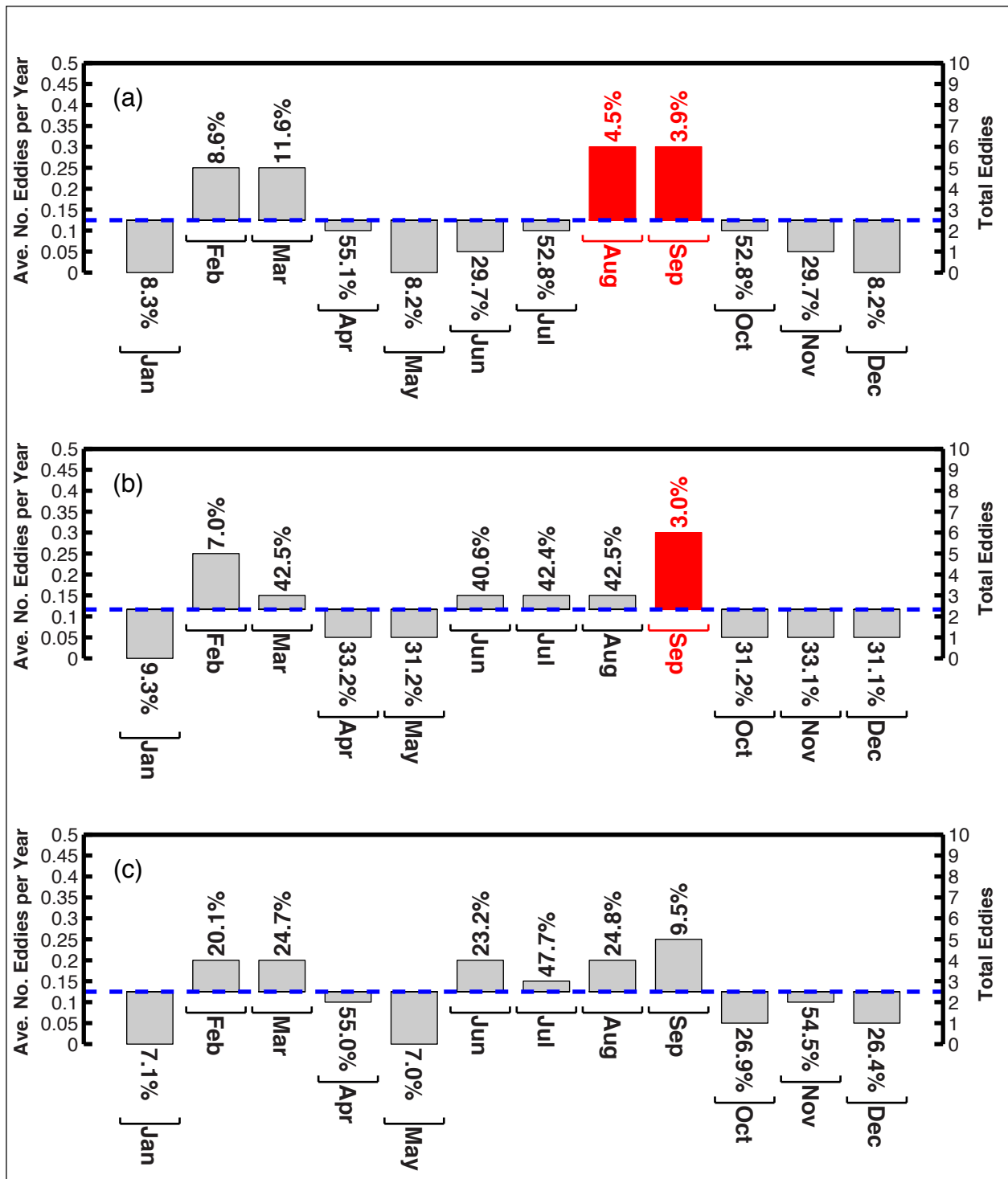


Figure 5.5-3. LC eddy separation dates (Table 5.4-2) binned monthly from (a) CCAR, (b) AVISO, and (c) AVISO-CUPOM altimetry (1993-2012). Blue dashed lines show the average number of LC eddies to separate per month, per year. The percent likelihood of observing an LC eddy count as extreme or more extreme by chance is displayed for each monthly bar. All bars at 5% or less are considered significant at the 95% confidence level and colored red.

Table 5.5-1. Results of significance testing of various sources of LC eddy separation event dates

Source	χ^2 Test			Randomization Test
	bin1	bin2	bin3	Significant Months
PRE-ALTIMETRY				
Re-analysis, 1978-1992	x	x		Aug(+)
Sturges (1993), 1965-1990				None
*Sturges (1994), 1973-1993		x	x	None
Vukovich (1988), 1973-1987		N/A		None
Vukovich (2012), 1972-1992				None
Vukovich (2012), 1978-1992		N/A		None
ALTIMETRY				
CCAR, 1993-2012	x	x		Aug(+), Sep(+)
†AVISO, 1993-2012	x	x		Sep(+)
AVISO-CUPOM, 1993-2012	x	x		None
§Alvera-Azcarate et al. (2009), 1993-2006	x	x		Mar(+), Sep(+)
⌘Chang and Oey (2012), 1993-2009	x	x		Sep(+)
Chang and Oey (2013b), 1993-2009	x	x	x	Mar(+), Sep(+)
Leben (2005), 1993-2004		N/A		Sep(+)
Lindo-Atichati et al. (2013), 1993-2009	x	x	x	Sep(+)
Vukovich (2012), 1993-2010	x	x		Mar(+)
COMBINED				
Re-analysis, 1978-1992+CCAR, 1993-2012	x	x	x	Aug(+), Sep(+), Dec(-)
∅Re-analysis, 1978-1992+AVISO, 1993-2012	x	x	x	Aug(+), Sep(+)
Re-analysis, 1978-1992+AVISO-CUPOM, 1993-2012	x	x	x	Aug(+), Sep(+)
Vukovich (2012), 1978-1992+CCAR, 1993-2012	x	x		Sep(+), Dec(-)
∅Vukovich (2012), 1978-1992+AVISO, 1993-2012	x	x		Sep(+)
Vukovich (2012), 1978-1992+AVISO-CUPOM, 1993-2012		x		None
⌘Chang and Oey (2012), 1974-2009	x	x	x	Dec(-)
Chang and Oey (2013b), 1974-2009	x	x	x	Mar(+), Dec(-)
Sturges and Leben (2000), 1973-1999	x	x		None
Vukovich (2012), 1972-2010	x	x		Mar(+), Dec(-)

For the χ^2 tests, binning1 (bin1) used month groupings Feb-Apr, May-Jul, Aug-Oct, and Nov-Jan, binning2 (bin2) used Jan-Mar, Apr-Jun, Jul-Sep, and Oct-Dec, and binning3 (bin3) used Mar-May, Jun-Aug, Sep-Nov, and Dec-Feb. "x" means the distribution was not uniform at the 95% confidence level. "N/A" means there are not enough separation events for the test to be valid. For the randomization tests, months with "+" signs are peaks, and months with "-" signs are troughs.

Additional notes on next page.

* Sturges (1994) presented one separation event occurring in 1993, beyond the limits of the pre-altimetry “era” ending in 1992. Even so, most of the dates in Sturges (1994) are pre-altimetry dates, and so Sturges (1994) is placed in the pre-altimetry category. Sturges (1994) was submitted before the end of 1993. Thus, the study year 1993 was not completed.

† In the AVISO date list (Table 5.4-2), two LC eddies shed in February 2006. However, if those two events are combined into one, the results of the χ^2 tests and randomization test remain the same.

§ Alvera-Azcarate et al. (2009) analyzed data ending in February 2006. Thus, the study year 2006 was not completed. Alvera-Azcarate et al. (2009) noted two separation events to have occurred on the same day, 6 March 2002. If those two events are combined into one, the results of the χ^2 tests remain the same, but the March peak is no longer significant.

⌘ No dates were explicitly given in Chang and Oey (2012), but we know the dates are very similar to dates in Chang and Oey (2013b). All dates in Chang and Oey (2013b) were taken to be dates in Chang and Oey (2012) “as is”, with the exception of three: Chang and Oey (2013b) dates in March 1996, April 1995 and May 2007 were included in Chang and Oey (2012), after each being shifted forward a month to ultimately match the altimetry histogram in Chang and Oey (2012). See further explanation in Section 5.4. Since the estimated Chang and Oey (2012) dates can be binned monthly to match the histogram in Chang and Oey (2012), the χ^2 test results included herein are valid even if the exact estimated dates are wrong. However, the corresponding randomization test will be impacted by incorrect dates.

⌘ In the AVISO date list (Table 5.4-2), two LC eddies shed in February 2006. However, if those two events are combined into one, the results of the χ^2 and randomization tests on the combined re-analysis/AVISO date set remain the same.

⌘ In the AVISO date list (Table 5.4-2), two LC eddies shed in February 2006. However, if those two events are combined into one, the results of the χ^2 and randomization tests on the combined Vukovich (2012)/AVISO date set remain the same.

season is significant in the CCAR seasonal distribution but not in the AVISO-CUPOM seasonal distribution. Differences in SSHA processing methods between CCAR and AVISO resulted in smaller and larger spreads, respectively, of separation dates around the center of the fall season. In addition, AVISO dates were clustered closer to the fall center than the AVISO-CUPOM dates, indicating that both SSHA processing and mean SSH impact the overall spread of the distribution. If the AVISO-CUPOM dates were the only dates available for analysis, there would have been insufficient evidence to prove seasonality based on the randomization test. With the null hypothesis that the counts come from a uniform distribution, χ^2 tests show that the null hypothesis can be rejected at the 95% confidence level for all three subplots with binning1 and binning2, indicating a seasonal preference. Thus, seasonality is also confirmed in the AVISO-CUPOM dataset although the preferred seasons cannot be identified.

Results of the statistical tests performed on the CCAR, AVISO, and AVISO-CUPOM datasets are given in Table 5.5-1 along with results of testing on additional LC eddy separation dates derived from altimetry. September is a significant month in all data sets except for AVISO-CUPOM, as mentioned before, and the Vukovich (2012) dates from 1993 through 2010. Vukovich (2012) was the only source in the Table 5.5-1 altimetry list to rely also on SST and ocean-color data besides altimetry to derive dates during the altimetry time period, which may have resulted in event dates different enough from other sources to suppress fall season significance. However, March was a significant month in the Vukovich (2012) altimetry dates. This month was also significant in Alvera-Azcarate et al. (2009) and Chang and Oey (2013b), but not Chang and Oey (2012). Lack of significance of the March peak in Chang and Oey (2012) illustrates the extreme sensitivity of significance testing to small changes in separation dates. (Please refer to Section 5.4 and Table 5.5-1 notes for details on the Chang and Oey (2012) dates.)

The pre-altimetry re-analysis date list is nearly consistent with the majority of the altimetry date lists because of its significant peak in August, close to the significant altimetry September peak. This rough agreement serves as additional evidence that the LC eddy separation dates determined by the re-analysis presented in this report are likely more accurate than the Vukovich (2012) dates.

Figure 5.5-4 displays the three altimetry date sets CCAR, AVISO, and AVISO-CUPOM paired with the pre-altimetry re-analysis dates. (Traditional histograms of the three combined lists are presented in Figures 5.5-2f, 5.5-2g, and 5.5-2h, respectively.) All three combined lists have significant peaks in August and September, including the combined list using the AVISO-CUPOM dates shown in Figure 5.5-4c. December has become a significant trough in the pre-altimetry/CCAR combined histogram (Figure 5.5-4a). Figure 5.5-5 displays the three altimeter-derived LC eddy separation date sets paired with the Vukovich (2012) pre-altimetry dates from 1978 through 1992. (Traditional histograms of the three combined lists are presented in Figures 5.5-2i, 5.5-2j, and 5.5-2k, respectively.) The August peak that appeared in the CCAR altimetry dates alone (Figure 5.5-3a) is no longer significant in the combined date list in Figure 5.5-5a. However, December has become a significant trough. Other months besides March, August, September, and December may also become significant as more separation events occur and are added to the record. The September peaks in the CCAR and AVISO altimetry lists (Figures 5.5-3a and 5.5-3b) are still significant in the combined lists (Figures 5.5-5a and 5.5-5b). No peaks are significant in the AVISO-CUPOM combined list (Figure 5.5-5c), which is not unexpected since neither the Vukovich (2012) pre-altimetry dates (Figure 5.5-1b) nor the AVISO-CUPOM altimetry dates (Figure 5.5-3c) had any significant peaks. The Vukovich (2012) pre-altimetry dates tend to suppress seasonal preference when combined with the altimeter record, whereas the pre-altimetry re-analysis dates tend to accentuate seasonality. Table 5.5-1 presents significance testing results for all six combinations of LC eddy separation dates along with results from published dates by other studies.

Significance testing indicates that the annual cycle of LC eddy separation has a strong significant peak in September, with a less distinct peak suggested in March. Therefore, it is natural to divide the cycle into the two seasons previously introduced, the spring and the fall, respectively peaking near the spring (March) and fall (September) equinoxes. Though the peaks of the two seasons are evident, the centers and boundaries are not. The seasonal centers (means), which account for all events within the respective season, may not necessarily match the seasonal peaks determined by significance testing of the distribution. To precisely define the boundaries of the seasons, it is useful for separation events to be arranged in a “circular” sense. “Linear” annual histograms, such as in Figure 5.5-1 through Figure 5.5-5, show the existence of seasonality well, but poorly represent the cycle of the seasons from year to year. Some publications such as Chang and Oey (2012) concatenate two identical annual cycles to illustrate the flow of one year into the next. However, regardless of how the data are plotted, January and December observations are often kept separate for statistical analyses. Since it is possible that a separation season can begin at the end of one year and end at the beginning of the next, it is imperative that all events have connectivity with each other mathematically so that seasonal boundaries can be objectively defined.

As an alternative to traditional “number-line” representations, separation event dates can be represented in a circular manner around the unit circle on a complex plane. First, the corresponding day-of-year (DOY) for each separation event date is converted to an angle with units of radians using:

$$\alpha = \frac{2\pi(DOY)}{365} \quad (5.5.1)$$

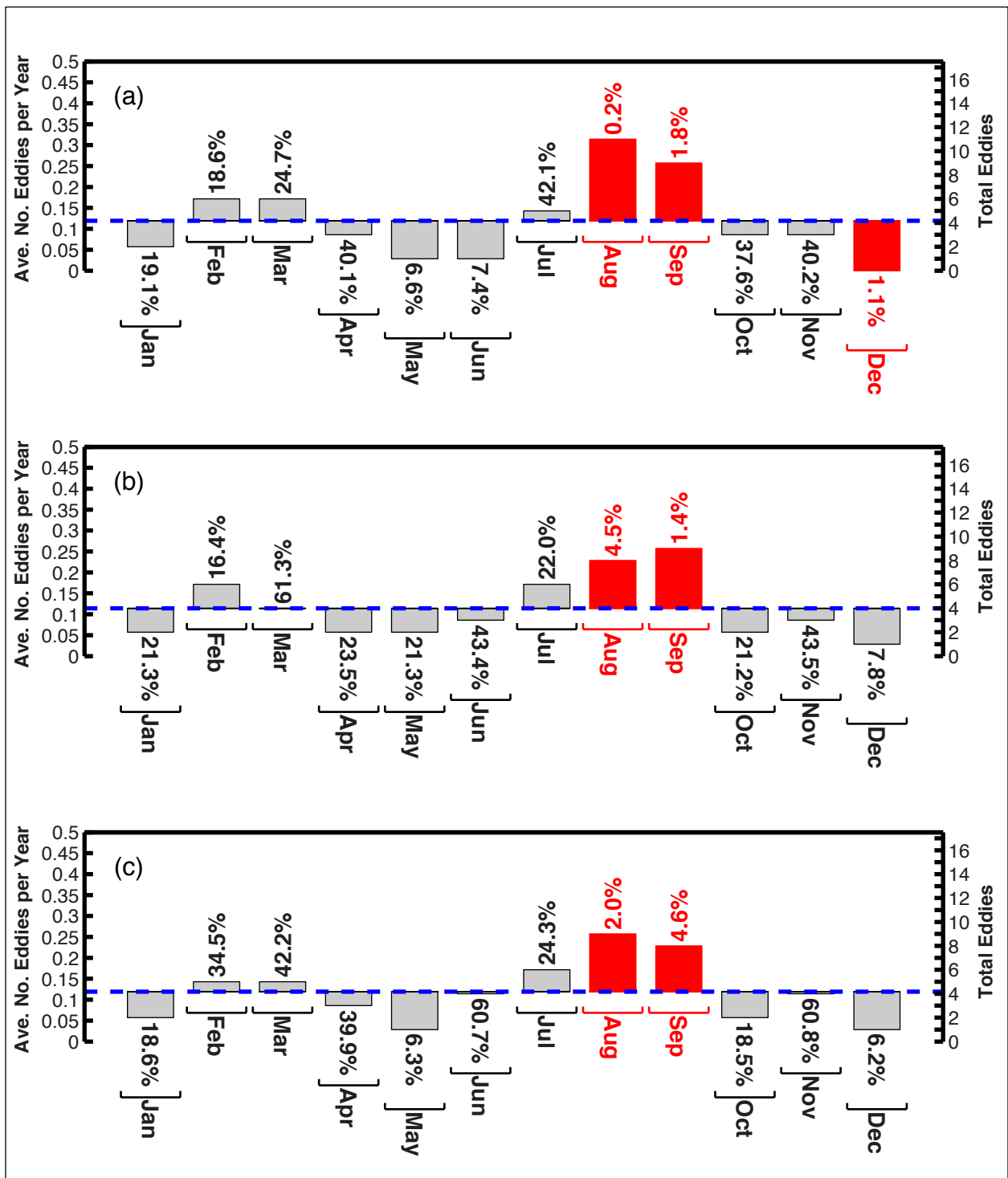


Figure 5.5-4. LC eddy separation dates binned monthly from combined pre-altimetry reanalysis (1978-1992) and (a) CCAR, (b) AVISO, and (c) AVISO-CUPOM altimetry (1993-2012). Blue dashed lines show the average number of LC eddies to separate per month, per year. The percent likelihood of observing an LC eddy count as extreme or more extreme by chance is displayed for each monthly bar. All bars at 5% or less are considered significant at the 95% confidence level and colored red.

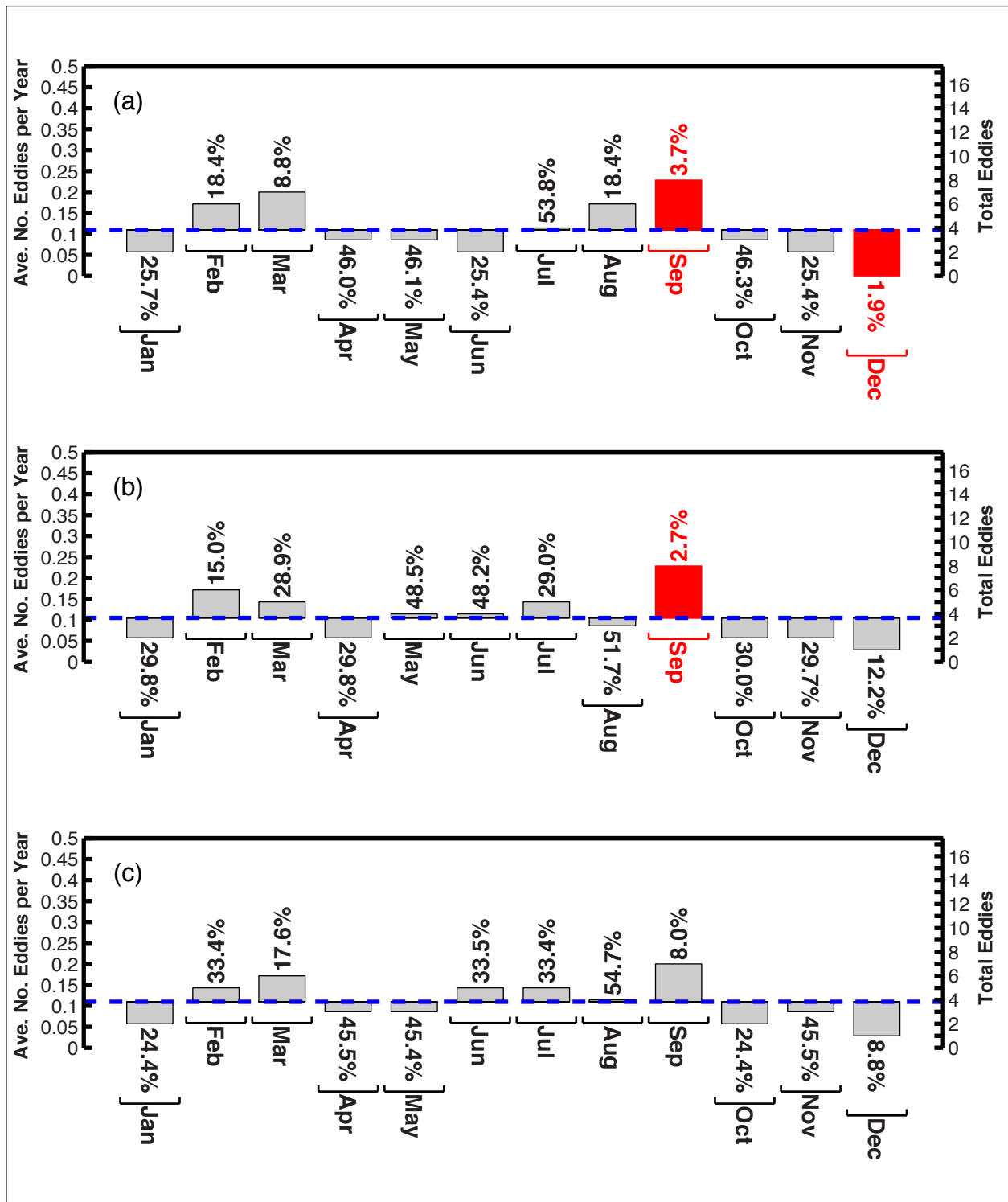


Figure 5.5-5. LC eddy separation dates binned monthly (1978-2012) from combined Vukovich (2012) pre-altimetry (1978-1992) and (a) CCAR, (b) AVISO, and (c) AVISO-CUPOM altimetry (1993-2012). Blue dashed lines show average number of LC eddy separations per month, per year. The percent likelihood of observing an LC eddy count as extreme or more extreme by chance is displayed for each monthly bar. All bars at 5% or less are considered significant and colored red.

Since DOY can be at most equal to 365 days and at least one day, α is always greater than zero and less than or equal to 2π . (Note that for a separation date falling in a leap year, the leap day is ignored and the DOY is calculated as for a non-leap year. In the case that a separation occurs on the leap day, Feb. 29, the DOY for Feb. 28 is used to keep the separation event in the correct month.) Then each angle α is transformed into a complex number:

$$z = \cos(\alpha) + i \sin(\alpha). \quad (5.5.2)$$

Separation dates in the form of complex numbers can then be plotted around the unit circle.

Figure 5.5-6 displays the pre-altimetry re-analysis date list from Table 5.3-1 plotted around the unit circle. Similar plots for the CCAR, AVISO, and AVISO-CUPOM altimetry date lists in Table 5.4-2 are shown in Figure 5.5-7, and plots of the combined pre-altimetry and altimetry date lists are shown in Figure 5.5-8. A k-means clustering algorithm was applied to each date list (seven altogether) to divide the events in each list into two distinct groups per plot, the spring (red dots) and fall (blue dots) seasons. (The results of a k-means scheme are dependent on the initialization of the algorithm; different initializations can result in different clusterings and, thus, different standard deviations of the two clusters in this situation. The k-means algorithm was semi-randomly initialized many times to identify the two event groups yielding the minimum-RMS of their standard deviations.) For each date list, the complex numbers corresponding to all dates in a season were averaged with Eq. (5.5.3) to find the geometric center or centroid of each season,

$$\bar{z} = \frac{1}{N} \sum_{j=1}^N z_j, \quad (5.5.3)$$

where the variable N represents the total number of events in the season. Then the mean angle was found as

$$\bar{\alpha} = \arg(\bar{z}), \quad (5.5.4)$$

where $0 < \bar{\alpha} \leq 2\pi$.

(Equation 5.5.1 can be used to calculate the DOY corresponding to the center of the season.) The colored triangles in each subplot of Figures 5.5-6 through 5.5-8 represent the centers of the two seasons. The spring and fall equinoxes occur after the respective centers of the separation seasons are reached during the year (moving counterclockwise around the circle). The dashed lines plotted between the seasonal means, each nearly pass through the origin of the corresponding unit circle, meaning that the centers of the two seasons are about six months apart in all seven date lists. (In fact, the dashed line in the pre-altimetry re-analysis figure, Figure 5.5-6, crosses through the origin almost exactly.) Notice that the triangles do not lie on the unit circles as the dots do. The distance between each triangle and the unit circle is a measure of dispersion (standard deviation) in the dates in each season. The approximate circular analogue of the basic linear standard deviation is given by the following equation:

$$\alpha_{std} = \sqrt{2(1-|\bar{z}|)}. \quad (5.5.5)$$

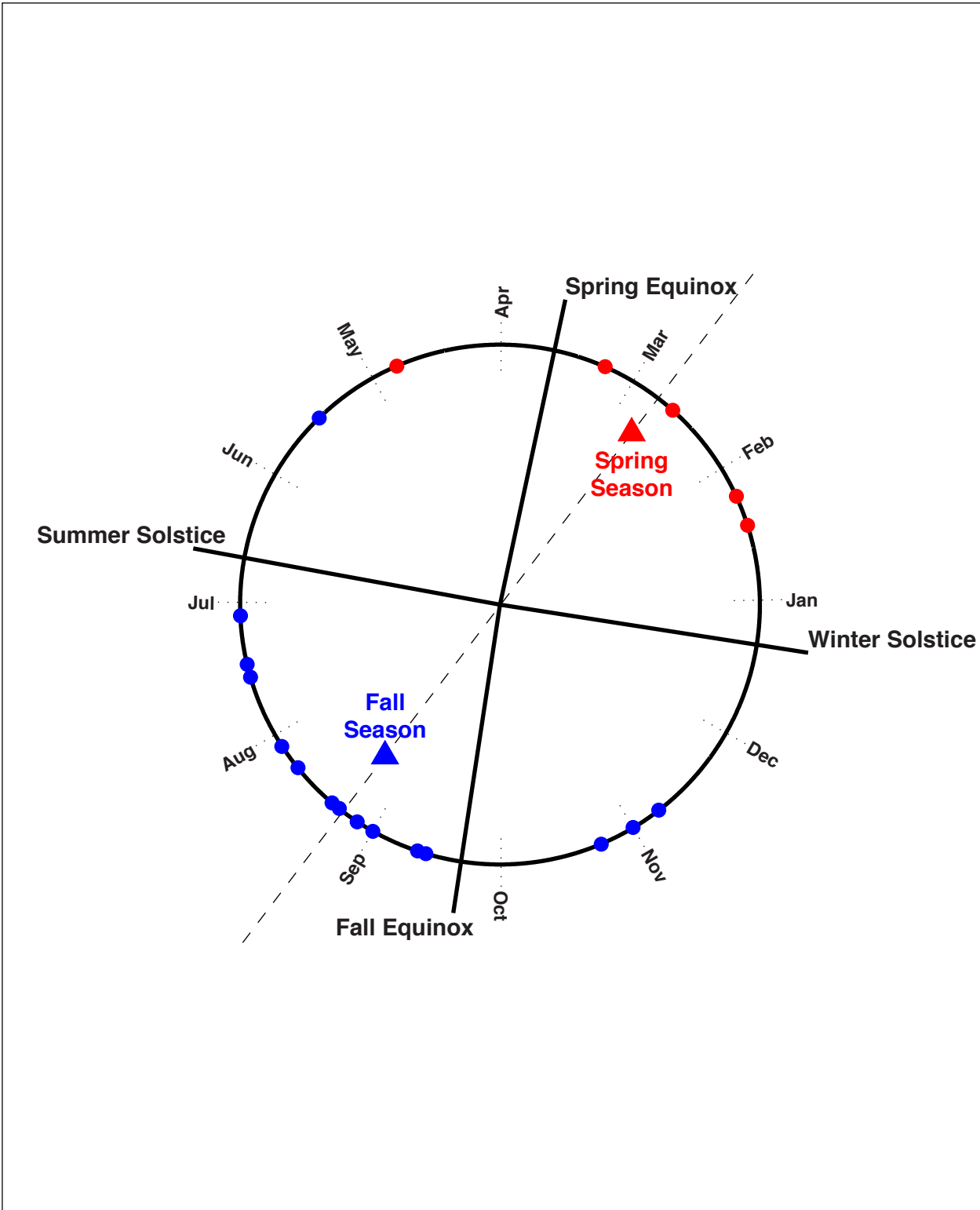


Figure 5.5-6. Pre-altimetry reanalysis LC eddy separation dates from 1978-1992 (Table 5.3-1) plotted as days-of-year on the unit circle in the complex plane, divided into two seasons. Each dot represents a separation event. The triangles represent the means of the two seasons.

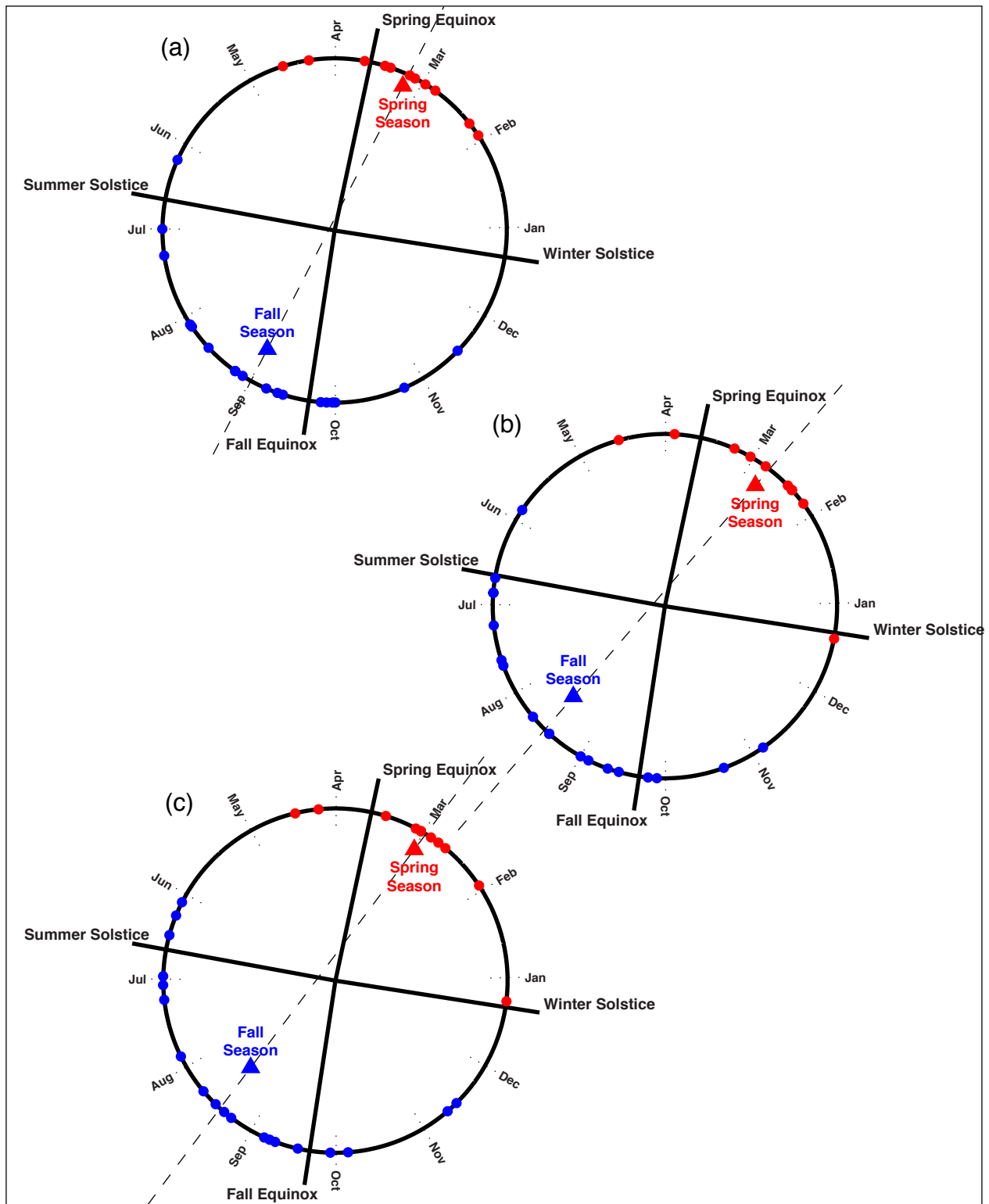


Figure 5.5-7. LC eddy separation dates (Table 5.4-2) from (a) CCAR, (b) AVISO, and (c) AVISO-CUPOM altimetry (1993-2012) plotted as days-of-year on the unit circle in the complex plane, and divided into two seasons. Each dot represents a separation event. The triangles represent the means of the two seasons.

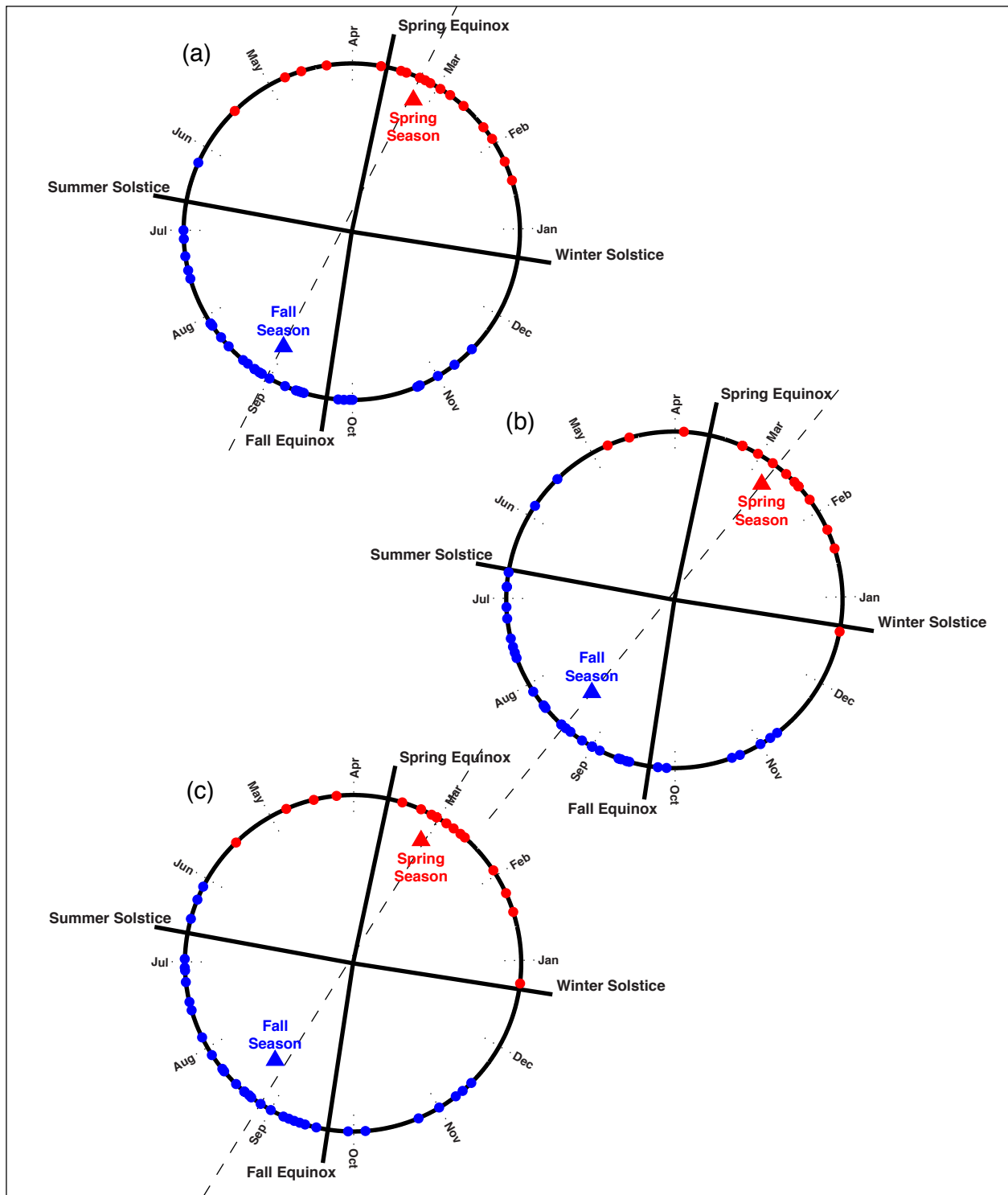


Figure 5.5-8. LC eddy separation dates (1978-2012) combining the reanalysis pre-altimetry with (a) CCAR, (b) AVISO, and (c) AVISO-CUPOM altimetry dates plotted as days-of-year on the unit circle in the complex plane, and divided into two seasons. Each dot represents a separation event. The triangles represent the means of the two seasons.

The angle α_{std} in Eq. 5.5.5 can be substituted into Eq. 5.5.1 to yield standard deviation in units of days (Berens 2009; Jammalamadaka and SenGupta 2001).

The centers and standard deviations obtained from circular statistical methods are given in Table 5.5-2. Linear means and standard deviations calculated using DOYs instead of complex numbers are also presented in the table for comparison. Considering all seven date lists, circular results indicate that the spring mean lies within approximately a two-week period from Feb. 22 through 7 March (~1 March); standard deviations are between 22 and 34 days. Linear results are much less reliable. They indicate that the spring mean lies within a period larger than a month, from 24 February through 2 April; standard deviations are between 23 and 96 days. The fall mean, according to circular methods, lies within approximately a two-week period from 16 August through 1 September (~24 August); standard deviations are between 37 and 45 days. Linear methods also indicate the mean lies in a two-week window from 16 August through 31 August; standard deviations are between 39 and 49 days. Mean circular and linear method results for the fall season are comparable. However, circular methods have a clear advantage for estimating the spring mean. The reason for this is because the AVISO and AVISO-CUPOM altimetry spring seasons start in December according to the clusterings in Figures 5.5-7b and 5.5-7c. In Table 5.5-2, the CCAR spring circular mean is very similar to its corresponding linear mean, but the AVISO and AVISO-CUPOM spring linear means are significantly different than their respective circular means. Also, in comparison to the CCAR spring linear standard deviation, the standard deviations of the other two date lists are very large. This discrepancy is caused by the DOY bias of Titanic, which separated in December in AVISO and AVISO-CUPOM but is part of the spring cluster. The Titanic DOY is high in the AVISO (354) and AVISO-CUPOM (358) date sets and low in the CCAR (39) dataset. Titanic not only has a noticeable impact on spring linear AVISO and AVISO-CUPOM altimetry statistics, but also the linear combined AVISO and AVISO-CUPOM statistics in Table 5.5-2 and Figures 5.5-8b and 5.5-8c.

Circular statistics account for relative positioning of the events better than standard linear (number-line) statistics, resulting in superior mean estimates. Note that each circular standard deviation in Table 5.5-2 is lower than the corresponding linear standard deviation, indicating that circular statistics have higher reliability. Linear statistics in Vukovich (2012) should be interpreted in light of the statistical discussion above. Instead of grouping separation events into two seasons, Table 2 of Vukovich (2012) reports that the average separation month of all events for three different year ranges is June, with a standard deviation of three months. The standard deviation was likely calculated assuming a normal distribution. However, none of the histograms in Figure 5.5-2 appear normally distributed. The mean of a normal distribution is equal to the most likely value, which Vukovich (2012) indicates is June, but most of the histograms in Figure 5.5-2 show that LC eddies are unlikely to separate in that month. Table 4 of Vukovich (2012) lists 48 LC eddy separation events from 1972 through 2010, only three (6%) of which were June events. Because the series of 12 calendar months repeats in a perpetual cycle, giving an “average” separation month on a number line, such as June, is meaningless and misleading since one might be led to believe that June events happen frequently. To the author’s credit, Vukovich (2012) also provides separation month mode, March, which has more statistical significance.

Table 5.5-2. Centers (means) and standard deviations (std.) of Table 5.2-1 and 5.4-2 separation events analyzed separately and combined, separated into spring and fall seasons and presented circularly and linearly

	Circular		Linear	
	<i>spring</i>	<i>fall</i>	<i>spring</i>	<i>fall</i>
PRE-ALTIMETRY				
Re-analysis, 1978-1992				
center (DOY)	53.2 (22 Feb)	236.0 (24 Aug)	54.8 (24 Feb)	235.5 (24 Aug)
std. (days)	33.6	42.5	38.9	47.3
ALTIMETRY				
CCAR, 1993-2012				
center (DOY)	65.6 (07 Mar)	243.8 (01 Sep)	65.8 (07 Mar)	242.9 (31 Aug)
std. (days)	22.0	37.4	23.3	40.6
AVISO, 1993-2012				
center (DOY)	53.9 (23 Feb)	227.7 (16 Aug)	90.0 (31 Mar)	227.8 (16 Aug)
std. (days)	28.9	41.3	95.4	44.7
AVISO-CUPOM, 1993-2012				
center (DOY)	59.8 (01 Mar)	228.9 (17 Aug)	92.3 (02 Apr)	229.7 (18 Aug)
std. (days)	27.4	44.6	90.4	48.7
COMBINED				
Re-analysis, 1978-1992+CCAR, 1993-2012				
center (DOY)	65.8 (07 Mar)	242.6 (31 Aug)	66.7 (08 Mar)	242.8 (31 Aug)
std. (days)	30.3	37.2	32.1	39.6
Re-analysis, 1978-1992+AVISO, 1993-2012				
center (DOY)	53.7 (23 Feb)	231.5 (20 Aug)	78.3 (19 Mar)	231.3 (19 Aug)
std. (days)	30.6	42.0	81.1	45.3
Re-analysis, 1978-1992+AVISO-CUPOM, 1993-2012				
center (DOY)	61.8 (03 Mar)	234.5 (23 Aug)	83.8 (25 Mar)	235.2 (23 Aug)
std. (days)	33.5	41.9	77.3	45.0
Re-analysis, 1978-1992+CCAR+AVISO+AVISO-CUPOM, 1993-2012				
center (DOY)	61.0 (02 Mar)	235.3 (23 Aug)	79.9 (21 Mar)	235.2 (23 Aug)
std. (days)	29.5	40.9	70.2	43.5

Seasonal clusterings in the analysis of the pre-altimetry re-analysis and CCAR, AVISO, and AVISO-CUPOM altimetry LC eddy separation date sets separately are somewhat sensitive to changes in event dates. The addition of a single new event to a list can cause events to be re-clustered into opposite seasons, shifting seasonal means by weeks. A larger number of events in each season must be observed before the seasons will “stabilize” and seasonal boundaries can be estimated. However, this number is not known a priori and depends on the stationarity of the process being observed. Even with the combined date sets, which include more separation events than do the pre-altimetry or altimetry date sets separately, the seasonal boundaries are not

well isolated. In Figure 5.5-8a, one boundary is between mid-May and early June, and the other between mid-November and mid-January. In Figure 5.5-8b, the boundaries are sometime in early May and between mid-November and mid-December. In Figure 5.5-8c, the boundaries are sometime in late May, and between mid-November and mid-December. For the best possible estimate of seasonal boundaries, the pre-altimetry re-analysis dates and the CCAR, AVISO, and AVISO-CUPOM dates were all combined together into one date list and clustered as before (not shown). The results indicate that the boundary between spring and fall is between 16 May and 28 May 28 (~22 May), and the boundary between fall and spring is between 16 November and 20 December (~3 December). Center and standard deviation statistics for this combined date list are included in Table 5.5-2. The spring center is 2 March, and the fall center is 23 August.

General Conclusions

In contrast to the new pre-altimetry re-analysis dates derived for this report, previously published pre-altimetry LC eddy separation dates do not exhibit seasonality. The re-analysis date list is thought to be more accurate than older date lists because the re-analysis is based on a more complete observational record and a careful re-analysis of that record. In addition, re-analysis significance- testing results are relatively consistent with altimetry-based results – that is, both the re-analysis dates and the dates from most altimetry lists show a significant LC eddy separation peak in the late summer/early fall – and most altimetry date lists are consistent with each other. Nevertheless, identification of LC eddy separation events in the pre-altimetry datasets (SST, chlorophyll-a, EddyWatchTM) is necessarily subjective. Caution is advised when using these data in combination with the more objective and quantitative altimetric record to detect subtle changes in long-term climate trends or seasonality since changes found could be an artifact of the heterogeneous record.

Analyses shown indicate at the 95% confidence level that the LC follows a seasonal pattern throughout the year. Figure 5.4-4 shows with a variety of different LC metrics and three different datasets that LC characteristics are different at some times of the year than at others. Statistical tests, using χ^2 on most date lists, indicate that there is seasonal preference to the timing of LC eddy separation since the distribution is not uniform. Randomization tests indicate that separations are most likely to occur in September and possibly March. Events are unlikely to happen in December. The annual cycle of LC eddy separation can be split into two seasons, the “spring” centered around 2 March and the “fall” centered around 23 August. The boundaries between these two seasons are approximately 22 May and 3 December.

5.6 INVESTIGATION OF DYNAMICS CONTRIBUTING TO LOOP CURRENT SEASONALITY

Statistically significant seasonality has been identified in this analysis, not only in the annual cycle of LC metrics (Section 5.4), but also in the biannual distribution of LC eddy separation events (Section 5.5). The primary cause of this seasonality can now be explored in detail.

As discussed in the introduction to this chapter, seasonality of LC eddy separation became more apparent over time as the length of the continuous record of altimetric monitoring of the LC and LC eddies increased. Industry concerns about the joint probability of eddy-hurricane events in the Gulf (Cooper and Stear 2009) and the potential impact of LC seasonality on the joint

probability motivated a preliminary re-analysis of the pre-altimetric and altimetric record of LC intrusion and eddy shedding. This information was presented at the 2010 Ocean Sciences Meeting (Leben and Hall 2010), and at the 2011 Gulf of Mexico Information Transfer Meeting (Leben et al. 2012). This generated a number of modeling studies supported by the LC study program that were performed independently from the observational studies. In those studies Chang and Oey (2012) hypothesized that the “biannually” varying combination of Gulf and Caribbean winds affect Gulf and Caribbean transports, which cause more LC eddies to shed in summer and winter and fewer to shed in spring and fall, based on a series of process-oriented modeling experiments. Chang and Oey (2013a) further stated that the LC shows bimodal, asymmetric growth/wane captured by the first two empirical orthogonal function (EOF) modes of SSH in the eastern Gulf/northern Caribbean Sea, with the more dominant growth/wane from summer to fall and the less dominant from winter to spring. In the following section, EOF analyses will be used to re-visit the findings determined from the process modeling studies and preliminary altimetric data analysis performed by Chang and Oey (2013a).

Deepwater EOF Analysis

EOFs are a powerful tool for identifying the dominant variability in a dataset and are useful for exploring seasonal variations in the LC as well. The following analysis 1) uses EOFs to capture the dominant LC variability in the 20-year altimeter time series, 2) shows that the dominant LC variability also contains seasonal variability, 3) extracts the seasonal EOF modes containing the annual variability, and 4) evaluates proposed physical mechanisms causing the seasonal modes and the annual LC variability.

Monthly SSH fields from 1993 through 2012 were generated from delayed-time weekly $\frac{1}{4}^{\circ}$ AVISO mapped SSH fields. A small amount of daily near-real-time data were included to complete the dataset through the end of the year 2012. The monthly data were demeaned in the deepwater by subtracting the averaged values of SSH from the monthly maps in Gulf waters deeper than 200 m to remove the steric signal associated with seasonal heating of the mixed layer. The steric signal is removed since it is an annual signal in the Gulf that would otherwise dominate the first mode of an EOF decomposition of SSH, but does not contribute to the dynamical variability of the LC. All data over the shelf were masked so that the EOF decomposition would reflect LC variability, which is predominately confined to the deep waters of the Gulf. This also prevents mode mixing (Kim and Wu 1999) of the deepwater and shelf variability in the EOF analyses. An EOF decomposition was calculated over the domain 98°W - 80°W , 18°N - 31°N . This is different than the EOF domain used by Chang and Oey (2013a) for analysis of the AVISO data, which covered 92°W - 80°W , 15°N - 31°N and included the continental shelf. In all deepwater EOF analyses shown in this chapter, the spatial signal over the shelf was reconstructed for each spatial EOF loading vector. This was accomplished by regressing the corresponding principal component time series (PCTS) onto the original SSH time series, over the shelf, to map the shelf signal correlated with the deepwater SSH variability.

The first two EOF loading vectors are shown in Figure 5.6-1 and account for 24.6% and 16.6% of the deepwater SSH variance. Gray dashed lines plotted on the loading vectors define the data masking boundaries of the EOF decomposition. With the exception of the lines that transect the Yucatan Channel and Florida Strait, the lines follow the 200-m isobath. In comparison to the first

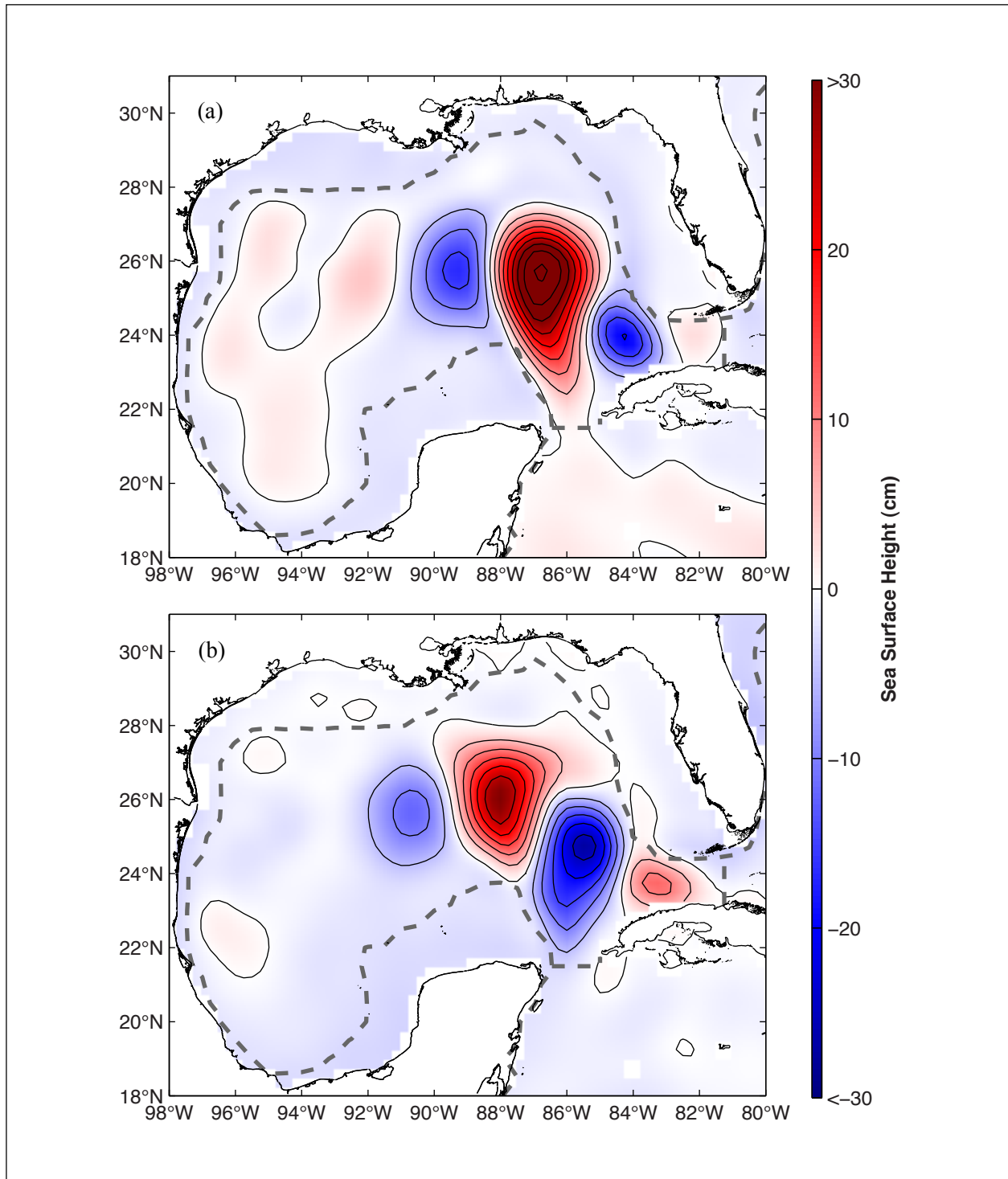


Figure 5.6-1. Deepwater (a) EOF mode 1 and (b) EOF mode 2 loading vectors, derived from monthly AVISO SSH with the steric signal removed. Mode 1 explains 24.6% of the variance, and mode 2 explains 16.6%. Black contours are at 5-cm intervals. Gray dashed lines signify the boundaries of the EOF decomposition. The lines follow the 200-m isobath everywhere except across the Yucatan Channel and Florida Strait.

two loading vectors, corresponding EOF modes shown in Figure 10 of Chang and Oey (2013a) accounted for 29.5% and 17.2% of the variance, slightly higher in both cases. This is due to differences in steric signal removal procedures, to differences in EOF decomposition domains, and likely to other differences in methods. The third and fourth EOF loading vectors are shown in Figure 5.6-2 and account for 11.1% and 6.6% of the deepwater variance. All together, the first four modes account for 58.9% of the variance in the monthly averaged data. EOF mode 1 leads EOF mode 2 by 55 days (EOFs derived from daily data were used to improve lag estimation only) based on a cross-correlation between PCTS 1 and 2. Further cross-correlation testing shows that mode 3 leads mode 4 by 65 days (see Figure 5.6-3).

When combined with the PCTS modes shown in Figure 5.6-3, the spatial patterns in Figures 5.6-1 and 5.6-2 blend into a continuous three-event sequence: LC penetration, LC eddy separation, and westward LC eddy propagation. Table 5.4-2 shows that 28 LC eddies were detected in the 20-year AVISO altimetry record. This averages out to about one LC eddy separation every 8.6 months. An approximate count of local peaks is 27 in PCTS 1 (using monthly EOFs); 26 in PCTS 2; 25 in PCTS 3; 29 in PCTS 4. There are about as many peaks in the PCTS as there are separation events, meaning that, on average, the propagating LC eddy pattern in the first four EOF modes repeats about as frequently as LC eddies separate in the AVISO data, between eight and nine months. This is approximately commensurate with the periods associated with the two quadrature pairs formed by the first four EOF modes, which are $7 \frac{1}{3}$ months (4×55 days) for modes 1 and 2, and $8 \frac{2}{3}$ months (4×65 days) for modes 3 and 4. The four deepwater EOFs in Figures 5.6-1 and 5.6-2 represent most of the LC and LC eddy SSH variability in the eastern Gulf.

These results are in contrast to the 3-month lagged correlation found between the first two EOF PCTS by Chang and Oey (2013a) in their EOF analysis of the monthly AVISO data. A 3-month lagged correlation corresponds to an annual period for the dominant quadrature pair. Why is there such a discrepancy, $7 \frac{1}{3}$ months versus 12 months, between the periods of the dominant quadrature pairs from these two EOF analyses of AVISO monthly data? An attempt was made to duplicate the EOF decomposition performed by Chang and Oey (2013a) to confirm the 3-month lag. The authors used monthly $1/3^\circ$ AVISO mapped SSH fields from January 1993 through December 2010. The steric signal was removed by averaging over the Gulf and northwestern Caribbean Sea (98°W - 80°W , 15°N - 31°N). Then, EOFs were computed over the domain 92°W - 80°W , 15°N - 31°N . Variance explained by the first EOF mode was 25.4%, and by the second EOF 15.9%, both still lower than the values quoted by Chang and Oey (2013a). Also, the lag computed between their first and second PCTS was two months, not three. Another EOF decomposition on the monthly AVISO dataset prepared for this report (not shown) was performed over the domain 92°W - 80°W , 18°N - 31°N , ignoring the western Gulf. Mode 1 led mode 2 by 54 days, and mode 3 led mode 4 by 65 days, comparable in both instances to the original lagged analysis results of 55 and 65 days, respectively. Including the western Gulf or northwestern Caribbean Sea, variability does not significantly affect the decomposition of the dominant LC variability modes.

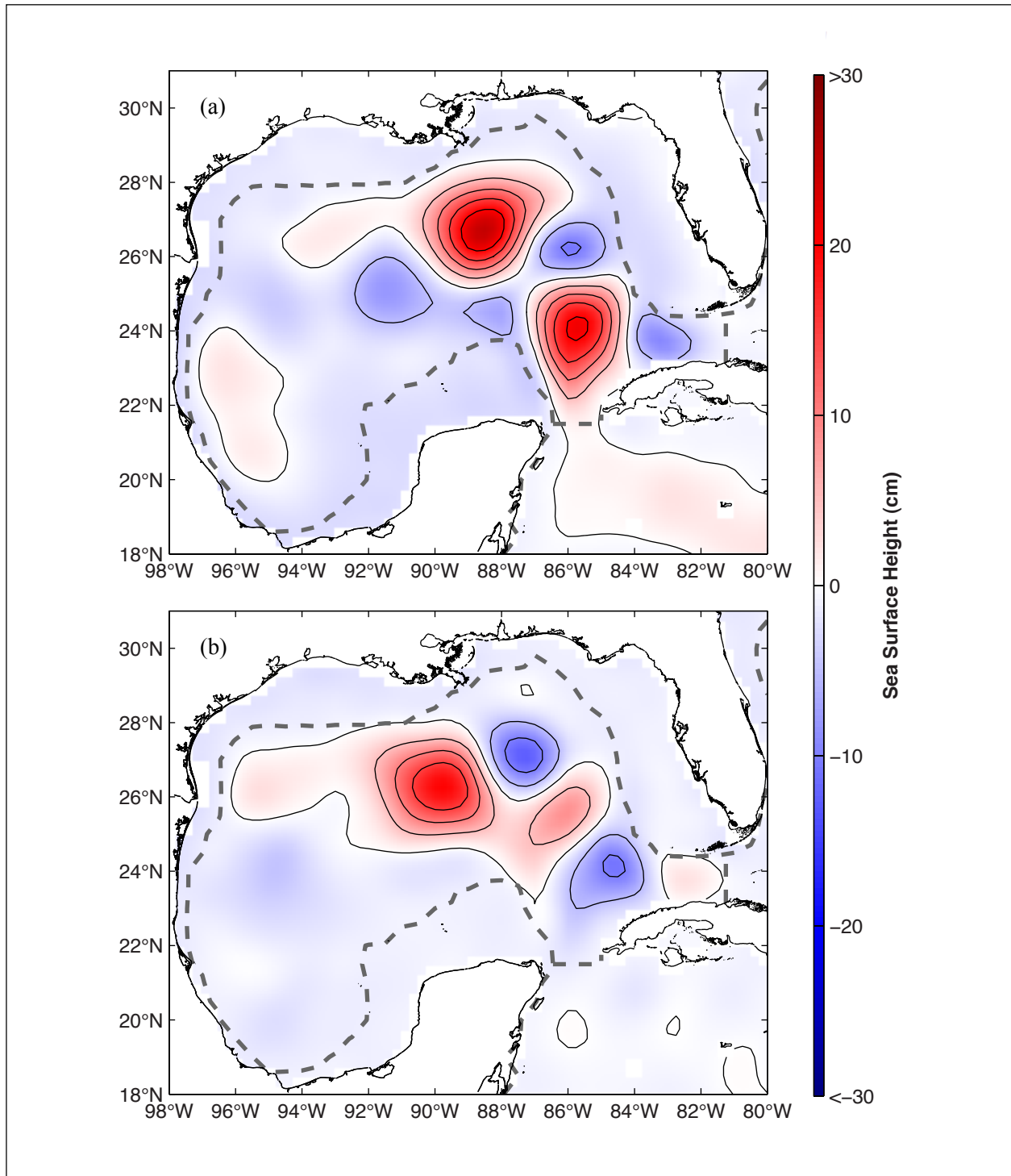


Figure 5.6-2. Deepwater (a) EOF mode 3 and (b) EOF mode 4 loading vectors, derived from monthly AVISO SSH with the steric signal removed. Mode 3 explains 11.1% of the variance, and mode 4 explains 6.6%. Black contours are at 5-cm intervals. Gray dashed lines signify the boundaries of the EOF decomposition. The lines follow the 200-m isobath everywhere except across the Yucatan Channel and Florida Strait.

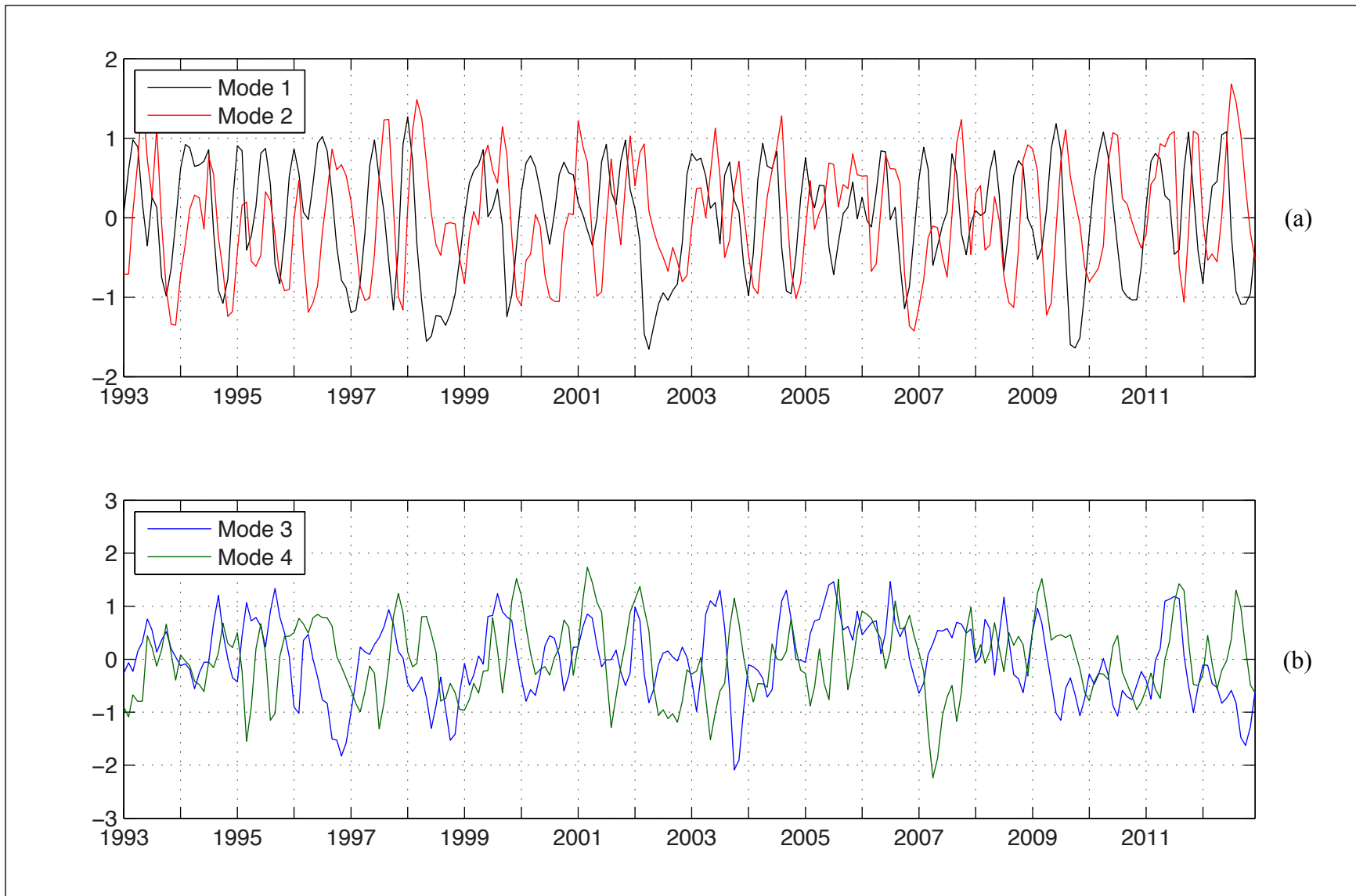


Figure 5.6-3. Deepwater principal component time series: (a) PCTS 1 and PCTS 2 and (b) PCTS 3 and PCTS 4, derived from monthly AVISO SSH with the steric signal removed.

Returning again to the original EOF decomposition, Figure 5.6-4 shows the composite annual cycle (CAC) of the PCTS computed by averaging all PCTS values shown in Figure 5.6-3 for each month, with 95% confidence intervals included. The CAC of PCTS 1 is dominantly annual, with the trough in October being statistically different than the months January through June. The CAC is weakly biannual with two small peaks in February and May, though this biannual signal is not significant. The CAC of PCTS 2 has no statistically significant monthly variance, but does exhibit some biannual variation with one peak in February and the other in July. February peaks in the CACs of both PCTS 1 and PCTS 2 are indicative of LC northward penetration and westward spreading. In contrast, the two-month delay between the May and July peaks of the first and second CACs, respectively, indicates LC northward penetration and LC eddy detachment or separation. The CAC of PCTS 3 is mainly annual with a significant trough in November, while the CAC of PCTS 4 is nondescript.

Figure 5.6-5a shows the sum of monthly variance of the AVISO data in the Gulf and northwestern Caribbean Sea, and Figure 5.6-5b provides the fraction of that variance contained within a monthly reconstruction of the first four deepwater EOF modes. The map shows that LC variance has been largely isolated and is upwards of 80% represented by the four modes. Notably, SSH variations along parts of the shelf are correlated with LC variations since the four EOF modes account for more than 30% of the variance in some areas of the Texas-Louisiana Shelf and more than 40% over some areas of the Campeche Bank. The map also shows that the variations in the western Gulf and northwestern Caribbean deep water are uncorrelated with the dominant LC variability.

The CACs of the LC metrics shown in Figure 5.4-4, derived from the complete 20-year AVISO monthly SSH dataset, capture the annual variability of the LC in the AVISO dataset very well. The CACs were computed by averaging all LC metric values for each month and each LC metric (area, area including detachments, volume, anticyclonic circulation, northernmost latitude, and westernmost longitude) to create a monthly mean time series for each metric. Using a different technique, CACs of the same LC metrics mentioned were computed from CAC SSH map sets derived from various monthly reconstructions using the first four deepwater EOF loading vectors shown in Figure 5.6-1 and Figure 5.6-2 to verify that the EOF modes contribute the majority of LC seasonal variability. Note that the LC metric CACs shown in Figure 5.4-4 were generated by averaging monthly LC metric values. The LC metric CACs shown here were created by generating an “average year” map set and then computing the corresponding LC metrics from that set. The first CAC SSH map set was calculated from the monthly-reconstructed deepwater EOF mode 1. SSH maps from each specific month were averaged to create a composite sequence of twelve maps, January through December, corresponding to the annual cycle, called CAC1. The second CAC SSH map set was calculated from the monthly reconstruction of modes 1 and 2 together and is CAC12. Similarly, two more EOF CAC map sets were calculated called CAC123 and CAC1234, and a final reference CAC map set was calculated from the original monthly AVISO SSH data called CAC_raw. The six listed LC metrics were calculated from each of the five CAC map sets. The names CAC_raw, CAC1, CAC12, CAC123, and CAC1234 will be used to refer to each respective twelve-month map sequence as well as individual LC metric CACs depending on the context. Since the LC metrics exhibit similar trends, only the maximum northern latitude and area are shown in Figures 5.6-6 and 5.6-7, respectively. Figures 5.6-6a and

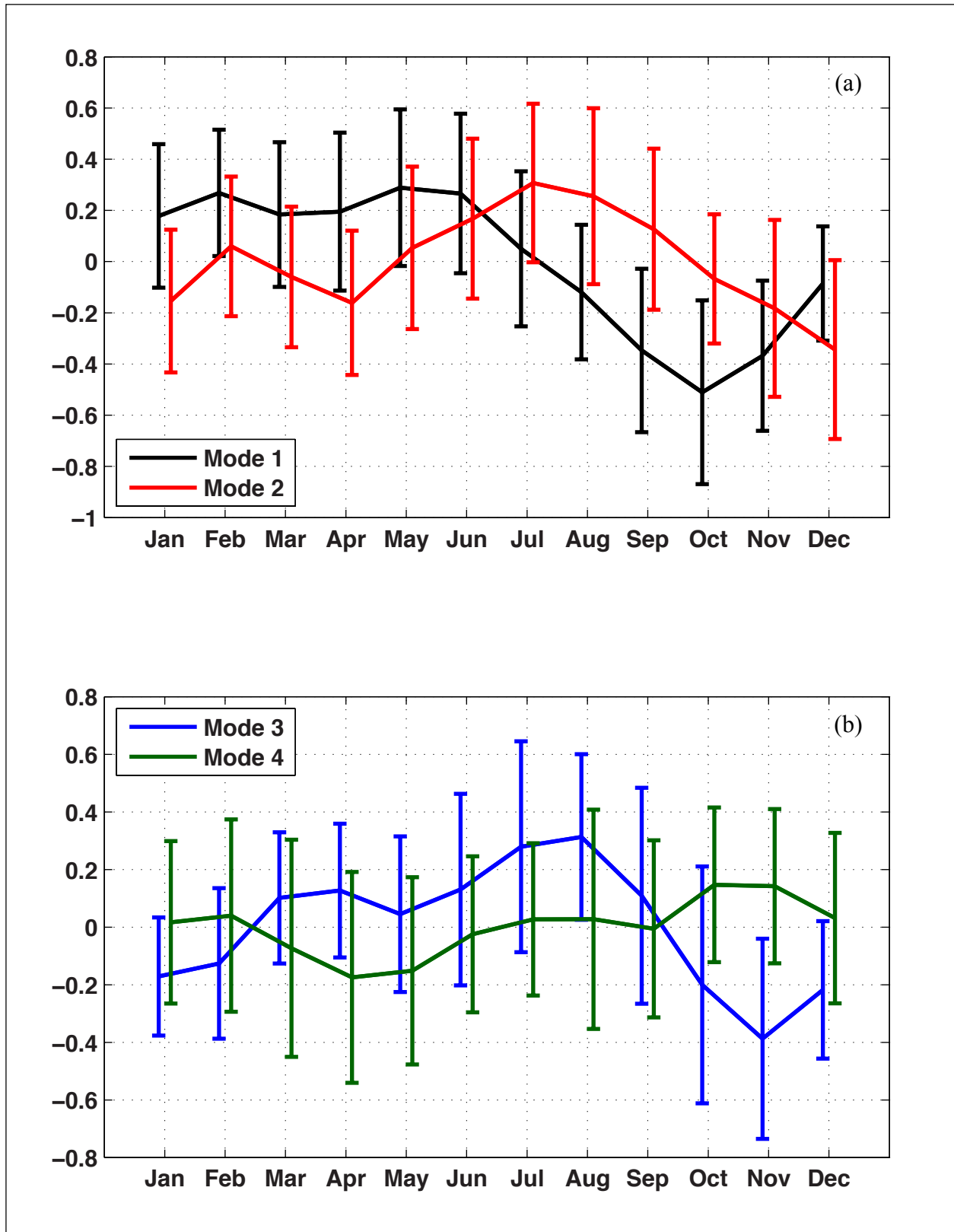


Figure 5.6-4. CACs generated from deepwater EOF mode (a) PCTS 1 and PCTS 2 and (b) PCTS 3 and PCTS 4. Error bars are 95% confidence intervals.

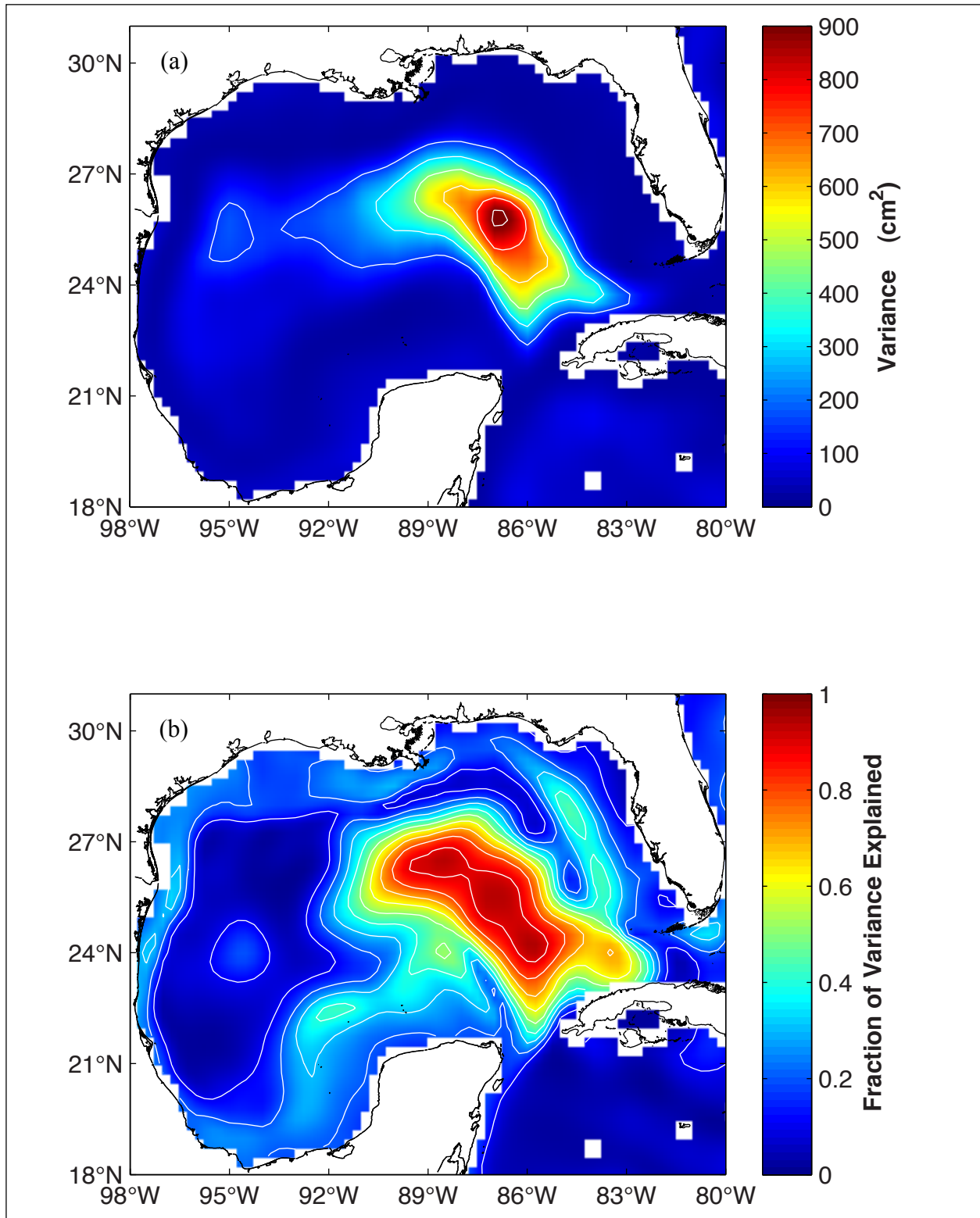


Figure 5.6-5. (a) Sum variance of monthly AVISO maps. Contour increment 150 cm^2 . (b) Fraction of total variance captured by first four deepwater EOF modes including correlated signals at depths less than 200 m. Contour increment 0.1.

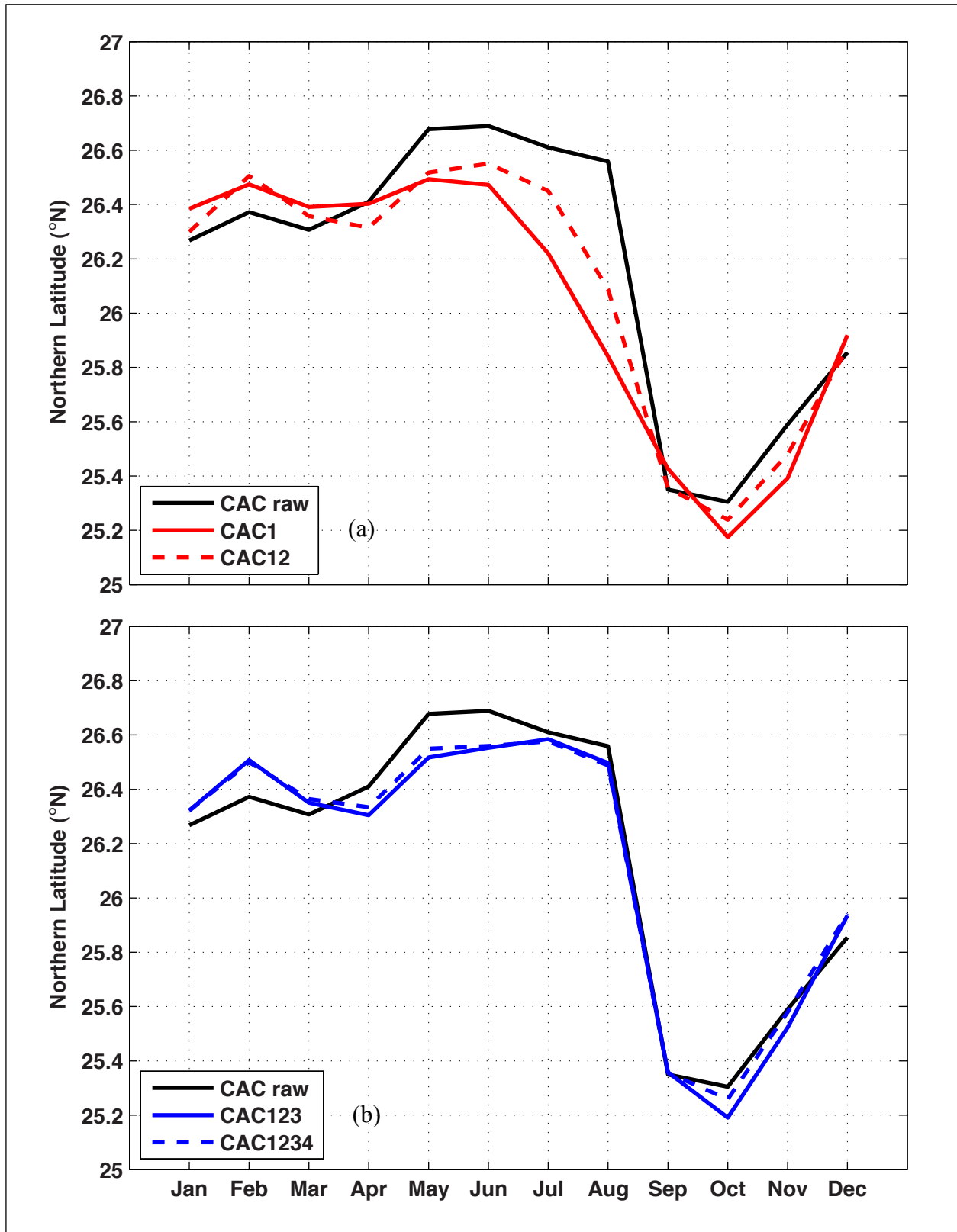


Figure 5.6-6. CAC of Loop Current northern boundary latitude. CAC_raw is plotted with: (a) CAC1 and CAC12; (b) CAC123 and CAC1234.

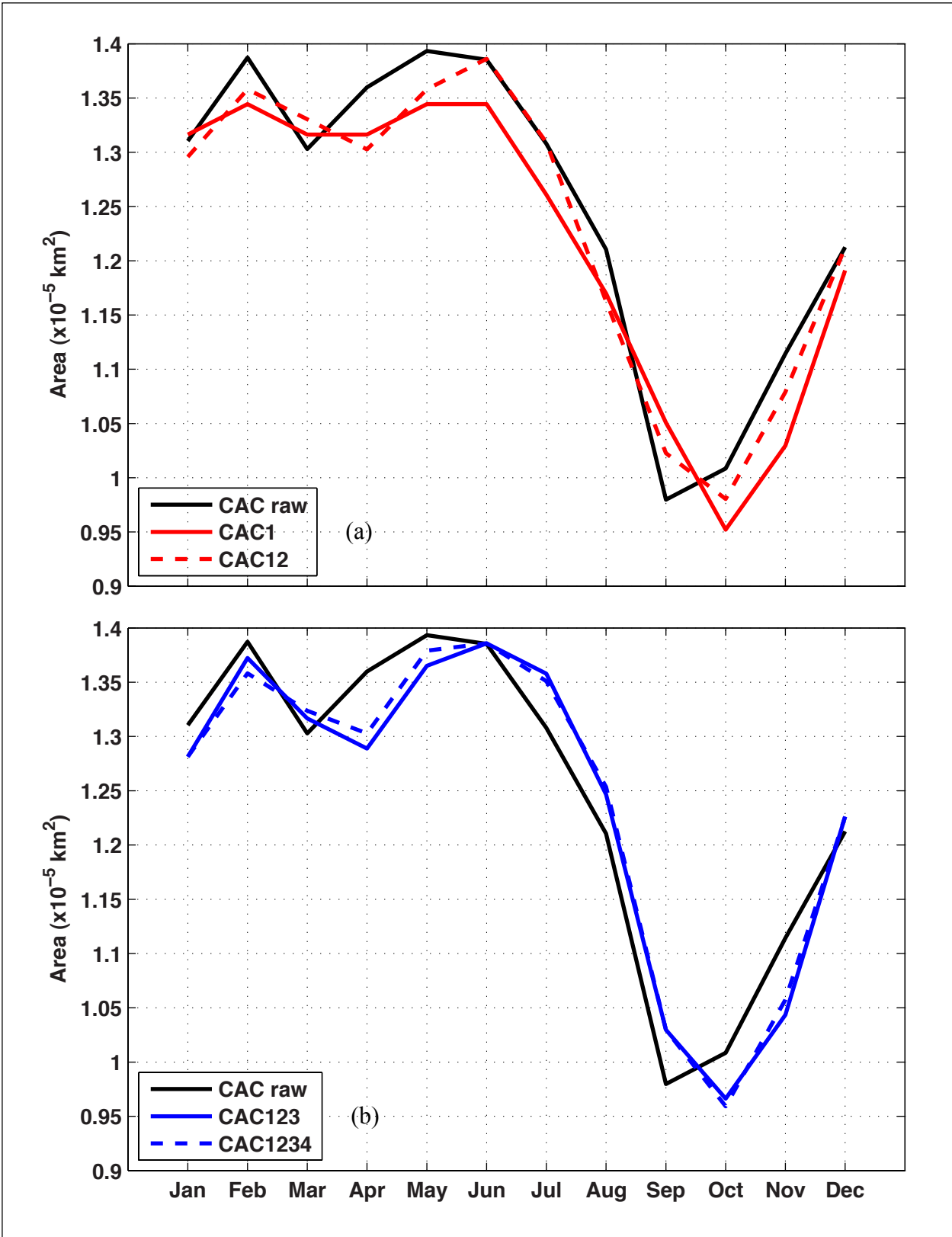


Figure 5.6-7. CAC of Loop Current area. CAC_raw is plotted with: (a) CAC1 and CAC12; (b) CAC123 and CAC1234.

5.6-7a show CAC_raw (metrics) compared to CAC1 and CAC12. Figures 5.6-6b and 5.6-7b show CAC_raw compared to CAC123 and CAC1234.

Figures 5.6-6 and 5.6-7 both show that CAC1 reproduces the dominant LC metric variability: relatively high values from January through June, low values during September and October, and then a rise to the end of the year. The next two EOF modes added in the CAC12 and in the CAC123 reconstructions additionally improve the metric approximation. Variance values are given in Table 5.6-1 for CACs and for the corresponding monthly-reconstructed time series for comparison. Area CAC variance explained reaches a maximum with only the first two modes. In contrast, monthly variance explained by the first two modes computed from the entire monthly time series is at a minimum for both northern latitude and area. The impact of the fourth EOF mode in CAC1234 is minimal. Minor improvements to the northern latitude approximation are found in April, May, and October of Figure 5.6-6b, and minor improvements to the area approximation are found in April and May of Figure 5.6-7b. The metric approximation will converge to the actual metric time series, CAC_raw, slowly as more EOF modes are added, though some EOF modes will “locally” make the approximation worse. Since approximation adjustments caused by the fourth EOF mode were so slight and since the fifth EOF mode (not shown) appeared to be more of a central/western Gulf mode than an eastern Gulf mode, it is likely that the dominant LC variability was captured by the first four EOF modes, so no further modes were added. In terms of fit, the LC northern latitude correlation between CAC_raw and CAC1234 is 0.9871 (variance 0.9744). The LC area correlation (R) is 0.9632 ($R^2 = 0.9277$).

Table 5.6-1. Proportion of LC northern latitude and area variance explained by first four deepwater EOF modes reconstructed as monthly time series and as CACs (CAC1, CAC12, CAC123, and CAC1234) with reference to complete monthly time series and CAC of original AVISO data (CAC_raw)

EOF	LC Northern Latitude Variance		LC Area Variance	
	Monthly	CAC	Monthly	CAC
EOF 1	0.2643	0.7668	0.2263	0.9212
EOF 1,2	0.1374	0.9084	0.1457	0.9574
EOF 1,2,3	0.5921	0.9662	0.6099	0.9179
EOF 1,2,3,4	0.6149	0.9744	0.6367	0.9277

Between the 20-year complete AVISO dataset and the 20-year reconstruction of the first four EOF modes, the LC northern latitude correlation is 0.7842 ($R^2 = 0.6149$), and the LC area correlation is 0.7980 ($R^2 = 0.6367$).

EOF modes of monthly data, as in Figures 5.6-1 and 5.6-2, capture LC variability very well, but are not optimal for describing seasonal signals. For instance, the CAC of PCTS 2 in Figure 5.6-4 indicates that the corresponding loading vector in Figure 5.6-1 has biannual power within a monthly context. However, the same biannual signal may not appear in an average year since the signal averages out. Additional EOF decompositions were performed on CAC_raw and CAC1234 for further insight into the LC variability. Figure 5.6-8 shows the deepwater mode 1

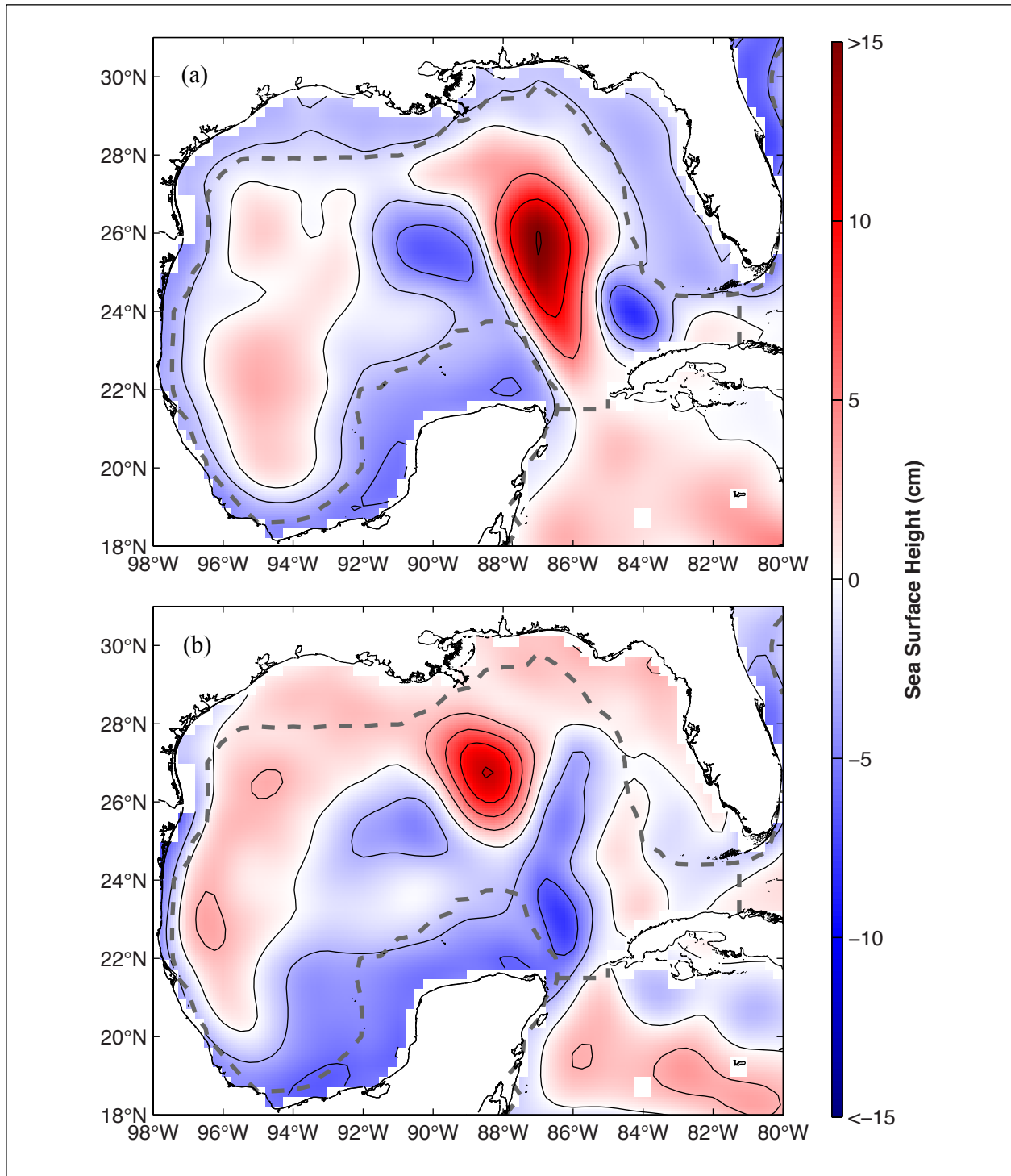


Figure 5.6-8. CAC_raw deepwater (a) EOF mode 1 and (b) EOF mode 2. Mode 1 explains 43.0% of the variance. Black contours are at -5, -2, 0, 5, 10, and 15 cm. Mode 2 explains 30.2% of the variance. Black contours are at 3-cm intervals. Gray dashed lines signify the boundaries of the EOF decomposition. The lines follow the 200-m isobath everywhere except across the Yucatan Channel and Florida Strait.

and mode 2 loading vectors of the CAC_raw EOF decomposition. Mode 1 in Figure 5.6-8a accounts for 43.0% of the SSH variance within CAC_raw, and mode 2 in Figure 5.6-8b accounts for 30.2%. Most of this variance is in the eastern Gulf. CAC_raw mode 3 and mode 4 loading vectors in Figure 5.6-9 account for 10.7% (Figure 5.6-9a) and 8.6% (Figure 5.6-9b) of the variance, respectively. The eight remaining EOF modes account for 7.5% total. PCTS corresponding to the first four EOF modes are shown in Figure 5.6-10. The PCTS of mode 1 and mode 2 are both mainly annual signals. Mode 1 has one main trough in October, which is associated with the fundamental variation of the LC metric CACs shown in Figure 5.4-4. The dominant peak in mode 2 is in August. Mode 2 also exhibits some weakly biannual signal associated with a small peak in March. In comparison, the monthly deepwater EOF mode 2 PCTS CAC in Figure 5.6-4 shows two noteworthy peaks in February and July (though the second one is larger), each occurring one month earlier than the respective peaks in March and August of the present CAC in Figure 5.6-10. The biannual variation mechanism present in the monthly AVISO data is mostly averaged away in CAC_raw with other inseparable variation mechanisms and noise. The CAC_raw EOF mode 2 loading vector in Figure 5.6-8b shares little in common with the monthly EOF mode 2 loading vector in Figure 5.6-1b except for a strong anticyclone at 88°W. Additionally, CAC_raw EOF mode 3 and mode 4 loading vectors in Figure 5.6-9 look nothing like monthly EOF mode 3 and mode 4 loading vectors in Figure 5.6-2. Conversely, the CAC_raw EOF mode 1 loading vector in Figure 5.6-8a closely resembles the monthly EOF mode 1 loading vector in Figure 5.6-1a. Both the CAC PCTS in Figure 5.6-10a and the CAC of PCTS 1 in Figure 5.6-4a follow an annual cycle remaining relatively stable from January through June, dropping to a minimum in October, and increasing to the end of the year. Since the first EOF mode of the monthly AVISO data and of the CAC of the monthly data (CAC_raw) are very similar with strongly annual Loop Current growth and subsidence. This is a mainly annual – not biannual – process.

The LC metrics plotted in Figures 5.6-6b and 5.6-7b demonstrate that the CAC of the first four EOF modes (CAC1234) captures most of the annual LC variability. Loading vectors of an EOF decomposition of CAC1234 are shown in Figures 5.6-11 and 5.6-12. The CAC1234 EOF decomposition captures 100% of CAC1234 variability as expected in the first four modes: 66.4%, 28.9%, 4.3%, and 0.4%, respectively. Note, however, that these modes do not capture 100% of the variability in CAC_raw. Figures 5.6-13 and 5.6-14 show, respectively, LC northern latitude and area CAC metrics of different reconstructions of the first three EOF modes of CAC1234 in comparison to CAC_raw and CAC1234. For both northern latitude and area, CAC1234 is almost perfectly reproduced by the reconstruction of the first three modes only, which is not surprising since the fourth mode captures only 0.4% of the variance in CAC1234.

The contribution of mode 4 to the seasonal signal is insignificant. The corresponding loading vector in Figure 5.6-12b reflects minimal impact on the LC. Table 5.6-2 lists proportions of variances explained using different reconstructions of the first four EOFs of CAC1234 in comparison to CAC1234 and CAC_raw. The first three modes explain about 97% of the northern latitude and 93% of the area variance in the annual cycle of the original AVISO data (CAC_raw). Note that the EOF 1 loading vector in Figure 5.6-11a closely resembles the CAC_raw EOF 1 loading vector in Figure 5.6-8a. However EOF 2, 3, and 4 loading vectors in Figures 5.6-11b and 5.6-12 do not match their CAC_raw EOF 2, 3, and 4 counterparts in Figures 5.6-8b and 5.6-9. The EOF loading vectors corresponding to CAC1234 have much less

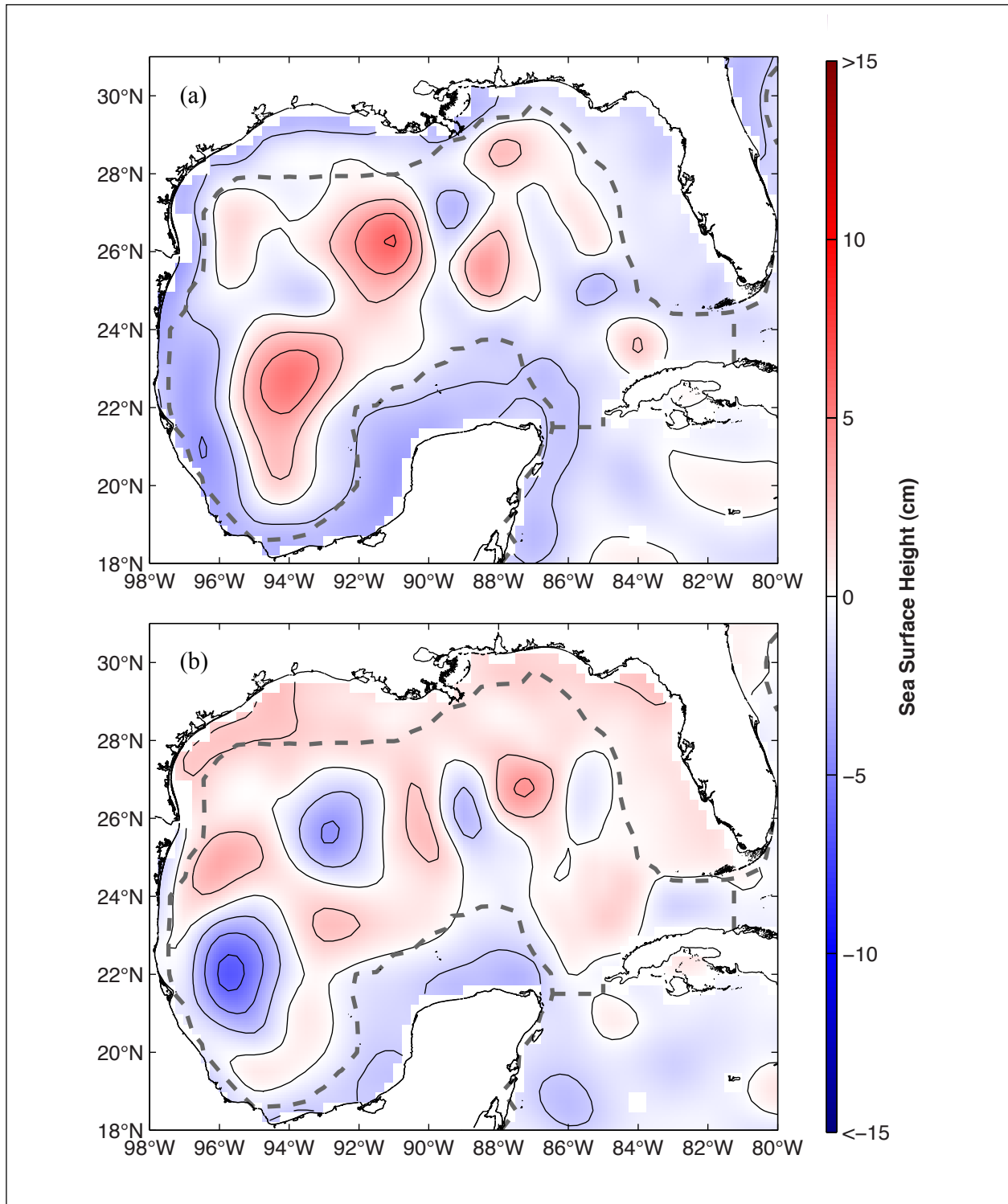


Figure 5.6-9. CAC_raw deepwater (a) EOF mode 3 and (b) EOF mode 4. Mode 3 explains 10.7% of the variance, and mode 4 explains 8.6%. Black contours are at 2-cm intervals. Gray dashed lines signify the boundaries of the EOF decomposition. The lines follow the 200-m isobath everywhere except across the Yucatan Channel and Florida Strait.

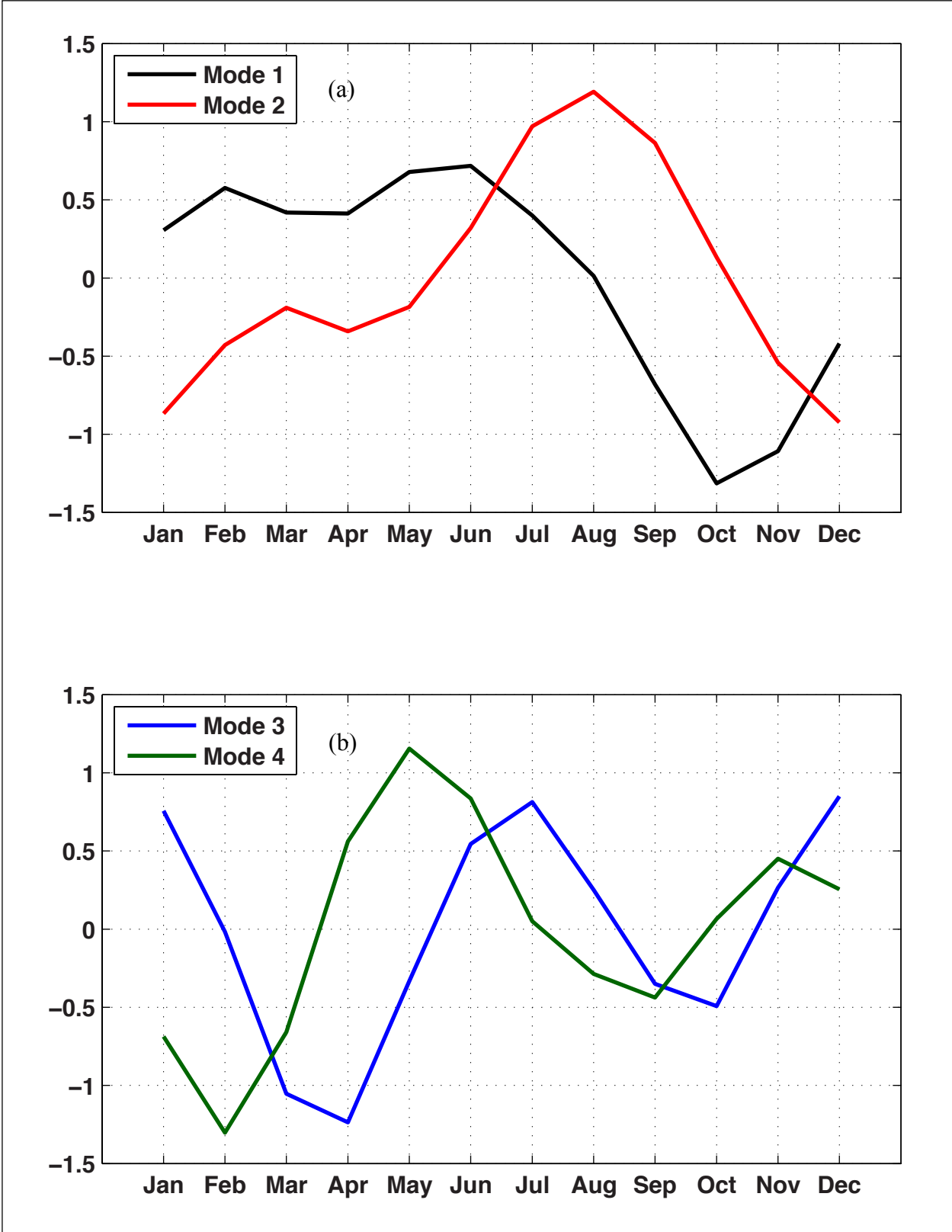


Figure 5.6-10. CAC_raw deepwater PCTS for (a) EOF mode 1 and EOF mode 2 and (b) EOF mode 3 and EOF mode 4.

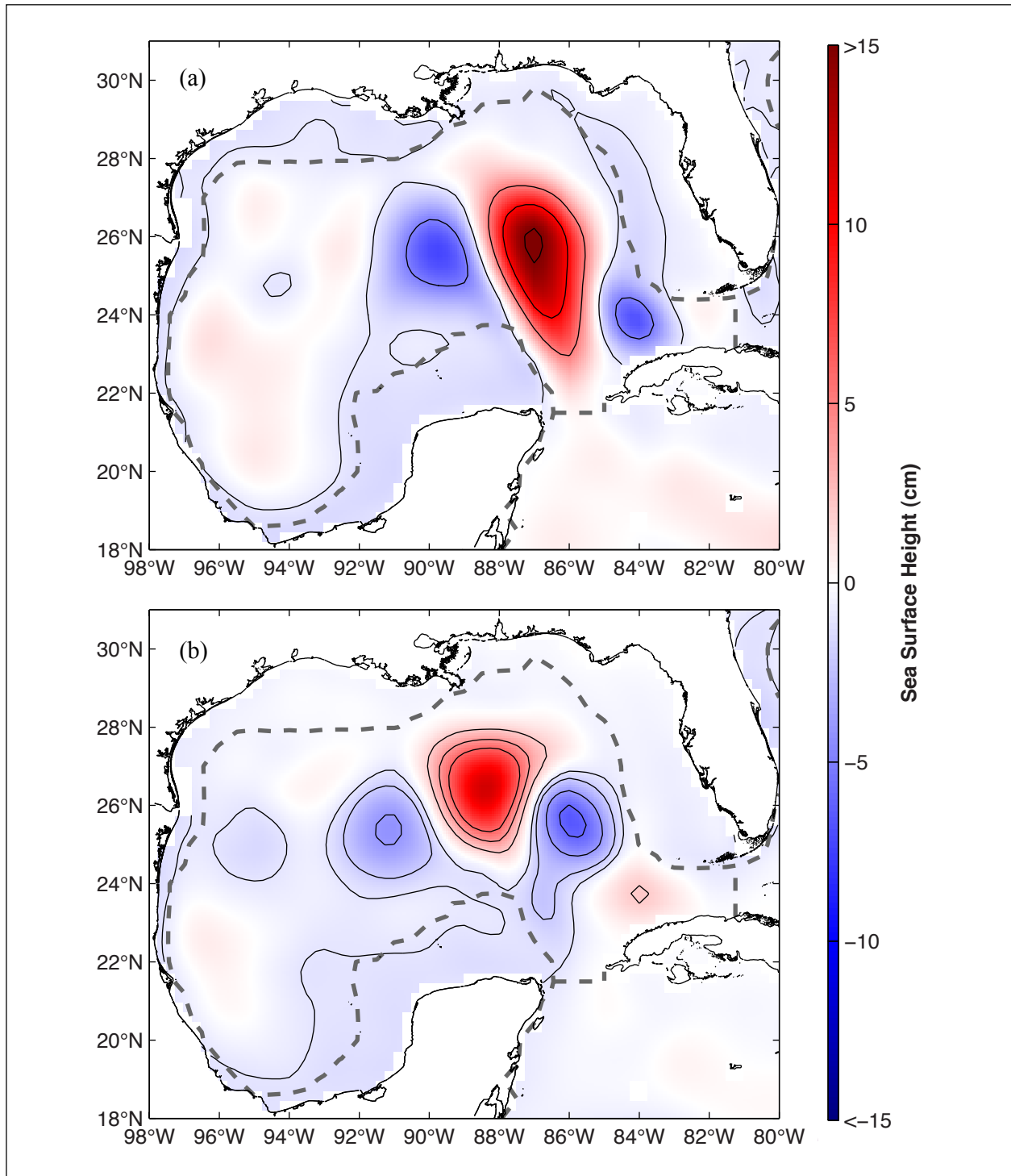


Figure 5.6-11. CAC1234 deepwater (a) EOF mode 1 and (b) EOF mode 2. Mode 1 explains 66.4% of the variance. Black contours are at -5, -0.9, 5, 10 and 15 cm. Mode 2 explains 28.9% of the variance. Black contours are at -6, -4, -2, -1, 2, 4 and 6 cm. Gray dashed lines signify the boundaries of the EOF decomposition. The lines follow the 200-m isobath everywhere except across the Yucatan Channel and Florida Strait.

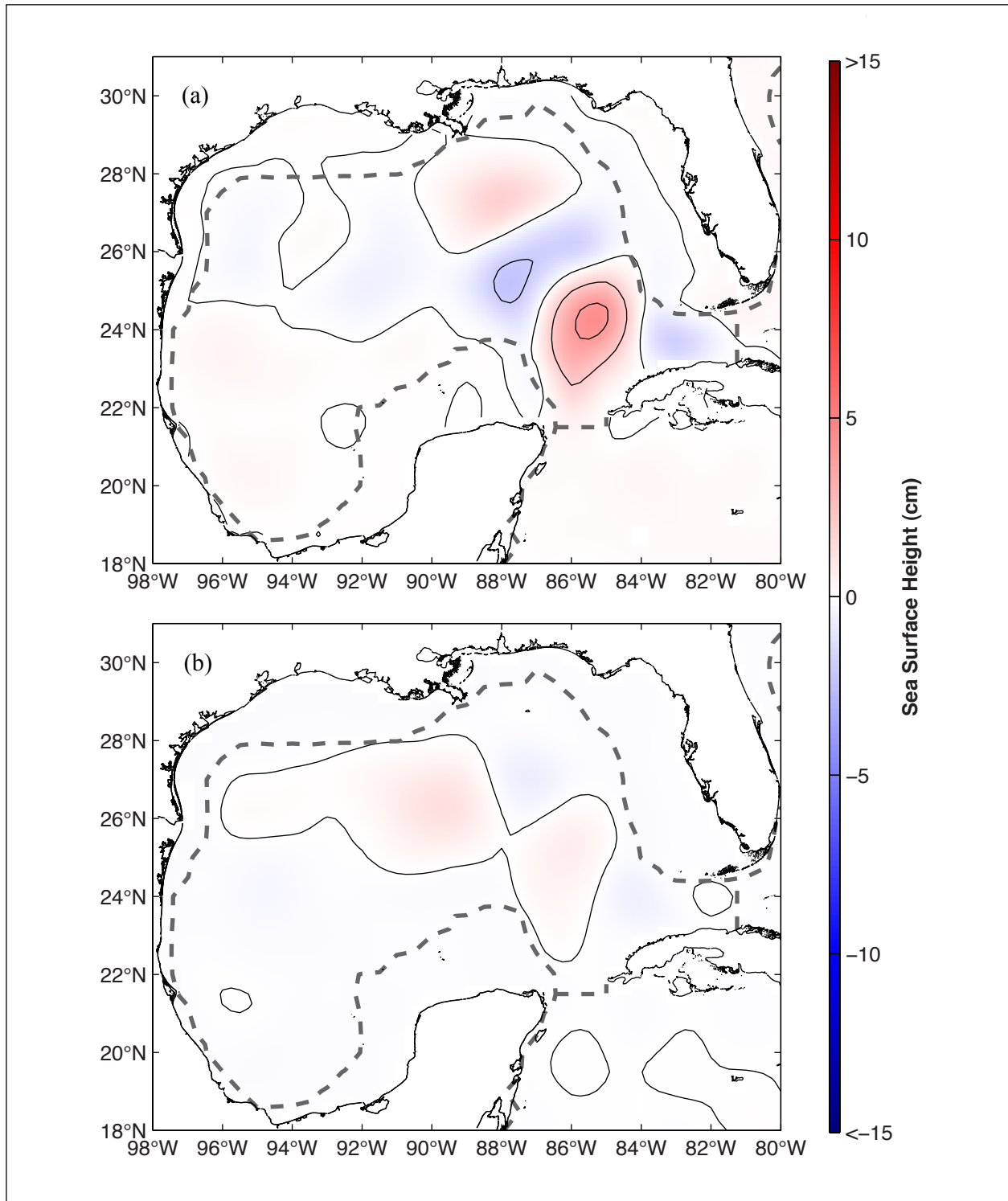


Figure 5.6-12. CAC1234 deepwater (a) EOF mode 3 and (b) EOF mode 4. Mode 3 explains 4.3%, and mode 4 explains 0.4%. Black contours are at 2-cm intervals. Gray dashed lines signify the boundaries of the EOF decomposition. The lines follow the 200-m isobath everywhere except across the Yucatan Channel and Florida Strait.

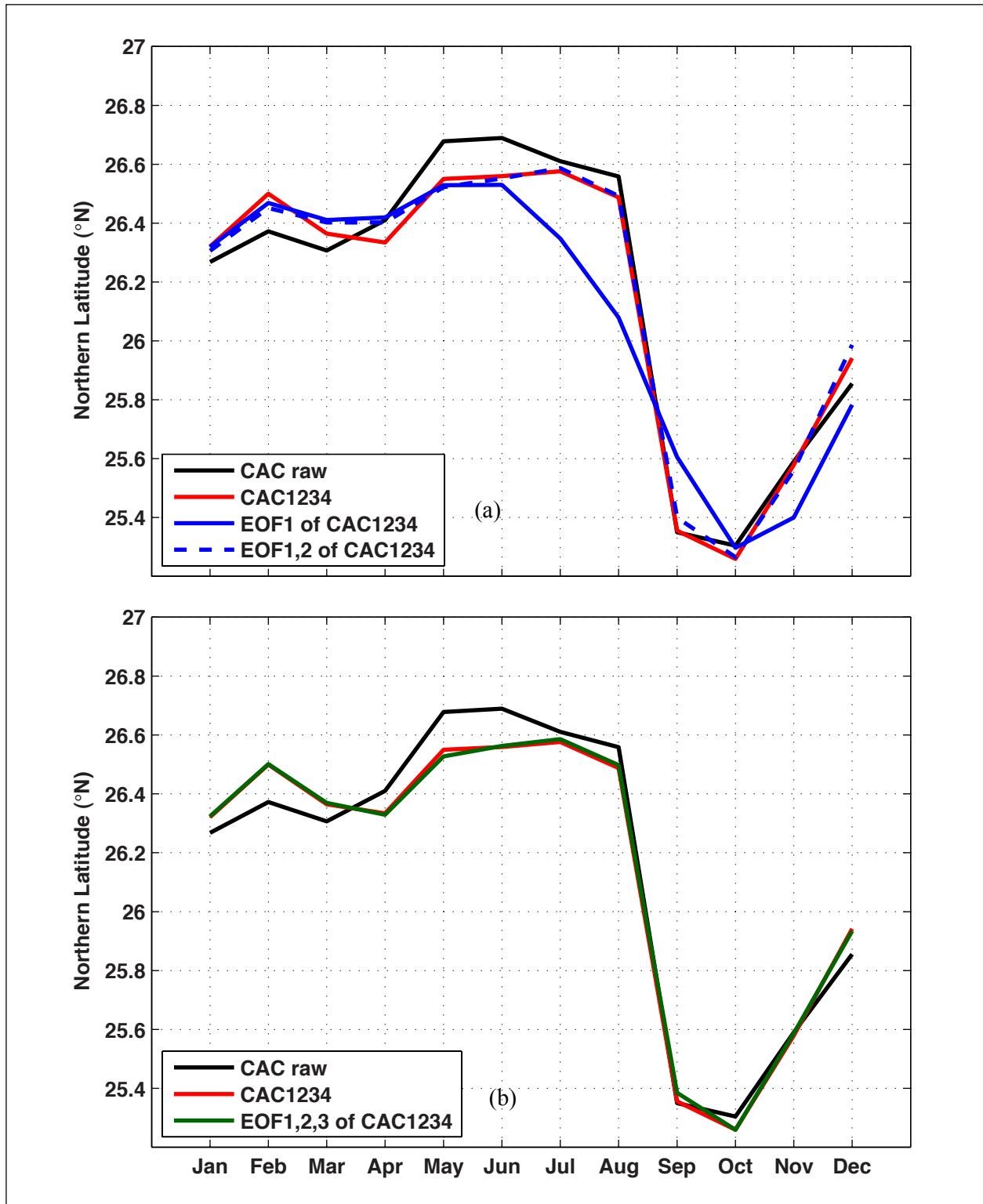


Figure 5.6-13. CAC of Loop Current northern boundary latitude. CAC_raw and CAC1234 are plotted with (a) CAC1234 EOF mode 1 and EOF modes 1 and 2 combined; (b) CAC1234 EOF modes 1, 2 and 3 combined and EOF modes 1, 2, 3 and 4 combined.

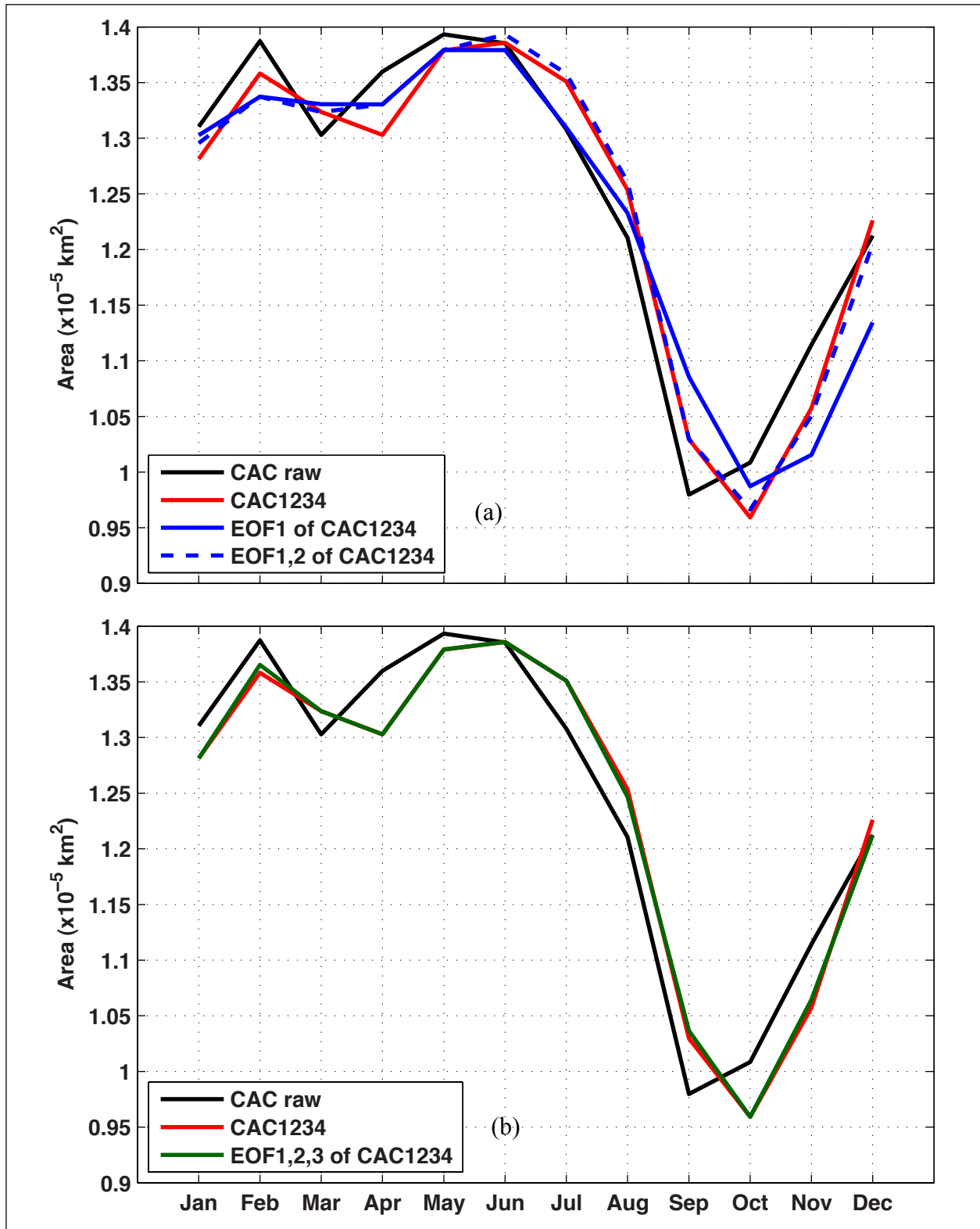


Figure 5.6-14. CAC of Loop Current area. CAC_raw and CAC1234 are plotted with (a) CAC1234 EOF mode 1 and EOF modes 1 and 2 combined; (b) CAC1234 EOF modes 1, 2 and 3 combined and EOF modes 1, 2, 3 and 4 combined.

extraneous variations and are, spatially, much less complex. The EOF processing and monthly averaging required to produce and decompose CAC1234 have reduced the degrees of freedom required to separate the dominant LC variability at seasonal time scales from the original monthly time series.

Table 5.6-2. Proportion of CAC_Raw and CAC1234 LC northern latitude and area variance explained by CACs of reconstructions of first four deepwater EOF modes of CAC1234

EOF	LC Northern Latitude Variance		LC Area Variance	
	CAC_raw	CAC1234	CAC_raw	CAC1234
EOF 1	0.8532	0.8801	0.8703	0.9265
EOF 1,2	0.9711	0.9952	0.9276	0.9915
EOF 1,2,3	0.9725	0.9994	0.9317	0.9984
EOF 1,2,3,4	0.9744	1.0000	0.9277	1.0000

The evidence presented so far of annual LC variability can be compared with the results published by Chang and Oey (2013a). Similar to Figure 5.6-4, Chang and Oey (2013a) also show CACs of EOF mode 1 and mode 2 PCTS (their Figure 10) derived from monthly AVISO data over the 18-year time period from 1993 through 2010, which are described as annual signals. In Figure 4 of Chang and Oey (2013a), the authors show the first two EOF modes of an ocean model, with the CACs of the PCTS showing clear biannual signals. Figure 8c of Chang and Oey (2013a) shows six CAC monthly LC fronts, indicating relatively steady LC shape from January to March, LC growth from March to July, LC wane from July to November, and LC growth again from November to January. All together, the fronts create an annual – not biannual – cycle with a maximum in July and minimum in November. Figure 8d is a Hovmöller CAC plot of SSH along the latitude 26.5°N (crossing the northern tip of the LC). Figure 8e shows a CAC of maximum SSH along 26.5°N, based on Figure 8d. Figure 8e is biannual and would be convincing if the results presented were achieved at a constant longitude. This would suggest that SSH and, thus, the LC varies biannually at a fixed point in space. However, the “maximum SSH” criterion enables capturing of the center of the January and June SSH peaks in Figure 8d, though they occur at different locations. The northern latitude of the LC and other metrics discussed in this chapter depend less on sensitive spatial amplitude variation and choice, and are therefore more likely indicators of LC variability. While it is true that most LC metrics in Figure 5.4-4 exhibit some biannual signal with local troughs in March or April and in October or November, the error bars show that the troughs in March or April are not significant. Assuming stationarity, these spring troughs may become statistically significant with more observations, but will still amount to only a small portion of seasonal LC variability.

Chang and Oey (2013a) explain that their Gulf-Caribbean model incorporated idealized wind forcing. The modeled Caribbean wind is a biannual sinusoid, maximum westward in December and June and minimum westward in March and September. This disagrees with observational wind data in that Caribbean wind is biannual but asymmetric, maximum westward in January and July and minimum westward in May and September (see Chang and Oey 2013a; Figure 8a). The September minimums are consistent with observations. The idealized modeled Gulf winds were 180° out of phase with modeled Caribbean winds, with westward peaks in March and

September and westward minimums in December and June. The modeled westward maximums are not a good match with observed Gulf wind peaks in either May or October. The modeled minimum in December matches the observed December/January minimum, but the modeled June minimum occurs earlier than the observed August minimum. Table 2 of Chang and Oey (2013a) indicates that the model run chosen for most of the analyses in the paper, “Exp.Carib” (or just “Carib”), showed most LC eddies separating in the months of June, December, and January, times when LC eddies are unlikely to separate in reality. Chang and Oey (2013a) attribute the discrepancy between the peak LC eddy separation months in the model and observations, to both the misalignment of the modeled wind peaks with the observed wind peaks and the symmetry of the modeled wind signal in comparison to the asymmetry of the observed wind data. In a separate comparison, the authors also attribute some of the discrepancy between modeled and observed north Caribbean CAC monthly maps (their Figure 9) to the idealized wind forcing in the model. Discrepancies between modeled results and observations need to be resolved by using more realistic annual wind forcing.

Chang and Oey (2013a) also note that two of the four model runs the authors performed, “Exp.Carib” and “Exp.GOMCarib,” show similar results. Peak eddy-shedding months are June, December, and January for both. Chang and Oey (2010a) argued that strong Gulf easterlies delay eddy separation, as discussed in Section 4.7. Both “Exp.Carib” and “Exp.GOMCarib” incorporate winds over the northwestern Caribbean Sea, but only “Exp.GOMCarib” incorporates winds over the Gulf also. If the same peak shedding times can be achieved with and without Gulf winds, the Gulf winds must not be causing any significant delay. The other two model runs the authors performed in Chang and Oey (2013a), “Steady22Sv,” with only far-field forcing, and “Exp.GOM,” incorporating Gulf winds as well, show no seasonal preference for eddy separation. “Steady22Sv” eddy separation periods are seven and eight months, while “Exp.GOM” separation periods are six, seven, and eight months. The authors state that though the Gulf winds in “Exp.GOM” do not cause seasonal preference, they still have the effect of delaying separation, even though their experiments seem to imply that Gulf winds decrease separation intervals.

Both Chang and Oey (2012) and Chang and Oey (2013a) use a Yucatan Channel transport CAC from Rousset and Beal (2010) to support their modeling result that the biannual LC eddy shedding is caused by biannual transport variations in the Yucatan Channel. However, Rousset and Beal (2010) do not claim any statistical significance for a biannual signal in their transport results. Figure 9e of Chang and Oey (2013a) presents a biannually varying CAC of SSHA within a specific domain capturing the Yucatan Channel and northern Caribbean Sea (17.5°N-22.5°N, 87°W-80°W), which the authors use to imply that SSHA variations in the region force biannual Yucatan Channel variations. The SSHA CAC does look somewhat like the Yucatan transport CAC in Figure 4b of Rousset and Beal (2010). However, the SSH anomalies that appear in the northern Caribbean Sea do not seem to propagate through the Channel in the corresponding CAC map set in Figures 9b and 9d. Evidence of a connection between SSHA and transport requires more extensive transport studies and more rigorous analyses. There may be some biannual transport through the Yucatan Channel forcing the LC, but that variation must account for only a small fraction of LC variability. The only clear evidence of biannual power associated with the LC is in the seasonal timing of LC eddy separation events.

In contrast to Chang and Oey's (2013a) results, all of the EOF analyses presented in this section indicate that variations of the LC itself are dominantly annual. Further inspection of the first two EOF loading vectors shown in Figure 5.6-11 indicates that annual LC variability is linked to coastal anomalies. The EOF 1 loading vector shows a nearly continuous low SSH anomaly around the entire Gulf shelf. The EOF 2 loading vector also shows a strong anomaly on the Campeche Bank. In the following subsection, results are shown from a coastal EOF analysis. It independently verifies the result that the LC co-varies with shelf signals and identifies coastal forcing as a possible dynamical source of the dominant LC annual variability.

Coastal EOF Analysis

Sea-level measurements from coastal tide gauges and satellite altimetry show that an inter-annual sea-level signal extends all around the Gulf (Li and Clarke 2005). This signal is both remotely and locally forced. Remotely forced inter-annual sea-level signals propagate along the U.S. Atlantic coast and into the Gulf as coastal-trapped waves (CTWs). Some of this coastal signal is forced by inter-annual Rossby waves that form in the Atlantic, propagate westward, cross the Gulf Stream, and impinge on the coast. Coastal Kelvin waves are generated as the Rossby waves reflect off of the southeast U. S. Atlantic coast. This mechanism is consistent with observations that show that the inter-annual sea-level signal on the coast is driven by wind-stress curl over the Atlantic, and oceanic Rossby wave propagation to the coast (Hong et al. 2000) and with the high correlation found between U.S. east coast annual mean sea level and sea level along the northern coast of the Gulf (Maul and Hanson 1991). Along the northern Gulf shelf, the remotely forced inter-annual coastal signal is amplified from Pensacola to the Louisiana-Texas shelf by inter-annual alongshore wind forcing (Li and Clarke 2005).

Li and Clarke (2005) identified inter-annual CTWs in the first EOF mode of historical monthly tide-gauge data (1986-2002) collected at 12 locations along the U.S. coast from Wilmington, North Carolina to Port Isabel, Texas. The first EOF mode captured 70% of the variance in the tide-gauge measurements, indicating an in-phase (at monthly resolution) signal spanning nearly 4500 km along the coast.

To ensure that the AVISO data in shallow waters are reliable in the Gulf, coastal EOF analyses were performed using monthly gridded $\frac{1}{4}^\circ$ AVISO SSH from 1993 through 2012 and compared with the tide-gauge results shown by Li and Clarke (2005). Near-coast SSH measurements are often excluded from gridded altimeter data products since wet tropospheric, high-frequency oceanographic, tidal, and other corrections applied to the altimetric range measurement tend to cause errors in the SSH values within 25 to 50 km of the coast (Saraceno et al. 2008). Consistent with the Li and Clarke (2005) analysis, the CAC was removed from the AVISO time series, and the data were low-pass-filtered using the Lanczos filter described in Trenberth (1984) to retain only inter-annual frequencies. After de-trending the data, all data in waters deeper than 500 m were masked to isolate the sea-level variations on the shelf and continental slope, and an EOF decomposition was then performed over the domain 98°W - 70°W , 18°N - 35°N . The EOF bounds were sufficiently far north to include the zone where the CTWs originate along the U.S. east coast and sufficiently far south to allow detection of the waves along the Gulf and northwestern Caribbean Sea coasts. The resulting PCTS and the original SSH were used to project the signal into the deep water (using a linear regression onto the original SSH time series as described in the earlier subsection on Deepwater EOF Analysis), yielding the monthly "low-passed" coastal

EOF mode 1 loading vector shown in Figure 5.6-15a. A second coastal EOF decomposition was performed on the monthly AVISO data without removing the CAC or low-pass filtering the data. This “raw” monthly coastal EOF mode 1 (CM1) loading vector is shown in Figure 5.6-15b for comparison.

The low-passed EOF mode 1 explains 60.4% of the low-frequency coastal AVISO variance, whereas CM1 explains 70.6% of the unfiltered coastal AVISO variance. Gray dashed lines in the Figure 5.6-15 maps designate the 500 m isobath. Loading vector sea level at the 12 tide gauge coastal locations from Figure 3 of Li and Clarke (2005) are plotted with corresponding loading vector sea-surface heights in Figure 5.6-16a. The low-passed loading vector SSH (blue curve) closely approximates the tide gauge loading vector (black curve) from Wilmington, North Carolina to about Pensacola, Florida, 2550 km down the coast. Beyond that point, the two loading vectors differ. Figure 5.6-16b shows the PCTS of the first tide gauge and AVISO coastal EOF modes. Note that though Li and Clarke (2005) used tide gauge data from 1986 through 2002, only tide gauge PCTS results from roughly June of 1993 into October 2001 were given. The correlation between the tide gauge PCTS and the low-passed AVISO PCTS is 0.5941, which is quite good considering the differences in the processing of the two datasets. There are several key differences: 1) EOF decompositions of the altimetry were not performed over the same time period as the tide gauge data since reliable gridded satellite altimetry products cannot be made prior to late 1992; 2) the AVISO analysis includes both shelf and slope variability; and 3) altimetry-derived values in the AVISO maps at the tide gauge locations are extrapolated from altimeter measurements further offshore. Given these processing differences and possible sources of error, the similarity of the two EOF analyses indicates that coastal AVISO data analyses are able to resolve most of the dominant signal observed by the coastal tide gauges.

Veracity of the near-coast AVISO data was also tested by analysis of the northward boundary current speeds using the CAC_raw SSH dataset. Note that CAC_raw was created from unmasked monthly AVISO data and possesses no intrinsic deepwater or coastal characteristics associated with the various EOF decompositions presented in this chapter of the report. Northward geostrophic speed anomalies were computed in the Gulf Western Boundary Current at 25.25°N between 97.5°W and 95.5°W using CAC_raw and were compared with Western Boundary Current ship-drift speed anomalies from Sturges (1993) in Figure 5.6-17a. Ship-drift speeds fall within the 95% confidence interval error bars for all months except February, April, and September, indicating that the near-shore geostrophic speeds derived from CAC_raw coastal SSH are reliable. Figure 5.6-17b plots the derived Gulf Western Boundary Current northward geostrophic speed anomaly CAC with CACs derived from Florida Current speed anomalies at 27.0°N between 80°W and 79°W and from Yucatan Current speed anomalies at 21.75°N between 86.75°W and 84.75°W. The CACs are consistent among the three currents in both speed and annual variation. Note that there is very little biannual seasonal variability in any of the western boundary currents.

Since comparison of the AVISO SSH with independent datasets indicates that coastal AVISO SSH data are valid, CM1 shown in Figure 5.6-18b can be compared with the first deepwater EOF loading vector derived from CAC1234 in Figure 5.6-18a. The two loading vectors are very

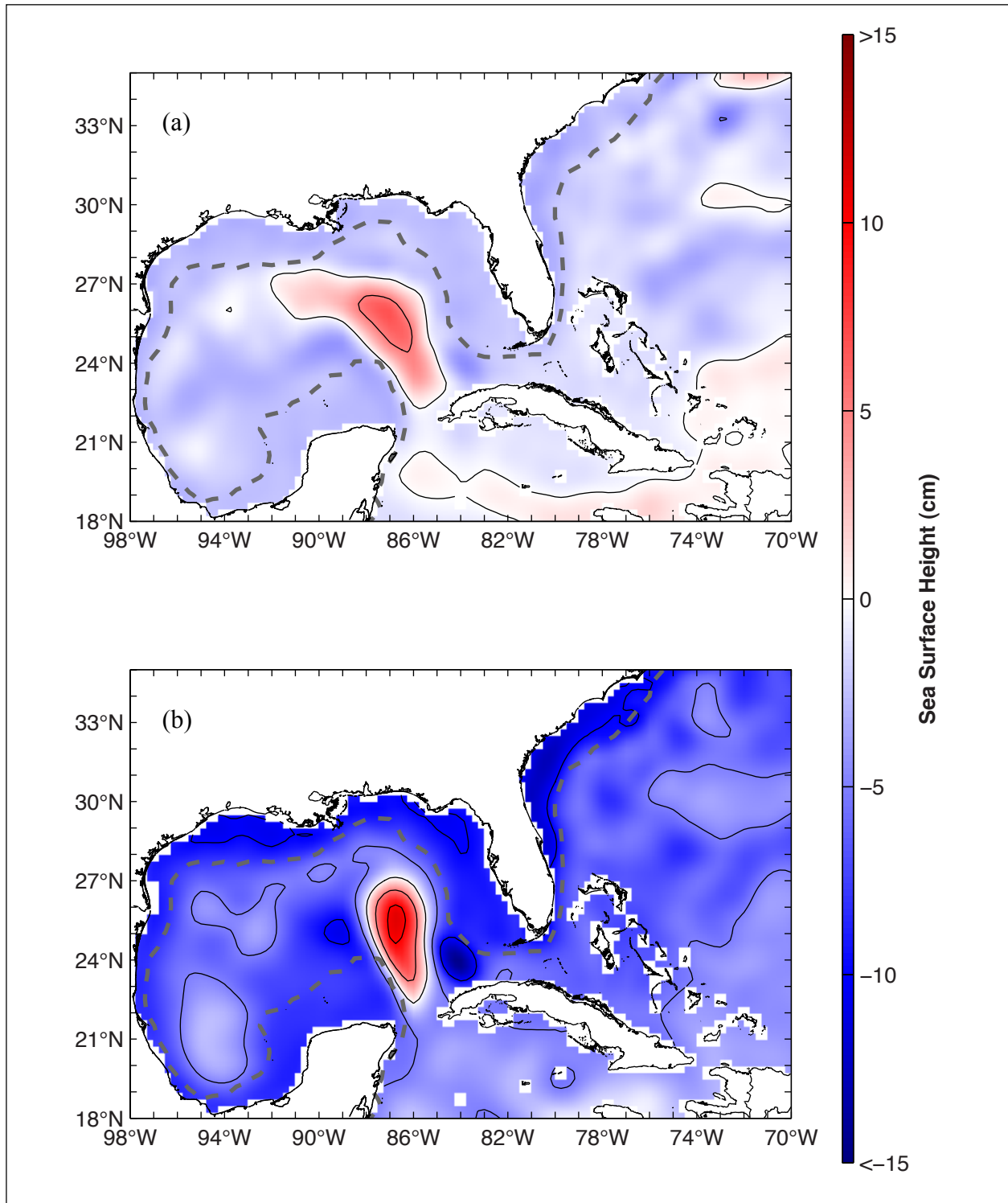


Figure 5.6-15. Coastal EOF mode 1 loading vector derived with monthly AVISO data from 1993 through 2012: (a) with CAC removed, low-pass-filtered using Lanczos filter design presented in Trenberth (1984), and detrended; (b) unfiltered (CM1). Black contours are at 5-cm intervals. Gray dashed lines follow the 500-m isobath and signify the boundaries of the EOF decomposition.

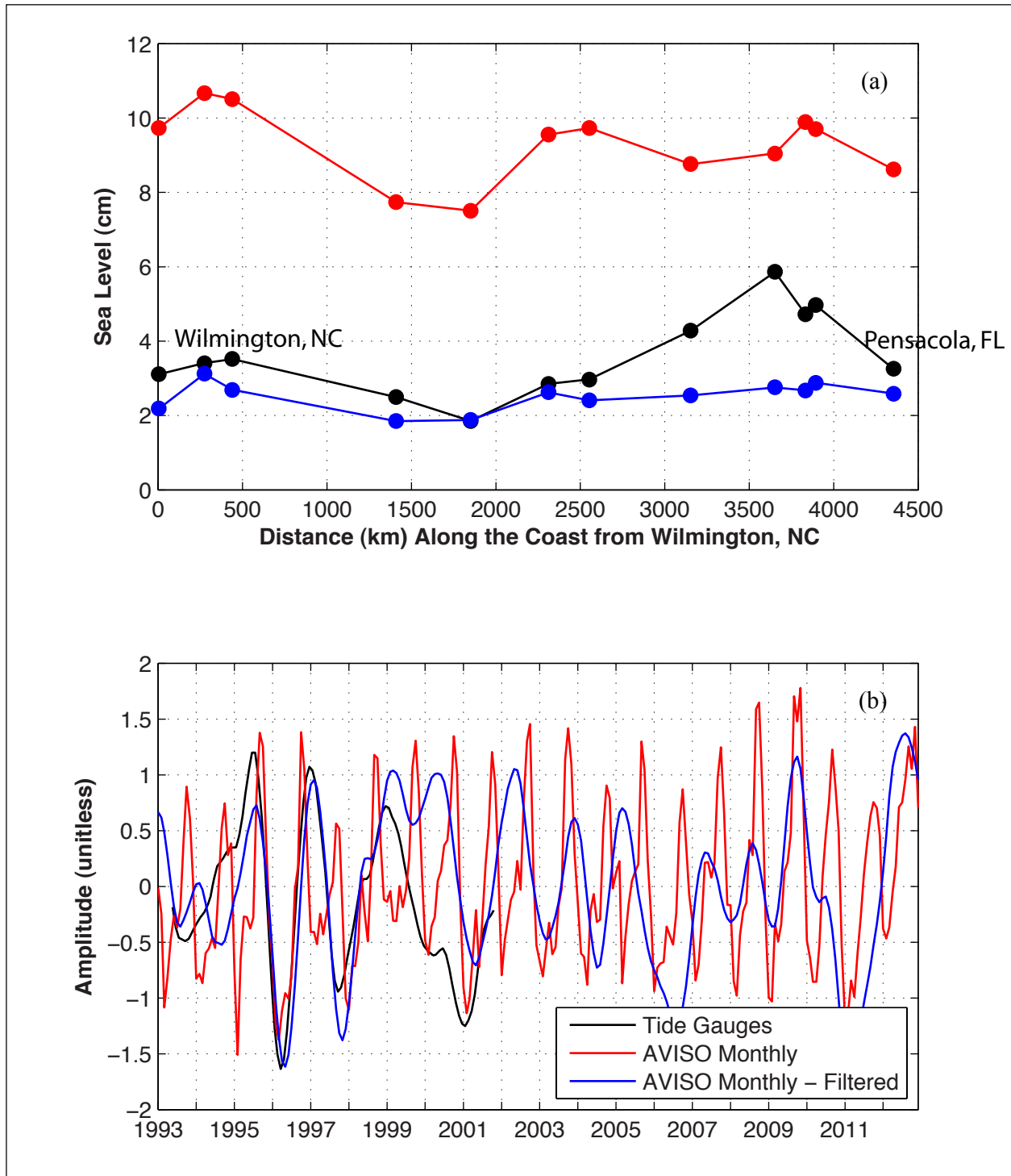


Figure 5.6-16. Interannual EOF mode 1 (black) from monthly tide gauge SSH data for June 1993 through October 2001 (Li and Clarke 2005) compared to EOF mode 1 derived from coastal AVISO SSH data low-pass-filtered with CAC/linear trend removed (blue) and unfiltered (red): (a) shows loading vector sea levels at specific distances along the coast south of Wilmington, North Carolina; (b) shows corresponding PCTS.

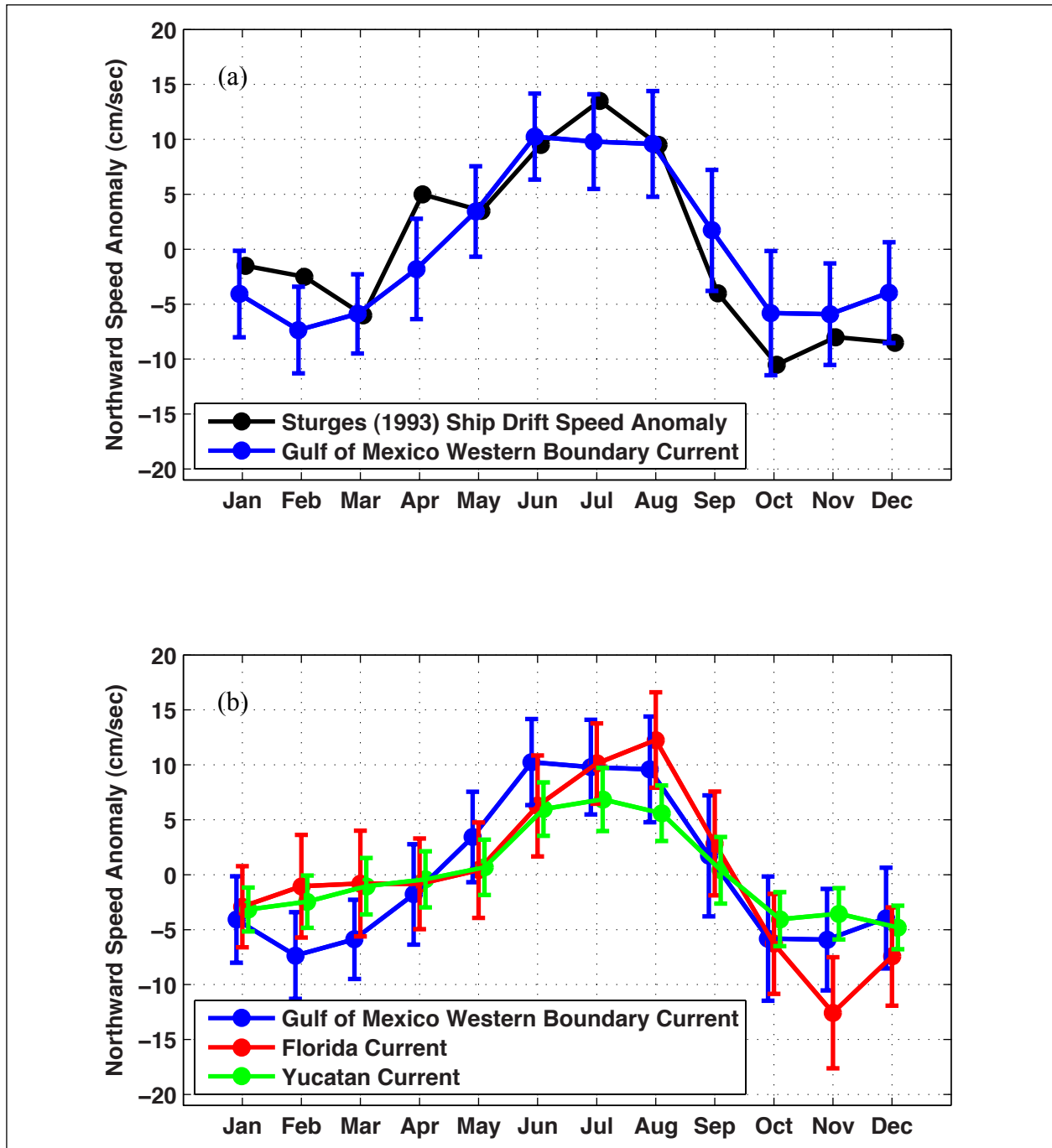


Figure 5.6-17. (a) Gulf Western Boundary Current ship drift speed anomaly CAC (Sturges 1993) as compared to the northward geostrophic speed anomaly derived from CAC_raw. (b) Northward geostrophic speed anomalies derived from CAC_raw within the Gulf Western Boundary Current, the Florida Current, and the Yucatan Current. Speed anomalies were computed in the Gulf Western Boundary Current at 25.25°N between 97.5°W and 95.5°W, in the Florida Current at 27°N between 80°W and 79°W, and in the Yucatan Current at 21.75°N between 86.75°W and 84.75°W. Error bars are 95% confidence intervals.

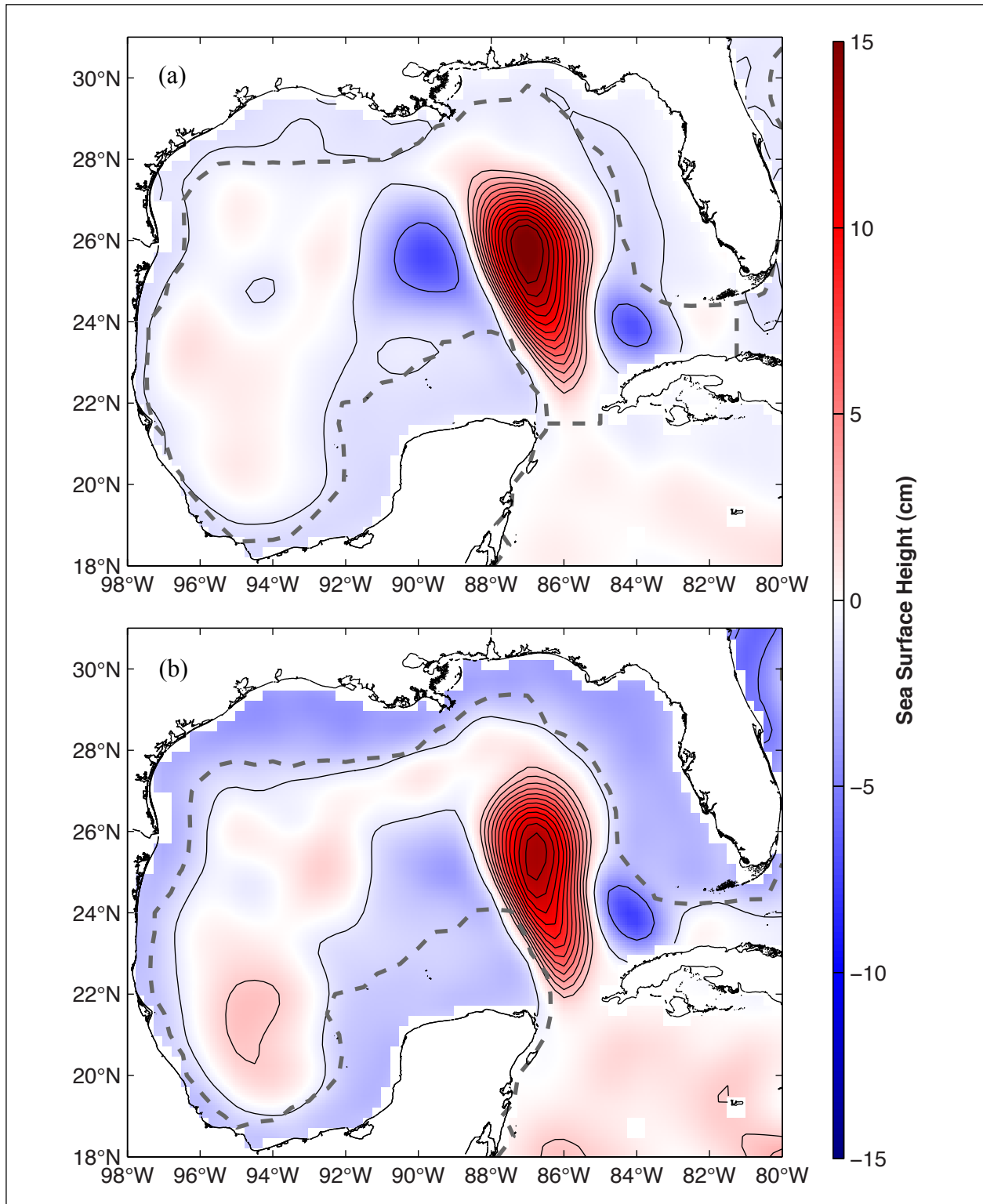


Figure 5.6-18. (a) CAC1234 EOF mode 1 loading vector (same as in Figure 5.6-11a). (b) CM1 loading vector with 5.07-cm offset applied. Black contours are at -5, -0.9, and 2 cm and then upwards at an interval of 2 cm. Gray dashed lines follow the 500-m isobath and signify the boundaries of the EOF decomposition.

similar in that they both show large anticyclonic anomalies over the LC and noticeable shelf signals as well, though the coastal loading vector shows a stronger coastal signal, as would be expected. The SSH correlation between the two loading vectors in the deepwater (deeper than 200 m) is 0.93 and is 0.85 overall. Figure 5.6-19a shows the sum of monthly variance of the AVISO data, and figure 5.6-19b provides the fraction of that variance contained within a monthly reconstruction of CM1. Variance explained is greater than 10% on the coast all the way around the Gulf from the West Florida Shelf to the Campeche Bank and within the LC. Variance explained is greater than 50% in some areas of the northern shelf.

Figure 5.6-20a compares the LC northern latitude metric of CAC_raw, CAC1234, and the CAC of the monthly CM1 reconstruction, while Figure 5.6-20b shows a similar comparison with LC area. Though no LC variance was included in the coastal EOF decomposition, LC variance is correlated with the coastal signal in the deepwater, and accounts for a large portion of the variance in the complete AVISO CAC, CAC_raw. Table 5.6-3 shows the proportion of CAC_raw and CAC1234 variance explained by the CAC of the monthly CM1 reconstruction for both LC metrics. The proportions in the table indicate that the CAC of the monthly CM1 reconstruction comes closer to approximating true LC area than LC intrusion/retreat characteristics. Minimum and maximum area values are approximately reproduced; only minimum northern latitudes are reproduced. In Figure 5.6-20a, the CAC of CM1 remains close in magnitude to CAC_raw from January through April. Then it drops below CAC_raw, providing a poor approximation to observed northern latitude from May through August. Then from September through December, it follows true northern latitude closely. For area in Figure 5.6-20b, the CAC of CM1 shows a similar trend as described for northern latitude from January through August. Then the CAC of the monthly CM1 reconstruction closely resembles CAC1234 for the rest of the year.

Table 5.6-3. Proportion of CAC_Raw and CAC1234 LC northern latitude and area variance explained by the monthly reconstruction of CM1

Variance	CAC_raw	CAC1234
LC Northern Latitude Variance	0.65	0.75
LC Area Variance	0.85	0.82

Clearly there is a close connection between CM1 and the dominant LC annual variability. The question then is why do the Kelvin waves have such a dramatic affect on the LC? At inter-annual time scales, flow on the shelf and at the shelf edge induces parallel flow in the adjacent deepwater as discussed by Li and Clarke (2005). Beyond the shelf break, the shelf wave SSH signal decays causing seaward changes in geostrophic velocities along the continental slope.

These deepwater near-shelf flow velocities vary depending on the orientation of the shelf (Li and Clarke 2005), but western boundaries theoretically induce the highest current speeds. In the Gulf, the Campeche Bank acts as a western boundary for the LC, which rapidly dissipates Kelvin wave energy in the form of eastward-propagating Rossby waves. The resulting changes in SSH at the shelf break induce a high-velocity jet over the continental slope that can either accelerate or decelerate the LC flow depending on the sign of the waves. The dynamics involved are valid at both annual and inter-annual frequencies. This effect may not be directly resolvable by satellite

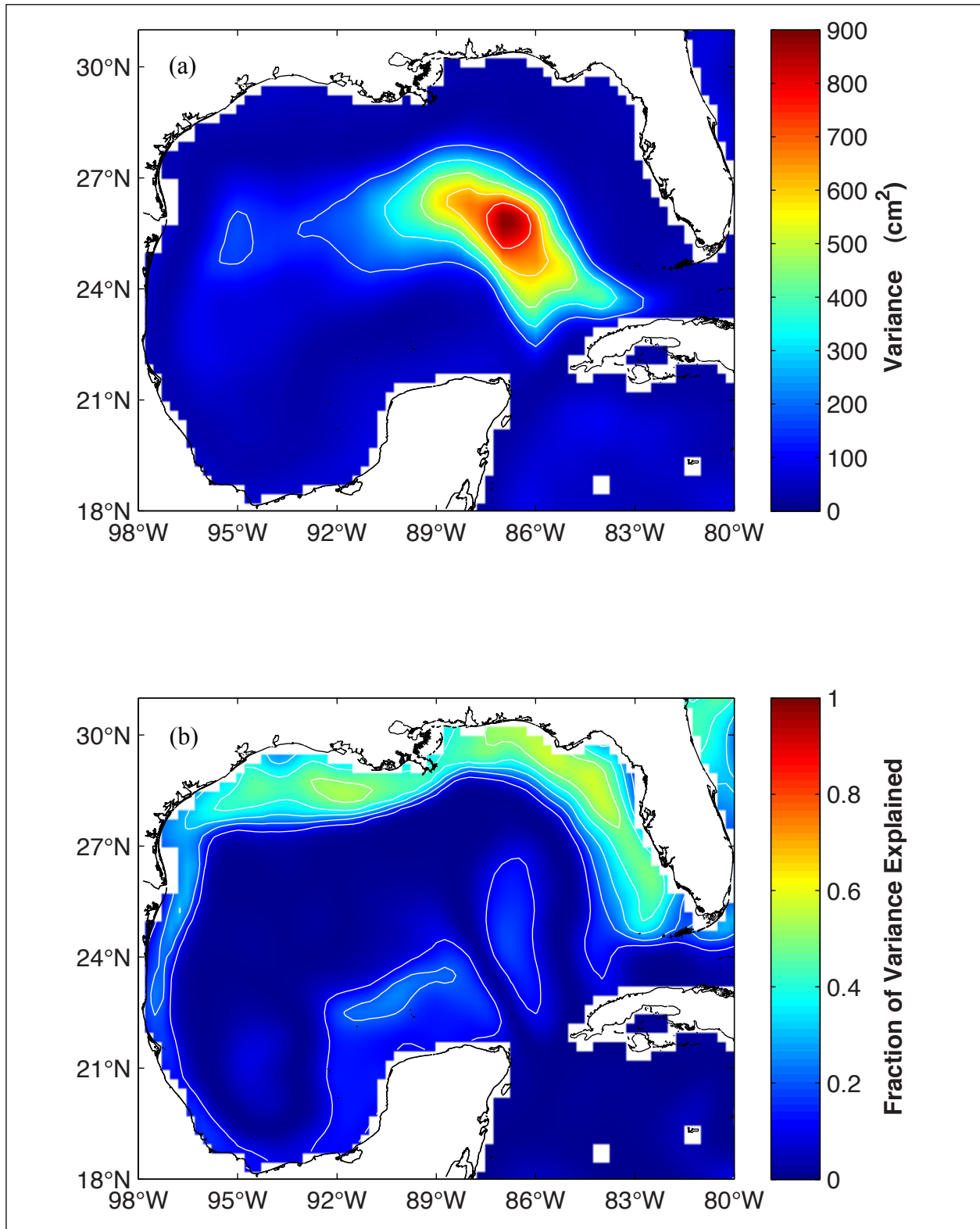


Figure 5.6-19. (a) Sum variance of monthly AVISO maps. Contour increment 150 cm^2 . (b) Fraction of total variance generated by monthly reconstruction of CM1. Contour increment 0.1.

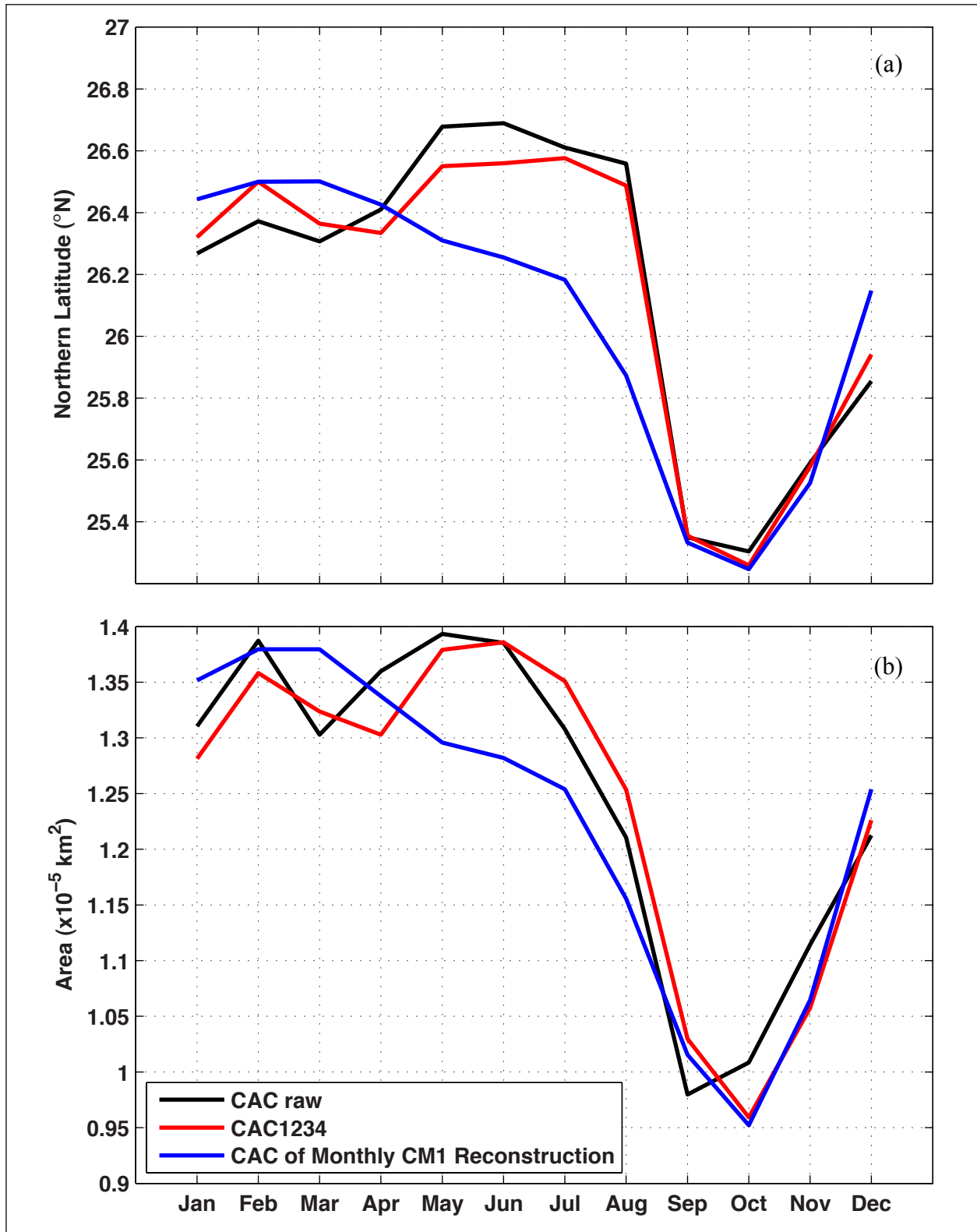


Figure 5.6-20. (a) CAC of Loop Current northern boundary latitude. (b) CAC of Loop Current area. Each of the two subplots shows CAC_raw, CAC1234 and CAC of monthly CM1 reconstruction.

altimetry since the shelf break SSH gradient is large over only a short distance; however, the net effect at seasonal, annual, and inter-annual time scales is apparent in the response of the LC in deepwater at these timescales. Reid (1972) has explained this type of LC response using a simple vorticity model that predicts the LC northern penetration as a function of current speed at the northern Campeche Bank shelf break and the departure angle of the LC at the shelf break. Greater current speed results in greater LC penetration for a fixed departure angle. Thus, CTWs propagating along the Gulf coast can and do affect LC variability through the generation of along-slope currents. This is one possible forcing mechanism for the observed annual variability in the LC. It is also possible that some LC variability is forced by the interaction of the eastern side of the LC with the remote shelf and slope along the West and South Florida slope. Further study of the CTW-induced currents is in progress using the in-situ data collected during the study program and an analysis of along-track altimeter data as performed by Li and Clarke (2005).

Conclusions

The seasonal LC variability is mainly annual. Altimeter-derived LC northern-boundary latitude and area metrics are relatively high from January through about July and low in September and October. The first three deepwater EOF modes of CAC1234 capture about 97% and 93% of the annual variability of LC northern latitude and area, respectively. Biannual LC seasonal variability is insignificant. It appears that inter-annual and annual coastal-trapped waves, energized mostly by wind-stress curl in the Atlantic and alongshore wind in the Gulf, are responsible for a large portion of LC variability. The CAC of the monthly CM1 reconstruction explains 65% of the variance in LC northern boundary latitude and 85% of the variance in LC area. Discussion and analysis of coastal EOF modes beyond CM1 will be the focus of future work.

CHAPTER 6: INERTIAL OSCILLATIONS

6.1 INTRODUCTION

Inertial oscillations are common in the Gulf of Mexico, and are the principal high-frequency motions observed in deep water. On the shallow continental shelves, diurnal and semi-diurnal tides become important, but in deep water, tidal fluctuations are generally very small. Wind-forced near-inertial internal waves are the major signal propagating down from the surface. During hurricanes, energetic inertial oscillations can penetrate to depths of 1000 m or more (Brooks 1983, Shay and Elsberry 1987, Shay et al. 1992). Hurricanes and tropical storms generate intense inertial-internal wave activity. In many cases, however, inertial oscillations may be generated by an abrupt shift in wind stress, and are observed throughout the year with less magnitude in summer, except for hurricanes, and larger magnitudes in winter as a response to cold fronts that are frequent in the northern and eastern parts of the Gulf. This chapter will be principally concerned with the observed and modeled response to Hurricane Ida, the only hurricane in the dataset. This will be discussed first, followed by a section on the variability of inertial motions through the 2½ years of current measurements.

The upper-ocean response to a moving hurricane has been studied extensively (e.g., Leipper 1967, Price 1981, Greatbatch 1983, Brink 1989, Dickey et al. 1998). The major response is characterized by sea-surface cooling and inertial oscillations that are most energetic to the right of the hurricane track. The hurricane-induced inertial energy then propagates both horizontally and vertically (Gill 1984). It is well known that under the β -effect, the inertial oscillations can only propagate equatorward into regions of smaller f as a result of beta-dispersion (Anderson and Gill 1979, Garrett 2001). On the other hand, the interaction of the inertial oscillations with the background flow can also influence its propagation. First derived by Mooers (1975), Kunze (1985) showed that the presence of relative vorticity, ζ , can alter the propagation of near-inertial waves through a change in the effective Coriolis parameter, f_{eff} , in the form of $f_{\text{eff}} = f + \zeta/2$. When the near-inertial wave approaches positive vorticity, the increase of f_{eff} prohibits the further free propagation of near-inertial waves; while when it approaches negative vorticity, f_{eff} becomes lower than f , creating a free propagation. Thus, to some extent, the horizontally non-uniform relative vorticity has the similar effect as the β -effect on the propagation of near-inertial energy. Numerical simulation work (Zhai et al. 2005a, Zhai et al. 2007) also shows that the distribution of near-inertial energy is strongly influenced by the background mesoscale eddy field and that anticyclonic eddies are important in draining near-inertial energy from the surface to the deep ocean.

Other than the effect of wave processes on the redistribution of hurricane-induced near-inertial energy, geostrophic advection is also important in carrying energy away from the hurricane track. Zhai et al. (2004) showed that the Gulf Stream can advect hurricane-induced near-inertial energy away from its generation site based on numerical simulations. Through mooring observations, Park et al. (2010) showed that the strong advection of the Kuroshio Extension dominates the near-inertial wave dispersion process, blocking the equatorward propagation of near-inertial energy.

In this study, the inertial oscillations induced by Hurricane Ida in November 2009 in the Gulf of Mexico (GOM) have been analyzed using both mooring observations and numerical models. Hurricane Ida was a category 2 storm that originated in the southwestern Caribbean Sea on 4 November and struck the Nicaraguan coast within 24 hours. It entered the GOM on 8 November, weakened and became an extratropical cyclone in the northern GOM before landfall in Alabama at Mobile Bay. It only took two days for Ida to cross the GOM (Figure 6.1-1; red line). To investigate the hurricane-induced inertial oscillations and the underlying mechanisms on the distribution of near-inertial energy, both mooring observations in the LC area and numerical models were utilized.

6.2 DATA AND METHODS

The LC mapping-array moorings (A-B-C transects) and CICESE moorings (E-transect) in the GOM have been employed for this inertial-wake study (Figure 6.1-1). The analysis concentrates on the upward-looking ADCPs that were deployed at 450 m (SAIC) and 500 m (CICESE) as these resolve the velocity profiles below ~ 60 m. Hurricane Ida went through the CICESE mooring transect, while the mapping-array moorings were on the right-hand side of the track (Figure 6.1-1), and both provide observational evidence on hurricane-induced motions.

For Hurricane Ida, the 3-HLP hourly velocity data from these moorings were extracted from 1 November 2009 to the end of December 2009. The currents were then 45-hour high-pass (45-HHP) filtered to extract the near-inertial components. The clockwise and anticlockwise rotary spectra were calculated from the U and V velocity components for a one-month period from 6 November to 6 December 2009. The relative vorticity normalized by local f (i.e., ζ/f) were also calculated using either triangle or least-square interpolation for the mapping array moorings, and direct computation for the CICESE moorings, as described in Section 2.9.

For the numerical model simulation, a 4-year ocean circulation hindcast from 2007 through 2010 was performed using the Regional Ocean Modeling System (ROMS) (Haidvogel et al. 2008; Shchepetkin and McWilliams 2005). ROMS is a free-surface, hydrostatic, primitive-equation model that employs split-explicit separation of fast-barotropic and slow-baroclinic modes and vertically-stretched terrain-following coordinates.

The model domain covers the entire Intra America Sea (IAS) including the Caribbean Sea, the GOM and the South Atlantic Bight. The model has a horizontal resolution of ~ 6 km (Figure 6.2-1). Vertically, there are 30 terrain-following levels in the water column with higher resolution near the surface and bottom to better resolve boundary-layer dynamics. The model is free running, forced by winds and atmospheric fluxes, with open boundary conditions given by data assimilated into the global Hybrid Coordinate Ocean Model (HYCOM data server [unknown date])

For the surface-wind forcing during Hurricane Ida, the 6-hourly, 6-km resolution Hurricane Research Division (HRD) wind, (Moon et al. 2008; Powell et al. 1998; HRD database) was blended with the National Center for Environmental Prediction (NCEP) reanalysis wind. Figure 6.2-2 shows the comparison of wind vector between the merged wind and National Data Buoy Center (NDBC) buoy 42003, whose location is indicated in Figure 6.1-1. It shows that the

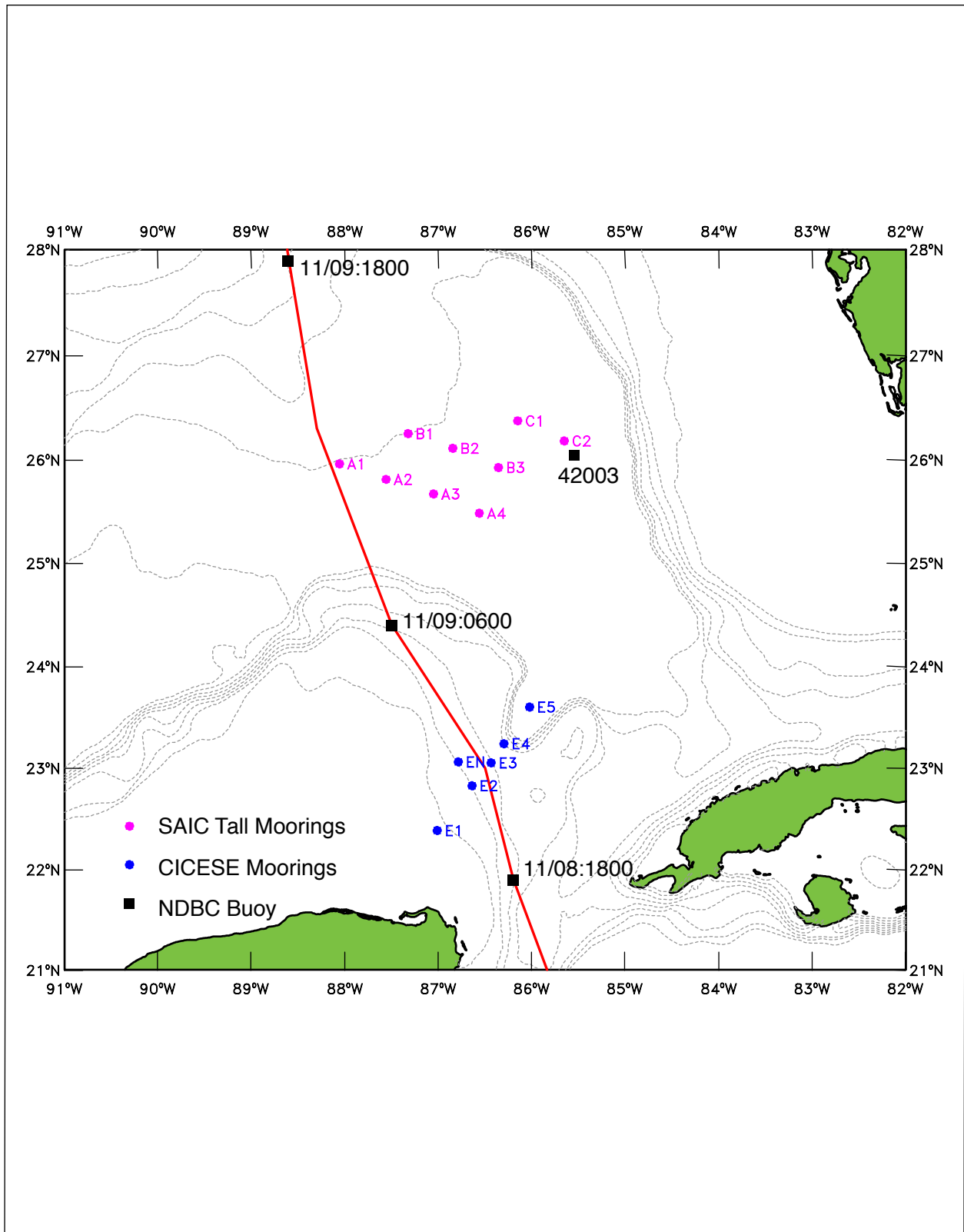


Figure 6.1-1. Locations for the mooring array in the Gulf of Mexico, the NDBC buoy and the track of Hurricane Ida.

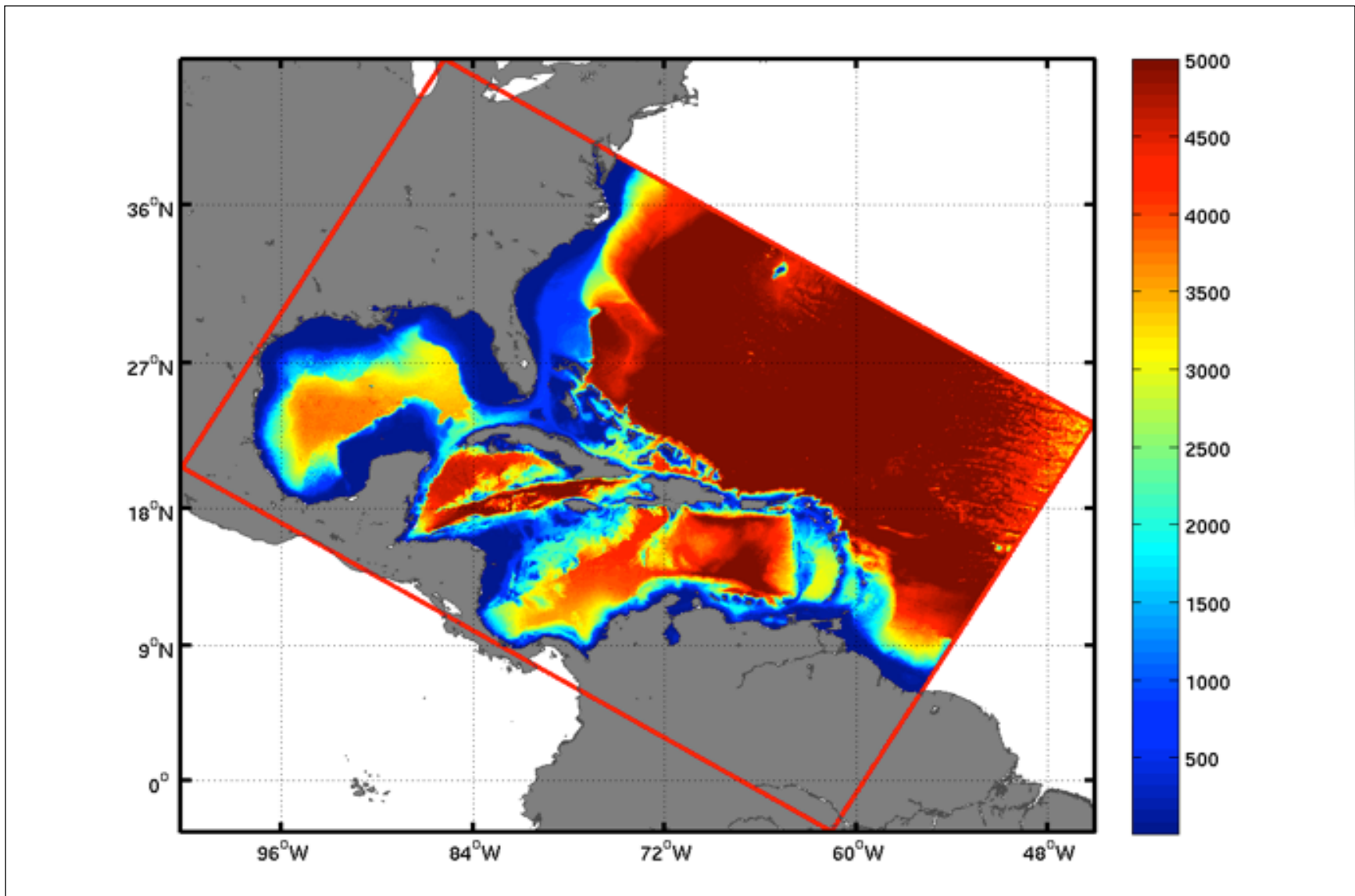


Figure 6.2-1. Six-kilometer (6-km) Intra-Americas Sea (IAS) circulation model domain. Both model boundaries and bathymetry (in meters) are shown.

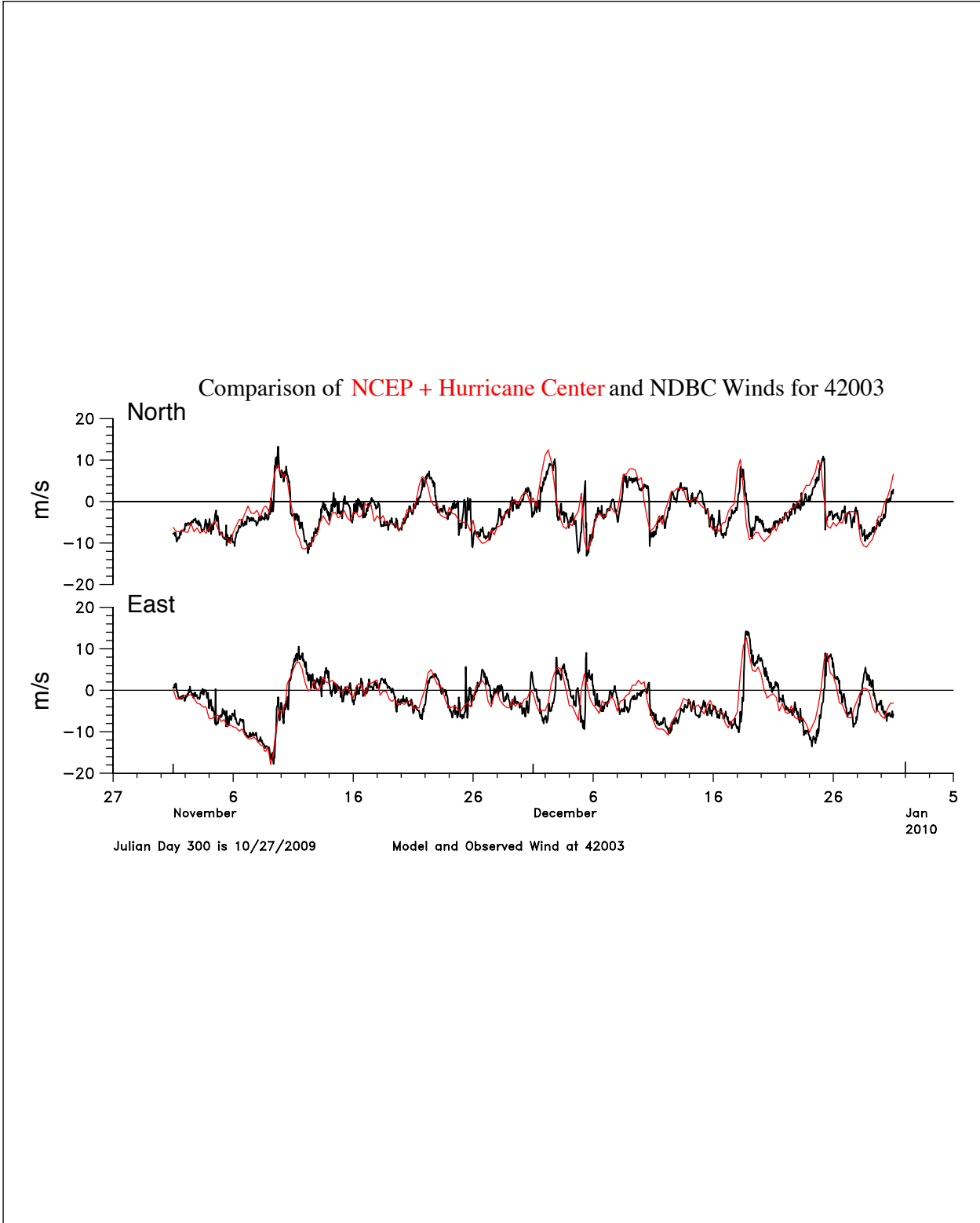


Figure 6.2-2. Time series comparison of east and north wind components between hourly 42003 buoy observations (black) and the merged 6-hourly product (red) used to drive the model in late 2009.

merged wind product agrees well with buoy observations, with a strong wind shift in early November when Hurricane Ida passed through.

In addition to the atmospheric conditions, the general ocean circulation condition is also presented. Figure 6.2-3 presents the time evolution of the wind field and LC conditions during Hurricane Ida, in the eastern Gulf of Mexico. From altimetry maps of SSH, a few weeks before the passage of Hurricane Ida, the LC had shed anticyclonic eddy Ekman and had retreated southward with its northern front south of 25° N. A very similar LC condition is found in a 4-year numerical simulation just before the passage of Hurricane Ida (Figure 6.2-4). Thus, because of similarity of the model-simulated LC and shed eddy at the beginning of November 2009 to observations, the model simulation for November 8, 2009 was taken as the initial conditions for the Hurricane Ida simulation. Over a 2-4 week period, the low-frequency flow evolves slowly and thus only small deviations in the background flow are expected. Together with the merged realistic wind field, the model was reinitialized and the circulation hindcast from 1 November to 7 December 2009, encompassing the entire life span of Hurricane Ida and its primary ocean response. The model hindcast along with model diagnostics were both saved at hourly intervals to keep the high frequency signals. To compare with observations, the simulated velocities at mooring locations were extracted and the same 45-HHP filter was applied. The model's diagnostics were also used in uncovering the possible mechanisms of hurricane induced inertial-oscillation distributions.

6.3 DESCRIPTION OF INERTIAL RESPONSE TO HURRICANE IDA

The hurricane-induced inertial oscillations are found in most of the mapping array moorings in the upper water column. For example, Figure 6.3-1a shows the time-series plot of 45-HHP filtered horizontal velocity at mooring A4 at various depth levels. It can be seen that near-inertial oscillation signals are present after the passage of Hurricane Ida (4-10 November 2009), starting around 10 November and lasting for 9-10 days at 84 m. The wave packets gradually propagate downward. At around 412 m, the inertial-oscillation signals are in the second half of November. Throughout the upper 400 m where ADCP measurements are available, a clear downward propagation of the near-inertial oscillation signal is well captured. Similar results are found in model simulations (Figure 6.3-1b). Although the model has approximately two inertial-wave packets, it successfully captured the hurricane induced inertial-oscillation signal though the downward propagation is not as well defined as in the observations.

On the other hand, observations from the CICESE E-transect moorings, deployed on the Campeche bank, show little inertial energy, though they were near the track of Hurricane Ida. Figure 6.3-2 shows an example of time series of high-pass-filtered horizontal velocity at E5. Throughout the upper water column, no strong inertial oscillations are induced after the passage of Hurricane Ida in early November.

Figure 6.3-3 shows a series of clockwise rotary spectra for the upper-water-column ADCP at nine selected moorings. In near-inertial waves, the velocity vector rotates clockwise with the wave period when viewed from above. It can be seen that for the A-B-C transects, the near-inertial power-spectral peaks are found and their near-inertial frequency is around f to $\sim 1.07f$, increasing with the increase in depth, which indicates the near-inertial waves have both local and far-field (north) origins. While further south, at the CICESE E-transect moorings, the inertial

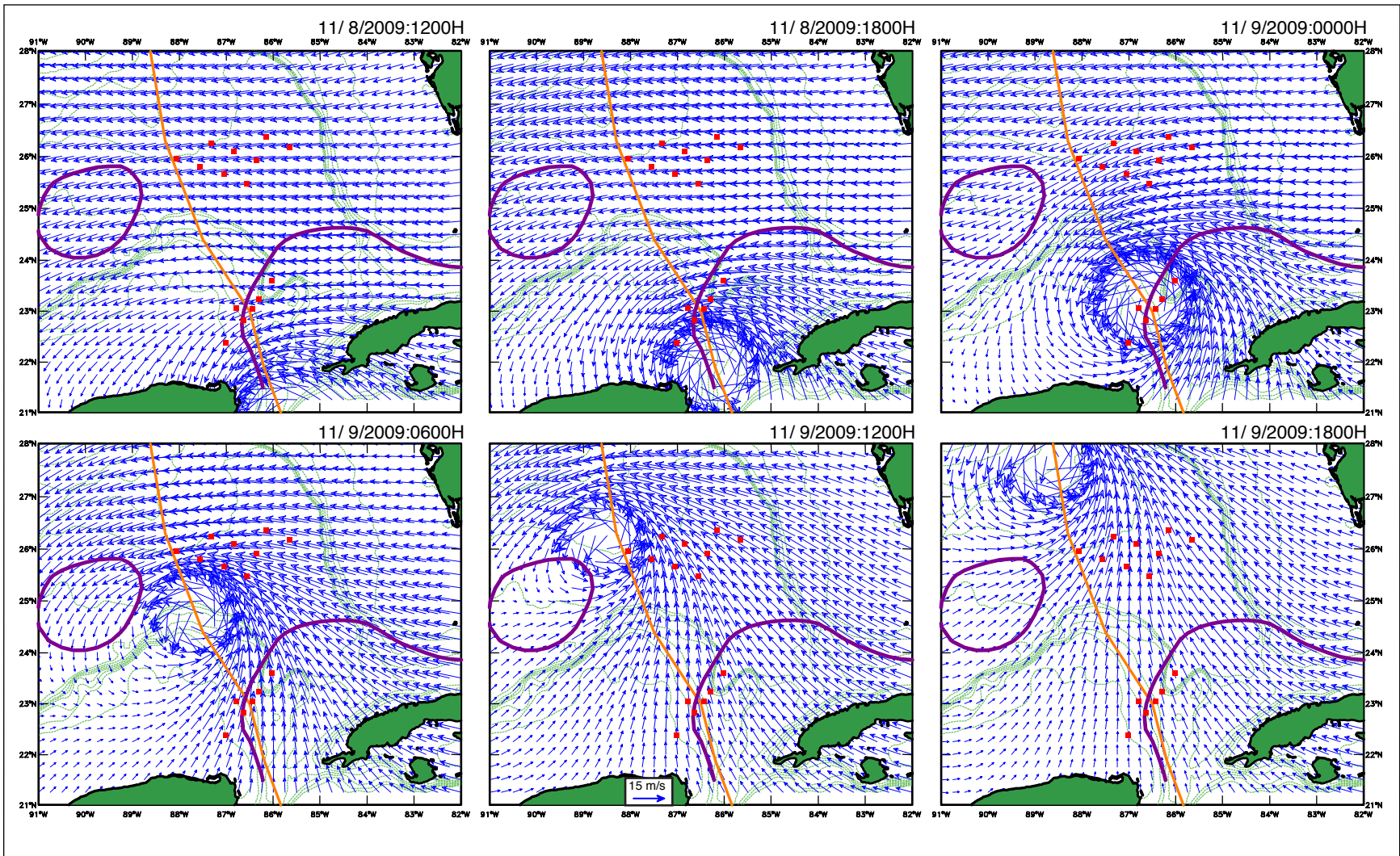


Figure 6.2-3. Winds during the passage of Hurricane Ida over the eastern Gulf from merged Hurricane Center and NCEP 10-m data. Mooring locations are indicated with red squares. The track of the central low pressure of Ida is given by the orange line, and the location of the 17-cm LC and eddy Ekman SSH front contour from the altimetry maps is given by the purple line.

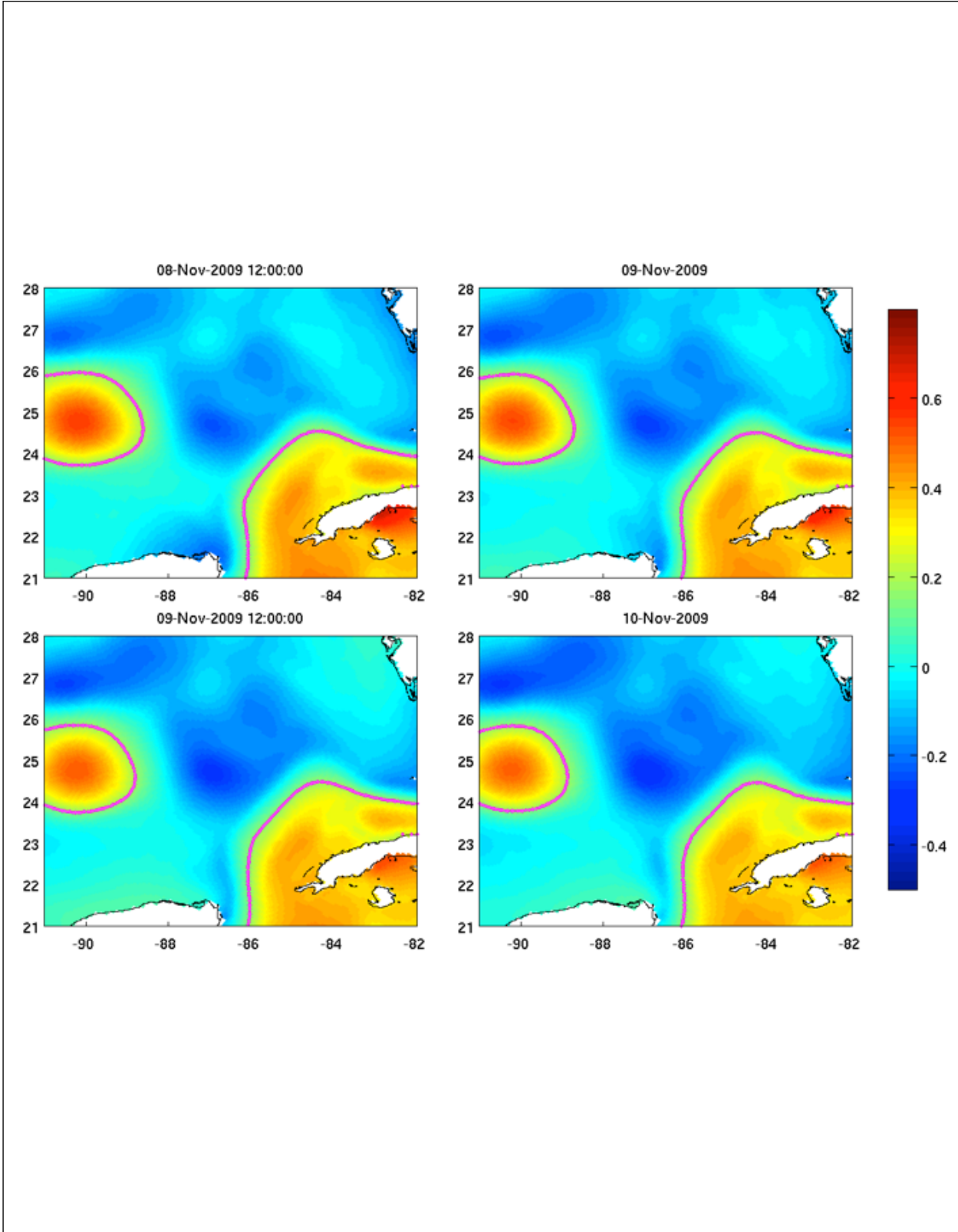


Figure 6.2-4. Model simulated Sea-Surface Height (SSH) in early November 2009. Purple line is the 17-cm SSH contour.

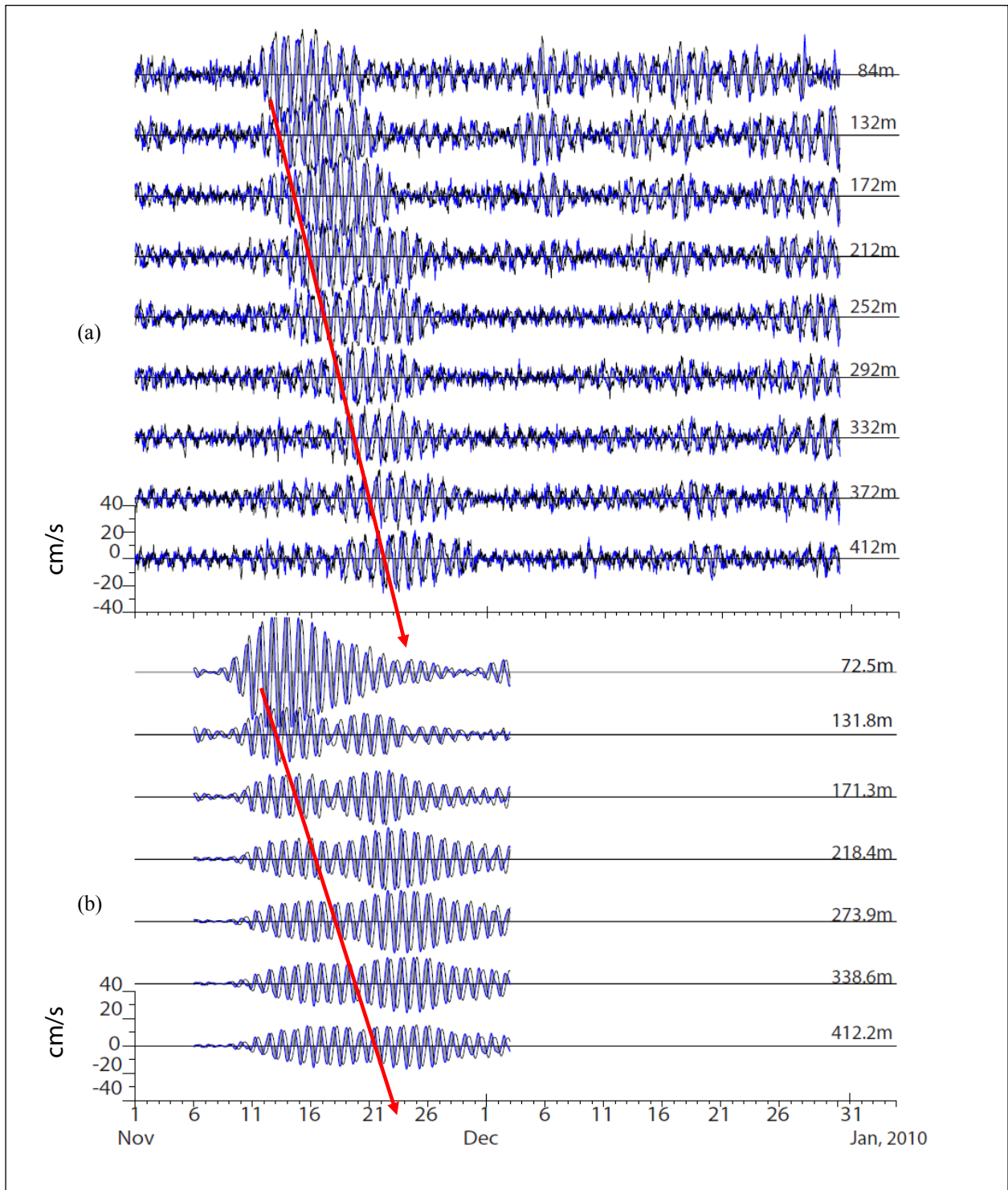


Figure 6.3-1. Time series of high-pass filtered horizontal velocity at various depths (a) from 450-m ADCP measurements at mooring A4 and (b) from model simulations at the same location. Blue line is the V-velocity (positive northward) and black line is U-velocity (positive eastward). Red arrow lines indicate the vertical packet propagation.

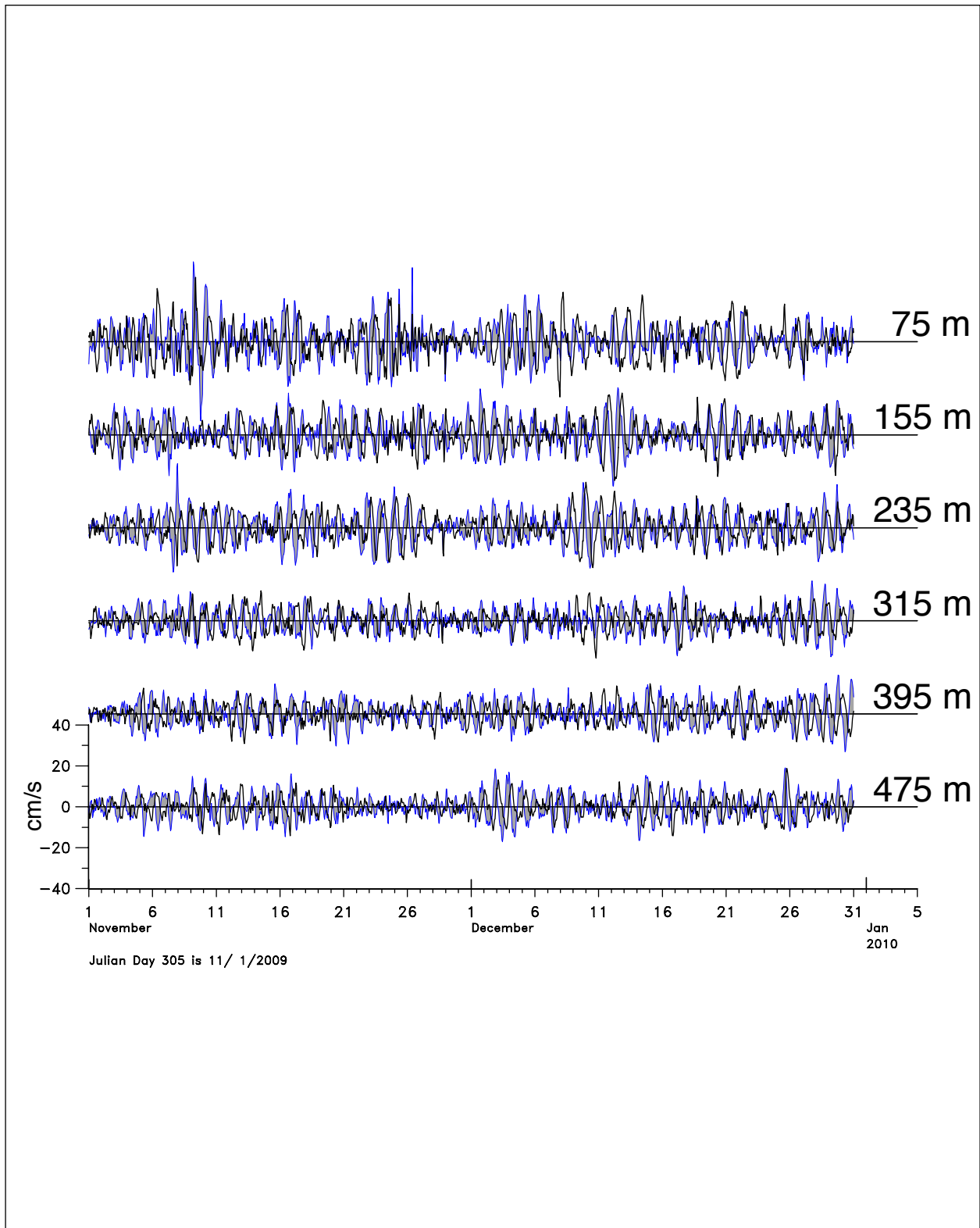


Figure 6.3-2. Time series of high-pass filtered horizontal velocity at various depths from 500-m ADCP measurements at mooring E5. Blue line is the V-velocity (positive north-ward) and black line is U-velocity (positive eastward).

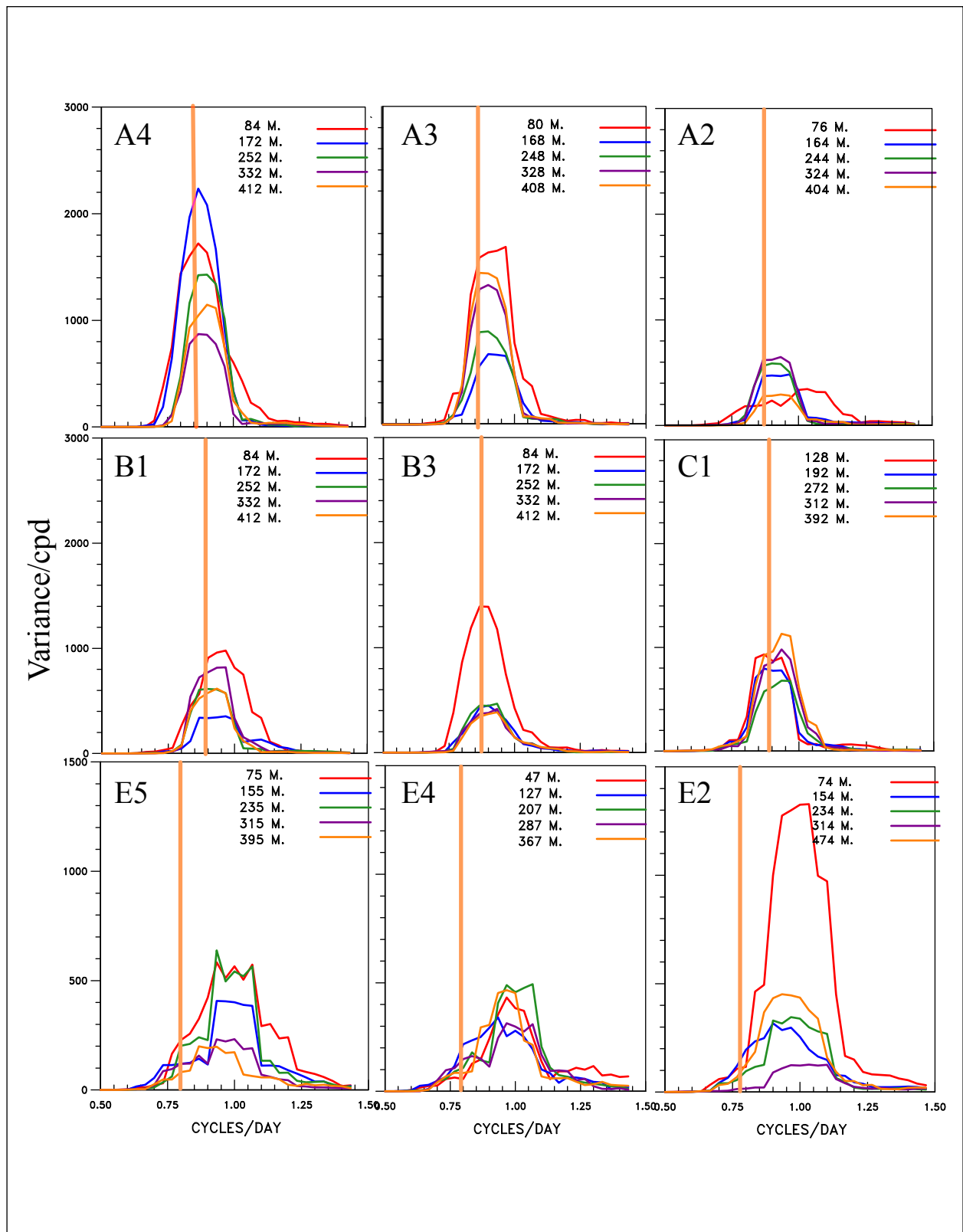


Figure 6.3-3. Clockwise rotary power spectra for high-pass filtered horizontal velocity at moorings for the upper 500 m. Orange vertical line shows the local inertial frequency.

oscillations are weaker and the frequencies corresponding to the power-spectral peaks are near the frequency of local diurnal tides, with a range of $\sim 1.13f$ to $1.25f$ throughout the water column.

In addition, the diurnal tidal energy at the E-transect moorings is much smaller than the near-inertial energy at the A-B-C transects (note the scale difference). Thus, the reduced amplitude high-frequency signal at the Campeche bank slope is dominated mainly by the local internal diurnal tides.

6.4 DISCUSSION

The different upper-ocean responses to the passage of Hurricane Ida in the two mooring groups in the vicinity of the hurricane track is an interesting phenomena and two possible factors in modulating the propagation of near-inertial waves are investigated here: relative vorticity and background advection. Because the LC had retreated, the trapping and deep penetration of near-inertial internal waves by anticyclonic eddies (Kunze, 1985) is not a factor for the mapping-array observations.

6.4.1 The Effect of Relative Vorticity on the Distribution of Inertial Oscillations

The presence of relative vorticity could alter the propagation of near-inertial waves through the effective Coriolis parameter f_{eff} . The mean distribution of normalized relative vorticity ζ / f at 200 m, as an example for the mapping-array moorings from 6 November to 6 December 2009 (Figure 6.4-1a), shows that the month-long mean relative vorticity is positive or cyclonic with a maximum of $0.11f$ near the center. According to Kunze (1985), the maximum f_{eff} then will be $1.05f$, which is still in the near-inertial frequency band. In that sense, this small positive relative vorticity in the region of the mapping-array moorings would not inhibit the propagation of near-inertial waves. Similar conditions are found at other depths, not limited to 200 m. However, the same month-long mean relative vorticity from the E-transect (Figure 6.4-1b) shows that the maximum relative vorticity appears at station 3 (between the E5 and E4 moorings) in the upper 200 m with a value of $0.4f$. This positive vorticity would increase the f_{eff} to $1.2f$, which exceeds the near-inertial frequency band, thus leading to the suppression of the propagation of near-inertial waves at these stations. Therefore, the strong positive relative vorticity is shown to be an important factor at the E-transect in prohibiting the propagation of near-inertial wave signals.

6.4.2 The Effect of the Loop Current on the Distribution of Inertial Oscillations

In addition to the suppression of the wave propagation process, strong background geostrophic advection may also be an important factor. This advection is shown in the altimeter SSH maps (Figure 6.2-3), with the E-transect moorings located near the front of the LC during the passage of Hurricane Ida. Using the theoretical approach of Zhai et al (2005b), the ratio between the dispersion processes of near-inertial waves and background circulation advective processes near the LC area can be estimated for the meridional component as:

$$R1 = \frac{\text{dispersive_process}}{\text{advective_process}} = \frac{N^2 l}{m^2 (\omega - V l) V} \quad (6.4.1)$$

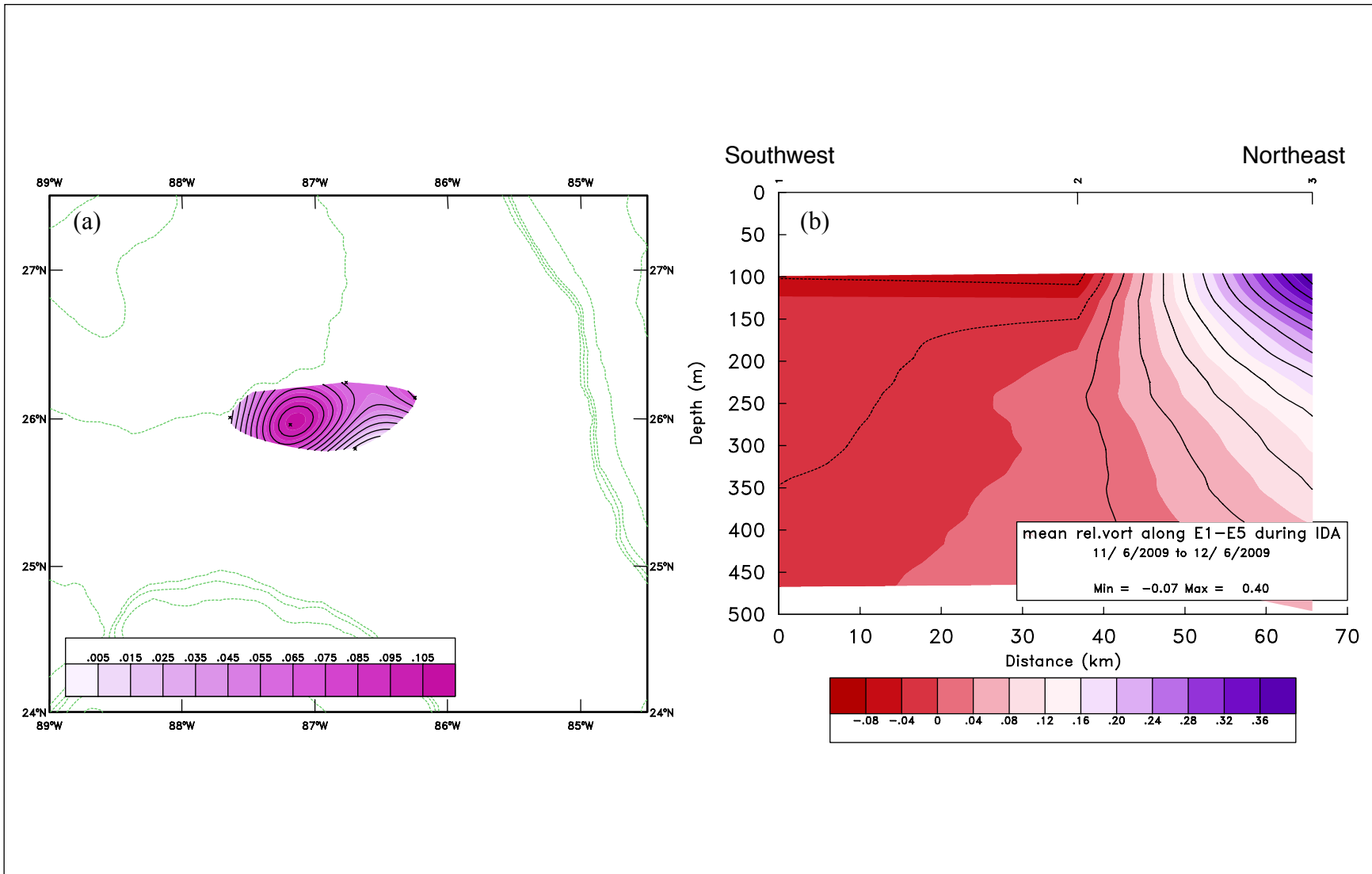


Figure 6.4-1. (a) Mean normalized relative vorticity plot for 6 November to 6 December 2009 at 200 m for the Loop Current study moorings (A-B-C transects). (b) Vertical plot of mean normalized relative vorticity at CICESE E-transect moorings for the same period.

and for the zonal component as:

$$R2 = \frac{\text{dispersive_process}}{\text{advective_process}} = \frac{N^2 k}{m^2 (\omega - V k) U} \quad (6.4.2)$$

where N is the buoyancy frequency near the thermocline, ω is wave frequency, l is the meridional wave number that is negative, k is zonal wave number, m is vertical wave number, V is meridional background flow and U is the zonal background flow. Typical values for $N = 0.01 \text{ s}^{-1}$, $l = 2\pi / 50 \text{ km}$, $k = 2\pi / 50 \text{ km}$, $m = 2\pi / 200 \text{ m}$ are used. At the E-transect, typically, $\omega = 7.3 \times 10^{-5} \text{ s}^{-1}$, and for the true northward flow of the LC ($V=1.5 \text{ m s}^{-1}$, $U=0$), the estimated ratio from Equation 6.4.1 is -0.0325, and the negative sign shows the equatorward propagation; for true eastward flow of the LC ($V=0$, $U=1.5 \text{ m s}^{-1}$), the estimated ratio from Equation 6.4.2 is 0.1163. Therefore, in both extreme conditions (true northward and true eastward flow) near the LC area, the estimated ratios indicate that at the Campeche bank slope, strong advection from the background flow dominates over the wave-dispersion processes, which is sufficient to block or reflect the equatorward propagation of near-inertial energy. Conversely, at the A-B-C transects, $\omega = 6.4 \times 10^{-5} \text{ s}^{-1}$, and the monthly means are $V=0.15 \text{ m s}^{-1}$ and $U=0.013 \text{ m s}^{-1}$. The estimated ratios for meridional and zonal components are -1.0245 and 21.7 respectively, indicating that the wave dispersion process overwhelms background advection, favoring the free propagation of near-inertial waves.

The model diagnostic output also provides some confirmation of the above conclusions. Figure 6.4-2 shows the time evolution of zonal-momentum budgets in November 2009 at moorings A4 and E5. On the left-hand side of the momentum equation is acceleration, while horizontal advection, Coriolis, the pressure gradient term and vertical viscosity are all on the right-hand side. The same 45-HHP filter was applied to all of these momentum terms to extract the high-frequency signal. It can be seen that at A4, the main momentum balance in the high-frequency band is between acceleration and the Coriolis term, resulting in strong inertial oscillations as observed, and these two terms are much larger compared to the rest of the terms in the momentum budget. However, at E5, which is near the LC front, horizontal advection becomes a major contributor in the momentum budget. It is comparable to the acceleration and Coriolis terms, dampening the inertial-oscillation signals.

Therefore, both ratio estimates from observations and model diagnostics confirm that on the Campeche bank slope, strong LC advection plays an important role in dampening the inertial-oscillation signals and blocking propagation. Conversely, at the A-B-C transect, with the retreat of the LC, after shedding of an anticyclonic eddy, inertial oscillations dominate and near-inertial waves propagate freely.

6.5 LONG-TERM VARIABILITY OF INERTIAL OSCILLATIONS

The variability of inertial oscillations over the 2½-year field program has been investigated using velocity observations in the eastern Gulf of Mexico. Complex demodulation (see Section 2.9) has been applied to the current velocity data to extract the amplitudes of fluctuations near the Coriolis frequency. Figure 6.5-1 shows time series of amplitude of velocity from complex demodulation at mooring locations A4, B2 and C1 as examples. For the observational interval, large amplitudes are generally found in winter, for instance from November 2009 to March 2010,

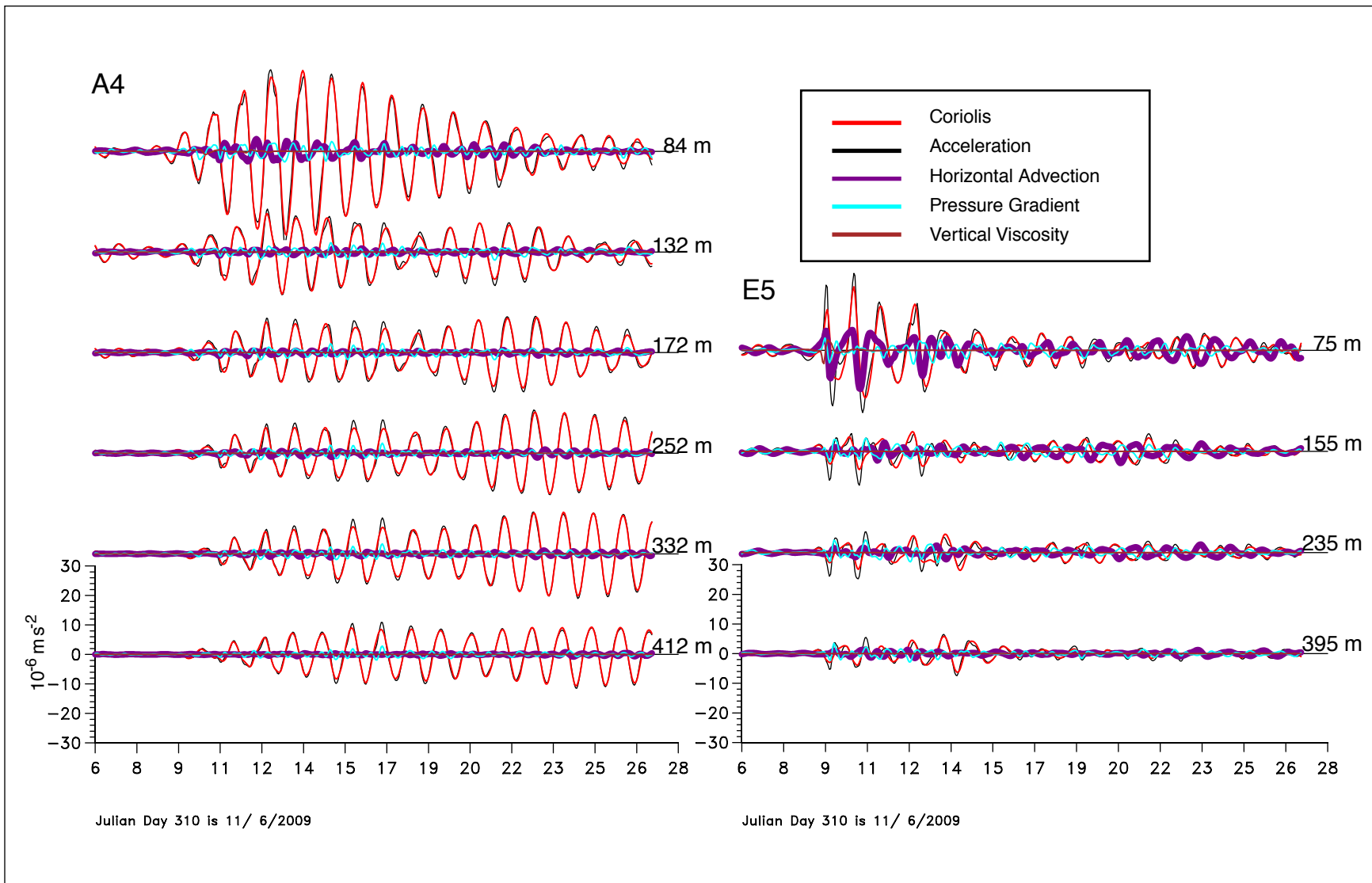


Figure 6.4-2. Time series evolution of zonal momentum budget at moorings A4 and E5 during the Hurricane Ida period (November 2009), red line is the Coriolis term, black line is acceleration term, purple line is horizontal advection, cyan line is pressure gradient term, and brown line is the vertical viscosity.

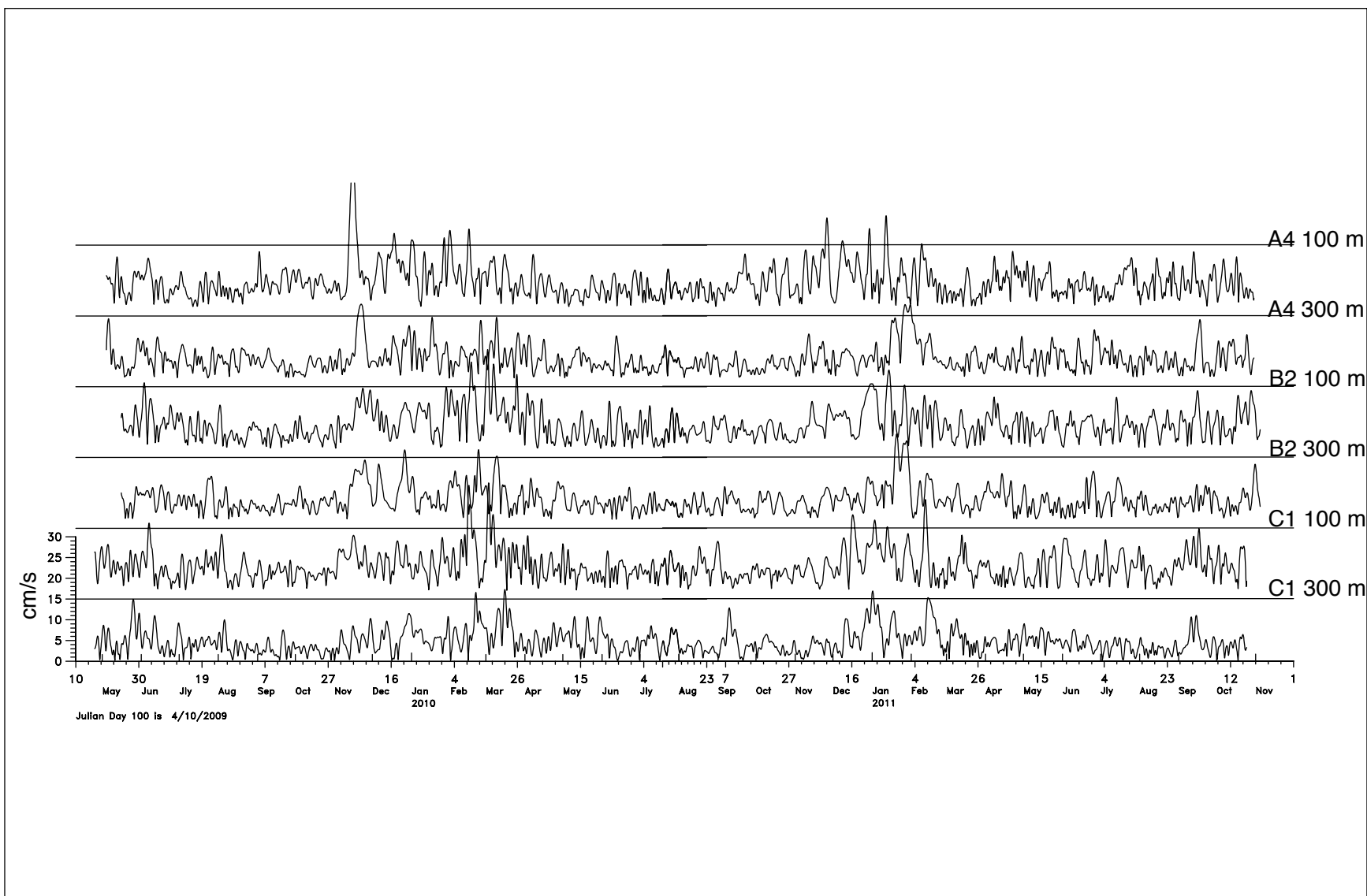


Figure 6.5-1. Time series (2.5 years long - from May 2009 to November 2011) of inertial frequency velocity amplitudes from complex demodulation at moorings A4, B2 and C1 for depths of 100 and 300 m, respectively.

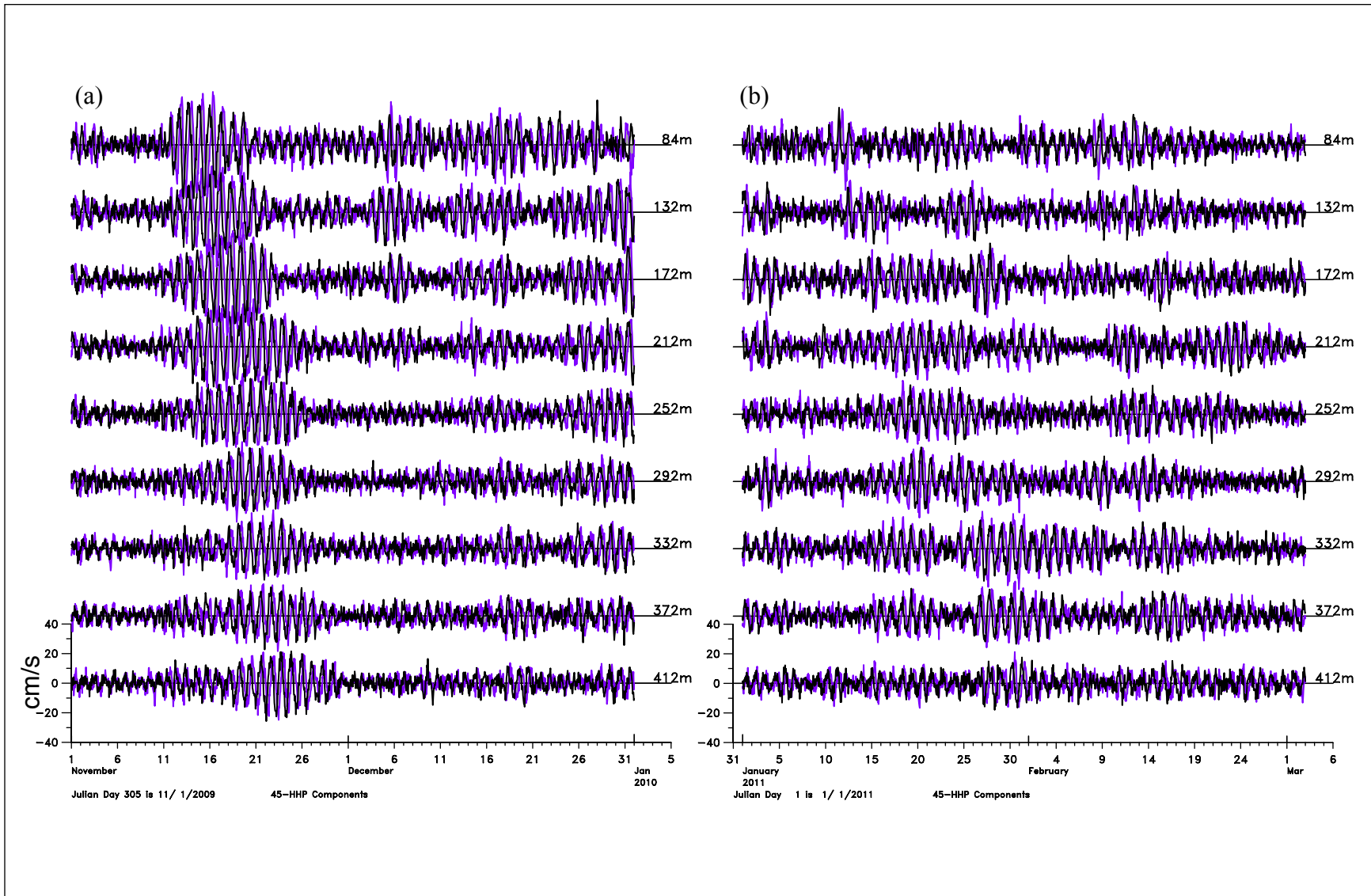


Figure 6.5-2. Time series of high-pass filtered horizontal velocity components at various depths from the 450-m ADCP measurements at mooring A4 for two periods (a) November 2009 and (b) January 2011.

and from November 2010 to March 2011. Although the specific peak amplitude time varies among mooring locations, they all peak in the winter season.

A 45-HHP filtered time series at these mooring locations further indicates the presence of inertial oscillations during the winter months. Figure 6.5-2 shows time series of the filtered velocity at various depths of mooring A4 for two winter periods. One is from November to the end of December 2009. In it, strong inertial-oscillation signals are present and inertial energy propagates downward. The other period is from January to the end of February 2011. In it, large-amplitude inertial oscillations are also present, but with less consistency with depth. This suggests the possibility that they are not of the same origin. Corresponding atmospheric conditions for these time periods (Figure 6.5-3) show that strong inertial oscillations occur when there is stronger wind, lower atmospheric temperature and lower atmospheric pressure.

Similar features are found at other mooring locations. At B2 (Figure 6.5-4), inertial oscillations are present throughout the upper 400 m in the second half of November 2009, as well as toward the end of December 2009 (Figure 6.5-4a). The inertial oscillations are also stronger at deeper depths from mid-January, 2011, while there is only a weak inertial-oscillation signal for the upper 200 m during this period (Figure 6.5-4b). The corresponding atmospheric conditions are shown in Figure 6.5-3.

At C1 (Figure 6.5-5), clear and strong inertial-oscillation signals are present in December 2010 and January 2011 throughout the upper 400 m, and in late February 2011 for the upper 250 m. Corresponding atmospheric conditions (Figure 6.5-6) show that strong winds had a direction shift along with a decrease in atmospheric temperature when there were strong inertial oscillations, indicating that the passage of winter cold fronts can cause these ocean velocity signals. Similar strong inertial oscillations are found at most of the A-B-C mooring sites. It is important to note that the inertial amplitudes generated by these winter storms and cold front passages appear to be as energetic and long lasting as those generated by Hurricane Ida.

6.6 SUMMARY AND CONCLUSIONS

Through the analyses of both moored-current observations in the Loop Current area in the eastern GOM and numerical model simulations, inertial oscillations induced by the passage of Hurricane Ida have been investigated. Strong hurricane-induced inertial oscillations are found in most of the mapping array moorings at all upper-layer depths, with the energy being transmitted downward as near-inertial waves. Similar features are well captured in the model simulations. The observations from the Campeche bank slope moorings, however, show that inertial oscillations are only weakly present. Instead, here, high-frequency oscillations are mainly dominated by local internal diurnal tides. It is noted that these may be the only observations of an internal diurnal tide in the Gulf, and warrant further investigation in the future.

This pattern of ocean response to the northward moving Hurricane Ida is found to be closely related to the background relative vorticity as well as background geostrophic advection. The slowly varying background relative vorticity changes the propagation of near-inertial waves through the change of the effective Coriolis parameter f_{eff} . From the relative vorticity analyses for the time of the storm, the mapping array moorings are located in the small positive relative vorticity area with a maximum around $0.1f$, resulting in a small change of f_{eff} to $1.05f$, which is

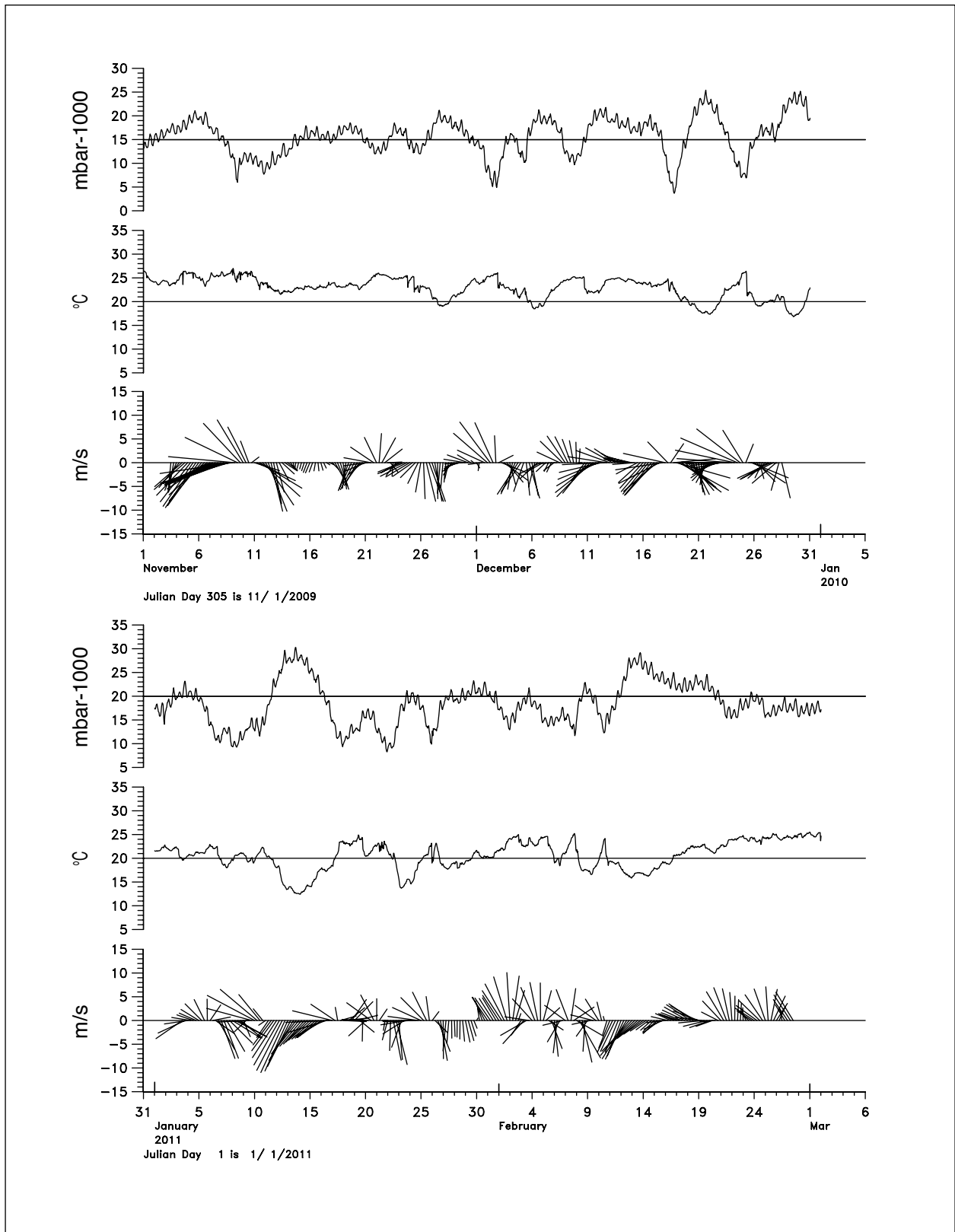


Figure 6.5-3. Time series of atmospheric pressure, atmospheric temperature, and wind vectors for two winter periods for NDBC buoy 42003.

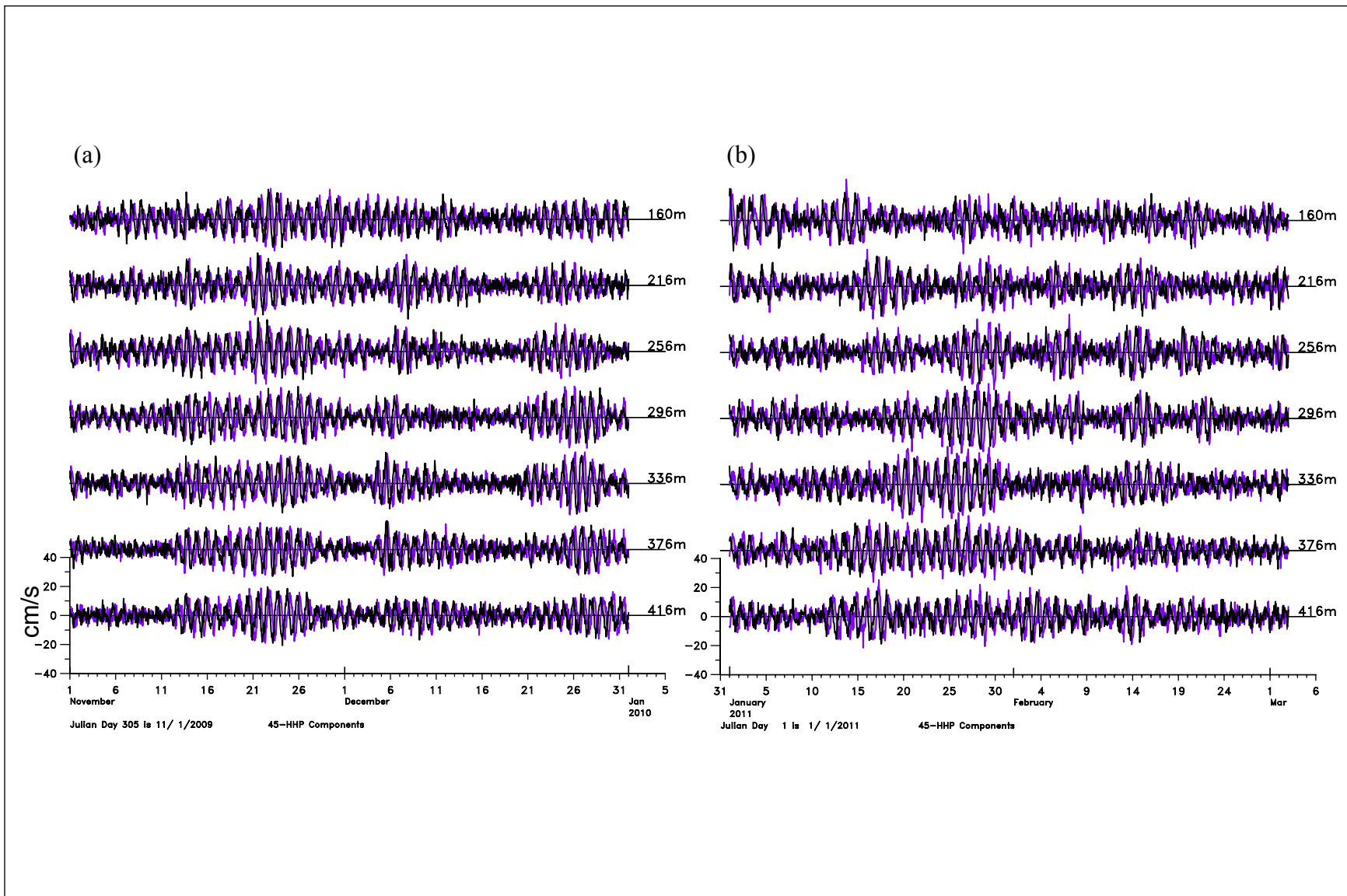


Figure 6.5-4. Time series of high-pass filtered horizontal velocity components at various depths from the 450-m ADCP measurements at mooring B2 for two periods (a) November 2009 and (b) January 2011.

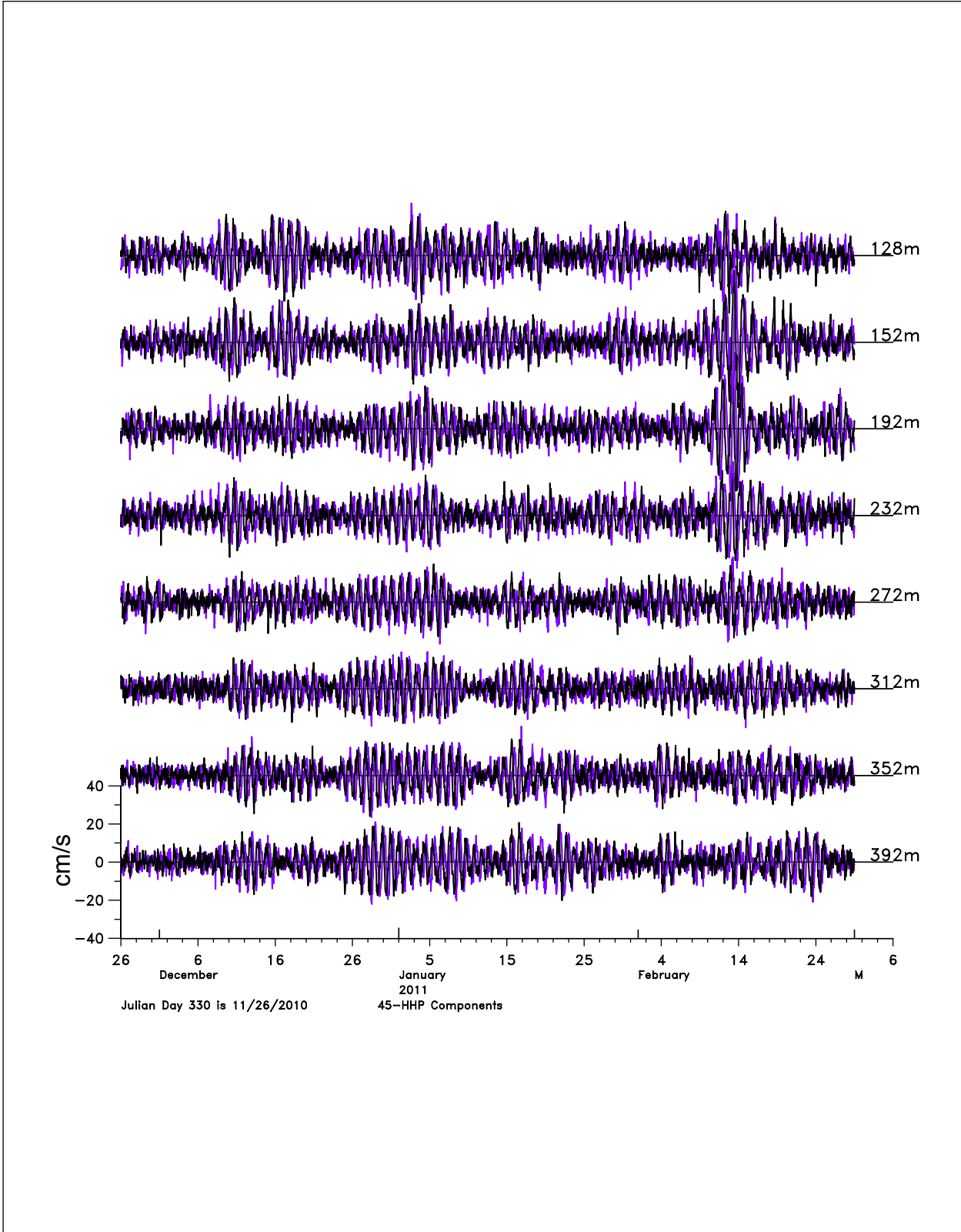


Figure 6.5-5. Time series of high-pass filtered horizontal velocity components at various depths from the 450-m ADCP measurements at mooring B2 for the 2010-2011 winter.

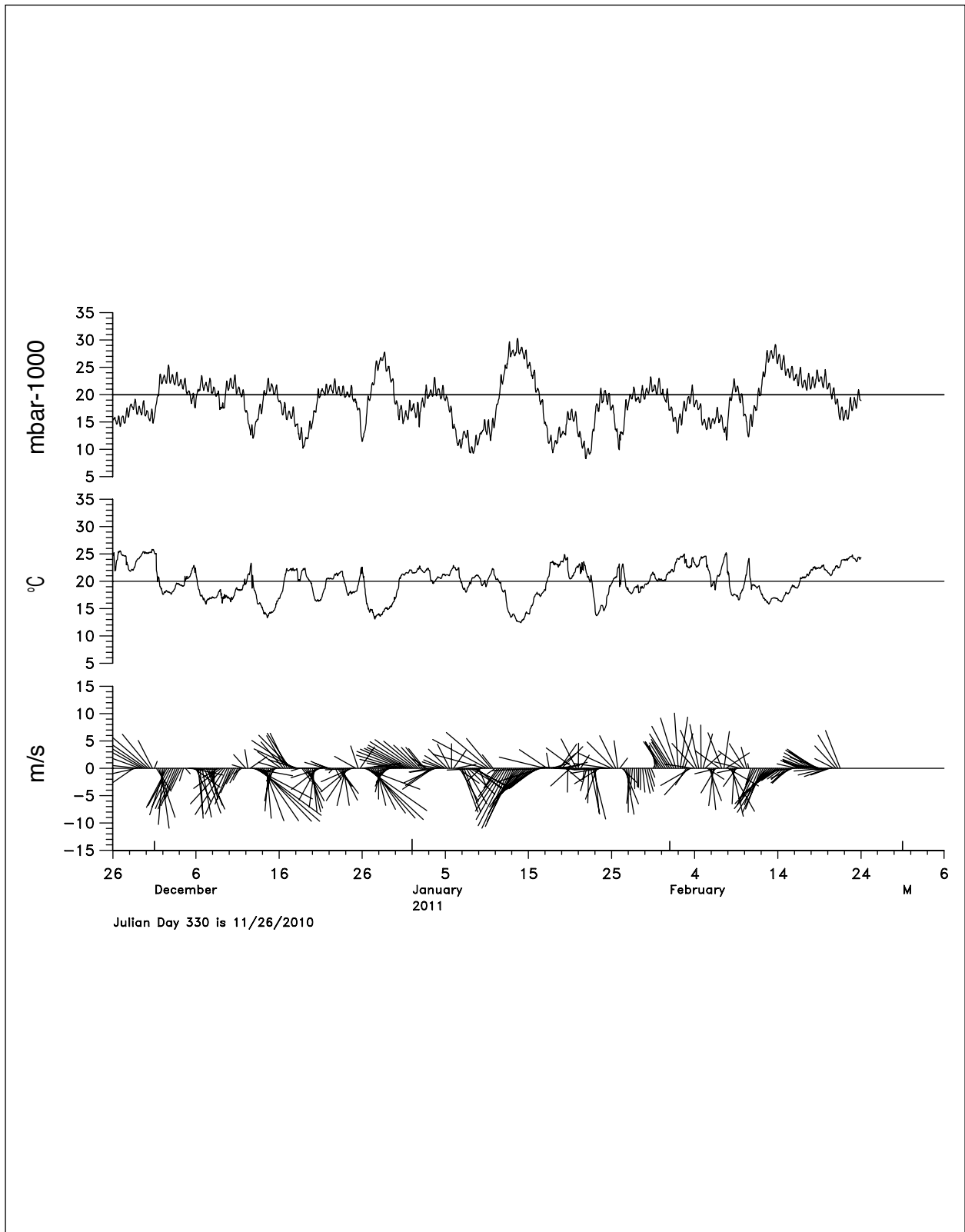


Figure 6.5-6. Time series of atmospheric pressure, atmospheric temperature, and wind vectors for the 2010-2011 winter periods for NDBC buoy 42003.

still in the near-inertial frequency band. However, for the Campeche bank slope moorings, the maximum relative vorticity on the cyclonic side of the LC front could be as high as $0.4f$, resulting in a big change of f_{eff} to $1.2f$, which exceeds the near-inertial frequency band, and suppresses the free propagation of near-inertial waves. Therefore, the presence of strong positive relative vorticity on the Campeche bank slope could be a contributor in suppressing the hurricane-induced inertial-oscillation signals. On the other hand, from the altimeter maps, when Hurricane Ida passed through the Gulf, the LC had shed an anticyclonic eddy and retreated southward, making its front close to the E-transect moorings on the Campeche bank slope. Thus, the background geostrophic flow near the E-transect moorings was just the strong LC, whose advection is non-negligible in modulating the propagation of near-inertial signals. From the ratio estimate of dispersive processes versus advective processes, using the method of Zhai et al. (2005b) in the Loop Current region, it is shown that over the Campeche bank slope, the Loop Current advection processes overwhelmed the wave dispersion processes, sufficiently blocking the inertial oscillation signals. Therefore, the strong background advection from the Loop Current serves as another factor in suppressing hurricane-induced inertial oscillations at the E-transect moorings. This evidence is also supported by the numerical model diagnostics.

Besides the inertial response to tropical storms and hurricanes, the observations show that near-inertial internal waves were present in the array most of the time with maximum amplitudes in the winter season. These winter events had magnitudes that were comparable to the response to Hurricane Ida. In the eastern Gulf, winter cold fronts generally move from west to east, but northward propagating fronts may also occur. The cause of these winter inertial events is most likely the passage of these cold fronts across the northern Gulf that produce abrupt shifts of strong winds that can initiate near-inertial waves that may be trapped and enhanced in anticyclonic flows such as the LC and LC eddies (Kunze 1985).

CHAPTER 7: SUMMARY DISCUSSION AND RECOMMENDATIONS

7.1 INTRODUCTION

This study was a measurement-based program into the characteristics, variability and dynamics of the LC. It consisted of a mapping array of PIES, tall and short current meter moorings deployed in U.S. waters, and tall mooring transects across the eastern slope of the Campeche Bank deployed in Mexican waters by CICESE. The U.S. array was deployed for 2 ½ years beginning in May 2009, and the CICESE array began in June 2009 and is still ongoing, though only two years of coincident observations are available. This report is not meant to supplant the future CICESE report on their observations, however, where appropriate, the two datasets have been combined to get a more complete description of LC processes. Because of the type of measurements and the lengths of the programs, the emphasis is on meso-scale variability. However, long-term interannual and intraannual variability has been addressed through a thorough analysis of the historical altimeter and SST records, and numerical modeling. Most of the numerical modeling performed under this program has been published (Chang and Oey 2010a, 2010b, 2011, 2012, 2013a; Xu et al. 2013a, 2013b), and therefore, in this report, model results are simply summarized and only results that are directly related to the observations have been highlighted. Numerical modeling was also used to study the ocean's inertial response to Hurricane Ida (Chapter 6). The reader will note some disagreements between the interpretations of published model results on some aspects of LC eddy-shedding processes as well as long-term variability, but this is the nature of scientific research, and will most likely be resolved in the future. Clearly, with such an extensive and comprehensive dataset, this report cannot hope to cover all aspects of complex phenomena associated with the LC, but it can be expected that these data will serve as a source for many future studies that will expand on the results presented here. These data are also an important resource for numerical modelers to evaluate the performance of their Gulf of Mexico models.

The LC is the most important circulation feature of the deep Gulf of Mexico because it is the feature with the highest energy. Remote effects, through the shedding of eddies, radiating TRWs, forcing mean flows, and influencing shelf flows, are felt throughout the Gulf. Until this study, there had been no comprehensive observational program for the LC, with most of the previous studies (summarized by Schmitz et al. (2005) and Vukovich (2007)) relying on remote sensing to investigate LC variability, which of course only describes the upper-layer patterns. Numerical models of the Gulf have also concentrated on upper-layer variability (see Oey et al. (2005) for a review), often seeking to reproduce eddy shedding. Model simulations have been used to speculate on LC processes controlling circulation (e.g., Oey (2008), Le Hénaff et al. (2012), and Morey and Dukhovskoy (2013)), but rarely have been directly compared with in-situ observations.

Perhaps the most important findings of the study are a significant revision of the ideas of how an eddy detachment takes place. The role of LCFEs is deemphasized in favor of baroclinic instabilities extracting energy from the mean flow, and jointly amplifying both the large scale meanders of the LC front, and the barotropic deep eddies. It is a steepening meander trough, in combination with the southwestward propagation of deep eddies, guided by the topography of

the southern part of the Mississippi Fan, that effects a detachment (see Section 7.4 for a more detailed discussion). Some of these mechanisms have been put forward in the literature, but have not been brought together in a proper sequence. For example, Schmitz (2005) discusses detachments by cyclones on the east and west side of the neck based on an analysis of SSH maps (the role of a large independent cyclone against the Campeche slope is not supported by this study's observations), and Xu et al. (2013b) discuss the role of baroclinic instabilities in model simulations, where they consider it a secondary mechanism that accelerates a detachment that is primarily a result of the Pichevin-Nof momentum paradox. The strong coupling of the upper and lower layers through barotropic flows has been observed in other strong baroclinic jets (e.g., the Gulf Stream); however, it has not been observed until this study for the LC. Coupling of barotropic and baroclinic flows is also not observed in other parts of the deep Gulf where moored velocity observations have been made (Hamilton 2009).

The other important results of the study pertain to the variability of the LC. In particular, the multi-decadal mean seasonal growth and wane of the LC has a dominant annual structure, with the consequence that eddy separation events have higher probabilities around the fall equinox and lower probabilities in late fall/early winter. This mean annual signal is correlated with the mean annual sea level signal along the U.S. southeastern coast, with the connection made through southward propagating coastal-trapped waves. How the remote signal on the west Florida shelf and slope affects the LC is not resolved by this study, nor is the tendency of eddy separation events to occur around the spring equinox.

This chapter is organized by first summarizing the results on statistics and dynamics (Chapters 3 and 4), followed by long-term and inertial variability (Chapters 5 and 6). These summaries are then followed with a discussion of processes that are not understood very well in the observational results, and some new study recommendations to fill the gaps.

7.2 LC EDDY SHEDDING EVENTS

The formation, detachment and separation of three major LC eddies were contained in the datasets. The three eddies were Ekman, Franklin and Hadal with first detachment dates of 6 July 2009, 8 June 2010, and 15 August 2011, respectively. All three followed similar sequences and the common features include a northward growth to an extended LC where the west-side front is relatively stationary along the Campeche upper slope. This western front then develops small-scale (50-100 km, 7 to 10-day period) cyclonic perturbations that grow in amplitude northwards along the slope, but then decay or are non-linearly transformed to longer period fluctuations over deep water on the northern part of the LC front. The east-side front of an extended LC, which is over the deep water of the eastern basin and thus not affected by the west Florida slope, develops large amplitude, long wavelength (~300 km), 40 to 60-day period meanders that propagate southward towards the Florida Straits. There is a simultaneous increase in lower-layer EKE, and the development of barotropic eddies that are displaced from the surface-layer crests and troughs by approximately $\frac{1}{4}$ wavelength (i.e., bottom-layer fluctuations lead the surface by $\sim 90^\circ$), which is a characteristic of a baroclinic instability. The interactions between the deep eddies (which are blocked from following the surface-layer meanders by the topography of the southern part of the eastern basin) with the meanders, causes a steepening of a trough that extends across the LC to cause a detachment.

According to theory, supported by numerical modeling (Chang and Oey, 2013a), if a detached eddy is large enough, and its center is far enough north so as not to be impeded by the Campeche Bank, it will move off to the west by β -advection, and a separation will be achieved. The Rossby wave westward velocity of $-\beta R_0^2$, where R_0 is the eddy's 1st baroclinic radius based on upper-layer depth, must exceed the LC growth for separation to occur, and LC growth depends on transport through the Yucatan Channel. Therefore, Yucatan transport is sometimes observed to decrease just before a detachment, which would facilitate a separation (Xu et al. 2013b). This reduction apparently occurred just prior to Franklin's final separation, based on CICESE's Yucatan transport calculations for 2010. However, the separated Franklin was small and weak and thus the westward β -advection did not apply.

The three individual eddies showed some differences in their behavior from this generalized pattern.

Ekman

The first detachment occurred in the south, along transect E, but the eddy remained in the southern part of the eastern basin and so was blocked from separating by the Campeche Bank. Final separation occurred when the LC and attached eddy extended to the west. After that time, meanders developed on the northern boundary and grew downstream until a separating trough, extending southwestward across the observational array, pinched off the LC neck. The final Ekman was smaller than for the first detachment. Ekman's final detachment illustrates that steepening meander troughs can occur anywhere along the northern or eastern front as long as they are over deep water, and deep barotropic flows can develop. Detachments are not restricted to regions just north of the Florida Straits.

Franklin

Franklin initially developed very similarly to Ekman and the first detachment occurred along transect E in the south, producing a southern eddy, also blocked by the Campeche Bank. The eddy remained in this southern position where the LC rejoined it multiple times, and instead of contributing to its growth, it extracted mean flow KE from the eddy. During this period of multiple reattachments and detachments, the CICESE-calculated Yucatan transports showed an overall increase of ~ 10 Sv, and may have been a factor in draining energy from the eddy. Eventually Franklin faded away under this repeated assault by the LC, and only separated a trivial anticyclone into the western Gulf.

Hadal

The LC underwent three extensions or growth spurts to the northwest. After each growth phase, large meanders developed on the eastern front, but seemed to be suppressed when the next extension of the LC and attached eddy occurred. Just prior to the first detachment and final separation, the steepening meander trough advected cyclonic vorticity of the trough from the eastern side of the extended LC to the western side, where it appeared as a large cyclonic displacement of the western front. Viewed as a frontal phenomena using SSH, it appeared that a large cyclone suddenly developed on the western boundary adjacent to the Campeche Bank. However, the transfer, primarily by advection with possible assistance by westward propagating deep cyclones, of relative vorticity from the eastern frontal boundary generated this apparent

western frontal perturbation growth. This observation contradicts Schmitz (2005) where it is asserted that some separations are effected by the simultaneous occurrence of cyclones on the eastern and western sides of the LC. Such occurrences may be artifacts of the SSH mapping algorithms. However, the formation of the west-side cyclone did assist in moving the separated Hadal, which was a large LC anticyclone, to the west. Numerical simulation using a free-running model over several months had some success in hindcasting Hadal's separation (Xu et al. 2013b) where the validation was provided by AVISO SSH.

7.3 STATISTICS AND DYNAMICS

Means and variances of velocity profiles are accounted for by two modes: a surface intensified unidirectional flow at the tall mooring location that occupies the upper layer from the surface to ~700 to 900 m, and a nearly depth-independent barotropic mode that is not always aligned with the surface-intensified baroclinic mode. These characteristics make the LC ideally suited to analysis by the PIES mapping array where geopotential height anomalies and bottom pressure accompany the bottom-referenced baroclinic mode, and its referencing barotropic velocity modes. The barotropic mode is not present along Campeche slope in water depths less than 1000 m, where mean flows and the baroclinic-mode fluctuations have about equal KE. In deep water, the KE is dominated by the barotropic mode, followed by the baroclinic and mean flow. Baroclinic and mean KE become more important in the vicinity of the LC or LC eddy fronts. Mean flows are strongly sheared in the upper layer and essentially depth-independent in the lower layer. Upper-layer means correspond to the mean LC configuration, but the lower-layer mean flows consist of an anticyclone-cyclone pair under the LC with the anticyclone to the west. This is consistent with potential vorticity conservation with the lower layer being squeezed and stretched on the leading and trailing edges, respectively, of a LC extending to the northwest. The shoaling topography of the Mississippi Fan to the northwest tends to intensify the deep anticyclone.

An illustration of how the weakly depth-dependent barotropic mode observed in the LC becomes more strongly bottom-trapped further north and west, away from the direct influence of the LC, is given in Figure 7.3-1. Here, depth-range-weighted CEOFs are given for mooring A3 (repeated from Figure 3.4-3), and mooring L4 that was deployed in a similar depth, west of the Mississippi Fan and near the Sigsbee escarpment, during the Exploratory study (Donohue et al. 2006). The modes have similar shapes at both locations, but at L4 the quasi-barotropic mode is distinctly more bottom trapped, decaying in amplitude towards the surface. Conversely, under the LC, at A3, the mode is essentially depth-independent. Though the near-surface-intensified mode at L4 has about half the amplitude of that at A3, the near-bottom amplitudes of the quasi-barotropic modes are quite similar. This suggests that barotropic signals originating in the LC propagate out to the west, becoming more bottom-trapped with the characteristics of TRWs, and thus become more disconnected from surface-layer eddies. TRW ray tracing in Hamilton (2009) [his Figure 15] shows possible connections of the L4 site with the LC for 60-day waves.

Neglecting the long periodicities associated with the LC eddy-shedding cycle, fluctuations in both layers are dominated by 100 to 20-day variability. Shorter period (< 20 days) fluctuations are important in the upper layer especially along the western front where it overlies the Campeche slope, and in the northwestern part of the array. These are characteristic of LCFEs propagating along the front. An analysis of ~10-day fluctuations along the Campeche slope

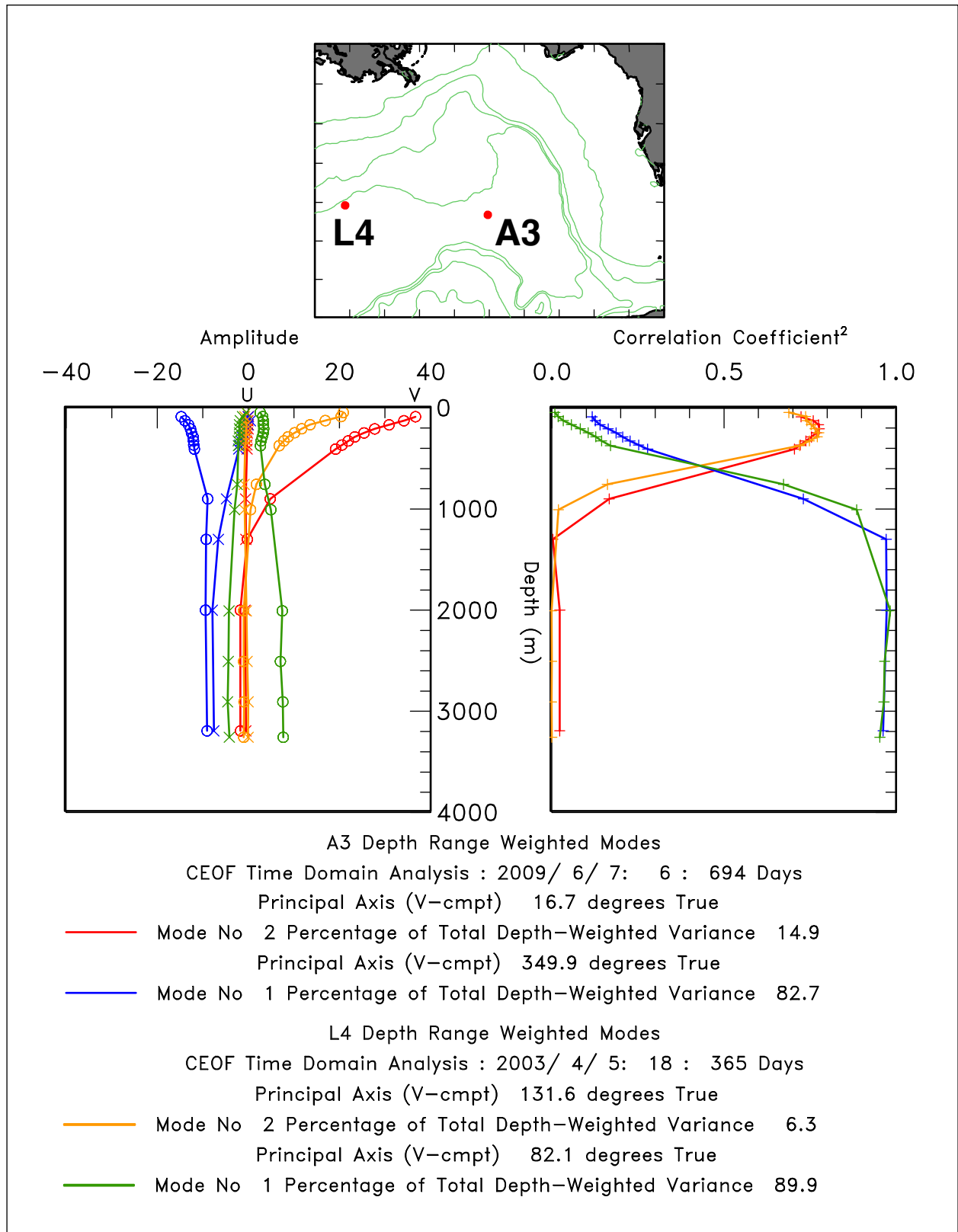


Figure 7.3-1. Depth range weighted CEOF modes for LC mooring A3 and Exploratory mooring L4.

shows that these fluctuations grow in amplitude between transects E, near the Yucatan, and N, near the northeast corner of the Campeche Bank. Bursts of LCFEs occurred during the northward extension or growth stage of the LC for all three eddies. After LCFEs leave the slope, growth appears to be inhibited, and they either decay or are transformed into longer period frontal perturbations. On the northeast side of the array, ~10-day fluctuations are only weakly observed. Furthermore, northeastward of the Campeche bank, along the LC front, over deep water, vertical coherence is low with similar weak fluctuations in the lower layer. This implies that LCFEs do not play an important role in developing deep eddies. This result does not support Oey's (2008) interpretation of model simulations where deep eddies were generated in this region from frontal eddies. The deep eddies in the model propagated off to the west and formed sources for TRWs radiating towards the Sigsbee escarpment.

The most energetic fluctuations are in the 100 to 20-day period band, and the large meander periods of 40 to 60 days tend to dominate. In the upper layer, 100 to 20-day fluctuations propagate clockwise around the LC with the highest amplitudes east of the Mississippi Fan. In the lower layer, amplitudes at these periodicities increase just prior to and during detachments, and are associated with baroclinic instabilities that feed the growth of both the eastern side meanders and lower-layer eddies. Lower-layer propagation is from the Mississippi Fan towards the southeast at periods > 40 days, but with more of a cross-LC direction towards the southwest in the higher 40 to 20-day band.

In the 20 to 10-day-period band, fluctuations tend to show an increase later in the detachment process, and are a relatively minor component of the total EKE. They are most prominent in the regions around the base of the Mississippi Fan, where stronger bottom slopes can support higher-frequency westward-propagating TRWs, and towards the southeast, where propagation is towards the northwest. The vertical modes of velocities and relative vorticity suggest that barotropic and bottom-trapped planetary wave motions, distinct from baroclinic instability, are possible and indeed likely. A wavenumber analysis indicates that the northwestern part of an extended LC has down or up-slope phase components that are consistent with longer-period (~40 to 60 days) TRWs. It is not clear, from observations, how such waves may be generated by the advance of the LC and/or LC eddy over shoaling topography, and whether wave dispersion, which depends on bottom slope, can radiate lower-layer EKE to the west and northwest.

7.4 LC EDDY SEPARATION DYNAMICS

In this section an attempt is made to concisely summarize the dynamics associated with a LC eddy detachment, as derived from the new observations. There are some aspects, particularly those related to the initiation of upper-lower layer baroclinic instabilities that were not resolved by the array. However, the authors are aware that the present study's results revise some of the earlier ideas on LC eddy separation, which were mainly derived from remote sensing (e.g., Schmitz (2005)) as a purely upper-layer phenomenon, or model studies.

The analysis does not support a paradigm where small LC meanders progressively grow downstream along their path, starting from small amplitudes near the Yucatan Channel and reaching large amplitudes along the eastern and southbound portion of the LC, where the resulting trough extends across the neck and pinches off an eddy. The reasons are: (1) Using the fine spatial and temporal resolution afforded by these new observations, meanders could be

traced along entering segments or northern or southward segments of the LC path, but it was difficult to connect any cases that transited this full path. (2) Meander frequencies along the northward and southward flowing portions were factors of two to four apart. (3) The path around the LC could not remain connected while neighboring portions oscillated at different frequencies. (4) Upper-deep coupling occurred along the southward-flowing portion of the LC for periods between 40 and 100 days, whereas meanders with these periods could not be traced back to the Yucatan Channel. Altogether, the observational evidence collected during this experiment, based upon spatial and temporal resolution capable of resolving the short spatial and temporal scales of the meanders, strongly argues against the concept of a continuous frontal-perturbation growth from the Yucatan around to the pinch-off near the Dry Tortugas.

The following multi-part scenario is suggested. The location of the LC within the Gulf and its positioning relative to the Mississippi Fan play important roles in determining the stability of the LC. It is speculated that the timing of this is related to the annual cycle discussed in Chapter 5. When the LC has extended sufficiently far north, with the well-observed tendency to lean towards the northwest (explained by the Pichevin-Nof momentum paradox), the following processes develop, involving vertical coupling with deep eddies that appear to depend upon interactions with the bottom topography of the southern extent of the Mississippi Fan.

A. Along the western edge of the LC, flowing northward from Yucatan Channel, small-amplitude meanders of 20 to 10-day period propagate northward. They became more energetic near the times that the three LC eddies detached and separated. However, in the case of Franklin, this variability notably preceded detachment and final separation, and in the case of Hadal the energy peaks followed the separation event. Furthermore, the deep eddies within the 20 to 10-day period exhibited southward phase propagation in that region, and the downstream-propagating upper meanders and deep-eddy perturbations did not couple effectively to jointly develop. Hence, they did not exhibit baroclinic instability that would enable them to draw efficiently upon the potential energy of the LC. Instead, they decayed in amplitude as they approached the northern section of the LC. Their fate suggests that they may either radiate deep eddies and deep topographic-wave variability as they approach the northern section, or they may simply feed their relatively meager energy and momentum back into the upper-current mean potential and kinetic energy field.

B. Along the northeastern portion of the LC, as it turns southward, deep eddies approach this section of the LC's path from the NNE. Deep eddies that may have originated externally encounter preexisting small-amplitude upper-jet meanders or they may have developed from baroclinic instability of the LC itself in this location. The combined upper and deep eddy/meander structures jointly intensify via baroclinic instability. These meanders are strongly energetic at 100 to 40-day periodicities, and they translate downstream (southward) and grow. This was a characteristic pattern in Ekman, Franklin, and Hadal, and the regional average EKE built to a peak in the 100 to 40-day band prior to eddy detachments and separation. The process involved a sequence of two or three deep eddies entering at the NNE side and the development of progressively steeper meanders. After this steepening – a sort of 1-2 or 1-2-3 punch sequence of anticyclones and cyclones – the meander trough amplified sufficiently to reach across the neck of the LC and pinch it off. The intensified deep eddies followed the topographic contours of the Mississippi Fan and propagated across the LC neck. Consequently, the location where this mode

of pinch-off occurred, enabled a conjoined process involving the full water-column. Deep eddies jointly intensify with upper meanders with a phase offset that drew upon the enormous pool of available potential energy in the LC and bottom topography. Subsequently, the deep eddies propagated across the neck and radiated energy northwesterly into the Gulf.

The observations did not extend far enough north to identify the source of the deep eddies that initiated the large-scale meander growth on the east side of the LC. Possible sources are eddies to the northeast of the array. Le Hénaff et al. (2012) indicate, from model studies, that the flow of the LC itself over the Mississippi Fan could generate a deep cyclone on the downstream side by the stretching of the lower water column through potential vorticity conservation. Against this concept, it is noted that the northern LC front barely reached the Mississippi Fan for Ekman and Franklin, and yet the meanders still developed. Le Hénaff et al.'s (2012) model LC tends to extend further into the Gulf than is usually observed, so in that case the Mississippi Fan topography is more a factor. Interpretations of remotely sensed SSTs have mentioned the merging and stalling of LCFEs on the northern LC boundary, producing a large cyclone in the surface layer. An example is Walker et al.'s (2011) "super" cyclone on the northern boundary of Franklin. Given the arguments above, it is thought more likely that northern cyclone development is from the generation of a large meander trough by the baroclinic instability process.

7.5 LONG-TERM AND SEASONAL VARIABILITY

Gulf of Mexico datasets, over the time period from 1978 through 1992, were reviewed to derive pre-altimetry LC eddy separation dates. Datasets used included Seasat and ERS-1 altimetry, CZCS chlorophyll-a, AVHRR SST, HMI EddyWatchTM reports, and CASE/EJIP GEM analyses. The reanalysis identified 20 separation events. Separation dates were estimated to be accurate to approximately ± 1.5 months and sufficient to detect statistically significant LC eddy separation seasonality, which was not the case for previously published records because of misidentification of separation events and their timing.

The reanalysis indicated that previous reported LC eddy separation dates, determined for the time period before the advent of continuous altimetric monitoring in the early 1990s, are inaccurate because of extensive reliance on SST imagery from polar orbiting satellites. Satellite sensors and sampling used were insufficient to detect the thermal signal of the LC and LC eddies due to the warm seasonal mixed layer and extensive cloudiness during the months of June through October, a limitation that was recognized at that time.

Automated LC tracking techniques were used to derive LC eddy separation dates in three different altimetry datasets over the time period from 1993 through 2012. Between 28 and 30 LC eddy separation events were identified. Differences in dataset means and in objective-analysis smoothing caused differences in corresponding separation events between the datasets. Significance tests on various altimetry and pre-altimetry/altimetry combined date lists show that LC eddy separation events are more likely in the months March, August, and September, and less likely in December. LC eddy separation event dates were objectively divided into spring and fall seasons using a k-means clustering algorithm. The estimated spring and fall centers are 2 March and 23 August, respectively, with seasonal boundaries on 22 May and 3 December. LC

growth and wane is dominantly an annual process. LC metrics such as area, northern latitude, etc. are relatively high from January through about July and low in September and October.

The SSH dominant mode of a coastal EOF analysis of the Southeast U.S. and Gulf of Mexico continental shelves indicates that the dominant coastal signal co-varies with the LC, and accounts for 65% and 85% of the annual variance in LC northern latitude and LC area, respectively. There is a statistically significant annual cycle embedded within the highly variable cycle of LC intrusion, eddy separation, and retreat. This annual cycle is primarily driven by and dynamically linked to geostrophic currents, seaward of the shelf break, forced by coastal-trapped waves generated on the Southeast U.S. and Gulf of Mexico continental shelves.

7.6 RECOMMENDATIONS

Some fundamental questions on LC dynamics have been raised by the results of this study that will require some detailed model investigations in relation to the observations. One group of questions relates to the east-side meanders: Why when meanders form, do they have seemingly preferred wavelengths of ~ 300 km and periods of 40 to 60 days? What mechanisms trigger the baroclinic instabilities that promote meander growth? What is the fate of the westward propagating deep cyclones after a detachment is achieved? Another set of questions arises from remote forcing mechanisms for the LC: How does the mean annual signal in LC growth and wane arise? How does the baroclinic instability mechanism for LC eddy detachments fit in with the mean annual variability in eddy separations? Statistical connections have been made between the remote SSH signal on the west Florida shelf and slope with LC variability, but dynamical connections are largely speculative. On a more practical level, models need to show that meander formation and growth and the interaction of barotropic and baroclinic flows conform to these observational results. A comparative analysis of multiple model diagnostics of these processes would likely be illuminating.

From the above discussion, some aspects of the LC circulation processes remain unclear, and could be tackled with a follow-on study. Principally, the mechanisms that trigger the baroclinic instability that grow the east-side meanders through coupling with the lower layer appear to be the primary agent for LC eddy detachment. The observations suggest that a possible triggering mechanism is the propagation of deep eddies from the northeast, a region with almost no previous in-situ measurements. If these eddies are pertinent, then a number of questions arise such as how are they formed, and how do they interact with the surface-layer circulation? The LC itself may be an agent through remote forcing in generating deep eddies in the northeast, perhaps using the combined topography along the Mississippi Fan and the west Florida escarpment as wave-guides for disturbances initiated further south. It is also noted that the southeastern part of the deep basin has had no significant long-term measurements, and would also be a candidate region for a comprehensive observational study.

The second set of major questions relate to how the LC radiates deep energy into the western and northwestern Gulf. The Mississippi Fan is the major abyssal topographic feature in the area and it may act as a wave-guide for TRWs and eddies, and also perhaps as a barrier for LC deep EKE reaching some parts of the northern slope. It is observed that velocity measurements along the base of the northern continental slope are very inhomogeneous in both frequency content and energy levels (Cox et al. 2010, Donohue et al. 2006, Hamilton 2009). An explanation is that the

flows along the base of the slope are primarily due to the impingement of TRWs of differing frequencies and wavelengths that are radiated from the LC and separated LC eddies translating westward across the basin (Oey and Lee 2002). Rectification of such waves by shoaling topography (Mizuta and Hogg 2004) was invoked as the driving force for the strong mean westward flows observed along the Sigsbee escarpment (DeHaan and Sturges 2005), though Chang and Oey (2011) argue that a cyclonic deep gyre is also a response to the LC eddy shedding cycle. Chang and Oey's (2011) model result of upwelling across the base of the upper layer (1000 m) in the eastern basin, after an eddy is shed, was partially supported by the calculation of area-averaged vertical velocities at 900 m from the moored velocity measurements. Thus, observations of the westward pathways of energetic flows emanating from the LC, along with the role of topography, would be an advance in the understanding of Gulf circulation processes.

The deployment of PIES/mooring arrays in various regions of the deep Gulf has proved to be a cost-effective means of observing the 3-D geostrophic currents, temperature and salinity, as well as SSH and bottom pressure on a daily basis over relatively large areas which also resolve important eddy scales. Mapping arrays that have been deployed in the eastern Gulf under BOEM/MMS funding are shown in Figure 7.6-1. It is clear that there is a large gap in deep-water coverage in the northeast (and also in the southeast). Though the LC and Exploratory arrays are adjacent, the deployments are not coincident in time, and that would be required for signals to be traced from the LC to the Sigsbee escarpment. To fulfill the objectives listed below, a minimal PIES/mooring mapping array is given in Figure 7.6-2 as a starting point for further LC related studies.

- Determine the pathways of deep energy generated under the Loop Current.
- Quantify the upper and deep-layer interaction along those pathways.
- Identify trigger mechanisms for Loop Current meanders that lead to Loop Current eddy separations.
- Provide benchmarks/metrics to validate processes simulated by general ocean circulation models.

The experimental design covers the northern part of the LC from the west Florida escarpment across the Mississippi Fan to the eastern part of the Sigsbee escarpment. Resolution is 40 to 50 km, which is adequate for mapping lower-layer eddies and TRWs. The array could be supplemented to cover a greater area with additional PIES, CPIES, near-bottom moorings and full-depth moorings. The measurements can also be supplemented with simultaneous deployments of upper and lower-layer RAFOS and APEX floats. Simultaneous Lagrangian and Eulerian measurements in the context of a PIES/mooring mapping array would provide a more fine-grained perspective on wave and eddy propagation. Similarly, the deployment of APEX profiling floats within the array would map water properties and provide calibration data for the PIES. It is recommended that this type of array be deployed for a minimum of two to three years so as to catch two to three LC eddy separations. Being able to compare three eddy separations during the present LC study was important to the subsequent analysis and made the results much more robust.

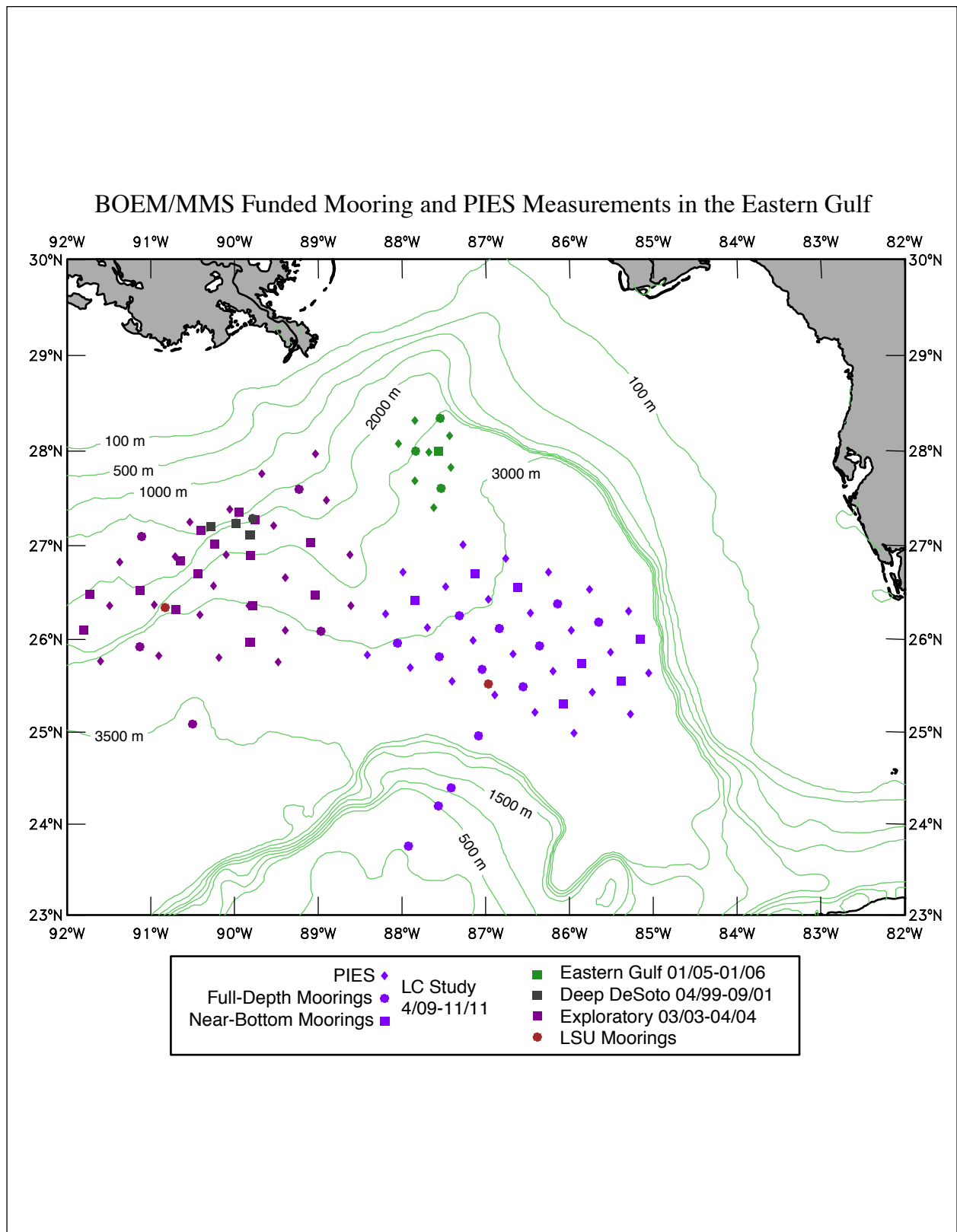


Figure 7.6-1. PIES/mooring arrays deployed in the eastern Gulf for this and prior BOEM/MMS programs.

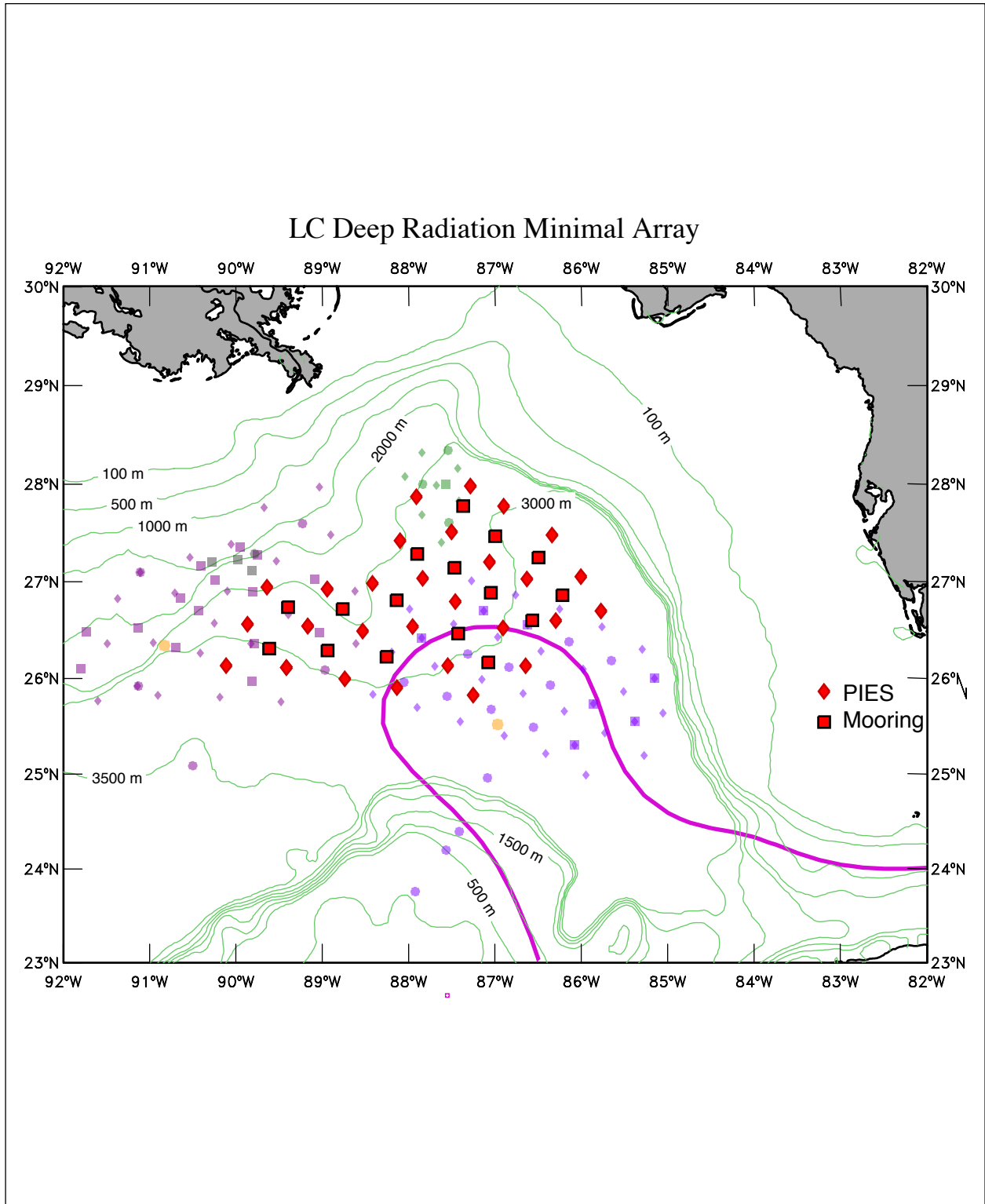


Figure 7.6-2. A possible configuration of PIES and moorings for a LC radiation experiment. The mean location of the 17-cm SSH contour for the 2 1/2 year LC study period is shown by the purple line. Previous locations of PIES and moorings from Figure 7.6-1 are shown in faded colors.

7.7 DEEPWATER HORIZON OIL SPILL

The *Deepwater Horizon* disaster on 20 April 2010, and the subsequent discharge of large quantities of oil and gas into the northern Gulf of Mexico over the next three months (Liu et al. 2011a) took place during the growth and first detachments of Franklin. Because the LC/Franklin had intruded north of 26°N, there was considerable concern at the time, that oil could be transported southwards to the Florida Keys and further east to Miami (Weisberg 2011), particularly as a large patch of surface oil accumulated in a northern meander trough or “super” cyclone in mid-May 2010 (Walker et al. 2011). However, hydrocarbon measurements made at PIES sites in July 2010 under the auspices of this program (Wade et al. 2011) showed no significant accumulation of oil within the LC. The implications of this finding were that any surface oil entrained into the LC was rapidly dispersed, or the Lagrangian flow fields within the meander trough and in the LC were distinct “manifolds” (Kuznetsov et al. 2002), and water parcels in the trough did not interact with those south of the LC boundary. Oil slicks were not observed south of the northern LC boundary, and surface drifters in the two regions did not intermingle and cross the LC front (Liu et al. 2011b). This may be explained by the relative isolation of LC and LC eddy water masses from external Gulf waters. In particular, as a further example of this isolation, it is noted that the sub-tropical underwater (SUW) salinity maximum (> 36.5 psu) at 100 to 200 m depth in LC eddies is still identifiable all the way to the western boundary of the basin (Brooks 1984; Donohue et al. 2008).

CHAPTER 8: REFERENCES

- Allen, M.R. and L.A. Smith. 1996. Monte Carlo SSA: Detecting irregular oscillations in the presence of colored noise. *J. Climate* 9(12):3373-3404. doi: 10.1175/1520-0442(1996)009<3373:MCSPIO>2.0.CO;2.
- Alvera-Azcarate, A., A. Barth, and R.H. Weisberg. 2009. The surface circulation of the Caribbean Sea and the Gulf of Mexico as inferred from satellite altimetry. *J. Phys. Oceanogr.* 39(3):640-657. doi: 10.1175/2008JPO3765.1.
- Anderson, D.L.T. and A.E. Gill. 1979. Beta dispersion of inertial waves. *J. Geophys. Res.* 84(C4):1836-1842. doi: 10.1029/JC084iC04p1836.
- Andrade-Canto, F., J. Sheinbaum, and L.Z. Sanson. 2013. A Lagrangian approach to the Loop Current eddy separation. *Nonlin. Process. Geophys.* 20:85-96. doi: 10.5194/npg-20-85-2013.
- AVISO+. Sea Surface Height Products [Internet]. Aviso User Service, CLS/DOS, 8-10 rue Hermès, Parc Technologique du Canal F-31520 Ramonville St-Agne, France. Available from: <http://www.aviso.altimetry.fr/en/data/products/sea-surface-height-products.html> .
- Bane, J.M., Jr., D.A. Brooks, and K.R. Lorenson. 1981. Synoptic observations of the three-dimensional structure and propagation of Gulf Stream meanders along the Carolina continental margin. *J. Geophys. Res.* 86(C7):6411-6425.
- Behringer, D.W., R.L. Molinari, and J.F. Festa. 1977. The variability of anticyclonic current patterns in the Gulf of Mexico. *J. Geophys. Res.* 82(34):5469-5478. doi: 10.1029/JC082i034p05469.
- Berens, P. 2009. CircStat: A Matlab toolbox for circular statistics. *J. Statistical Software* 31(10):1-21.
- Berntsen, J. and L.-Y. Oey. 2010. Estimation of the internal pressure gradient in σ -coordinate ocean models: comparison of second-, fourth-, and sixth-order schemes. *Ocean Dynamics* 60:317-330. doi: 10.1007/s10236-009-0245-y.
- Bishop, S.P., D.R. Watts, J.-H. Park, and N.G. Hogg. 2012. Evidence of bottom-trapped currents in the Kuroshio extension region. *J. Phys. Oceanogr.* 42(2):321-328. doi: 10.1175/JPO-D-11-0144.1.
- Bretherton, F.P., R.E. Davis, and C.B. Fandry. 1976. A technique for objective analysis and design of oceanographic experiments applied to MODE-73. *Deep Sea Res.* 23:559-582.
- Briggs, W.L. 1987. A multigrid tutorial. Philadelphia, PA: Soc. For Ind. and Appl. Math.. 88 pp.

- Brink, K.H. 1989. Observations of the response of thermocline currents to a hurricane. *J. Phys. Oceanogr.* 19(7):1017-1022. doi: 10.1175/1520-0485(1989)019<1017:OOTROT>2.0.CO;2.
- Brooks, D.A. 1983. The wake of Hurricane Allen in the western Gulf of Mexico. *J. Phys. Oceanogr.* 13(1):117-129.
- Brooks, D.A. 1984. Current and hydrographic variability in the northwestern Gulf of Mexico. *J. Geophys. Res.* 89(C5):8022-8032. doi: 10.1029/JC089iC05p08022.
- Bunge, L., J. Ochoa, A. Badan, J. Candela, and J. Scheinbaum. 2002. Deep flows in the Yucatan Channel and their relation to changes in the Loop Current extension. *J. Geophys. Res.* 107(C12):3233. doi: 10.1029/2001JC001256.
- Candela, J., J. Scheinbaum, J. Ochoa, A. Badan, and R. Leben. 2002. The potential vorticity flux through the Yucatan Channel and the Loop Current in the Gulf of Mexico. *Geophys. Res. Lett.* 29(22):2059. doi:10.1029/2002GL015587.
- Carrère, L. and F. Lyard. 2003. Modeling the barotropic response of the global ocean to atmospheric wind and pressure forcing - comparisons with observations. *Geophys. Res. Lett.* 30(6):1275. doi: 10.1029/2002GL016473.
- Casey, K.S., T.B. Brandon, P. Cornillon, and R. Evans. 2010. The past, present, and future of the AVHRR Pathfinder SST Program [Internet]. In: Barale, V., J.F.R. Gower, and L. Alberotanza, eds. *Oceanography from Space: Revisited*. Springer. pp. 323-341. Available from: <http://www.nodc.noaa.gov/SatelliteData/pathfinder4km/>.
- Chang, Y.-L. and L.-Y. Oey. 2010a. Why can wind delay the shedding of Loop Current eddies? *J. Phys. Oceanogr.* 40(11):2481-2495. doi: 10.1175/2010JPO4460.1.
- Chang, Y.-L. and L.-Y. Oey. 2010b. Eddy and wind-forced heat transports in the Gulf of Mexico. *J. Phys. Oceanogr.* 40(12):2728-2742. doi: 10.1175/2010JPO4474.1.
- Chang, Y.-L. and L.-Y. Oey. 2011. Loop Current cycle: Coupled response of the Loop Current with deep flows. *J. Phys. Oceanogr.* 41(3):458-471. doi: 10.1175/2010JPO4479.1.
- Chang, Y.-L. and L.-Y. Oey. 2012. Why does the Loop Current tend to shed more eddies in summer and winter? *Geophys. Res. Lett.* 39(5):L05605. doi: 10.1029/2011GL050773.
- Chang, Y.-L. and L.-Y. Oey. 2013a. Loop Current growth and eddy shedding using models and observations: Numerical process experiments and satellite altimetry data. *J. Phys. Oceanogr.* 43(3):669-689. doi: 10.1175/JPO-D-12-0139.1.
- Chang, Y.-L. and L.-Y. Oey. 2013b. Coupled response of the Trade Wind, SST gradient, and SST in the Caribbean Sea, and the potential impact on Loop Current's interannual variability. *J. Phys. Oceanogr.* 43(7):1325-1344. doi: 10.1175/JPO-D-12-0183.1.

- Chelton, D.B., M.G. Schlax, and R.M. Samelson. 2011. Global observations of nonlinear mesoscale eddies. *Progr. Oceanogr.* 91:167-216.
- Cheney, R.E., J.G. Marsh, and B.D. Beckley. 1983. Global mesoscale variability from collinear tracks of SEASAT altimeter data. *J. Geophys. Res.* 88(C7):4343-4354. doi: 10.1029/JC088iC07p04343.
- Chereskin, T.K., M.Y. Morris, P.P. Niiler, P.M. Kosro, R.L. Smith, S.R. Ramp, C.A. Collins, and D.L. Musgrave. 2000. Spatial and temporal characteristics of the mesoscale circulation of the California Current for eddy-resolving moored and shipboard measurements. *J. Geophys. Res.* 105(C1):1245-1270. doi: 10.1029/1999JC900252.
- Chérubin, L.M., W. Sturges, and E.P. Chassignet. 2005. Deep flow variability in the vicinity of the Yucatan Straits from a high-resolution numerical simulation. *J. Geophys. Res.* 110(C4):C04009. doi: 10.1029/2004JC002280.
- Chérubin, L.M., Y. Morel, and E.P. Chassignet. 2006. Loop Current ring shedding: The formation of cyclones and the effect of topography. *J. Phys. Oceanogr.* 36(4):569-591.
- Chin, T.M. Multi-scale ultra-high resolution sea surface temperature [Internet]. NASA JPL Physical Oceanography DAAC, Pasadena, CA [cited 2012 January]. Available from: <http://mur.jpl.nasa.gov/>.
- Cochrane, J.D. 1965. The Yucatan Current and equatorial currents of the western Atlantic. In: Unpublished Report Ref. 65-17-T. Dept. of Oceanography and Meteorology, Texas A&M University, College Station, TX. pp. 6-27.
- Coholan, P.D., J.W. Feeney, and S.P. Anderson. 2008. Life and times of Eddy Zorro: A review of the 2007 Gulf of Mexico Loop Current activity. Offshore Technology Conference, 5-8 May 2008, Houston, TX, USA. Paper OTC-19413-MS, 9 pp., doi: 10.4043/19413-MS.
- Cooper, C. and J. Stear. 2009. Estimating design currents during Joint Eddy-TRWs and Joint Eddy-Hurricanes. Offshore Technology Conference, 4-7 May 2009, Houston, TX, USA. Paper OTC-19985-MS, 10 pp., doi: 10.4043/19985-MS.
- Cox, J., C. Coomes, S. DiMarco, K. Donohue, G.Z. Forristall, P. Hamilton, R.R. Leben, and D.R. Watts. 2010. Study of deepwater currents in the Eastern Gulf of Mexico. U.S. Dept. of the Interior, Bureau of Ocean Energy Management, Regulation, and Enforcement, Gulf of Mexico OCS Region, New Orleans, LA. OCS Study BOEMRE 2010-041. 473pp.
- Craig, P.D. and M.L. Banner. 1994. Modeling wave-enhanced turbulence in the ocean surface layer. *J. Phys. Oceanogr.* 24(12):2546-2559. doi:10.1175/1520-0485(1994)024<2546:MWETIT>2.0.CO;2.
- Cressman, G.P. 1959. An operational objective analysis system. *Mon. Weather Rev.* 87(10):367-374.

- Cronin, M. and D.R. Watts. 1996. Eddy-mean flow interaction in the Gulf Stream at 68°W. Part I: Eddy energetics. *J. Phys. Oceanogr.* 26:2107-2131.
- Cushman-Roisin, B. and J.-M. Beckers. 2011. *Introduction to Geophysical Fluid Dynamics: Physical and Numerical Aspects*. 2nd ed. International Geophysics Series, 101. Waltham, MA: Academic Press. 828 pp.
- Cushman-Roisin, B. 1994. *Introduction to geophysical fluid dynamics*. New Jersey: Prentice-Hall. 320 pp.
- Cushman-Roisin, B., L. Pratt, and E. Ralph. 1993. A general theory for equivalent barotropic thin jets. *J. Phys. Oceanogr.* 23:91-103.
- CZCS. 2008. The Coastal Zone Color Scanner experiment [Internet]. National Aeronautics and Space Administration. Available from: <http://oceancolor.gsfc.nasa.gov/CZCS/>.
- DeHaan, C.J. and W. Sturges. 2005. Deep cyclonic circulation in the Gulf of Mexico. *J. Phys. Oceanogr.* 35(10):1801-1812.
- Dibarboure, G., M.-I. Pujol, F. Briol, P.Y. Le Traon, G. Larnicol, N. Picot, F. Mertz, and M. Ablain. 2011. Jason-2 in DUACS: Updated system description, first tandem results and impact on processing and products. *Mar. Geodesy* 34(3-4):214-241.
- Dickey, T., D. Frye, J. McNeil, D. Manov, N. Nelson, D. Sigurdson, H. Jannasch, D. Siegel, T. Michaels, and R. Johnson. 1998. Upper-ocean temperature response to hurricane Felix as measured by the Bermuda testbed mooring. *Mon. Weather Rev.* 126(5):1195-1201. doi: 10.1175/1520-0493(1998)126<1195:UOTRTH>2.0.CO;2.
- Donohue, K.A., D.R. Watts, K.L. Tracey, A.D. Greene, and M. Kennelly. 2010. Mapping circulation in the Kuroshio Extension with an array of current and pressure recording Inverted Echo Sounders. *J. Atmos. Oceanic Technol.* 27(3):507-527. doi: 10.1175/2009JTECHO686.1.
- Donohue, K., P. Hamilton, K. Leaman, R. Leben, M. Prater, D.R. Watts, and E. Waddell. 2006. Exploratory study of deepwater currents in the Gulf of Mexico. Volume II: Technical report. U.S. Dept. of the Interior, Minerals Management Service, Gulf of Mexico OCS Region, New Orleans, LA. OCS Study MMS 2006-074. 430 pp.
- Donohue, K., P. Hamilton, R. Leben, R. Watts, and E. Waddell. 2008. Survey of deepwater currents in the northwestern Gulf of Mexico. Volume II: Technical report. U.S. Dept. of the Interior, Minerals Management Service, Gulf of Mexico OCS Region, New Orleans, LA. OCS Study MMS 2008-031. 375 pp.
- Ducet, N., P.Y. Le Traon, and G. Reverdin. 2000. Global high-resolution mapping of ocean circulation from TOPEX/Poseidon and ERS-1 and -2. *J. Geophys. Res.* 105(C8):19477-19498. doi: 10.1029/2000JC900063.

- Egbert, G.D. and S.Y. Erofeeva. 2002. Efficient inverse modeling of barotropic ocean tides. *J. Atmos. Oceanic Technol.* 19(2):183-204. doi: 10.1175/1520-0426(2002)019 <0183:EIMOBO>2.0.CO;2.
- Evans Hamilton, Inc. (EHI). 1992. The climatology and simulation of eddies. Final report to Exxon Prod. Res. Co. 216 pp.
- Fan, S., L.-Y. Oey, and P. Hamilton. 2004. Assimilation of drifter and satellite data in a model of the northeastern Gulf of Mexico. *Cont. Shelf Res.* 24(9):1001-1013.
- Fofonoff, N.P. and R.M. Hendry. 1985. Current variability near the southeast Newfoundland Ridge. *J. Phys. Oceanogr.* 15(7):963-984.
- Forristall, G.Z., R.R. Leben, and C.A. Hall. 2010. A statistical hindcast and forecast model for the Loop Current (OTC-20602-MS). In: Offshore Technology Conference 2010 (OTC 2010), Houston, Texas, USA, 3-6 May 2010, Volume 2. Curran Associates, Inc., Red Hook, NY. pp.1201-1212.
- Franz, B. 2006. Implementation of SST processing within OBPG [Internet]. National Aeronautics and Space Administration (NASA). Available from: http://oceancolor.gsfc.nasa.gov/DOCS/modis_sst/.
- Fu, L.-L. and B. Holt. 1982. Seasat Views Ocean and Sea Ice with Synthetic-Aperture Radar. JPL Publication 81-120. Jet Propulsion Laboratory, California Institute of Technology, Pasadena, CA. pp. 52-53.
- Fu, L.-L., D. Stammer, R.R. Leben, and D.B. Chelton. 2003. Improved spatial resolution of ocean surface topography from the T/P-Jason-1 altimeter mission. *EOS, Trans. Amer. Geophys. Un.* 84(26):241-248. doi: 10.1029/2003EO260002.
- Garrett, C. 2001. What is the "Near-Inertial" band and why is it different from the rest of the internal wave spectrum? *J. Phys. Oceanogr.* 31(4):962-971. doi: 10.1175/1520-0485(2001)031<0962:WITNIB>2.0.CO;2.
- Gill, A.E. 1984. On the behavior of internal waves in the wakes of storms. *J. Phys. Oceanogr.* 14(7):1129-1151.
- Gille, S.T. and C.W. Hughes. 2001. Aliasing of high-frequency variability by altimetry: Evaluation from bottom pressure recorders. *Geophys. Res. Lett.* 28(9):1755-1758. doi: 10.1029/2000GL012244.
- Glenn, S.M., G.Z. Forristall, P. Cornillon, and G. Milkowski. 1990. Observations of Gulf Stream ring 83-E and their interpretation using feature models. *J. Geophys. Res.* 95(C8):13043-13063.

- GCMD. U.S. Naval Oceanographic Office (NAVOCEANO)'s AVHRR MCSST global satellite daily Sea Surface Temperature (SST) retrievals [Internet]. NASA Global Change Master Directory (GCMD) [cited 2012]. Available from: http://gcmd.nasa.gov/records/GCMD_NAVOCEANO_MCSST.html .
- GHRSSST. GHRSSST Level 4 MUR Global Foundation Sea Surface Temperature Analysis [Internet]. NASA JPL Physical Oceanography DAAC, Pasadena, CA [cited 2012 January]. Available from: <http://podaac.jpl.nasa.gov/dataset/JPL-L4UHfnd-GLOB-MUR> .
- GOES3 c2009. GOES Level 3 6km Near Real Time SST 24 Hour [Internet]. NASA JPL Physical Oceanography DAAC, Pasadena, CA. Available from: http://podaac.jpl.nasa.gov/dataset/GOES_L3_SST_6km_NRT_SST_24HOUR .
- Grant, W.D. and O.S. Madsen. 1979. Combined wave and current interaction with a rough bottom. *J. Geophys. Res.* 84(C4):1797-1808.
- Greatbatch, R.J. 1983. On the response of the ocean to a moving storm: the nonlinear dynamics. *J. Phys. Oceanogr.* 13(3):357-367. doi: 10.1175/1520-0485(1983)013<0357:OTROTO>2.0.CO;2.
- Greenslade, D.J.M., D.B. Chelton, and M.G. Schlax. 1997. The midlatitude resolution capability of sea level fields constructed from single and multiple altimeter datasets. *J. Atmos. Oceanic Technol.* 14(4):849-870.
- Gregg, W.W., M.E. Conkright, J.E. O'Reilly, F.S. Patt, M.H. Wang, J.A. Yoder, and N.W. Casey. 2002. NOAA-NASA coastal zone color scanner reanalysis effort. *Appl. Optics* 41(9):1615-1628. doi: 10.1364/AO.41.001615.
- Griesel, A., S.T. Gille, J. Sprintall, J.L. McClean, and M.E. Maltrud. 2009. Assessing eddy heat flux and its parameterization: A wavenumber perspective from a $1/10^\circ$ ocean simulation. *Ocean Modelling* 29:248-260.
- Grinsted, A., J.C. Moore, and S. Jevrejeva. 2004. Application of the cross wavelet transform and wavelet coherence to geophysical time series. *Nonlin. Process. Geophys.* 11:561-566. doi: 10.5194/npg-11-561-2004.
- Haidvogel, D.B., H. Arango, W.P. Budgell, B.D. Cornuelle, E. Curchitser, E. DiLorenzo, K. Fennel, W.R. Geyer, A.J. Hermann, L. Lanerolle, J. Levin, J.C. McWilliams, A.J. Miller, A.M. Moore, T.M. Powell, A.F. Shchepetkin, C.R. Sherwood, R.P. Signell, J.C. Warner, and J. Wilkin. 2008. Ocean forecasting in terrain-following coordinates: Formulation and skill assessment of the Regional Ocean Modeling System. *J. Compu. Phys.* 227(7):3595-3624. doi: 10.1016/j.jcp.2007.06.016.
- Hamilton, P. 1990. Deep currents in the Gulf of Mexico. *J. Phys. Oceanogr.* 20(7):1087-1104.

- Hamilton, P. 2007. Deep-current variability near the Sigsbee Escarpment in the Gulf of Mexico. *J. Phys. Oceanogr.* 37:708-726.
- Hamilton, P. 2009. Topographic Rossby waves in the Gulf of Mexico. *Progr. Oceanogr.* 82:1-31. doi: 10.1016/J.POCEAN.2009.04.019.
- Hamilton, P. and A. Lugo-Fernández. 2001. Observations of high speed deep currents in the northern Gulf of Mexico. *Geophys. Res. Lett.* 28(14):2867-2870. doi: 10.1029/2001GL013039.
- Hamilton, P. and T.N. Lee. 2005. Eddies and jets over the slope of the northeast Gulf of Mexico. In: Sturges, W. and A. Lugo-Fernández, eds. *Circulation in the Gulf of Mexico: Observations and models*, Geophysical Monograph 161. American Geophysical Union, Washington, DC. pp. 123-142.
- Hamilton, P., J.J. Singer, E. Waddell, and K. Donohue. 2003. Deepwater observations in the northern Gulf of Mexico from in-situ current meters and PIES. Final report. Volume II: Technical report. U.S. Dept. of the Interior, Minerals Management Service, Gulf of Mexico OCS Region, New Orleans, LA. OCS Study MMS 2003-049. 95 pp.
- Hamilton, P., K.A. Donohue, R.R. Leben, A. Lugo-Fernández, and R.E. Green. 2011. Loop Current observations during spring and summer of 2010: Description and historical perspective. In: Liu, Y., A. MacFadyen, Z.-G. Ji, and R.H. Weisberg, eds. *Monitoring and modeling the Deepwater Horizon oil spill: A record-breaking enterprise*, Geophysical Monograph 195. American Geophysical Union, Washington, DC. pp.117-130. doi: 10.1029/2011GM001116.
- Hamilton, P., T.J. Berger, J.J. Singer, E. Waddell, J.H. Churchill, R.R. Leben, T.N. Lee, and W. Sturges. 2000. DeSoto Canyon eddy intrusion study. Final report. Volume II: Technical report. U.S. Dept. of the Interior, Minerals Management Service, Gulf of Mexico OCS Region, New Orleans, LA. OCS Study MMS 2000-080. 275 pp.
- Hendricks, J.R., R.R. Leben, G.H. Born, and C.J. Koblinsky. 1996. Empirical orthogonal function analysis of global TOPEX/POSEIDON altimeter data and implications for detection of global sea level rise. *J. Geophys. Res.* 101(C6):14131-14146. doi: 10.1029/96JC00922.
- Hendry, R.M., D.R. Watts, and C.S. Meinen. 2002. Newfoundland Basin sea-level variability from TOPEX/POSEIDON altimetry and inverted echo sounder-bottom pressure measurements. *Can. J. Remote Sensing* 28(4):544-555.
- Hogg, N.G. 2000. Low-frequency variability on the western flanks of the Grand Banks. *J. Mar. Res.* 58(4):523-545.

- Hong, B.G., W. Sturges, and A.J. Clarke. 2000. Sea level on the U.S. east coast: Decadal variability caused by open ocean wind-curl forcing. *J. Phys. Oceanogr.* 30(8):2088-2098. doi: 10.1175/1520-0485(2000)030<2088:SLOTUS>2.0.CO;2.
- Howden, S.D. 2000. The three-dimensional secondary circulation in developing Gulf Stream meanders. *J. Phys. Oceanogr.* 30(5):888-915. doi: 10.1175/1520-0485(2000)030<0888:TTDSCI>2.0.CO;2.
- HRD. H*Wind Analyses [Internet]. Hurricane Research Division, Atlantic Oceanographic and Meteorological Laboratory, NOAA, Miami, FL. Available from: http://www.aoml.noaa.gov/hrd/data_sub/wind.html .
- Huh, O.K., W.J. Wiseman, Jr., and L.J. Rouse, Jr. 1981. Intrusion of Loop Current waters onto the west Florida continental shelf. *J. Geophys. Res.* 86(C5):4186-4192.
- Hurlburt, H.E. and J.D. Thompson. 1980. A numerical study of Loop Current intrusions and eddy shedding. *J. Phys. Oceanogr.* 10(10):1611-1651. doi: 10.1175/1520-0485(1980)010<1611:ANSOLC>2.0.CO;2.
- Hurlburt, H.E. and J.D. Thompson. 1982. The dynamics of the Loop Current and shed eddies in a numerical model of the Gulf of Mexico. In: Nihoul, J.C.J., ed. *Hydrodynamics of semi-enclosed seas*, Vol. 34, Elsevier Oceanography Series. Elsevier Scientific Publ. Co., New York. pp. 243-297. doi: 10.1016/S0422-9894(08)71247-9.
- HYCOM. Hybrid Coordinate Ocean Model data server [Internet]. Consortium for Data Assimilative Modeling, COAPS, Florida State University, Tallahassee, FL. Available from: <http://hycom.org/dataserver> .
- Inoue, M., S.E. Welsh, L.J. Rouse, Jr., and E. Weeks. 2008. Deepwater currents in the eastern Gulf of Mexico: Observations at 25.5°N and 87°W. U.S. Dept. of the Interior, Minerals Management Service, Gulf of Mexico OCS Region, New Orleans, LA. OCS Study MMS 2008-001. 95 pp.
- Jammalamadaka, S.R. and A. SenGupta. 2001. *Topics in circular statistics. Series on multivariate analysis, Volume 5*, Singapore: World Scientific Publishing. 336 pp.
- Jordi, A. and D.-P. Wang. 2012. sbPOM: A parallel implementation of the Princeton Ocean Model. *Environmental Modeling & Software*, 39: 58-61. doi: 10.1016/j.envsoft.2012.05.013. Available from: <http://www.imedea.uib-csic.es/users/toni/sbpom/> .
- Kantha, L., J.-K. Choi, K.J. Schaudt, and C.K. Cooper. 2005. A regional data-assimilative model for operational use in the Gulf of Mexico. In: Sturges, W. and A. Lugo-Fernández, eds. *Circulation in the Gulf of Mexico: Observations and models*, Geophysical Monograph 161. American Geophysical Union, Washington DC. pp. 165-180.

- Kim, K.-Y. and Q. Wu. 1999. A comparison study of EOF techniques: Analysis of nonstationary data with periodic statistics. *J. Climate* 12(1):185-199. doi: 10.1175/1520-0442-12.1.185.
- Kirwan, A.D., Jr., G. McNally, and J. Coehlo. 1976. Gulf Stream kinematics inferred from a satellite-tracked drifter. *J. Phys. Oceanogr.* 6(5):750-755. doi: 10.1175/1520-0485(1976)006<0750:GSKIFA>2.0.CO;2.
- Kirwan, A.D., Jr., W.J. Merrell, Jr., J.K. Lewis, and R.E. Whitaker. 1984. Lagrangian observations of an anticyclonic ring in the western Gulf of Mexico. *J. Geophys. Res.* 89(C3):3417-3424. doi: 10.1029/JC089iC03p03417.
- Koblinsky, C.J., B.D. Beckley, R.D. Ray, Y.-M. Wang, L. Tsaoussi, A. Brenner, and R. Williamson. 1998. NASA Ocean altimeter pathfinder project. Report 1: Data processing handbook. NASA/TM-1998-208605.
- Kontoyiannis, H. and D.R. Watts. 1994. Observations on the variability of the Gulf Stream path between 74°W and 70°W. *J. Phys. Oceanogr.* 24(9):1999-2013. doi: 10.1175/1520-0485(1994)024<1999:OOTVOT>2.0.CO;2.
- Kramer, H.J. 2002. *Observation of the earth and its environment: Survey of missions and sensors.* 4th ed.: Springer-Verlag. 1510 pp.
- Kundu, P.K. and J.S. Allen. 1976. Some three-dimensional characteristics of low-frequency current fluctuations near the Oregon coast. *J. Phys. Oceanogr.* 6(2):181-199.
- Kunze, E. 1985. Near-inertial wave propagation in geostrophic shear. *J. Phys. Oceanogr.* 15(5):544-565.
- Kuznetsov, L., M. Toner, A.D. Kirwan, Jr., C.K.R.T. Jones, L.H. Kantha, and J. Choi. 2002. The Loop Current and adjacent rings delineated by Lagrangian analysis of the near-surface flow. *J. Mar. Res.* 60(3):405-429. doi: 10.1357/002224002762231151.
- LaCasce, J.H. 1998. A geostrophic vortex over a slope. *J. Phys. Oceanogr.* 28(12):2362-2381. doi: 10.1175/1520-0485(1998)028<2362:AGVOAS>2.0.CO;2.
- Leben, R.R. 2005. Altimeter-derived Loop Current metrics. In: Sturges, W. and A. Lugo-Fernández, eds. *Circulation in the Gulf of Mexico: Observations and models*, Geophysical Monograph 161. American Geophysical Union, Washington, DC. pp. 181-201.
- Leben, R.R. and C.A. Hall. 2010. A 30-year record of Loop Current eddy separation events. *EOS, Trans. Amer. Geophys. Un.* 91(26). *Ocean Sci. Meet. Suppl.*, Abstract PO45E-02.
- Leben, R.R. and G.H. Born. 1993. Tracking Loop Current eddies with satellite altimetry. *Adv. Space Res.* 13(11):325-333.

- Leben, R.R., C.A. Hall, and N.G. Hoffmann. 2012. The relationship between Loop Current separation period and retreat latitude revisited. In: McKay, M. and J. Nides, eds. Proceedings: Twenty-sixth Gulf of Mexico information transfer meeting, March 2011. U.S.Dept. of the Interior, Bureau of Ocean Energy Management, Gulf of Mexico OCS Region, New Orleans, LA. OCS Study BOEM-2012-107. pp.37-41.
- Leben, R.R., G.H. Born, and B.R. Engebret. 2002. Operational altimeter data processing for mesoscale monitoring. *Mar. Geodesy* 25(1-2):3-18. doi: 10.1080/014904102753516697.
- Lee, T. and P. Cornillon. 1996. Propagation of Gulf Stream meanders between 74° and 70°W. *J. Phys. Oceanogr.* 26(2):205-224. doi: 10.1175/1520-0485(1996)026<0205:POGSMB>2.0.CO;2.
- Lee, T.N. and L.P. Atkinson. 1983. Low-frequency current and temperature variability from Gulf Stream frontal eddies and atmospheric forcing along the southeast U.S. outer continental shelf. *J. Geophys. Res.* 88(C8):4541-4567.
- Legeckis, R. 1976. Present and planned satellite observations of the Gulf of Mexico and the Caribbean Sea (abstract). In: H.B. Stewart, Jr., ed. Progress in Marine Research in the Caribbean and Adjacent Regions, CICAR-II Symposium, 12-16 July 1976, Caracas, Venezuela. p.239.
- Le Hénaff, M., V.H. Kourafalou, Y. Morel, and A. Srinivasan. 2012. Simulating the dynamics and intensification of cyclonic Loop Current frontal eddies in the Gulf of Mexico. *J. Geophys. Res.* 117(C2):2034. doi: 10.1029/2011JC007279.
- Leipper, D.F. 1967. Observed ocean conditions and Hurricane Hilda. *J. Atmos. Sci.* 24(2):182–196.
- Leipper, D.F. 1970. A sequence of current patterns in the Gulf of Mexico. *J. Geophys. Res.* 75(3):637-657.
- Le Traon, P.Y., F. Nadal, and N. Ducet. 1998. An improved mapping method of multisatellite altimeter data. *J. Atmos. Oceanic Technol.* 15(2):522-534. doi: 10.1175/1520-0426(1998)015<0522:AIMMOM>2.0.CO;2.
- Le Traon, P.Y., Y. Faugère, F. Hernandez, J. Dorandeu, F. Mertz, and M. Ablain. 2003. Can we merge GEOSAT follow-on with TOPEX/POSEIDON and ERS-2 for an improved description of the ocean circulation? *J. Atmos. Oceanic Technol.* 20(6):889-895. doi: 10.1175/1520-0426(2003)020<0889:CWMGFV>2.0.CO;2.
- Li, J. and A.J. Clarke. 2005. Interannual flow along the northern coast of the Gulf of Mexico. *J. Geophys. Res.* 110(C11):C11002. doi: 10.1029/2004JC002606.
- Lin, X.-H., L.-Y. Oey, and D.-P. Wang. 2007. Altimetry and drifter assimilations of Loop Current and eddies. *J. Geophys. Res.* 112(C5):C05046. doi:10.1029/2006JC003779.

- Lindo-Atichati, D., F. Bringas, and G. Goni. 2013. Loop Current excursions and ring detachments during 1993-2009. *Intl. J. Rem. Sens.* 34(14):5042-5053. doi: 10.1080/01431161.2013.787504.
- Lindstrom, S.S. and D.R. Watts. 1994. Vertical motion in the Gulf Stream near 68°W. *J. Phys. Oceanogr.* 24:2321-2333.
- Liu, Y., A. MacFadyen, Z.-G. Ji, and R.H. Weisberg, eds. 2011a. Monitoring and modeling the Deepwater Horizon oil spill: A record breaking enterprise. *Geophysical Monograph* 195. Washington, DC: American Geophysical Union. 271 pp.
- Liu, Y., R.H. Weisberg, C. Hu, C. Kovach, and R. Riethmüller. 2011b. Evolution of the Loop Current system during the Deepwater Horizon oil spill event as observed with drifters and satellites. In: Liu, Y., A. MacFadyen, Z.-G. Ji, and R.H. Weisberg, eds. *Monitoring and modeling the Deepwater Horizon oil spill: A record-breaking enterprise*, *Geophysical Monograph* 195. American Geophysical Union, Washington, DC. pp. 91-102. doi: 10.1029/2011GM001127.
- Lugo-Fernández, A. and R.R. Leben. 2010. On the linear relationship between Loop Current retreat latitude and eddy separation period. *J. Phys. Oceanogr.* 40(12):2778-2784. doi: 1175/2010JPO4354.1.
- Luther, M.E. and J.M. Bane. 1985. Mixed instabilities in the Gulf Stream over the continental slope. *J. Phys. Oceanogr.* 15(1):3-23.
- Malanotte-Rizzoli, P., D.B. Haidvogel, and R.E. Young. 1987. Numerical simulation of transient boundary-forced radiation, Part I: The linear regime. *J. Phys. Oceanogr.* 17(9):1439-1457. doi: 10.1175/1520-0485(1987)017<1439:NSOTBF>2.0.CO;2.
- Maltrud, M., S. Peacock, and M. Visbeck. 2010. On the possible long-term fate of oil released in the Deepwater Horizon incident, estimated using ensembles of dye release simulations. *Environ. Res. Lett.* 5(3):1-7. doi: 10.1088/1748-9326/5/3/035301.
- Maul, G.A. 1975. An evaluation of the use of the earth resources technology satellite for observing ocean current boundaries in the Gulf Stream system. Tech. Rep. ERL 335 AOML-18:125. NOAA, NWS.
- Maul, G.A. 1977. The annual cycle of the Gulf Loop Current, Part 1: Observations during a one-year time series. *J. Mar. Res.* 35(1):29-47.
- Maul, G.A. and F.M. Vukovich. 1993. The relationship between variations in the Gulf of Mexico Loop Current and Straits of Florida volume transport. *J. Phys. Oceanogr.* 23(5):785-796. doi: 10.1175/1520-0485(1993)023<0785:TRBVIT>2.0.CO;2.

- Maul, G.A. and K. Hanson. 1991. Interannual coherence between North Atlantic atmospheric surface pressure and composite southern U.S.A. sealevel. *Geophys. Res. Lett.* 18(4):653-656. doi: 10.1029/91GL00141.
- Maul, G.A., F. Williams, M. Roffer, and F.M. Sousa. 1984. Remotely sensed oceanographic patterns and variability of blue fin tuna catch in the Gulf of Mexico. *Oceanol. Acta.* 7(4):469-479.
- Maul, G.A., P.W. DeWitt, A. Yanaway, and S.R. Baig. 1978. Geostationary satellite observations of Gulf Stream meanders: Infrared measurements and time series analysis. *J. Geophys. Res.* 83(C12):6123-6135. doi: 10.1029/JC083iC12p06123.
- McWilliams, J.C. 2006. *Fundamentals of Geophysical Fluid Dynamics*. Cambridge, UK: Cambridge University Press. 249 pp.
- Meinen, C.S. and D.R. Watts. 2000. Vertical structure and transport on a transect across the North Atlantic Current near 42°N: Time series and mean. *J. Geophys. Res.* 105(C9):21869-21891. doi: 10.1029/2000JC900097.
- Mellor, G.L. and T. Yamada. 1982. Development of a turbulence closure model for geophysical fluid problems. *Rev. Geophys.* 20(4):851-875. doi: 10.1029/RG020i0040p00851.
- Merrifield, M.A. and C.D. Winant. 1989. Shelf circulation in the Gulf of California: A description of the variability. *J. Geophys. Res.* 94(C12):18133-18160.
- Mizuta, G. and N.G. Hogg. 2004. Structure of the circulation induced by a shoaling topographic wave. *J. Phys. Oceanogr.* 34(8):1793-1810.
doi: 10.1175/1520-0485(2004)034<1793:SOTCIB> 2.0.CO;2.
- Molinari, R.L., S. Baig, D.W. Behringer, G.A. Maul, and R. Legeckis. 1977. Winter intrusions of the Loop Current. *Science* 198:505-507. doi: 10.1126/science.198.4316.505.
- Mooers, C.N.K. 1975. Several effects of a baroclinic current on the cross-stream propagation of inertial-internal waves. *Geophys. Fluid Dyn.* 6:245-275.
- Moon, I.-J., I. Ginis, and T. Hara. 2008. Impact of the reduced drag coefficient on ocean wave modeling under hurricane conditions. *Mon. Weather Rev.* 136:1217-1223.
doi: 10.1175/2007MWR2131.1.
- Morey, S.L. and D.S. Dukhovskoy. 2013. A downscaling method for simulating deep current interactions with topography: Application to the Sigsbee Escarpment. *Ocean Modelling* 69:50-63. doi: 10.1016/j.ocemod.2013.05.008.
- Müller-Karger, F.E., J.J. Walsh, R.H. Evans, and M.B. Meyers. 1991. On the seasonal phytoplankton concentration and sea surface temperature cycles of the Gulf of Mexico as determined by satellites. *J. Geophys. Res.* 96(C7):12645-12665.

- Munk, W.H. and D.E. Cartwright. 1966. Tidal spectroscopy and prediction. *Phil. Trans. Roy. Soc. Lon., Series A, Mathemat. Phys. Sci.* 259(1105):533-581.
doi: 10.1098/rsta.1966.0024.
- Naeije, M., E. Schrama, and R. Scharroo. 2000. The radar altimeter database system project RADS. In: *Proceedings of the International Geoscience and Remote Sensing Symposium (IGARSS)*, vol. 2, 24-28 July 2000, Honolulu, HA. pp.487-490.
- Naeije, M., R. Scharroo, E. Doornbos, and E. Schrama. 2008. GLobal altimetry sea-level service: GLASS, final report, December 2008. NUSP-2 report GO 52320 DEO. NIVR/DEOS publ., Delft, NL. 107pp.
- NODC. 2005. World Ocean Atlas 2005 [Internet]. National Oceanographic Data Center, NOAA, Washington, DC. Available from: http://www.nodc.noaa.gov/OC5/WOA05/pr_woa05.html .
- Nof, D. 1981. On the beta-induced movement of isolated baroclinic eddies. *J. Phys. Oceanogr.* 11(12):1662-1672.
- Nof, D. 2005. The momentum imbalance paradox revisited. *J. Phys. Oceanogr.* 35(10):1928-1939. doi: 10.1175/JPO2772.1.
- Nowlin, W.D., Jr., A.E. Jochens, S.F. DiMarco, R.O. Reid, and M.K. Howard. 2001. Deepwater physical oceanography reanalysis and synthesis of historical data, synthesis report. U.S. Dept. of the Interior, Minerals Management Service, Gulf of Mexico OCS Region, New Orleans, LA. OCS Study MMS 2001-064. 530 pp.
- OBPG [Ocean Biology Processing Group] 2010. Oceancolor Validation: Processing flags and masks [Internet]. National Aeronautics and Space Administration (NASA). Available from: <http://oceancolor.gsfc.nasa.gov/VALIDATION/flags.html> .
- OBPG [Ocean Biology Processing Group] c2012. Oceancolor Web: Data Services [Internet]. National Aeronautics and Space Administration (NASA) [cited 2012 January]. Available from: <http://oceancolor.gsfc.nasa.gov/> .
- Oey, L.-Y. 1996. Simulation of mesoscale variability in the Gulf of Mexico: sensitivity studies, comparison with observations, and trapped wave propagation. *J. Phys. Oceanogr.* 26(2):145-175.
- Oey, L.-Y. 2008. Loop Current and deep eddies. *J. Phys. Oceanogr.* 38(7):1426-1449. doi: 10.1175/2007JPO3818.1.
- Oey, L.-Y. and H.-C. Lee. 2002. Deep eddy energy and topographic Rossby waves in the Gulf of Mexico. *J. Phys. Oceanogr.* 32(12):3499-3527.

- Oey, L.-Y., P. Hamilton, and H.-C. Lee. 2003a. Modeling and data analyses of circulation processes in the Gulf of Mexico, final report. U.S. Dept. of the Interior, Minerals Management Service, Gulf of Mexico OCS Region, New Orleans, LA. OCS Study MMS 2003-074. 129 pp.
- Oey, L.-Y., H.-C. Lee, and W.J. Schmitz, Jr. 2003b. Effects of winds and Caribbean eddies on the frequency of Loop Current eddy shedding: A numerical model study. *J. Geophys. Res.* 108(C10):3324. doi:10.1029/2002JC001698.
- Oey, L.-Y., T. Ezer, and G. Forristall, C. Cooper, S. DiMarco, and S. Fan. 2005. An exercise in forecasting Loop Current and eddy frontal positions in the Gulf of Mexico. *Geophys. Res. Lett.* 32:L12611. doi: 10.1029/2005GL023253.
- Oey, L.-Y., T. Ezer, and H.-C. Lee. 2005. Loop Current, rings and related circulation in the Gulf of Mexico: a review of numerical models and future challenges. In: Sturges, W. and A. Lugo-Fernández, eds. *Circulation in the Gulf of Mexico: Observations and models*, Geophysical Monograph 161. American Geophysical Union, Washington, DC. pp. 31-56.
- Oey, L.-Y., T. Ezer, and W. Sturges. 2004. Modeled and observed empirical orthogonal functions of currents in the Yucatan Channel, Gulf of Mexico. *J. Geophys. Res.* 109:C08011. doi: 10.1029/2004JC002345.
- O'Reilly, J.E. and 24 Coauthors. 2000. SeaWiFS postlaunch calibration and validation analyses, Part 3. In: Hooker, S.B. and E.R. Firestone, eds. *NASA Tech. Memo 2000-206892*. vol. 11. 49 pp. NASA Goddard Space Flight Center, Greenbelt, MD. pp. 9-23.
- Ott, R.L. and M. Longnecker. 2001. *An introduction to statistical methods and data analysis*. 5th ed. Pacific Grove, CA: Duxbury Press. 1152 pp.
- Park, J.-H., D.R. Watts, K.A. Donohue, and K.L. Tracey. 2012. Comparisons of sea surface height variability observed by pressure-recording inverted echo sounders and satellite altimetry in the Kuroshio Extension. *J. Oceanogr.* 68:401-416. doi: 10.1007/s10872-012-0108-x.
- Park, J.-H., K.A. Donohue, D.R. Watts, and L. Rainville. 2010. Distribution of deep near-inertial waves observed in the Kuroshio Extension. *J. Phys. Oceanogr.* 66(5):709-717. doi: 10.1007/S10872-010-0058-0.
- Parke, M.E., G. Born, R. Leben, C. McLaughlin, and C. Tierney. 1998. Altimeter sampling characteristics using a single satellite. *J. Geophys. Res.* 103(C5):10513-10526. doi: 10.1029/97JC02175.
- Parke, M.E., R.H. Stewart, D.L. Farless, and D.E. Cartwright. 1987. On the choice of orbits for an altimetric satellite to study ocean circulation and tides. *J. Geophys. Res.* 92(C11):11693-11707.

- Pedder, M.A. 1989. Limited area kinematic analysis by a multivariate statistical interpolation method. *Mon. Wea. Rev.* 117(8):1695-1709.
doi: 10.1175/1520-0493(1989)117<1695:LAKABA>2.0.CO;2.
- Pedder, M.A. 1993. Interpolation and filtering of spatial observations using successive corrections and Gaussian filters. *Mon. Weather Rev.* 121(10):2889-2902.
- Pichevin, T. and D. Nof. 1997. The momentum imbalance paradox. *Tellus* 49A(2):298-319.
doi:10.1034/j.1600-0870.1997.t01-1-00009.x.
- Powell, M.D., S.H. Houston, L.R. Amat, and N. Morisseau-Leroy. 1998. The HRD real-time hurricane wind analysis system. *J. Wind Eng. Ind. Aerodyn* 77 & 78:53-64.
- Preisendorfer, R.W. and C.D. Mobley. 1988. Principal component analysis in meteorology and oceanography. *Developments in Atmospheric Science, Vol. 17.* New York: Elsevier. 425 pp.
- Press, W.H., S.A. Teukolsky, W.T. Vetterling, and B.P. Flannery. 1992. *Numerical recipes in FORTRAN, the art of scientific computing.* 2nd ed. New York: Cambridge University Press. 963 pp.
- Press, W.H., S.A. Teukolsky, W.T. Vetterling, and B.P. Flannery. 2007. *Numerical recipes: The art of scientific computing.* 3rd ed. New York: Cambridge University Press. 1235 pp.
- Price, J.F. 1981. Upper ocean response to a hurricane. *J. Phys. Oceanogr.* 11(2):153-175.
- Ray, R.D. 1999. A global ocean tide model from TOPEX/POSEIDON altimetry:GOT99.2. NASA Tech. MEMO 1999-209478. NASA Goddard Space Flight Center, Greenbelt, MD. 58 pp.
- Reid, R.O. 1972. A simple dynamic model of the Loop Current. In: Capurro, L.R.A. and J.L. Reid, eds. *Contributions on the physical oceanography of the Gulf of Mexico, Texas A&M University Oceanographic Studies, Vol. 2.* Gulf Publishing Co., Houston, TX. pp. 157-159.
- Rhines, P.B. 1970. Edge-, bottom-, and Rossby waves in a rotating stratified fluid. *Geophys. Fluid Dyn.* 1(3-4):273-302. doi: 10.1080/03091927009365776.
- Rio, M.-H. and F. Hernandez. 2004. A mean dynamic topography computed over the world ocean from altimetry, in situ measurements, and a geoid model. *J. Geophys. Res.* 109(C12):C12032. doi: 10.1029/2003JC002226.
- Rio, M.-H. and G. Larnicol. 2010. The CNES/CLS mean dynamic topography. In: *Proceedings of the Ocean Surface Topography Science Team Meeting, October 2010, Lisbon, Portugal.*

- Rousset, C. and L.M. Beal. 2010. Observations of the Florida and Yucatan Currents from a Caribbean cruise ship. *J. Phys. Oceanogr.* 40(7):1575-1581.
doi: 10.1175/2010JPO4447.1.
- Sandwell, D.T. and D.C. McAdoo. 1988. Marine gravity of the southern ocean and Antarctic margin from Geosat. *J. Geophys. Res.* 93(B9):10389-10396.
doi: 10.1029/JB093iB09p10389.
- Saraceno, M., P.T. Strub, and P.M. Kosro. 2008. Estimates of sea surface height and near-surface alongshore coastal currents from combinations of altimeters and tide gauges. *J. Geophys. Res.* 113(C11):C11013. doi: 10.1029/2008JC004756.
- Schaeffer, P., Y. Faugère, J.F. Legeais, A. Ollivier, T. Guinle, and N. Picot. 2012. The CNES_CLS11 global mean sea surface computed from 16 years of satellite altimeter data. *Mar. Geodesy* 35(Suppl. 1):3-19.
- Schlax, M.G. and D.B. Chelton. 1994. Detecting aliased tidal errors in altimeter height measurements. *J. Geophys. Res.* 99(C6):12603-12612. doi: 10.1029/94JC00568.
- Schmitz, W.J., Jr. 2005. Cyclones and westward propagation in the shedding of anticyclonic rings from the Loop Current. In: Sturges, W. and A. Lugo-Fernández, eds. *Circulation in the Gulf of Mexico: Observations and models*, Geophysical Monograph 161. American Geophysical Union, Washington, DC. pp. 241-261.
- Schmitz, W.J., Jr., D.C. Biggs, A. Lugo-Fernández, L.-Y. Oey, and W. Sturges. 2005. A synopsis of the circulation in the Gulf of Mexico and on its continental margins. In: Sturges, W. and A. Lugo-Fernández, eds. *Circulation in the Gulf of Mexico: Observations and models*, Geophysical Monograph 161. American Geophysical Union, Washington, DC. pp. 11-29.
- Schnapf, A. 1981. TIROS-N-operational environmental satellite of the 80's. *J. Spacecraft and Rockets* 18(2):172-177. doi: 10.2514/3.57800.
- Science Applications International Corp. (SAIC). 1989. Gulf of Mexico physical oceanography program. Final report: Year 5. Volume II: Technical report. U.S. Dept. of the Interior, Minerals Management Service, Gulf of Mexico OCS Region, New Orleans, LA. OCS Study MMS 89-0068. 333 pp.
- Shay, L.K. and R.L. Elsberry. 1987. Near-inertial ocean current response to Hurricane "Frederic". *J. Phys. Oceanogr.* 17(8):1249-1269.
- Shay, L.K., P.G. Black, A.J. Mariano, J.D. Hawkins, and R.L. Elsberry. 1992. Upper ocean response to Hurricane Gilbert. *J. Geophys. Res.* 97(C12):20227-20248.

- Shchepetkin, A.F. and J.C. McWilliams. 2005. The Regional Oceanic Modeling System (ROMS): a split-explicit, free-surface, topography-following-coordinates ocean model. *Ocean Modelling* 9:347-404. doi: 10.1016/j.ocemod.2004.08.002.
- Smagorinsky, J. 1963. General circulation experiments with the primitive equations. *Mon. Weather Rev.* 91(3):99-164.
doi: 10.1175/1520-0493(1963)091<0099:GCEWTP>2.3.CO;2.
- Smith, W.H.F. and D.T. Sandwell. 1997. Global sea floor topography from satellite altimetry and ship depth soundings. *Science* 277(5334):1956-1962.
doi: 10.1126/science.277.5334.1956.
- Sturges, W. 1992. The spectrum of Loop Current variability from gappy data. *J. Phys. Oceanogr.* 22(11):1245-1256.
- Sturges, W. 1993. The annual cycle of the western boundary current in the Gulf of Mexico. *J. Geophys. Res.* 98(C10):18053-18068.
- Sturges, W. 1994. The frequency of ring separations from the Loop Current. *J. Phys. Oceanogr.* 24(7):1647-1651.
- Sturges, W. and A. Bozec. 2013. A puzzling disagreement between observations and numerical models in the central Gulf of Mexico. *J. Phys. Oceanogr.* 43(12):2673-2681. doi: 10.1175/JPO-D-13-081.1.
- Sturges, W. and J.C. Evans. 1983. On the variability of the Loop Current in the Gulf of Mexico. *J. Mar. Res.* 41(4):639-653.
- Sturges, W. and R. Leben. 2000. Frequency of ring separations from the Loop Current in the Gulf of Mexico: A revised estimate. *J. Phys. Oceanogr.* 30(7):1814-1819.
- Tai, C.-K. 2009. The temporal aliasing formulas for the tandem mission of Jason-1 and TOPEX/Poseidon. *J. Atmos. Oceanic Technol.* 26(2):352-367.
doi: 10.1175/2008JTECHO610.1.
- Torrence, C. and G.P. Compo. 1998. A practical guide to wavelet analysis. *Bull. Amer. Meteorol. Soc.* 79:61-78.
- Trenberth, K.E. 1984. Signal versus noise in the Southern Oscillation. *Mon. Weather Rev.* 112(2):326-332. doi: 10.1175/1520-0493(1984)112<0326:SVNITS>2.0.CO;2.
- Vukovich, F.M. 1986. Aspects of the behavior of cold perturbations in the eastern Gulf of Mexico: A case study. *J. Phys. Oceanogr.* 16(1):175-188.
- Vukovich, F.M. 1988. Loop Current boundary variations. *J. Geophys. Res.* 93(C12):15585-15591. doi: 10.1029/JC093iC12p15585.

- Vukovich, F.M. 2007. Climatology of ocean features in the Gulf of Mexico using satellite remote sensing data. *J. Phys. Oceanogr.* 37(3):689-707. doi: 10.1175/JPO2989.1.
- Vukovich, F.M. 2012. Changes in the Loop Current's Eddy Shedding in the Period 2001-2010. *Intl. J. Oceanogr.* 2012(Article ID 439042):1-18. doi: 10.1155/2012/439042.
- Vukovich, F.M. and B.W. Crissman. 1986. Aspects of warm rings in the Gulf of Mexico. *J. Geophys. Res.* 91(C2):2645-2660.
- Vukovich, F.M. and G.A. Maul. 1985. Cyclonic eddies in the eastern Gulf of Mexico. *J. Phys. Oceanogr.* 15(1):105-117.
- Vukovich, F.M., B.W. Crissman, M. Bushnell, and W.J. King. 1978. Sea-surface temperature variability analysis of potential OTEC sites utilizing satellite data, Final Report DOE Contract No. EG-77-C-05-0544. Res. Triangle Inst., Research Triangle Park, NC. 153 pp.
- Vukovich, F.M., B.W. Crissman, M. Bushnell, and W.J. King. 1979. Some aspects of the oceanography of the Gulf of Mexico using satellite and in-situ data. *J. Geophys. Res.* 84(C12):7749-7768. doi: 10.1029/JC084iC12p07749.
- Wade, T.L., S.T. Sweet, J.N. Walpert, J.L. Sericano, J.J. Singer, and N.L. Guinasso, Jr. 2011. Evaluation of possible inputs of oil from the Deepwater Horizon spill to the Loop Current and associated eddies in the Gulf of Mexico. In: Liu, Y., A. MacFadyen, Z.-G. Ji, and R.H. Weisberg, eds. *Monitoring and modeling the Deepwater Horizon oil spill: A record breaking enterprise*, Geophysical Monograph 195. American Geophysical Union, Washington, DC. pp. 83-90.
- Walker, N.D., C.T. Pilley, V.V. Raghunathan, E.J. D'Sa, R.R. Leben, N.G. Hoffmann, P.J. Brickley, P.D. Coholan, N. Sharma, H.C. Graber, and R.E. Turner. 2011. Impacts of Loop Current frontal cyclonic eddies and wind forcing on the 2010 Gulf of Mexico oil spill. In: Liu, Y., A. MacFadyen, Z.-G. Ji, and R.H. Weisberg, eds. *Monitoring and modeling the Deepwater Horizon oil spil: A record breaking enterprise*, Geophysical Monograph 195. American Geophysical Union, Washington, DC. pp. 103 -116.
- Walker, N., R. Leben, S. Anderson, J. Feeney, P. Coholan, and N. Sharma. 2009. Loop Current frontal eddies based on satellite remote sensing and drifter data. U.S.Dept. of the Interior, Minerals Management Service, Gulf of Mexico OCS Region, New Orleans, LA. OCS Study MMS 2009-023. 88pp.
- Walker, N., S. Myint, A. Babin, and A. Haag. 2003. Advances in satellite radiometry for the surveillance of surface temperatures, ocean eddies and upwelling processes in the Gulf of Mexico using GOES-8 during summer. *Geophys. Res. Lett.* 30(16):1854. doi:10.1029/2003GL017555.

- Wang, D.-P., L.-Y. Oey, T. Ezer, and P. Hamilton. 2003. Nearsurface currents in DeSoto Canyon (1997-1999): comparison of current meters, satellite observations, and model simulations. *J. Phys. Oceanogr.* 33(1):313-326.
- Watts, D.R., K.L. Tracey, and A.I. Friedlander. 1989. Producing accurate maps of the Gulf Stream thermal front using objective analysis. *J. Geophys. Res.* 94(C6):8040-8052.
- Watts, D.R., X. Qian, and K.L. Tracey. 2001. Mapping abyssal current and pressure fields under the meandering Gulf Stream. *J. Atmos. Oceanic Technol.* 18(6):1052-1067.
- Weisberg, R.H. 2011. Coastal ocean pollution, water quality and ecology: A commentary. *Mar. Technol. Soc. J.* 45(2):35-42.
- Welch, P.D. 1967. The use of fast Fourier transform for the estimation of power spectra: A method based on time averaging over short, modified periodograms. *IEEE Trans. Audio Electroacoustics* AU-15(2):70-73. doi: 10.1109/TAU.1967.1161901.
- Willmott, C.J. 1981. On the validation of models. *Phys. Geogr.* 2(2):184-194. doi: 10.1080/02723646.1981.10642213.
- Xu, F.-H., L.-Y. Oey, Y. Miyazawa, and P. Hamilton. 2013a. Hindcasts and forecasts of Loop Current and eddies in the Gulf of Mexico using local ensemble transform Kalman filter and optimum-interpolation assimilation schemes. *Ocean Modelling* 69:22-38. doi: 10.1016/j.ocemod.2013.05.002.(SCI).
- Xu, F.-H., Y.-L. Chang, L.-Y. Oey, and P. Hamilton. 2013b. Loop Current growth and eddy shedding using models and observations: Analyses of the July 2011 eddy-shedding event. *J. Phys. Oceanogr.* 43(5):1015-1027. doi: 10.1175/JPO-D-12-0138.1.
- Yin, X.-Q. and L.-Y. Oey. 2007. Bred-ensemble ocean forecast of Loop Current and rings. *Ocean Modelling* 17(4):300-326.
- Zhai, X., R.J. Greatbatch, and C. Eden. 2007. Spreading of near-inertial energy in a 1/12° model of the North Atlantic Ocean. *Geophys. Res. Lett.* 34(10):10609. doi: 10.1029/2007GL029895.
- Zhai, X., R.J. Greatbatch, and J. Sheng. 2004. Advective spreading of storm-induced inertial oscillations in a model of the northwest Atlantic Ocean. *Geophys. Res. Lett.* 31(14):L14315. doi: 10.1029/2004GL020084.
- Zhai, X., R.J. Greatbatch, and J. Sheng. 2005a. Doppler-shifted inertial oscillations on a β plane. *J. Phys. Oceanogr.* 35(8):1480-1488. doi: 10.1175/JPO2764.1.
- Zhai, X., R.J. Greatbatch, and J. Zhao. 2005b. Enhanced vertical propagation of storm-induced near-inertial energy in an eddying ocean channel model. *Geophys. Res. Lett.* 32(18):L18602. doi: 10.1029/2005GL023643.

APPENDIX: BAROTROPIC TIDES

Tidal response analysis (Munk and Cartwright, 1966) determined the amplitude and phase for eight major tidal constituents (O1, K1, Q1, P1, M2, K2, N2, S2) from the twenty-five recovered bottom pressure records (PIES 51 through 75) within the array (Figures A-1 and A-2, and Tables A-1 and A-2). Estimated phase and amplitude vary smoothly across the array as expected. Tidal amplitudes are generally small. The largest tidal amplitudes are near 13 cm for O1 and K1, near 5 cm for P1 and M2, and less than 5 cm for the remaining four constituents. Amplitudes have been converted to meters by dividing pressure by density times gravity, $\rho g = 1.02$.

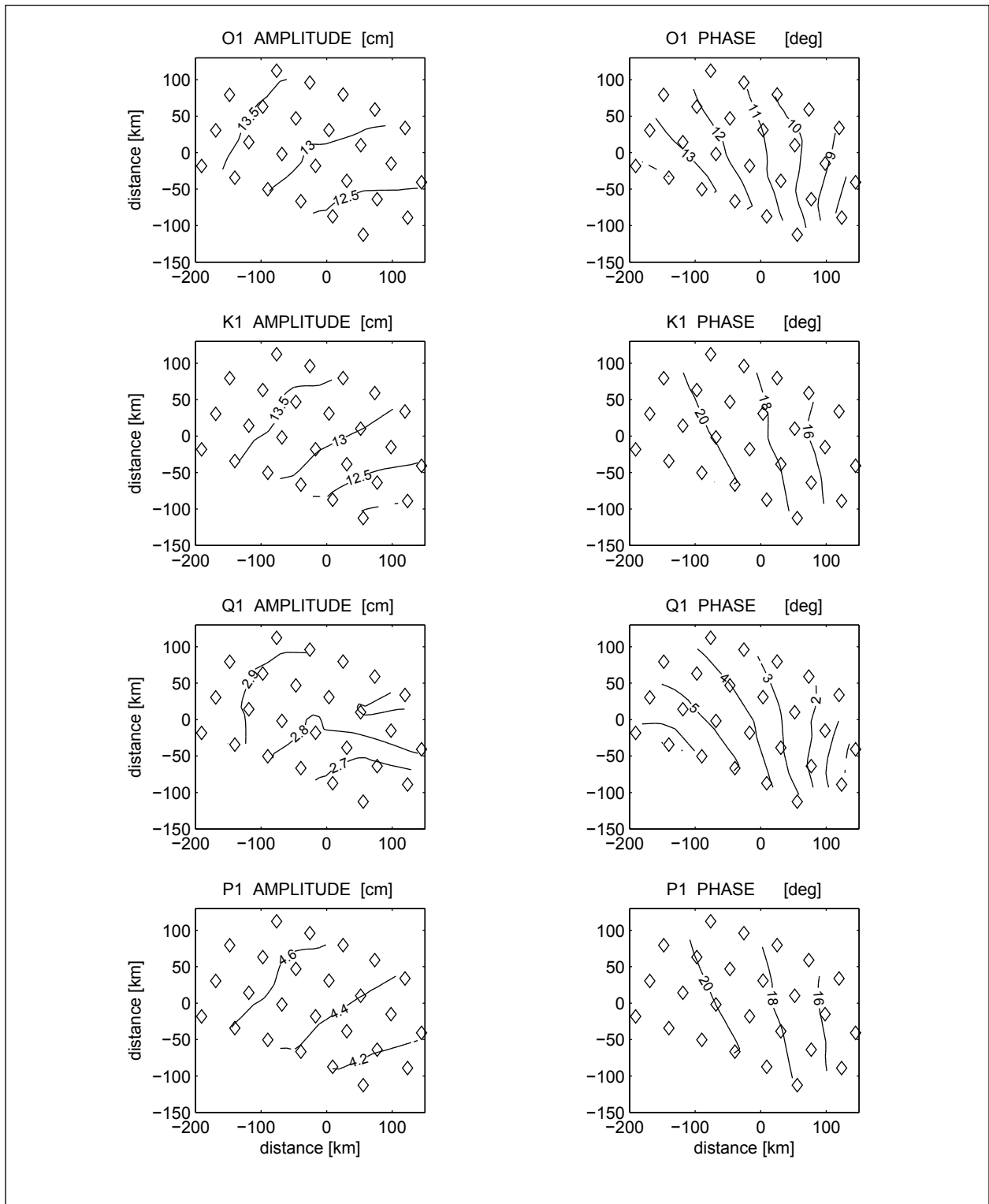


Figure A-1. Amplitude (left column) and phase (right column) of the O1, K1, Q1, and P1 constituents determined with the tidal response method (Munk and Cartwright, 1966) from the 25 bottom pressure records. PIES locations denoted by open diamonds.

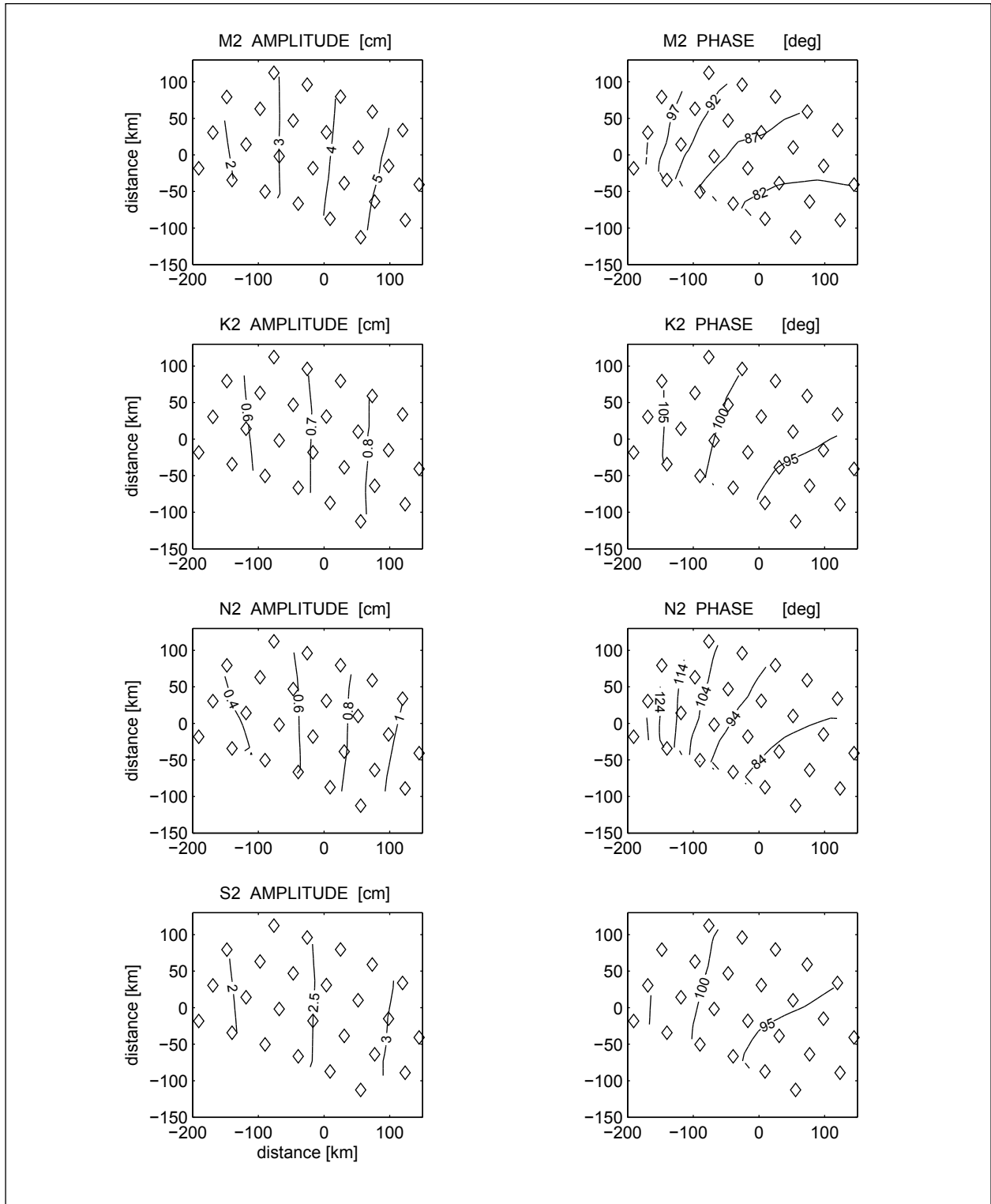


Figure A-2. Amplitude (left column) and phase (right column) of the M2, K2, N2, and S2 constituents determined with the tidal response method (Munk and Cartwright, 1966) from the 25 bottom pressure records. PIES locations denoted by open diamonds.

Table A-1. Amplitude in CM and Phase in Degrees for Four Major Tidal Constituents (O1, K1, Q1, P1)

Determined with the Tidal Response Method of Munk and Cartwright (1966)

Site	O1		K1		Q1		P1	
	Amplitude (cm)	Phase (degrees)	Amplitude (cm)	Phase (degrees)	Amplitude (cm)	Phase (degrees)	Amplitude (cm)	Phase (degrees)
P51	13.65	12.54	13.90	20.43	2.93	4.64	4.73	20.55
P52	13.69	13.27	13.87	21.20	2.94	5.28	4.72	21.32
P53	13.69	14.16	13.86	22.05	2.95	6.24	4.72	22.18
P54	13.59	11.59	13.84	19.32	2.93	3.65	4.71	19.48
P55	13.47	12.05	13.70	19.87	2.89	4.40	4.66	19.96
P56	13.42	12.83	13.64	20.59	2.89	5.25	4.64	20.69
P57	13.37	14.04	13.54	21.36	2.95	6.60	4.59	21.55
P58	13.43	11.04	13.67	18.49	2.91	3.37	4.65	18.66
P59	13.14	11.70	13.36	19.31	2.83	4.02	4.54	19.44
P60	13.19	12.24	13.40	19.88	2.84	4.78	4.56	19.98
P61	13.01	13.47	13.18	21.24	2.80	5.93	4.48	21.33
P62	13.27	9.88	13.48	17.12	2.87	2.42	4.58	17.28
P63	13.08	10.99	13.26	18.30	2.83	3.50	4.51	18.45
P64	12.88	11.50	13.04	19.01	2.78	4.24	4.43	19.11
P65	12.76	12.56	12.88	20.14	2.75	5.18	4.38	20.24
P66	13.09	9.56	13.22	16.32	2.84	2.16	4.50	16.54
P67	12.92	10.24	13.01	16.52	2.91	2.51	4.40	16.94
P68	12.61	10.58	12.69	17.96	2.72	3.10	4.32	18.10
P69	12.41	11.64	12.42	19.03	2.68	4.21	4.23	19.16
P70	12.98	8.92	12.92	14.69	2.93	1.47	4.37	15.13
P71	12.77	9.17	12.73	15.37	2.86	1.54	4.31	15.78
P72	12.41	9.34	12.36	16.59	2.68	1.81	4.21	16.76
P73	11.96	10.63	11.87	17.65	2.59	3.23	4.05	17.84
P74	12.58	7.48	12.47	14.10	2.83	359.56	4.23	14.51
P75	12.10	7.64	12.01	14.94	2.61	0.12	4.10	15.10

Table A-2. Amplitude in CM and Phase in Degrees for Four Major Tidal Constituents (M2, K2, N2, S2)

Determined with the Tidal Response Method of Munk and Cartwright (1966)

Site	M2		K2		N2		S2	
	Amplitude (cm)	Phase (degrees)	Amplitude (cm)	Phase (degrees)	Amplitude (cm)	Phase (degrees)	Amplitude (cm)	Phase (degrees)
P51	2.10	99.88	0.57	105.20	0.41	122.09	1.99	103.83
P52	1.75	102.13	0.55	106.97	0.36	131.90	1.88	105.44
P53	1.37	106.66	0.52	108.59	0.31	146.62	1.77	106.94
P54	2.91	94.04	0.64	101.66	0.54	106.23	2.26	100.45
P55	2.66	93.71	0.62	102.34	0.49	108.00	2.18	101.01
P56	2.33	93.53	0.60	102.99	0.42	111.75	2.07	101.53
P57	1.97	93.52	0.57	104.42	0.34	118.45	1.97	102.79
P58	3.49	90.98	0.70	100.01	0.64	98.19	2.47	98.89
P59	3.23	89.13	0.67	99.76	0.58	97.83	2.36	98.47
P60	3.01	88.06	0.65	99.96	0.53	97.26	2.29	98.60
P61	2.66	86.44	0.62	100.56	0.44	97.26	2.17	99.05
P62	4.09	88.49	0.75	97.64	0.76	92.98	2.67	96.61
P63	3.86	87.25	0.72	98.05	0.70	91.53	2.57	96.91
P64	3.67	84.43	0.70	97.22	0.65	89.10	2.50	95.92
P65	3.41	82.33	0.68	96.96	0.59	86.71	2.41	95.58
P66	4.67	86.92	0.80	96.77	0.87	88.80	2.88	95.80
P67	4.55	85.20	0.78	96.82	0.85	86.39	2.80	95.75
P68	4.32	82.10	0.76	94.87	0.79	82.29	2.70	93.78
P69	4.15	79.86	0.73	94.30	0.74	79.29	2.62	93.11
P70	5.23	86.17	0.85	96.02	1.00	86.60	3.05	95.12
P71	5.16	83.15	0.84	94.62	0.97	81.83	3.01	93.71
P72	5.07	80.21	0.82	93.01	0.94	78.02	2.94	92.03
P73	4.88	77.68	0.79	91.95	0.90	73.78	2.84	90.96
P74	5.77	82.12	0.89	93.04	1.12	79.53	3.19	92.26
P75	5.76	78.03	0.88	90.65	1.09	74.19	3.16	89.78



The Department of the Interior Mission

As the Nation's principal conservation agency, the Department of the Interior has responsibility for most of our nationally owned public lands and natural resources. This includes fostering the sound use of our land and water resources; protecting our fish, wildlife, and biological diversity; preserving the environmental and cultural values of our national parks and historical places; and providing for the enjoyment of life through outdoor recreation. The Department assesses our energy and mineral resources and works to ensure that their development is in the best interests of all our people by encouraging stewardship and citizen participation in their care. The Department also has a major responsibility for American Indian reservation communities and for people who live in island communities.

The Bureau of Ocean Energy Management Mission

The Bureau of Ocean Energy Management (BOEM) works to manage the exploration and development of the nation's offshore resources in a way that appropriately balances economic development, energy independence, and environmental protection through oil and gas leases, renewable energy development and environmental reviews and studies.